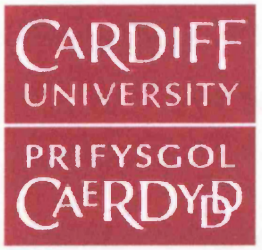

3D GEOMETRY AND KINEMATICS OF NON-COLINEAR FAULT INTERSECTIONS

MÀIRI A. NELSON

Submitted in partial fulfilment of the requirements for the degree of Ph.D.

Cardiff University

November 2006

ProQuest LLC
789 East Eisenhower Parkway
P.O. Box 1346
Ann Arbor, MI 48106-1346

DECLARATION

This work has not previously been accepted in substance for any degree and is not concurrently submitted in candidature for any degree.

Signed ..... (candidate)
Date 27th November 2006

STATEMENT 1

This thesis is the result of my own independent work/investigation, except where otherwise stated. Other sources are acknowledged by explicit references.

Signed ..... (candidate)
Date 27th November 2006

STATEMENT 2

I hereby give consent for my thesis, if accepted, to be available for photocopying and for inter-library loan, and for the title and summary to be made available to outside organisations.

Signed ..... (candidate)
Date 27th November 2006

SUMMARY

Extensional fault arrays at all scales and from different settings, commonly consist of fault sets with different strikes, either due to basement influence, or because of local stress perturbations. These non-colinear fault arrays are characterised by different types of high-angled fault intersections. Significant research has been undertaken into the process and product of colinear fault propagation and linkage in three dimensions, but there is little understanding of the kinematics of multidirectional fault array evolution.

Detailed interpretation of the 3D geometry and displacement distributions of intersecting faults has been carried out in four case-study areas in order to further the understanding of kinematic interaction of non-colinear faults. These studies are: a polygonal fault system from the Vøring Basin; cross-cutting faults from the Gulf of Mexico; extensional faults at the tip of a strike-slip fault in the Levant Basin and intersections between grabens trends in Canyonlands National Park, Utah. Intersections display a range of geometries that have been classified into five groups. An intersection may vary between classes within the vertical section. It is not possible to determine the evolutionary style of an intersection by geometry alone but detailed analysis of displacement distributions can reveal the growth histories of the intersecting faults.

Faults that meet at high-angled intersections are interpreted to interact kinematically, and show two distinct evolutionary styles: accidental and branching intersections. Accidental intersections form where the intersecting fault propagates toward the main fault plane and relationships that fit this style are defined as abutment, soft and hard linkage and cross-cutting. Evolutionary sequences from abutment to hard linkage, soft to hard linkage and abutment to cross-cutting are identified. Branching intersections form where the intersecting fault propagates away from the main fault plane. A new method for network evolution, termed lateral bifurcation, is proposed for this style of intersection.

AKNOWLEDGEMENTS

A number of people deserve a special mention for the help and support that they have provided during my time in Cardiff. Firstly, I am extremely grateful to my supervisor, Joe Cartwright, who gave me the opportunity to pursue this research and whose patience and advice throughout the work was invaluable.

Thanks are due to the BG-Group, Norsk Hydro and Western Geco for data contribution. The Geological Society Elspeth Matthews Fund is thanked for providing external funding for my field research. Financial support from the Sir Frank Dixie scholarship is also gratefully acknowledged. I am grateful to the managers of the 3DLab, Neil Ferguson and Gwen Pettigrew, for technical support and for sorting out many computer problems.

I have benefited greatly from the friendship and support of the members of the 3DLab and the department, past and present, including Mads, Dorthe, Andy R., Mike, Andy H., Richard, Valente, Cat, Päivi, Rob, Mostyn, Simon H. Rich L., Vicky, and particularly my office mates Claudia and Thomas who were always available for a chat. Special thanks go to Dorthe Hansen and Catherine Baudon for their enthusiasm in the field and for numerous thought-provoking technical discussions from which this work has greatly benefited. I am especially grateful to Päivi Heiniö for making it possible for me to submit this work remotely.

Beyond the department, I would like to thank all the friends who have persuaded me into mountain biking, climbing, running and more during my time in Cardiff. Special thanks go to Gwyn and Claire for recent contact that has kept me cheery. I would like to thank Helen for understanding and, of course, Dr. M. Nelson (#1) for fun times beyond the PhD. I have received a lot of support during my time in Cairo. I greatly appreciate the understanding of my boss, Ashley Price, and I thank my housemate, Paul, for his help with reviewing my work and for always providing me with a hot dinner.

For immeasurable encouragement and support, I thank all my family. My mum and dad could not have been more patient, nor given more support to help me through this. Finally, I am deeply grateful to Tim for his limitless positive nature, for practical and for emotional support throughout.

CONTENTS

LIST OF FIGURES

CHAPTER 1: INTRODUCTION

CHAPTER 2: GJALLAR RIDGE POLYGONAL FAULT SYSTEM, VØRING BASIN

CHAPTER 3: CROSS-CUTTING FAULTS, GULF OF MEXICO

CHAPTER 4: STRIKE-SLIP FAULT TIP, LEVANT BASIN

CHAPTER 5: GRABENS FAULT ARRAY, CANYONLANDS NATIONAL PARK

CHAPTER 6: DISCUSSION

APPENDIX A

APPENDIX B

LIST OF TABLES

CHAPTER 1: INTRODUCTION

1.1 RATIONALE

Non-colinear fault networks are characterised by fault sets that have variable strike directions. They are a common feature in extensional fault arrays from different basinal settings (e.g. Maerten et al., 2002; Needham et al., 1996). The strike variability is often explained by invoking multiple tectonic episodes, requiring a change in the regional stress field (e.g. Faerseth et al., 1997). However, multiple fault sets can also develop contemporaneously, and this can be explained by local perturbations of the stress field (e.g. Maerten, et al., 2002), reactivation of basement trends (e.g. Younes and McClay, 2002) or evolution of fault networks under 3D strain (e.g. Reches, 1983; Krantz, 1988). Despite their ubiquity, there has been no systematic study of the 3D geometry or kinematics of interacting faults in non-colinear fault systems.

The kinematics of fault interaction during growth of colinear, extensional fault arrays has been the subject of numerous studies (Peacock and Sanderson, 1991; Walsh and Watterson, 1991; Trudgill and Cartwright, 1994; Dawers and Schlische, 1995). These studies have wide implications for different fault growth models (Cartwright et al., 1995). Important differences exist between fault interactions in colinear versus non-colinear fault systems. Most notably, multi-directional arrays are characterised by high-angled fault intersections. In order to understand the fault interactions in contemporaneous non-colinear arrays, it is important to understand the 3D geometry of intersecting faults and the methods of evolution of these intersections.

This chapter summarises the significance of the research project and provides a list of aims for the thesis. The key methods used in this study are described and the thesis layout is defined.

1.2 BACKGROUND AND SCOPE

Fundamental advances in the understanding of normal fault geometries and evolution have been made over the past 20 years. The subject of fault growth and interaction from colinear

fault arrays has received considerable attention. These studies have hinged around development of the technique and associated understanding of displacement analysis (Muraoka and Kumata, 1983; Walsh and Watterson, Rippon, 1985; Watterson, 1986; Barnett et al., 1987; Walsh and Watterson, 1988). Displacement distributions provide insight into the propagation history of a normal fault.

The conceptual framework for fault propagation and growth was based on analysis of isolated normal faults that did not intersect a free surface or another fault (Rippon, 1985; Watterson, 1986; Barnett et al., 1987; Walsh and Watterson, 1987, 1988). These faults were found to display characteristic displacement distributions that ideally have a central maximum that decreases to a broadly elliptical tip line of zero displacement value. From these observations, a model of radial fault propagation for an isolated fault was proposed (e.g. Barnett et al., 1987). It was argued that regions of maximum fault displacement correspond to the sites of most slip events, and therefore to the location of nucleation of the fault.

Different models proposed a scale invariant growth for faults suggesting a constant slip-to-length ratio (Walsh and Watterson, 1988; Cowie and Scholz, 1992; Dawers et al., 1993; Schlische et al., 1996) within a particular setting. The model of growth by radial propagation proposed for an ideal isolated normal fault assumes that the same ellipsoidal shape is maintained throughout growth, that the rock volume is a homogneous elastic material, that the whole surface slips in every slip event and that there is a constant rate of growth. However, displacement distributions were found to vary from idealised examples due to variations in elastic properties along a fault (Burgmann et al., 1994), interaction with a mechanical barrier such as a major lithological boundary (Wilkins and Gross, 2002) and, more importantly, in proximity to another fault (Nicol et al., 1996).

In a colinear fault array, where parallel fault segment tips overlap with one another, both faults were found to display asymmetric displacement distributions (Peacock and Sanderson, 1991; 1994; Childs et al., 1995). The displacement gradient steepens in the overlap region and the position of maximum displacement moves toward the overlapping fault tips (Willemse, et al., 1996; Peacock and Sanderson, 1996), provided that the segments are in close enough proximity to allow their respective elastic strain fields to interact during growth. Fault interaction, as described above, is termed soft linkage (Walsh and Watterson, 1991). When interacting fault planes become contiguous with one another, they are defined as hard linked.

Further, entire fault arrays were found to have kinematic coherence when the sum of the individual D-L profiles of the constituent faults were found to demonstrate the displacement profile of an idealised isolated fault (Walsh and Watterson, 1991).

Quantification of displacement distributions to further the understanding of the modes of fault growth, interaction and linkage has yet to be applied to faults from multi-directional arrays.

1.2.1 Non-colinear fault studies

Fault networks with plan view traces that have more than one strike orientation are prevalent in a number of tectonic settings. Structural maps from faulted petroleum reservoirs almost invariably show faults of different orientations that form high-angled intersections e.g. Gullfaks field, N. Sea (Fossen and Rornes, 1996); Oseberg field, northern N. Sea (Maerten et al., 2002); Gulf of Mexico (Needham et al., 1996); Timor Sea (Gartrell et al., 2002) and the Reconcavo Rift, Brazil (Destro, 2003).

Explanations for the occurrence of intersecting faults and mutli-directional fault systems include poly-phase faulting (e.g. Donath, 1962); faulting in a 3D strain field (e.g. Reches, 1983), control of basement lineaments (e.g. Younes and McClay, 2002) or simultaneous development of faults in a locally perturbed stress field (Maerten et al., 2002). The types of fault systems within which contemporaneous intersecting faults occur range from extensional rift systems e.g. Gulf of Suez, North Sea (Patton et al., 1994, Hesthammer and Fossen, 2001); horsetail faults at the termination of strike-slip faults (e.g. Segall and Pollard, 1980); polygonal fault systems (e.g. Cartwright, 1996); crestal collapse structures (e.g. Suppe, 1985); domal salt and salt withdrawal structures (Rowan et al., 1998); release faults (e.g. Destro, 2004; Stewart, 2001) and cross-cutting faults (Dickinson, 1954) amongst others. Despite the ubiquity of non-colinear fault intersections, the nature of their evolution is poorly understood.

Previous work has included a geometric classification of fault intersections (Fossen et al., 2005; Bruhn et al., 1990). These fault intersections have been found to be sites of increased dilation and deformation. They have also been reported as focused pathways of fluid flow (Gartrell et al., 2002) and locations of localised ore (Newhouse, 1942; Park and MacDiarmid, 1970).

Interactions of non-colinear mode I fractures have received attention in the ceramics and fracture mechanics literature (e.g. Tuckwell, 2003; Bourne and Willemse, Oeschner et al., 1996). Nieto-Samantiaego and Alaniz-Alvarez (1997) draw attention to problems caused by slip vector orientation in multiple set fault patterns and use this to illustrate problems arising from using inversion methods to obtain the regional stress tensor. The dynamic interaction of strike-slip faults has been investigated and intersections have been found to be the sites of high strain accumulation (e.g. Talwani, 1999).

Maerten (2000) and Maerten et al., (1999, 2002) have progressed the topic of normal fault intersection by comparison of the dip-slip distribution of faults in mechanical models of non-colinear intersections to natural examples from industry reflections surveys and to analogue sandbox models. A predictable response is obtained from the main fault and it is argued that there is a mechanical interaction between the intersecting faults. This mechanical interaction is largely attributed to the elastic deformation that modifies the local shear stress acting on one fault as induced by slip on another.

In this work, attention is focused on the growth of intersecting faults and their evolution through interaction and intersection, by analysis of detailed observations of slip distributions. This approach will attempt to address outstanding questions pertaining to the kinematics of fault interaction in non-colinear fault arrays.

Four case studies areas were chosen to investigate fault interaction in non-colinear arrays: a polygonal fault system from the Vøring Basin, northern North Sea; cross-cutting faults above domal structures in the Gulf of Mexico; a horsetail structure at a strike-slip fault termination in the Levant basin and intersecting grabens trends in the Canyonlands National Park, Utah. The highly interconnected geometry of the polygonal fault system from the Voring basin offered the opportunity to classify intersection geometries and to investigate whether the geometry of an intersection is related to its style of evolution. The Gulf of Mexico dataset offered the potential to understand how faults can evolve to become cross-cutting – a question that is not addressed in the current literature. The strike-slip fault structure in the Levant dataset was a unique example of a well-imaged tip structure that could be investigated in three dimensions due to the very high quality of the dataset. This dataset provided not only the opportunity to investigate evolution of the faults in the system through displacement analyses, but also a chance to study the architecture of a strike-slip fault and to relate this to its

evolution. Finally, the Canyonlands Grabens case study was chosen for the ability to gain detailed displacement measurements in the field due to excellent exposure of fault scarps and for the capacity to describe sub-seismic scale structures that are related to non-colinear fault intersections.

1.3 AIMS OF THESIS

The main purpose of this research is to characterise the 3D geometries and kinematics of types of non-colinear fault intersections. This overall aim is tackled by systematically addressing a number of key aims within four case study areas. These key aims are to:

- Define a classification of intersection geometry.
- Investigate the relationship between intersection geometry and intersection evolution.
- Describe geometries of fault intersections in 3D.
- Devise criteria to differentiate between key types of intersection.
- Determine the kinematics of fault propagation in multi-directional systems.
- Define evolution styles in non-colinear fault arrays.
- Investigate whether non-colinear faults can be kinematically coherent.
- Develop a methodology for analysis of 3D fault intersections.
- Investigate branch line evolution.
- Explore sub-seismic response to fault intersection.

1.4 METHODOLOGY AND LIMITATIONS

The results provided in this thesis were obtained through analysis of three 3D seismic datasets and from one field study. The methodology used for analysis of the investigated faults is outlined in this section, with particular focus on the methods generally applicable to all the 3D seismic studies (Chapters 2 – 4). Within each of the subsequent chapters, further details of procedures used that are specific to each case study will be described. The seismic data were interpreted on a UNIX workstation running Schlumberger GeoFrame 3.7 software.

1.4.1 Fault Interpretation on 3D seismic

The high resolution 3D seismic datasets used in this study permitted interpretation of faults with relative ease. Faults were identified on seismic profiles from dim zones that cross-cut the stratigraphic reflections at high angles, and systematically offset these reflections. Actual fault

planes were not imaged by the datasets as the seismic reflection method is not suited to image near-vertical features (Badley, 1985).

The best definition of plan view traces of fault networks was provided by horizontal slicing of a coherence volume. This provided superior images to time-structure horizons and permitted rapid analysis of intersection geometries and their variations within the vertical depth section. A coherence cube was created for each of the 3D seismic datasets used in this study. The coherence cube is the result of processing seismic data for imaging discontinuities i.e. faults and channels. Calculation of localised waveform similarity in both in-line and cross-line directions produces interpretable changes in both directions (Bahorich and Farmer, 1995; Chopra, 2002). A short study confirmed the optimal vertical analysis window to be between 40ms and 100ms for each of the datasets. In general, a spatial analysis window of five traces provided maximum lateral resolution.

Mapping of seismic reflections provided the most accurate fault network geometries, as defined at a particular stratigraphic time, by eliminating uncertainty incurred by comparison across surveys that have a significant element of stratigraphic dip. This had the added benefit of providing a method of rapid visual analysis of displacement variations (particularly when viewed in 3D). Mapped horizons were chosen with the primary aim of delineating the plan view fault geometry, rather than as important stratigraphic markers. Consequently, mapped reflections were chosen for their regional continuity and high amplitudes, thus minimising interpretation problems.

Where regional stratigraphic dip was thought to be a limiting factor to interpretation of coherence slices, but time available for interpretation was restricted, isoproportional slices (Zeng et al., 1998) were created. This involved portioning of the vertical dataset between two bounding regional horizons, as defined by the interpreters input. The output slices were created by weighting the influence of the structural variation of the bounding regional horizons with proximity to each horizon. Slicing the volume in this way adheres more carefully to stratigraphic dip in comparison to horizontal slicing.

Finally, coherence extractions were created on mapped horizons and isoproportional slices to enhance fault definition and to provide a basemap where working with complex plan view geometries. The lateral resolution of the 3D seismic data is an important limiting factor to

definition of intersection locations and geometries. Details of seismic resolution, phase and general quality are presented in subsequent case studies (Chapters 2 – 4).

1.4.2 Fault throw measurement on 3D seismic

Throw measurements were taken as a proxy for displacement which was deemed to be a valid methodology because faults were dominantly planar. A simple approach to measurement of fault throw from 3D seismic profile lines was developed. Seismic cross-sectional lines were taken perpendicular to fault traces on mapped horizons (Section 1.4.1), in order to measure throw in the true dip direction. This assumes that faults are predominantly dip-slip in the absence of further information.

The x, y and z co-ordinates of both the footwall and hangingwall intersections of the horizon of interest with the studied fault were noted from the seismic display. Throw value was gained from subtraction of the footwall depth from the hangingwall depth (ms, TWT) (Fig. 1.1). The x and y co-ordinates permitted reconstruction of the precise measurement locations in 3D space, using plotting software such as Origin 7.4, and this was extremely useful for accurate location of intersection branch lines. Throw values are given in ms (TWT) throughout this thesis but a seismic Pwave velocity is provided in each case study (Chapters 2 – 4) to allow conversion to depth (m). There will be variations in seismic Pwave velocity throughout the vertical section and this will therefore induce errors to specific values. These errors are not thought to be significant, and particularly unlikely to greatly affect throw profile trends which are interpreted in this thesis. Further errors in measurement will have been incurred during the measurement phase with relation to the accuracy of the cursor location. These combined errors are quantified at ±2ms in each example.

The value of offset that could be measured is limited by the sample rate of the data, and was equal to 4ms for the 3D seismic datasets used in these case studies. Throw values that approach this limit are therefore made with less confidence. The error on throw measurements increases in areas directly adjacent to fault intersections. Seismic resolution decreases when two faults approach and it can be difficult to resolve two separate fault throw measurements (Fig. 1.2). Intersecting faults that have synthetic dip directions in cross-section will cause greater throw values to be measured from the intersection location (Fig. 1.2a), while antithetic faults will result in reduced throw values (Fig 1.2b). Examples where either of these has occurred are easily identifiable and can be removed from throw analysis.

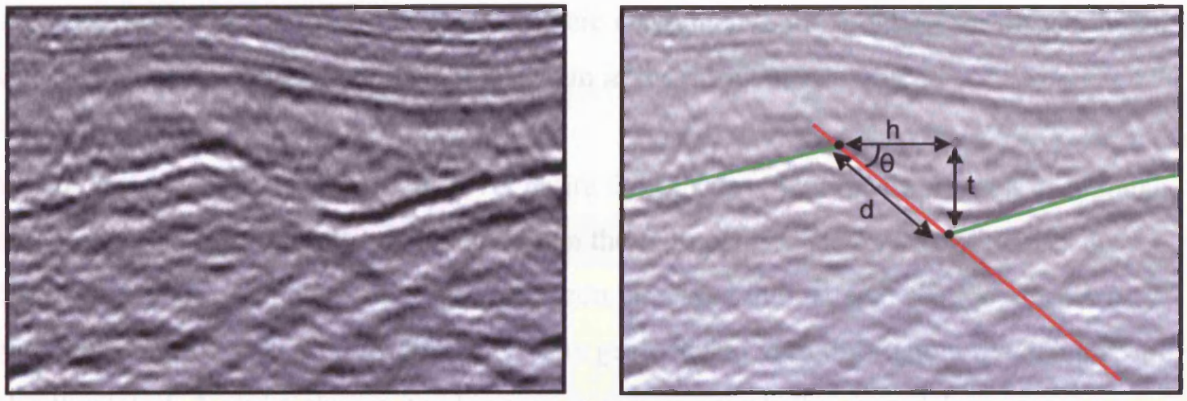

Figure. 1.1. Methodology of throw measurement from seismic data. (a) Seismic section showing an offset horizon. (b) interpreted seismic section showing the vertical (throw, t) and horizontal (heave, h) components of displacement (d). The x, y and z co-ordinates of the footwall and hangingwall intersections of the horizon of interest with the fault plane (black dots) are noted. Throw is calculated by subtracting the footwall depth value from the hangingwall depth value. Heave is calculated from the distance between the x, y co-ordinates. These variables permit the calculation of dip and displacement using trigonometry.

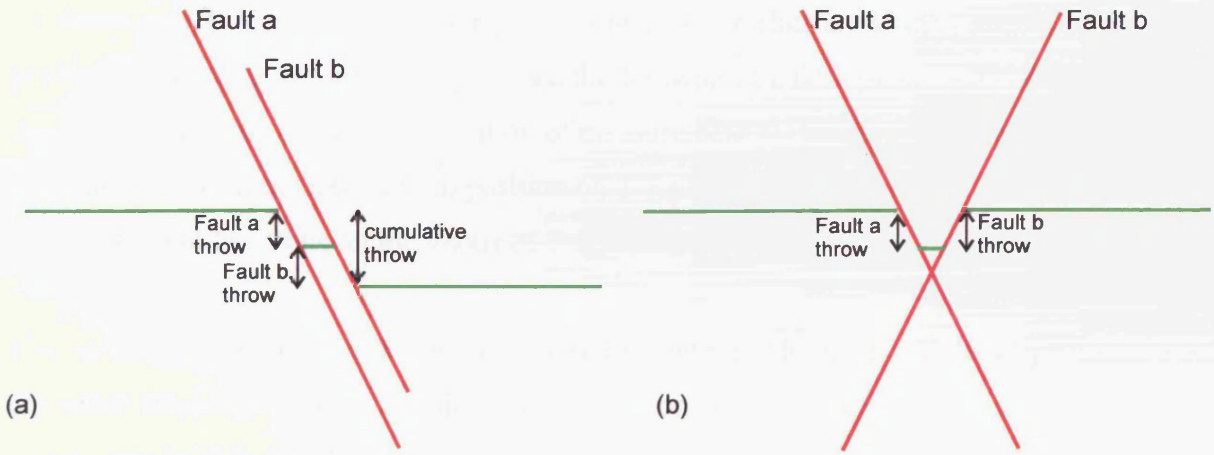

Figure 1.2. Schematic diagram of the limitation caused by two faults that distribute horizon offset between them. This offset cannot be resolved on the seismic data in the area that is proximal to the intersection of the faults. (a) two synthetic faults approach one another and the limit of resolution. The throw measurement taken is the addition of Fault a throw and Fault b throw. (b) Two antithetic faults approach one another and the limit of resolution. The throw measurement is reduced to zero as Fault b throw is subtracted from Fault a throw.

Further limitations to the throw measurement technique were encountered where short wavelength fold structures were identified on seismic profile lines adjacent to faults. These were interpreted as fault drag structures. Where encountered, the criterion for measurement was to include this ductile component of strain in the throw measurement.

Where measurements were collated over entire fault planes (Section 1.4.3), cross-sectional profile lines were commonly chosen based on the fault plane trace on a key horizon. As distance from this mapped stratigraphic horizon increased in the depth section, uncertainty with respect to the potential for the fault plane geometry to vary throughout the depth section also increased. A strike change would result in measurements that were taken on non-perpendicular lines. Additionally, in complex structural settings, it may be difficult to ascertain from cross-sections alone, that the same fault is being sampled. To reduce these errors, sampled faults were commonly mapped in three-dimensions in order to best define their 3D geometry.

1.4.3 Fault display and limitations

The throw data are displayed as throw variation with length (T-x) plots, throw variation with depth (T-z) plots and throw distribution on vertical fault plane projections, that are contoured for throw values. Vertical fault plane projections and T-x plots are always displayed from a position in the hangingwall looking toward the footwall of a fault plane that is dipping out of the page, toward the reader. The location of measurement points are plotted with relation to their distance from the intersection position on T-x plots. Measured values are plotted as midpoint depth locations on the y-axis of T-z plots.

The vertical fault plane projections were initially contoured by hand and then by Surfer 7.0 computer mapping software in order to assess any contouring errors. The gridding method chosen was kriging which generates an interpolated grid by estimating values of points at grid nodes over the whole graph using a distance-weighted function from real data points. The computer-contoured plots closely resembled the hand-contoured plots adding confidence to the original interpretation.

A limitation of the technique of plotting data on vertical fault plane projections is that the true 3D geometry of the fault plane is not represented. True positioning of measurement locations in 3D space that could be contoured for throw value was not possible with any software

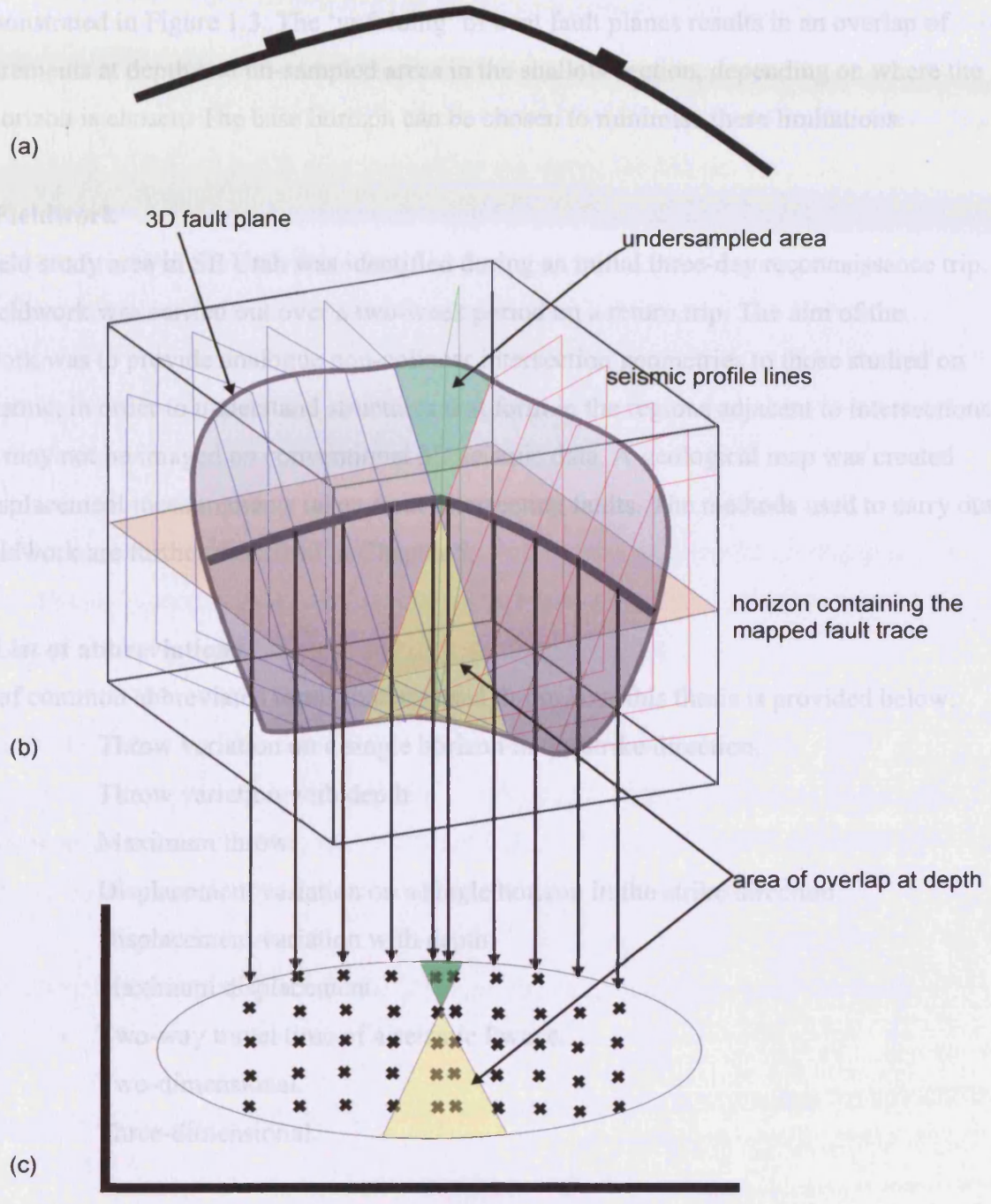

Figure 1.3. Example of limitations of the vertical projection method for displaying throw data. (a) The plan view fault trace displays a significant strike change. This mapped plan view geometry is used as a basemap for profile lines taken perpendicular to the fault trace. (b) 3D geometry of the fault plane. Profile lines are taken perpendicular to the mapped plan view trace in (a), therefore they vary in orientation along the length of the structure (red, green and blue lines). Profile lines overlap at depth, therefore the same area of the fault plane is sampled more than once (yellow shading). The shallow section in the area of the fault bend is characterised by undersampling (green shading). (c) The bent fault is 'unfolded' to plot on a 2D vertical fault plane projection. Throw values are displayed across the entire fault plane (x locations). The shaded areas represent the areas of duplicate sampling (yellow) and undersampling (green).

available for this study. Any strike variations of the fault planes therefore incurred errors on the vertical projection. An extreme example of the limitations associated with this technique is demonstrated in Figure 1.3. The 'unfolding' of bent fault planes results in an overlap of measurements at depth and un-sampled areas in the shallow section, depending on where the base horizon is chosen. The base horizon can be chosen to minimise these limitations.

1.4.4 Fieldwork

The field study area in SE Utah was identified during an initial three-day reconnaissance trip. The fieldwork was carried out over a two-week period on a return trip. The aim of the fieldwork was to provide analogue non-colinear intersection geometries to those studied on 3D seismic, in order to understand structures that form in the regions adjacent to intersections, which may not be imaged on conventional 3D seismic data. A geological map was created and displacement measurements taken from intersecting faults. The methods used to carry out the fieldwork are further described in Chapter 5.

1.4.5 List of abbreviations

A list of common abbreviated terms that are used throughout this thesis is provided below:

T-x	Throw variation on a single horizon in the strike direction.
T-z	Throw variation with depth.
Tmax.	Maximum throw.
D-x	Displacement variation on a single horizon in the strike direction.
D-z	Displacement variation with depth.
Dmax.	Maximum displacement.
TWT	Two-way travel time of a seismic Pwave.
2D	Two-dimensional.
3D	Three-dimensional.

1.5 STRUCTURE OF THESIS

The work presented in this thesis was carried out in four separate geographical areas, each with varying structural styles. Each case study (Vøring Basin, Gulf of Mexico, Levant Basin and Canyonlands) constitutes a chapter in this thesis (Chapters 2, 3, 4 and 5 respectively). Many of the observations described in this thesis are discussed within individual chapters, whilst the discussion chapter of this thesis (Chapter 6) focuses on specific themes that draw

on a compilation of observations made across the case study areas. The thesis comprises a total of seven chapters and the content of Chapters 2 – 7 is briefly summarised below:

Chapter 2 provides a classification of plan view intersection geometries and a detailed analysis of throw variations within each classification. The terminology of styles of evolution of intersections is defined and is used throughout the rest of the thesis.

Chapter 3 reconstructs 3D geometries and displacement variations of cross-cutting intersections. It investigates whether cross-cutting faults can have kinematic coherence.

Chapter 4 provides a 3D architecture of strike-slip fault zones and relates this to the evolution of fault intersections at the tip of a strike-slip fault.

Chapter 5 provides a new geological map of a study area in the Canyonlands National Park, SE Utah. Displacement measurements and description of intersection geometries are used to propose an evolutionary model for intersection development in this area.

Chapter 6 forms the main discussion of this thesis and draws on observations made throughout the thesis. Characteristic styles of intersection evolution are further investigated and compared in order to provide an evolutionary model of non-colinear fault interaction. Branch line development is investigated and related to fault interaction models.

Chapter 7 is a short conclusion chapter that summarises the main findings of this thesis.

CHAPTER 2: GJALLAR RIDGE POLYGONAL FAULT SYSTEM, VØRING BASIN

2.1 INTRODUCTION

The growth of polygonal fault systems (PFS) involves the contemporaneous propagation of many faults with a large range of strikes, which expand their tip lines, interact with neighbouring faults and eventually intersect to form a highly interconnected network (Cartwright, 1994a, 1996; Cartwright and Lonergan, 1996; Lonergan et al. 1998). As such, PFS represent an ideal subject for this thesis investigation into non-colinear fault linkage. The aim of this chapter is to document the plan view geometries and throw distributions that develop in the Gjallar Ridge (GR) PFS in order to determine any relationship between geometry of intersection and its evolution and to investigate how the intersecting faults interact in this setting.

The chapter begins with an introductory review of PFS which outlines the possible mechanisms for their formation. The descriptive section of the chapter can be divided into two parts. Part I, titled structural characteristics (Section 2.2), firstly describes and groups the main plan view geometries within the array thus defining a simple intersection classification based on intersection angles. Secondly, it addresses the propagation style within the array by separating the faults into three distinct groups defined by their throw variation with depth. This is important to establish as it impacts the way that the Part II intersection examples are interpreted. Therefore a summary interpretation is provided in Section 2.2.2.3.

The remainder of the results from this study are presented in Part II, a kinematic analysis of fault intersections. The sub-sections are grouped by geometrical class, as defined in Part I, and include a number of 2D and 3D throw analyses that are interpreted in the context of evolution of the intersections. Each main descriptive section (Sections 2.3.1 – 2.3.4) concludes with a summary interpretation preparing for further discussion in Section 2.4. The main results provide a basis for geometrical classification, types of fault evolution and the terminology of both that is used throughout the thesis.

2.1.1 Introduction to Polygonal Fault Systems

PFS have been identified from over 50 passive margin and intra-cratonic basinal settings worldwide (Cartwright et al., 2003; Cartwright and Dewhurst, 1998; Lonergan et al., 1998). They are defined by these authors as an array of layer-bound extensional faults within a mainly fine-grained stratigraphic interval that exhibit a diverse range of fault strikes which partially or fully intersect to form a polygonal pattern in map view. The faults typically have small throw values of less than 100m and fault trace lengths of 500-1000m (Cartwright, 1994a, b; Lonergan et al., 1998). Plan view geometries range from truly polygonal to curved and rectangular (Lonergan et al., 1998). Strain is distributed within the stratigraphic layer in contrast to fault patterns arising from tectonic forces where strain is concentrated into discrete zones (Lonergan et al., 1998).

The mechanisms responsible for polygonal fault formation are currently under debate. This review is not intended to provide an exhaustive account of proposed methods of formation mechanisms of PFS. Instead, it aims to draw attention to work that is applicable to this piece of research i.e. where it relates to intersection geometry and evolution. For a detailed review of current understanding of PFS see Cartwright et al. (2003).

Four genetic mechanisms have been invoked to explain PFS formation. These are gravity collapse, density inversion, syneresis and compactional loading. Of these, gravity collapse is not considered to be a viable primary controlling process as no dominant alignment of fault strikes is recognised (Cartwright et al., 2003). It is important to consider the consequences of the remaining three processes on intersection evolution. In the Lake Hope fault system (South Australia), Watterson et al. (2000) observed downward convergence of conjugate fault pairs which meet and terminate at the Cadna-owie horizon. They note this basal tip horizon to have the most spatially organised plan view polygonal geometry and argue that this clearly points to nucleation at and propagation upward from this layer. By comparing the Cadna-owie plan view geometry with the structural pattern produced by Raleigh-Taylor instabilities (e.g. Talbot et al., 1991) they invoked a density inversion mechanism for origination of the PFS. In support of this mechanism they described a folded, low density layer above the Cadna-owie horizon and argued that this strained the overburden in such a way as to promote polygonal faults. Watterson et al. (2000) do not adequately address the observation that maximum throw values are recorded approximately 400m above the basal termination. Their upward propagation model therefore cannot be reconciled with fault models that describe maximum

displacement as the site of nucleation (e.g. Barnett et al., 1987, Walsh and Watterson, 1987). In response to this criticism, put forward by James (2000), Watterson et al. (2000) offer only that the Lake Hope faults are consistent with a non-tectonic origin and thus open up the question of whether polygonal faults actually grow in a similar manner to tectonic normal faults.

Goulty (2001) also noted spatial regularity at the base of PFS and suggested upward propagation resulting from compactional loading. Berndt et al. (2003) and Stuevold (2003) also recorded upward propagation from their analysis of T-z plots. However there is some confusion in that Berndt et al. (2003) noted that some faults may propagate downwards, and assumed that the point of maximum displacement marked the nucleation location.

In contrast, the syneresis model is based on the fact that each PFS described thus far in the literature deforms very fine-grained sediments (Cartwright and Dewhurst, 1998). Lachenbruch (1962) observed that naturally-occurring polygons are identified from ice-wedges, cooling lava, desiccation cracks in sediments as well as in drying cement and ceramics and that these all form through volumetric contraction. Cartwright and Dewhurst (1998) invoked a volumetric contraction mechanism of syneresis and this model implies central nucleation and radial propagation of the PFS. Indeed, this is also recorded by Dewhurst et al., (1999), Hansen (2004) and Lonergan et al., (1998) who interpreted radial fault growth based on observations of fault plane shapes and 3D geometries. However, a model of radial fault propagation for all faults in the system does not easily explain the spatial ordering described at the base of many PFS (e.g. the Gjallar Ridge dataset studied herein).

According to Tuckwell (2003) , the development of a fracture network is strongly controlled by the stress state present during formation, mechanical interactions between adjacent fractures, the material properties of the rock and local heterogeneities in the rock mass (e.g. Lawn and Wilshaw, 1975; Cotterel and Rice, 1980; Atkinson, 1987). Isotropic stress states have been described from PFS and the deformed rock masses are largely fine-grained clays or siliceous oozes. Therefore regional stress and lithological heterogeneities are minimal, suggesting that the most important factor may be the mechanical interactions between adjacent fractures, and these interactions are the focus of this chapter. It should be noted that additional stresses arising due to variations in layer thickness and dip may also act to further complicate the growth of the system.

2.1.2 Study Area Location and Geology

The study area is located on the western margin of the Cretaceous Vøring Basin, in the northern North Sea, part of the Norwegian continental margin (Fig. 2.1). The polygonally faulted succession forming the main focus of this chapter is developed within post-rift Miocene to Recent sediments lying above the Gjallar Ridge (Fig. 2.1). The Gjallar Ridge is a structurally complex fault-bounded, arcuate high that trends NE-SW over a distance of 250km (Corfield et. al., 2004). A late Middle Jurassic to Late Cenomanian extensional phase related to continental rifting created the deep basin area that had developed into the Vøring Basin by the Early Palaeocene (Brekke et al., 1999).

Due to the difficulty of tying wells to deep reflections, there is some uncertainty over the timing of the development of the Gjallar Ridge. Cretaceous reflections are identified onlapping the ridge and Bjornseth et al. (1997) interpreted this to represent Early Cenomanian uplift and the first tectonic event to be recognised in the Vøring Basin. Corfield et al. (2004) dated the initiation of the Gjallar Ridge structure as Lower Cretaceous; however Brekke et al. (1999) dated it as being Late Cretaceous. Onlap of the upper Cretaceous was proposed by Corfield et al. (2004) to represent a later upper Cretaceous to Palaeocene extensional phase. A further Miocene uplift event is recorded by truncated Miocene reflections beneath a base upper Pliocene unconformity (Corfield et al., 2004; Norsk Hydro unpublished report) (see Fig. 2.5).

Following the cessation of an Eocene break-up event, the Vøring margin subsided due to thermal cooling and sedimentation and the regional stress regime remained in overall compression (Norsk Hydro unpublished report; Bjornseth et al., 1997; Hjulsteun et al., 1997; Brekke et al., 1999). Sedimentation was dominated by the deposition of siliceous oozes in hemipelagic and pelagic environments (Norsk Hydro unpublished report; Berndt et al., 2003).

2.1.3 Dataset and methodology

The dataset used in this study was a 3D seismic survey from the area of the Norwegian sector of the northern North Sea between 4°00' - 5°00'E and 66°40' – 67°20'N (Fig. 2.2), which has an areal extent of 47 x 39 km and a depth of c. 3250ms TWT.

The 3D seismic data are displayed with positive polarity (SEG standard) i.e. the acoustic impedance increase at seabed is a peak displayed as black on the seismic profile. The seabed

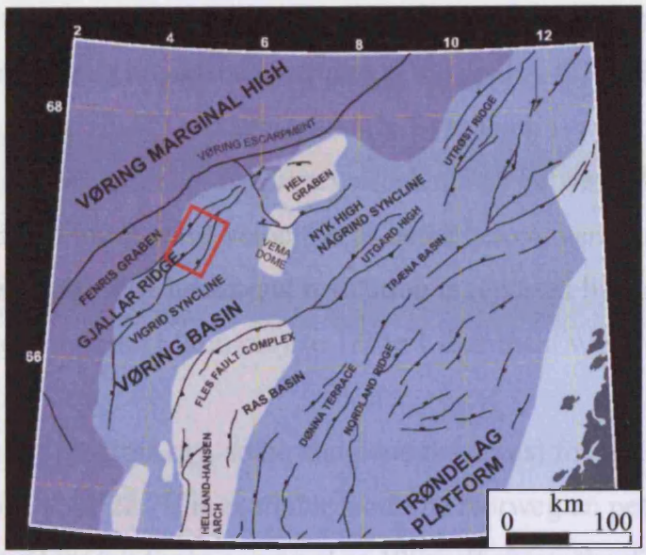

Figure 2.1. Regional structure map of the mid-Norwegian margin showing the study area location on the Gjallar Ridge. Modified from Hansen et al., 2005.

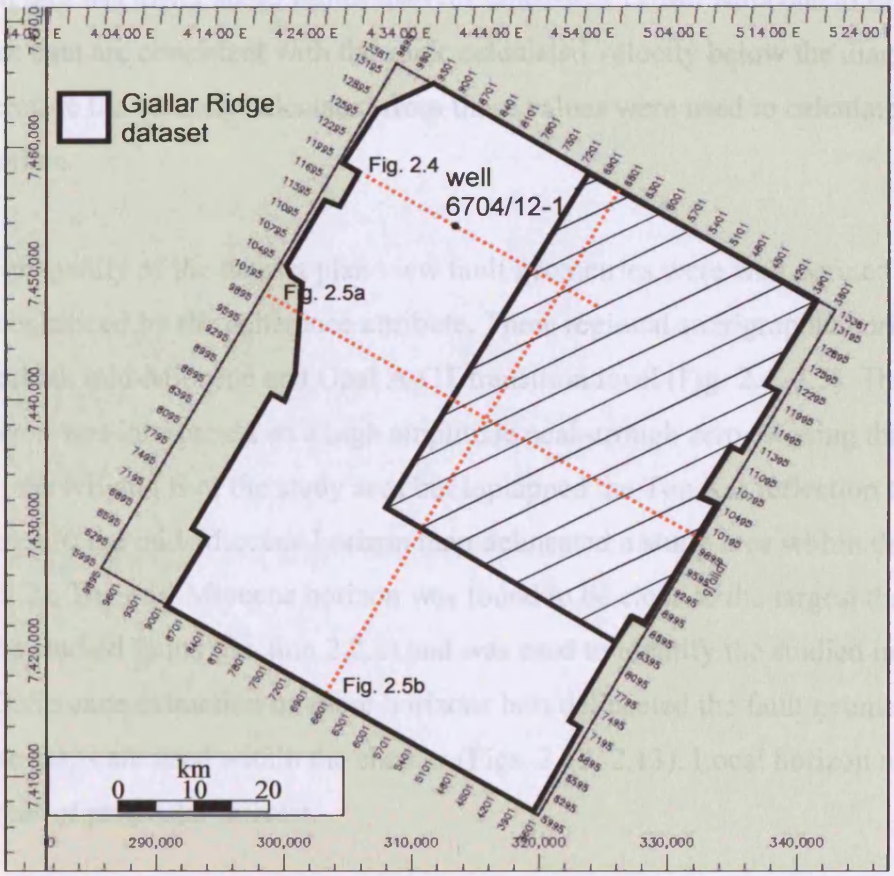

Figure 2.2. Map showing the outline of the Gjallar Ridge seismic survey area. The cross-hatched boxed area is the extent of the middle Miocene horizon and the sub-area chosen for detailed analysis. Note the location of regional seismic lines shown in Figure 2.4 and 2.5.

reflection is a high amplitude peak surrounded by troughs (Fig. 2.3) and this same character is recognised from the acoustic impedance increase at the opal A-CT reflection. Therefore, the data are zero phase. Inline (E-W) and cross-line (N-S) spacing is approximately 12.5m. The data are 3D migrated. The dominant frequency is calculated between 40 and 50Hz. Using this frequency range and seismic P-wave velocities as listed below, vertical resolution is ~10-12m (1/4 dominant wavelength). The horizontal resolution is reported by Hansen et al. (2005) as 30-50m, which corresponds approximately to 1/2 to 1 dominant wavelength.

The composite well log (gamma ray, sonic and density curves) for well 6704/12-1 with coordinates 67°7'25N 4°42'22.7E is available from the Norwegian petroleum directorate (www.npd.no). Interval transit times averaged as 190μs/ft above the diagenetic transition corresponding to an average seismic velocity of 1.6km/s and increased to 125μs/ft = ~2.4km/s below the diagenetic front. Checkshot data were available for the Top Kai to seabed unit (1900ms TWT) and for the Lower Miocene (2500ms TWT). The sonic log shows that the Top Kai to Seabed unit has lower sonic values than the consistent Lower Miocene to Pliocene unit. The checkshot data are consistent with the sonic calculated velocity below the diagenetic transition therefore the velocity calculated from these values were used to calculate fault dips where appropriate.

Due to the high quality of the dataset plan view fault geometries were well defined by horizon mapping and enhanced by the coherence attribute. Three regional stratigraphic horizons were mapped at Seabed, mid-Miocene and Opal A-CT transition level (Fig. 2.4, 2.5). The mid-Miocene horizon was interpreted on a high amplitude peak-trough zero crossing that was continuous in the NE and E of the study area but toplapped the Top Kai reflection to the NW and W. As a result, the mid-Miocene horizon map delineated a study area within the larger dataset (Fig. 2.2). The mid-Miocene horizon was found to be close to the largest throw on the majority of the studied faults (Section 2.2.2) and was used to identify the studied intersection geometries. Coherence extraction on these horizons best delineated the fault geometries and therefore these maps are used within the chapter (Figs. 2.12, 2.13). Local horizon maps were created for areas of particular interest.

In an attempt to follow stratigraphy more accurately than could be achieved using flat coherence slices, isoproportional slices (Zeng et al., 1998) were created at approximately

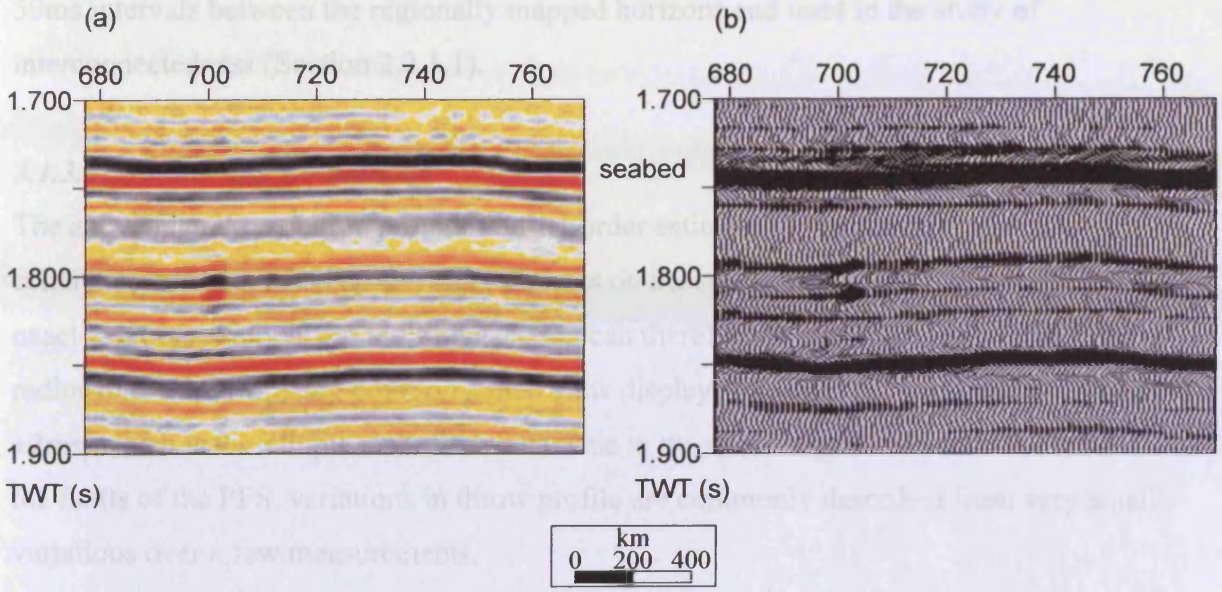

Figure. 2.3. Seismic character of the seabed reflection. (a) Variable area (VA) display. (b) Variable intensity (VI) display. The data are close to zero phase migrated and are displayed using positive standard polarity (SEG standards).

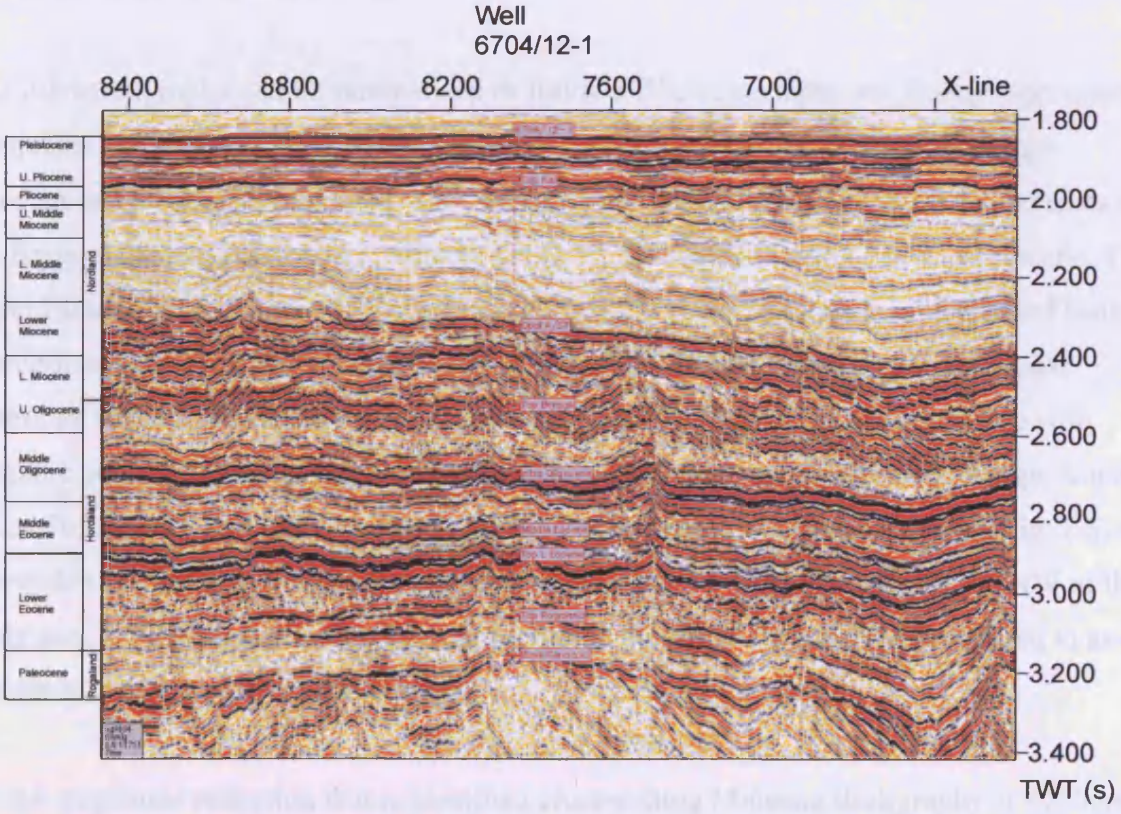

Figure 2.4. Seismic line (in-line 11695) through the 6704/12-1 well showing well tie to reflections. See Fig. 2.2 for line location

50ms intervals between the regionally mapped horizons and used in the study of interconnectedness (Section 2.2.1.1).

2.1.3.1 Errors and Limitations

The above lateral resolution provides a first-order estimate for the spatial resolution of coherence attribute data and therefore impacts on the spatial location of intersections. The exact location of any given fault intersection can therefore at best be defined to within a radius of c. 25m from any point on a map view display. The error on throw measurements is ±2ms, which is the sample rate of the data. Due to the short length and small throw values of the faults of the PFS, variations in throw profile are commonly described from very small variations over a few measurements.

2.1.4 Stratigraphic context of the study area

The seismic survey used in this study displays a Cenozoic stratigraphic section (Fig. 2.4). Horizons tops are correlated from well 6704/12-1 in Figure 2.4 and the correlation follows that of Hansen et al. (2005).

The lithostratigraphy can be summarised as follows. The Palaeocene and Eocene succession comprises claystone with minor sandstone interbeds (Hansen et al., 2005). The Oligo-Miocene succession is dominantly bio-siliceous ooze (Hjelstund et al., 1997) and consists of the Brygge and Kai Formations, with the youngest Kai deposits being dated as Pliocene. The upper Pliocene to Pleistocene succession is termed the Naust Formation. The Kai and Naust Formations consist of alternating claystones, siltstones and sandstones with occasional limestone in the Kai Formation, whereas the Brygge Formation is largely claystone with biogenic ooze. The polygonally faulted succession includes the fine-grained Brygge, Kai and Naust Formations. A further horizon is mapped on the regional seismic sections (Fig. 2.5) and lies within the Kai Formation. It is truncated against the Top Kai reflection to the NW of the study area highlighting Pliocene missing section in this area. This horizon is referred to as the middle Miocene horizon in this chapter.

A high amplitude reflection that is identified cross-cutting Miocene stratigraphy at ~2300ms TWT is attributed to the diagenetic transition of Opal-A to Opal-CT where the siliceous oozes through which it runs provide an ample supply of Opal-A in the form of skeletal debris (Norsk-Hydro unpublished report). Seismic amplitudes increase below the diagenetic

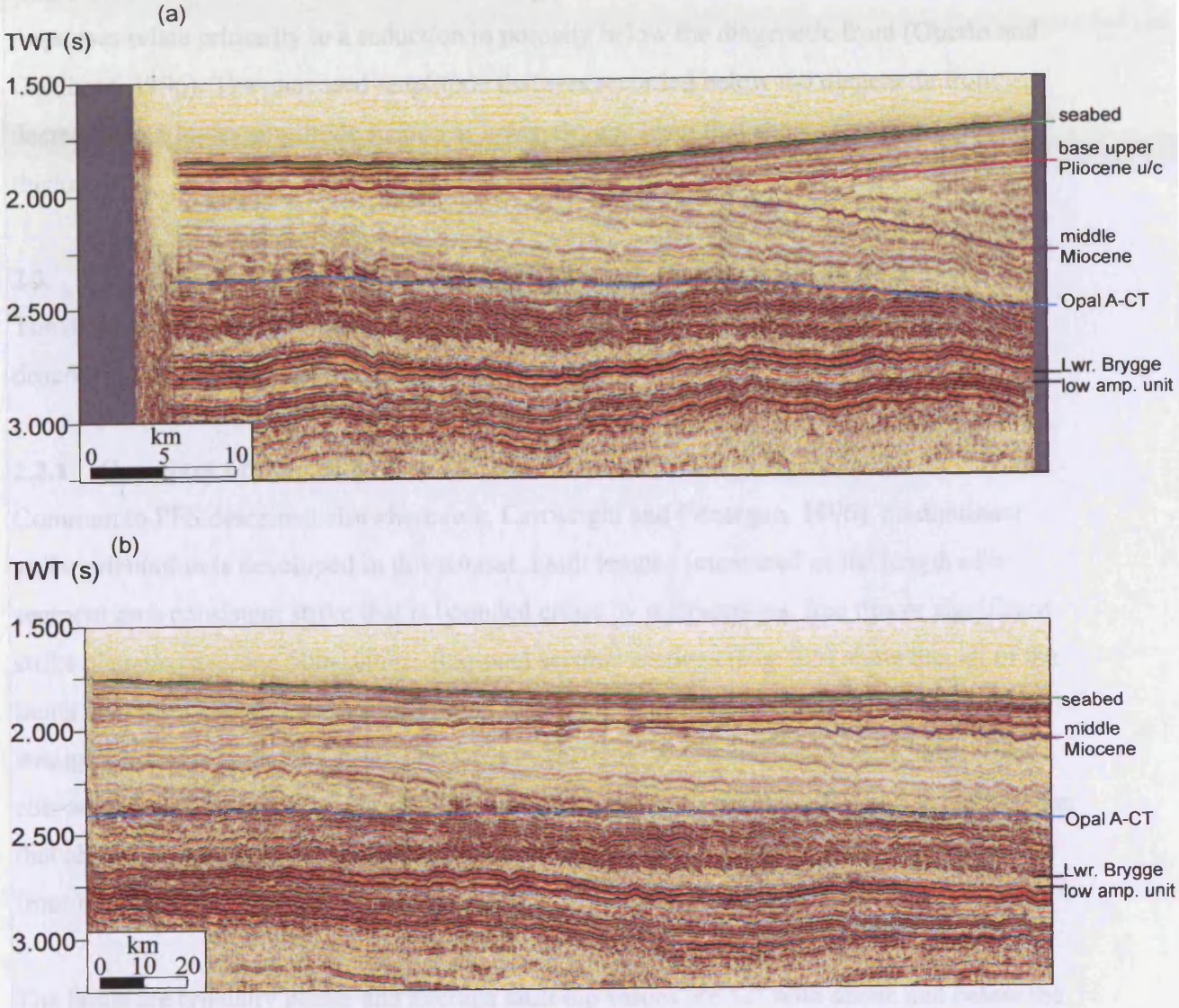

Figure 2.5. Regional seismic profile lines (a) In-line 10000. The middle Miocene horizon is truncated by the base upper Pliocene unconformity. (b) Cross-line 6622. Amplitudes are higher, and density of polygonal faulting greater, below the reflection of the Opal A-CT diagenetic transition. The polygonal faults do not continue through the Lower Brygge low amplitude unit. See Fig. 2.2 for line locations.

boundary and an increase in seismic velocity is recorded from the well logs (Hansen et al., 2005). Brekke et al. (1999) relates this to fluid loss from the transition of Opal-A to Opal-CT where 30-40% of the volume is released during phase transitions. The variation in log responses relate primarily to a reduction in porosity below the diagenetic front (Guerin and Goldberg, 1996). The increased amplitude that was recorded below the diagenetic front decreases to a lower amplitude section at lower Brygge level that shows some variation in thickness.

2.2 PART I: STRUCTURAL CHARACTERISTICS OF THE GJALLAR RIDGE PFS

The description of the structural characteristics of the GR PFS is sub-divided into a description of geometry and of kinematics.

2.2.1 Geometry of the GR PFS

Common to PFS described elsewhere (e.g. Cartwright and Lonergan, 1996), no dominant strike orientation is developed in this dataset. Fault lengths (measured as the length of a segment on a consistent strike that is bounded either by intersections, free tips or significant strike changes) average 500-1000m. Regional seismic sections (Fig. 2.5) show that all of the faults are closely spaced extensional faults that deform the intra-Oligocene to seabed stratigraphy. The faulted units are dissected by the Opal A-CT diagenetic reflection, which cuts across stratigraphy. The density of faulting below the diagenetic reflection is greater than that above. Some faults are confined to the stratigraphy either above or below the diagenetic front but others cut across it (Section 2.2.2.2).

The faults are typically planar and average fault dip values are 52° both above and below the reflection. Some evidence is seen of listric fault profiles below the Opal A-CT transition with dips shallowing to 42°. Basal tips are reached above the Intra-Oligocene unconformity, across which no faults continue.

2.2.1.1 Interconnectedness of the fault array

The term PFS implies a spatially ordered and entirely connected plan view geometry and indeed, a near-perfect polygonal system is identified from the base of the faulted section (Fig. 2.6). Above the diagenetic transition the system is less truly polygonal and can be described as an irregular system (c.f. Lonergan et al., 1998). Interconnectedness of the fault array provides a measurable attribute to help define the state of evolution of the system.

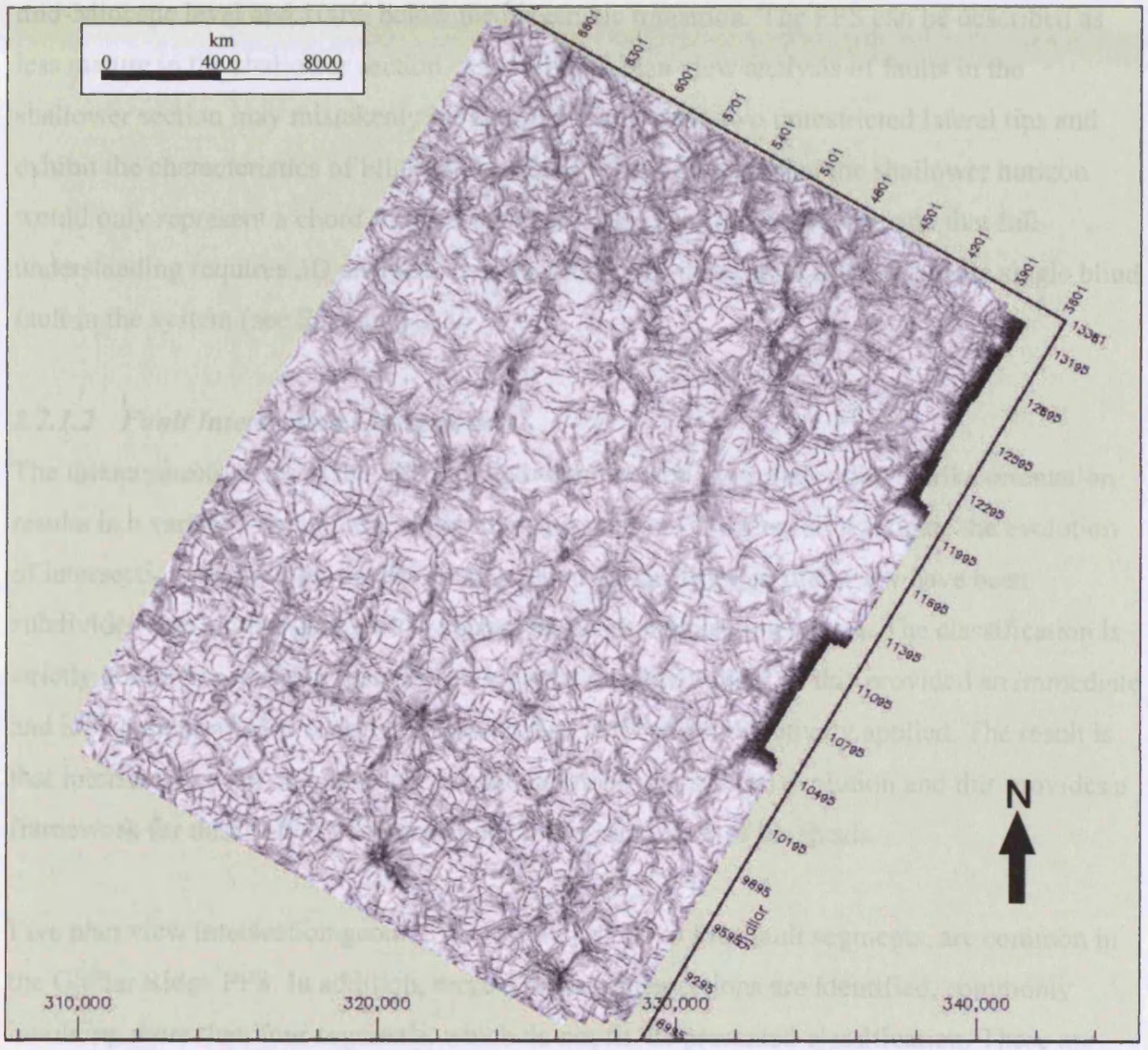

Figure 2.6. Coherence extraction map of an isoproportional slice taken near the base of the polygonally faulted succession. Linear coherence anomalies (low continuity) represent faults that intersect to form near-perfect polygon shapes in plan view.

The GR PFS is characterised by many intersections in a highly connected system. Comparison of the number of free tips to intersecting tips in sample areas from two horizons at different depths in the vertical section produced a ratio of degree of connectedness. The two horizons were the upper Pliocene and the middle Miocene study horizon (Figs. 2.4, 2.5). The upper Pliocene horizon records 66% connectedness and this increases with depth to 93% at mid-Miocene level and 100% below the diagenetic transition. The PFS can be described as less mature in the shallower section. Accordingly, plan view analysis of faults in the shallower section may mistakenly indicate that faults have two unrestricted lateral tips and exhibit the characteristics of blind faults. These results indicate that the shallower horizon would only represent a chord through the upper section of the fault plane and that full understanding requires 3D analysis. It is therefore very difficult to identify a truly single blind fault in the system (see Section 2.2.2.1).

2.2.1.2 Fault Intersection classification.

The interconnectedness of the PFS coupled with the lack of preferred fault strike orientation results in a variety of plan view intersection geometries. In order to investigate the evolution of intersection geometries, the different geometries identified in plan view have been subdivided into simple geometrical classes based on intersection angles. The classification is strictly geometric, without reference to kinematics of evolution, as this provided an immediate and indisputable way to classify an intersection that can be objectively applied. The result is that intersections can be classified independently of intersection evolution and this provides a framework for description of intersections in the remainder of the thesis.

Five plan view intersection geometries, involving two to four fault segments, are common in the Gjallar Ridge PFS. In addition, more complex intersections are identified, commonly involving more than four segments, which do not fit the presented classification. These are not included in this study.

CLASS	IDEAL GEOMETRY	DESCRIPTION
T	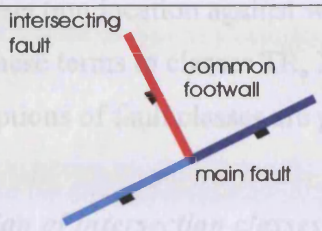	Three segments meet at a single intersection. Main fault is top bar of T and has an angle approximating 180 (actual average = 173°) on its two constituent fault segments. Intersecting fault meets main fault at angles 60-120°.
Y	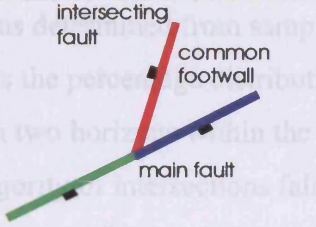	Three segments meet at a single intersection. Main fault as for T. Intersecting fault makes an acute angle between 10° and 60° with main fault.
TR	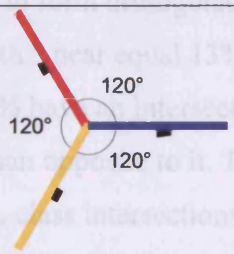	Three segments meet at a single intersection. Angles between all three segments are ≤ 145° with the ideal case being a perfect triple junction of all angles = 120°. Few intersections have near-equal angles of intersection and most have the smallest angle between 85° and 95° with two other angles ranging between 122°-133° and 128° - 145°.
X	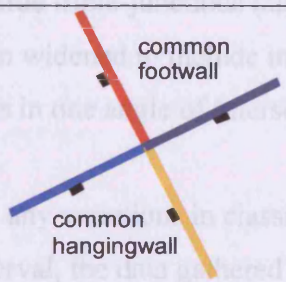	Four segments meet at a single intersection with any angle between intersecting segments. Commonly two sets of two segments, that do not vary in strike and dip across intersection, meet at near-orthogonal angles.
L	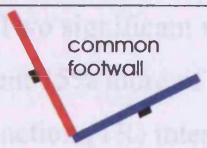	Two fault segments meet at a single intersection at any angle but commonly near-orthogonal and commonly with synthetic dip directions.

Table 2.1. Summary of intersection geometry classification and terminology.

In each intersection the constituent faults are broken down into distinct fault segments that are separated at the intersection location. Thus, even where a plan view trend maintains a continuous strike from one side of an intersection to the other (e.g. the main fault in a class T or Y intersection) it will be defined as two segments and displayed accordingly in T-x plots (Sections 2.3.1 – 2.3.4).

Classes T and Y use the terms main fault and intersecting fault to define their constituent fault segments. The main fault is defined as the two segments that maintain a constant strike and dip across the intersection location against which the intersecting fault terminates. It is not possible to apply these terms to classes TR, X and L based on plan view geometry alone. The geometrical descriptions of fault classes are presented in Table 2.1.

2.2.1.3 Distribution of intersection classes

Based on the geometrical classification described above, the relative distribution of each intersection type was determined from sample areas within the GR PFS. The pie chart in Figure 2.7a presents the percentage distribution of each class gathered from 386 measurements from two horizons within the lower middle Miocene – Pleistocene section of the dataset. The majority of intersections fall within the T class (68%), which shows a tendency for the system to form orthogonal intersections. Classes of X and Y geometries are less well represented with a near equal 13% and 14% respectively. Of the Y class intersections, almost 75% have an intersecting fault segment that dips in the same direction as the main faults, rather than opposite to it. There are fewer still occurrences of TR class intersections (3%) and L class intersections (2%). In the Miocene – Pleistocene section of the Gjallar Ridge system true triple-junctions (all angles equal to 120°) are very rare and the classification has been widened to include intersections where all three angles are <145°. This commonly results in one angle of intersection significantly larger than the other two.

In order to investigate any variations in classification distribution that pertain to location within the vertical interval, the data gathered from each studied horizon are presented separately (Fig. 2.7b, c). Two significant variations are noted between the horizons. Firstly, T class intersections represent 15% more of the class distribution in the upper Pliocene horizon and secondly, all triple junction (TR) intersections that were included in the entire distribution (Fig. 2.7a) are solely from the middle Miocene horizon (Fig. 2.7b). These results show a preference for initial near-orthogonal intersection throughout the vertical interval of study and indicate that other types may form as a result of the density of the polygonal fault array.

2.2.1.4 Orthogonal intersections

Further observations on the most common T class intersections are made below. In this dataset, 95% of T class intersections occur in the footwall of the main fault. By definition T class intersections have a range of geometries as intersection angles can vary between 60° and

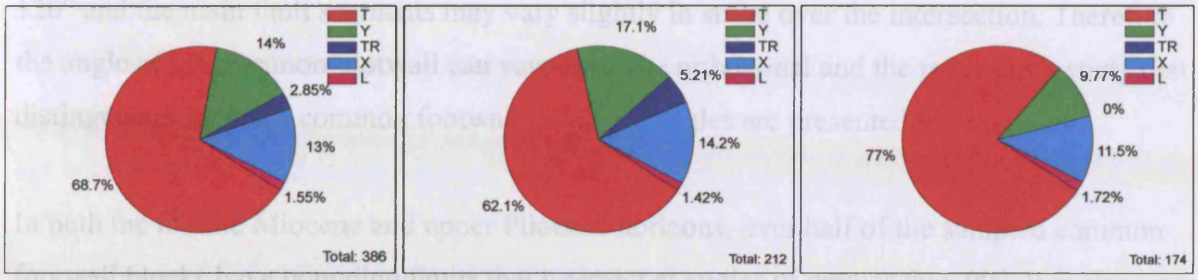

(a) (b) (c)

Figure 2.7. Pie charts of the percentage distribution of intersection classes. (a) all sampled data. (b) data from middle Miocene horizon. (c) data from upper Pliocene horizon.

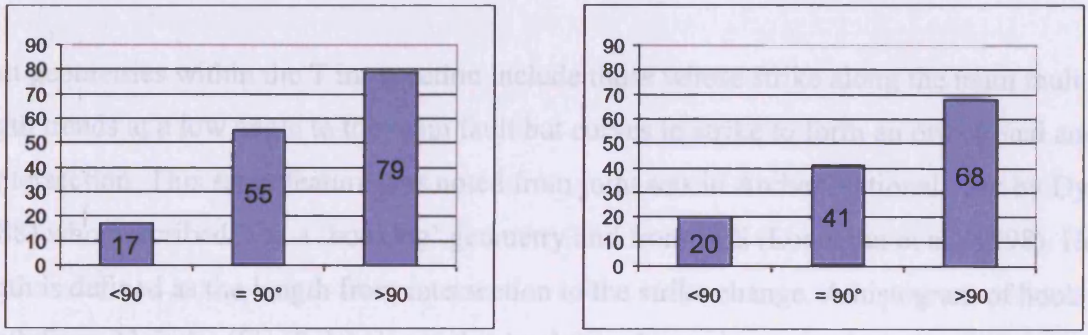

(a) (b)

Figure 2.8. Frequency of acute, orthogonal and obtuse common footwall bounding angles. (a) middle Miocene horizon. (b) upper Pliocene horizon.

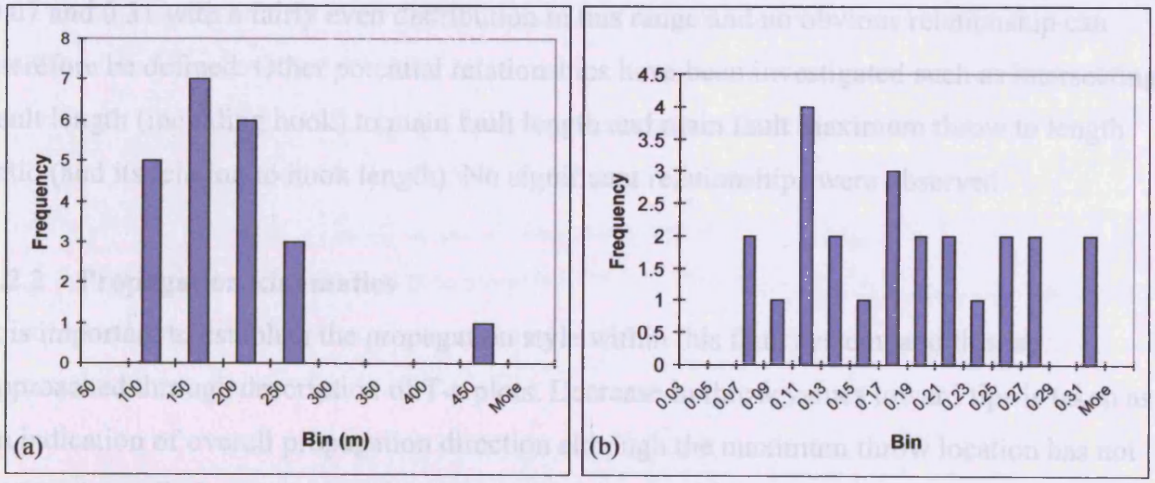

(a) (b)

Figure 2.9. Histograms investigating hook relationships. (a) Frequency of hook length. (b) Frequency of ratio of hook length to main fault length.

120° and the main fault segments may vary slightly in strike over the intersection. Therefore the angle of the common footwall can vary from the orthogonal and the results of a study that distinguishes between common footwall bounding angles are presented in Figure 2.8.

In both the middle Miocene and upper Pliocene horizons, over half of the sampled common footwall blocks have bounding faults that intersect at angles of greater than 90°. It is also very common for footwall blocks to have a 90° angle. Both horizons show that it is far less common for acute angled common footwall blocks to occur (11% for the middle Miocene and 16% for the shallower horizon). To summarise, the data finds that c. 85% of common footwalls are bounded by faults that intersect at angles of 90° or greater and that T class footwall intersection is therefore not favoured by angles <90°.

Fault geometries within the T intersection include those whose strike along the main fault length trends at a low angle to the main fault but curves in strike to form an orthogonal angle at intersection. This same feature was noted from joint sets in Arches National Park by Dyer (1988) who described it as a 'hooking' geometry and from PFS (Lonergan et al., 1998). Hook length is defined as the length from intersection to the strike change. A histogram of hook length from 22 faults (Fig. 2.9a) shows that hook lengths tend to range between 50m and 250m with 60% of measured lengths in the range 100-200m. One value is significantly higher at 430m.

The histogram of hook length to main fault length (Fig. 2.9b) shows the ratio to vary between 0.07 and 0.31 with a fairly even distribution in this range and no obvious relationship can therefore be defined. Other potential relationships have been investigated such as intersecting fault length (including hook) to main fault length and main fault maximum throw to length ratio (and its relation to hook length). No significant relationships were observed.

2.2.2 Propagation kinematics

It is important to establish the propagation style within this fault system, and this is approached through description of T-z plots. Decrease in throw values toward tips is taken as an indication of overall propagation direction although the maximum throw location has not been universally interpreted as the site of nucleation in a PFS (Watterson et al., 2000).

2.2.2.1 Blind Fault

As described in Section 2.2.1.1, it is difficult to identify a fault that does not intersect a free surface or another fault either in plan view or dip profile. Only one fault that fits these criteria has been identified and this section will describe its throw distribution with a view to calibrating the throw variation due to isolated, blind fault growth (Barnett et al. 1987) in this system. The fault, termed Blind Fault 1 (BF1), (see Fig. 2.12 for location) cuts the Miocene section from 1904ms to 2190ms and decreases in throw toward its upper and lower tip. It is therefore classified as a Type 3 fault (see Section 2.2.2.2).

The throw distribution (Fig. 2.10a) has a maximum value in the centre of the fault plane, decreasing outward to a zero tip line that has a near-elliptical to rectangular shape. Throw contours also have a broadly elliptical shape but vary around single values. Toward the upper tip the contours vary around values where broad folds (i.e. no brittle offset) have been measured and therefore represent the upper tip ductile expression of deformation. The measured throw distribution on a horizon midway down the fault surface exhibits a central maximum (Fig. 2.10b). Lateral tip gradients are difficult to quantify due to limited seismic resolution but an increase in profile gradient by a factor of approximately 10 is recorded from the blind fault tips (Fig. 2.10b). T-z plots (Fig. 2.10c) also display a near-central maximum throw but are slightly asymmetric. Upper and lower tip gradients average between 0.116 and 0.256. Toward the lateral tips of BF1 the T-z profile is flat.

2.2.2.2 Throw variation with depth

Models describing the formation of PFS have been summarised by Cartwright et al. (2003) and introduced in Section 2.1.1 with respect to fault propagation mechanisms. Both initiation by upward or by radial growth have been proposed and previous work has used throw variations to distinguish between these different growth mechanisms. This section will describe throw variation with depth for 30 faults measured from the Gjallar Ridge system in order to assess growth styles in this system (Fig. 2.11). The throw profile lines are taken from the approximate location of maximum throw along the length of the fault and this location typically occurs near the centre of map view fault segments (Fig. 2.12).

The T-z plots (Fig. 2.11) are sub-divided into three types:

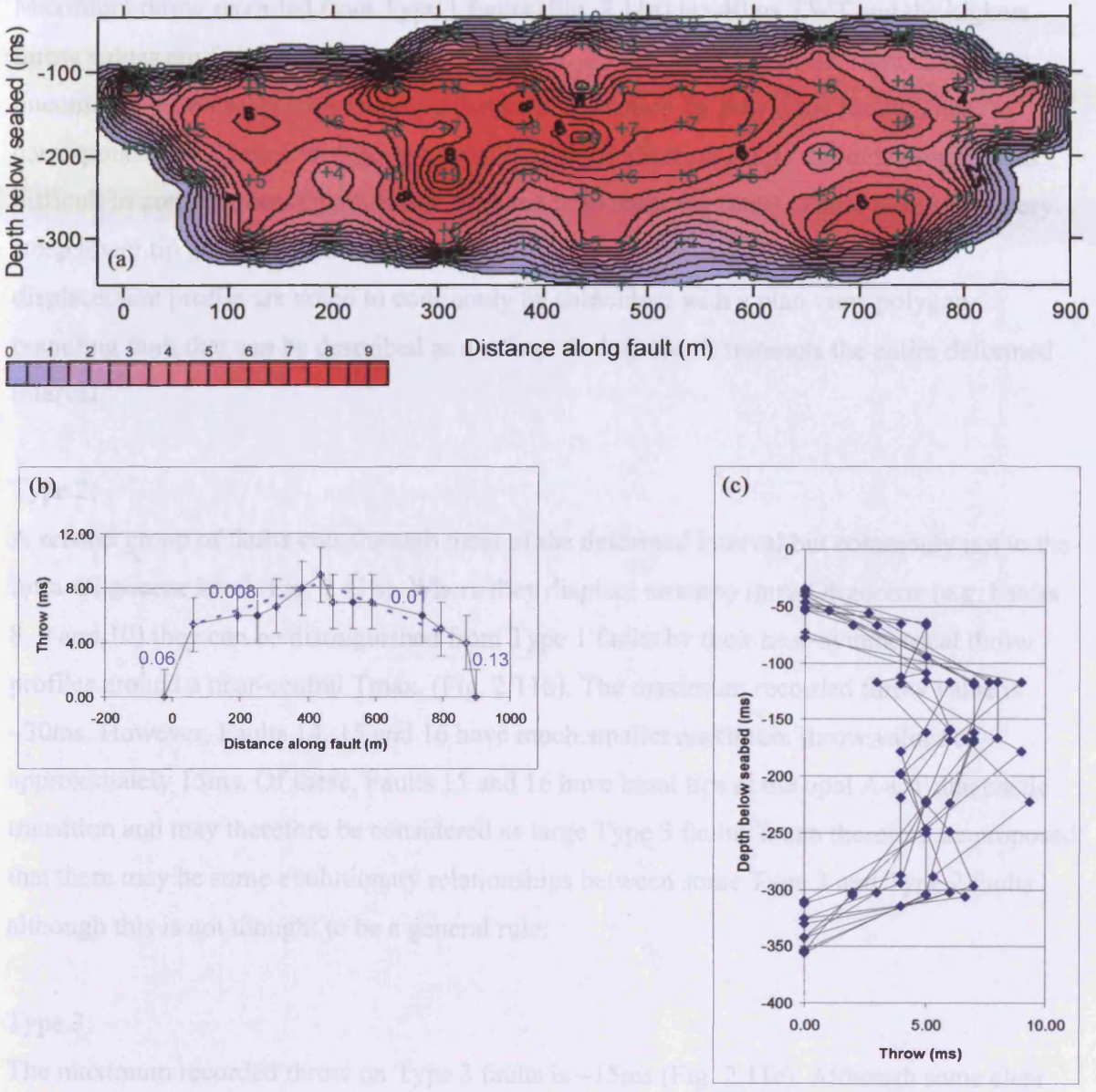

Figure 2.10. Throw distribution of BF1. (a) Vertical fault projection of 3D throw distribution. Measurement locations are represented by a cross and throw values are shown alongside. The data are contoured at 1ms intervals. (b) T-x plot from a representative horizon has a near-central Tmax. Gradients taken between inflection points on the T-x plot show steepening toward the tips, though this is limited by resolution of the tip location. (c) T-z plots from profile lines. Upper and lower tip gradients are measured from tips to first inflections and average between c. 0.1 and 0.2.

Type 1:

Maximum throw recorded from Type 1 faults (Fig. 2.11a) is ~40ms TWT and the highest throw values are found near their basal tips, up to 200ms TWT above the Intra-Oligocene unconformity below which there is no further deformation by polygonal faults. This corresponds to the lower Brygge low amplitude layer (Section 2.1.4) through which it was difficult to correlate continuous reflections and to identify the faults. These faults have very steep lower tip gradients and much shallower upper tip gradients. Faults with this displacement profile are noted to commonly be coincident with a plan view polygon-bounding fault that can be described as a master fault in that it transects the entire deformed interval.

Type 2:

A second group of faults cuts through most of the deformed interval but commonly not to the Intra-Oligocene level (Fig. 2.11b). Where they displace strata to Intra-Oligocene (e.g. Faults 8, 9 and 10) they can be distinguished from Type 1 faults by their near-symmetrical throw profiles around a near-central Tmax. (Fig. 2.11b). The maximum recorded throw value is ~30ms. However, Faults 14, 15 and 16 have much smaller maximum throw values of approximately 15ms. Of these, Faults 15 and 16 have basal tips at the opal A-CT diagenetic transition and may therefore be considered as large Type 3 faults. It can therefore be proposed that there may be some evolutionary relationships between some Type 3 and Type 2 faults although this is not thought to be a general rule.

Type 3:

The maximum recorded throw on Type 3 faults is ~15ms (Fig. 2.11c). Although some clear variation in shape of throw distribution against depth is recognised the faults commonly display symmetry around a near-central maximum throw. The maximum throw does not consistently occur at the same stratigraphic horizon. The measurement value that was taken from the middle Miocene horizon is situated close to the maximum throw value in most examples.

In summary, faults of the study area fit into the following categories:

(1) those that deform the section from the Intra-Oligocene unconformity to the Plio-Pleistocene and have asymmetric T-z profiles (Type 1, Fig. 2.11a);

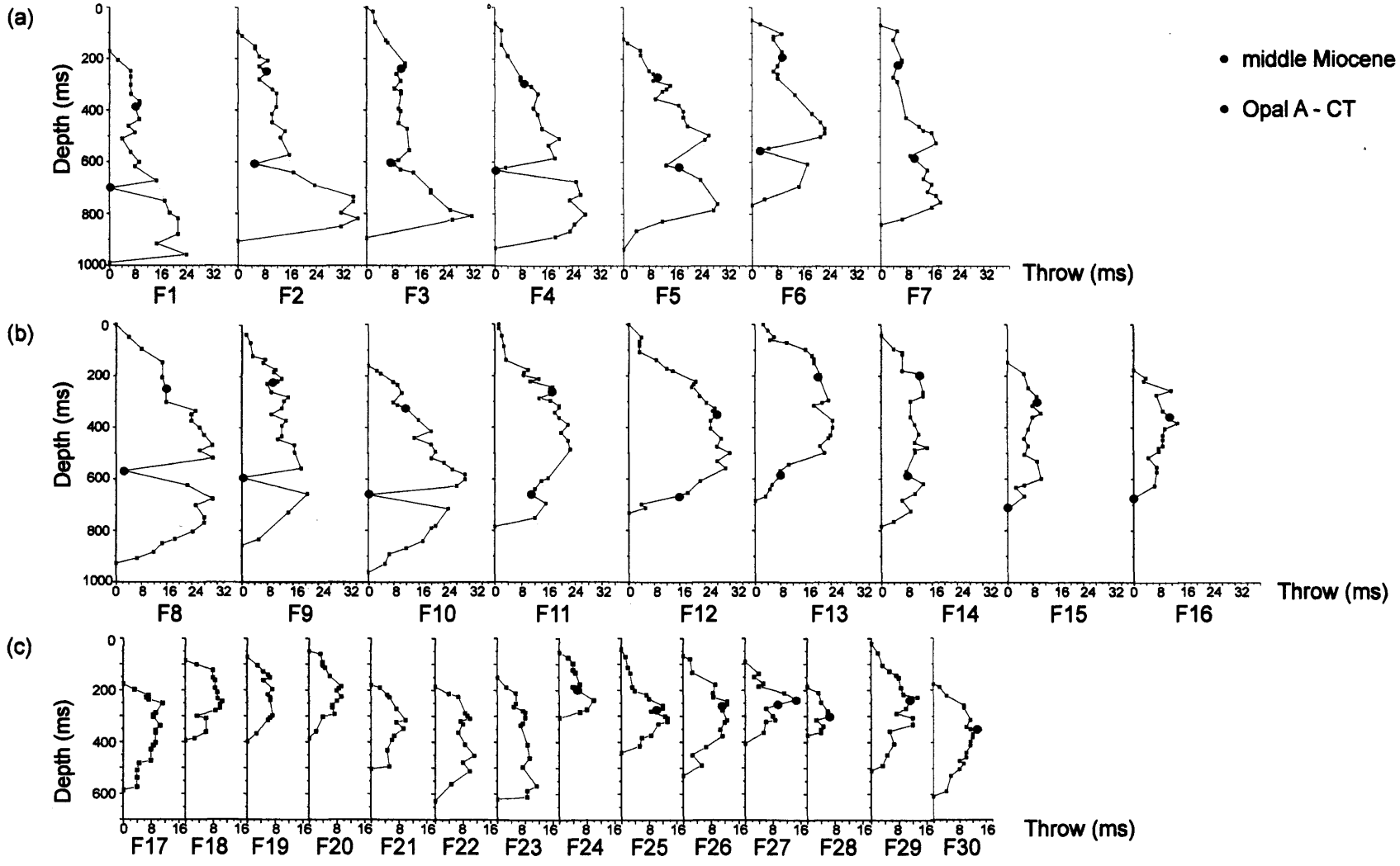

Figure 2.11. T-z plots for 30 faults within the polygonally faulted succession. (a) Type 1 faults. (b) Type 2 faults. (c) Type 3 faults. See Fig. 2.12 for fault locations. Local minimum throw values are commonly identified from the Opal A - CT horizon. Dashed orange lines are added to aid identification of overall profile shape. See section 2.2.2.3.

(2) those that deform the lower Miocene – Pleistocene section and have symmetric throw profiles (Type 2, Fig. 2.11b); and
(3) those which are confined to the lower middle Miocene – Pleistocene section and display symmetric throw profiles (Type 3, Fig. 2.11c).

The measurement value that represents offset of the opal A-CT reflection frequently shows a minimum value. This can give information about the relative timing of movement of the faults with respect to the occurrence of diagenesis (Section 2.2.2.3).

2.2.2.3 Propagation kinematics summary

The Type 1 faults (Fig. 2.11a) also commonly form polygon-bounding faults in the most spatially organised horizon which is close to their level of maximum throw. The basal tips are not well imaged as they lie within the Brygge low amplitude layer. Watterson (2000) suggests that a low density layer may be fundamental to upward propagation from the base of a polygonally faulted tier. Propagation upward from the basal tips requires that the downward tip either detaches in a highly ductile or mobile layer or buttresses against a rheologically more competent layer. There is no evidence from the available well logs to suggest that the Brygge low amplitude event is a mobile or weak unit. However, the T-z profiles suggest that propagation mainly upward from the lower Brygge interval can be interpreted from these faults while still fitting the model of nucleation near the maximum throw level.

The central throw maximum and elliptical nature of the 3D throw distribution of BF1 (Fig. 2.10) would be interpreted in a tectonic system as having evolved through radial propagation (Watterson, 1986). As the BF1 cannot have nucleated at the base of the polygonally faulted section, the same interpretation is applied here. This Type 3 fault most probably nucleated in a mid-fault position and evolved through radial propagation and the T-z profiles of the Type 3 faults also support this interpretation as they show a near-symmetrical distribution with a near-central Tmax. location (Fig. 2.11c). The near-symmetrical throw distribution of the Type 2 faults which rarely displace strata to the lower Brygge, (Fig. 2.11b) is therefore also indicative of radial propagation. In addition, the fact that the maximum throw profile lines were taken from near-central locations on plan view fault segment traces (Fig. 2.12) also supports radial growth. This suggests that both upward and radial fault growth styles are present in the Gjallar Ridge fault system.

Faults with an Opal A-CT throw measurement of near zero are interpreted as having arrested growth prior to the arrest of diagenetic transformation (Davies and Cartwright, 2002); those with an Opal A-CT throw value that does not deviate from the profile trend are interpreted as having entirely post-diagenetic movement; and those with a value in between record movement both pre- and post formation of the diagenetic reflection.

Type 1 faults grew mainly prior to the arrest of diagenesis. However, faults 2, 3, 5 and 7 all show that they had some post-diagenetic movement. Of the Type 2 group, the faults that cut through the largest section – faults 8, 9 and 10 - have entirely pre-diagenetic movement. The others show very little variation in their throw profiles at the opal A-CT measurement and are interpreted to have post-diagenetic movement. A very brief study attempted to investigate if there were spatial relationships between faults with pre-, pre- and post- and post-diagenetic transition. No relationships were found.

As the Type 3 faults display the simplest growth characteristics the focus on intersection geometries and throw measurement will be largely concentrated within this fault group. The interpretation of radial growth of Type 2 and 3 faults in the Gjallar Ridge PFS is fundamentally important for interpretations that are offered of intersection evolution throughout the remainder of the chapter. This interpretation is supported by 3D studies throughout the chapter.

The results of this section allow proposal of an evolutionary growth model that fits within the rules of nucleation relating to throw distribution as defined for tectonic faults (Barnett et al., 1987; Walsh and Watterson, 1987) (Section 2.4.1).

2.3 PART II: KINEMATIC ANALYSIS OF INTERSECTION CLASSES

The second part of this chapter distinguishes intersections based on the classification given above and presents throw data to allow a kinematic analysis with the aim of understanding how the different geometries evolved.

2.3.1 Kinematic analysis of T intersections

A key observation from the structural characteristics of the Gjallar Ridge PFS (Section 2.2) was that approximately 70% of sampled intersections fall within the T geometry classification

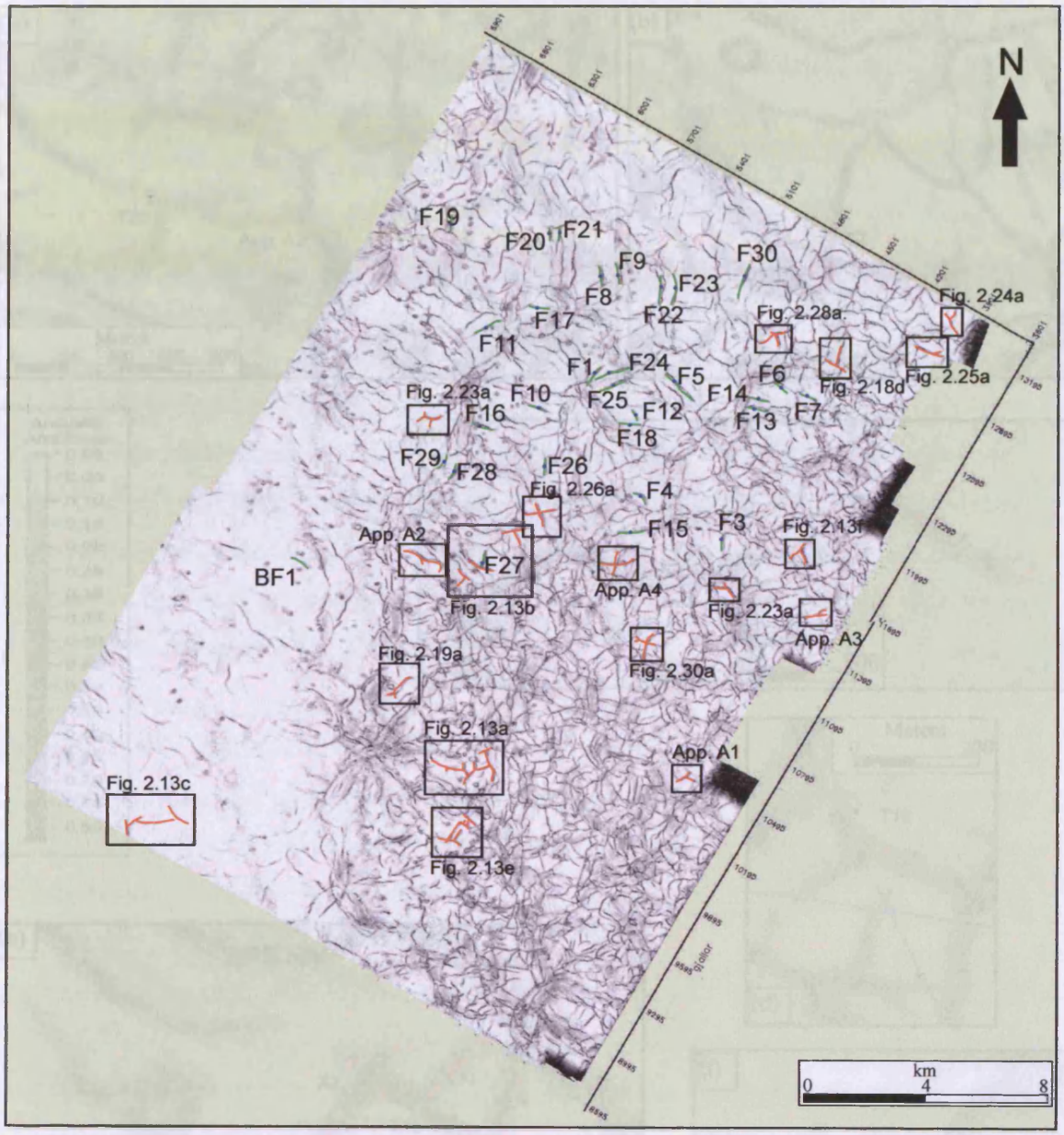

Figure 2.12. Coherence extraction of middle Miocene basemap. The sampled faults presented in Fig. 2.11 are highlighted in green and blue dots mark the location of the profile line. Note that blue dots are commonly near the centre of the highlighted fault traces. Boxed areas encompassing fault traces that are highlighted in orange are the study areas used in the remainder of the chapter.

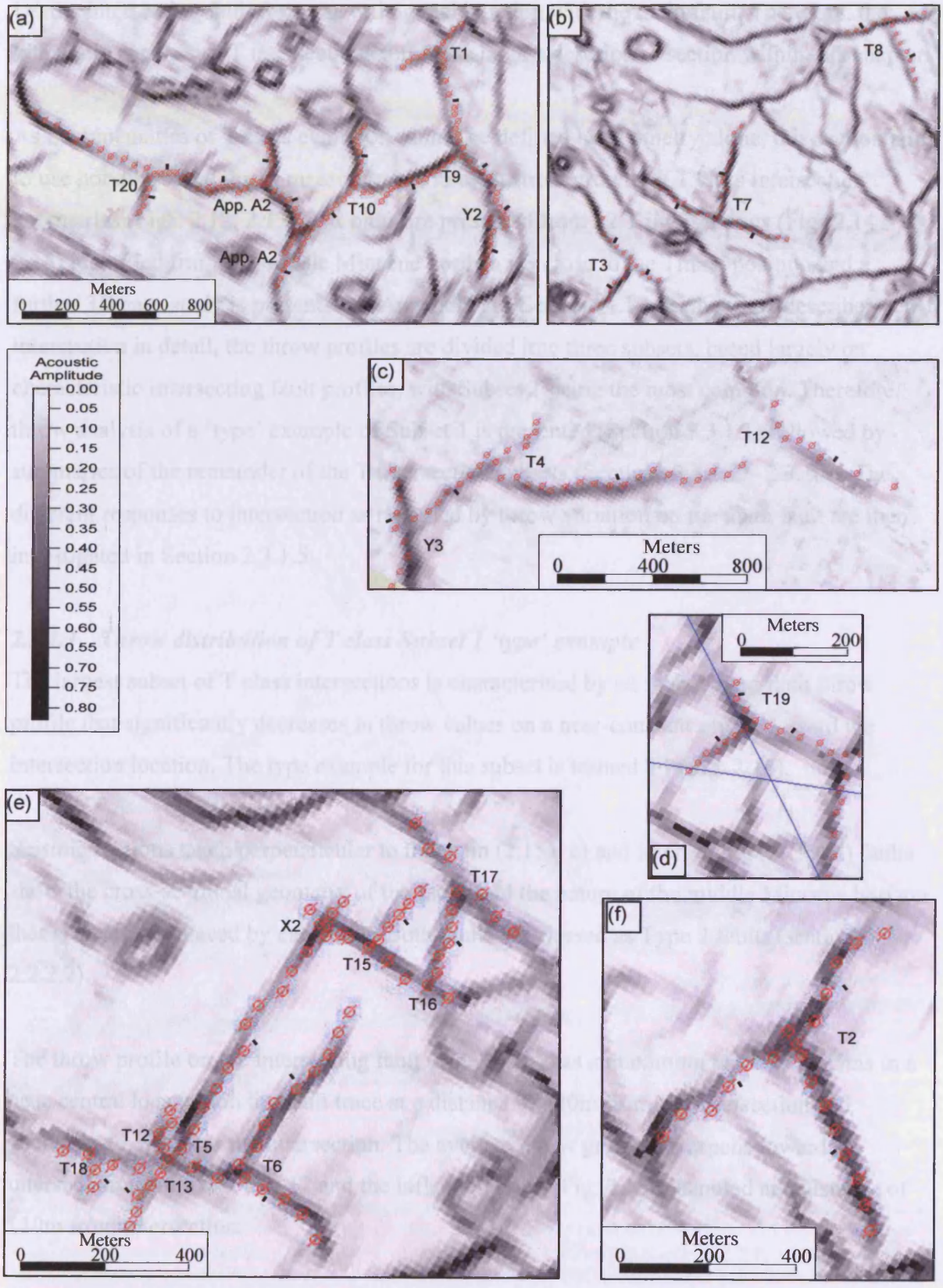

Figure 2.13. Zoomed excerpts of the middle Miocene coherence extraction (Fig. 2.12). (a) - (f) Plan view geometries of the studied T intersections (Figs. 2.15 - 2.18). Red markers indicate the location of profile lines taken perpendicular to each fault trace and from which throw measurements were taken.

i.e. the intersecting fault forms an orthogonal junction with the main fault. Therefore, the kinematic analysis of T intersections forms the largest descriptive section within this chapter.

As the kinematics of T class evolution cannot be defined by geometry alone, this section aims to use horizon-based throw measurements to reconstruct growth of T class intersection geometries (Figs. 2.12, 2.13). T-x plots are presented from 22 T intersections (Figs 2.14 – 2.18) identified from the middle Miocene horizon i.e. close to the Tmax. position and a further 3D case study is presented as Appendix A. (Section A.1.). Rather than describe each T intersection in detail, the throw profiles are divided into three subsets, based largely on characteristic intersecting fault profiles, with Subset 1 being the most common. Therefore, throw analysis of a 'type' example of Subset 1 is presented (Section 2.3.1.1) followed by summaries of the remainder of the T intersection subsets (Sections 2.3.1.2 – 2.3.1.4). The different responses to intersection as recorded by throw variation on the main fault are then investigated in Section 2.3.1.5.

2.3.1.1 Throw distribution of T class Subset 1 'type' example

The largest subset of T class intersections is characterised by an intersecting fault throw profile that significantly decreases in throw values on a near-constant profile toward the intersection location. The type example for this subset is termed T1 (Fig. 2.15).

Seismic sections taken perpendicular to the main (2.15a, c) and intersecting (2.15a, d) faults show the cross-sectional geometry of the faults and the nature of the middle Miocene horizon that is clearly displaced by each fault. Both faults are classed as Type 2 faults (section 2.2.2.2).

The throw profile on the intersecting fault (Fig. 2.15b) has a maximum value of c. 25ms in a near-central location on the fault trace at a distance of 430m from the intersection and decreases to 3ms near the intersection. The average throw gradient steepens toward the intersection from 0.047 to 0.12 and the inflection point (Fig. 2.15b) is noted at a distance of 110m from intersection.

2.3.1.2 Subset 1: Intersecting fault throw decreases toward intersection

The decrease in throw toward the intersection on the intersecting fault that was described from T1 (Section 2.3.1.1) is a key characteristic common to many orthogonal intersections,

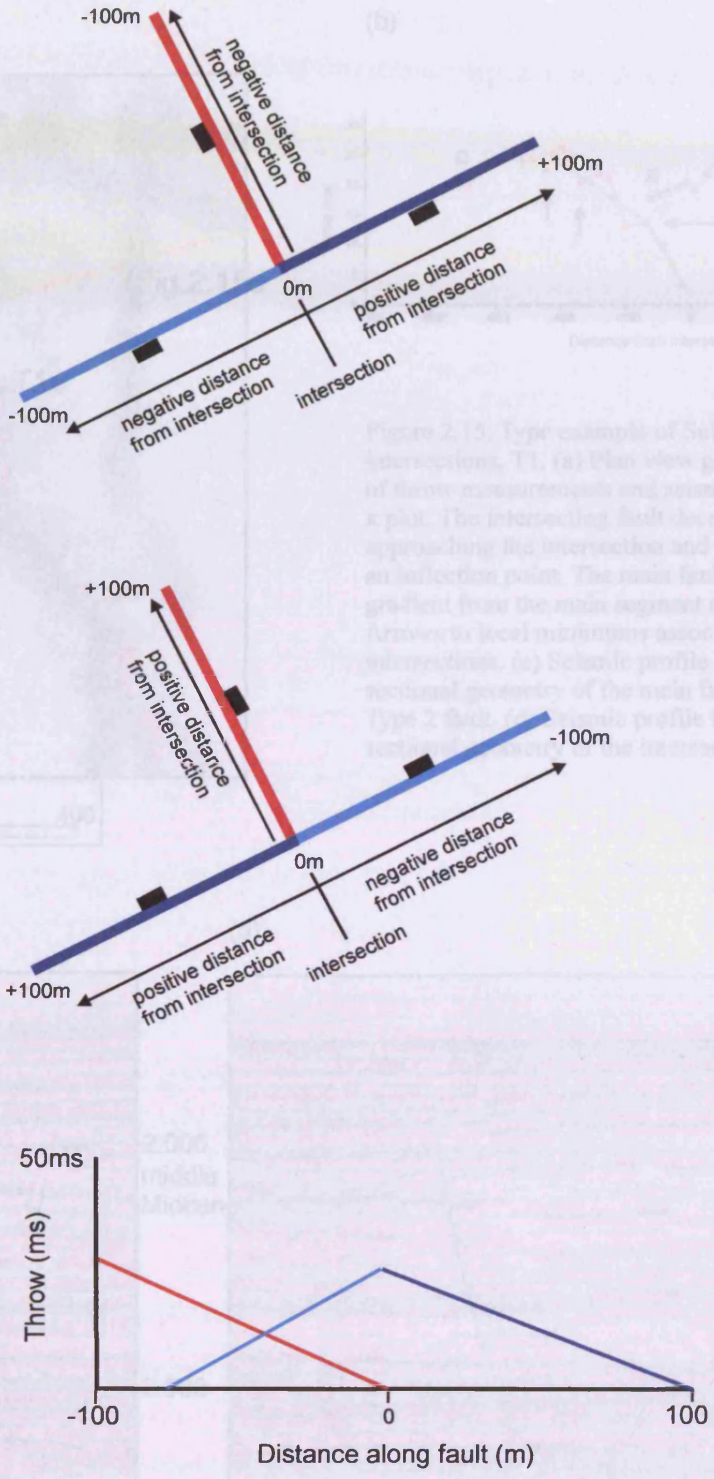

Figure. 2.14. Summary diagram showing how T-x plots are constructed. The intersecting fault is displayed on the same T-x profile as the main fault. The distance along each segment is measured from the intersection location which is always at 0m along the x-axis. Plots are always constructed looking toward the footwall main fault plane that is dipping out of the page. Red is the intersecting fault, navy is the main fault segment that is a positive distance from the intersection and blue is the main fault segment that is a negative distance from the intersection. (a) Footwall intersection. The intersecting fault is a negative distance from intersection. (b) Hangingwall intersection. The intersecting fault is a positive distance from intersection. (c) Schematic T-x plot of a footwall intersection.

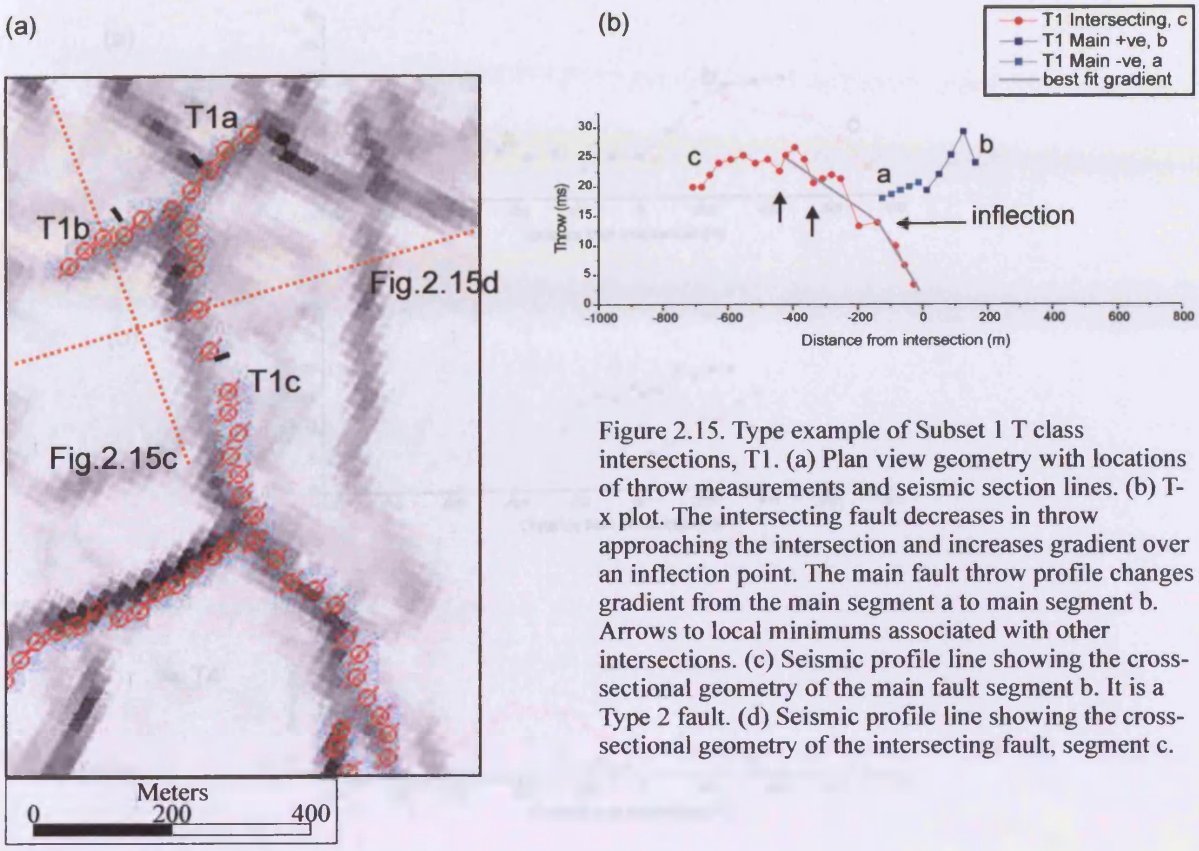

Figure 2.15. Type example of Subset 1 T class intersections, T1. (a) Plan view geometry with locations of throw measurements and seismic section lines. (b) T-x plot. The intersecting fault decreases in throw approaching the intersection and increases gradient over an inflection point. The main fault throw profile changes gradient from the main segment a to main segment b. Arrows to local minimums associated with other intersections. (c) Seismic profile line showing the cross-sectional geometry of the main fault segment b. It is a Type 2 fault. (d) Seismic profile line showing the cross-sectional geometry of the intersecting fault, segment c.

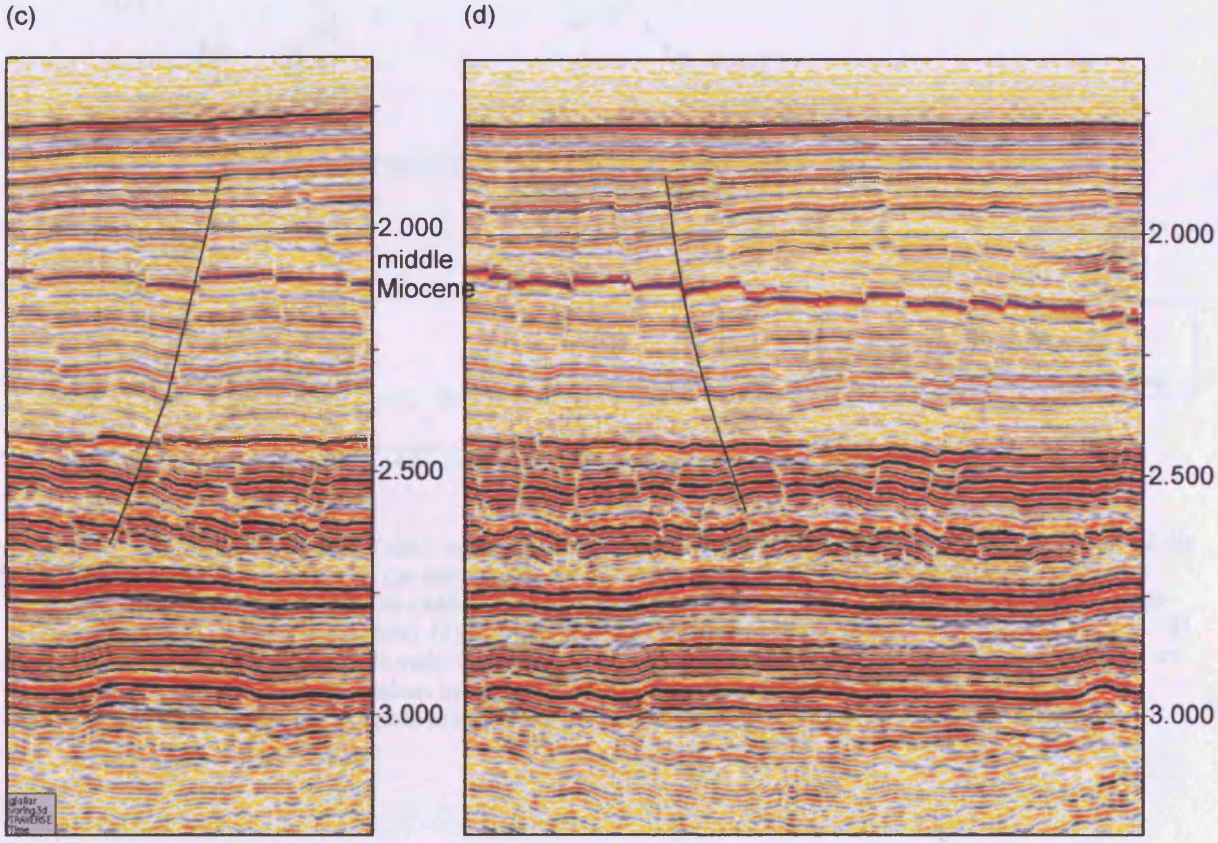

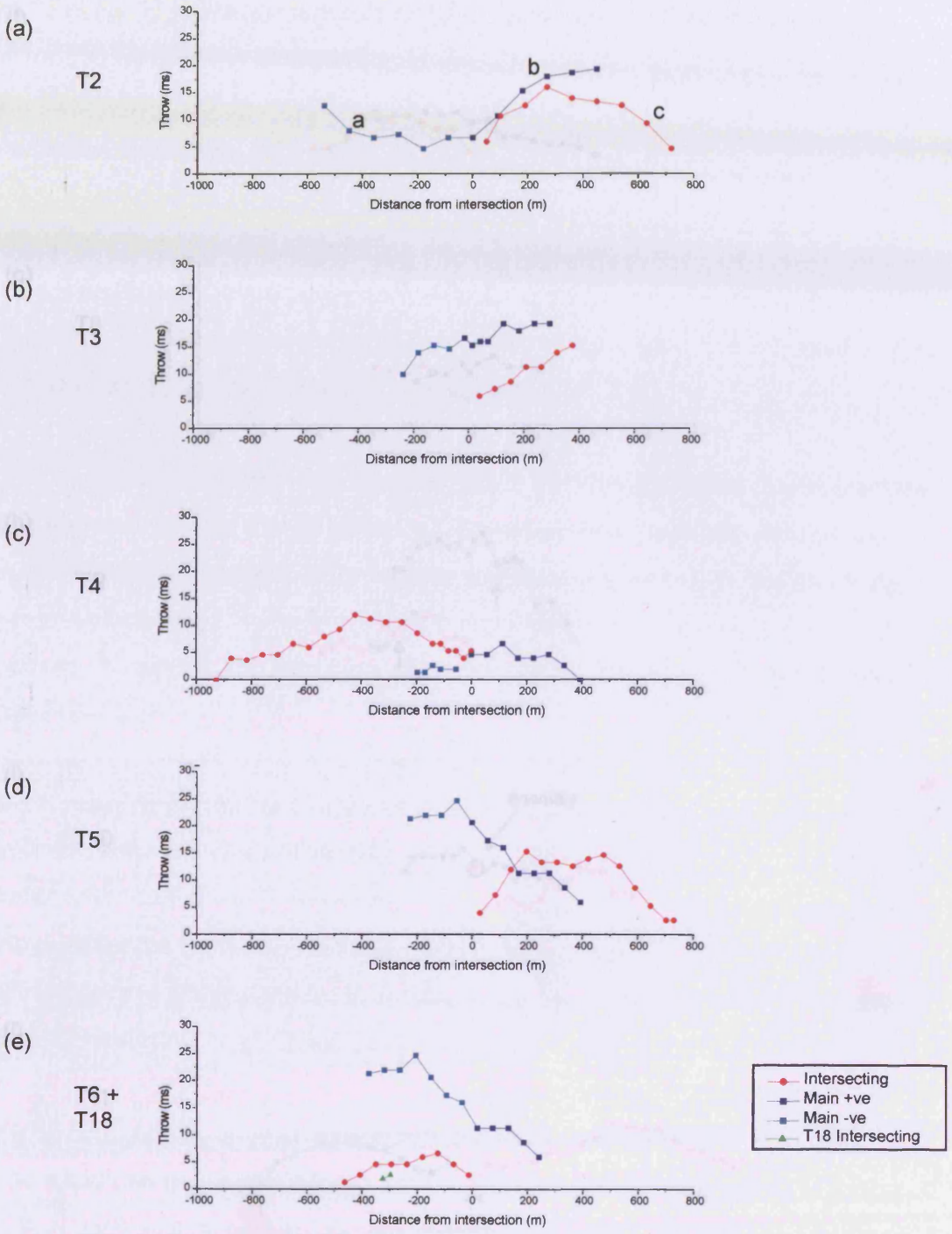

Figure 2.16. T-x plots of Subset 1 T class intersections. (a) - (j). The intersecting fault decreases throw toward the intersection. A gradient increase on the intersecting fault is frequently noted. The main fault displays varying responses to intersection including no change, a local minimum, a local gradient variation and a profile change across intersection (see text for details). (e) includes the T18 intersection from Subset 2 (see Section 2.3.1.3). (h) arrows show local minimums on the main fault that relate to sites of intersection with intersecting faults that are not sampled. (i) the localised anomalous measurement at the intersection location is an example of a measurement where it was not possible to resolve two separate faults (addition of throw, Chapter 1).

(f)

T7

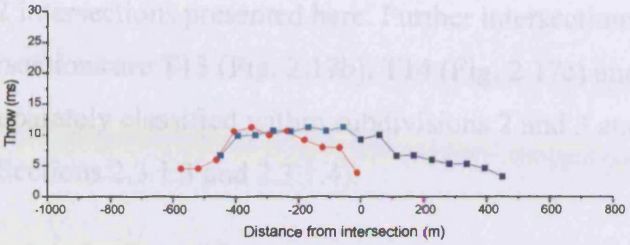

(g)

T8

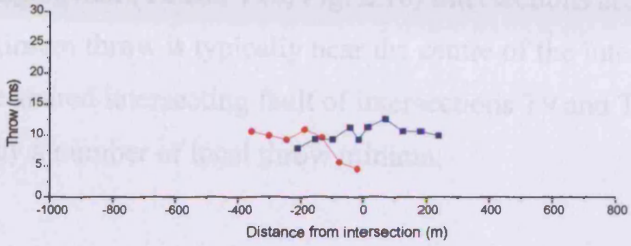

(h)

T9

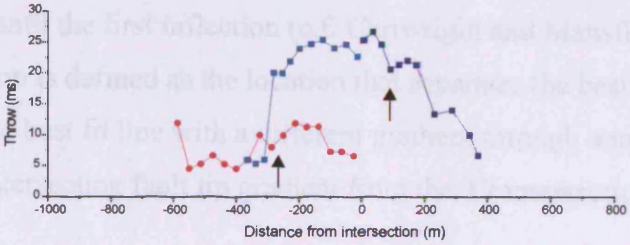

(i)

T10

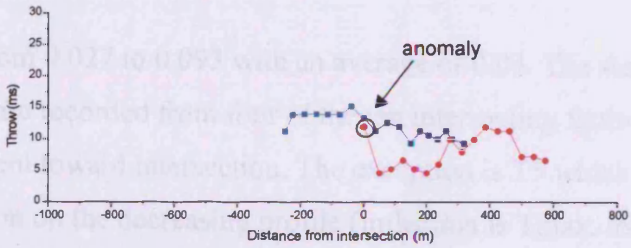

(j)

T11

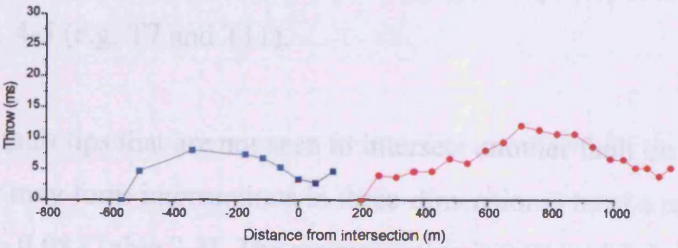

Figure 2.16 (continued)

and from 15 of the 22 intersections presented here. Further intersections that have throw decrease toward intersections are T13 (Fig. 2.17b), T14 (Fig. 2.17c) and T21 (Fig. 2.18c). However, these are separately classified within subdivisions 2 and 3 and reasons for this given in each subdivision (Sections 2.3.1.3 and 2.3.1.4).

Both footwall and hangingwall (T2 and T10, Fig. 2.16) intersections are recorded from this subdivision. The maximum throw is typically near the centre of the intersecting fault profile (where sampled). The shared intersecting fault of intersections T9 and T10 is termed 'ragged' as it is characterised by a number of local throw minima.

Intersecting tip gradients are measured from the best fit line through measurements from the intersection location until the first inflection (c.f. Cartwright and Mansfield, 1998) (Table 2.2). The first inflection is defined as the location that separates the best fit line for the tip gradient from a second best fit line with a different gradient through another set of measurements. The intersecting fault tip gradient from the T9 intersection is omitted because of its ragged profile.

Tip gradients range from 0.027 to 0.093 with an average of 0.03. The steeper values from this range (0.07 to 0.093) are recorded from four of the ten intersecting faults that show evidence of steepening in gradient toward intersection. The exception is T5 which has a throw gradient of 0.07 but no inflection on the decreasing profile (inflection is Tmax. location). Throw profiles that steepen in gradient toward their intersecting tips steepen by a factor between c.2 (e.g. T1 and T2) and c. 4-5 (e.g. T7 and T11).

Throw gradients from fault tips that are not seen to intersect another fault on the middle Miocene basemap (but may form intersections in three-dimensions) have a range of recorded gradients from 0.004 to 0.08 (Table 2.2). The average value is 0.04 which is similar to the average throw gradient recorded above. However, the lower end of this range is well below the lower end of the range for the intersecting fault tips. This observation that steeper tip profiles are recorded from intersecting tips has potential significance in understanding the mechanics of intersection (Section 2.3.1.6).

Values of displacement on the intersecting faults that are measured from the sample location closest to intersection, range between 3ms and 7ms (Table 2.2) (excluding the 0ms tip value

Intersection	Figure number	Intersecting or Main Fault	Increasing (I)/Decreasing (D) toward intersection	Footwall or Hangingwall	Tmax. Value (ms)	Tmax. Location	Throw gradient from intersection to 1st inflection	Throw gradient beyond 1st inflection	Free tip gradient	Main fault change over intersection	Interpretation
T1	2.15	Intersecting	D	F	26.66	centre of profile	0.12	~0.047	-		Abutment
		Main			29.33	away from intersection	0.02 | 0.75	-	-	1.34ms decrease	
T2	2.16a	Intersecting	D	H	16	away from intersection	0.093	0.05	0.044		Abutment/intersection of three separate segments
		Main			19.33	away from intersection	0.048 | flat	-	-	significant profile + gradient change	
T3	2.16b	Intersecting	D	F	15.33	away from intersection	0.028	-	-		Abutment
		Main			19.33	away from intersection	0.016	-	-	none	
T4	2.16c	Intersecting	D	F	12	centre of profile	0.03	0.008	0.07		Abutment/soft linkage (FW linkage)
		Main			6.67	centre of profile	0.047	-	Flat	2.67ms decrease and gradient increase	
T5	2.16d	Intersecting	D	F	15.33	1st inflection	0.07	Flat	-		Abutment
		Main			24.67	near intersection	0.05	-	0.04	gradient flattens after intersection	
T6	2.16e	Intersecting	D	F	6.67	1st inflection	0.036	0.009	0.03		Abutment
		Main			15.33	away from intersection	0.04	-	0.05	gradient steepens over intersection	
T7	2.16f	Intersecting	D	F	11.33	away from intersection	0.07	0.017	-		Abutment/soft linkage (FW linkage)
		Main			11.33	near intersection	-	0.016	0.024	Local minimum	
T8	2.16g	Intersecting	D	F	11	away from intersection	0.044	-	-		Abutment
		Main			12.67	away from intersection	-	-	0.024	Local minimum	
T9	2.16h	Intersecting	D	F	12	centre of profile			-		Abutment
		Main			26.66	near intersection	~0.047	-	-	Local minimum	
T10	2.16i	Intersecting	D	H	12	away from intersection	0.027	~0.018	-		Abutment
		Main			15.33	near intersection	0.05		-	Gradient increase	
T11	2.16j	Intersecting	D	F	12	centre of profile	0.07	0.014	0.07		Abutment
		Main			8	centre of profile	-	-	0.08	Local minimum	
T12	2.17a	Intersecting	I	F	4.67	near intersection	0.047	-	-		Splay/bud
		Main			15.33	centre of profile				None	
T13	2.17b	Intersecting	D	H	3.33	near intersection	0.095	0.016	0.016		Splay/bud
		Main			15.33	centre of profile				None	
T14	2.17c	Intersecting	D	F	3.33	near intersection	-	-	-		Splay/bud
		Main			10.66	near intersection	0.005	-	-	1.99ms decrease	
T15	2.17d	Intersecting	I	F	4	near intersection	-	-	-		Abutment
		Main			11.33	away from intersection	-	-	-	Local minimum	
T16	2.17e	Intersecting	I	F	4.67	intersection	-	-	-		Abutment
		Main			11.33	near intersection	-	-	-	Local minimum	
T17	2.17f	Intersecting	I	F	4.67	intersection	-	-	-		Splay/bud
		Main			26	away from intersection	-	-	-	Significant minimum	
T18	2.16e	Intersecting	I	H	2.67	intersection	0.024	-	-		Splay/bud
		Main			24.67	away from intersection	Flat	-	-	None	
T19	2.18a	Intersecting	I	F	9.33	intersection	0.05	-	0.05		Tip bifurcation
		Main			21.34	away from intersection	0.02	-	-	Significant decrease of 10ms	
T20	2.18b	Intersecting	I	F	5.33	intersection	0.02	-	0.02		Tip bifurcation
		Main			18.67	intersection	0.02	-	-	Significant decrease of 4.67ms	
T21	2.18c	Intersecting	D	F	15.33	away from intersection	0.02	Flat	-		Soft linkage/footwall linkage
		Main			30.67	intersection	-	-	-	Significant decrease of 10.67ms	
TA	App. A1	Intersecting	D	F	12	away from intersection					Footwall linkage; intersection of three separate segments
		Main			10.67	near intersection					

Table 2.2. Summary table of T class intersection fault attributes.

from T11). It is clear from intersections T3, T4, T6, T7, T9 and T10 (Figs. 2.16) that projection of the measured displacement gradient of the intersecting faults toward the intersection would result in a zero tip location beyond the site of intersection (even at the lower end of the error range). This raises the question: do the intersecting faults have throw profiles that decrease rapidly to a zero tip value (i.e. increase in gradient as above) below seismic resolution? Alternatively, do they intersect with a small value of throw remaining at this location? These questions have implications for the interpretation of the role of interaction between the main fault and the intersecting fault (see Section 2.4.3.2).

2.3.1.3 Subset 2: Intersecting fault characterised by small throw values

This second subset of the orthogonal intersection class is also defined by a specific throw magnitude characteristic of the intersecting fault, namely a maximum cutoff limit of 5ms for the throw on the intersecting fault. Seven T intersections (T12 - T18) fall within this subset (Figs. 2.17 and 2.16e). Intersections T16 and T17 share their intersecting fault.

Intersecting faults from intersections T14, T16, T17 and T18 can be described as having a throw profile with little lateral throw variation. An overall increase in throw toward intersection is described from intersecting faults of T12 and T15 because the lowest measurement on each lies at its non-intersecting tip and is just greater than the error range of all other measurements. The final intersecting fault that fits this subdivision is that of T14. As it is closer to 250m in length it seems unusual that it has not accrued any throw values greater than c. 3ms.

The intersecting faults are typically short and reach a non-intersecting tip within approximately 150m of intersection. Interpretation of the observations provided here is given in Section 2.3.1.6.

2.3.1.4 Subset 3: Main Fault characterised by significant throw decrease at intersection

Three intersections fall within this subset, T19, T20 and T21 (Figs. 2.13 and 2.18), which are characterised by an abrupt decrease in throw values at the intersection location from one segment of the main fault to the other (Fig. 2.18). Significantly, at the intersection location, the sum of the throw value of the intersecting fault can be added to the lesser throw fault segment to equal the throw value on the greater throw fault segment.

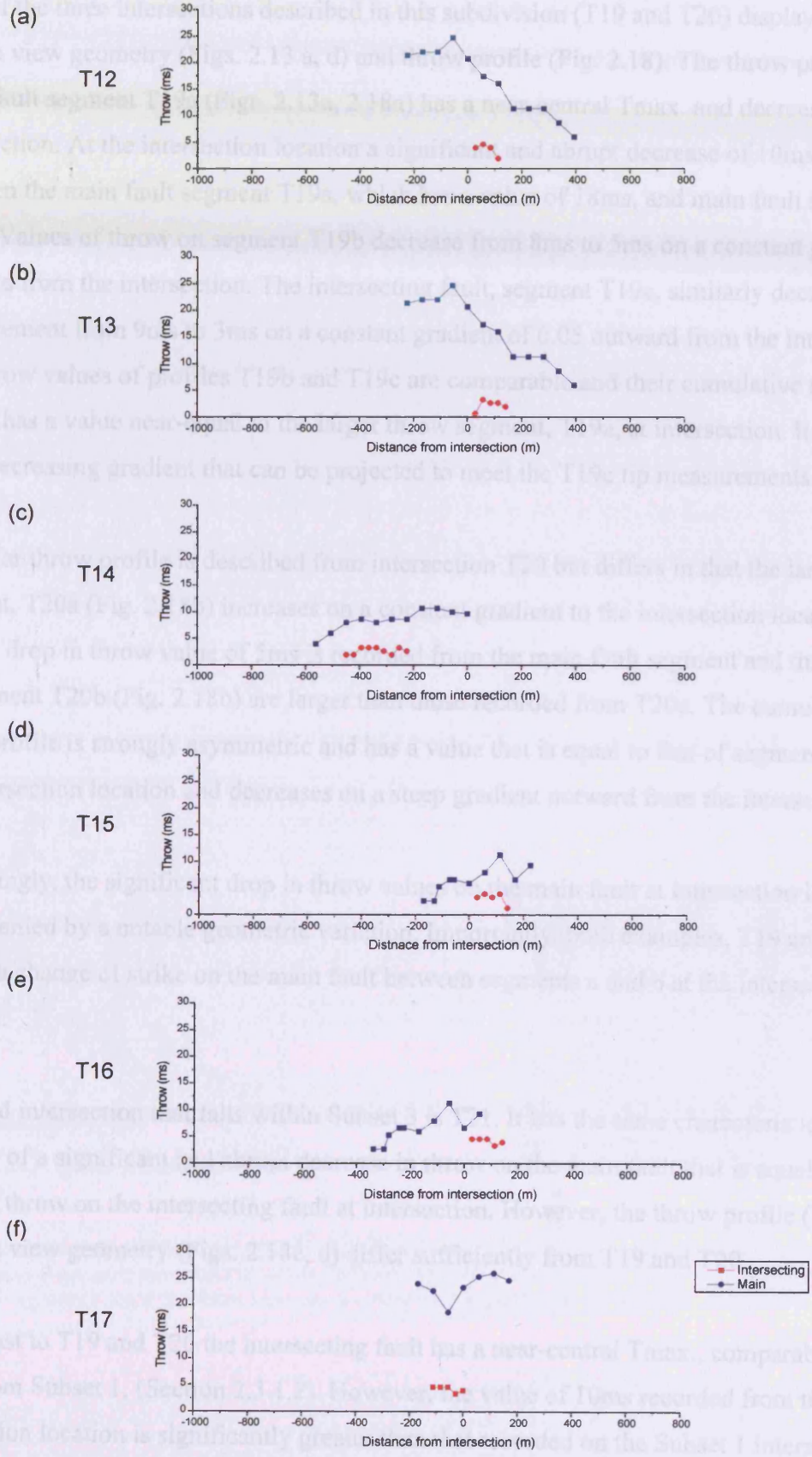

Figure 2.17. T-x plots of Subset 2 T class intersections. (a) - (f) Intersecting faults are characterised by small lengths and small throw values. The main fault displays varying responses to intersection (see text for details).

Two of the three intersections described in this subdivision (T19 and T20) display similarities in plan view geometry (Figs. 2.13 a, d) and throw profile (Fig. 2.18). The throw profile of main fault segment T19a (Figs. 2.13a, 2.18a) has a near-central Tmax. and decreases toward intersection. At the intersection location a significant and abrupt decrease of 10ms is recorded between the main fault segment T19a, which has a value of 18ms, and main fault segment T19b. Values of throw on segment T19b decrease from 8ms to 5ms on a constant gradient outward from the intersection. The intersecting fault, segment T19c, similarly decreases in displacement from 9ms to 3ms on a constant gradient of 0.05 outward from the intersection. The throw values of profiles T19b and T19c are comparable and their cumulative throw profile has a value near-equal to the larger throw segment, T19a, at intersection. It shows a steep decreasing gradient that can be projected to meet the T19c tip measurements.

A similar throw profile is described from intersection T20 but differs in that the larger throw segment, T20a (Fig. 2.18b) increases on a constant gradient to the intersection location. A smaller drop in throw value of 5ms is recorded from the main fault segment and throw values on segment T20b (Fig. 2.18b) are larger than those recorded from T20c. The cumulative throw profile is strongly asymmetric and has a value that is equal to that of segment T20a at the intersection location and decreases on a steep gradient outward from the intersection.

Interestingly, the significant drop in throw values on the main fault at intersection is accompanied by a notable geometric variation. Importantly, both examples, T19 and T20, exhibit a change of strike on the main fault between segments a and b at the intersection location.

The third intersection that falls within Subset 3 is T21. It has the same characteristics as T19 and T20 of a significant and abrupt decrease in throw on the main fault that is equal to the value of throw on the intersecting fault at intersection. However, the throw profile (Fig. 2.18c) and plan view geometry (Figs. 2.18c, d) differ sufficiently from T19 and T20.

In contrast to T19 and T20 the intersecting fault has a near-central Tmax., comparable to those from Subset 1, (Section 2.3.1.2). However, the value of 10ms recorded from the intersection location is significantly greater than that recorded on the Subset 1 intersecting faults and this value equals that of the displacement decrease between the main fault segments

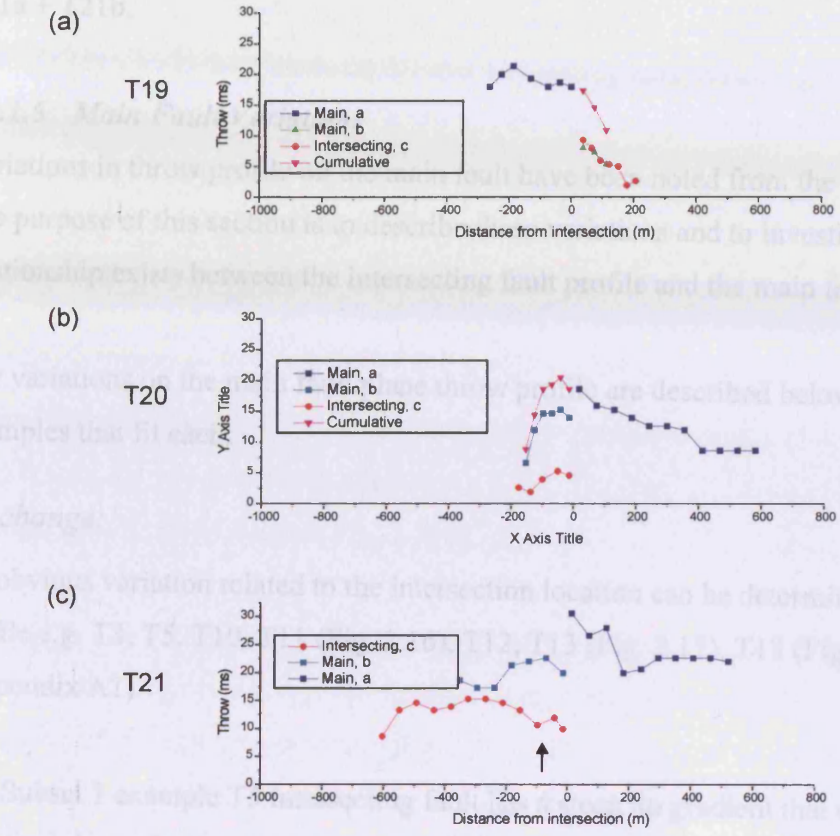

(d)

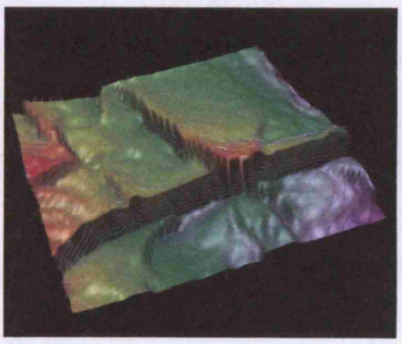

(e)

Figure 2.18. (a) - (c) T-x plots of Subset 3 T class intersections. (d) Plan view geometry of T21 intersection. (e) 3D perspective image of the middle Miocene horizon. Cumulative throw values on the intersecting fault and main fault segment b equal the throw value on the main fault segment a at the intersection location.

T21a + T21b.

2.3.1.5 Main Fault Variations

Variations in throw profile on the main fault have been noted from the intersection location. The purpose of this section is to describe these variations and to investigate whether a relationship exists between the intersecting fault profile and the main fault response.

The variations on the main fault plane throw profile are described below with T class examples that fit each.

No change:

No obvious variation related to the intersection location can be determined on the main fault profile e.g. T3, T5, T10, T11 (Fig. 2.16), T12, T13 (Fig. 2.17), T18 (Fig. 2.16e) + TA (Appendix A1).

The Subset 1 example T5 intersecting fault has a steep tip gradient that can be projected to a zero tip value at intersection. An increased tip gradient is predicted from intersecting faults of T3 and T10 and the T11 intersection exhibits a steepened tip gradient that reaches a tip a small distance from intersection.

Intersections from Subset 2 that show no variation over the main fault plane are those that have small values of throw, or no throw (T13) on their intersecting faults at intersection, with the exception of the throw profile of the T12 intersecting fault which decreases away from the intersection.

Local minimum:

A single throw value decreases from the overall trend. This may also include a localised gradient increase on the main fault profile e.g. T4, T6, T7, T8, T9 (Fig. 2.16), T15 and T16 (Fig. 2.17).

Commonly, the local minimum values lie within the error bar range of the throw values to either side therefore, it is not certain that they are always a real feature. Nevertheless, they occur frequently and are even noted at locations on main faults where unsampled intersecting faults meet (e.g. Figs. 2.15, 2.16h and 2.18c).

Rather than a local minimum, the T4 and T6 intersections record a gradient increase but they are included as they can be thought to form through the same process (see Section 2.4.3). Throw values on the intersecting fault and the main fault segment T4a are equal. Values of throw on the main fault segment T4b are very low and the main fault profile is not symmetrical.

Profile change:

A significant difference exists between the throw profiles in terms of throw values and gradients of the two main fault segments e.g. T1, T2, (Fig. 2.16), T17 (Fig. 2.17) and one example that is not described (Fig. 2.18c).

Two of the main faults that record a profile change at intersection are from Subset 1. Intersection T1 shows a complete gradient change across intersection (Fig. 2.15b), that is accompanied by a change in strike (Fig. 2.15a). The main fault of intersection T2 also displays a clear profile variation. Segment T2b (Fig. 2.16a) has a central Tmax. that decreases on a gradient of c.0.8 toward intersection. The T2a (Fig. 2.16b) segment has low values and a uniform gradient toward intersection. It is interesting to note that all three segments of these intersections have the same value of throw at intersection.

Significant decrease:

A significant and abrupt throw decrease exists at the site of intersection (with lower values maintained beyond intersection location) e.g. T19, T20 + T21 (Fig. 2.18).

Main faults that display significant decrease in throw at intersection are Subset 3 faults and have been described in Section 2.3.1.4.

2.3.1.6 Kinematic Interpretation of T class

The purpose of this section is to provide a summary interpretation of the results of the descriptive section above in order to define key propagation styles within the geometrical classes. New terminology is defined and this summary provides a basis for discussion of evolutionary styles within the GR PFS (Section 2.4).

By far the majority of intersections have a throw profile of the intersecting fault that decreases in throw from a near-central Tmax. value toward the intersection location. This characteristic is indicative of Subset 1 of the T class (Sections 2.3.1.1, 2.3.1.2) and is interpreted to represent lateral propagation of the intersecting fault toward the main fault. This type of intersection, which forms through propagation of an intersecting fault toward a main fault, is termed Accidental Intersection in this thesis, to reflect the totally separate initial propagation of each fault.

From the observed changes in the throw close to intersection and the observation that intersecting tip gradients have higher values than non-intersecting tip gradients, an interpretation of a mechanical inter-relationship between the intersecting faults can be reached. It is interpreted that the presence of the main fault restricts, and leads to arrested propagation of the intersecting fault, a relationship that is herein termed Abutment (See Section 2.4.3) (c.f. Nicol et al, 1996; Wilkins and Gross, 2002).

Where the main faults of the accidental intersections exhibit no change in throw at the intersection location, it is suggested that they were unaffected by the approaching intersecting fault. Examples of variation in throw profile of the main fault – either a local minimum or a local gradient change – were recorded for some Subset 1 intersections. This is interpreted to record the relationship with the intersecting fault and may relate to the area ahead of the propagating tip of the intersecting fault which may be ductile deformation (Section 2.4.3.2). Where throw values decrease toward the error limit close to the intersection point, caution must be applied in interpreting the significance of profile trends and tip variations may exist below seismic resolution.

A good example of very pronounced variation in throw in the vicinity of an intersection was recorded from the T21 Subset 3 intersection. In this example, the cumulative throw of the intersecting fault and the main fault segment with lesser throw was equal to the main fault segment with greater throw at intersection. This relationship strongly suggests that the three segments are mechanically interrelated. From the decrease in throw profile toward the intersection, the T21 intersection is also interpreted to form initially through accidental intersection. This is a clear example where the intersecting fault can be interpreted to have linked to the main fault. This is a hard linkage state (c.f. Walsh and Watterson, 1991) and is a

rare type of intersection reported from the GR PFS. Hard linkage at a non-colinear intersection will be discussed in Section 2.4.3.2.

Where an abrupt change in throw profile is seen along the main fault at the intersection zone, all three segments are interpreted to have propagated separately, with potential linkage of the two main segments. This is a likely interpretation for intersection T1, for example, since a strike change on the main fault is also mapped at this point. Alternatively, it is possible that the gradient variation is related to other factors such as relation to other, unsampled fault intersections. In such examples it is interesting that all three segments, that were initially propagating separately, intersected in the same location. An explanation for why this occurs should be sought.

The second T class subset encompasses short intersecting faults from which it was difficult to describe a throw profile trend as throw values were dominantly <5ms. Examples T15 and T16 exhibited a local minimum relationship with the main fault, and no change on the main fault throw profile was exhibited by the other examples. These observations are interpreted to show that the majority of Subset 2 intersecting faults are in a very early stage of growth that can be described as splaying or budding outward from the main fault plane. Propagation outward from a main fault is termed Branching Intersection within this thesis.

An exception to the interpretation of branching is identified from the intersecting fault of T16 and T17 as propagation was either from one main fault to the other or the intersecting fault initiated somewhere between the structures. It is suggested that this small intersecting fault formed to accommodate strain in this region (i.e. a breach fault) and may thus have propagated from the centre toward the intersections.

In summary, the small values of throw that have accrued on the intersecting faults within this subdivision coupled with their short length point to a propagation style initiating at or close to the main fault and propagating outward. These can therefore be broadly termed splay intersections. It is expected that these faults can grow and propagate toward abutting intersections with other planes.

The final propagation relationship described from this analysis is also largely identified by the throw variation on the main fault plane profile. It is characterised by a throw value on the

main fault segment that is equal to the cumulative throw on the other two segments. These lesser throw segments decrease in throw from the intersection location thus defining this intersection type as a branching intersection. In addition, both lesser throw segments vary in strike from the main fault trend and this may be a definitive characteristic of this type of evolution. This relationship is termed Lateral Bifurcation as it is interpreted that the main fault bifurcates and shares its displacement between the two new segments. This lateral bifurcation mode of evolution is also recorded from Y class (Section 2.3.3) and TR class (Section 2.3.2) geometries where a 3D case study describes the growth style in more detail.

Throw profiles characteristic of lateral bifurcation are unique in that a significant and abrupt decrease in throw is recorded from the main fault at intersection and that the intersecting fault and the lesser throw main fault segment effectively share the throw distribution on the greater throw main fault segment. Combined with the variation in strike that is identified on the main fault at the intersection location, the observations are consistent with a lateral bifurcation style of evolution (see also Sections 2.3.2 and 2.3.3).

In summary, interpretation of intersection evolution is gained by combining the interpretations of intersecting fault propagation direction from the T class subdivisions with the variation in throw recorded on the main fault. In almost all recorded cases it can be argued that an interaction exists between the main fault and the intersecting fault in a T class intersection. T class intersections form most commonly through accidental intersection. Of these, abutment is the most common stage of T class evolution.

2.3.2 Kinematic analysis of TR Intersections

Throw data for 7 TR class intersections was acquired and analysed. The results mainly support interpretation of propagation kinematics that have been described from previous T class geometries therefore only 4 examples are presented here (and a further 3 in Appendix A2). The first example is a detailed 3D throw analysis of a TR intersection that displays a characteristic profile that is repeatedly found within the dataset and is extremely important for understanding propagation style in the GR PFS.

2.3.2.1 3D analysis of a TR class intersection

TRA Geometry

The plan view geometry (Fig. 2.19a) of the TRA intersection has three free tips at the middle Miocene horizon level and segment TRAa is significantly greater in length than the other two segments. This greater length is also reflected in the greater depth of section that it deforms (Figs. 2.19b-e). Two seismic profiles are presented from the TRAa segment, the first at its southern extent (Fig. 2.19b) and the second toward the north (Fig. 2.19c). The southern profile displays the TRAa segment cutting through the Miocene section with a dip of ~50° and a maximum throw at 2180ms TWT. It can be interpreted as crossing the diagenetic reflection below which the dip value decreases significantly to ~38° and a second throw maxima is identified at 2600ms TWT. In contrast, the northern seismic profile (Fig. 2.19c) shows two distinct faults – one that deforms Miocene sediments and the other that deforms Oligocene sediments. They are not linked in the dip direction. Each sampled profile line showed one of the above relationships – either a shallower dip with depth or a separation of the faults. Therefore the faults are interpreted to be two separate structures and the deeper fault is cut obliquely by some profile lines (explaining the shallow dip) and is thus excluded from further analysis.

The TRAb segment seismic profile (Fig. 2.19d) shows this fault segment to have very little expression in the depth section and displays brittle offset between 1943ms to 2292ms TWT. The TRAc segment trace (Fig. 33d) dips 50° and is deformed between 1891ms and 2194ms TWT. The perspective view of the mapped fault planes (Fig. 2.20a) shows a branch line with a consistent plunge and dip between segments TrAa and TRAc that is also shared in part by segment TRAb. The TRAb fault plane is displayed as significantly smaller than the other segments (in part due to cropping by the software gridding tools) and the TRAc segment decreases in vertical extent towards its tip.

The 3D perspective view of the middle Miocene horizon (Fig. 2.20b) is an important image as it visually describes throw profiles from this horizon. Notably, segments TRAb and TRAc have throw values that equal the value of throw on segment TRAa at the intersection location. A common footwall is shared by segments TRAa and TRAc and a common hangingwall between segments TRAa and TRAb.

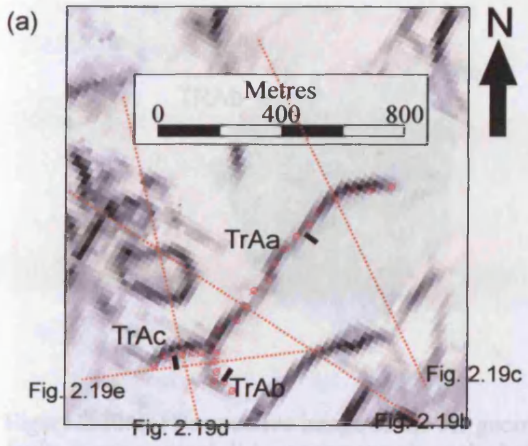

Figure 2.19. Geometry of the TRA intersection. (a) Plan view geometry on the middle Miocene horizon. Segment TRAa is significantly longer than Segments TRAb and TRAc. The strike of segment TRAa bisects the strike orientations of the other segments. (b) Seismic profile line through segment TRAa. Two faults can be identified that are separated by the diagenetic transition. (c) Seismic profile line through segment TRAa. The fault trace appears to be continuous from above to below the diagenetic transition, but shallows in gradient. (d) Seismic profile line through segment TRAb. The fault is entirely constrained within the Miocene interval and displays small throw values. (d) Seismic profile line through segment TRAc. The fault is entirely constrained within the Miocene interval and displays small throw values.

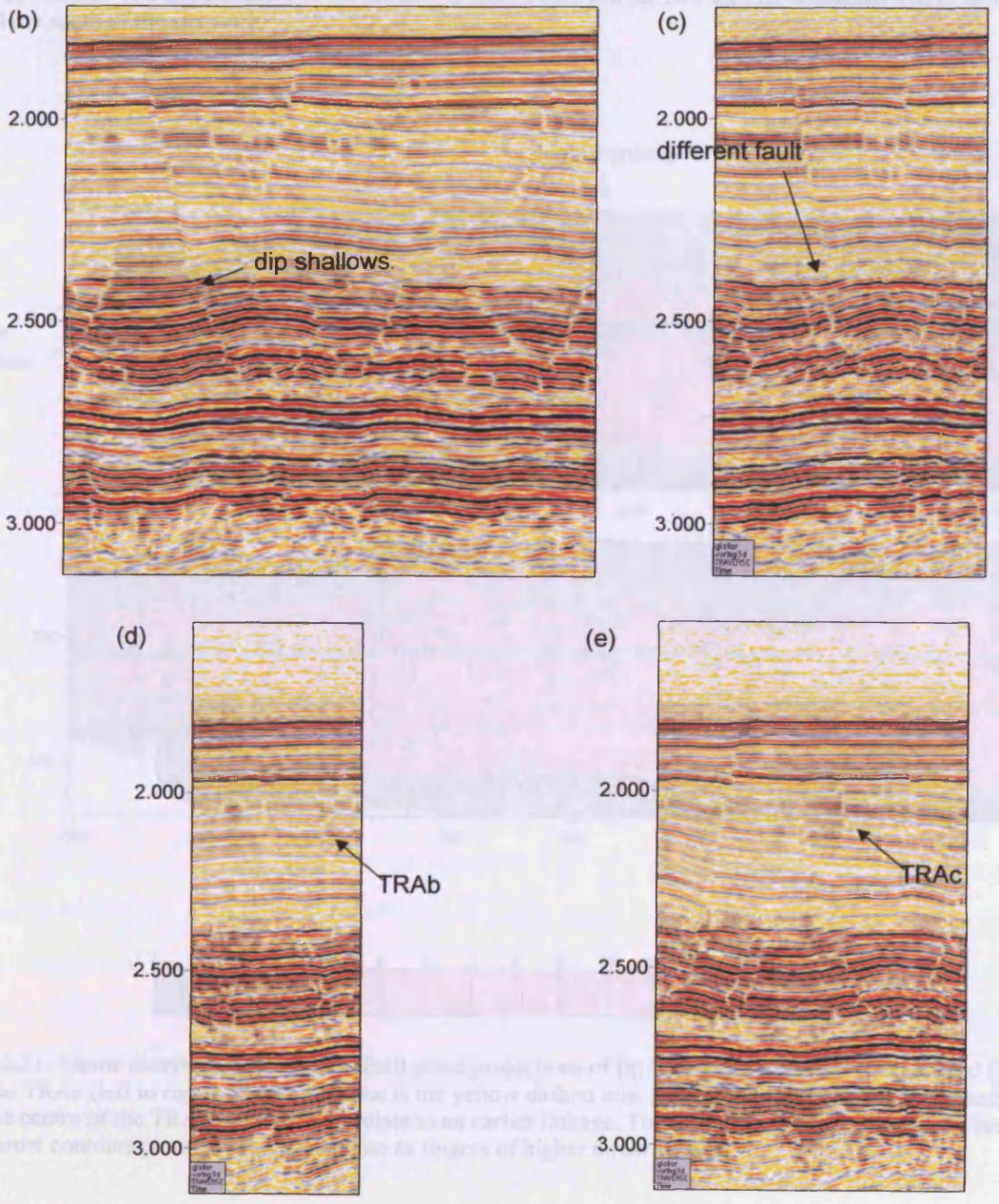

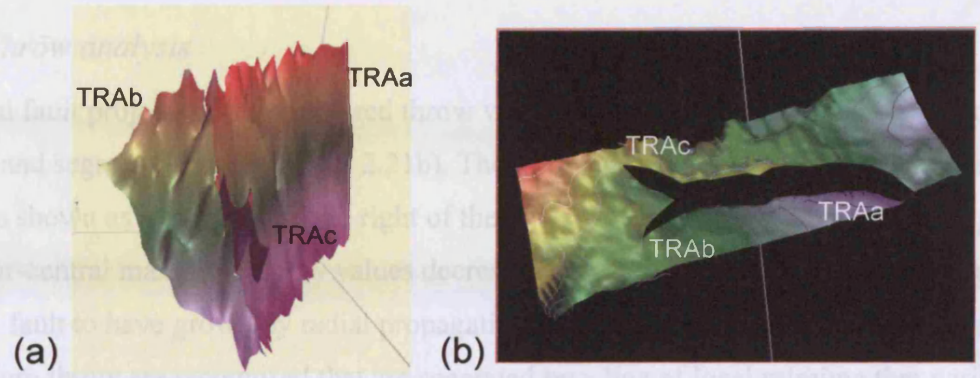

Figure 2.20. (a) Perspective image of the 3D geometry of the mapped fault planes. The branch line between the faults is sub-vertical. It is continuous along the height of the faults for the TRAa and TRAb segments. The TRAc segment shares the branch line over a shorter height (this is partly limited because of clipping by the software tools). Segments TRAb and TRAc strike obliquely to the TRAa segment. (b) Perspective image of the middle Miocene horizon. The displacement of the horizon is shared between the two smaller segments, TRAb and TRAc toward the south of the structure.

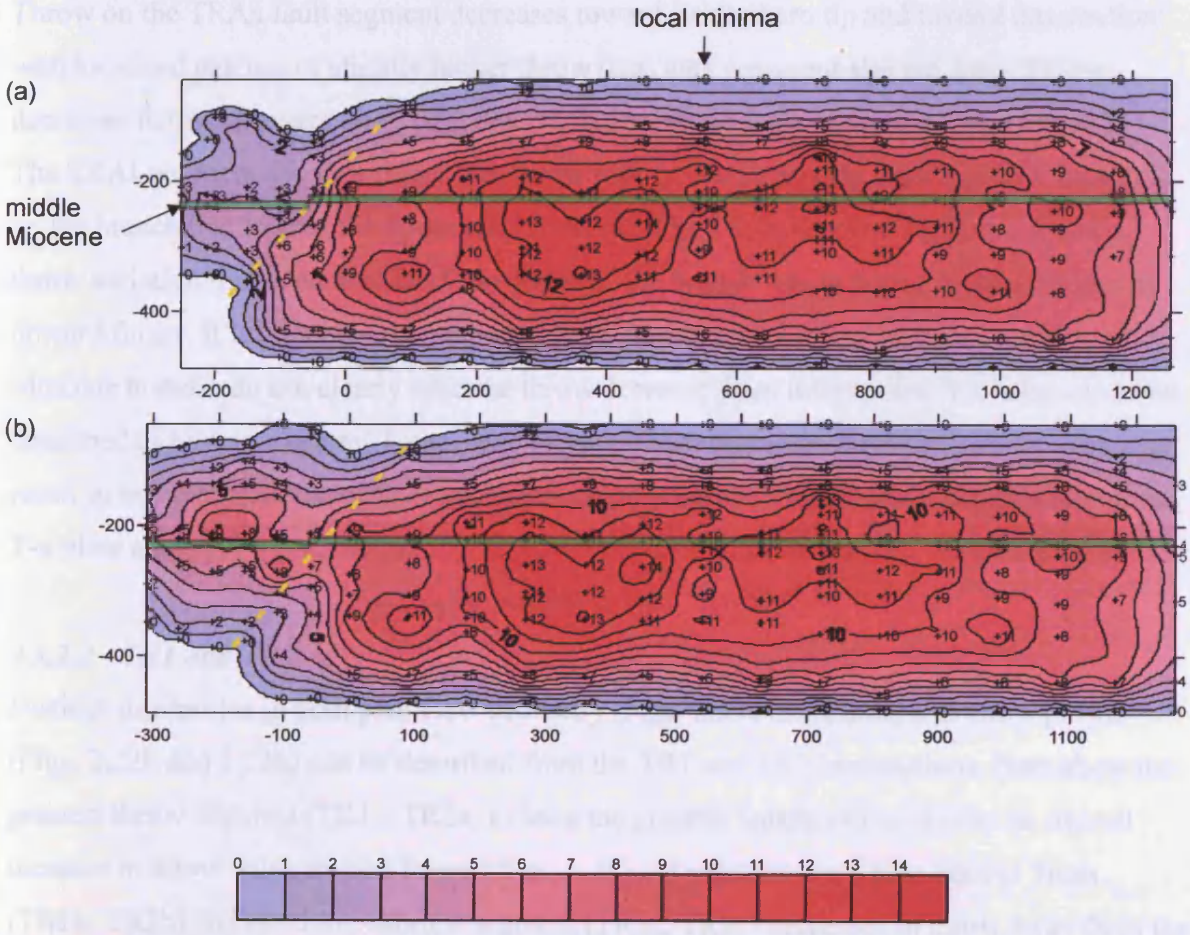

Figure 2.21. Throw distribution on vertical fault plane projections of (a) TRAc to TRAa (left to right) and (b) TRAb to TRAa (left to right). The branch line is the yellow dashed line. A local minimum of throw is identified from the centre of the TRAa plot that may relate to an earlier linkage. Throw values decrease toward the branch line. Throw contours penetrate the branch line as fingers of higher throw values.

TRA Throw analysis

Vertical fault projections of contoured throw values are displayed as segment TrAa to b (Fig. 2.21a) and segment TrAa to c (Fig. 2.21b). The throw distribution on fault plane segment TrAa is shown as everything to the right of the intersection location on both plots (Figs. 2.21a, b). Near-central maximum throw values decrease to an elliptical zero tip line showing this Type 3 fault to have grown by radial propagation. However, two distinct central areas of maximum throw are recognised that are separated by a line of local mimima that varies between 1 and 3ms below the values to either side. This is a very small throw variation but can be interpreted to show an early linkage between two fault planes. Although no obvious variations are seen at this location from the base map in Figure 2.19a, a small strike change may be imaged on the 3d horizon perspective image (Fig. 2.20b).

Throw on the TRAa fault segment decreases toward its northern tip and toward intersection with localised patches of slightly higher throw (that may represent slip patches). Throw decreases across intersection to both the TRAb and TRAc fault segment planes (Fig. 2.21). The TRAb segment shows a finger-like throw pattern that decreases from a central location on the branch line toward the upper and lateral tip. The TRAc segment similarly shows a throw variation that decreases from the centre of the branch line to a zero tip in a diagonally upward finger. It is interesting to note that throw variations extracted from the middle Miocene horizon do not clearly describe throw decrease from intersection but rather could be described as having a central Tmax. (c.f. TR1b + TR2b segments, Section 2.3.2.2). This may result in misinterpretation of fault evolution and highlights a limitation of interpretation from T-x plots alone.

2.3.2.2 TR1 and TR2

Distinct similarities in both plan view geometry (Figs. 2.22a and 2.23a) and throw profile (Figs. 2.22b and 2.23b) can be described from the TR1 and TR2 intersections. Both show the greatest throw segment (TR1a, TR2a) to have the greatest length and to display an overall increase in throw value toward intersection. A second segment has a near-central Tmax. (TR1b, TR2b) and the third, shortest segment (TR1c, TR2c) decreases in throw away from the intersection location. The cumulative plot from the lesser throw segments TR1b and TR1c has a throw value at intersection that is equal to that of the TR1a segment. Additionally, the cumulative plot smoothes the profile between segment TR1a and TR1b. The throw value of

(a)

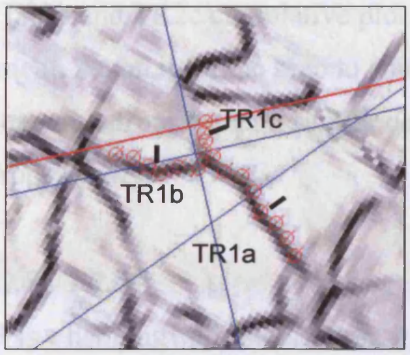

(b)

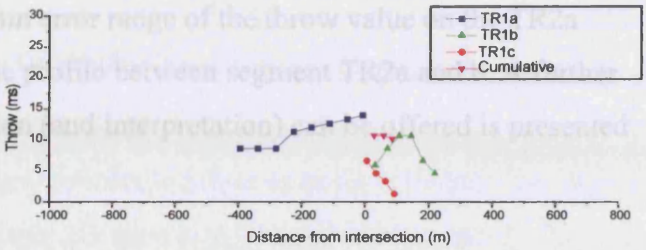

Figure 2.22. (a) Plan view geometry of the TR1 intersection at middle Miocene level. (b) T-x plot of the TR1 intersection at middle Miocene level. The cumulative throw 'bridges' the TR1a to TR1b profile.

(a)

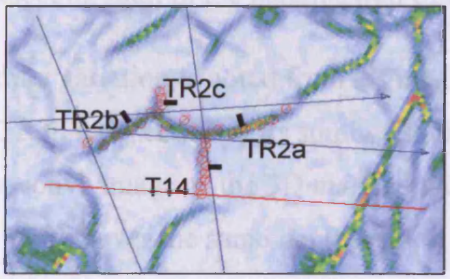

(b)

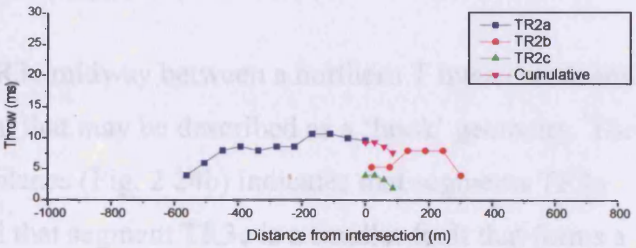

Figure 2.23. (a) Plan view geometry of the TR2 intersection at middle Miocene level. (b) T-x plot of the TR2 intersection at middle Miocene level. The cumulative throw 'bridges' the TR1a to TR1b profile.

(a)

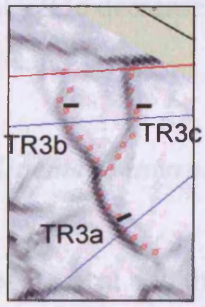

(b)

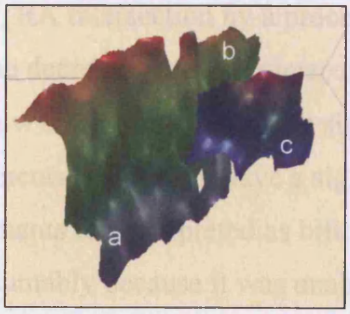

(c)

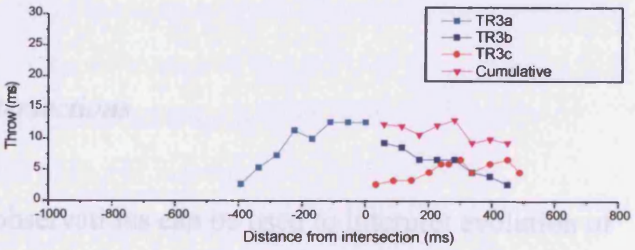

Figure 2.24. (a) Plan view geometry of the hangingwall intersection, TR3, at middle Miocene level. (b) Perspective view of the mapped fault planes in 3D. (c) the intersecting fault decreases in throw toward intersection. The cumulative profile of the TR3b and TR3c fault segments has a value equal to TR3a at the intersection location.

the TR2b and TR2c cumulative plot is within error range of the throw value on the TR2a segment. Again it can be seen to smooth the profile between segment TR2a and b. A further TR example from which a similar description (and interpretation) can be offered is presented as Appendix A2.

2.3.2.3 TR3

TR3 is a hangingwall intersection. It has a plan view geometry (Fig. 2.24a) that fits the classification of triple-junction from angles measured in close proximity to the intersection. However, an overall alignment in strike between segments TR3a and TR3b (which varies notably at intersection) suggests that these formed the main fault and segment TR3c is the intersecting fault in the hangingwall of the main fault.

A strike variation is noted from segment TR3c midway between a northern T intersection and the TR3c intersection at its southwest extent that may be described as a 'hook' geometry. The perspective image of the 3D mapped fault planes (Fig. 2.24b) indicates that segments TR3a and TR3b cover the same depth section and that segment TR3c is a smaller fault that forms a consistently plunging branch line with the main fault plane.

The throw profile for the TR3 intersection (Fig. 2.24c) is particularly interesting. Once again, the throw values on the lesser throw plots equal the greater throw profile at intersection. In this case, throw of both segments TR3a and TR3b increase toward the intersection and throw of segment TR3c decreases. The cumulative plot forms a near-symmetrical profile with segment TR3a.

2.3.2.4 Kinematic interpretation of TR intersections

TRA

The 3D geometrical and throw distribution observations can be used to interpret evolution of the TRA intersection by a process of lateral bifurcation. Throw distribution on the TRAa plane decreases toward intersection suggesting that this segment propagated toward this point. Throw distribution decreases significantly at the intersection location to the TRAb and TRAc segments which both have a significantly different strike to the TRAa segment. These segments are interpreted as bifurcating from the propagating tip of segment TRAa, presumably because it was unable to continue propagation on the same strike (possibly due to a local inhomogeneity), and the segments TRAb and TRAc share the displacement that has

been distributed from the segment TRAa fault plane. Segment TRAa can be projected to show a near-equal bisection angle (Fig. 2.19a).

The fault projections highlight the location of the middle Miocene horizon intersection with the fault planes. Because of the diagonal finger of higher slip (instead of horizontal) a T-x description of throw distribution from the middle Miocene horizon would show a local minimum near the intersection location. Therefore the interpretation of lateral bifurcation may not have been reached without the extra information that is gained from a throw-contoured vertical fault plane map. In particular, where fault segments display a C-shaped profile (particularly within error bar range of one another) they are typically interpreted as a separate segment. However they may evolve outward and upward, as in this case (see TR1 + TR2).

The observation that the value of throw on the two lesser segments adds up to the value on the larger throw segment is thought to be critical and was also noted from T class intersections, T19 and T20 (and from Y class intersection, Y1, see Section 2.3.3). This strongly suggests that a kinematic relationship exists between the three segments and that evolution of the intersection is in some way linked.

TR1 and TR2

It is not easy to explain why the maximum throw value on TR1a and TR2a are located at the intersection location. Indeed, maximum throw has been interpreted to relate to nucleation location, however, asymmetric throw profiles are known from interaction with other fault segments (Peacock and Sanderson, 1991) creating maximum throw locations closer to one tip than another. It may be possible to propose that these examples accord with the interpretation of Lonergan et al. (1998) that all three segments evolved from a single nucleation position (strain distribution focused on the larger throw segment more than the others). This observation supports growth by lateral bifurcation. However, the TRb segments both show a minimum rather than a maximum at the intersection location although this may be a function only of the single horizon on which throw is analysed (see case study TRA). An alternative interpretation is that the TRa and TRb segments linked requiring that segment TRc splayed from the intersection to accommodate excess strain. It would also be necessary for this linkage to create the asymmetric throw profile that results in a throw increase toward intersection on the TRa segments. The systems can be described as kinematically closed.

TR3

From the observation that the main fault segments TR3a to TR3b have a near-central Tmax. value that is offset by the value of throw on the intersecting fault at the intersection location, a hangingwall linkage interpretation can be put forward for evolution of this intersection. This has not previously been reported from a PFS or a tectonic fault system and is thought to be very rare as only 5% of orthogonal intersections were recorded as occurring in the hangingwall. It is suggested that linkage is in an early stage as the throw value recorded at the intersection location on the intersecting fault is only 3ms.

In summary, the kinematic interrelationship between segments in a triple-junction class intersection is typically characterised by the cumulative throw values of the two lesser throw segments being equal to the larger throw value. TRA, TR1 and TR2 are interpreted to have evolved through lateral bifurcation.

2.3.3 Kinematic analysis of Y intersections

The throw distribution from three selected Y class intersections is described in order to investigate their evolution. Four Y intersections were studied in the course of this work. A further example is presented in Appendix A3.T

2.3.3.1 Y1 and Y2 throw analysis

Fault intersections Y1 and Y2 are characterised by cumulative throw profiles on the lesser throw segments that are equal to the larger throw segment at the intersection location (c.f. Subset 3 of T class intersections, Section 2.3.1.4).

Throw on the Y1a segment (Fig. 2.25a, b) increases toward a maximum of 20ms at a distance of 75m from the intersection on a fairly constant gradient of 0.03, then decreases to a value of 15ms at intersection. The throw on the Y1b segment (Fig. 2.25b) has a value of ~7ms at intersection and approximately maintains this value to the sampled tip. Throw on the intersecting fault decreases from a value of 8ms near intersection to 4ms at its northern tip. The cumulative throw values of the Y1b and c segments form a throw profile that is equal to the Y1a segment throw at intersection and decreases outward from intersection on a gradient that mirrors that of the throw profile increase on the Y1a segment. In this way, the Y1a profile, together with the cumulative profile, displays a near-symmetrical profile with a central Tmax. position.

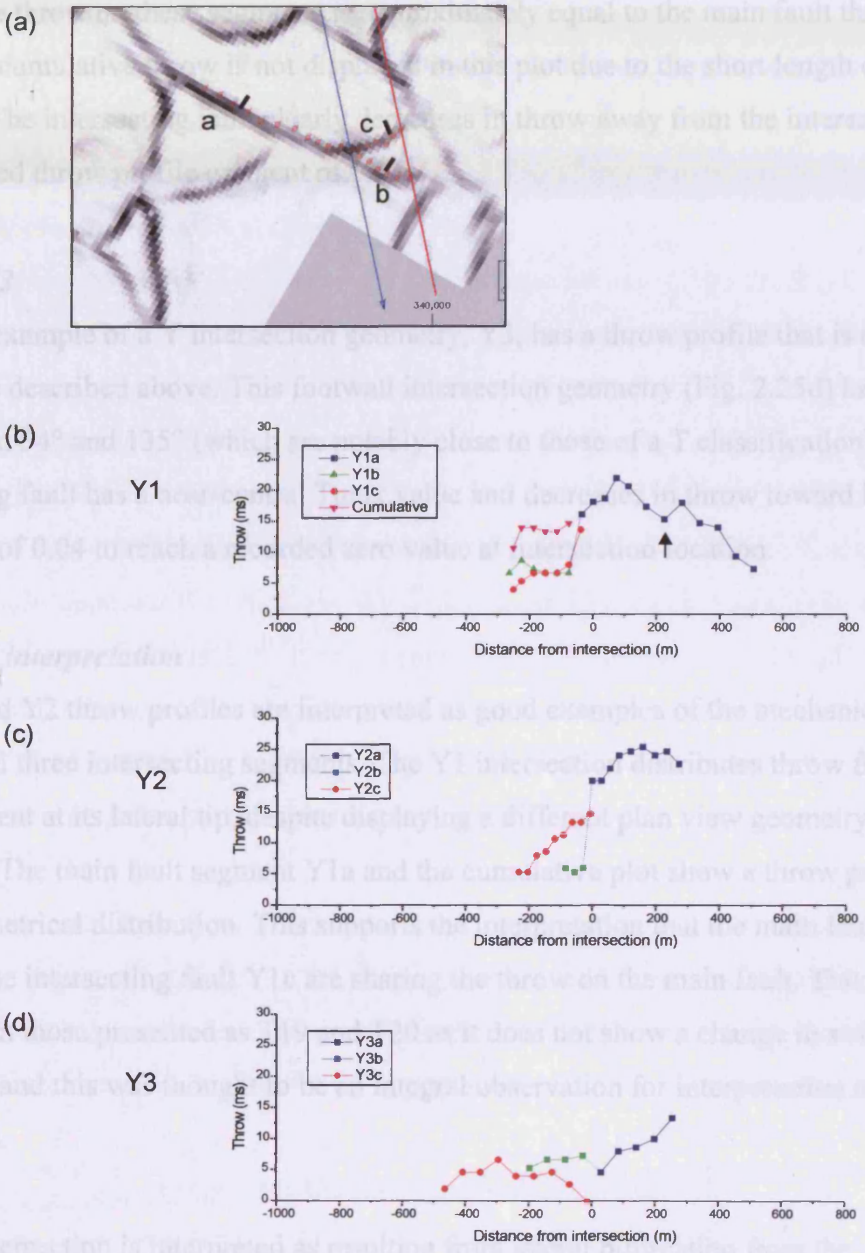

Figure 2.25. Throw distribution of Y intersections. (a) Plan view of the Y1 intersection at middle Miocene level. (b) T-x plot of the Y1 intersection at middle Miocene level. Throw on the Y1a segment decreases abruptly at the intersection location. The cumulative throw of segments Y1b and Y1c is equal to the throw of segment Y1a at intersection, and the cumulative profile mirrors the Y1a profile. (c) T-x plot of the Y2 intersection. The Y2c, intersecting fault, segment decreases in throw outward from the intersection. Cumulative throw values on the Y2c and Y2b segments equal the throw value of the Y2a segment at the intersection location. (d) T-x plot of the Y3 intersection. Throw on the Y3c segment decreases toward intersection. The throw location is marked on the main fault by a local minimum.

The throw profile of the Y2 footwall intersection (Fig. 2.25c) shows some similarities to Y1 in that throw decreases over the intersection on the main fault. At the intersection location cumulative throw on these segments is approximately equal to the main fault throw value. However, cumulative throw is not displayed in this plot due to the short length of the Y2b segment. The intersecting fault clearly decreases in throw away from the intersection on a well-defined throw profile gradient of 0.04.

2.3.3.2 Y3

The third example of a Y intersection geometry, Y3, has a throw profile that is quite different from those described above. This footwall intersection geometry (Fig. 2.25d) has angles of intersection 54° and 135° (which are notably close to those of a T classification). The intersecting fault has a near-central Tmax.value and decreases in throw toward intersection on a gradient of 0.04 to reach a recorded zero value at intersection location.

2.3.3.3 Y interpretation

The Y1 and Y2 throw profiles are interpreted as good examples of the mechanical interaction between all three intersecting segments. The Y1 intersection distributes throw from the main fault segment at its lateral tip, despite displaying a different plan view geometry to previous examples. The main fault segment Y1a and the cumulative plot show a throw profile with a near-symmetrical distribution. This supports the interpretation that the main fault segment Y1b and the intersecting fault Y1c are sharing the throw on the main fault. This example differs from those presented as T19 and T20 as it does not show a change in strike on the main fault and this was thought to be an integral observation for interpretation of lateral bifurcation.

The Y2 intersection is interpreted as resulting from lateral bifurcation from the observations that the main fault throw value decreases by a value that is equal to the intersecting fault throw at intersection. Previously described examples of bifurcating intersections exhibit either equal values of displacement on bifurcating segments (T19 and Y1) or the bifurcating main fault segment has greater throw than the intersecting segment (T20). In contrast, this example (Y2) shows most clearly that throw on the intersecting fault is a maximum at the intersection and that it decreases away from it. This is believed to best match a model of lateral bifurcation.

2.3.4 Kinematic analysis of X intersections

The occurrence of X class intersections in the GR PFS is rare, but they are worthy of further consideration. This section presents observations of 3D geometry and throw analysis from two X class intersections and T-x analysis from two further examples (see also Appendix A.4) in order to address the question of how they evolve.

2.3.4.1 3D analysis of X class intersection, XA

The plan view geometry of XA on the middle Miocene horizon (Figs. 2.26a, d) is a near-orthogonal intersection and fault segments show no variation in strike and dip to their opposite segment across intersection. The plan view geometry varies through the depth section and this is illustrated by a series of coherence slices (Fig. 2.26b), and from the mapped fault planes displayed in 3D space (Fig. 2.26c). The plan view geometry varies between a T class intersection in the shallow vertical section (e.g. 1932ms TWT) to an X class intersection within the mid-depth vertical window (e.g. 2028ms TWT) then back to a T class geometry again at depth (e.g. 2336ms TWT). The mapped fault planes (Fig. 2.26c) highlight that at greater depth the two fault planes do not intersect in the upper Oligocene – lower Miocene section. This image shows that the T class geometries can be limited in the depth section where intersecting fault tip shapes are near-elliptical.

The three segments XAa, XAc and XAd all deform the sedimentary section from the seabed to close to the Intra Oligocene unconformity. Segment XAb differs considerably from the other three segments in that it cuts through only the upper Miocene-Pliocene stratigraphy (Type 3 fault, section 3.2.2.2) as described above.

XA Throw analysis

T-z plots (Fig. 2.27a) show that fault segments XAc, XAd and XAa are Type 2 faults (section 3.2.2.2). Both the XAc and XAd segments have very similar profile shapes and support an interpretation that the XAc segment to XAd segment can be interpreted as one fault plane. Segment XAb is a Type 3 fault therefore all faults in this description grew by radial propagation.

Further information on propagation style can be gained from 3D throw distributions of the faults (Fig. 2.27b - d). Fault segments XAc - XAd have a common central maximum throw area located around 500ms below the seabed. The fault plane has an overall elliptical throw

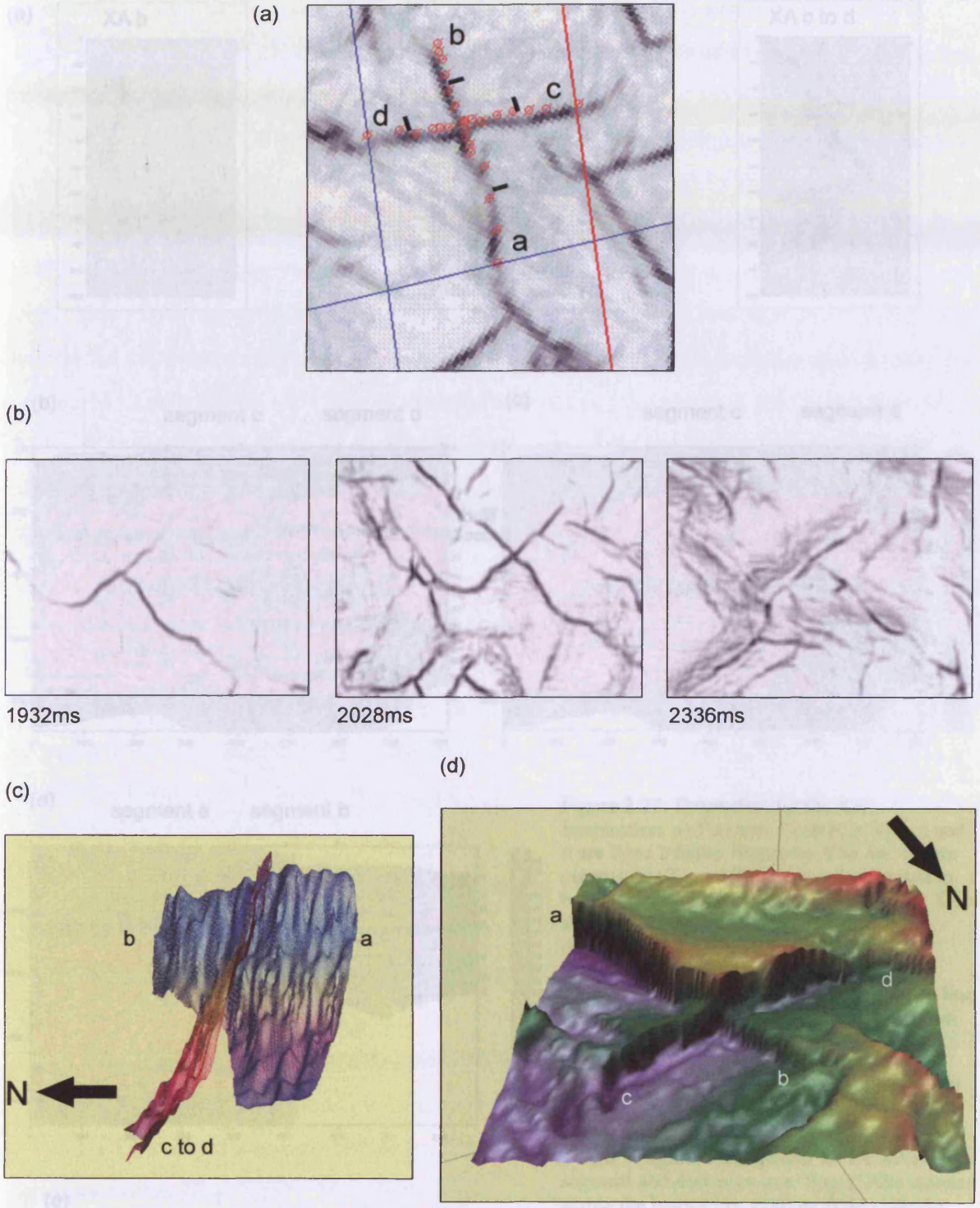

Figures 2.27. Geometry of the XA intersection. (a) Plan view geometry at the middle Miocene level. The cross-cutting intersection is orthogonal. Fault segments are continuous in strike and dip across the intersection. (b) Coherence slices illustrate that the geometry changes within the vertical section from a T class intersection to an X class intersection then back to a T class intersection at depth. (c) 3D image of mapped fault planes. The cross-cutting geometry is only maintained over a limited vertical interval in the shallow section. At depth, there is no intersection between the fault planes. (d) 3D image of the offset of the middle Miocene horizon by the XA faults. Segment b has less throw than the other segments in the system.

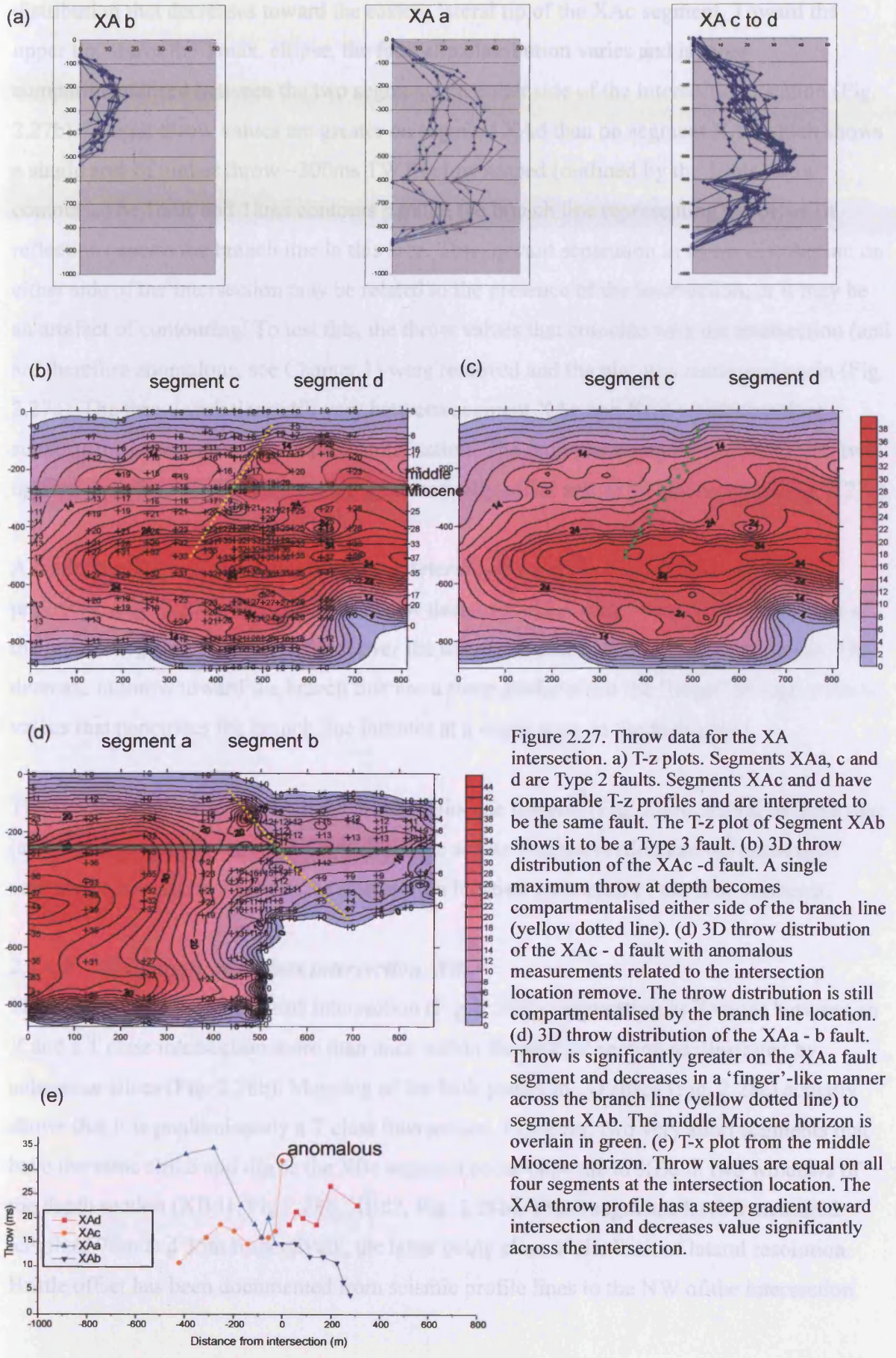

Figure 2.27. Throw data for the XA intersection. a) T-z plots. Segments XAa, c and d are Type 2 faults. Segments XAc and d have comparable T-z profiles and are interpreted to be the same fault. The T-z plot of Segment XAb shows it to be a Type 3 fault. (b) 3D throw distribution of the XAc -d fault. A single maximum throw at depth becomes compartmentalised either side of the branch line (yellow dotted line). (d) 3D throw distribution of the XAc - d fault with anomalous measurements related to the intersection location remove. The throw distribution is still compartmentalised by the branch line location. (d) 3D throw distribution of the XAa - b fault. Throw is significantly greater on the XAa fault segment and decreases in a 'finger'-like manner across the branch line (yellow dotted line) to segment XAb. The middle Miocene horizon is overlain in green. (e) T-x plot from the middle Miocene horizon. Throw values are equal on all four segments at the intersection location. The XAa throw profile has a steep gradient toward intersection and decreases value significantly across the intersection.

distribution that decreases toward the eastern lateral tip of the XAc segment. Toward the upper tip, above the Tmax. ellipse, the fault slip distribution varies and is more compartmentalised between the two segments on either side of the intersection location (Fig. 2.27b). Overall throw values are greater on segment XAd than on segment XAc which shows a single area of higher throw ~200ms TWT below seabed (outlined by the 16ms throw contour). The 16ms and 18ms contours parallel the branch line representing the offset of reflections across the branch line in this area. This upward separation in throw distribution on either side of the intersection may be related to the presence of the intersection, or it may be an artefact of contouring. To test this, the throw values that coincide with the intersection (and are therefore anomalous, see Chapter 1) were removed and the plot was contoured again (Fig. 2.27c). The throw variations still vary between segment XAc and XAd which therefore supports the observation of compartmentalisation. The fault plane may be separated into two upward growth areas. Reflections are systematically offset across the intersection (Fig. 2.27c).

A distinctly different throw distribution is determined from the XAa to XAb vertical projection (Fig. 2.27d). Most notably, throw decreases elliptically from the southern edge of the plot on segment XAa toward and over the intersection in a 'finger'-like distribution. The decrease in throw toward the branch line has a steep gradient and the 'finger' of higher throw values that penetrates the branch line initiates at a single area on the fault plane.

Throw values are extracted from the middle Miocene horizon (Fig. 2.27e. 2.26d) to show that (a) there is no notable variation on each profile across the intersection and (b) near-equal values of throw are recorded at the intersection location from each of the four segments.

2.3.4.2 3D analysis of X class intersection, XB

This plan view geometry of this intersection (Fig. 2.28a) is interesting as it varies between an X and a T class intersection more than once within the vertical section as illustrated by coherence slices (Fig. 2.28b). Mapping of the fault planes in 3D space (Fig. 2.28c) actually shows that it is predominantly a T class intersection. However, two very short segments that have the same strike and dip as the XBc segment occur opposite to XBc in two windows of the depth section (XBd1, Fig.2.28b, XBd2, Fig. 2.28b). These segments have a measured length of 70m and 35m respectively, the latter being close to the limit of lateral resolution. Brittle offset has been documented from seismic profile lines to the NW of the intersection.

(a)

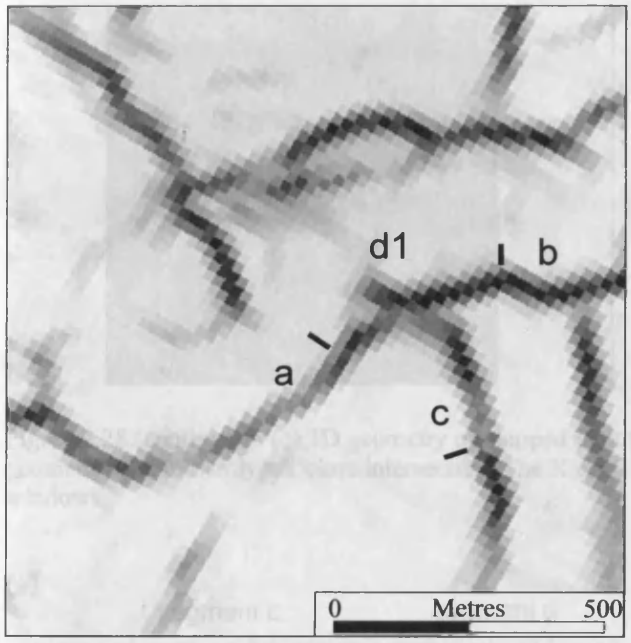

Figures 2.28 Geometry of the XB intersection. (a) coherence extraction of the middle Miocene horizon showing the plan view geometry of the XB intersection. A short segment, XBd1 has a continuous strike and dip to segment XBc across the intersection with XAa to XAb. (b) Series of coherence slices that describe the XB geometry variation throughout the vertical section. The upper and central sections are a T class intersection (2140ms and 2340ms). Segments XBd1 and XBd2 cross-cut the main fault plane in two windows of the vertical section (2240ms and 2440ms).

(b)

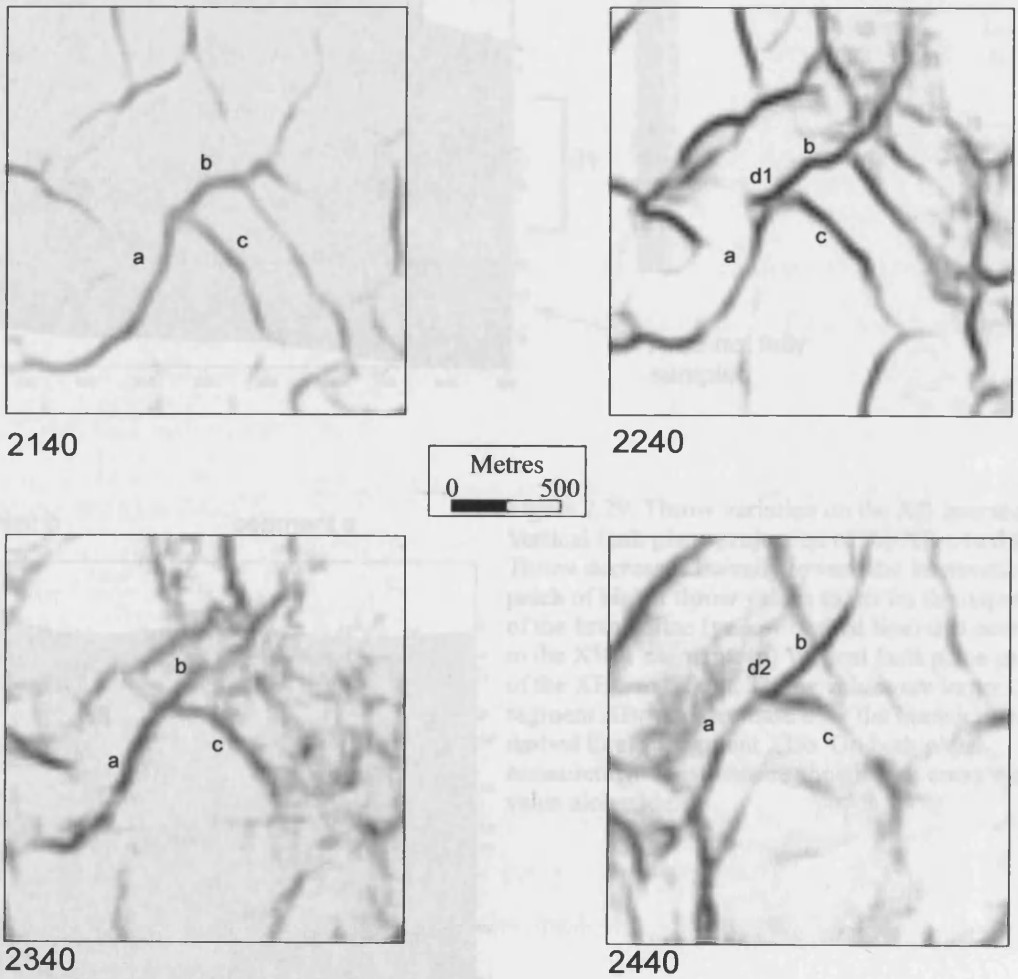

(c)

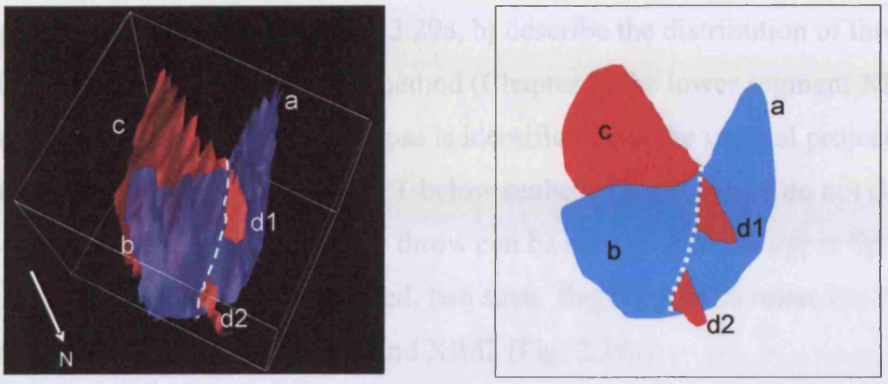

Figure 2.28 (continued). (c) 3D geometry of mapped fault planes of XB and schematic diagram. The intersection geometry is dominantly a T class intersection. The X class intersection exists in two limited and distinct vertical windows.

(a)

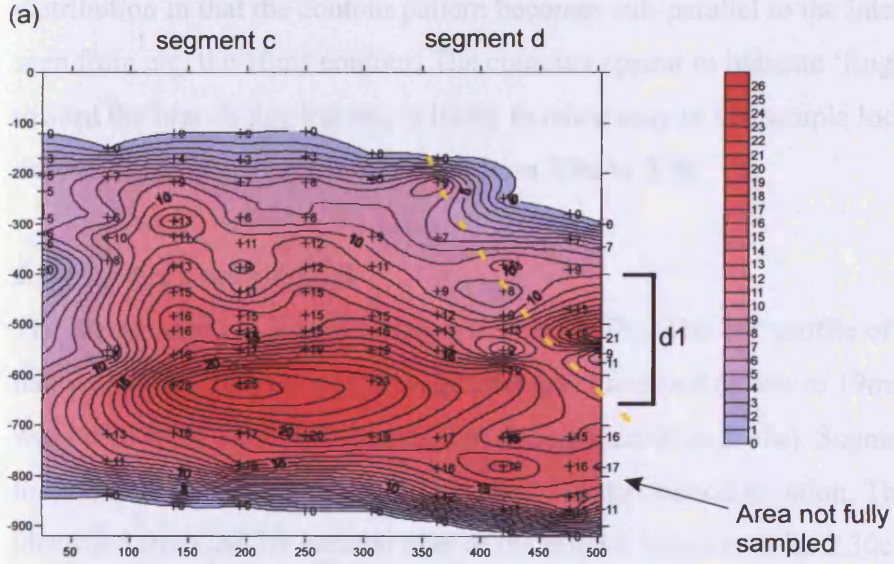

(b)

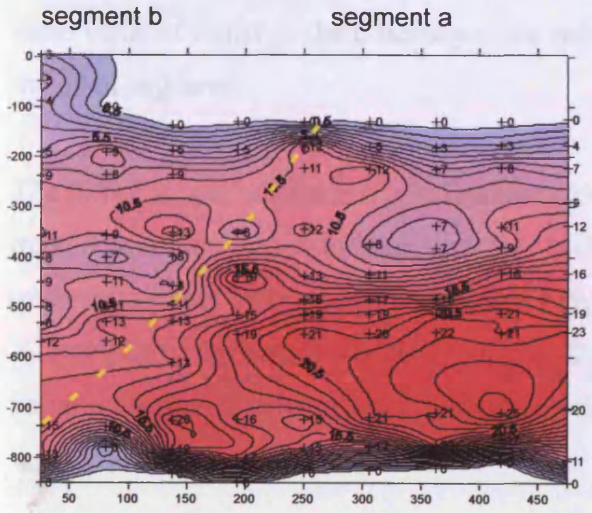

Figure 2.29. Throw variation on the XB intersection. (a) Vertical fault plane projection of the XB c to d fault. Throw decreases laterally toward the intersection. A patch of higher throw values exists on the opposite side of the branch line (yellow dashed line) that corresponds to the XBd1 segment. (b) Vertical fault plane projection of the XB a to b fault. Throw values are larger on segment XBa and decrease over the branch line (yellow dashed line) to segment XBb. On both plots, measurement locations are shown by a cross with throw value alongside.

XB Throw analysis

Vertical fault plane projections (Figs. 2.29a, b) describe the distribution of throw. Due to the limitations of the vertical projection method (Chapter 1) the lower segment XBd2 has not been sampled. A maximum throw ellipse is identified from the vertical projection of Segments XBc to XBd at ~600ms TWT below seabed. Throw values do not decrease elliptically. Instead 'fingers' of higher throw can be seen toward the upper tip and importantly toward the northern intersection. Indeed, two such 'fingers' can be related to the vertical windows of the two segments XBd1 and XBd2 (Fig. 2.29a).

The XBa_b vertical fault projection (Fig. 2.29b) shows that throw is concentrated in segment XBa where largest throw values are recorded. XBa also has a very intersecting throw distribution in that the contour pattern becomes sub-parallel to the intersection branch line as seen from e.g. the 10ms contour. The contours appear to indicate 'fingering' of this lateral tip toward the branch line but this is likely to relate only to the sample locations. Throw values decrease across the fault intersection from XBa to XBb.

2.3.4.3 T-x analysis of X1

The X1 intersection is near orthogonal (Fig. 2.30a). The T-x profile of X1 (Fig. 2.30b) shows that values of throw on all four segments are near-equal (17ms to 19ms) at intersection, as was noted from the XA intersection at this horizon (Fig. 2.27e). Segment X1a increases in throw toward intersection but decreases at the intersection location. This is not clearly identified from the 3D horizon map of the middle Miocene (Fig. 2.30c) and the value was noted as being difficult to measure due to the proximity of intersection at the time of data acquisition. However, it may actually represent a genuine throw reduction in order to have the same value of throw as the other segments and this would suggest an interrelationship with the other segments.

The throw profile of segment X1c increases toward intersection and shows no variation in trend across intersection to segment X1d which has a local maximum ~100m from intersection then decreases toward its tip (T19, section 3.3.4). The throw profile from segment X1c to X1d to the cumulative X1d1 and X1d2 plots is near-symmetrical. Very little throw variation is therefore recorded at this intersection with the exception of the local decrease in

(a)

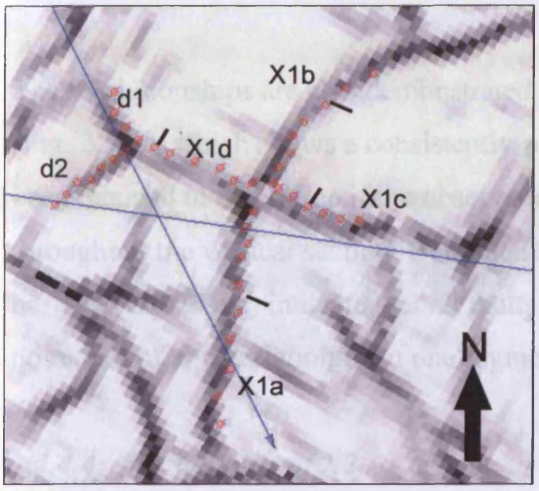

(b)

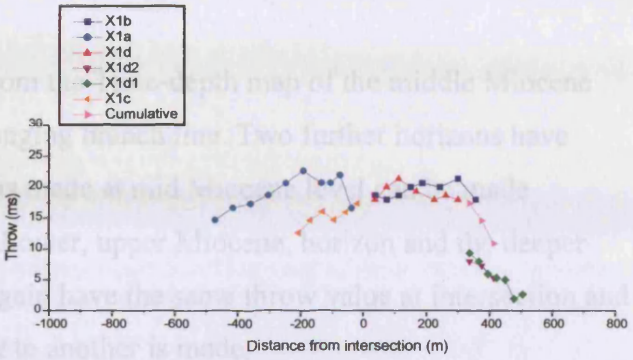

(c)

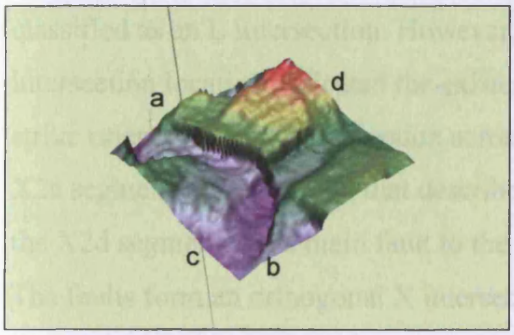

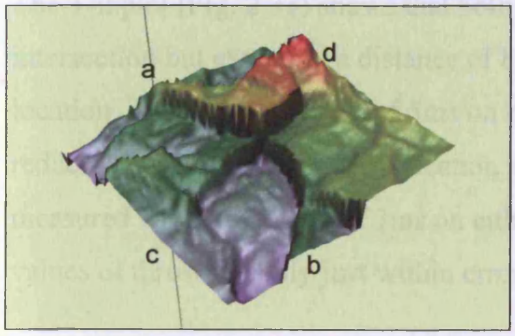

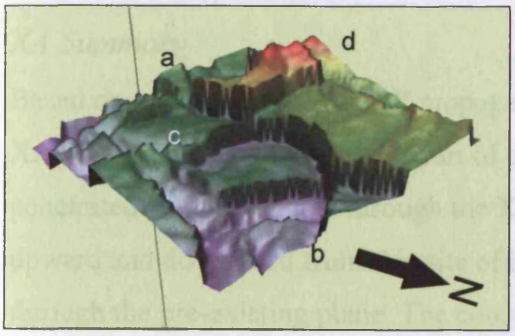

Figure 2.30 Geometry and throw distribution of the X1 intersection. (a) Coherence extraction of the middle Miocene horizon showing the plan view geometry of the X1 intersection. The faults are orthogonal and have continuous strike and dip values across intersection. The X1d segment bifurcates at its lateral tip. This is also the T19 intersection. (b) T-x plot from the middle Miocene horizon. There is very little variation in throw on the faults across the intersection. Throw values are equal on all four segments at the intersection. The cumulative profile of X1d1 and d2 is continuous with the X1d to c profile resulting in a symmetrical throw profile. (c) 3D perspective images of upper Pliocene, middle Miocene and lower Miocene horizons that are offset systematically by the X1 faults. The lack of throw variation across intersection is consistent throughout the depth section. Additionally, throw values on each fault segment are equal at the intersection location on each horizon.

throw on the X1a segment. The throw profiles of the X1a and X1d segments are near-symmetric and these bound the common footwall block (Fig. 2.30c).

These relationships are also demonstrated from the Time-depth map of the middle Miocene (Fig. 2.30c), which shows a consistently-plunging branch line. Two further horizons have been mapped to determine if the observations made at mid Miocene level can be made throughout the vertical section. Both the shallower, upper Miocene, horizon and the deeper horizon (Fig. 2.30c) indicate that all faults again have the same throw value at intersection and no record of any variation from one segment to another is made.

2.3.4.4 T-x analysis of X2

The final example, X2, has a plan view geometry that is significantly different from those previously described (Fig. 2.13e). From the coherence extraction alone it was initially classified as an L intersection. However, recognition of offset horizons in the area past the intersection location indicated the existence of two further short fault segments with the same strike orientation and dip direction across the intersection from the two main segments. The X2a segment is the same as that described in Section 2.3.1.2 as the T5 intersecting fault and the X2d segment is the main fault to the T15 and T16 T class intersections (Section 2.3.1.3). The faults form an orthogonal X intersection.

The T-x plot (Fig. 2.31) shows that both main fault segments decrease in throw toward intersection but extend to a distance of 85m (X2a_b) and 55m (X2c_d) past the intersection location. The value of throw of 5ms on both segments is equal at the intersection. Throw then reduces across the intersection location and the two faults mirror one another with two measured values of throw of 3ms on either segment. It should be cautioned that these small values of throw are only just within error of seismic resolution.

2.3.4.5 X Interpretation

XA Summary

Based on a model of radial fault propagation, the throw distribution that decreases from the XAa fault plane across a central part of the branch line strongly suggests that segment XAa penetrated and propagated through the XAc – d plane. The branch line would have evolved upward and downward from this site of initiation as the relatively later fault plane developed through the pre-existing plane. The compartmentalisation of throw contours on both fault

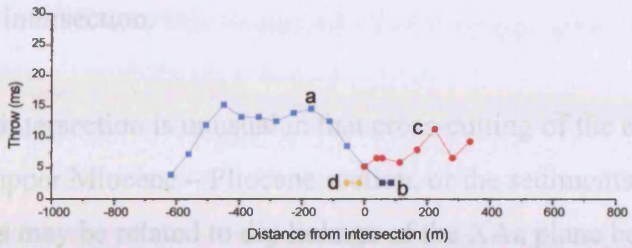

Figure 2.31. T-x plot for the X2 intersection. Throw values are equal on all segments at the intersection location. Throw values on segments X2a and X2c are decreasing toward intersection.

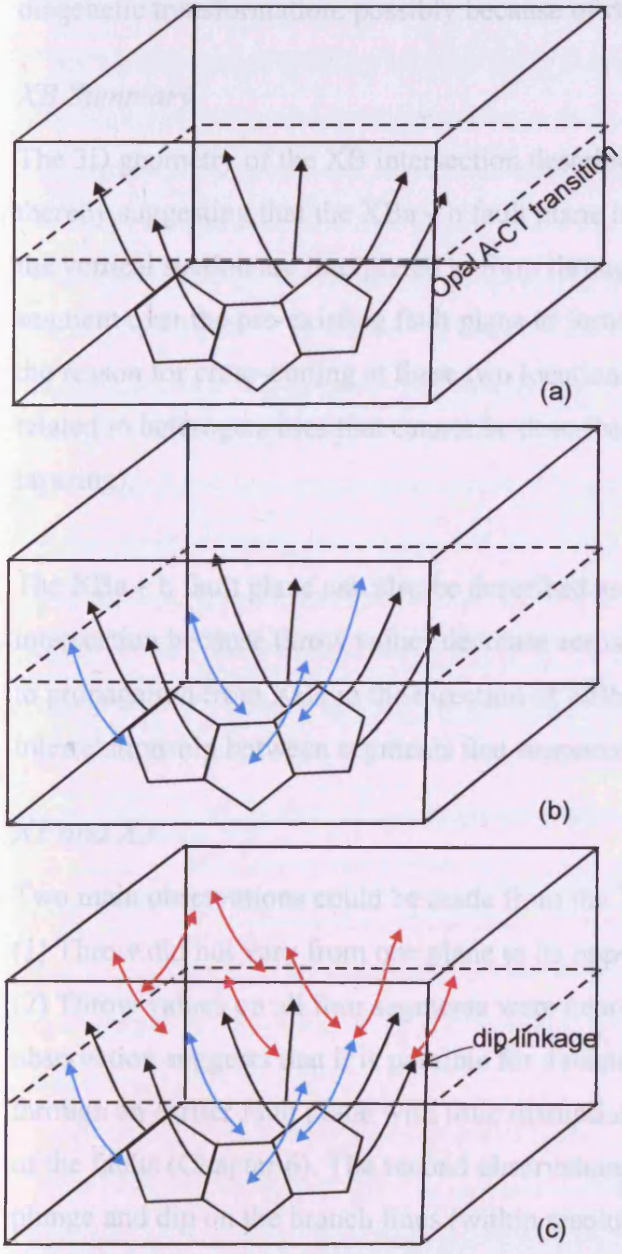

Figure 2.32. Schematic diagram of evolutionary model of vertical propagation of a PFS. (a) Stage 1. The polygonal fault system develops from the base of a stratigraphic layer. Ideal plan view polygon geometries are formed and fault propagation is upward (Type 1 faults, single-headed black arrows). Some faults can propagate across the diagenetic transition (dashed horizon). (b) Stage 2. A second set of faults are formed that infill the spaces in the original system and propagate radially (Type 2 faults, double-headed blue arrows). These faults can propagate across the diagenetic transition. (c) Stage 3. A later set of polygonal faults forms and is confined to the vertical section above the diagenetic transition. These faults propagate radially (Type 3 faults, double-headed red arrows). They can form dip linkages with Type 2 and Type 3 faults.

planes shows that the intersection affected the growth of each fault. It is possible that both faults were active during intersection.

The 3D geometry of this intersection is unusual in that cross-cutting of the earlier fault plane is entirely limited to the upper Miocene – Pliocene section, or the sediments above the diagenetic transition. This may be related to dip linkage of the XAa plane between a fault below and a fault above the diagenetic transition i.e. only the upper part of the fault plane is propagating across the intersection. An alternative explanation is that the later fault plane is only able to cross-cut the existing fault plane in the sediments that are unaffected by the diagenetic transformation, possibly because of rheological changes related to the diagenesis.

XB Summary

The 3D geometry of the XB intersection describes is predominantly a T class intersection thereby suggesting that the XBa – b fault plane is pre-existing. The areas of X intersection in the vertical section are interpreted to form through propagation of slip patches on the XBc segment over the pre-existing fault plane to form the XBd segments. It is difficult to explain the reason for cross-cutting at these two locations from the current database but it may be related to heterogeneities that cannot be described from the available dataset (e.g. lithological layering).

The XBa – b fault plane can also be described as showing a relationship with the XBc – d intersection because throw values decrease across this branch line. This may be related solely to propagation from XBa in the direction of XBb but can also be considered to show an interrelationship between segments that supports interpretation of a kinematic relationship.

X1 and X2

Two main observations could be made from the T-x examples presented above:
(1) Throw did not vary from one plane to its opposite across the intersection location, and
(2) Throw values on all four segments were near-equal at the intersection location. The first observation suggests that it is possible for a relatively later fault to penetrate and propagate through an earlier fault plane with little disruption. This raises the question of relative activity of the faults (Chapter 6). The second observation, along with the observation of constant plunge and dip on the branch lines (within resolution), suggests that the fault evolution may be inter-related.

The X2 intersection is interesting as it suggests that the faults met as an L class intersection and that rather than linking they were able to interact in such a way that both could propagate slightly past the intersection. In contrast an L class intersection is described from Chapter 5 which is interpreted as linking with no fault propagation past intersection. The mechanical interaction is likely to be related to the way in which the process zones at the tips of propagating faults interact.

2.4 Discussion: Intersection Evolution in the GR PFS

The aims of this chapter included providing a classification of intersection geometries and investigation of whether geometries can be related to their style of evolution. In order to meaningfully interpret and relate the throw measurements to intersection evolutions the propagation style within the system had to be understood. The results from the propagation kinematics study (Section 2.2.2) validated the interpretation that maximum throw represented the zone of nucleation and that Type 2 and Type 3 faults propagated radially. From these results, Section 2.4.1 proposes an evolutionary sequence for the three types of faults in the GR PFS. Following this, a summary of observations relating the geometrical classes to their intersection style is discussed. (Section 2.4.2).

The remainder of this discussion is then devoted to further analysis of the different styles of intersection that have been recognised from this study (Section 2.4.3). It is clear from the previous description that the evolution of intersection classes can be sorted into two groups, namely 1) accidental intersections and 2) branching intersections. Accidental intersections are defined by the intersecting fault that propagates toward, and to form, an intersection with a master fault, termed main fault in the description. Branching intersections form through the propagation away from a master or parent fault and include splays and lateral bifurcations. The majority of intersections fit into the accidental intersection group so the structural evolution of these provides the main focus to this section (Section 2.4.3). Following discussion of the different stages of accidental intersection, the question of whether an evolutionary sequence can form between the stages will be addressed.

Section 2.4.4 discusses the structural evolution of branching intersections. Within this section a short comparison between throw profiles of branch-type intersections and footwall capture intersections will aid understanding of the definition of each.

2.4.1 Vertical evolution of the Gjallar Ridge PFS

The results of the throw analysis in Section 2.2.2 validated the interpretation of radial propagation of the fault system for Type 2 and Type 3 faults. In addition, the division of the Type 1 – 3 faults allows an evolutionary growth model to be proposed that fits within the rules of nucleation relating to throw distribution as defined for tectonic faults (Barnett et al., 1987; Walsh and Watterson,1987) and relates to the diagenetic transition. The line drawing (Fig. 2.32) summarises the stages of evolution as follows: 1) propagation upward of a spatially-organised set of polygon-bounding faults (Type 1); 2) a set of radially propagating faults form as space-filling faults; 3) faulting occurs that is largely confined to the lower Middle Miocene to Pleistocene section (i.e. above the diagenetic transition). This relationship will have evolved synchronously with continued faulting and background processes of diagenesis and sedimentation. The fact that Type 3 faults are almost entirely constrained within the section above the diagenetic front, and that the density of faulting increases below this boundary, points toward a change in the mechanics of the system above and below the diagenetic transition once this was established. Indeed, it has been suggested that the polygonal faulting may have occurred in response to Opal A-CT conversion (Hansen et al., 2005). However, recent work suggests that the diagenetic transition is not thought to be responsible for origin of the PFS but may cause modification of it (J.A. Cartwright, pers comm., 2005).

A very brief study attempted to investigate if there were partial relationships between faults with pre-, pre- and post- and post-diagenetic transition. However, no relationships were found. It would be an interesting study to attempt to track the spatial development of faults with different timing relationships to the diagenetic front e.g. separating Type 1 faults from Type 2 faults as these are thought to have evolved at different times. However, neither fault evolution nor diagenetic transformation are instantaneous. Therefore it would be difficult to determine any such relationship.

2.4.2 Geometrical relation to evolution

Examples of both accidental and branching intersections were identified from the T, Y and TR intersection classes. Therefore, it is not possible to confidently apply a kinematic interpretation based on classification of geometry alone. However, the observations described previously in this chapter allow a few generalizations to be proposed. Sixty percent of the sampled T class intersection can be grouped in the accidental category. Of these, the most

commonly formed relationship (>92%) is abutment of the intersecting fault against the master fault. The single accidental abutment relationship described from the Y class (Section 2.3.3) closely approximated a T class geometry at middle Miocene level (and may have a T intersection elsewhere in the depth section). In a well developed T intersection (see below), the intersecting fault will most likely form an abutting accidental intersection with the main fault.

Subdivision 2 of the T class displayed intersections with very small lengths. The small faults also had very small throw values and were interpreted to form as early stage 'buds' as part of the branching intersections group. These can be distinguished from the abutting geometries largely on length and throw value. They form 33% of the described T intersections. Only the remaining 7% of T class structures, interpreted as linkages, cannot be identified in any way from intersection geometry alone (however, there is some evidence that they will have obtuse intersection angles).

From the observations of an acute intersection angle, coupled with the fact that dip direction is largely consistent between the main and intersecting faults, Y intersections typically form branching relationships. Lateral tip bifurcation occurs in acute-angled Y or TR class intersections at the tip of a main fault. Confidence in interpreting this style of branching evolution can be gained where a longer segment is contiguous with two shorter segments and typically (but not necessarily) incurs a strike change from the main to both 'splays'. Growth after bifurcation offers another method of network evolution within a PFS. Potential candidates for lateral bifurcation that have been identified from geometry alone within the GR PFS are shown on Figure 2.33.

In summary:

- T class intersections (with large intersecting faults) commonly form accidental abutment relationships.
- T class intersections with intersecting faults that are very small in length and throw value, commonly originate as 'buds' from the main fault plane.
- Intersections that display a hook geometry typically form through accidental intersection.
- Acute-angled intersections (angles less than c.40°) are often formed as branching intersections. The branch fault has the same dip direction as the main fault segment.

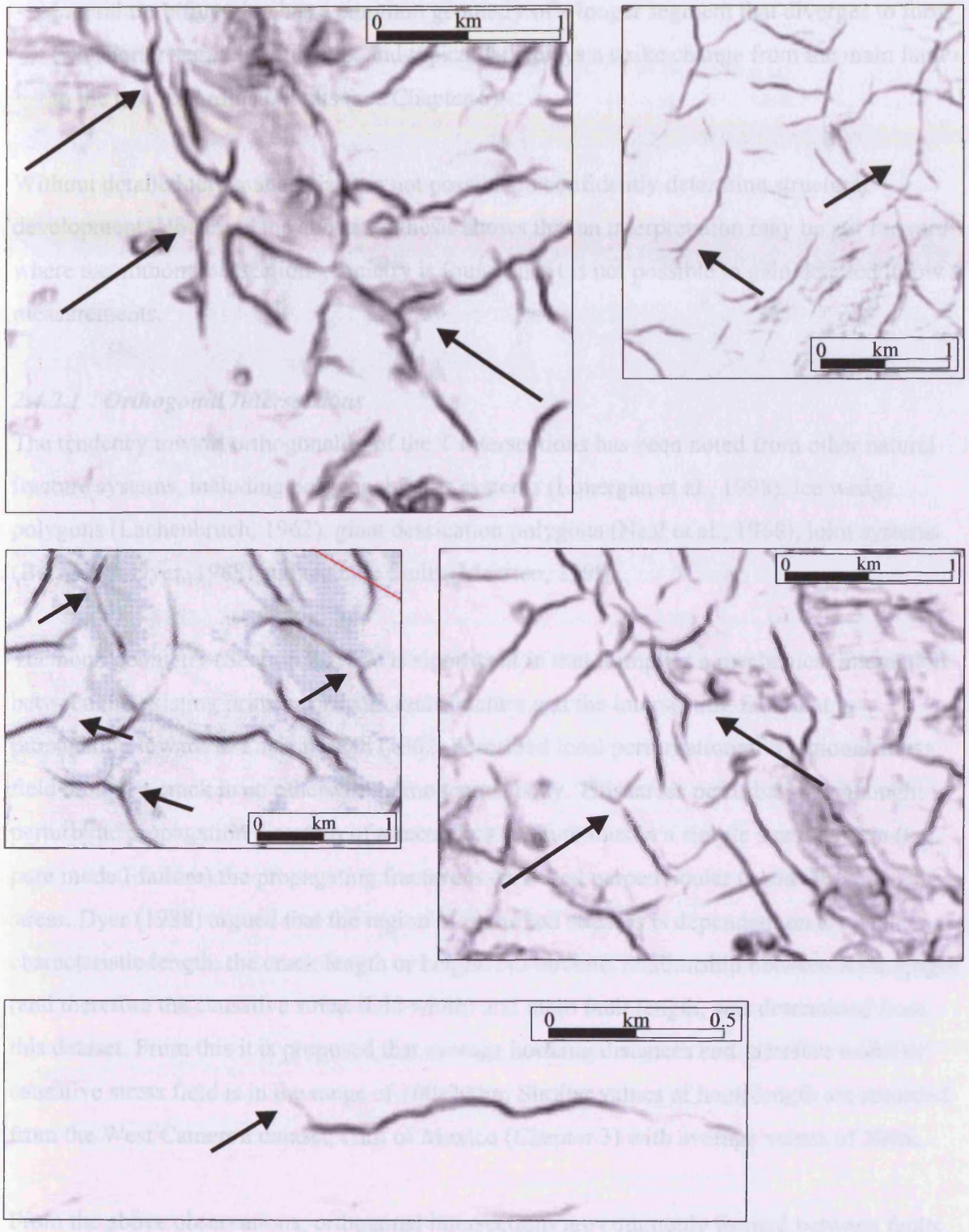

Figure 2.33. Coherence extractions from the middle Miocene and upper Pliocene horizons. The images display fault trace geometries that show a change of strike of the main fault toward its lateral tip. Two shorter segments trend at oblique angles to the main fault, which commonly bisects the intersection angle. These fault intersections display the characteristic geometries of intersections that form through lateral bifurcation. Therefore they are candidates for interpretation of their intersection evolution from geometry alone.

- Lateral tip bifurcation has a common geometry of a longer segment that diverges to form two shorter segments at its tip, and typically displays a strike change from the main fault to the two subordinate faults (see Chapter 6).

Without detailed throw analysis, it is not possible to confidently determine structural development. However, the above synthesis shows that an interpretation may be put forward where a common intersection geometry is found and it is not possible to gain detailed throw measurements.

2.4.2.1 Orthogonal Intersections

The tendency toward orthogonality of the T intersections has been noted from other natural fracture systems, including polgyonal faults systems (Lonergan et al., 1998), ice wedge polygons (Lachenbruch, 1962), giant dessication polygons (Neal et al., 1968), joint systems (Bai, 2002; Dyer, 1988) and tectonic faults (Maerten, 1999).

The hook geometry (Section 2.2.1.4) is significant in that it implies a mechanical interaction between the existing primary or main fault fracture and the intersecting fault that is propagating toward it. Lachenbruch (1962) described local perturbation of a regional stress field around a crack in an otherwise homogenous body. This stress perturbation is thought to perturb the propagation direction of a secondary fracture thus in a simple stress system (e.g. pure mode I failure) the propagating fracture is deflected perpendicular to maximum tensile stress. Dyer (1988) argued that the region of perturbed stresses is dependent on a characteristic length, the crack length or height. No obvious relationship between hook length (and therefore the causative stress field width) and main fault length, was determined from this dataset. From this it is proposed that average hooking distances and therefore width of causative stress field is in the range of 100-200m. Similar values of hook length are recorded from the West Cameron dataset, Gulf of Mexico (Chapter 3) with average values of 300m.

From the above observations, orthogonal intersections are commonly formed between faults that are propagating at high angles to the main fault (e.g. faults of the T class). They can also be facilitated through deflection of an intersecting fault, that is propagating at a low angle to the main fault, to become strike-normal to the main fault.

2.4.3 Structural evolution of accidental intersections

The most frequently documented type of accidental intersection in this work is abutment where the intersecting fault arrests propagation at the master fault plane. Linkage and cross-cutting types of accidental intersection are less frequently reported. The kinematics of these three types of accidental intersection are summarised below followed by some consideration of their potential to evolve from one type to another. This implies a relative time relationship where the main fault is pre-existing and the intersecting fault is later. Accidental intersections encompass intersections that form from abutment relationships, footwall or hangingwall linkage and examples of cross-cutting relationships.

2.4.3.1 Abutment

From the observation that propagation of the intersecting fault arrests at the location of the master fault, the simplest interpretation is that the presence of the master fault is responsible for arrest of the intersecting fault. It may be possible to explain this from the stress perturbation around the master fault that is caused by the stress drop associated with slip on the master fault. The main fault plane can be likened to a free surface that has no traction after a slip event e.g. Ackermann and Schlische (1997) and Engelder (1993). This creates a stress reduction shadow that forms because stress within the rock volume cannot be transmitted across the free surface of the fracture (Gross et al., 1995). It follows that propagation of the intersecting fault which requires that stress concentration at fault tips equals the yield strength of the rock, is arrested as it enters the stress shadow. The stress perturbation manifests itself as an area around the fault in which no parallel faults can propagate (Ackermann and Schlische, 1997) or nucleate (Gupta and Scholtz, 2000). This has the effect of polarising stress such that any polygonal faults propagating into this stress shadow realign into an orthogonal direction with respect to the primary fault. The local reorientation of the stress field varies along the length of the main fault according to heterogeneities such as material properties, boundary conditions and growth mechanisms (Gupta and Scholz, 2000).

Accidental intersection relationships of linkage and cross-cutting are also described in this section and show that the intersecting fault does not indefinitely halt its propagation as it enters the shadow zone. It should be noted that this mechanical context does not take into account any changes in strength which might occur during silica diagenesis, and which could further complicate the processes involved during abutment of an intersecting fault.

2.4.3.2 Linkage

Few intersections in the GR PFS were interpreted to have formed through linkage of an accidental intersection. Examples from the T class (Section 2.3.1.4), the Y class (Appendix A.3) and the TR class (Appendix A.2) descriptions have been interpreted as hard linked structures. The intersection that best displays characteristics of hard linkage is T21 and the discussion will focus on this example.

This section aims to discuss the kinematics of hard linkage in a PFS in the context of the model of footwall capture and linkage put forward by Nicol et al, (2003). These authors describe a highly interconnected PFS from the Lake Hope basin (Australia) that results in predominantly footwall intersections. They propose that the intersecting fault links with a segment of the main fault plane (the intersected fault) resulting in a distinct change in strike of the active fault plane and relative inactivity on the unlinked fault segment of the main fault which they term the inactive hangingwall splay. The fault segments which share a mutual footwall are favoured for linkage and continue movement as a single fault after linkage. What criteria are used to define footwall linkage?

Nicol et al (2003) proposes the rule that those fault segments that share a footwall will form linked structures. From this, can the recognition of a mutual footwall be interpreted as a linked fault thereby allowing a geometrical method of identification? This interpretation is questionable since, for example, cross-cutting faults form mutual footwalls through geometry alone. Therefore kinematic evidence is required. For the faults to be kinematically compatible, the aggregate throw on the intersecting fault and the hangingwall splay must equal throw on the linked main fault segment at the intersection location. This relationship has been described from several of the intersections in the GR PFS and it is noted that interpretation of lateral bifurcation has been put forward for some and footwall linkage for others. The key criterion for interpretation of footwall linkage is a throw decrease on the intersecting fault toward the intersection (Section 2.4.4) A further criterion for positive identification of footwall capture is the recognition of the inactive hangingwall splay. However, there are no growth intervals to tie down active periods irrefutably. The GR PFS has been reported to have an interconnected ratio of >0.7 which suggests that 'inactive' hangingwall splays will themselves be involved in further intersections and kinematic relationships. Therefore the strongest evidence for a footwall capture method of linkage is by preserving the original profile of the intersecting fault as in the case of T21.

The previous section proposed that the tendency for accidental abutment intersections to occur is driven by the lack of traction on the main fault planes toward which the intersecting fault is propagating. How then, does the intersecting fault reach a state of hard linkage with a segment of this original plane? The observation that over 80% of T class intersections form an obtuse angle bounding the mutual footwall (Section 2.2.1.4), perhaps offers a route to explaining this type of hard linkage. Park (1989) describes the influence of a second fault that locally releases stress in the strained zone causing modification of the stress field around its active region which influences further fault movements. This causes superimposition of new stresses parallel to the fault on an oblique set of pre-faulting stress axes to create a new set of stress trajectories. These superimposed trajectories may facilitate linkage and slip movement parallel to the branch line.

Consider that the intersecting fault is propagating in the perturbed stress field and is able to propagate toward the main fault. Slip events that occur over the intersecting fault may then serve to break the main fault footwall until a situation is reached where the intersecting tip is near forming a branch line with the main fault and both faults are bounding a coherent block of rock termed the mutual footwall. The perturbed stress field is locally aligned to favour slip on the intersecting fault and a further event may cause reactivation of the footwall-bounding segment of the main fault. If sufficient traction has built up on the main fault plane since the last slip event it is possible that the intersecting fault will be able to propagate close enough to the master fault plane to cause such reactivation.

Soft linkage

Where recognised from Subset 1 intersections, local minimum and locally anomalous displacement gradients at the intersection location, are thought to relate to the variations of the rock volume ahead of the propagating tip of the intersecting fault. Specifically, the strain ahead of the propagating intersecting fault tip may be expressed as ductile bending of beds, i.e. a lateral tip fold (Peacock and Parfitt, 2002). The impact that propagation of the intersecting fault has on the main fault T-x profile may be considered as a soft linkage stage (Fig. 2.34) (see Chapter 6).

The possibility of a linkage stage is an important observation from the multidirectional PFS. It shows that an analogy may be made with the evolution of unidirectional fault arrays through along-strike segment linkage. However, there is clearly a geometrical variation between non-

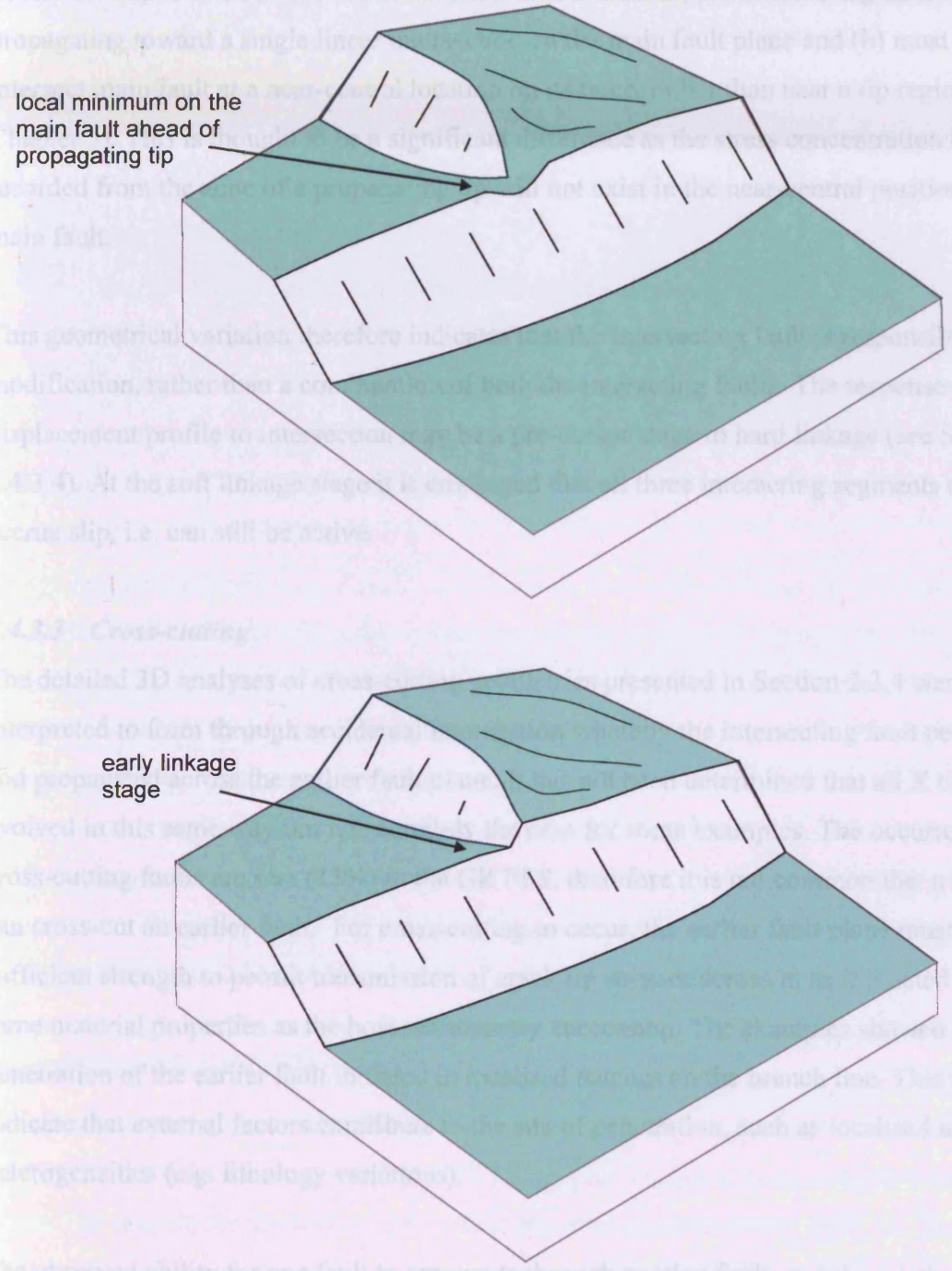

Figure 2.34. Schematic diagrams of the possible evolution of early-stage linkage. (a) The main fault displays a variation on its displacement profile in the intersection location, related to bending ahead of the propagating tip of the intersecting fault. Both segments of the main fault can continue to slip together. (b) Increased influence of the intersecting fault on the main fault profile and the near-field stress orientation may lead to an early-stage hard linkage between the non-colinear faults.

colinear and colinear fault arrays. An overlapping or underlapping geometry is fundamental to the linkage of sub-parallel faults. Complimentary modification of T-x profiles is recognised from this overlap (Willemse, 1996; Gupta and Scholz, 2000). In contrast, non-colinear arrays do not overlap to form an area of mutual interaction. Instead, the intersecting fault will be (a) propagating toward a single linear intersection on the main fault plane and (b) most likely to intersect main fault at a near-central location on its trace, rather than near a tip region (see Chapter 5). This is thought to be a significant difference as the stress concentration that is recorded from the zone of a propagating tip will not exist in the near-central position on the main fault.

This geometrical variation therefore indicates that the intersecting fault is responsible for T-x modification, rather than a combination of both the interacting faults. The response of the displacement profile to intersection may be a pre-cursor stage to hard linkage (see Section 2.4.3.4). At the soft linkage stage it is envisaged that all three interacting segments can still accrue slip, i.e. can still be active.

2.4.3.3 Cross-cutting

The detailed 3D analyses of cross-cutting geometries presented in Section 2.3.4 were interpreted to form through accidental intersection whereby the intersecting fault penetrated and propagated across the earlier fault plane. It has not been determined that all X class faults evolved in this same way but it is certainly the case for some examples. The occurrence of cross-cutting faults are rare (13%) in the GR PFS, therefore it is not common that a later fault can cross-cut an earlier fault. For cross-cutting to occur, the earlier fault plane must have sufficient strength to permit transmission of crack tip stresses across it, as if it acted with the same material properties as the host sedimentary succession. The examples showed that penetration of the earlier fault initiated in localised patches on the branch line. This may indicate that external factors contribute to the site of penetration, such as localised mechanical heterogeneities (e.g. lithology variations).

The observed ability for one fault to propagate through another fault, and the relation to relative shear strength on the pre-existing plane raises the question of relative activity on the faults. Needham (1996) implied that inactivity of the earlier fault plane was necessary for cross-fault propagation. This interpretation could be supported by the lack of variation of T-x profiles recorded from the intersection location (Section 2.3.4). However, the

compartmentalisation of the pre-existing fault plane, XAc_d in the XA intersection, suggests either that slip accrued after intersection and that it was altered by the intersection or that the intersection sufficiently altered palaeo-throw distributions. The latter case seems less likely. In addition, the observation that throw values on all intersecting faults are the same at intersection (and that they may alter to achieve this relationship) suggests that some interrelation between cross-cutting faults, and therefore activity on both, may be possible. This idea of a kinematic inter-relationship does not suggest that the faults are actually hard linked.

2.4.3.4 Evolutionary Sequence of accidental intersections

The above section argued that abutment intersections are the most common accidental type but that circumstances exist in which hard linkage and cross-cutting accidental intersections occur. This section aims to discuss the question – are the relationships of abutment, linkage and cross-cutting related by an evolutionary sequence?

a) Abutment to linkage?

Evidence for accidental intersection comes from throw profiles decreasing in value toward intersection. Where this was observed to decrease to a tip the intersection was interpreted to form an abutment relationship with the pre-existing main fault. A potential soft linkage stage has been proposed that has similar characteristics to the abutment stage but impacts the T-x profile of the main fault. This requires that the rock volume between the intersecting faults is modified by ductile bending. Therefore, the abutting intersection varies from the soft-linked intersection. The preference for one to form over the other may be related to factors such as strain rate. It is not considered likely that abutment can evolve to soft linkage (see Chapter 6). In contrast, faults displaying abutment and soft linkage states may evolve to hard-linked faults. The existence of a soft-linked state prior to hard linkage may benefit this transition as it has already modified the T-x profile of the main fault. An example of an early stage soft-to-hard linkage may be example T4 (Fig. 2.13). Abutment to hard linkage requires conditions that are favourable for mechanical interaction between the intersecting faults i.e. the main fault can be reactivated by propagation of the intersecting fault

b) Linkage to cross-cutting?

The accidental intersection hard linkage state can only be confidently recognised when throw values from the intersecting and hangingwall splay fault segments add up to the throw value on the main fault segment at the intersection location. Cross-cutting intersections do not show such a relationship. For a linked structure to evolve to an X geometry it would have to effectively 'break' the linkage with the main fault plane and cut across this lower traction surface. This would be recorded in a throw profile whereby the original main fault plane would have varying throw across the intersection, as defined from its state of one linked segment and one inactive hangingwall splay. In addition, the throw values on the intersecting fault would also vary abruptly at intersection as the segment that propagates across would have significantly less throw than that which had previously been linked as an active fault. This relationship has not been recorded from X intersection throw profiles and the possibility of an evolutionary stage from hard linkage to cross-cutting is therefore discounted.

c) Abutment to cross-cutting?

Comparison of the intersection classification distribution of T to X (disregarding all other classes) indicates a distinct preference for T class intersections (83%) as contrasted with the X class (17%), despite the high levels of connectivity (and therefore maturity) of this system. Both the XA and XB examples provided evidence that a T class intersection can evolve to an X class intersection within the vertical interval. The throw distribution on the XA intersecting fault was noted to have a steep lateral displacement gradient toward the intersection. The throw contours were rectangular in shape. Throw contours that cut across the fault plane initiated from a single location on the branch line, and grew upward and downward from that position (see Chapter 6). It can be interpreted from these observations that the intersecting fault was initially arrested (from the anomalously high tip gradient) and that propagation through the pre-existing fault plane started from one slip event and evolved through radial propagation. It is probable that an arrested fault accrues more slip at its intersecting tip, creating a high displacement gradient, before it gains sufficient tip stresses to propagate across the main fault. Therefore an evolutionary sequence of abutment to cross-cutting is thought to be most likely.

In summary, a sequence of abutment to linkage to cross-cutting can be discounted. However, it is considered reasonable to predict an evolutionary sequence of soft to hard linkage and abutment to cross-cutting in the GR PFS (see Fig. 6.6).

2.4.4 Structural evolution of Branching intersections

A most significant result from this analysis is the identification of a method of network evolution of PFS through lateral bifurcation at the tip of a fault plane. The fault plane bifurcates at its lateral extent (potentially because of a heterogeneity in the medium through which it is propagating) thus distributing its throw between, and creating, two fault segments typically of different strikes. Growth outward of the bifurcations are part of the evolving PFS network and will act as intersecting faults to other intersections.

Lateral bifurcation is identified from throw distribution and decrease outward from the main fault plane, which is the criteria for branching intersection. The cumulative throw profiles ideally reflect a single fault throw profile. Maximum throw on the parent fault plane is identified either from a location adjacent to the intersection or from a near-central location. Where it is not adjacent to the intersection the fault is thought to have been propagating as a single structure that bifurcated toward its tip. Where the maximum throw value on the parent fault is adjacent to the intersection, bifurcation may have occurred at an earlier stage, thus the throw profile has redistributed over further slip events.

The observation that two smaller throw segments can be added to equal the value of throw on the larger throw segment is common to interpretation of both accidental intersection by footwall linkage and branching intersection by lateral bifurcation (and by splaying). It is not easy to distinguish between these and this can only be achieved with certainty from careful analysis of the intersecting fault throw profiles. Where the intersecting fault throw decreases outward from the intersection location at the tip of a fault, ideally associated with a strike change, it can be interpreted as lateral bifurcation. In contrast, where the intersecting fault profile decreases in throw toward the intersection it can be interpreted as footwall linkage. Nicol et al. (2003) suggest that the maximum incremental slip on the intersecting fault will move nearer to the branch point, i.e. toward the centre of the linked fault, post-linkage. Therefore mature intersections will have 'overprinted' the early linkage throw profile and may display a near maximum at the intersection corner between the intersecting and main linked segment. This stage has not been reached in the examples given here. Indeed, as such few linkages are recorded from the GR PFS, it may be implied that the system, although highly interconnected, is not mature in terms of linkage. It can therefore be argued that this early linkage system will still preserve a decrease in throw toward intersection on a footwall capture structure.

Further branching relationships have been proposed from evolution of TR intersections and from Subset 2 T class intersections. The TR class examples display throw profiles that appear to indicate propagation of two separate faults that require a third splay to accommodate strain where their tips interact. This interpretation is cautioned by the TRA example where a similar 2D profile was taken from the 3D example that was interpreted as lateral bifurcation. Accuracy of interpretation of the throw profiles within the error range is required and 3D interpretation is preferable.

2.4.5 Summary

The polygonal fault network is extremely interconnected. Each of the studied intersections has displayed a relationship between the fault segments involved in intersection. From this observation, the network evolution is identified to be entirely related as it is expected that the studied fault segments also form relationships with other fault segments with which they intersect. However, the system is not mature in terms of linkage as identified from the abundance of abutment relationships in comparison to the rare linkage structures in the accidental intersection group. From geometry alone, the degree of linkage cannot be interpreted which has implications for interpretation of compartmentalisation and fluid flow in the network.

2.5 CONCLUSIONS

This case study has focused on three fundamental themes pertaining to this research: (1) the geometry of non-colinear intersections, (2) the style of fault propagation and (3) the kinematics of evolution of non-colinear intersections. The key findings related to these themes are summarised below.

Geometry

- The ratio of intersecting to non-intersecting fault tips is c.0.8 and therefore the system is highly interconnected.
- Interconnectedness is lower (c.0.6) toward the upper tips of the faults. This relates to shorter fault lengths as horizons sample a chord through the upper tip.
- Fault tip lines are predominantly elliptical in shape.
- Non-colinear faults meet at predictable intersection geometries. Where intersections involve between two and four fault segments, a classification has been produced.

- The classification defines 5 geometries of intersection – T (68%), Y (14%), X (13%), TR (3%), L (2%).
- There is a preference for near-orthogonal, i.e. T class, intersection.
- Hooking geometries frequently facilitate near-orthogonal intersection. They have characteristic lengths of c.100-200m as measured from the strike change to the intersection location on the intersecting fault.
- The hook geometry indicates that the intersecting fault has propagated into the perturbed stress field caused by the presence of the pre-existing fault.
- 95% of T class intersections occur in the footwall of the main fault.
- c.85% of common footwalls of T class intersections are bounded by faults that have intersection angles of 90° - 120°.
- It is not possible to fully interpret intersection evolution from geometry alone.
- 3D studies are recommended for interpretation of intersection evolution.

Fault propagation

- The distribution of throw can be related to the growth histories of faults in the PFS.
- Three types of faults exist in the GR PFS as defined by characteristic T-z profiles:
  - Type 1 faults develop through dominantly upward propagation and span the entire polygonally faulted succession from the Intra-Oligocene unconformity to the Plio-Pleistocene.
  - Type 2 faults develop through radial propagation and deform the lower Miocene to the Pleistocene.
  - Type 3 faults develop through radial propagation and are confined to the lower middle Miocene to the Pleistocene section (above the diagenetic transition).
- Radial propagation is the dominant mode of fault growth in the GR PFS.
- An evolutionary model of vertical development of the fault system proposes that Type 1 faults formed during the earliest development of the system, Type 2 faults then filled the interim spaces and Type 3 faults formed latest, and were related to evolution of the diagenetic transition.

Kinematics of intersection evolution

- Fault intersections form either as accidental or as branching intersection styles.

- Accidental intersections form through propagation of an intersecting fault toward the intersection location.
- Branching intersections form through propagation of an intersecting fault away from the intersection location.
- The evolution of the entire fault network of the GR PFS is mechanically interrelated. Each studied intersection displays a relationship between the intersecting faults indicating that this is pervasive throughout the system.

Accidental Intersections

- Accidental intersections are defined by a decrease in throw on the intersecting fault toward the intersection location.
- Accidental intersection is the predominant style of intersection evolution in the GR PFS.
- Accidental intersection is the predominant style of intersection evolution of the T class and X class. Less frequently, accidental intersection forms TR and Y classes.
- There are four types of fault relationships that form through accidental intersection:
    - Abutment: throw on the intersecting fault decreases systematically. The gradient of the T-x profile commonly increases over an inflection toward the zero throw tip.
    - Soft linkage: the main fault T-x profile is altered by the intersection.
    - Hard linkage: the intersecting fault is contiguous with the main fault. A value of throw is measured from the intersecting fault at the intersection location.
    - Cross-cutting: the intersecting fault has penetrated and propagated across the main fault.
- Each type of accidental intersection indicates that there is a mechanical interaction between the intersecting faults.
- Accidental intersections can evolve from abutment to hard linkage or cross-cutting, or from soft linkage to hard linkage.
- Abutment examples are the most common type of accidental intersection.
- Few hard linkages exist indicating that the GR PFS is in an early stage of linkage evolution.

Branching Intersections

- Branching intersections are defined by a decrease in throw on the intersecting fault outward from the intersection location.

CHAPTER 3: CROSS-CUTTING FAULTS, GULF OF MEXICO

3.1 INTRODUCTION

The occurrence of cross-cutting fault intersections raises interesting questions regarding their mode of evolution and how their constituent faults interact kinematically. The West Cameron area of the Gulf of Mexico provides a unique opportunity to investigate evolution of such structures that are pervasive throughout a large vertical interval.

This chapter will describe in detail the three-dimensional geometries and throw variations of two cross-cutting intersection examples (Section 3.2). Further observations from this dataset of Y class geometries are presented in Section 3.3. A structural evolution of each example will be provided at the end of the descriptive sections and the discussion (Section 3.4) will then compare and contrast the evolution of the cross-cutting intersection examples. Two different methods of cross-cutting intersection evolution are proposed. These have considerable implications for how we interpret the development of branch lines.

3.1.1 Geological Setting

The study area is located offshore Louisiana, on the shallow water continental margin of the northern central Gulf of Mexico (Fig. 3.1). The area is actively deforming through gravitational collapse following deposition of a thick Cenozoic deltaic and pro-deltaic sequence above the Jurassic Louann evaporates (Wu et al., 1990b). The deformed sands, silts and shales of the study area are Miocene to Pleistocene in age.

The post-depositional salt movement has resulted in an extensive series of large growth faults. Faults in the study area are arcuate to linear in plan view and have a dominantly NE-SW trend (Fig. 3.2). A second, E-W, trend also exists within the study area and it is interaction between these trends that creates the intersections of interest.

Villamil et al. (1998) describe creation of minibasins through sediment loading onto, and evacuation of, allochthonous salt. These minibasins are bounded by positive salt structures

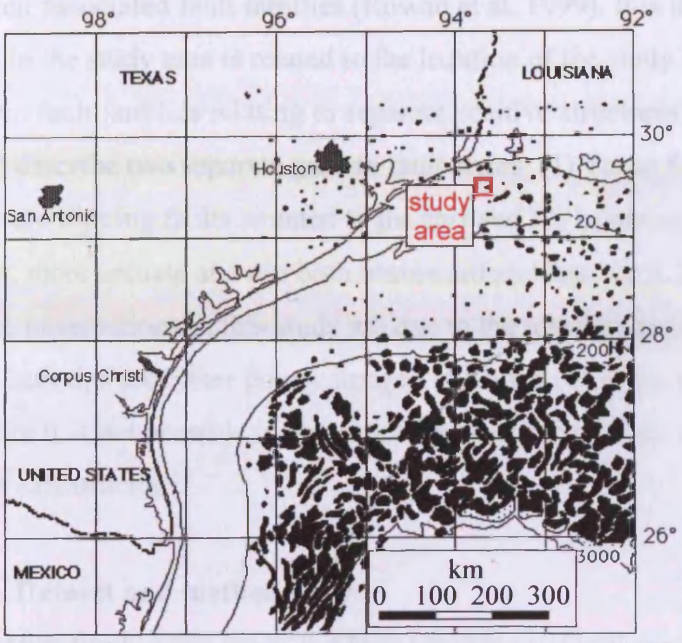

Figure 3.1. Location of the Gulf of Mexico highlighting the West Cameron study area, offshore Louisiana. Salt domes are represented in black. Modified from Reymond, 1994.

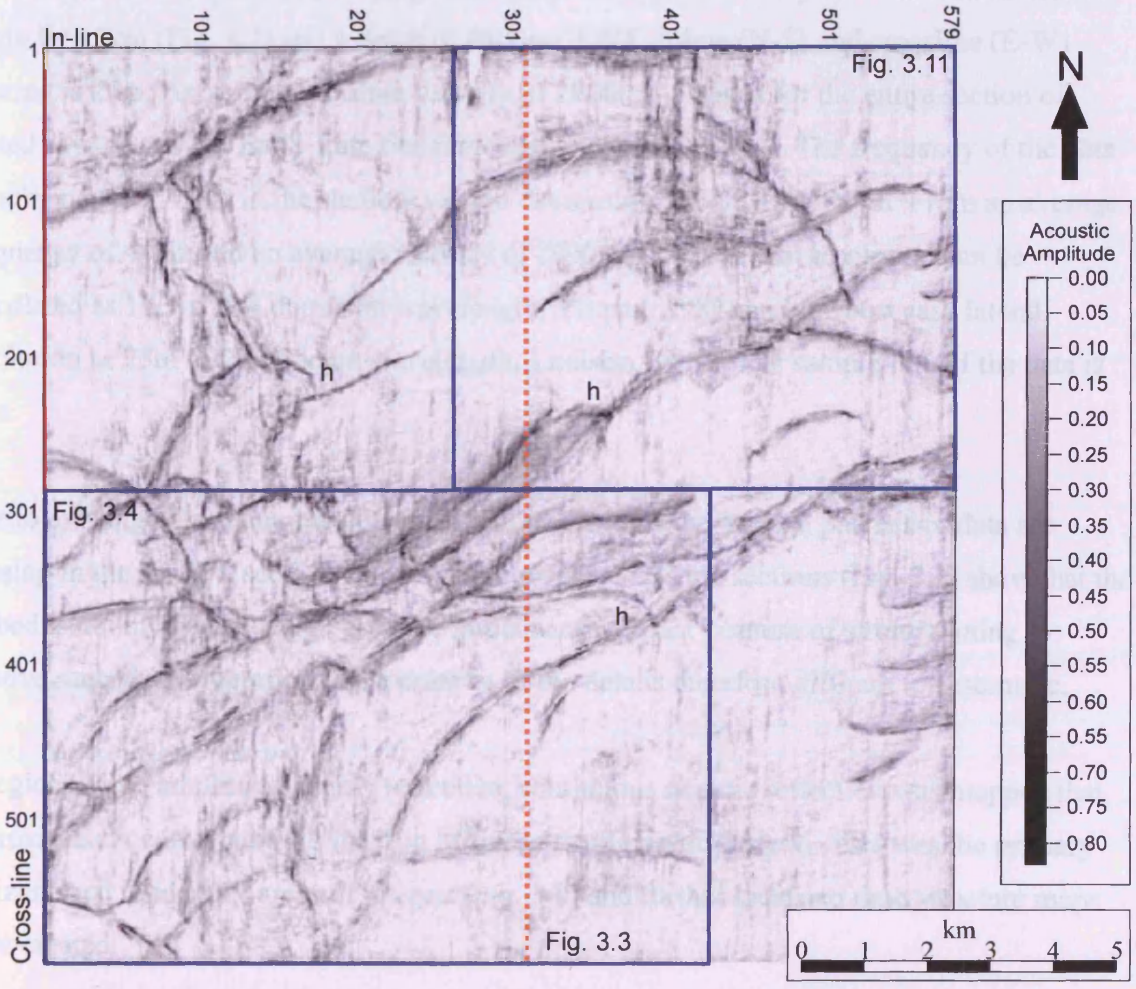

Figure 3.2. Dataset area shown by coherence extraction of Top Miocene mapped horizon. Dark lineaments represent faults which have a dominant NE-SW trend. Boxed areas are those used for further study. Location of the regional seismic line shown in orange. h: 'hook' geometries. See text for further explanation.

and their associated fault families (Rowan et al. 1999). It is likely that the interaction of fault trends in the study area is related to the location of the study area in a transitional zone between fault families relating to separate positive structures. However, Worral and Snelson (1989) describe two separate growth fault styles: (1) Texas Style with elongate, rectilinear, basinward dipping faults situated to the east and (2) Louisiana Style growth faults, which are shorter, more arcuate and dip both basinward and landward. It is implied by Reymond (1994) that the intersections in this study are due to the interference between these two styles. The lower fault tips are either poorly imaged or truncated by the available dataset (Figs. 3.2, 3.3), therefore it is not possible to determine whether they detach in salt structures and if so, which type of salt structure.

3.1.2 Dataset and methodology

The dataset used in this study is a high resolution 3D seismic survey that has dimensions 15km by 15km (Fig. 3.2) and a depth of 4500ms TWT. Inline (N-S) and crossline (E-W) spacing is 25m. An average seismic velocity of $2000ms^{-1}$ is used for the entire section of mixed siliciclastics of Early-Late Cenozoic age (Reymond, 1994). The frequency of the data is estimated at c.45Hz in the shallow section decreasing to c.30Hz at depth. From an average frequency of 40Hz and an average velocity of $2000ms^{-1}$ the vertical resolution can be calculated as 12.5m (1/4 dominant wavelength, Yilmaz, 1987) and the best case lateral resolution as 25m (1/2 dominant wavelength, Lindsey, 1989). The sample rate of the data is 2ms.

Due to existing petroleum development infrastructure on the seabed, patches of data are missing in the shallow section. Furthermore, regional seismic sections (Fig. 3.3) show that the seabed is not imaged as a high acoustic impedance contrast because of strong muting to remove seabed reverberations. The polarity of the data is therefore difficult to determine.

A regional high amplitude, highly reflective, continuous seismic reflection was mapped that approximately corresponds to the Top Miocene stratigraphic horizon. This was the primary horizon used to identify areas of interest (Fig. 3.2) and further localised time structure maps were created.

A coherency volume of the entire dataset was created to assist in the delineation of the fault pattern and its variations within the seismic volume. Faults were identified from linear

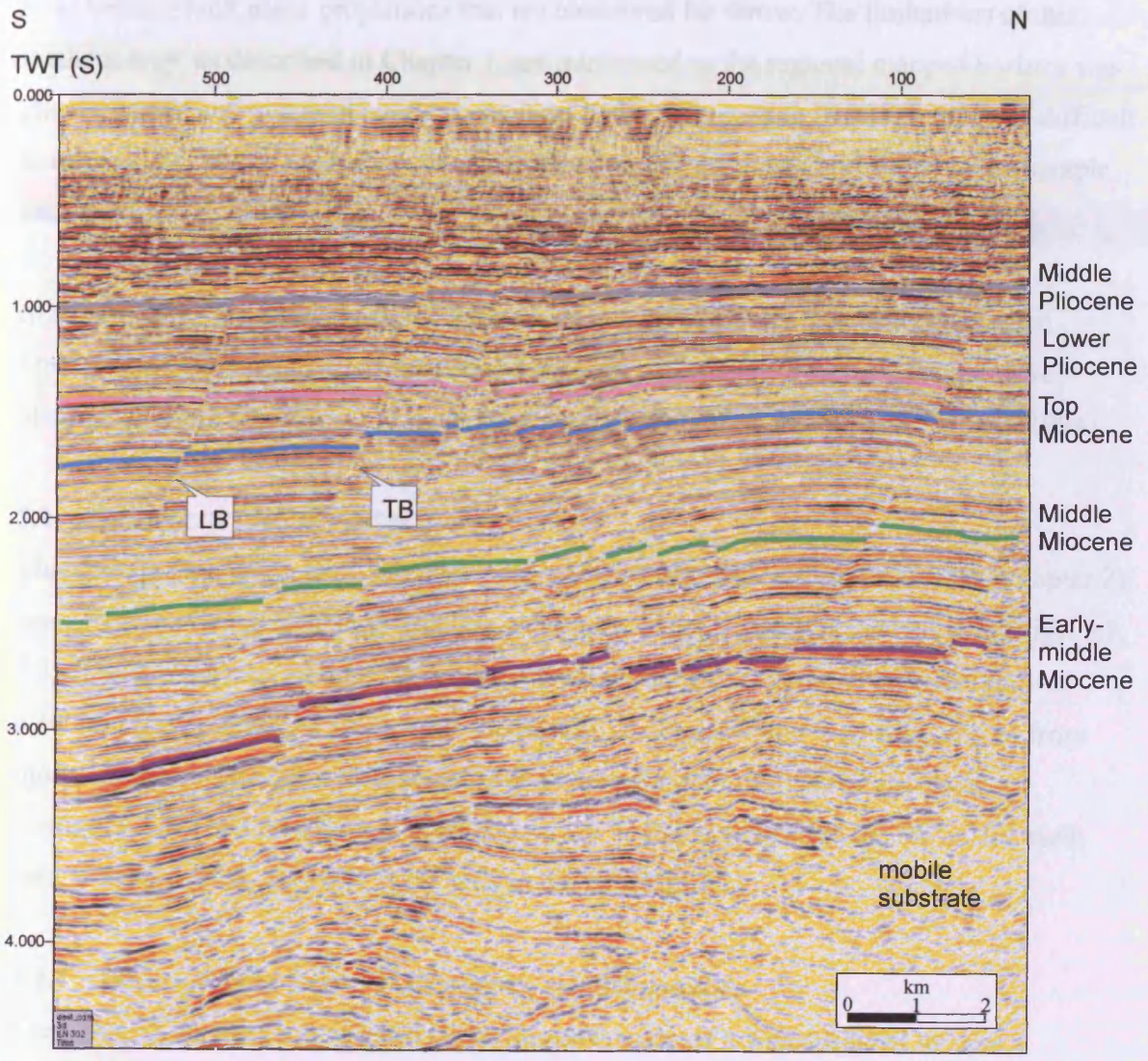

Figure 3.3. Regional seismic section In-line 302 (see Fig. 3.2 for location). Landward and basinward dipping faults identified by systematic offset of reflections. Reflections tied to stratigraphy from Reymond, 1994. Top Miocene horizon is regionally mapped and used as a basemap (Fig. 3.2). LB: Louisiana B; TB: Texas B.

coherence anomalies, representing low continuity, and from sub-vertical zones of low reflectivity and systematically offset reflection terminations. Data are presented as T-x plots or as vertical fault plane projections that are contoured for throw. The limitations of this methodology, as described in Chapter 1, are minimised as the regional mapped horizon was chosen so that any potential overlaps occurred in the deep section from where it was difficult to obtain data. Throw measurement errors are ±2ms (c.2m), related primarily to the sample rate.

In the absence of available well log data the seismic stratigraphy is poorly constrained. Stratigraphic markers are displayed on the regional seismic profile (Fig. 3.3) and were obtained through comparison to the limited seismic sections available in Reymond (1994).

3.2 CROSS-CUTTING INTERSECTIONS

This section focuses on two fault intersection areas with cross-cutting or X class (Chapter 2) geometries that were identified from the regionally mapped Top Miocene horizon (Figs. 3.2, 3.3). The X class intersections described in this section persist vertically over a range of c.3000ms TWT and this provides the opportunity to describe branch line topologies from these complex structures over a considerable vertical extent of the total structural configuration. The first example is termed Lower X and is situated in the SW of the study area and the second, Upper X, is situated in the NE (Fig. 3.2).

3.2.1 Description of Lower X Geometry and Kinematics

The Lower X intersection was chosen for detailed study as it was observed to have a consistent cross-cutting intersection throughout the imaged interval. It has also been described to a more limited extent by Mansfield (1996), Mansfield and Cartwright (1996) and by Needham et. al (1996).

The Lower X intersection is formed between the traces of two faults, termed the E-W trending Louisiana Fault and the NE-SW trending Texas Fault (Fig. 3.4). The faults dip to the south and south-west respectively. The southern edge of the dataset limits the lateral extent to which both faults can be traced, therefore their true length is unknown. Within the dataset, the Texas Fault has a total length of 11.5km and is part of the predominant NE-SW trend (Section

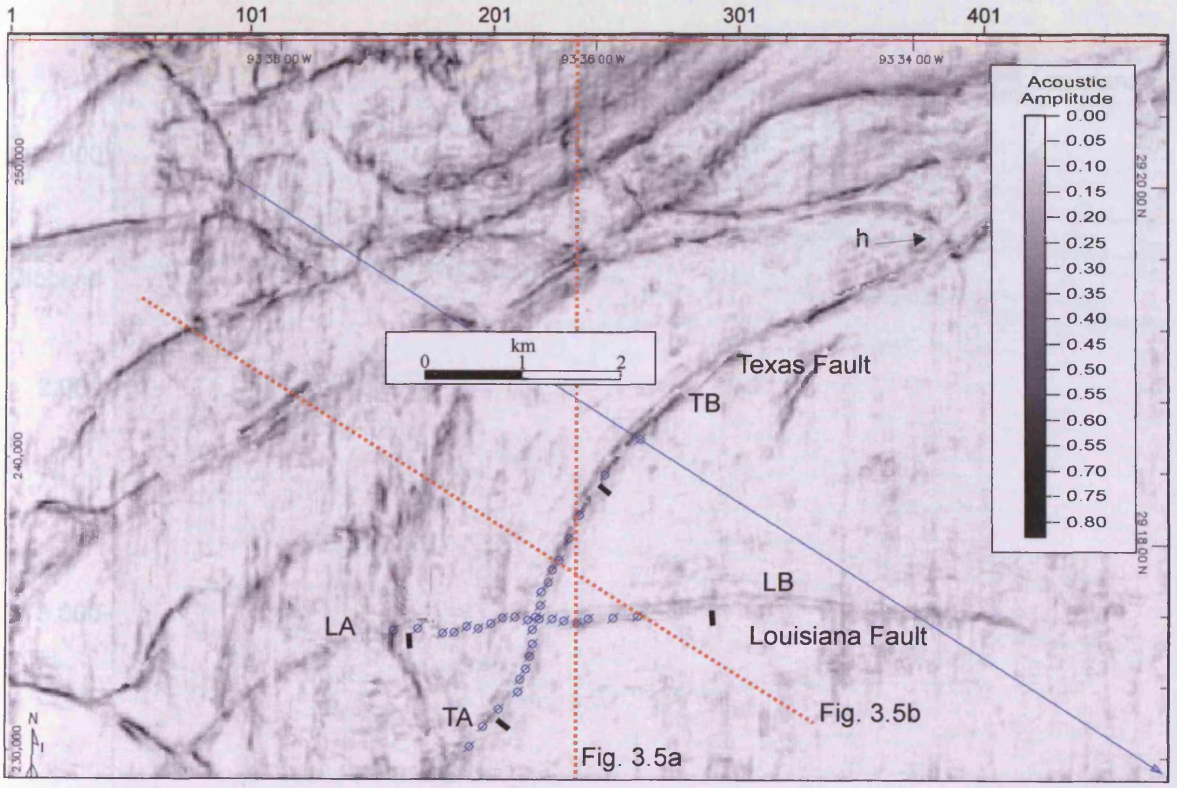

Figure 3.4. Coherence extraction of Top Miocene horizon showing the X geometry of the Lower X intersection. The intersecting fault traces form two acute and two obtuse angles. Navy coloured circular markers are locations of displacement measurement profile lines. Location of seismic section lines of Figure 3.5 are shown. LA: Louisiana A; LB: Louisiana B; TA: Texas A; TB: Texas B; h: hook geometry.

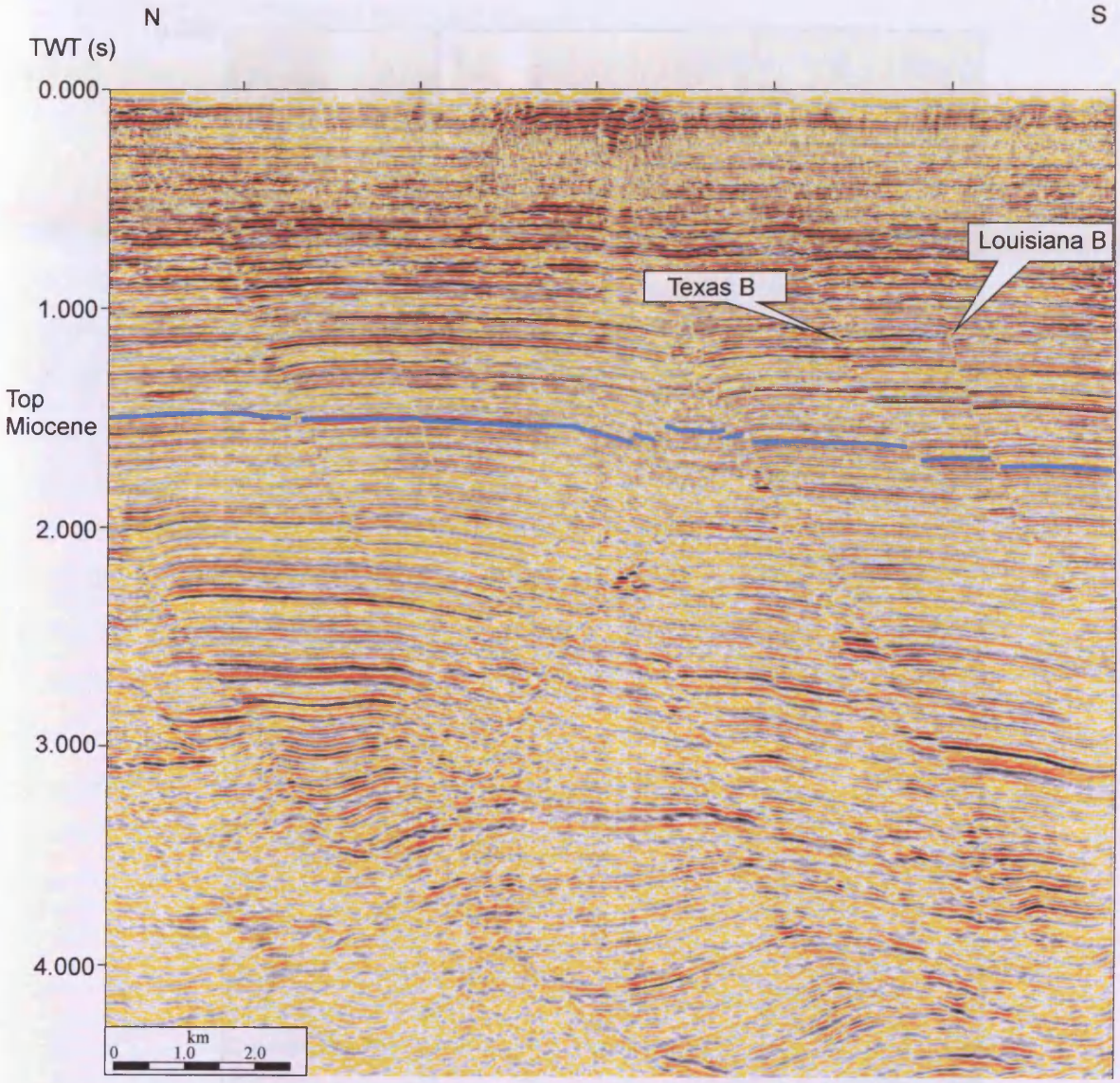

Figure 3.5a. Seismic profile line taken perpendicular to the Louisiana Fault. The Louisiana Fault is truncated at its lower extent by the edge of the dataset. The Texas B fault is cut obliquely by this seismic section (accounting for its shallow angle) and resolution is decreased in the area where the two faults cross-cut.

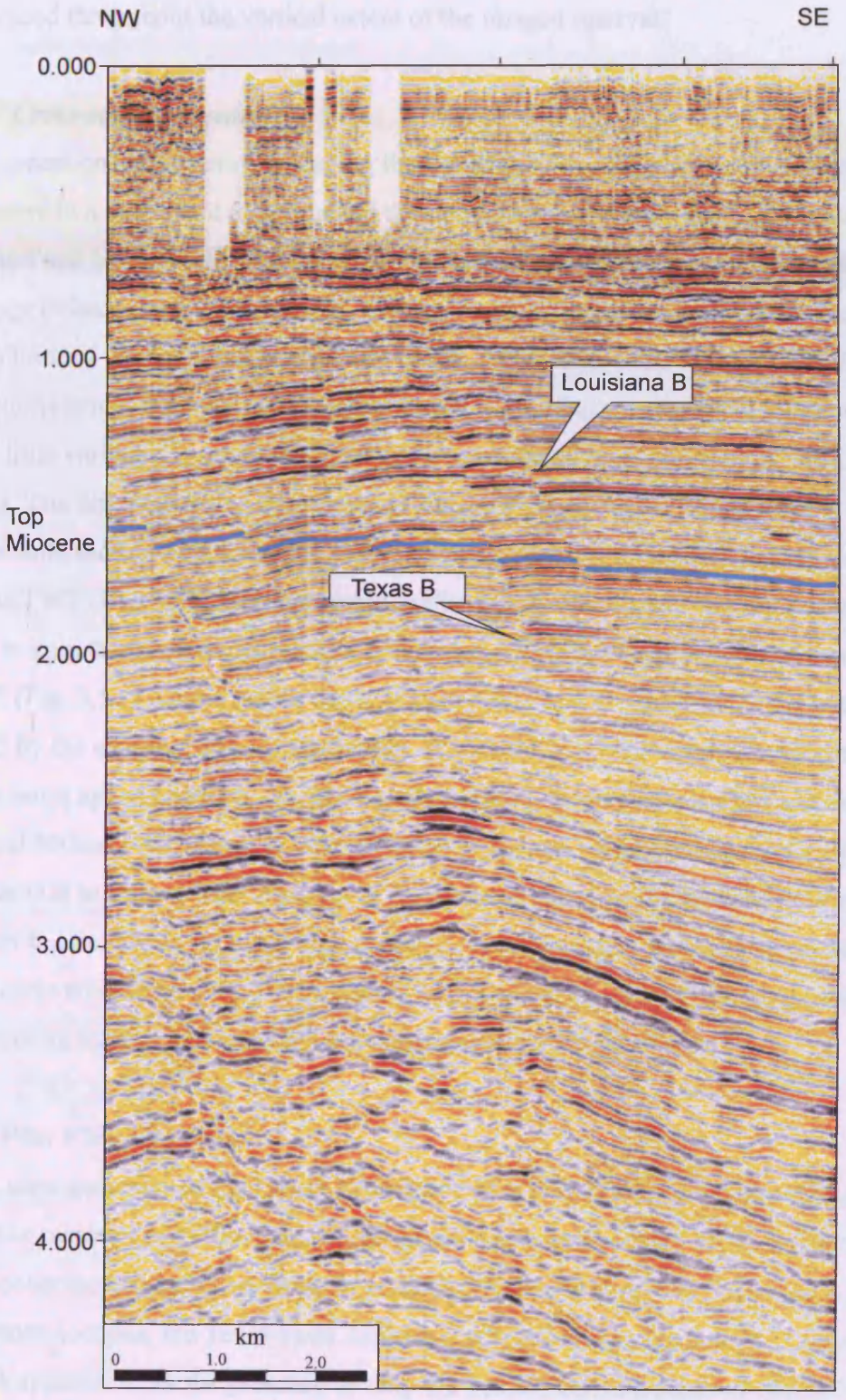

Figure 3.5b. Seismic profile line taken perpendicular to the Texas Fault. Both the Texas and Louisiana Faults are imaged. Throw values increase with depth.

3.1.1). The Louisiana Fault has a shorter trace length within the study area and its eastern tip can be traced throughout the vertical extent of the imaged interval.

3.2.1.1 Cross-sectional geometry

The cross-sectional fault array, including the Louisiana Fault (Fig. 3.5a), dominantly downthrows in a basinward direction and the faults have a typically listric geometry. The Louisiana Fault has a southward dip of 30° and is locally offset in the dip direction indicating dip linkage (Mansfield and Cartwright, 1996). The lower tip of the fault is truncated by the southern limit of the dataset. The upper tip lies between 300ms and 700ms TWT. Correlation of reflections across the fault indicates that throw values show a general increase with depth. There is little variation in cross-sectional geometry between the Louisiana A and Louisiana B segments. The dip intersection between the Louisiana Fault and the Texas Fault is expressed on the seismic section by a widening of the low reflectivity zone where they cross-cut at c.2125ms TWT (Fig. 3.5a). Seismic resolution is therefore decreased locally and it was difficult to gain throw measurements from this area of intersection. The Texas Fault dips 35° to the SE (Fig. 3.5b). Throw values increase with depth and the basal tip of the fault is truncated by the southern edge of the dataset. It is difficult to define the exact location of the upper tip but it appears to have reached a position that is close to the seabed and lies between 250ms and 500ms TWT. There is little variation in the cross-sectional geometry of the Texas A and Texas B segments. The lower tip of the Texas A segment is truncated by the limit of the dataset but the Texas B fault segment can be traced into the deep section and becomes slightly listric with depth (Fig. 3.5b). Throw values increase and reflectivity decreases with depth therefore there is less confidence in seismic reflection correlation.

3.2.1.2 Plan View Geometry

The plan view geometry of the Lower X intersection is remarkably consistent throughout the dataset. The persistence of the intersection branch line over the depth range is illustrated by a series of coherence slices taken throughout the depth section (Fig. 3.6). As evident from seismic cross-sections, the Texas Fault deforms shallower sediments than the Louisiana Fault, and this is apparent from the presence of only the Texas Fault at a depth of 768ms TWT (Fig. 3.6a). At this time slice position, both lateral fault tips of the Texas Fault can be identified.

The Louisiana Fault has an irregular upper tip as shown by its presence as two (Fig. 3.6b), or three (Fig. 3.6c), separate segments, rather than a single trace cross-cutting the Texas Fault at

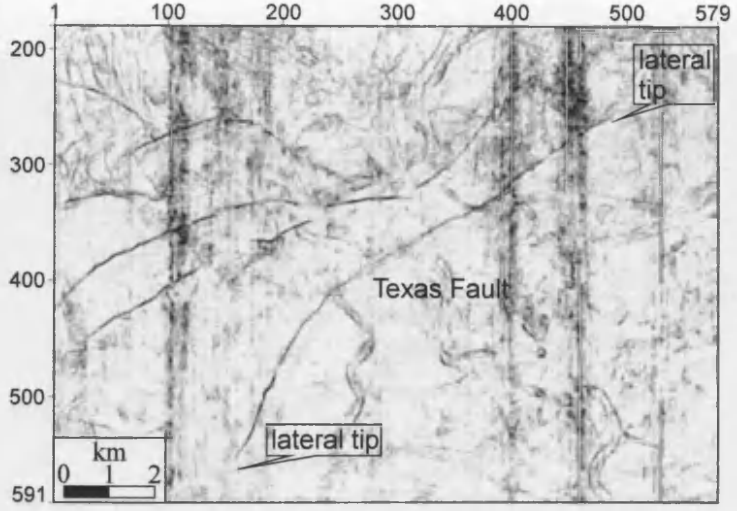

(a) 768ms TWT

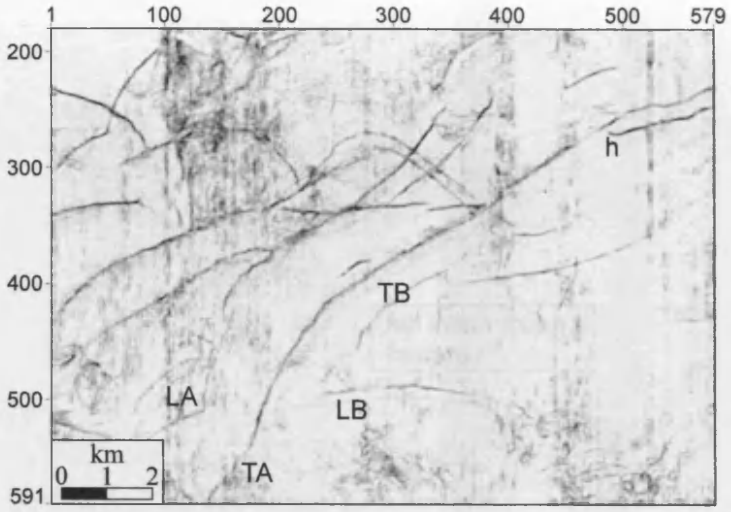

(b) 968ms TWT

Figure 3.6. Series of coherence slices through the 3D seismic volume illustrating the plan view geometry of the Lower X intersection. The Lower X structure shows very little variation in plan view geometry throughout the depth section and is therefore a very stable structure. (a) Only the Texas Fault is imaged and both lateral tips are seen. (b) The upper tips of segments LA and LB are imaged but no intersection is identified. (c) Three upper tip segments of the Louisiana Fault are seen. (d) A full intersection is identified at a single branch point. (e) - (j) The branch line migrates toward the south of the dataset. No offset of either fault is recorded at intersection. LA: Louisiana A; LB: Louisiana B; TA: Texas A; TB: Texas B; h: hook.

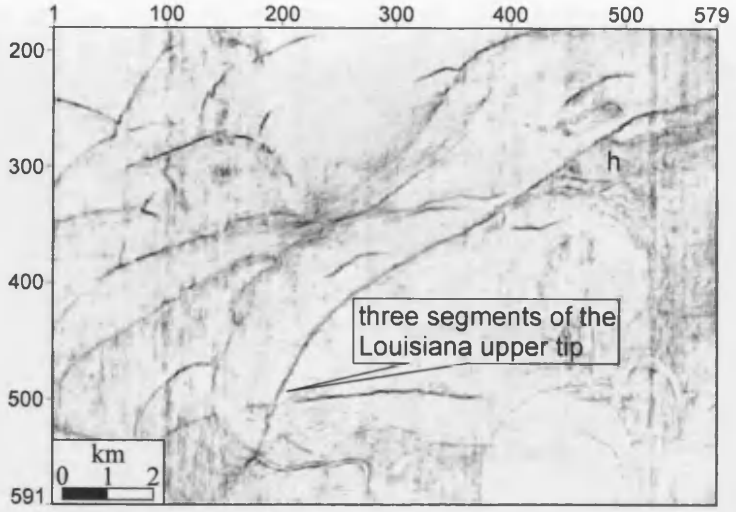

(c) 1148ms TWT

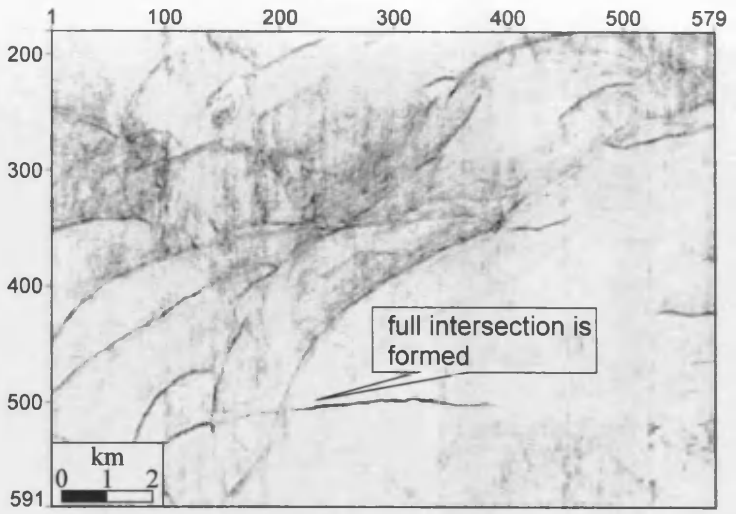

(d) 1260ms TWT

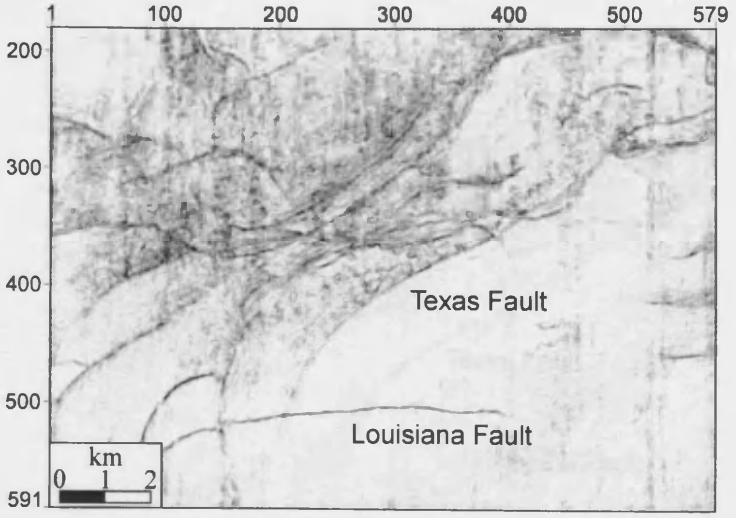

(e) 1428ms TWT

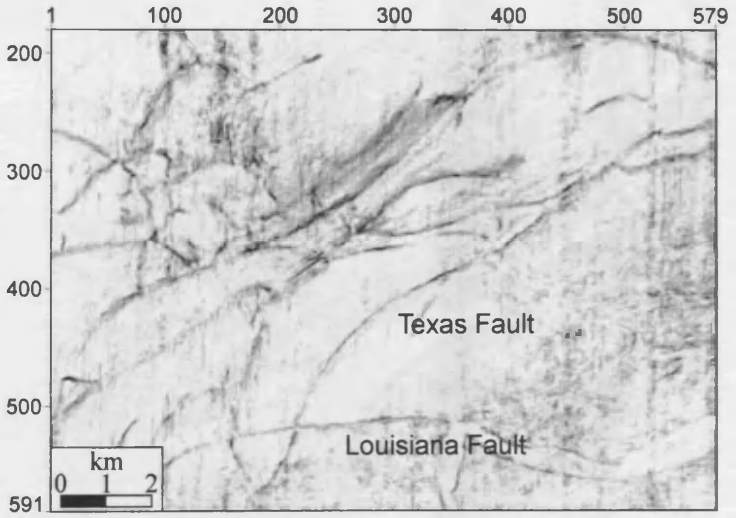

(f) 1600ms TWT

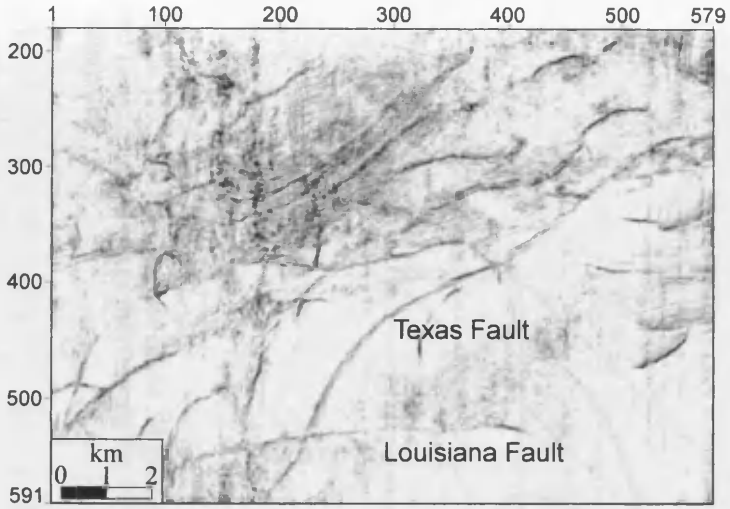

(g) 1840ms TWT

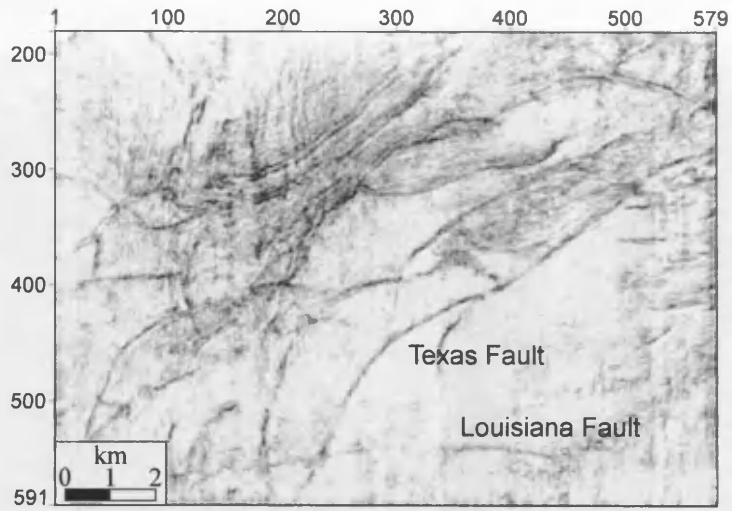

(h) 2108ms TWT

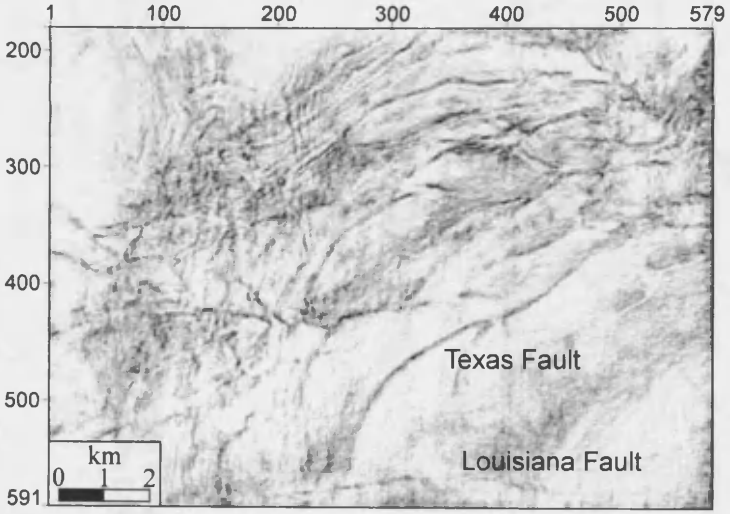

(i) 2500ms TWT

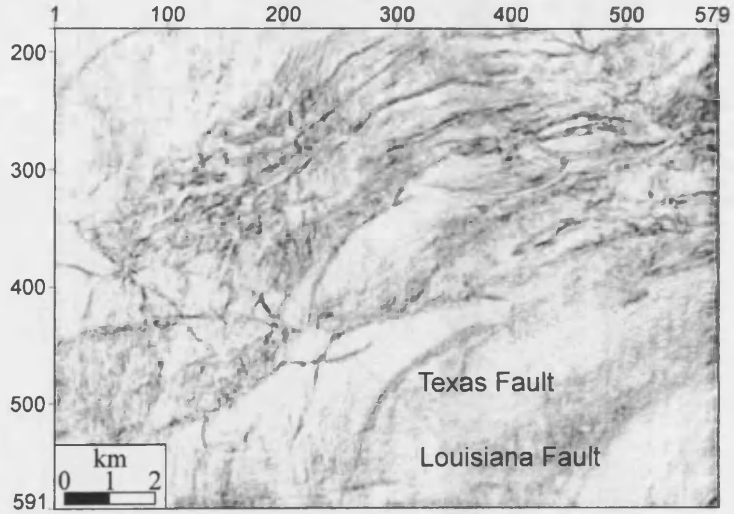

(j) 2548ms TWT

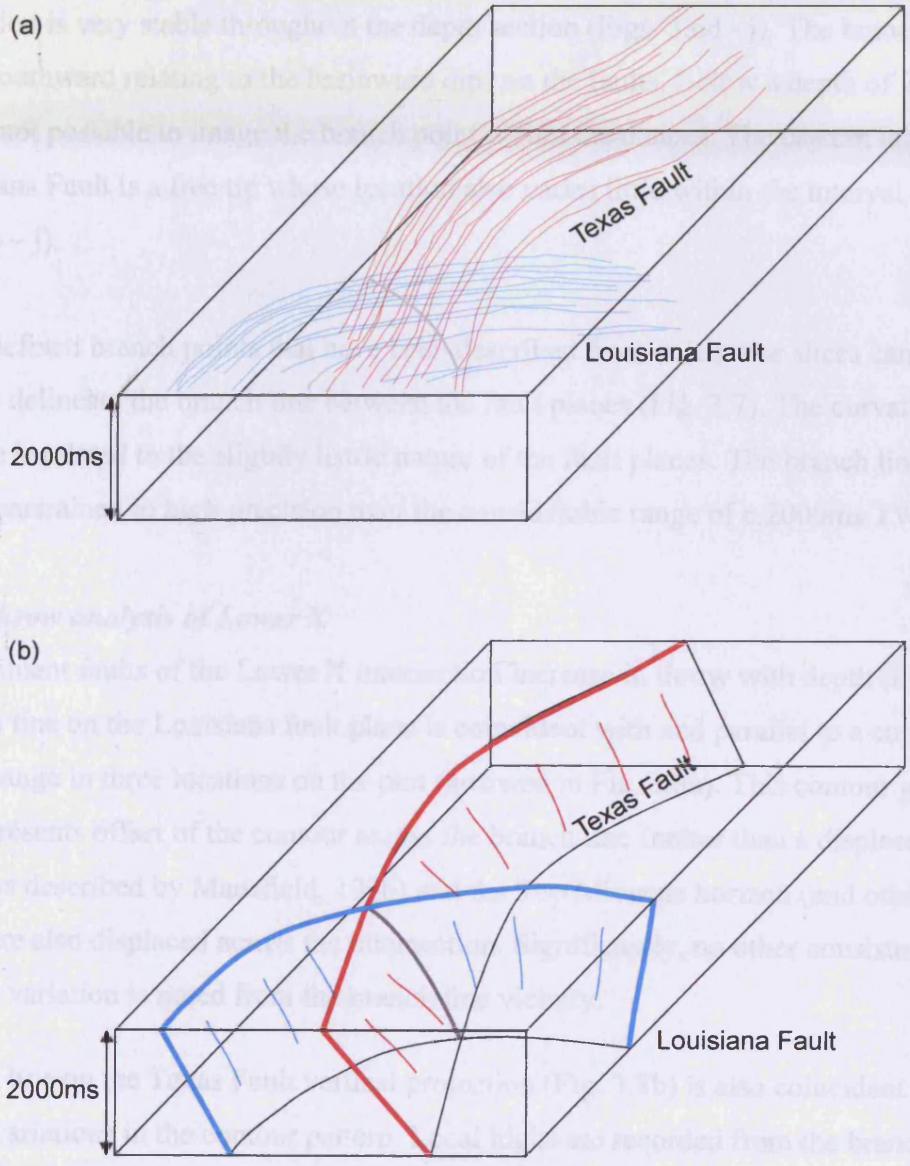

Figure 3. 7. Synoptic diagram of the 3D geometry of the Lower X intersection. (a) Reconstruction of the Texas and Louisiana Fault traces from tracing the series of coherence slices. (b) Schematic diagram of the Lower X intersection.

968ms TWT. The Texas Fault increases length with depth and neither tip is imaged within the dataset below 968ms. The Louisiana Fault is a throughgoing fault trace which forms a full X intersection geometry with the Texas fault trace at 1260ms TWT and below (Figs. 3.6d - j). Within seismic resolution, the X intersection can be described as a single branch point. This configuration is very stable throughout the depth section (Figs. 3.6d - j). The branch point migrates southward relating to the basinward dips on the faults. Below a depth of 2548ms TWT it is not possible to image the branch point within the dataset. The eastern lateral tip of the Louisiana Fault is a free tip whose location also varies little within the interval of interest (Figs. 3.6b – j).

The well-defined branch points that have been described from coherence slices can be joined together to delineate the branch line between the fault planes (Fig. 3.7). The curvature of the branch line is related to the slightly listric nature of the fault planes. The branch line is spatially constrained to high precision over the considerable range of c.2000ms TWT.

3.2.1.3 Throw analysis of Lower X

Both constituent faults of the Lower X intersection increase in throw with depth (Fig. 3.8). The branch line on the Louisiana fault plane is coincident with and parallel to a contour gradient change in three locations on the plot (arrowed in Fig. 3.8a). This contour gradient change represents offset of the contour across the branch line (rather than a displacement minimum as described by Mansfield, 1996) and the Top Miocene horizon (and other horizons) are also displaced across the intersection. Significantly, no other consistent or remarkable variation is noted from the branch line vicinity.

The branch line on the Texas Fault vertical projection (Fig. 3.8b) is also coincident with and parallel to variations in the contour pattern. Local highs are recorded from the branch line at approximate depths of 1400ms, 1650ms and 1900ms (Fig. 3.8b). These localised highs can best be explained by the inability to resolve two distinct horizon offsets at the intersection location, resulting in a zone of combined throw (Fig. 3.9, Chapter 1).

The offset of horizons across both fault planes is clearly demonstrated by the Top Miocene horizon (Fig. 3.9). No variation in throw is seen on either fault plane approaching the intersection location. Each horizon offset that represents a fault plane on the time-structure map (Fig. 3.9) is displaced by the exact value of throw across the other fault plane.

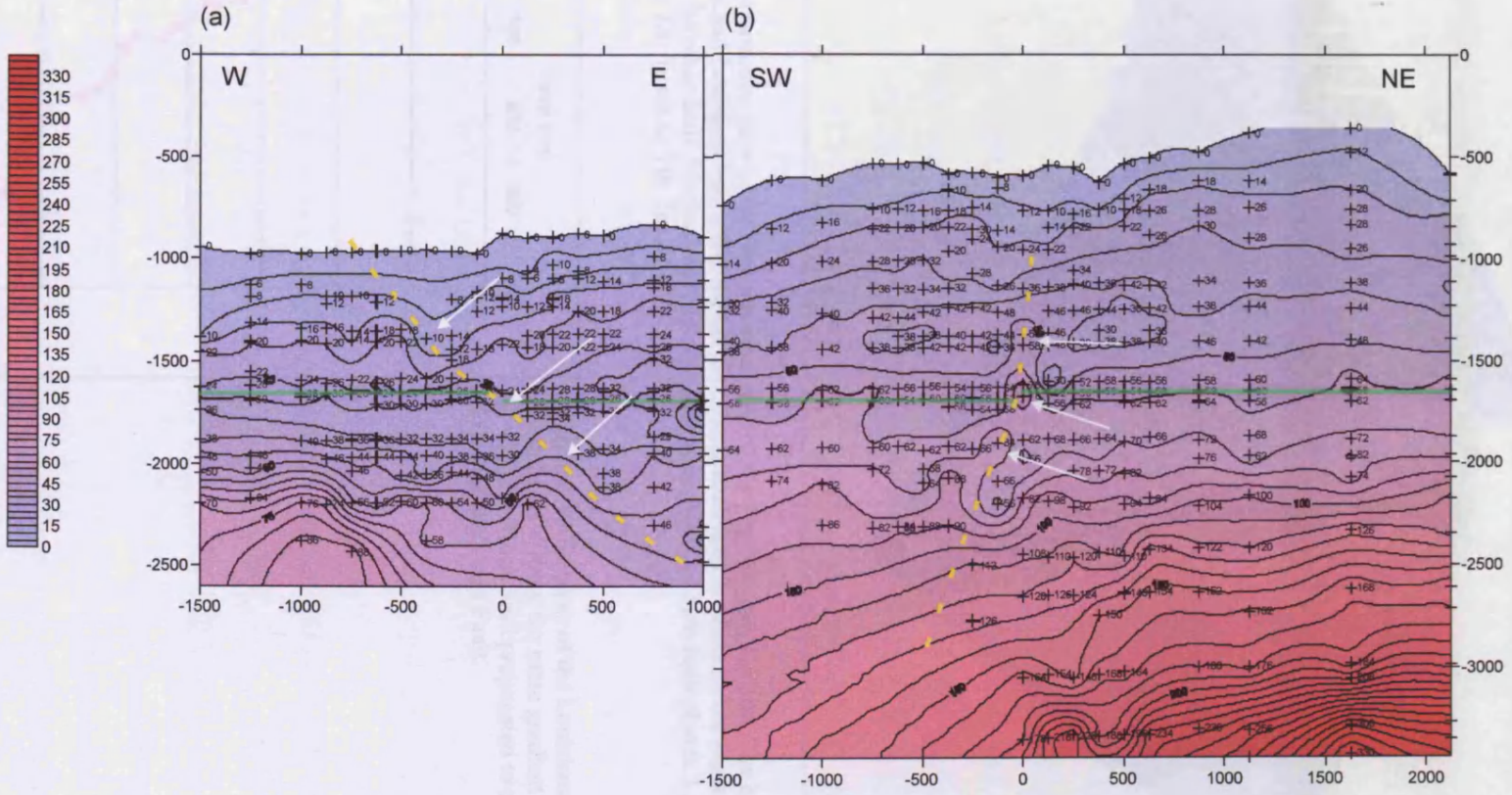

Figure 3 8. Throw distribution displayed as vertical fault projections. (a) Louisiana Fault. (b) Texas Fault. Note offset of Top Miocene horizon. The plots are displayed at the same scale with the same colour bar. The branch line is dotted in yellow and shows an apparent shallowing of dip with depth that is related to the limitation of the methodology of vertical projection (Chapter 1). White arrows indicate where branch line parallels throw contours or highs

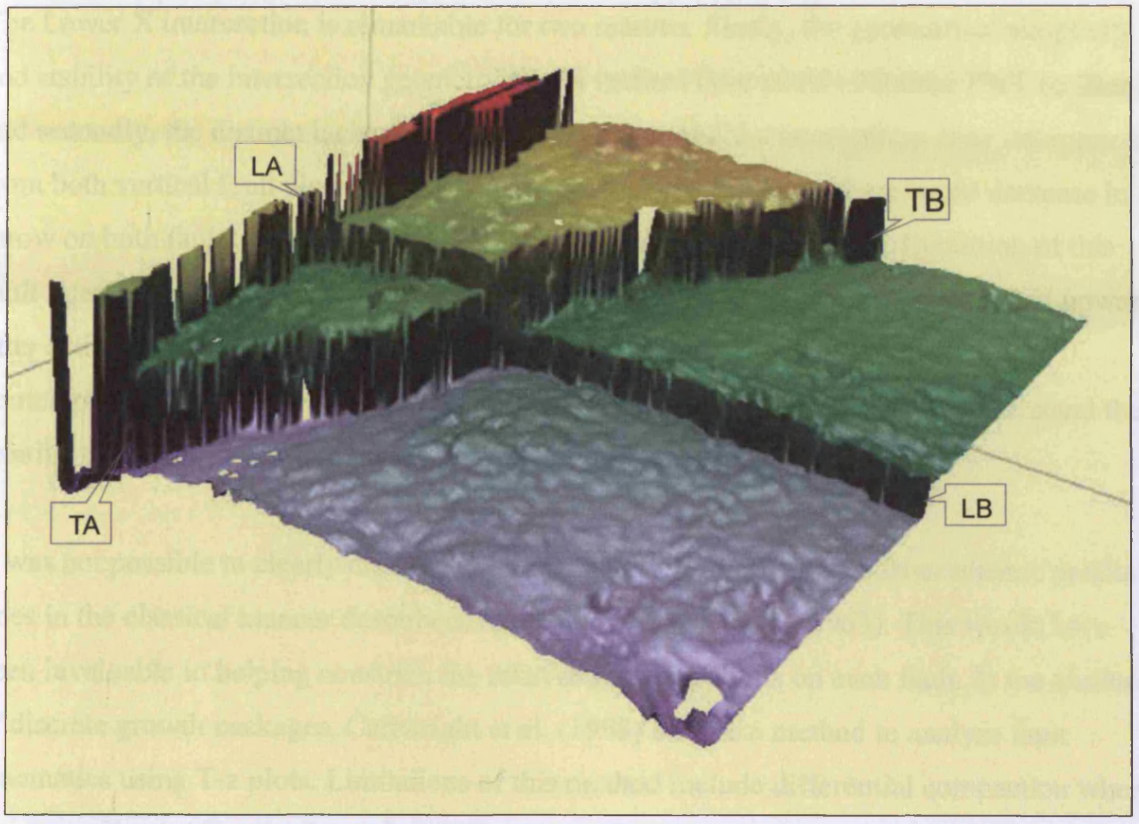

Figure 3.9. 3D perspective view of the time-structure map of the Top Miocene horizon. The horizon is displaced by both the Texas and Louisiana Faults and the horizon across each fault is offset by the exact value of displacement on the other fault. Displacement values are near-constant on both fault planes. LA: Louisiana A; LB: Louisiana B; TA: Texas A; TB: Texas B.

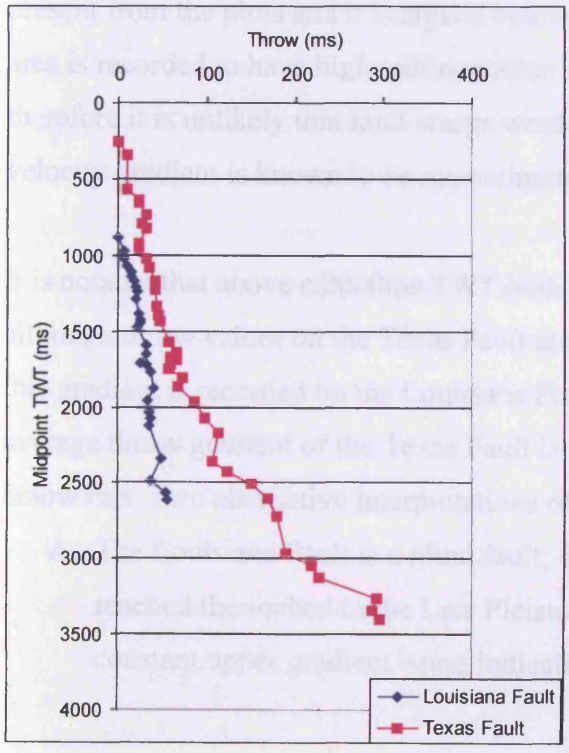

Figure 3.10 T-z plots of the Louisiana and Texas Faults. Both faults display the same gradient above c. 2000ms TWT. The Texas fault propagated to a shallower level than the Louisiana Fault.

3.2.1.4 Structural Evolution of the Lower X intersection

The Lower X intersection is remarkable for two reasons. Firstly, the geometrical simplicity and stability of the intersection geometry over a vertical interval of ~2000ms TWT (c. 2km) and secondly, the distinct lack of variation in strain around the intersection zone interpreted from both vertical fault plane projections and time structure maps. The upward decrease in throw on both faults is interpreted as upward Mode II style propagation. Evolution of this fault intersection therefore requires either (a) that the younger fault plane propagated upward after activity on the older fault plane ceased, or (b) that fault movement was contemporaneous. For further analysis, it is therefore necessary to attempt to understand the relative timing of the fault motion.

It was not possible to clearly distinguish sedimentary growth packages from seismic profile lines in the classical manner described, for example, by Thorsen (1963). This would have been invaluable in helping constrain the relative growth periods on each fault. In the absence of discrete growth packages, Cartwright et al. (1998) outline a method to analyse fault kinematics using T-z plots. Limitations of this method include differential compaction where throws are large (Cartwright et al., 1998) and the assumption that sedimentation always fills topographies created by growth structures (Castelltort et al., 2004). Increased compaction in the hangingwall would serve to increase throw values and therefore periods of non-growth may be mis-interpreted as growth. This can be discounted as potential growth intervals are not present from the plots and it is argued below that the faults are blind faults. Further, the study area is recorded to have high sedimentation rates throughout the Cenozoic (Reymond, 1994) therefore it is unlikely that fault scarps would exist over a prolonged period of time. The velocity gradient is known to be approximately linear through the interval in question.

It is notable that above c.2000ms TWT both faults display a similar vertical throw gradient although throw values on the Texas Fault are consistently higher (Fig. 3.10). No variation to this gradient is recorded on the Louisiana Fault and it has an approximate value of 0.04. The average throw gradient of the Texas Fault is recorded as 0.047 above ~2250ms TWT and 0.15 below this. Two alternative interpretations of these T-z plots can be proposed:

A. The Louisiana Fault is a blind fault; the Texas Fault propagated as a blind fault and reached the seabed in the Late Pleistocene. This is based on the interpretation of the constant upper gradient being indicative of blind fault propagation, and the small

differences in throw being due to wallrock strains necessary to accommodate vertical variation in throw (Walsh and Watterson, 1987).

B. Both faults were active growth faults, from the Early Pleistocene (1.5Ma BP), with the throw variation being indicative of small but persistent stratigraphic thickness variation across the fault, i.e. syn-sedimentary growth. The average rate of growth is therefore 50m in 1.5Ma, or 1m/30000years. This is an order of magnitude lower than reported average growth rates from similar settings in the Gulf of Mexico (Berryhill et al. 1987).

The favoured interpretation is that both faults are blind. As described in Section 3.1.2, the dataset does not allow study of the deeper continuation of these structures. Therefore it is not possible to investigate timing of e.g. growth of the fold, above which these faults are interpreted to form. Evolution of this intersection will be further discussed in Section 3.4.2.

3.2.2 Description of Upper X Geometry and Kinematics

The second X intersection study area, termed upper X, is located in the NE of the West Cameron dataset (Fig. 3.2). It consists of two near-orthogonal intersections that share a NW-SE trending fault, termed the Mississippi Fault, which intersects with two NE-SW trending faults, termed the Sabine and the Sigsbee Faults (Fig. 3.11).

3.2.2.1 Cross-sectional geometry

In cross-section, the Mississippi Fault (Fig. 3.12a) has an upper tip that is close to the seabed, at approximately 750ms TWT. The fault trace is gently curved and cuts through almost the entire vertical extent represented by the seismic dataset. However, the reduction in data quality with depth makes it difficult to identify the location and nature of the lower tip. Along strike, beyond the Sabine intersection, the upper tip is c. 1200ms TWT.

The Sabine and Sigsbee Fault traces (Fig. 3.12b) are parallel and slightly curved with an approximate dip of 35° to the southeast. The upper tips of both faults occur at c.600ms TWT. The lower tips are difficult to define due to reduction in data quality with depth but the Sabine Fault lower tip is recorded at c.3000ms TWT where the fault may terminate in layer parallel shear within a muddy sequence.

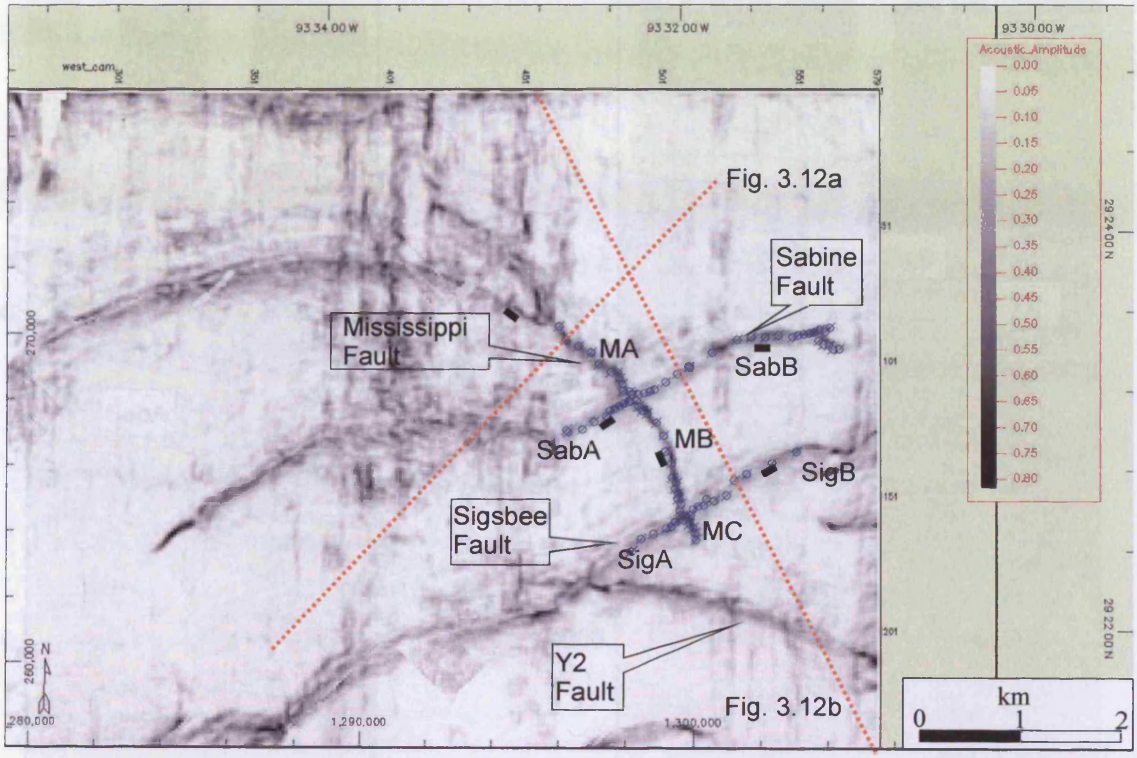

Figure 3.11 Coherence extraction of Top Miocene horizon showing the X geometries of the Upper X intersections. Navy coloured circular markers are locations of displacement measurement profile lines. Location of seismic section lines of Figure 3.12 are shown. MA: Mississippi A; MB: Mississippi B; MC: Mississippi C; SabA: Sabine A; SabB: Sabine B; SigA: Sigsbee A; SigB: Sigsbee B.

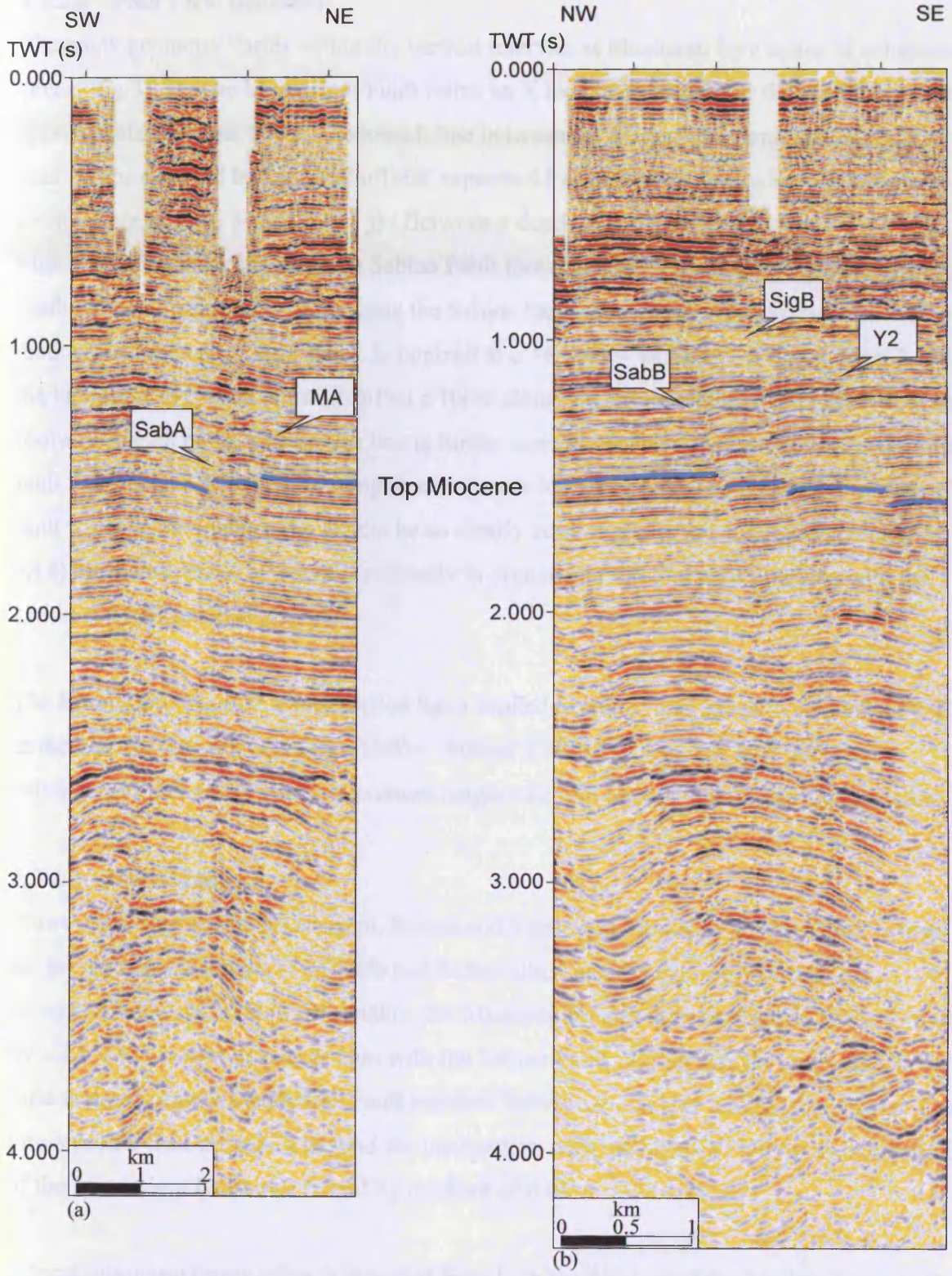

Figure 3.12. Seismic section lines showing the cross-sectional nature of (a) the Mississippi and Sabine Faults and (b) the Sabine, Sigsbee and Y2 faults. Seismic reflections become more difficult to correlate across the faults at depth.

3.2.2.2 Plan View Geometry

Plan view geometry varies within the vertical interval, as illustrated by a series of coherency slices (Fig.3.13). The Mississippi Fault forms an X intersection with the Sabine Fault below approximately 900ms TWT. The branch line between the Mississippi Fault and the Sabine Fault is complicated by localised offsets, separated by vertical sections where no offset is identified (e.g. Figs. 3.13a, e, h, i, j) . Between a depth of c. 950ms and 1150ms TWT (e.g. Figs. 3.13b, d), the location of the Sabine Fault footwall branch point with the Mississippi Fault is laterally shifted c.100m along the Sabine Fault trace to the NE, forming a second distinct hangingwall branch point. In contrast at c.1400ms – 1450ms TWT (e.g. Figs. 3.13f, g) the hangingwall branch point is shifted c.100m along the Sabine Fault trace to the SW of the footwall branch point. The branch line is further complicated by localised mutual offset of the fault traces, e.g. Fig. 3.13k, creating three separate branch points. These localised offsets of fault traces at the intersection cannot be so clearly seen on the schematic line drawing (Fig. 3.14) but it does show an overall continuity in plunge and dip that is comparable with the Lower X intersection (Fig. 3.7).

The Mississippi/Sigsbee X intersection has a limited extent of approximately 300ms (TWT) in the vertical interval, between c.1500 – 1800ms TWT (e.g. Figs. 3.13h-l), and the Mississippi Fault extends for a maximum length of 250m beyond the intersection location.

3.2.2.3 Throw analysis

Throw variations on the Mississippi, Sabine and Sigsbee Fault planes at Top Miocene level are presented as T-x plots (Fig. 3.15) and further illustrated by the Top Miocene time-structure map (Fig. 3.16). Most notably, the Mississippi Fault throw values decrease abruptly by c.20s TWT across its intersection with the Sabine Fault. Values remain lower and show little variation on the Mississippi Fault segment between the Sabine and Sigsbee Faults. The throw profile then decreases beyond the intersection with the Sigsbee Fault to the southern tip of the Mississippi Fault on a lateral tip gradient of 0.05.

A local minimum throw value is recorded from both the Sabine and the Sigsbee Faults at their intersections with the Mississippi Fault. The Sabine Fault has a predominantly uniform profile with throw decreasing towards its NE lateral tip. The throw gradient increases over an inflection from an average value of 0.03 to a tip gradient of 0.1. The strike of the fault varies at the north-eastern tip, where it appears to 'split' into two short fault segments in plan view,

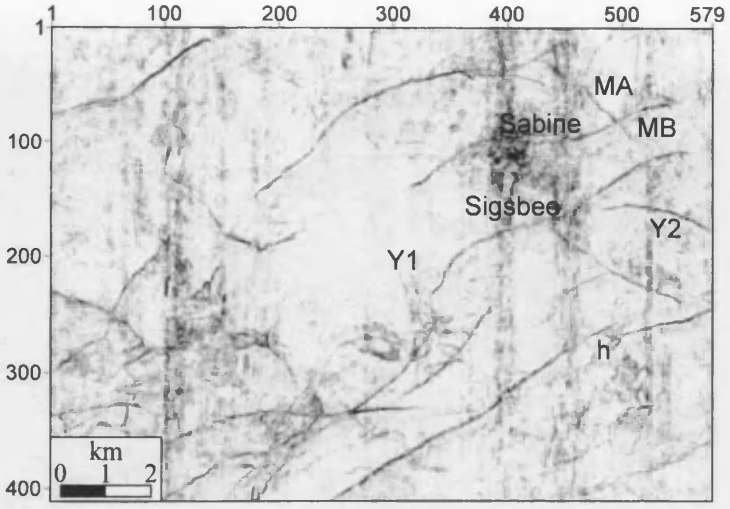

(a) 916ms TWT.

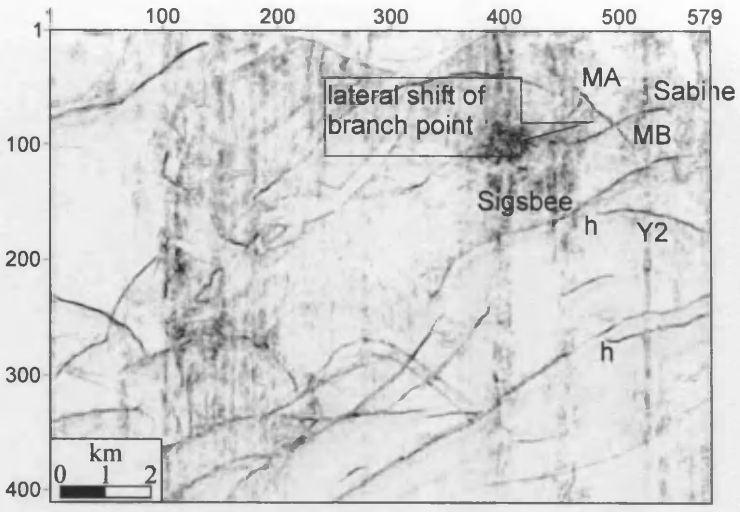

(b) 956ms TWT.

Figure 3.13. Series of coherence slices through the 3D volume illustrating the plan view geometry of the Upper X, Y1, Y2 and Y3 intersections. (a) The Mississippi Fault forms an X intersection with the Sabine Fault; no intersection occurs between the Mississippi and Sigsbee Faults. (b) The Mississippi/Sabine branch point is laterally offset c.100m to the NE. (c) The Mississippi/Sabine branch point is laterally offset c.100m to the NE. The Y1 fault forms a hook geometry. (d) The Mississippi/Sabine branch point is laterally offset c.100m to the NE. The Y1 and Y2 faults form pronounced hooking geometries. (e) No lateral offset is recorded on the Mississippi/Sabine intersection. The Mississippi Fault forms a T intersection with the Sigsbee Fault. (f) The Mississippi/Sabine branch point is laterally offset c.100m to the SW. (g) The Mississippi/Sabine branch point is laterally offset c.100m to the SW. The Y2 fault exhibits a less pronounced hook geometry. (h), (i), (j) The Mississippi Fault forms an X intersection with the Sigsbee Fault. No lateral offset is recorded on the Mississippi/Sabine intersection. The Y2 intersection does not exhibit a hook geometry. The Y3 intersection is formed at the eastern tip of the Sabine Fault. (k) Three separate branch points are imaged at the Mississippi/Sabine intersection as highlighted by arrows. The Mississippi Faults extends a short distance into the Sigsbee hangingwall. (l) No lateral offset is recorded on the Mississippi/Sabine intersection. The Y2 intersection does not exhibit a hook geometry. MA: Mississippi A; MB: Mississippi B; MC: Mississippi C; SabA: Sabine A; SabB: Sabine B; SigA: Sigsbee A; SigB: Sigsbee B; h: hook.

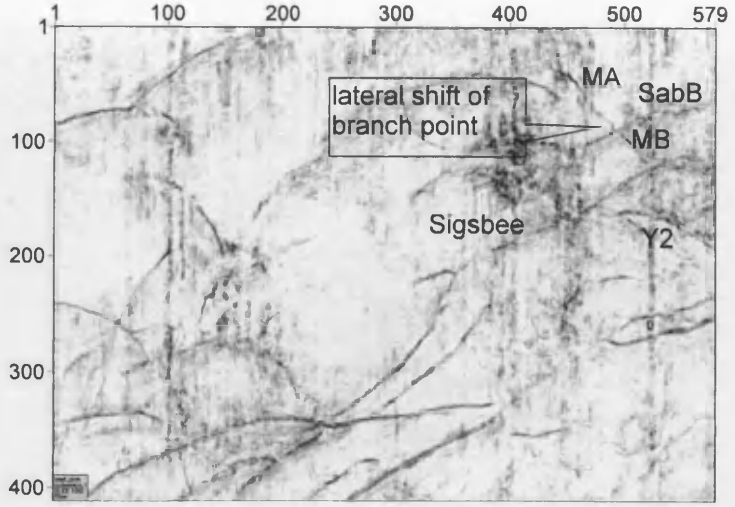

(c) 1092ms TWT.

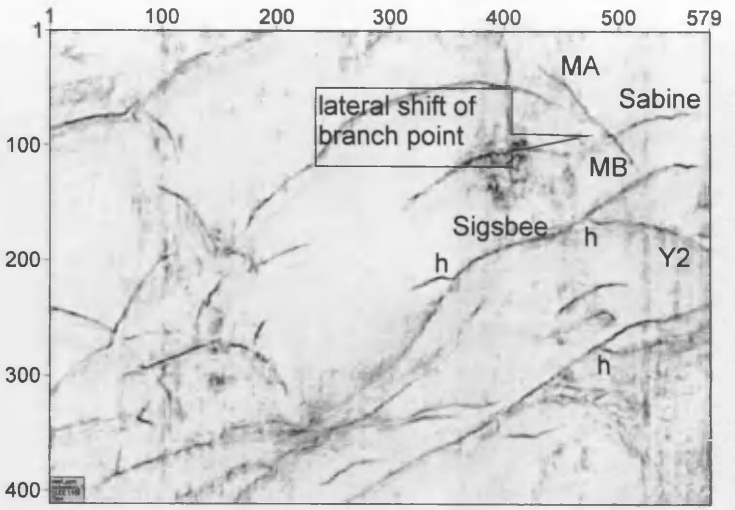

(d) 1156ms TWT.

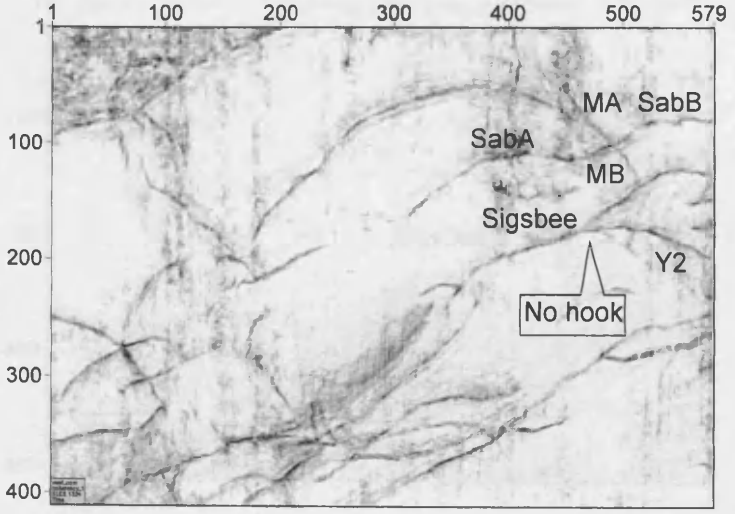

(e) 1324ms TWT.

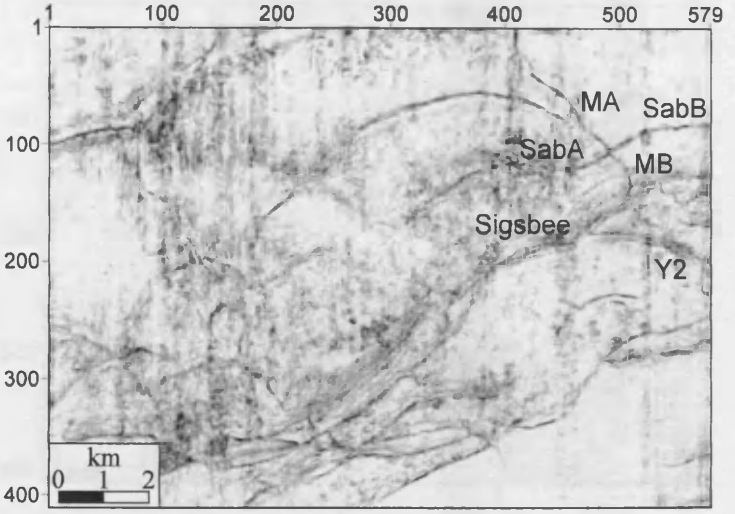

(f) 1412ms TWT.

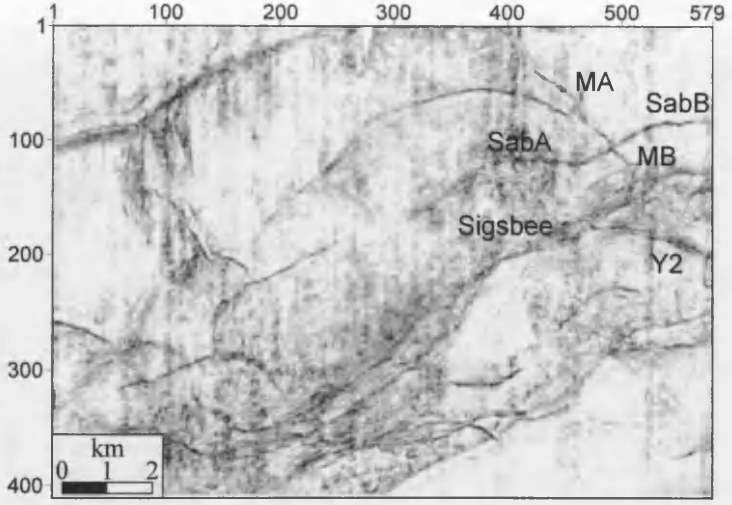

(g) 1440ms TWT.

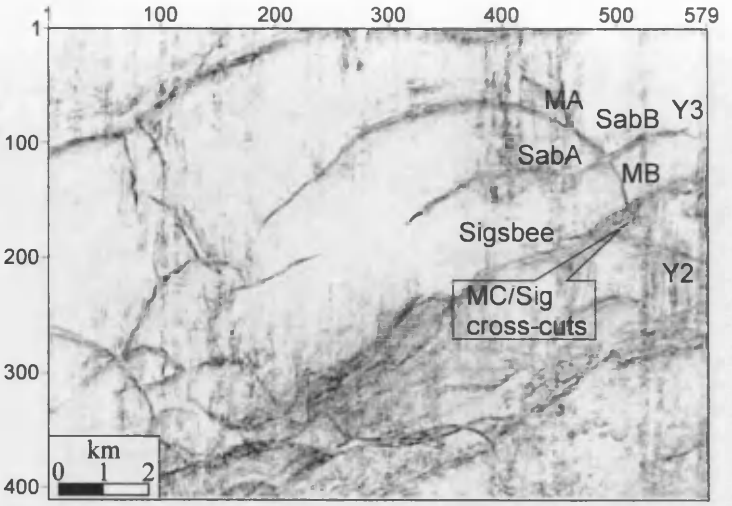

(h) 1496ms TWT.

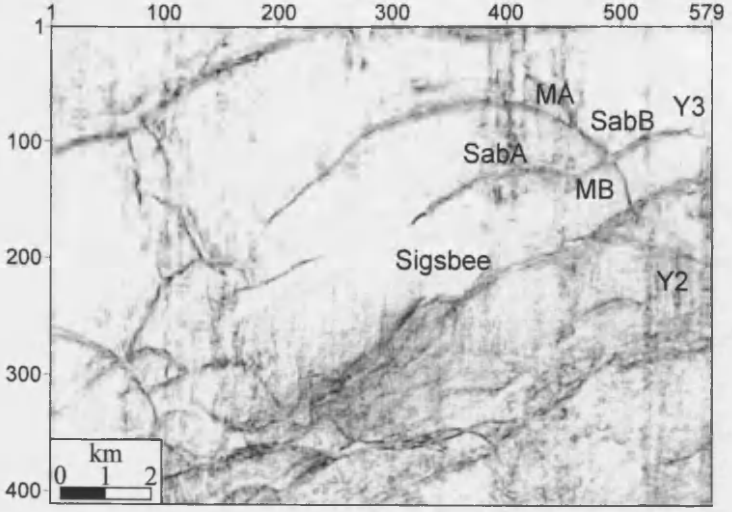

(i) 1500ms TWT.

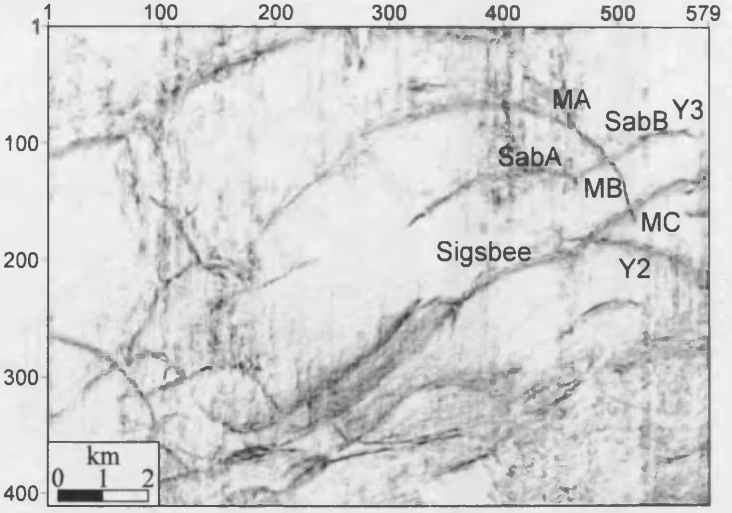

(j) 1524ms TWT.

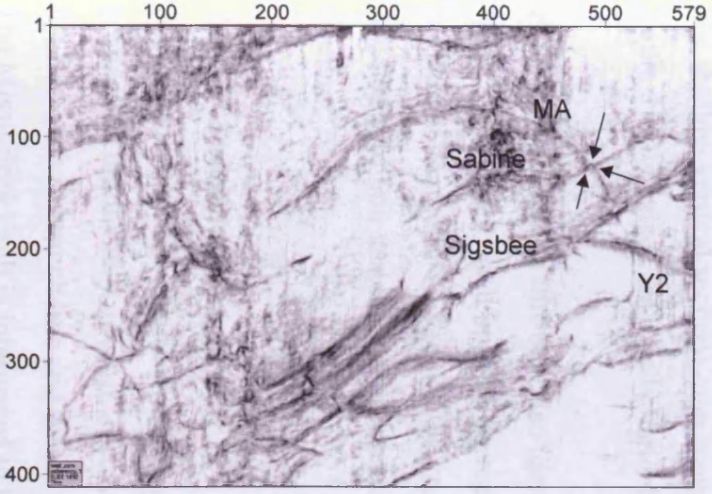

(k) 1692ms TWT

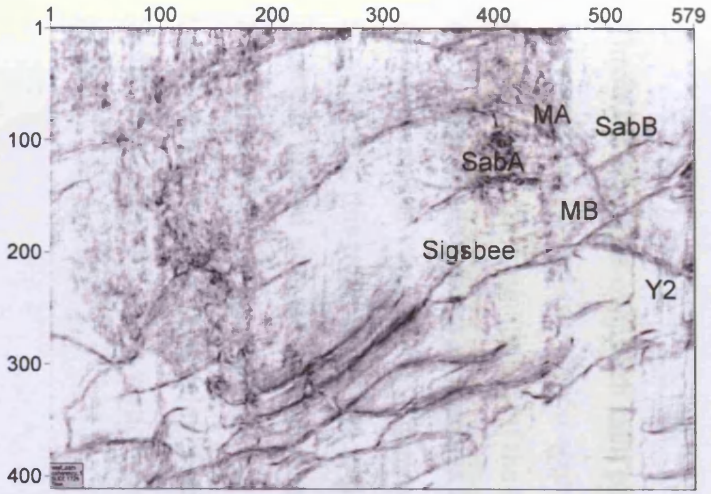

(l) 1724ms TWT.

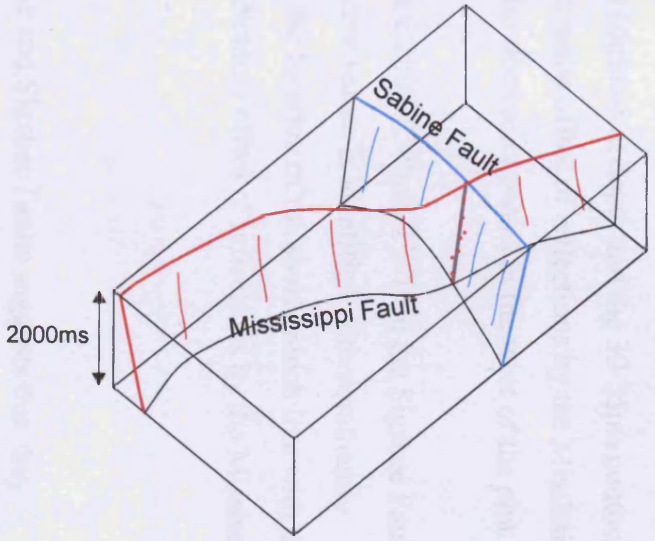

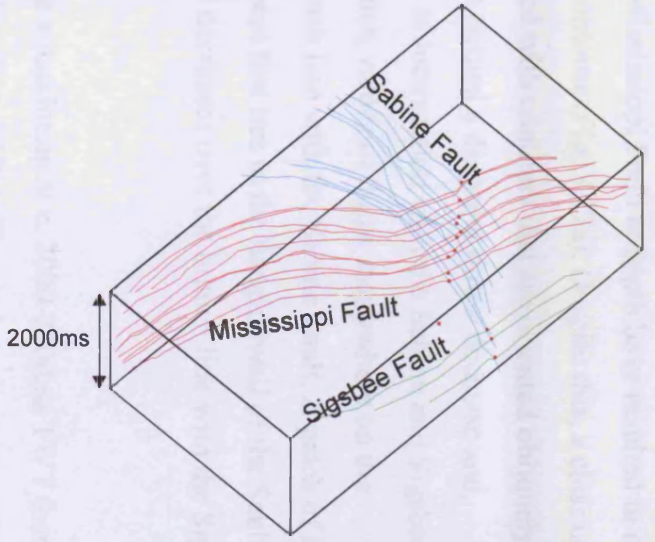

Figure 3.14. Synoptic diagram of the 3D geometry of the Upper X intersection. (a) Reconstruction of the Mississippi, Sabine and Sigsbee Fault traces from tracing the series of coherence slices. (b) Schematic diagram of the Upper X Mississippi/Sabine intersection. Red dots are branch points, highlighting that no single branch line exists.

termed the Y3 intersection (Section 3.3.2) (Fig. 3.13h-l). The Sigsbee Fault also has a uniform throw profile with very few throw variations over its sampled length.

Throw distributions over each fault plane are presented in Figure 3.17. Complexities in interpretation of, and correlation across, the Mississippi Fault at depth have resulted in many short wavelength irregularities of the throw contours (Fig. 3.17a). Despite this, a clear upward and lateral trend of throw decrease is identified with contours that are oriented obliquely to the horizontal or vertical. For this reason, it is termed a diagonal throw decrease and, significantly, this trend is parallel to the lines of intersection with the Sabine and Sigsbee Faults. In accord with the Top Miocene T-x plot, values of throw everywhere on the Mississippi Fault decrease abruptly at the branch line with the Sabine Fault. A patch of higher throw values from the Mississippi Fault segment that lies in the hangingwall of the Sabine Fault (Fig. 3.17a) has a sub-vertical trend and decreases over the branch line with the Sigsbee Fault.

The throw distribution on the Sabine Fault has a maximum at c. 2000-2500ms TWT that is entirely constrained to the east of the branch line (Fig. 3,17b). Throw decreases upwards as described by predominantly horizontal throw contours, but they locally parallel the branch line of the Mississippi Fault (e.g. the 45-55ms contours at depth and the 30-35ms contours in the shallow vertical section), representing systematic offset of reflections by the Mississippi Fault. Throw values are locally variable but also decrease upward in the west of the plot.

A band of maximum throw is also identified at c.2000-2500ms TWT on the Sigsbee Fault (Fig. 3.17c). An overall upward decrease in throw values is identified with dominantly horizontal contours. This varies locally where the location of the short branch line with the Mississippi Fault varies the contour pattern indicating offset of reflections by the Mississippi Fault.

3.2.2.4 Structural Evolution

Analysis of the throw distribution of the Sabine and Sigsbee Faults suggests that they propagated dominantly upward. Throw contours on the Mississippi Fault are sub-parallel to the Sabine fault branch line and throw values decrease toward and across this intersection. The Mississippi Fault is interpreted to have propagated toward and across intersection with the Sabine Fault to form an X geometry through accidental intersection. Similarly, a higher

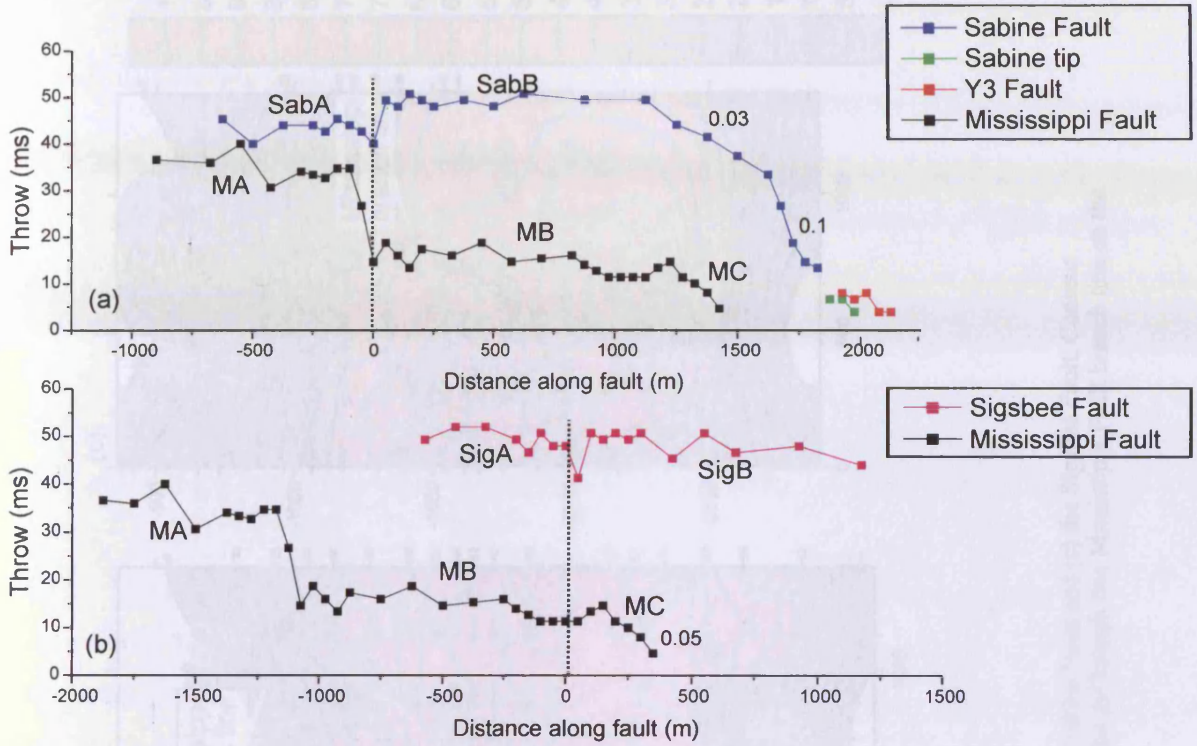

Figure 3.15 T-x plots of Upper X intersections. (a) Mississippi/Sabine and Y3 intersections. (b) Mississippi/Sigsbee intersection. Dotted line is location of intersection.

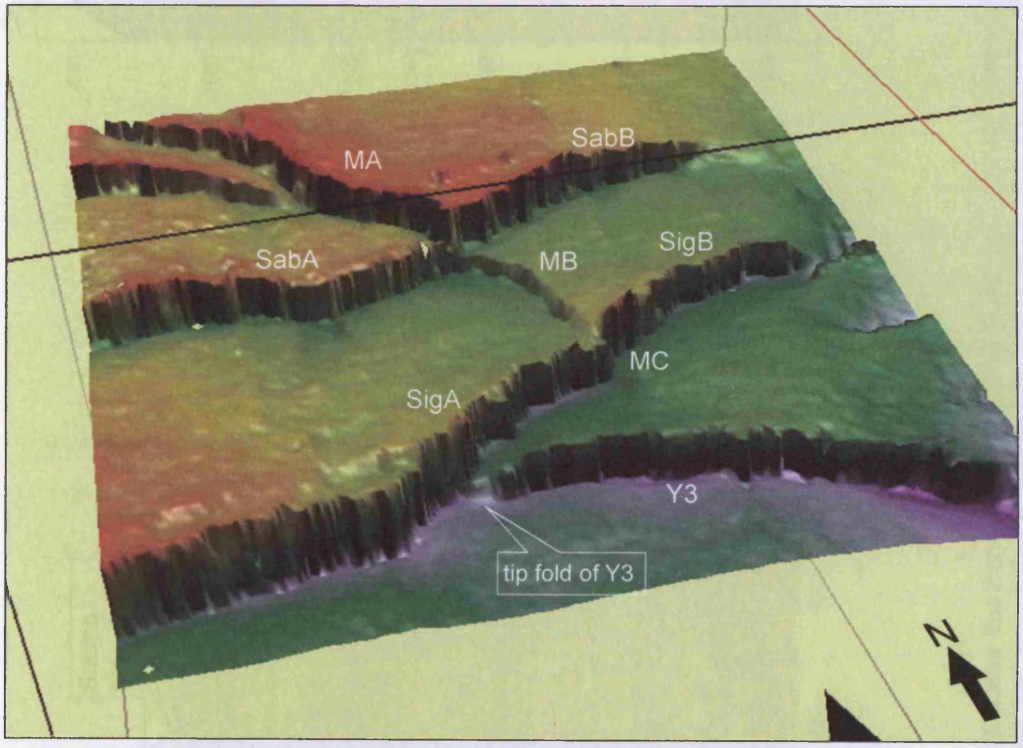

Figure 3.16 3D perspective view of the time-structure map of the Top Miocene horizon illustrating the Upper X and Y3 geometries. The MB segment of the Mississippi Fault has significantly lower values of throw than the MA segment. An area of folding at the intersecting tip of the Y3 fault can be seen. MA: Mississippi A; MB: Mississippi B; MC: Mississippi C; SabA: Sabine A; SabB: Sabine B; SigA: Sigsbee A; SigB: Sigsbee B.

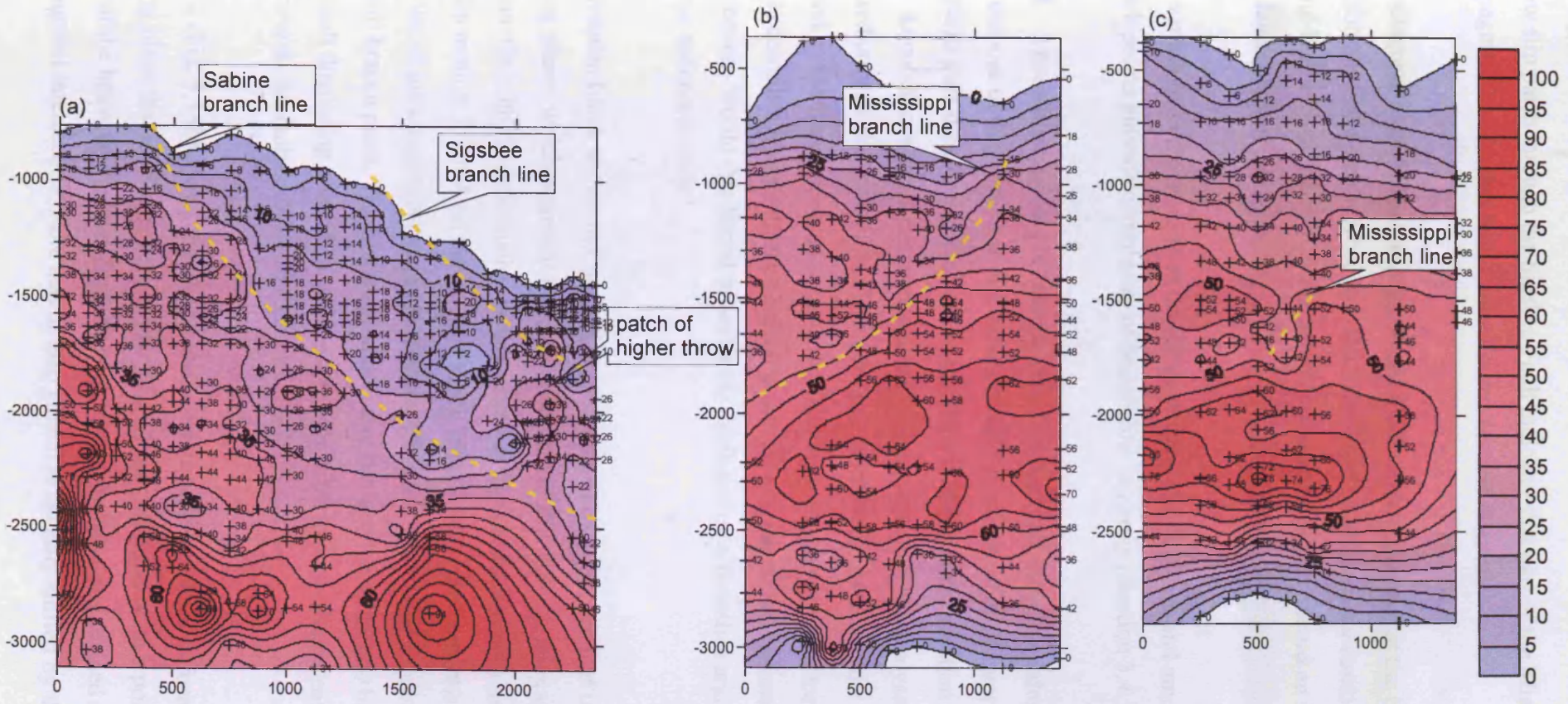

Figure 3.17. Throw distributions on vertical fault projections of (a) the Mississippi Fault, (b) the Sabine Fault and (c) the Sigsbee Fault. Contour intervals are 5ms. Branch lines represented by dashed yellow lines. Throw contours locally parallel the branch line Mississippi Fault branch line on the Sabine and Sigsbee vertical fault projections.

throw slip patch through the Sigsbee Fault indicates that part of the Mississippi Fault plane propagated through this fault over a limited vertical interval.

The diagonal contours on the Mississippi Fault are not localised at the branch line where horizontal offsets are recorded (c.f. the Sabine and Sigsbee throw contours) suggesting that the tip line was sub-parallel to the Sabine plane and this may record an inter-relationship with this fault (Section 3.4.1).

The variations in the number of branch points and the direction and amount of lateral shift of branch points indicate complexity of branch line topology (Section 3.4.3).

3.2.3 Three-dimensional X Intersection Geometry: a simple analogue model

The purpose of this section is to examine the 3D geometry of an X intersection structure, that maintains pure dip-slip motion with a later fault forming after cessation of movement on the first. As coherence slices do not necessarily follow stratigraphy, analysis of branch lines that is based only on the coherence slices does not describe the nature of the branch line that is defined by the intersection of a mapped reflection with the fault intersections. Dickinson (1954) describes lateral offset of branch points on a stratigraphic horizon from such an intersection. Would this lateral offset be (a) exhibited on a timeslice and (b) resolved on a 3D seismic coherence slice?

The wooden block shown in Fig. 3.18 represents a volume of rock that is deformed by two dipping planes which represent faults. The surface of this volume represents a stratigraphic horizon. Only brittle deformation is considered in this model and both fault planes have pure dip-slip motion. Point A on the wooden block (Fig. 3.18a) represents the location that will be the point of intersection between two dipping planes in the mutual footwall i.e. the mutual footwall branch point. The first stage shows that the wooden block has been deformed by an E-W fault displacing point A to point A'. In map view this translation can be represented by the heave of the fault.

Stage 2 (Fig. 3.18b) shows that the wooden block has been further deformed by a second dipping plane that is oblique to the first. It has translated point A' to a point A'' again by the value of the heave of the later fault. Point A'' is the branch point formed at the mutual hangingwall intersection. Note that in map view it is laterally shifted by the resultant vector of

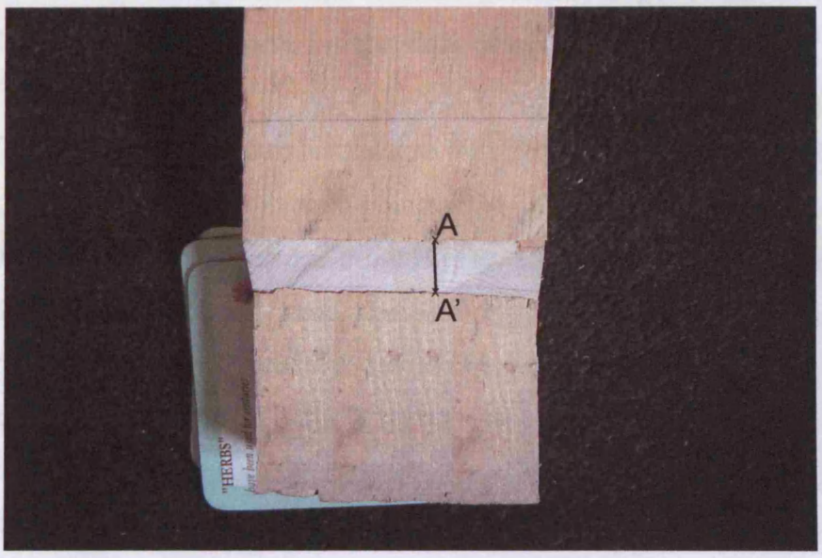

(a)

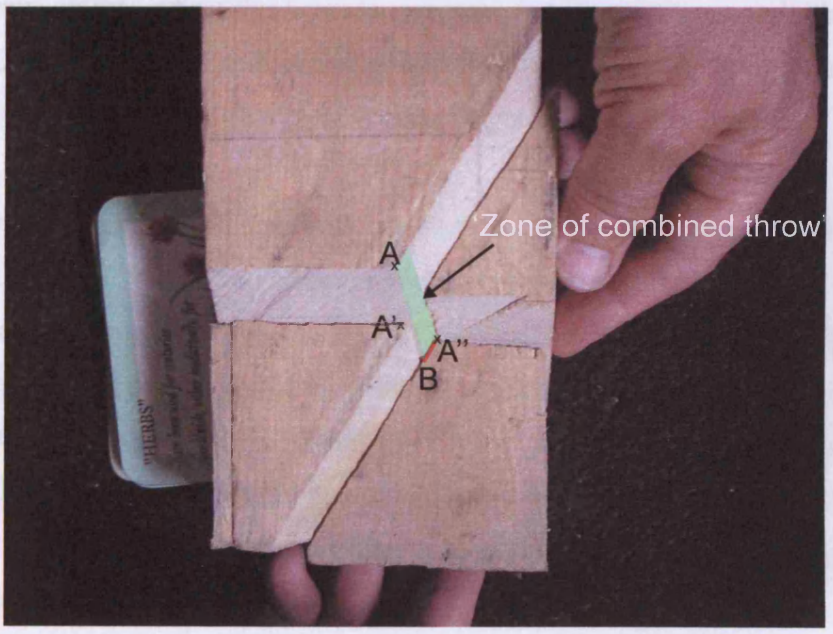

(b)

Figure 3.18. Simple analogue model of cross-cutting faults. Photographs are taken from a bird's eye view to represent the configuration in map view. (a) Stage 1. The wooden block is displaced by a single fault with dip-slip motion and point A is translated to point A'. This translation is represented by the heave of the fault in map view. (b) Stage 2. A second fault deforms the configuration of Stage 1. Point A' is translated to point A", a distance that is equal to the heave of the second fault in map view. Separate footwall and hangingwall branch lines are formed. These bound a zone of combined throw where separate throw on each fault cannot be measured. A slice through the volume would image a footwall branch point at position B and a hangingwall branch point at position A".

heave 1 plus heave 2. This lateral shift is therefore entirely related to the value of dip and throw on the constituent fault planes. The resultant geometry of the deformed block after two phases of fault movement is the same independent of which fault moved first.

If the level of a slice is considered to be equal to the depth of the lowest block in Stage 2 (Fig. 3.18b) then it can be seen that two branch points exist on the time slice. These are Point A'' or the mutual hangingwall intersection and Point B (Fig. 3.18b). Point B is the location of the intersection of the mutual footwall branch line with the horizontal slice of interest. Therefore Point A is translated to Point B directly down the footwall branch line and its position in map view can be calculated from the total throw on both faults and the dip of the footwall branch line. A slice through the volume would therefore show lateral offset between the mutual footwall branch line (B) and the mutual hangingwall branch line (A''). The magnitude of this offset is dependent on throw values and orientations of the constituent fault. A parallelogram with boundaries of this lateral offset and the footwall and hangingwall branch lines (Fig. 3.18b) represents an area where throw measurement would equal throw on both fault movements. Dickinson (1954) defines this parallelogram as the 'zone of combined throw' that is a geometrical requirement of two cross-cutting faults with dip-slip motion.

A scaled example (Appendix B) is therefore used to determine the value of lateral offset on a time slice of 1700ms TWT (c. Top Miocene) through the Lower X intersection which has been described as having only one branch point. The calculated horizontal distance between the hangingwall branch point (B) and the footwall branch point (A'') is 75m and therefore much greater than the limit of lateral resolution. As throw values increase this lateral offset will increase. It is therefore intriguing that only one branch line is recorded and suggests that the Lower X example does not conform to the criteria stated of dip-slip motion and relative activity for this analogue.

3.3 DESCRIPTION OF Y INTERSECTION GEOMETRIES

This section presents two types of examples of Y intersections in order to make a comparison with evolution of Y intersections described in Chapter 2. In contrast to intersections described from Chapter 2, T class intersections are not the dominant geometry and occur only locally (Section 3.3.1).

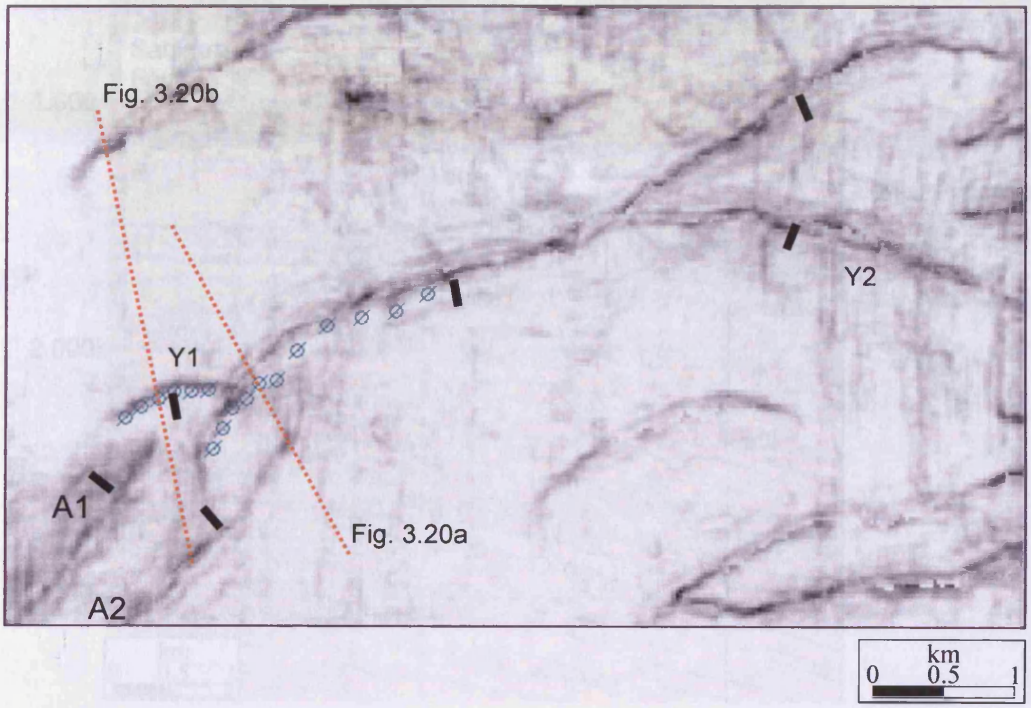

Figure 3.19 Coherence extraction of Lower Pliocene horizon showing the geometries of the Y1 and Y2 intersections. Green markers are the locations of profiles for throw measurements (Fig. 3.21). The location of seismic profile lines in Fig. 3.20 are shown.

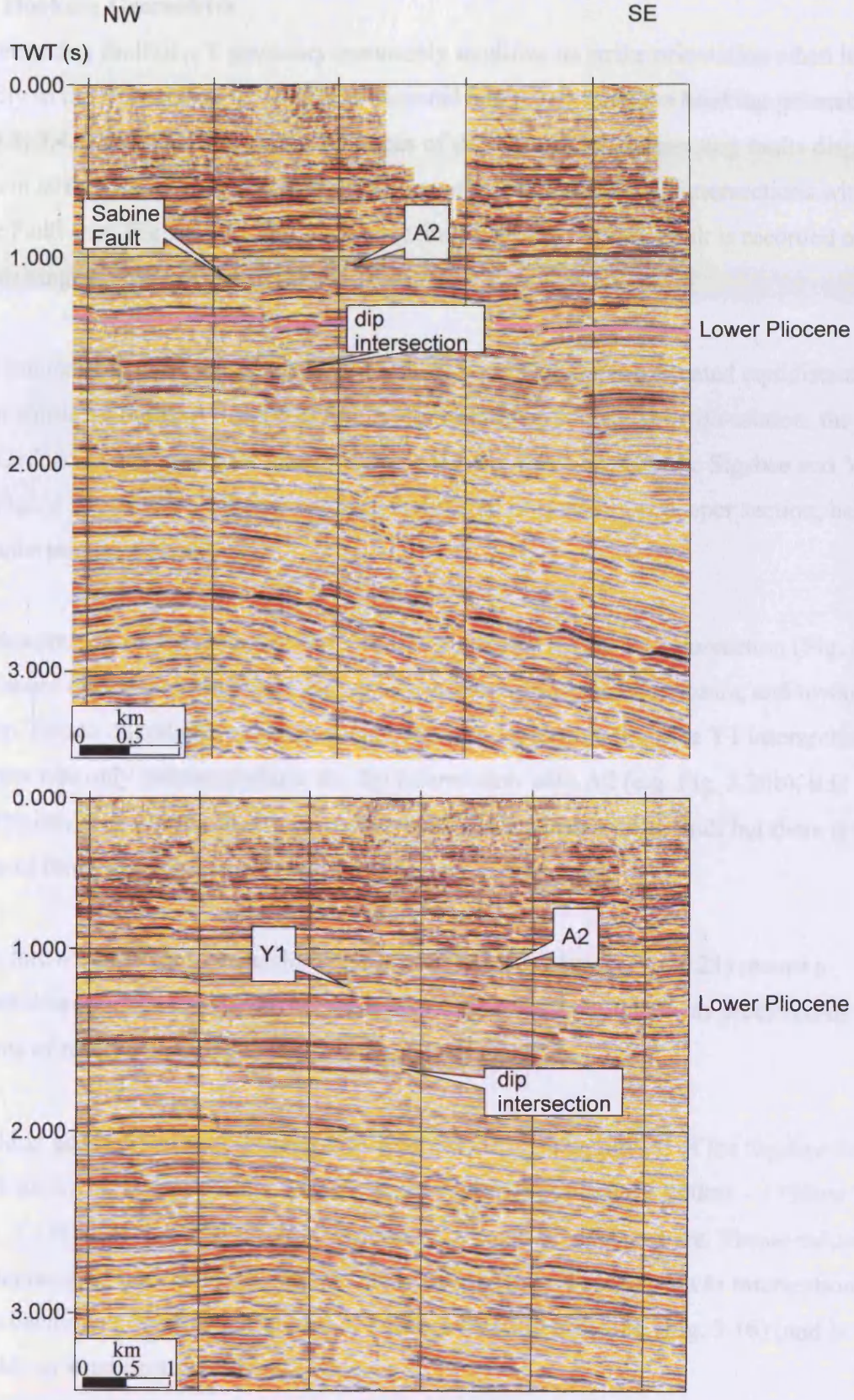

Figure 3.20. Seismic profile lines through (a) the Sabine and A2 faults and (b) the Y1 and A2 faults.

3.3.1 Hooking Geometries

The intersecting fault of a Y geometry commonly modifies its strike orientation when in close proximity to the intersection to become orthogonal and this is termed a hooking geometry (Figs. 3.2, 3.4, 3.6, 3.13). The plan view traces of the Y1 and Y2 intersecting faults display a prominent strike change that occurs at a distance of c. 300m from their intersections with the Sigsbee Fault (e.g. Fig. 3.13d). The Y1 intersection with the Sigsbee Fault is recorded over the depth range below c.900ms TWT.

The Y1 intersecting and main Sigsbee faults are sub-parallel and are situated equidistant between antithetic faults, A1 and A2 (Fig. 3.19), of the same trend. In cross-section, the A2 fault trace forms conjugate-type intersections in the dip direction with the Sigsbee and Y1 faults (Figs. 3.20). The Y1 intersecting fault is difficult to trace in the deeper section, below the dip intersection with A2.

Throw distribution on the main Sigsbee Fault is unaffected by the Y1 intersection (Fig. 3.21). Throw values decrease toward the upper tip, as shown by horizontal contours, and toward the lateral tip. Due to uncertainty with the deeper structural interpretation, the Y1 intersecting fault throw was only measured above the dip intersection with A2 (e.g. Fig. 3.20b). it is difficult to interpret a throw distribution pattern for the Y1 intersecting fault but there is some evidence of throw decrease toward its lateral tip and intersection.

Both the throw distributions from the Sigsbee and Y1 fault planes (Fig. 3.21) record a horizontal decrease in throw where they intersect with the A2 conjugate, as predicted by the limitations of resolving antithetic throw on faults (Chapter 1).

The hooking geometry of the Y2 intersection occurs in the hangingwall of the Sigsbee Fault. The hook geometry is only locally well defined over the depth range c.900ms – 1750ms TWT (e.g. Fig. 3.13d, g) and displays a true Y geometry with no hook elsewhere. Throw values on the Y2 intersecting fault decrease toward intersection (Fig 3.16). Adjacent to intersection, localised bending of bedding in the area of reduced throw is observed (Fig. 3.16) (and is comparable to structures described in Chapter 5).

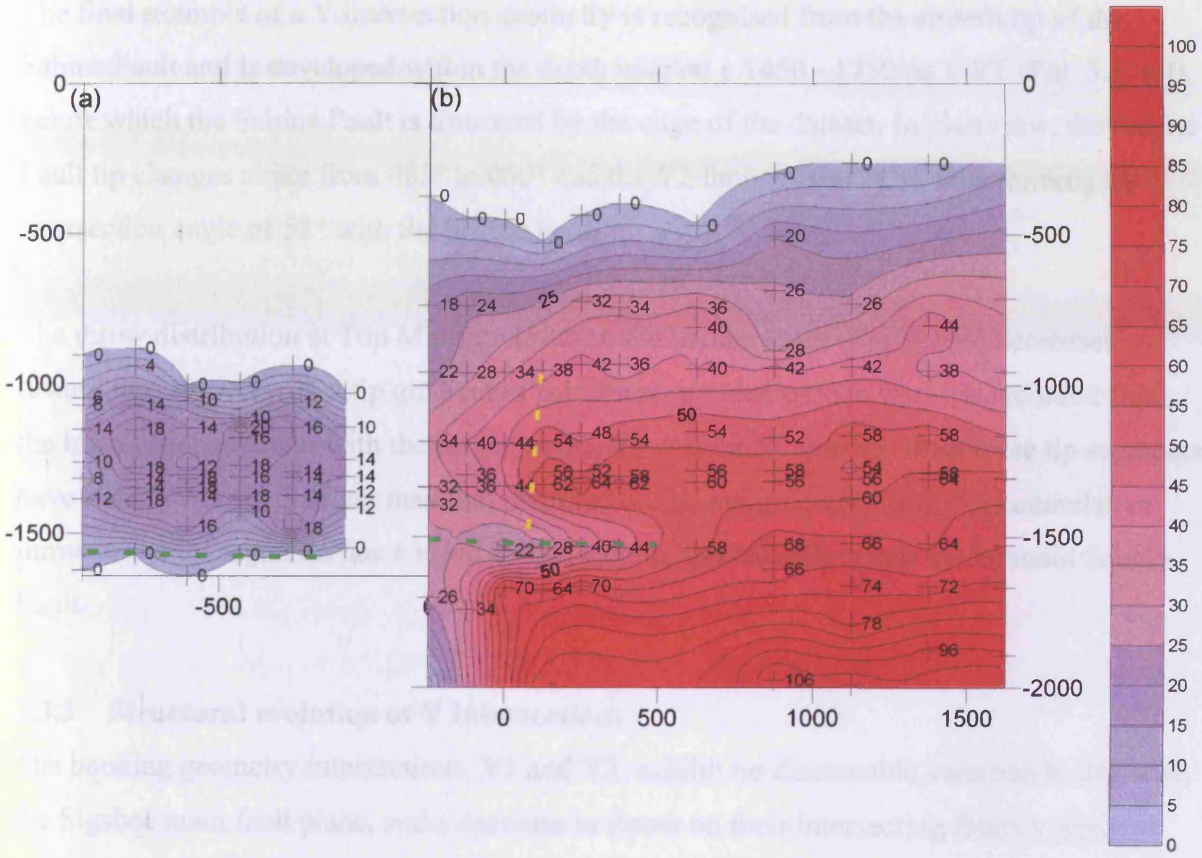

Figure 3.21. Vertical fault projections contoured for displacement. (a) Y2 Fault. (b) Sabine Fault. Yellow dashed line is branch line with Y2. Horizontal green dashed line is branch line with the A2 Fault.

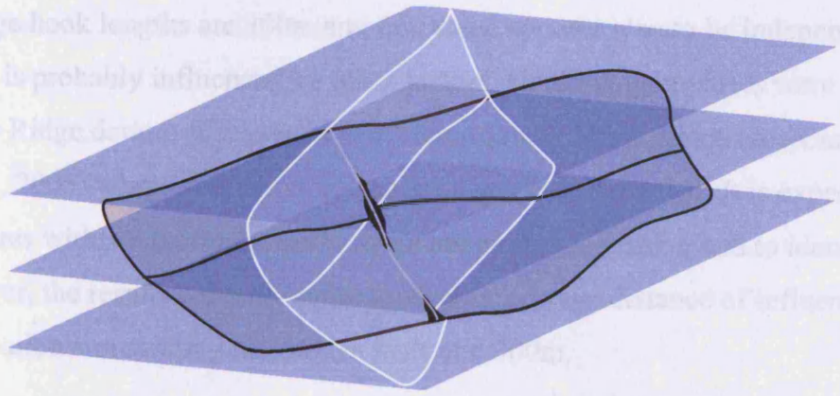

Figure 3.22. Complexities of branch line topology are the result of mutual offsetting of two cross-cutting faults. Black areas mark zones of dilation and potentially tortuous fluid pathways.

3.3.2 Description of Y3 intersection

The final example of a Y intersection geometry is recognised from the eastern tip of the Sabine Fault and is developed within the depth interval c.1450 - 1750ms TWT (Fig. 3.13h-l), below which the Sabine Fault is truncated by the edge of the dataset. In plan view, the Sabine Fault tip changes strike from 085° to 060° and the Y2 fault strikes 112°, thus forming an intersection angle of 52° with the Sabine Fault.

The throw distribution at Top Miocene level on the Sabine Fault (Fig. 3.15a) decreases toward intersection with a tip gradient of 0.1. An abrupt decrease in throw is recorded from the intersection location with the tip segments, Y3 and the Sabine tip. Both these tip segments have a shallower tip gradient than that recorded on the main Sabine Fault. The cumulative throw of the tip segments has a value at intersection approximating that on the main Sabine Fault.

3.3.3 Structural evolution of Y Intersections

The hooking geometry intersections, Y1 and Y2, exhibit no discernable variation in throw on the Sigsbee main fault plane, and a decrease in throw on their intersecting faults toward intersection. In addition, the intersecting fault of Y2 displayed localised bending at the intersecting fault tip location that can be interpreted to occur ahead of a propagating tip. From these observations, an interpretation of evolution through accidental intersection is proposed. It is argued that recognition of accidental intersection can be positively inferred from the observation of a hooking geometry.

Average hook lengths are 300m and this value appears also to be independent of fault lengths and so is probably influenced by other factors. Hooking geometries were recorded from the Gjallar Ridge dataset (Chapter 2) and from offshore West Africa (Joe Cartwright, pers. comm., 2005) where similar hook length ranges were recorded. It is expected that hook structures within a particular scale range are easiest to resolve and to identify on seismic data. However, the results certainly point toward an average distance of influence/stress perturbation surrounding the master fault of c.300m.

The hook geometry is therefore indicative of a mechanical relationship between the propagating intersecting fault and the main fault which has implications for identifying activity on the main fault plane. In the case of the Y2 intersection, the hook geometry is only

developed over limited vertical intervals, which may help interpretation of relative activity on the intersecting faults. It can be proposed that the hook geometry will only form on the intersecting fault if the main fault plane is active and therefore inducing a stress perturbation. The main fault cannot have been active throughout the entire interval when the intersecting fault had propagated into the area adjacent to the intersection. This is an interesting topic to pursue further but there is not scope for this work in this chapter.

An interpretation of lateral bifurcation is plausible for the Y3 intersection geometry because the main fault throw distribution is shared between the tip segments. Decrease in throw value from the intersection location to its tip on the intersecting fault, along with the characteristic strike change, is consistent with an evolutionary progression through branching. This intersection differs from examples in Chapter 2 because the cumulative throw profile of the tip segments has a shallower gradient to the main fault tip profile. Due to dominant upward growth, these tip splays most probably represent upper tip bifurcation (c.f. Childs 1996).

3.4 DISCUSSION: EVOLUTION OF X INTERSECTIONS

From comparison of the Upper and Lower X examples, it can be inferred that X geometry intersections can evolve in different ways within a single structural domain. This discussion will compare and contrast the evolution of these structures to examine whether X intersections represent kinematically coherent structures.

3.4.1 Accidental Intersection X Evolution

The Mississippi/Sabine fault intersection is an example of evolution of an X geometry through accidental intersection. In this example, the Mississippi Fault propagated toward and then through the Sabine Fault plane. This intersection is characterised by an abrupt decrease in throw on the Mississippi Fault at the intersection location from values in the footwall of the Sabine Fault to the values in the hangingwall of the Sabine Fault. It is therefore inferred that this identification of a throw decrease across an X intersection is indicative of evolution through accidental intersection and continued propagation across the earlier formed fault.

The near-horizontal contours that parallel the upper tip line of the Sabine Fault demonstrate upward growth. In contrast, the Mississippi Fault throw contours are sub-parallel to the branch line, and this has been informally termed 'diagonal' propagation (Section 3.2.2.3). Two important points arise:

(1) The Sabine Fault must have been the dominant fault and its presence modified the growth of the Mississippi Fault.
(2) The diagonal growth toward the Sabine Fault plane effectively resolved 'space' problems that arise in laterally propagating systems (see Chapter 6).

These observation imply that the Mississippi Fault is responding to the presence of the Sabine Fault by modification of the shape of the fault tip. The pre-existing fault therefore perturbs the stress field in 3D, indicating that both faults were active while the Mississippi Fault propagated toward the Sabine Fault. This theme will be developed in Chapter 6.

The complex nature of the branch line (Section 3.2.2.2) with mutual offsetting of the Mississippi and Sabine Faults indicates that there was reactivation of movement on the faults as they evolved to become an X, i.e. the less active fault is offset, then reactivated, then able to offset the other fault at a different level. This interpretation is supported by a decrease in throw on the Sabine Fault (to a lesser extent than the Mississippi Fault) across intersection with maximum throw constrained to the east of the branch line.

Due to the identification of lateral shifts of branch points on horizontal slices, it is not possible to link branch points on horizons into a continuous branch line. In 3D this complexity can be seen to widen the zone of associated deformation around the branch line (Fig. 3.22) and may be explained by a zone of dilation or intense fracturing. Further, deformation of the fault plane is envisaged to be required in the form of bends along strike on the fault plane and steepening/shallowing with depth to accommodate the lateral shifts. The occurrence of more than one branch point on horizontal slices through the dataset also implies that dip-slip movement on each fault was maintained (Section 3.2.3).

3.4.2 Kinematically-related X Evolution

In contrast to the evolution of an accidental X intersection, the Texas/Louisiana X intersection does not exhibit throw variations, tip line modification or complexity of its branch line that can be resolved on 3D seismic. Instead, a simple throw distribution that decreases upward with horizontal contours shows upward propagation of both fault planes. The throw distribution is unaffected by the intersection. This is an intriguing observation as it contrasts with previously modelled intersections (e.g. Maerten, 1999). Further, the intersection has a remarkably stable and consistent 3D geometry throughout the imaged interval, with only a

single branch line (i.e. neither fault offsets the location of the branch line) and very little variation of the location of the Louisiana Fault eastern free tip.

To fulfil the kinematic requirements of such a stable structure, two possible interpretations can be put forward:

(1) Fault movement on one fault plane ceased entirely before movement on the other fault plane began and the later fault propagated across the earlier fault plane, as if it had the mechanical properties of the undeformed host rock.

(2) Growth on both faults was contemporaneous.

It is assumed that if fault activity ceased on the earlier fault before activity on the later fault, then both faults have accrued displacement with purely extensional dip-slip motion, and more than one branch line should have formed (Section 3.2.3). The single branch line that has been described from the Lower X example, requires that slip vectors are readjusted on one or both faults, most probably both, so that they parallel the branch line. The stability of the Lower X configuration therefore argues in favour of a kinematic interdependence of the faults, and therefore contemporaneous growth.

In addition, the constant position of the eastern tip of the Louisiana Fault indicates that fault length varies little within the vertical interval of interest and the fault tip has a rectangular shape. Therefore, it is likely that fault length was established early and displacement was added without significant addition of length (c.f. Walsh, 2002). This implies that formation of the X geometry may have occurred at early stages of evolution of the structure.

The onset of growth of the Louisiana or Texas Faults cannot be constrained with the data available. Conventionally, as the Texas Fault has larger throw values and a greater length (within the dataset limits), it could be thought to have been active for longer than the Louisiana Fault. However, slip rate is unknown and therefore it is not possible to specify the earlier formed fault with certainty. The upper tip gradients of both faults are remarkably similar and this may argue toward a relationship between the faults. The Louisiana Fault has less throw at a given depth and has not propagated to the near-seabed location of the upper tip of the Texas Fault. Therefore, displacement was not added in equal amounts on all four intersecting segments since initiation of the structure. But if the Louisiana Fault was relatively later then slip may have been added simultaneously over both faults since the structure was added.

In conclusion, the Lower X structure is an intriguing structure that is thought to exhibit kinematic coherence of its constituent faults.

3.4.3 Branch line Evolution

Using the examples of the Upper X and Lower X intersections, branch lines in X geometry intersections can be shown to vary in their evolution. The accidental intersection of a diagonally propagating tip will have more initial points of contact with the main fault than e.g. a laterally propagating tip (see Chapter 6). In the Upper X example, the fault tip had an irregular edge and it is proposed that slip patches propagated ahead of the main tip to intersect with the Sabine Fault contemporaneously. Consequently, short discontinuous branch line segments will simultaneously increase in length until, with further propagation through the main fault, a continuous branch line is achieved. Deformation associated with the evolution of this branch line is likely to be distributed over the whole length of the branch line as it evolves through the linkage of a number of small sections in the process zone ahead of the propagating intersecting tip.

Branch line evolution in the case of the Lower X intersection evolved in an entirely different way. Upward growth with no recorded anomalous throws creates an upward-propagating branch line, whose plunge and dip are resolved from the 3D orientation of its constituent fault planes. Deformation will be concentrated vertically ahead of the slip events on either fault plane. The branch line will evolve with evolution of the plane with relative youngest motion and will not be fully evolved until movement on the younger plane catches up with the older i.e. will not be fully established as a line between the two planes until both planes are fully developed.

3.4.4 Summary

Evidence has been given that there can be contemporaneity in the system and that fault growth is potentially episodic. While active, it is expected to affect the other fault plane as in the case of the Upper X and Y3 intersections. The Lower X intersection is therefore remarkable in that it seems likely that both faults were contemporaneous and were able to grow as a coherent single structure with different slip events on the two fault planes.

The cross-cutting geometries in the study area form in relation to positive salt structures that bound mini-basins in the Gulf of Mexico. Reches (1983) describes the mechanics of propagation of multi-directional faults that evolve above domal structures. It is therefore quite plausible that both faults were able to propagate at the same time. If this were indeed the case then it is an intriguing structure to study in more detail as it shows that faults can act independently while in contact with the other plane. Further, they are able to share the same branch line which appears to require a variation in slip vectors but no recorded effect on throw patterns. It would take a considerable amount of further work to resolve this issue.

3.5 CONCLUSIONS

The primary objectives of this study were to describe the 3D geometries of X class intersections and to attempt to understand the evolutions of these structures in the West Cameron study area, Gulf of Mexico. A secondary objective was to describe the evolution of Y class geometries. The major findings relating to these two themes are summarised below:

Evolution of cross-cutting faults

- The X class intersections formed through dominantly upward propagation.
- Displacement on cross-cutting faults with predominantly dip-slip motion will create two branch points which can be resolved on a slice through the coherence volume (where the branch points are separated by a distance that is greater than the lateral resolution).
- An abrupt decrease in throw of one fault across the intersection with the other fault is indicative of evolution through accidental intersection
- A later fault plane can propagate through an earlier fault plane through evolution of an accidental intersection.
- 'Diagonal' propagation has been described where the intersecting fault tip is modified by the stress perturbation caused by the presence of the pre-existing fault plane. The tip shape of the intersecting fault is modified to become sub-parallel to the cross-section of the earlier plane. This tip modification removes 'space-filling' issues.
- There is evidence for kinematic coherence of cross-cutting planes. The throw magnitudes in this system are sufficient to resolve more than one branch point where slip vectors remain dip-slip. Therefore, where only a single branch point is resolved, it is likely that slip vectors have modified to accommodate contemporaneous faulting.

- Further evidence in support of kinematic coherence is recognised from the overall stability of the Lower X intersection and the comparable T-z profiles the constituent faults of the Lower X intersection.
- Kinematically coherent cross-cutting faults do not modify the throw distribution on the fault planes of their constituent faults.

Evolution of Y class intersections

- Hooking geometries of intersecting faults are indicative of accidental intersection. Hook values are comparable with those from other basinal settings, suggesting that the shape and magnitude of the stress perturbation around a fault may be predictable.
- A hook geometry signifies activity on the main fault plane. Within the same intersection, periods of inactivity and activity may then be quantified through recognition of the presence or absence of a hook geometry on the intersecting fault.
- Intersection evolution through the process of lateral tip bifurcation is identified within this fault system.

CHAPTER 4: STRIKE-SLIP FAULT TIP, LEVANT BASIN

4.1 INTRODUCTION

An exceptionally well-imaged intersecting fault system, termed the Afiq Fault system, is observed on 3D seismic data from the Levant Basin, eastern Mediterranean. Intersections of faults with dominantly extensional dip-slip motion occur at the tip of the strike-slip Afiq Fault, as defined from careful study of displaced markers. This chapter aims to reconstruct the evolution of the strike-slip fault and its associated minor structures including the related extensional faults.

Previously published work has described cross-sectional strike-slip fault geometries from 2D seismic lines (e.g. Harding, 1990). Detailed plan view geometries are frequently described from surface exposure on scales of 1-100m (e.g. Granier, 1985; Martel, 1990) and 10s to 100s of kilometres (e.g. Kim et al., 2001, Fu et al., 2005), and more rarely from 1-10km (e.g. Pachell et al., 2002). Descriptions of analogue models also provide some understanding of three-dimensional geometries and processes. However, this study is unique in that the 3D seismic dataset acts as a natural laboratory in which to study the detailed 3D fault architecture and intersection geometries in the scale range of 1-10km. A new methodology for quantification of strike-slip displacements and displacement gradients is presented.

The chapter is structured by firstly introducing the regional geology of the study area and providing the stratigraphic and structural context for the Afiq Fault. This is followed by description of the geometries of the structures that are integral to the array. These are studied separately in Sections 4.4 (strike-slip faults) and 4.5 (normal faults) respectively and the 3D branch line geometries are described in Section 4.6. Kinematic analyses are presented in Section 4.7 and the results are integrated with the geometric understanding leading to the interpretation of evolution of the system in Section 4.8. This chapter therefore addresses the main aims of the thesis of fault intersection evolution and definition of branch line topology.

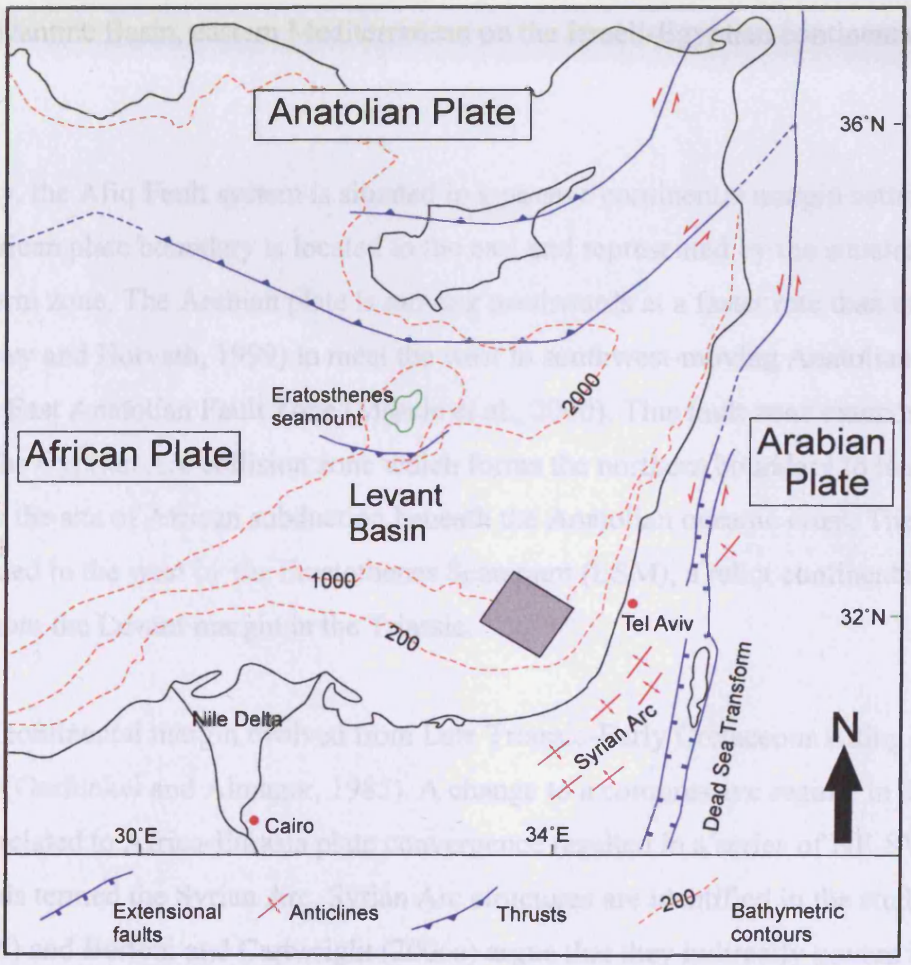

Figure 4.1. Regional geological map (modified from Bertoni and Cartwright, 2005). The boxed area represents the location of the 3D seismic survey used in this study on the continental margin of the Levant Basin.

The intersection geometries described herein can be classified as branching intersections. The study adds to understanding of secondary fault evolution in a strike-slip system.

4.1.1 Regional setting of the Afiq Fault system

This section summarises the main regional geological factors contributing to the study area in order to place the Afiq Fault system in its regional context. The study area is located in the southern Levantine Basin, eastern Mediterranean on the Israeli-Egyptian continental slope (Fig. 4.1).

Geologically, the Afiq Fault system is situated in a passive continental margin setting. The Arabian-African plate boundary is located to the east and represented by the sinistral Dead Sea Transform zone. The Arabian plate is moving northwards at a faster rate than the African plate (Badawy and Horvath, 1999) to meet the west to southwest-moving Anatolian plate at the sinistral East Anatolian Fault Zone (Mascle et al., 2000). This fault zone extends westward to become the Cyprian Arc collision zone which forms the northern boundary to the Levant Basin and is the site of African subduction beneath the Anatolian oceanic crust. The basin is partly bounded in the west by the Erastothenes Seamount (ESM), a relict continental fragment that rifted from the Levant margin in the Triassic.

The Levant continental margin evolved from Late Triassic-Early Cretaceous rifting in the Tethys area (Garfunkel and Almagor, 1985). A change to a compressive regime in the late Cretaceous related to Africa-Eurasia plate convergence resulted in a series of NE-SW trending folds termed the Syrian Arc. Syrian Arc structures are identified in the study area (e.g. Fig. 4.6) and Bertoni and Cartwright (2006a) argue that they indirectly govern the landward extension of Miocene evaporites. Evaporitic deposition occurred in the Late Miocene following a period of erosion and localised emergence that started in the Early Miocene.

NW-SE trending slope canyons developed whose orientations were related to basement structural trends by Bertoni and Cartwright (2006a). These canyons developed headward into deeply incised valleys as the late Miocene sea level dropped by greater than 1000m (Gaullier et al., 2000). Thick evaporites were deposited on the basin floor and in the canyons which therefore controlled salt edge morphology (Bertoni and Cartwright, 2006a).

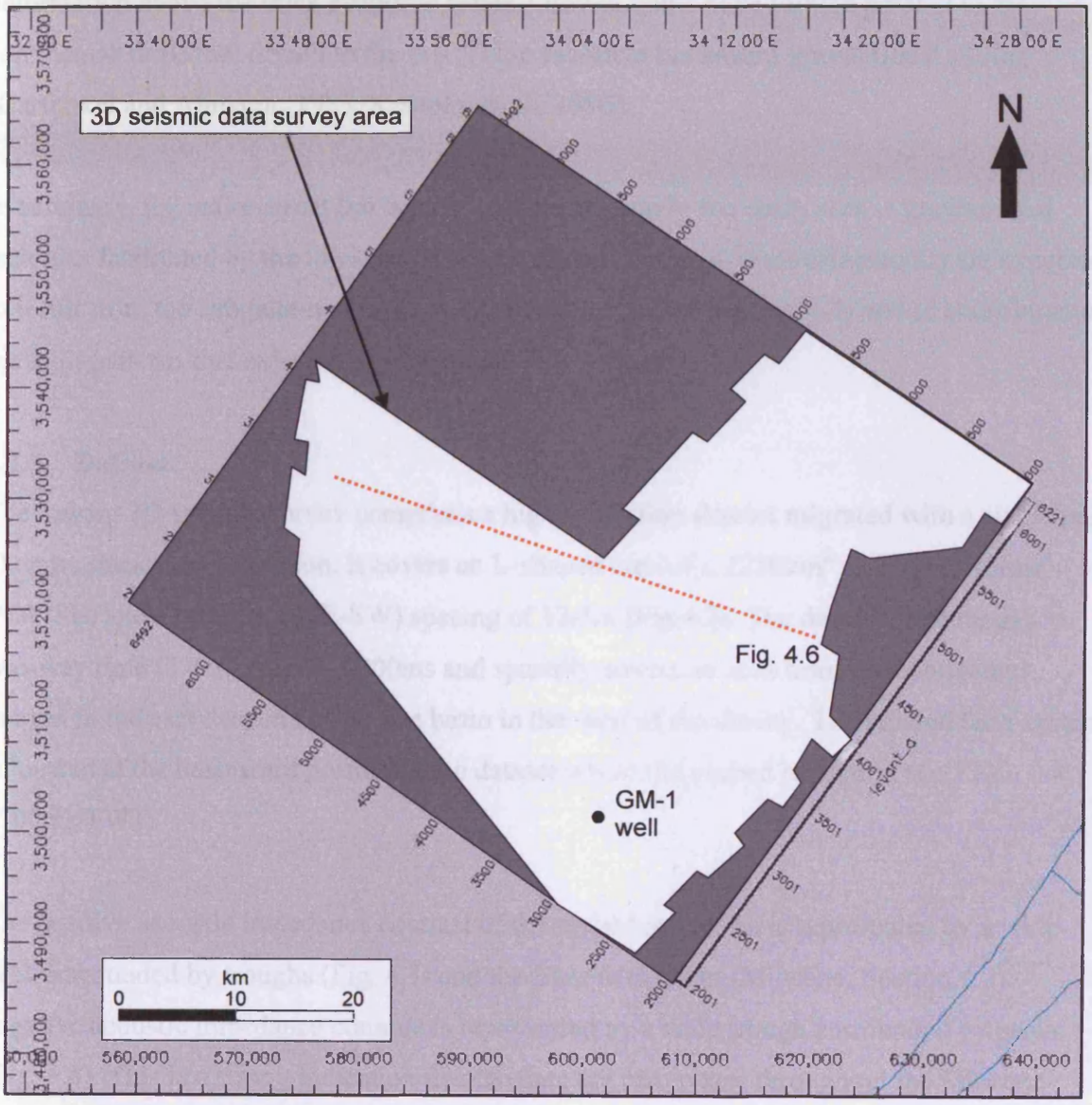

Figure 4.2. Map showing the outline of the 3D seismic dataset used in this study. Note the location of the GM-1 well and the regional seismic line. Levant coastline is delineated in blue.

Throughout the Pliocene-Recent interval the Nile River delta provided the predominant source of sediment to the Levant Basin. The resultant thick accumulation of progradational-aggradational clays and silts loaded the continental margin leading to thin-skinned deformation above the thick evaporite series. Growth faults have formed parallel to the continental slope that detach in the salt. These facilitate basinward gravitational sliding (Garfunkel and Almagor, 1985; Kempler et al., 1996).

In summary, the major structural control on deformation in the study area is gravitational tectonics facilitated by the thick salt layer. Local variations in stress orientations are expected to result from the irregular morphology of the salt edge (see Section 4.3) and to contribute to the fault patterns that exist in the study area.

4.1.2 Dataset

The Levant 3D seismic survey comprises a high resolution dataset migrated with a single pass 3D post-stack time migration. It covers an L-shaped area of c.2250km^2 and has an inline (NW-SE) and a crossline (NE-SW) spacing of 12.5m (Fig 4.2). The data volume ranges in two-way time (TWT) from 0–6000ms and spatially covers an area from the continental margin in the east deepening into the basin in the west of the survey. The studied fault system is located at the basinward portion of the dataset where the seabed reflection is c.1200-1300ms TWT.

The positive acoustic impedance contrast of the seabed reflection is represented by a wide peak surrounded by troughs (Fig. 4.3) and the Base Messinian (Miocene, Section 4.2) negative acoustic impedance contrast is represented by a wide trough surrounded by peaks (Fig. 4.4). This is a strong indication that the data are zero phase throughout the Miocene-Recent interval. A flat gas water contact is also displayed from the dataset and supports this interpretation.

The bandwidth of the dataset and its variation with depth has been investigated (Fig. 4.5). The average bandwidth of both the entire depth interval and the post-Miocene interval is 20-80Hz with a centre frequency of 50Hz (Fig. 4.5a, b, c). A reduction in dataset quality is observed from the pre-Messinian section which has an average bandwidth of 12-48Hz and a centre frequency of ~30Hz (Fig. 4.5a, d). BG Group reports (unpublished) confirm that the target

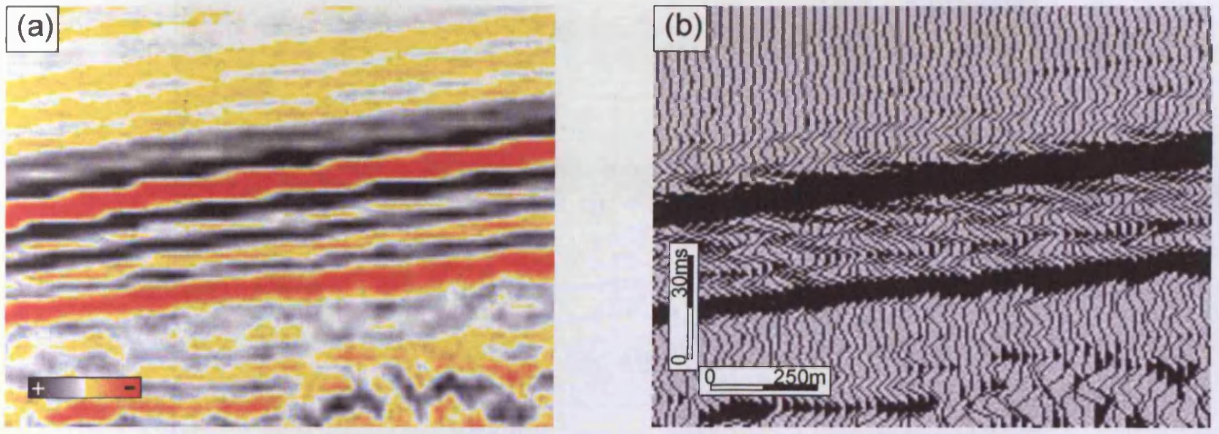

Figure 4.3. Seismic character of the seabed reflection. a) Variable area (VA) display. b) Variable intensity (VI) display. The data are zero phase migrated and displayed using positive normal polarity (SEG standard, Sheriff, 1991).

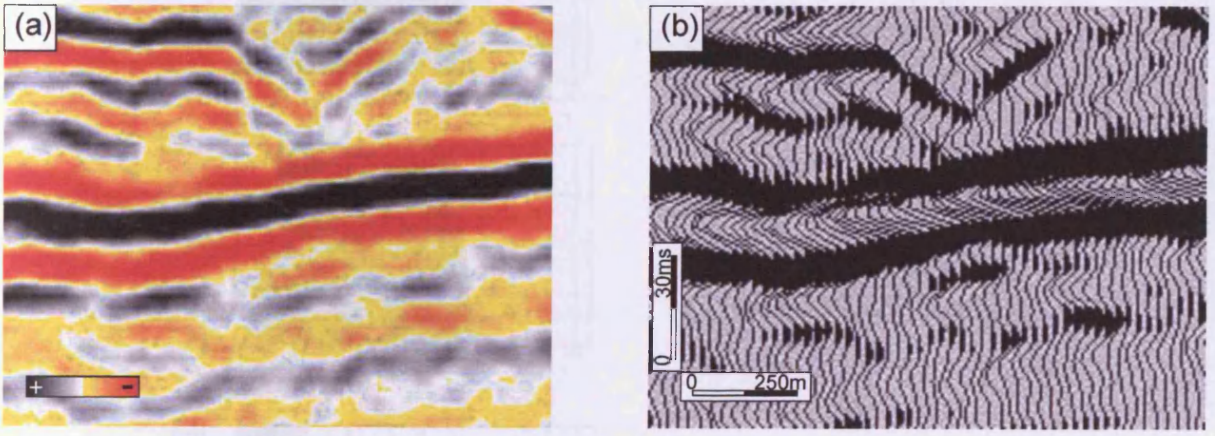

Figure 4.4. Seismic character of the Base Messinian reflection. a) Variable area (VA) display. b) Variable intensity (VI) display. The data are zero phase migrated and displayed using positive normal polarity (SEG standard, Sheriff, 1991).

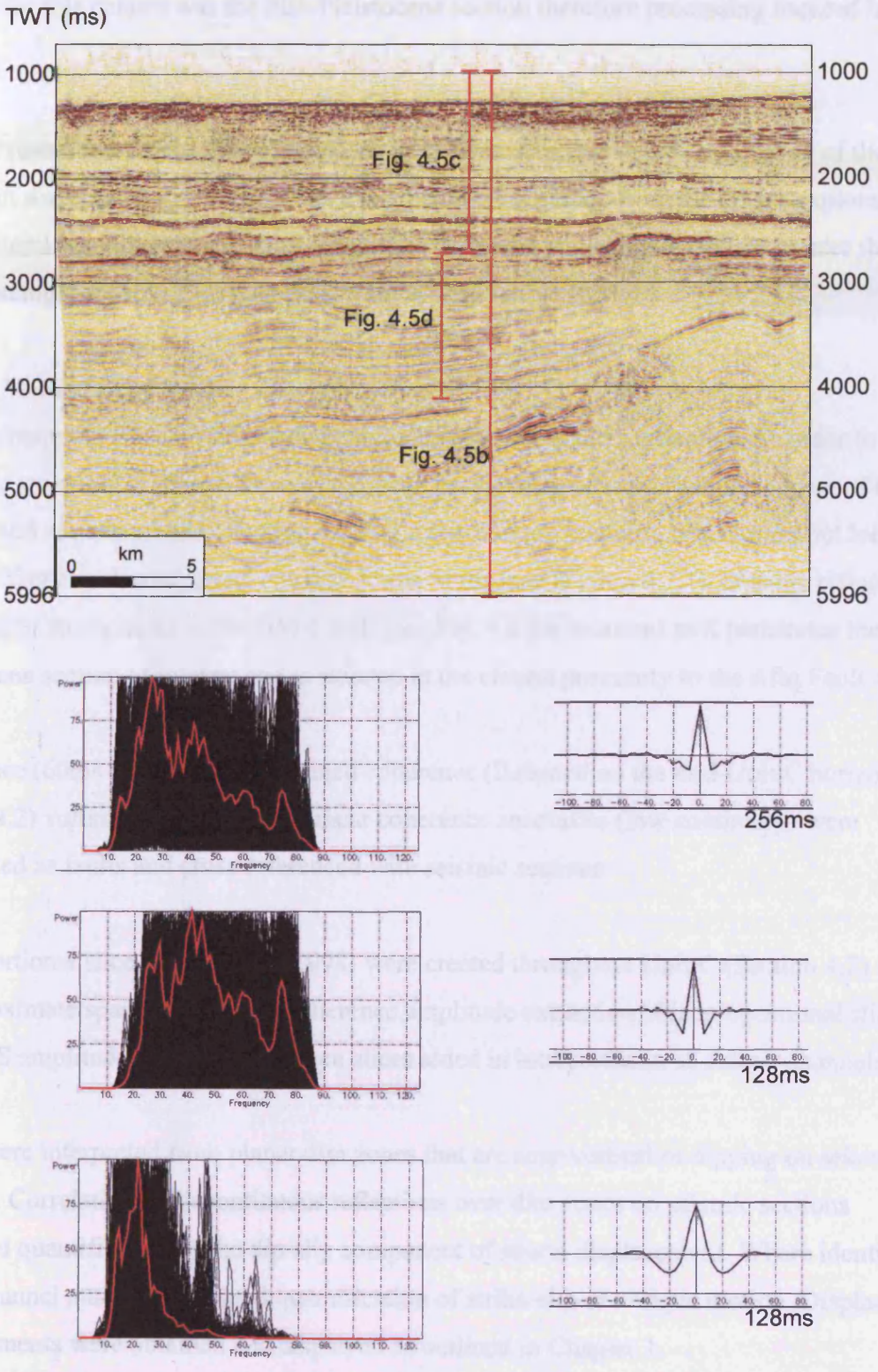

Figure 4.5. Frequency spectra analysis of 3D seismic dataset. a) seismic profile (Line 3901) from which frequency spectra were extracted over the bracketed depth windows. b) Frequency spectra extracted from the entire depth window (1000-6000ms TWT) using the 256ms wavelet shown. Average bandwidth is 20-80Hz. Centre frequency is 50Hz. c) Frequency spectra extracted from the post-Miocene interval (including the Messinian evaporites, 1000-2750ms TWT) using the 128ms wavelet shown. Average bandwidth is 20-80Hz. Centre frequency is 50Hz. d) Frequency spectra extracted from the pre-Messinian section (2750-4100ms TWT) using the 128ms wavelet shown. Average bandwidth is 12-48Hz. Centre frequency is 30Hz.

interval for this dataset was the Plio-Pleistocene section therefore processing focused in this interval.

Vertical resolution for the Plio-Pleistocene interval is 10m calculated as a quarter of the dominant wavelength (Yilmaz, 1987), using parameters gained from the GM-1 exploration well. Lateral resolution is estimated as half the dominant wavelength, (where greater than trace spacing, Lindsey, 1989), and therefore as 20m in this survey.

4.1.3 Methodology

Horizon mapping was carried out on continuous regional marker reflections in order to delineate structural features. Three of these are particularly referred to in the course of the chapter and are described in Section 4.2.2. Further horizon mapping was carried out locally to define offset of palaeo-channel markers across faults (see Section 4.7.1). Seismic reflections were tied to stratigraphy in the GM-1 well (see Fig. 4.2 for location) as it penetrates the Plio-Pleistocene section of interest and is situated in the closest proximity to the Afiq Fault zone.

Coherence (60ms window) and flattened coherence (flattened on the mid-Unit C horizon, section 4.2) volumes were created. Linear coherence anomalies (low continuity) were interpreted as faults and cross-referenced with seismic sections.

Isoproportional slices (Zeng et al., 1998) were created throughout Unit C (Section 4.2) with an approximate spacing of 50ms. Coherence amplitude extraction of isoproportional slices and RMS amplitude extraction between slices aided in interpretation of palaeo-channels.

Faults were interpreted from planar dim zones that are near-vertical or dipping on seismic sections. Correlation of discontinuous reflections over dim zones on seismic sections permitted quantification of the dip-slip component of stratal displacement. Where identified, paleo-channel markers permitted quantification of strike-slip or oblique motion. Displacement measurements were obtained and displayed as outlined in Chapter 1.

4.2 Stratigraphic Context

Stratigraphic units defined from wells were tied to the 3D seismic dataset in order to place the study area into stratigraphic context. Bertoni and Cartwright (2005) have outlined three basic units that correspond to Late Cretaceous-Late Miocene (Unit A), Messinian evaporites (Unit

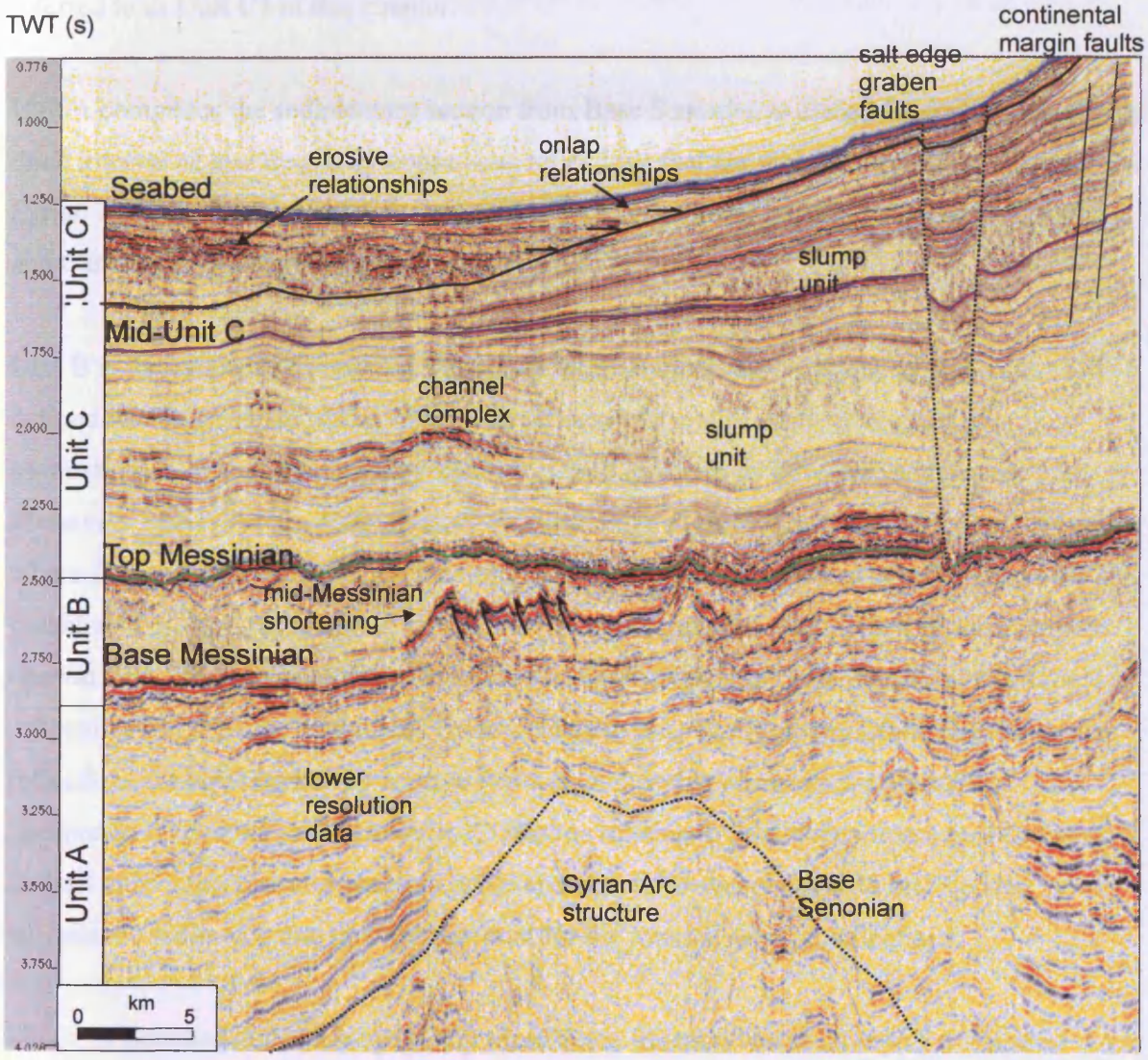

Figure 4.6. Regional seismic section (see Fig. 4.2 for location) displaying characteristic structures and stratigraphic features of Units A (pre-Messinian), B (Messinian evaporites), C (Pliocene-Recent) and C1 (Upper Pleistocene-Recent). A Syrian Arc feature is identified in Unit A. The generally low amplitude seismic character of Unit B is interbedded with high amplitude layers that have experienced shortening. Channels and slumps characterise Unit C and an onlap surface defines the boundary between Unit C and Unit C1 that is heavily channelised. A graben feature extends from the seabed to Top Unit B and terminates at the eastern pinchout of Unit B. Stratal geometries display a depression that is contained by the graben faults. Continental margin faults deform the upper part of Unit C.

B) and Pliocene-Recent (Unit C) (Fig. 4.6). These were defined on the basis of seismic character, geometrical relationships and well calibration. A unit at the top of Unit C was also interpreted as it has a distinctive seismic character that impairs accurate fault displacement measurements. This unit corresponds to Unit T10 in Frey-Martinez et al. (2005) but will be referred to as Unit C1 in this chapter.

Unit A comprises the sedimentary section from Base Senonian to Base Messinian. It is a 1km thick interval of low frequency continuous reflections that are mainly deep-water clastics. The Syrian Arc anticlines, and canyon systems, are identified from this interval (Fig. 4.6, Bertoni and Cartwright, 2006a; Frey-Martinez et al., 2005).

Unit B is the evaporite-dominated Messinian interval. Regional mapping by Hsü et al. (1973) defined the top and base of this interval as reflectors M and N respectively and this terminology is still in use, but they will be referred to herein as Top/Base Messinian. The Messinian evaporites are 400m thick at the distal edge of the dataset but thin toward the east where Top and Base Messinian reflections combine to become one single reflection at the salt pinchout (Fig. 4.6), representing a correlative landward unconformity. Unit B has a largely chaotic transparent seismic facies. However, medium-high amplitude, locally continuous, reflections can often be determined from within the unit. The high amplitude mid-Messinian reflections are often broken by reverse faults (Fig. 4.6) that represent the shortening interpreted by Bertoni and Cartwright (2006a) as relating to post-depositional movement of the salt units. Unit B is composed of halite and anhydrite evaporites with interbedded siliciclastic sediments that probably account for the internal seismic reflections.

Unit C is bounded at its base by the top Messinian reflection and at its top by the seabed. Unit C is deformed by gravitational tectonics above the Messinian salt layer including the Afiq Fault system on which this chapter focuses. It has been further divided into Unit C1 at the top 100-200ms of the dataset comprising upper Pleistocene-Recent sediments. Between the Top Messinian and base C1, Unit C has a seismic character of high frequency, mostly continuous medium-high amplitude and largely parallel reflections. These represent a wedge of prograding-aggrading shelf to base of slope claystones,alternating with sandstones and siltstones.

Within this sequence, lensoid to sheet-like, chaotic, low amplitude units occur that are interpreted as slump complexes by Frey-Martinez et al. (2005) with a frequency of occurrence that increases up-section. Individual very high amplitude bodies exist that display erosive relationships with sediments below and are identified on coherence slices as ribbon-like features with a width of ~100-300m. These are interpreted to be channel complexes, and in some cases channel bodies with lateral accretion and levee deposits can be determined (c.f. Abreu et al., 2003).

The base of Unit C1 is defined in the east by a horizon against which Unit C1 reflections onlap, which becomes conformable with Unit C1 reflections toward the west (Fig. 4.6). Unit C1 comprises mainly fine-grained clastic sediments that form an aggrading sigmoidal clinoform geometry on the continental slope. Frey-Martinez et al. (2005) also report numerous slump bodies from within this unit.

The majority of Unit C1 is characterised by discontinuous high amplitude reflections that can only be tracked locally and are difficult to correlate across faults. The thickness of this discontinuous high amplitude package is variable and in some cases is thicker in the hangingwall of a normal fault. These reflections show clear erosive relationships with deeper reflections. This seismic character is interpreted as a highly channelised package. The difficulty in correlation across faults creates greater uncertainty in fault displacement measurements made within this unit (see Section 4.7.2). Above this package Unit C1 is superseded by parallel, continuous low amplitude reflections.

4.2.1 Regional Mapping

Three major regional interpreted horizons are referred to throughout this text and shown in seismic section in Figure 4.6. The main function of these horizons is to delineate the fault system and they were therefore chosen based on their continuous seismic character rather than as key stratigraphic boundaries. The mapped horizons are Top Messinian, a mid Unit C horizon that correlates to the approximate location of the Pliocene/Pleistocene boundary, and the seabed horizon.

4.2.1.1 Top Messinian

The Top Messinian horizon is a continuous high amplitude peak representing the acoustic impedance contrast from the deep-water clastics of Unit C into the high velocity evaporites of

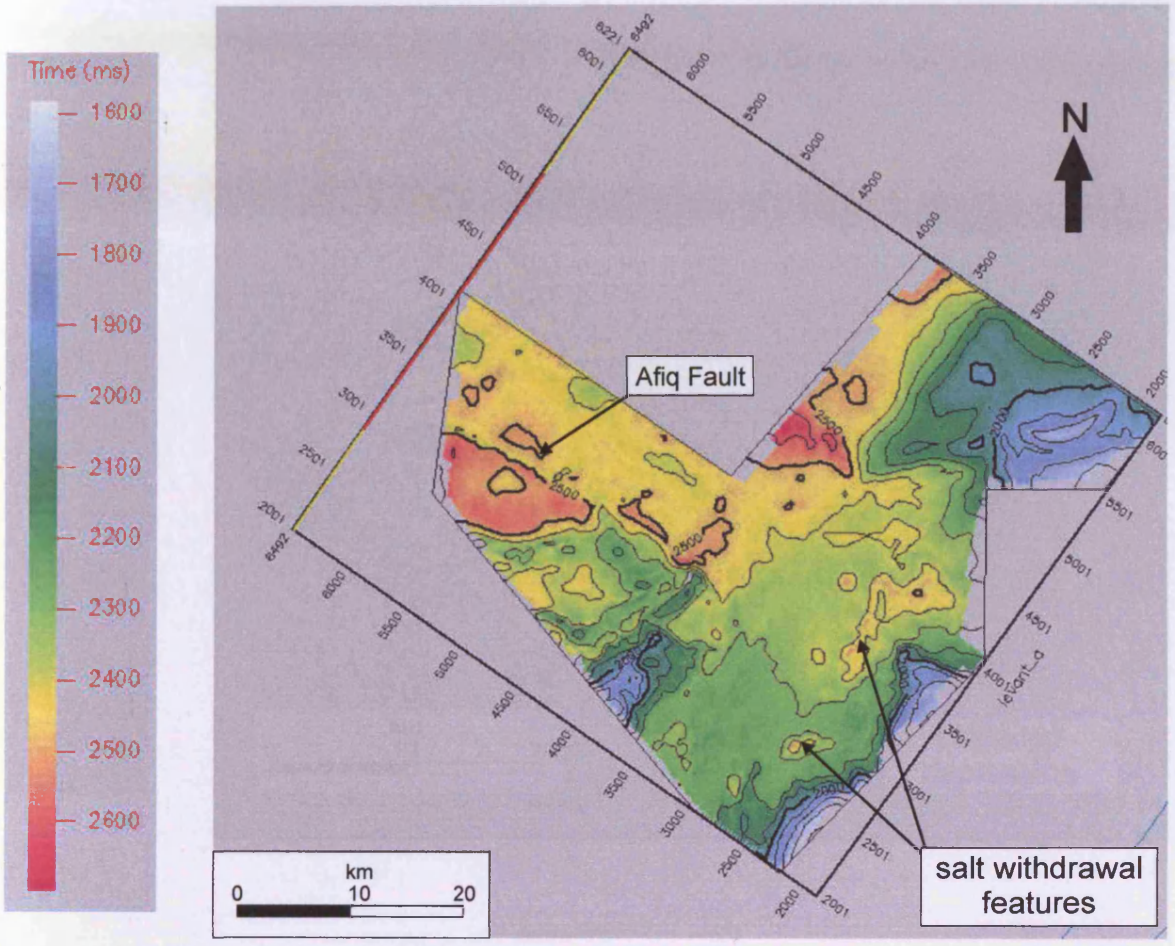

Figure 4.7. Two-way time (ms) structure map of the Top Messinian horizon. Localised variations in the contour pattern in the distal section of the dataset reflect irregularity on the top salt reflection. The trace of the Afiq Fault can be identified. More proximal irregularities represent post-depositional salt evacuation.

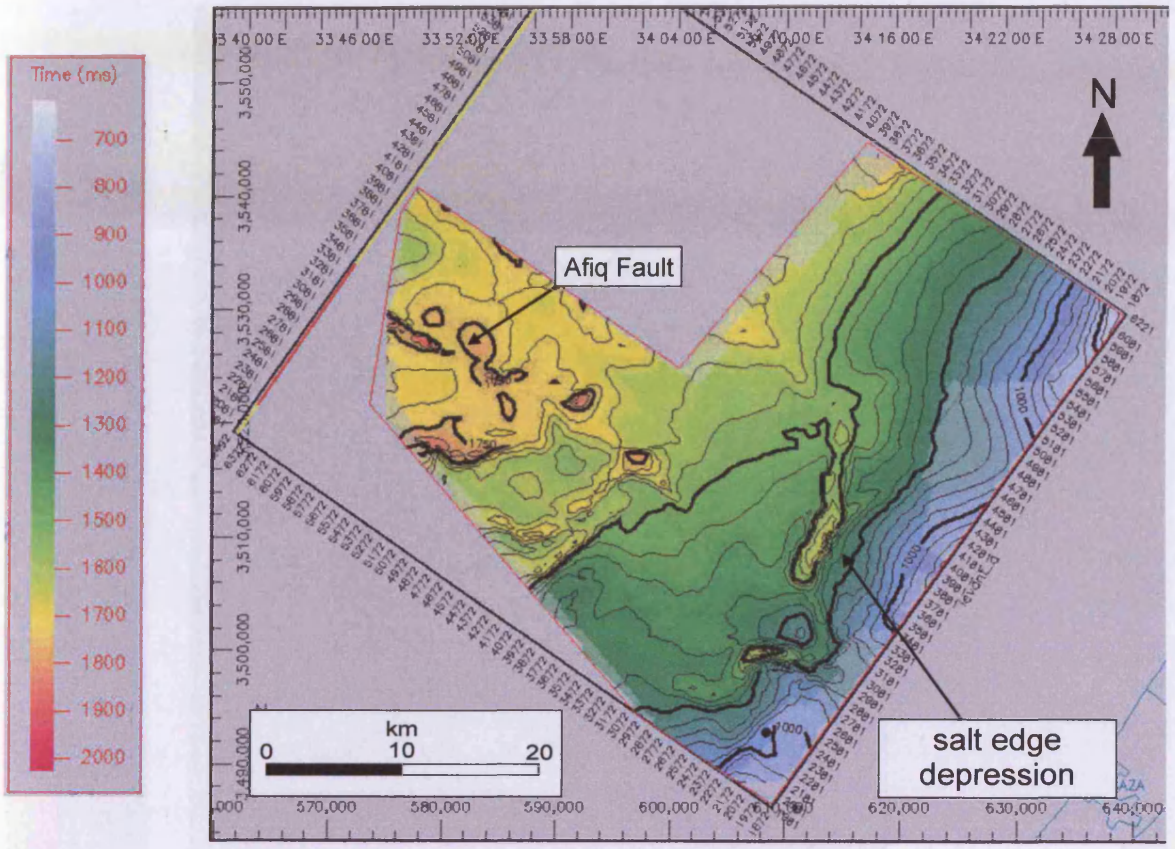

Figure 4.8 Two-way time (ms) structure map of the mid-Unit C horizon. A gentle decrease in slope from the continental margin into the basin is locally varied with relation to deformation of the horizon including a salt edge depression.

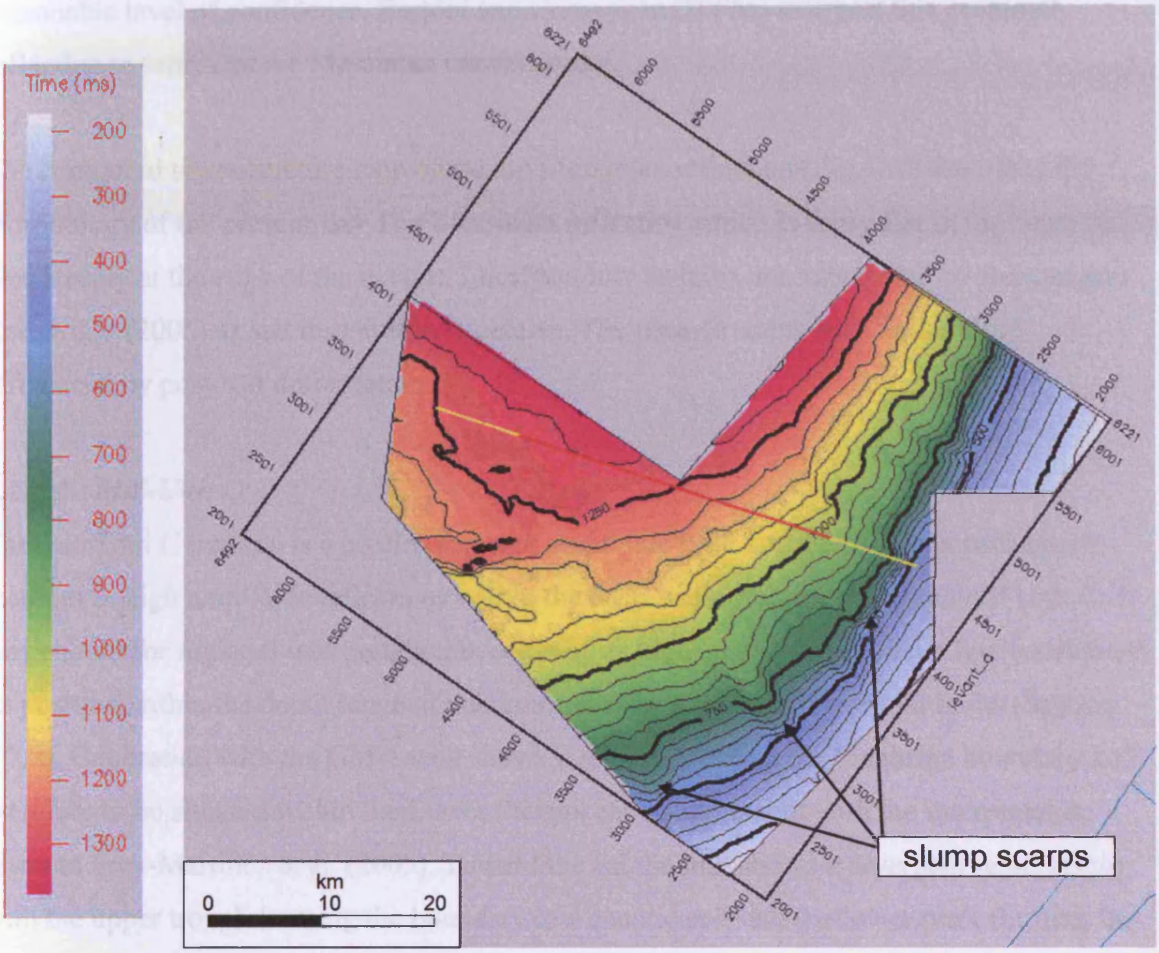

Figure 4.9 Two-way time (ms) structure map of the seabed horizon. The continental slope gradually decreases toward the basin and slump scarps disrupt the proximal contour pattern.

Unit B. In the proximal part of the study area, where the Messinian unit pinches out, it is possible to trace this high amplitude reflection to the landward limit of the dataset with a reasonable level of confidence. Bertoni and Cartwright (2006a) interpret this proximal reflection to represent the Messinian unconformity.

The contoured time-structure map of the top Messinian reflection (Fig. 4.7) describes the morphology of the present-day Top Messinian reflection which is fairly flat in the basin but dips steeply at the edge of the dataset. Localised low features are interpreted by Bertoni and Cartwright (2005) as salt dissolution structures. The time-structure map is therefore influenced by post-salt deformation.

4.2.1.2 Mid-Unit C

The mid-Unit C horizon is a continuous high amplitude peak situated within a package of medium to high amplitude reflections within the deep-water clastic stratigraphy of Unit C. It was chosen for regional interpretation because of its high amplitude character and because of its position within the depth range of maximum displacement on the normal faults (Section 4.7.2). Calibration with the GM-1 well shows it to tie just above the Calabrian boundary and therefore to be situated within the Lower Pleistocene in agreement with the interpretation given in Frey-Martinez et al. (2005). Toward the SE the unit shows a divergent relationship with the upper trough forming the boundary to a chaotic unit and the lower peak forming the lower boundary. The chaotic unit is interpreted as a slump deposit and the mid-Unit C horizon is traced as the top boundary.

The contoured time-structure map of the mid-Unit C horizon (Fig. 4.8) shows that the slope of the continental margin gently decreases toward the basin. Variations in this general deepening pattern are seen as linear bullseye contour patterns on the slope that relate to salt depressions (Section 4.3.2.1). In the basin, the Afiq Fault trace can be identified from offset of the contour pattern.

4.2.1.3 Seabed

The seabed horizon is mapped with a high level of confidence as a continuous high amplitude peak at the positive acoustic impedance water/sediment interface (Fig. 4.6). The contoured TWT (ms) structure map (Fig. 4.9) of the seabed horizon displays a gradual slope from the

Israeli shelf into the basin. A number of scarp features are identified as the heads of slump deposits (Frey-Martinez et al., 2005).

4.3 STRUCTURAL CONTEXT

The aim of this section is to describe the structural elements of the study area and to place these into the regional setting to provide a structural context for the Afiq Fault system. The fault system studied herein is related to the gravitational tectonics above the mobile evaporite layer (Section 4.4) and therefore the structural context focuses on salt-related deformation that can be identified from the study area.

The main structural elements that deform Unit C are shown on a synoptic diagram (Fig. 4.10) that superimposes them upon an isochron map of Unit B and will be referred to in the course of this section.

4.3.1 Salt thickness and canyons

The distribution of evaporites in the study area can be related to the Cretaceous-Miocene canyon systems as described by Bertoni and Cartwright (2006a). This distribution ultimately affects the structures identified within the study area and will therefore be described in this section. Bertoni and Cartwright (2006a) present a Messinian salt isochron map (their Fig. 7), the contours of which define an irregular edge to the salt pinchout. They show that the dataset used in this study is located entirely within an embayment that relocates the salt pinchout approximately 35km landward of the location of the generally linear NE-SW trending salt edge elsewhere on the Israeli margin. In addition, the head of the El Arish and Afiq canyon systems are mapped from Unit A directly below this embayment. On the scale of the Levant dataset used in this study, salt edge irregularities form small embayments that are interpreted to be situated stratigraphically above the El-Arish and Afiq canyons and their tributaries. Bertoni and Cartwright (2006a) argue a strong case for preferential Messinian erosion and salt deposition above the axes of the older canyons. In turn, they provide evidence for NW-SE basement structural trends acting as a controlling factor in defining the location of the canyon axes in the onshore/offshore transition.

4.3.2 Fault systems

The distribution of faulting that deforms Unit C in the study area is related to its governing factors of post-depositional salt deformation and sediment loading. The fault pattern (Fig.

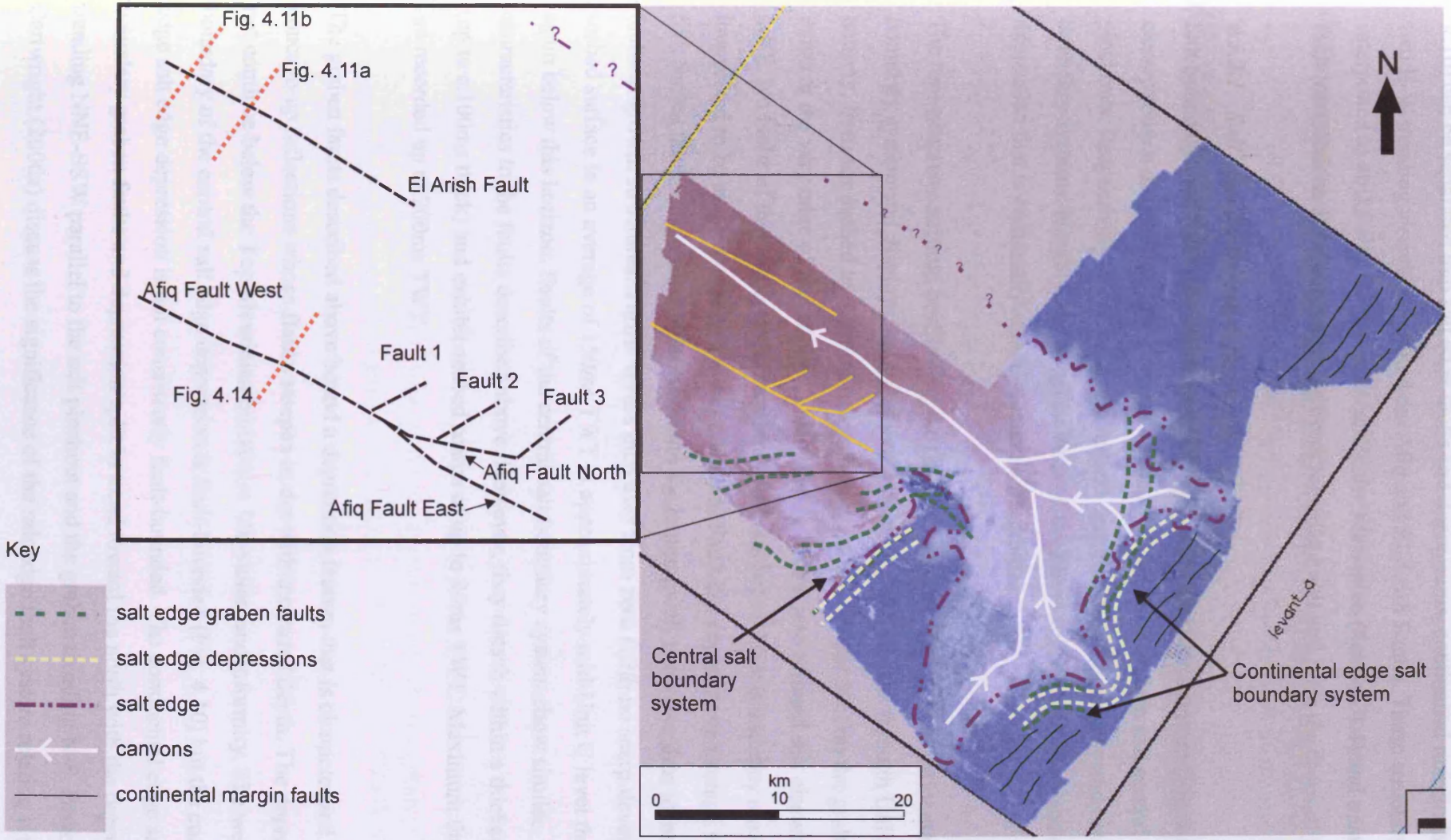

Figure. 4.10. Synoptic diagram of the main structural elements in the study area and the Cretacous-Miocene canyon system (Bertoni and Cartwright, 2006) superimposed upon an isochron map of Unit B. The irregular edge of the Unit B salt pinchout correlates closely with the positions of the heads of the Unit A canyons. Grabens and depressions are located at, and follow the trend of, the updip edge of the salt pinchout.

4.10) can be separated into salt edge faults and depressions, continental margin faults and the two E-W trending structures, termed the Afiq and El-Arish Faults. These structures are interpreted as strike-slip faults that detach in the Messinian (Section 4.4) and a number of fault intersections are identified at the tip of the Afiq Fault and form the focus of this chapter.

4.3.2.1 Salt edge faults and depressions

Salt boundary faults and depressions are labelled on the synoptic diagram (Fig. 4.10) and clearly show a distribution that is related to the salt edge at its eastern and central updip pinchouts. Respectively, these faults are termed continental salt boundary and central salt boundary systems. Notably, the irregular edge of the salt is followed by the trace of a depression that is commonly also associated with faulting.

The representative seismic profile (Fig 4.6) is taken through part of the continental edge salt boundary system and displays a graben-bounding fault pair that cuts through Unit C in its entirety, from the seabed to the top Messinian salt. In this seismic section the graben system exists at the very edge of the salt but is also seen to detach into thinned salt elsewhere (Fig. 4.10). No faults of this salt boundary system penetrate below Unit B and they are therefore interpreted to be associated with the salt pinchout. Fault dip angles have average values of 50-55°. Stratal thickening from the footwall into the hangingwall is shown, thus identifying these faults as growth structures. Throw values increases from zero (with no scarp developed) at the seabed surface to an average of 150ms TWT at approximately mid-Unit C level then decrease again below this horizon. Faults of the central salt boundary system show similar characteristics to the faults described above. However, they detach within a thicker salt unit (up to c.100ms thick) and exhibit seabed scarps of up to 80ms TWT. Maximum throw values are recorded up to 200ms TWT.

The graben faults described above bound a depression feature that is characterised by concave-up reflections whose flanks steepen in dip with increased depth. The depression does not continue below the Top Messinian horizon or Messinian unconformity. The western boundary of the central salt edge depression is fault-bounded (Fig. 4.10) but the continental edge salt edge depression is not consistently fault-bounded. The continental edge salt boundary graben faults and depression split in trend toward the north with the depression trending NNE-SSW parallel to the salt pinchout and the graben trending N-S. Bertoni and Cartwright (2006a) discuss the significance of the salt edge fault system relating it to post-

depositional salt withdrawal. The closer relation of the depressions rather than the fault pattern to the present day salt pinchout noted here suggests that the depressions form in direct response to salt withdrawal. Where grabens encompass depressions it is suggested that steepening flanks with depth lead to faulting at inflexion points. The greater displacement associated with salt edge faults that detach in thicker salt (i.e. the central salt edge system) suggests that the ability of the faults to propagate and grow in Unit C is governed by the thickness of the salt in which they detach. Similar geometries to these are seen at the edge of many salt basins e.g. the North Sea (Stewart and Clark, 1999).

4.3.2.2 Continental margin faults

The continental margin faults system (Figs. 4.6, 4.10) is a broadly parallel, NE-SW trending linear array of faults on the continental slope. Fault lengths reach over 16km. All continental margin faults dip downslope and have an average dip angle of 45°. Two different categories of continental margin fault exist, Type A and Type B, as defined by their characteristics and location on the margin.

Type A faults are situated closest to the shelf edge. They deform entirely within Unit C and frequently deform the seabed. They have straight to curved plan view traces and are longer than type B faults. They have a maximum displacement of approximately 50ms and are separated by an average spacing of 1km.

Type B faults have a maximum displacement of <10ms and a regular spacing of approximately 250m. They are parallel and straight in plan view and have average lengths of approximately 2km. They deform entirely within Unit C and do not reach the seabed surface. They are situated further landward than type A in the continental margin system.

It is interpreted that Type B faults are less well developed than type A faults and may evolve through propagation and linkage to become Type A faults. These faults do not detach into the Messinian salt system but are nevertheless interpreted to be the result of sediment loading of the continental margin (e.g. Garfunkel and Almagor, 1985).

4.3.3 Structural context summary

The structural evolution of the Pliocene-Recent of the study area is heavily influenced by the depositional morphology of the Messinian salt units and its embayments and salients. The salt

boundary system detaches in the updip extent of the salt and mirrors the irregular edge of the evaporite pinchout. It is interpreted to facilitate deformation by thin-skinned tectonics above the evaporite layer. The continental margin faults are also moving the sediment downslope under gravity. In turn the location of the salt embayments is related to an older canyon system (Fig. 4.10) whose position may have been defined by basement faulting trends (Bertoni and Cartwright, 2006a).

In addition to the structures described above, the E-W trending Afiq and El-Arish Fault systems are highlighted on the synoptic diagram (Fig. 4.10). They trend parallel the palaeo-canyon axis and also to the boundaries of the embayment related to the canyon system as defined by Bertoni and Cartwright (2006a). Therefore their origin is interpreted to be related to the salient of the Messinian evaporite system (see Section 4.4.2).

4.4 3D GEOMETRY OF STRIKE-SLIP FAULTS

The main focus of this chapter is to document the relationship between the Afiq Fault and a series of moderate throw normal faults, and in particular their intersection. However, the initial description of structure focuses on the El-Arish Fault because it is better imaged and can be used as an analogue for interpretation of the Afiq Fault.

The detailed descriptions that are provided below are possible because of the high-resolution dataset and allow a unique insight into the 3D geometries of early-stage strike-slip fault systems. Structures that are found to be integral to the evolution of the Afiq Fault are also found to be integral to the evolution of its intersections with extensional faults. The architecture of the strike-slip faults is described in this section, followed by a description of the 3D geometries of the normal faults (Section 4.5).

4.4.1 3D Geometry of the El-Arish Fault

The El-Arish Fault is an ENE-WSW trending structure that is located 8km north of the Afiq Fault of the same trend (Fig. 4.10). It is a sub-vertical fault that is composed of a principal fault zone at depth and more than one discrete fault toward its upper tip (Fig. 4.11). It deforms Unit C from the seabed to the Top Messinian in the central region but displays a more limited vertical extent toward its lateral tips where it reaches neither the seabed nor the Top Messinian (Fig. 4.11b). Its length varies with depth but is recorded as 10.6km at the seabed surface.

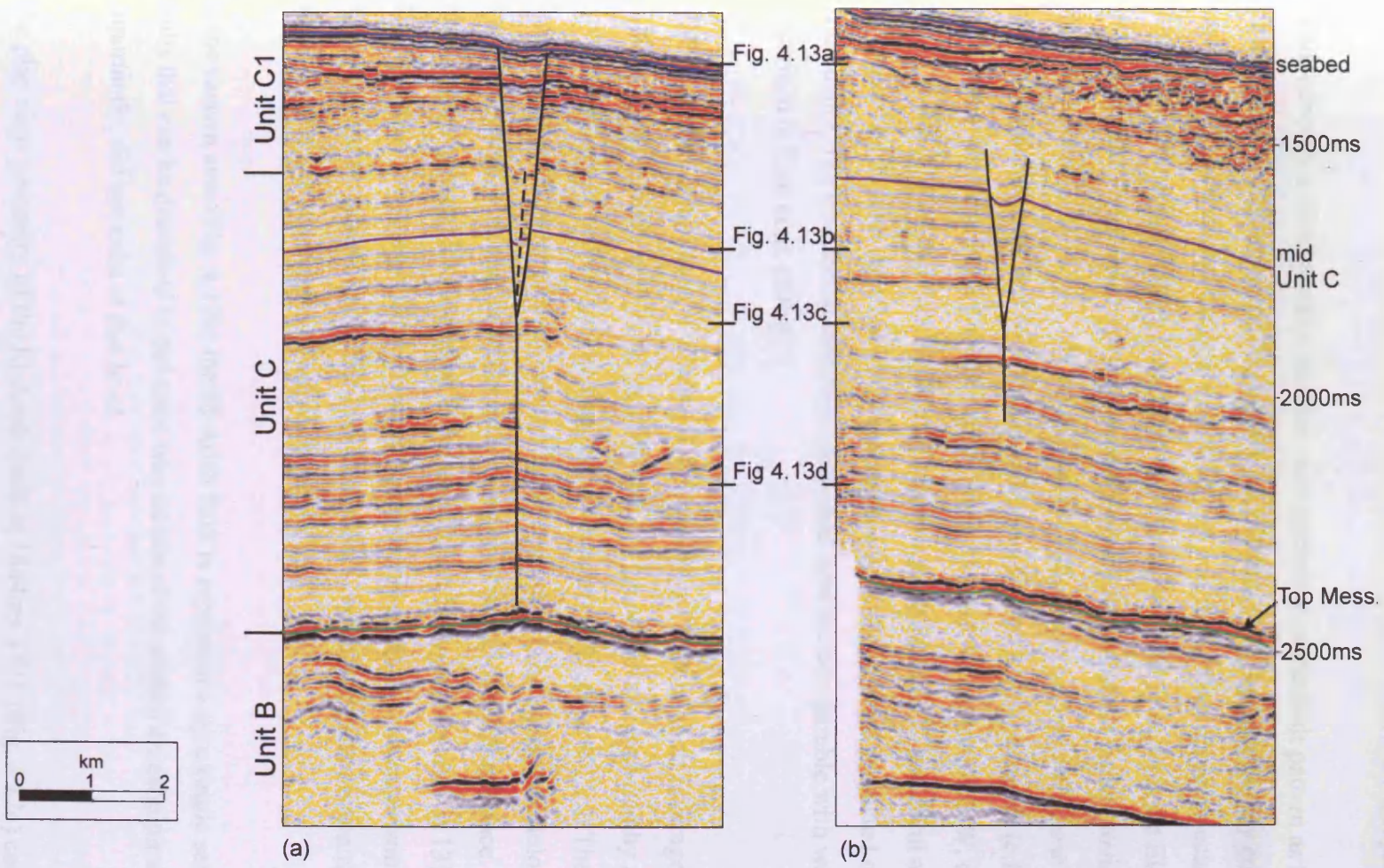

Figure 4.11. Seismic profiles displaying the cross-sectional trace of the El-Arish Fault. See Fig. 4.10 for locations. (a) Seismic section through central location of El-Arish Fault trace. The fault deforms Unit C from the seabed to the Top Messinian. Below c. 1950ms TWT it is interpreted as a single vertical fault trace, above this is diverges to become two bounding faults that display dip-slip kinematics. (b) Seismic section through near-tip location of El-Arish Fault trace. The fault displays the same geometrical characteristics of upward-divergence but notably does not deform the entire vertical interval of Unit C.

The cross-sectional fault trace diverges upward from a single mapped principal fault into two faults that bound a zone of faulting (Fig. 4.11). It is therefore comparable to negative flower structures as described by Harding (1985). These bounding structures have a component of dip-slip extension (max. throw of 20ms) as identified from offset stratigraphic horizons.

Four coherence slices portray the plan view geometry of the fault pattern as it varies throughout the depth section (Fig. 4.12). At 1316ms TWT, approximately coincident with the seabed, the El-Arish fault is represented by two sets of right-stepping en-echelon faults that have a NE-SW trend (Fig. 4.12a). Each set dips toward and joins with the El-Arish principal fault at depth. These faults are the upwardly-diverging bounding faults previously described in cross-section (Fig. 4.11). All faults from set 1 dip southward and all those from set 2 dip northward so that both sets join the throughgoing El-Arish Fault at depth (c.f. Fig 4.11). The continuous El-Arish Fault trace at depth (Fig. 4.11a and 4.12d) trends E-W, midway between sets 1 and 2. The en-echelon faults have an average strike of 078° and form an angle ranging between 43-52° with the trace of the throughgoing El-Arish Fault projected onto the seabed from depth. The en-echelon structures described here are comparable with wall damage zones described in Kim et al. (2004).

The El-Arish Fault pattern at 1700ms TWT constitutes a set of short (average length of c.300m), right-stepping en-echelon faults that are generally encompassed by a set of long (average length of c.800m), right-stepping en-echelon faults (Fig. 4.12b). These are termed high-angled and low-angled en-echelon faults respectively and this terminology relates to their orientation with respect to the underlying principal El-Arish Fault trace. The high-angled faults have comparable orientation to the en-echelon fault sets recorded at 1316ms TWT (Fig. 4.12a) and are interpreted to be the same faults at this depth from comparison with cross-sectional seismic profile lines. The low-angle faults each encompass on average 6-10 high-angle faults and have lengths of approximately 1km.

In the eastern area (Fig. 4.12b) the El-Arish fault is represented by a single set of en-echelon faults that can be described in the same way as one of the seabed en-echelon sets but, importantly, did not exist at that level.

The plan view geometry of the El-Arish Fault at 1844ms TWT (Fig. 4.12c) consists of two sets of low angle right-stepping segments of lengths c.1000m. They are spaced closely

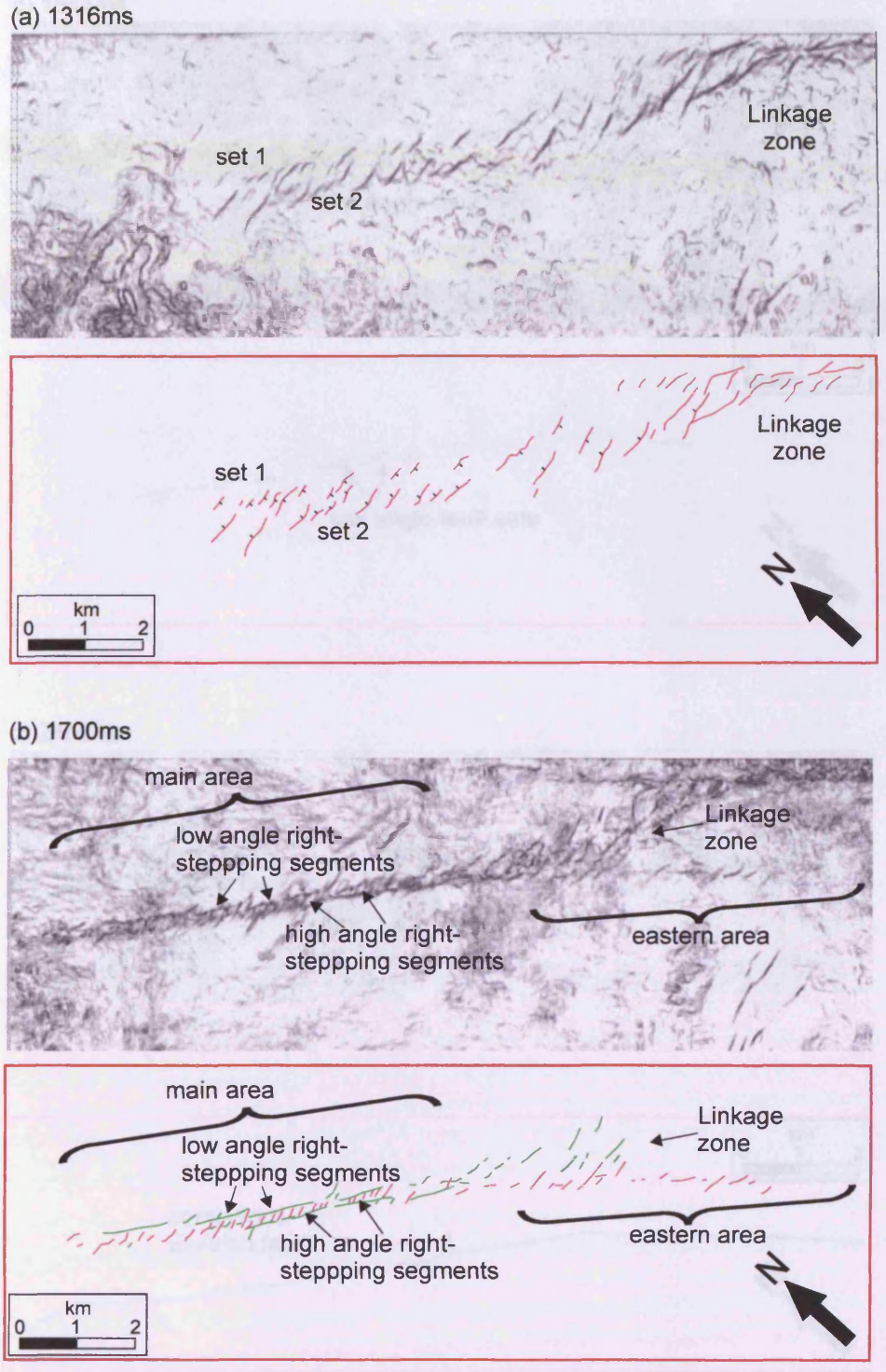

Figure 4.12. Coherence slices and line drawing interpretations displaying the plan view variation in the El-Arish geometry with depth. (a) 1316ms TWT. Two sets of en-echelon faults are imaged. Set 1dips to the south and set 2 dips to the north therefore each set dips toward and joins with the El-Arish Fault at depth. The El-Arish Fault trends through the centre of this fault zone at depth. (b) 1700ms TWT. Fault sets of the same orientation as those at 1316ms TWT are shorter in length and bounded by longer en-echelon faults. These sets are termed high-angle and low-angle respectively, based on their orientation to the principal El-Arish Fault. (c) 1844ms TWT. Only low-angled fault sets are imaged. Note that channel forms are imaged and display sinistral offset across the El-Arish Fault. d) 2168ms TWT. The El-Arish Fault is represented by a single and continuous plan view trace.

c) 1844ms

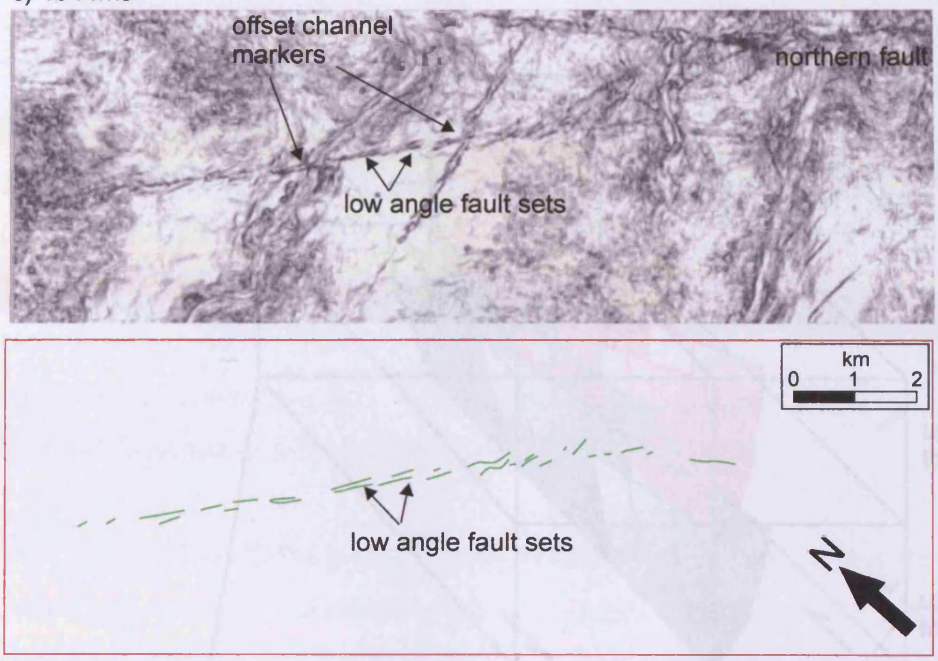

d) 2168ms

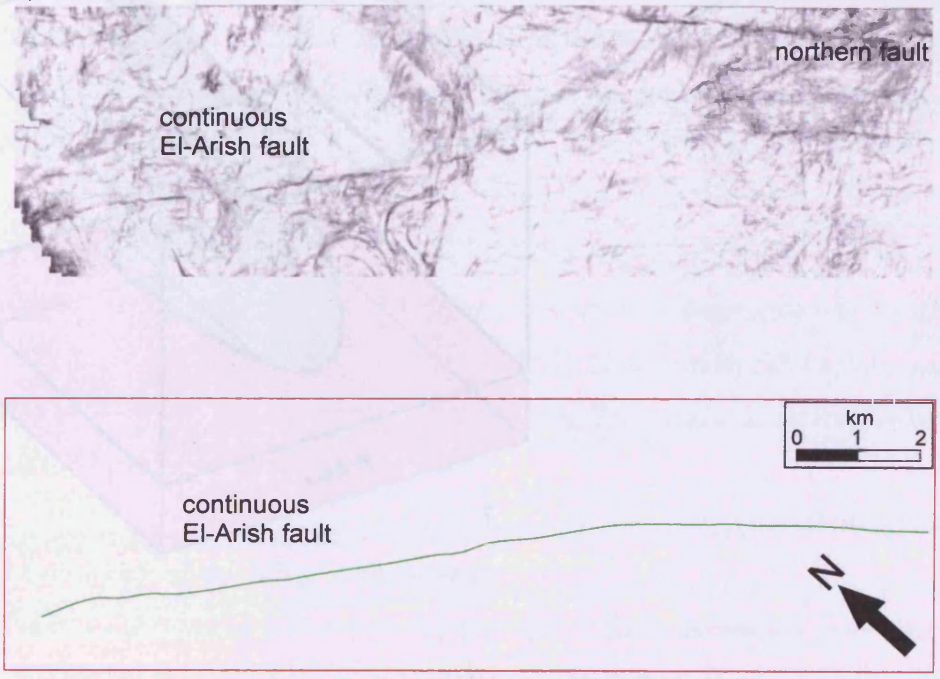

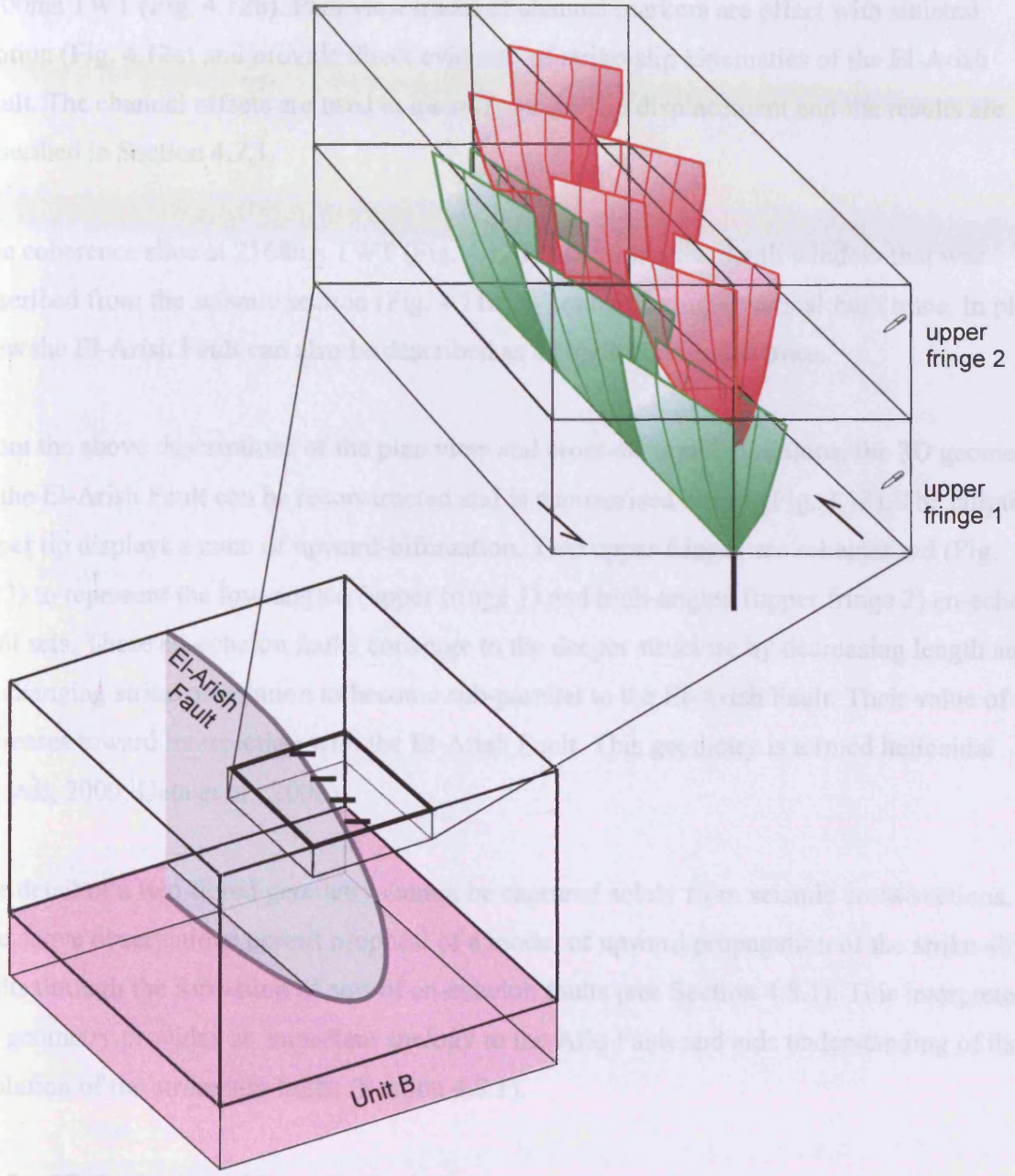

Figure 4.13. Synoptic diagram of the 3D geometry of the El-Arish Fault. The tip line is elliptical and the and the basal tip detaches in the Unit B Messinian evaporites. Structures in the upper portion of the fault plane form two fringes of en-echelon faults.

together and trend sub-parallel to the deeper El-Arish Fault trace. They are interpreted to be the low angle, right-stepping en-echelon faults that were described from the coherence slice at 1700ms TWT (Fig. 4.12b). Plan view traces of channel markers are offset with sinistral motion (Fig. 4.12c) and provide direct evidence of strike-slip kinematics of the El-Arish Fault. The channel offsets are used to quantify strike-slip displacement and the results are described in Section 4.7.1.

The coherence slice at 2168ms TWT (Fig. 4.12d) lies within the depth window that was described from the seismic section (Fig. 4.11a) to contain a single vertical fault trace. In plan view the El-Arish Fault can also be described as a single continuous trace.

From the above descriptions of the plan view and cross-sectional variations, the 3D geometry of the El-Arish Fault can be reconstructed and is summarised below (Fig. 4.13). The elliptical upper tip displays a zone of upward-bifurcation. Two upper fringes are schematised (Fig. 4.13) to represent the low-angled (upper fringe 1) and high-angled (upper fringe 2) en-echelon fault sets. These en-echelon faults converge to the deeper structure by decreasing length and by changing strike orientation to become sub-parallel to the El-Arish Fault. Their value of dip increases toward intersection with the El-Arish Fault. This geometry is termed helicoidal (Mandl, 2000; Ueta et al., 2000).

The detail of a two-tiered geometry cannot be captured solely from seismic cross-sections. The above observations permit proposal of a model of upward propagation of the strike-slip faults through the formation of sets of en-echelon faults (see Section 4.8.1). This interpreted 3D geometry provides an important analogy to the Afiq Fault and aids understanding of the evolution of the strike-slip faults (Section 4.8.1).

4.4.2 3D Geometry of the Afiq Fault System

The Afiq Fault is a sub-vertical fault that deforms Unit C from the seabed to its lower tip within the Messinian evaporites. It has a Y-shaped plan view geometry, similar to that described from the Kunlun Fault trace (Fu et al., 2004), and is therefore divided into three sections for descriptive purposes – the Afiq West, the Afiq North and the Afiq East (Fig. 4.10). The Afiq West will be shown below to be the most developed section of the fault and exhibits a principal vertical fault zone through the entire Unit C section (Figs. 4.14, 4.15). The Afiq Fault (in particular the Afiq East and Afiq North) is commonly associated with more

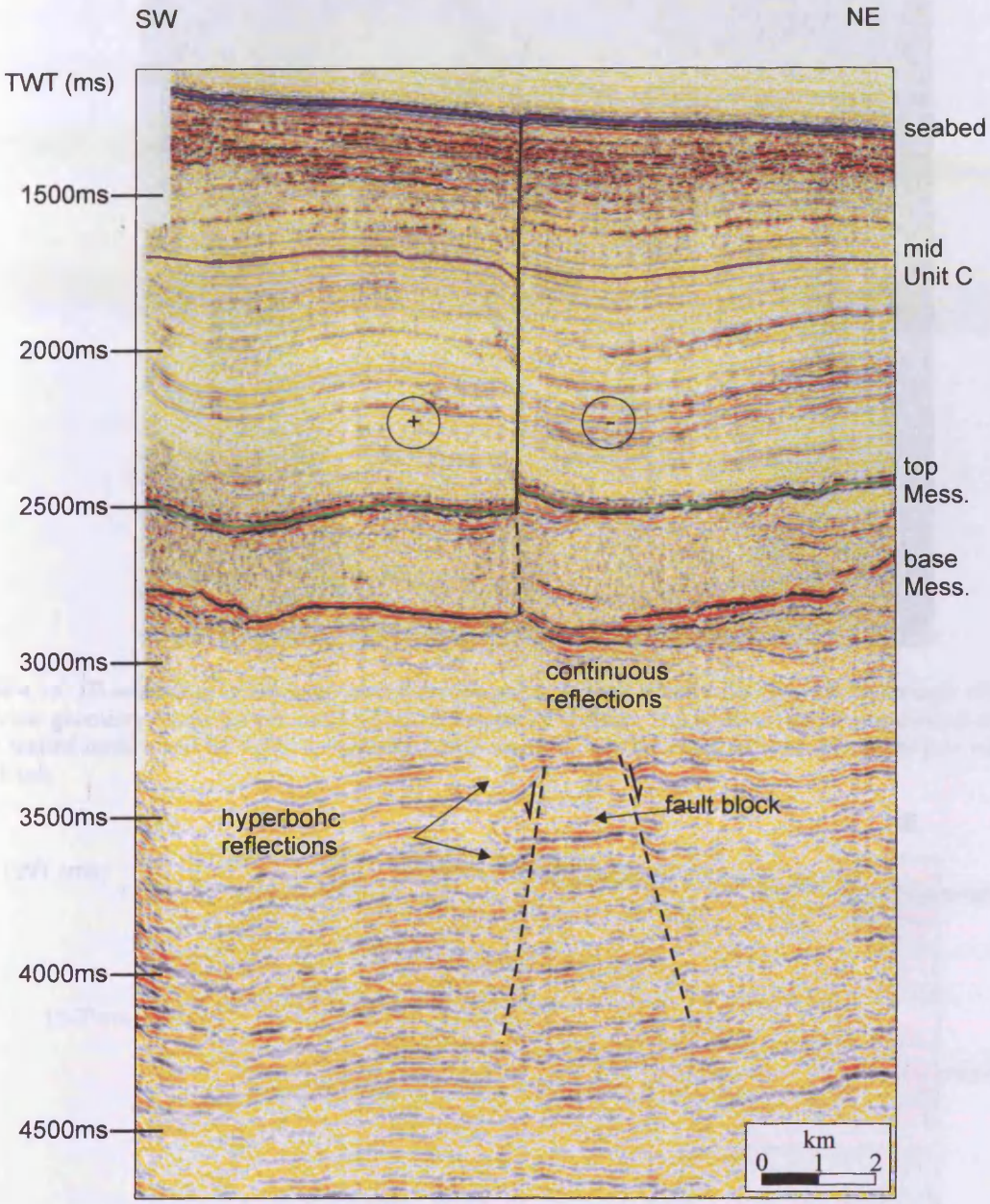

Figure 4.14. Seismic profile showing the cross-sectional geometry of the Afiq Fault. See Fig. 4.17 for location. The Afiq Fault trace is sub-vertical and deforms the entire vertical section of Unit C, detaching within Unit B. The geophysical response of the Base Messinian reflection and the underlying Unit A reflections are disrupted due to seismic artefacts resulting from the presence of the Afiq Fault. Reflections are offset with a component of dip-slip motion that is localised to the area adjacent to the fault plane only..

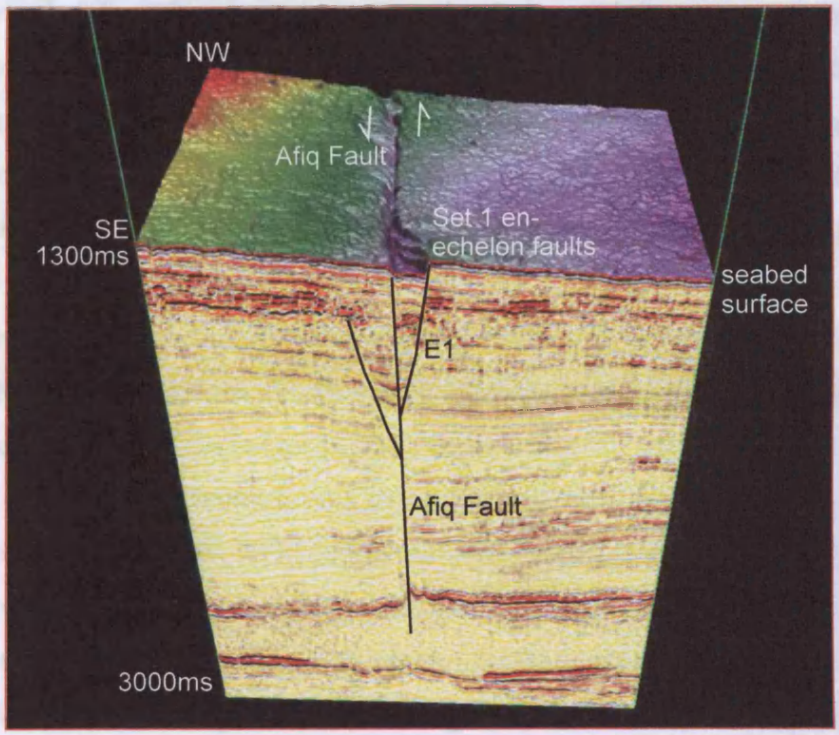

Figure 4.15. 3D seismic cube showing the cross-sectional geometry of the Afiq Fault on the seismic slice and its plan view geometry on the time-structure map of the seabed surface. The northern set of en-echelons are imaged at the seabed surface and E1 forms a signficiant fault scarp. E1 can be traced in cross-section to join with the Afiq Fault.

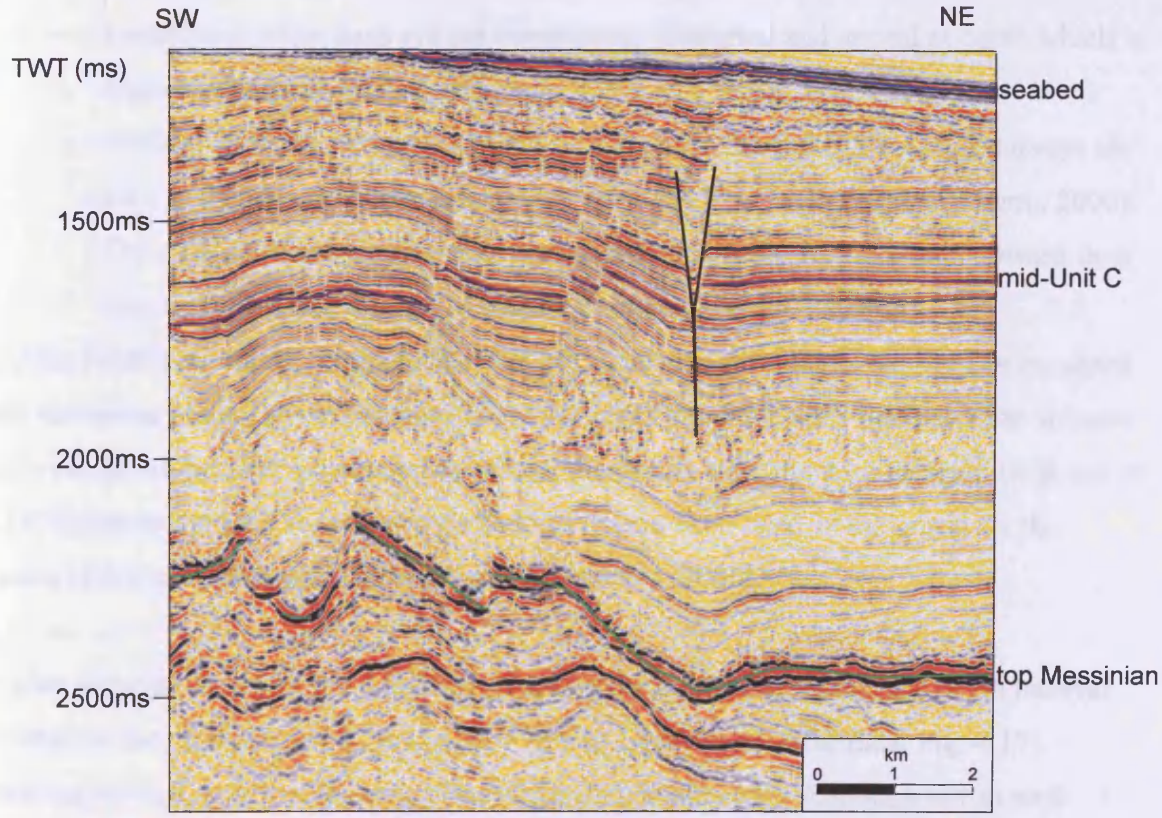

Figure 4.16. Cross-sectional profile showing the geometry of the Afiq Fault toward its eastern extent. See Fig. 4.10 for location. The Afiq Fault maintains its geometry of upward-bifurcation but does not intersect the seabed at its upper tip nor the Top Messinian at its basal tip.

than one discrete fault in the upper Pliocene-Recent section and the upwardly-diverging structure is comparable to a negative flower structure (c.f. Harding, 1985). This three-dimensional geometry is captured in Figure 4.15 and it can be seen that the upwardly-diverging structures form an en-echelon pattern and have significant dip-slip motion at the seabed. Localised dip-slip motion is identified adjacent to the Afiq Fault (Fig. 4.14).

The upper tip of the Afiq Fault plunges below the seabed on the Afiq East and North sections (Fig. 4.16). Significantly, the lower tip does not intersect with the Messinian evaporites in the Afiq East section (Fig. 4.16). Therefore the fault plane geometry is elliptical, and comparable to the El-Arish Fault plane. The exact location of the lower tip is unknown but the Afiq Fault is interpreted to detach within the Messinian evaporites rather than being interpreted as a basement-linked structure. The geophysical response of the Base Messinian reflection and the underlying Unit A reflections are disrupted, but this is interpreted as resulting from seismic artefacts. The Afiq Fault is interpreted as detaching within the Messinian evaporates for the following reasons:

- Clastic depositional bodies intercalated in the basal part of the Messinian are not offset by the Afiq Fault (Bertoni and Cartwright, 2006b).
- Underlying reflections are not consistently disrupted and anneal at depth which is typical of seismic pull-up artefacts.
- Analogous faults to the NW of the study area in the Gal C and Gal B surveys are seen to detach in the Messinian evaporates (M.P.A. Jackson, pers. comm., 2006).
- The Afiq East and North Faults are contained entirely within Unit C toward their tips, therefore they cannot be basement linked in these locations.

The Afiq Fault most likely originated as a lateral ramp structure that is required by localised stress variations related to the irregular edge of the salt pinchout. This interpretation is based largely on its sub-parallel orientation to the salt pinchout embayment boundary (Garfunkel et al., 1979) and to the Unit A canyon axis that has in turn been cited as the origin for the location of the salt embayment (Bertoni and Cartwright, 2006a).

The plan view geometry of the Afiq Fault displays variations throughout the depth interval and between the three fault sections (Afiq West, Afiq North and Afiq East, Fig. 4.17), enhancing understanding of its fault plane shape and architecture. Although not so well defined as the El-Arish Fault architecture, en-echelon faults are identified from the Afiq Fault, and its evolution is therefore thought to be comparable to the El-Arish Fault.

The near-seabed plan view geometry (e.g. 1316ms TWT, Fig. 4.17a) clearly displays sets of en-echelon fractures that lie to the north and south of the through-going Afiq West Fault and become convergent with the Afiq Fault where they intersect with it. The Afiq North Fault is represented by two sets of oppositely dipping, right-stepping, en-echelon faults that dip toward and join with the Afiq North trace at depth, as was described from the El-Arish Fault. Therefore, in contrast to the Afiq West, the Afiq North has not propagated to the seabed. This is also the case for the Afiq East which is represented by only one set of northward-dipping en-echelon faults. In seismic profile this single en-echelon set has a south-dipping pair that has not reached the surface. It can be inferred from this that the en-echelon faults sets do form as pairs but that one set can develop in preference to its opposite set. The en-echelon faults can be described as high-angled from this coherence slice (Fig. 4.17a). They have a sigmoidal plan view geometry in the Afiq West and North sections but are linear in the Afiq East area. This is likely to be related to the relative evolutionary stage of the different sections of the Afiq Fault (see Section 4.8.2). The three normal faults that will be described in Section 4.5 are contiguous with three en-echelon faults of this system.

The plan view architecture of the Afiq Fault at 1760ms TWT (Fig. 4.17b) is complicated and the geometry varies between the three main sections (Afiq West, Afiq North and Afiq East). The Afiq West has a single principal fault trace that is primarily represented by one linear trace on the coherence slice. The Afiq North Fault is more complicated and comprises a densely faulted, anastomosing zone of approximately 300m width. The Afiq East Fault has a throughgoing fault trace at this level and has a segmented nature (Fig. 4.17b) that is comparable to that described from the El-Arish Fault at 1700ms TWT. Low-angled, right-stepping, en-echelon faults are identified, along with and commonly bounding, high-angled fault sets. The eastern tip of the Afiq East is difficult to identify on the coherence slice because of interaction with the central salt boundary graben faults (Section 4.3.2.1).

The Afiq Fault plan view trace at 2260ms TWT (Fig. 4.17c) is located approximately 200ms above the top Messinian horizon (Fig. 4.14) and has a clearly defined, single trace in all three sections. The Afiq West is continuous with the Afiq North, while the Afiq East intersects at a deflection (Fig. 4.17c).

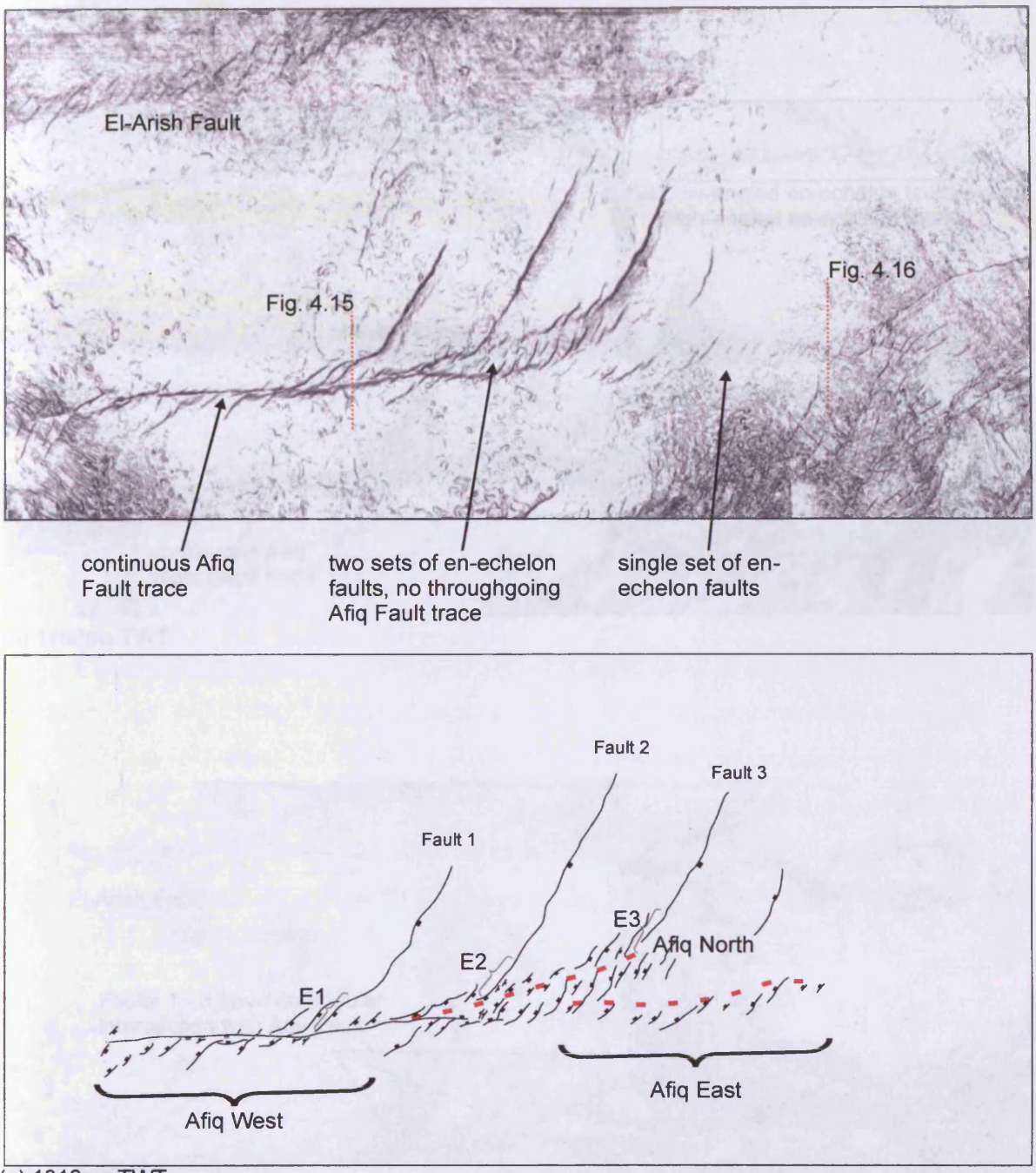

(a) 1316ms TWT

Figure 4.17. Coherence slices illustrating the plan view variation in the Afiq Fault geometry with depth. (a) 1316ms TWT. Coherence slice and line drawing interpretation. The near-surface plan-view geometry of the Afiq Fault shows that the fault has a throughgoing trace on the Afiq West section. The upper tip plunges below the surface to the east where the Afiq North and Afiq East sections are represented by sets of sigmoidal en-echelon faults. Two sets of en-echelons are imaged at the surface above the Afiq North Fault but only one set represents the Afiq East Fault. Note location of seismic profiles in Figs. 4.15 and 4.16. (b) 1760ms TWT. The Afiq West Fault is a throughgoing trace. The Afiq North Fault has an anastomosing geometry. High-angled and Low-angled sets of en-echelon faults are imaged in the Afiq East (see inset). (c) 2260ms TWT. The Afiq West, North and East are all throughgoing, continuous faults. The Afiq North is contiguous with the Afiq West, the Afiq East intersects the Afiq North at the arrowed location.

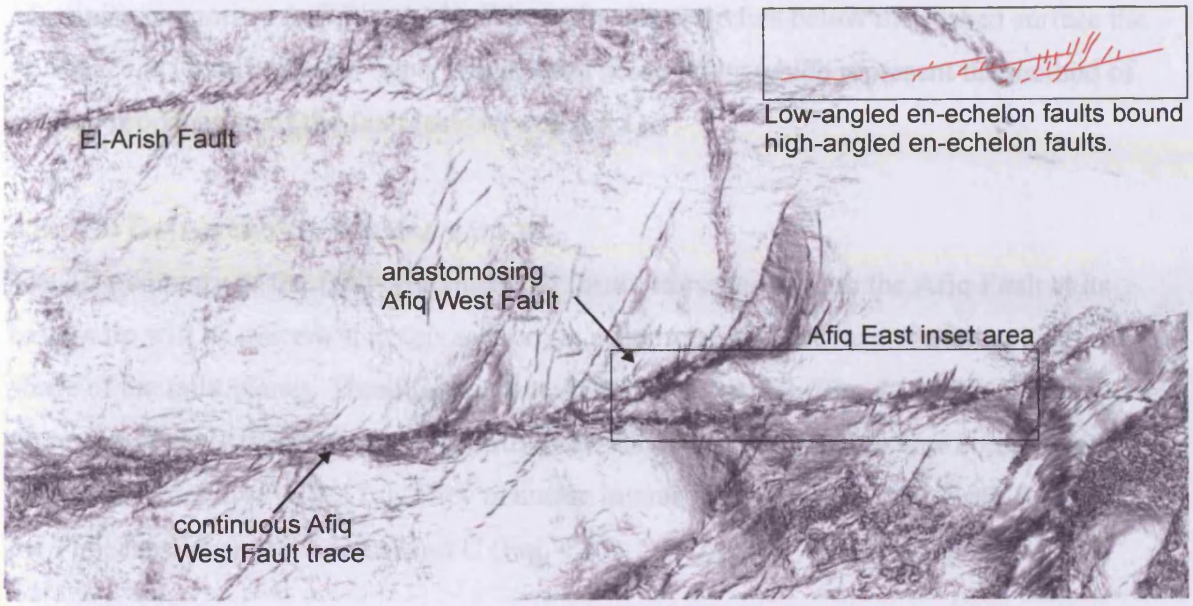

(b) 1760ms TWT

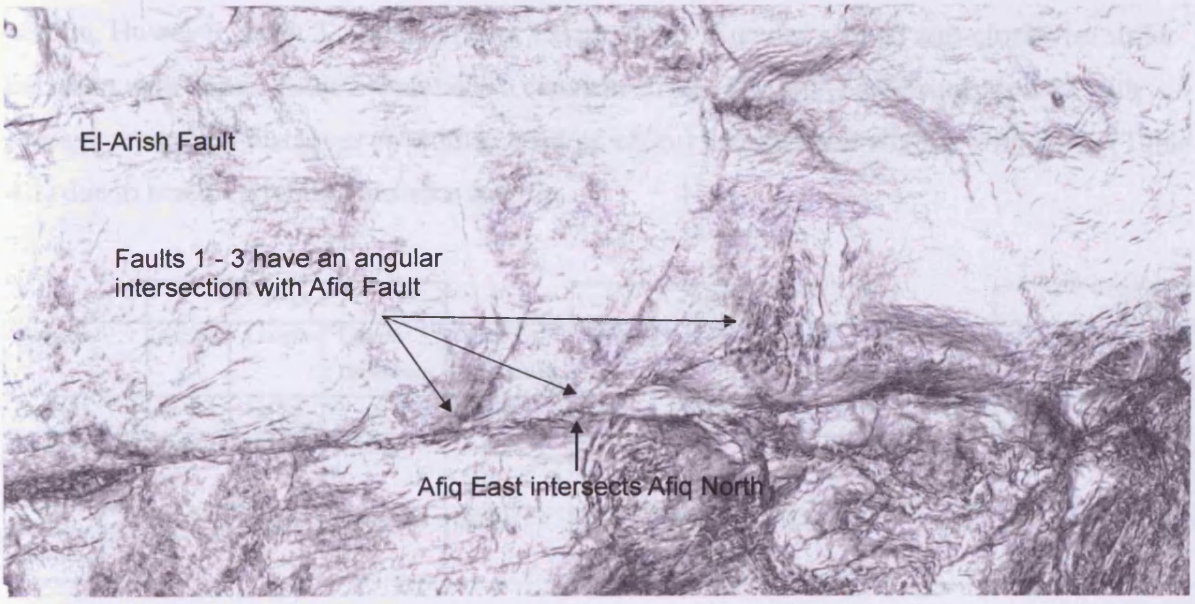

(c) 2260ms TWT

In summary, the 3D geometry of the Afiq Fault is elliptical with a throughgoing fault trace in the west that plunges below the seabed surface in the east and does not intersect with the Messinian evaporites (c.f. Fig. 4.13). Where the upper tip lies below the seabed surface the fault trace is identified from upper fringe en-echelon faults which represent the method of vertical propagation of the fault (see Section 4.8.1).

4.5 3D GEOMETRY OF NORMAL FAULTS

The 3D geometry of the fault structures that form intersections with the Afiq Fault at its eastern tip will be described in this section, in order to establish sense of motion and the 3D shape of the fault planes. Three faults, named Faults 1, 2 and 3 (Fig. 4.10), are situated in the tip region of the Afiq West to Afiq North fault, which is interpreted to be a continuous lineament at depth (Fig. 4.17c). They maintain intersections with the Afiq Fault throughout the Pliocene-Recent section of Unit C (Fig. 4.17).

The linear structures are near-parallel with a NE-SW trend and a near-constant separation distance (Figs. 4.17, 4.18, Table 4.1). Small variations in plan view geometries with depth (Fig. 4.17) are summarised in Table 4.1. Fault strikes are broadly maintained throughout the section. However, Fault 3, and to a lesser extent, Fault 1, record a small anti-clockwise strike variation with depth. Fault 2 maintains a constant strike. The faults are evenly spaced with average separation distances (within an error of ±80m) that increase slightly with depth (Table 4.1) due to small variations in strike and dip.

	Fault 1				Fault 2				Fault 3		
Horizon	**Strike**	**Length**	**Length Difference**	**Fault 1-2 Separation**	**Strike**	**Length**	**Length Difference**	**Fault 2-3 Separation**	**Strike**	**Length**	**Length Difference**
Seabed	066°	3350m		2077m	063°	5100m		2231	062°	3200m	
Mid-Pliocene	066°	3657m	+307m	2171m	063°	5087m	-13m	2286	057°	3771m	+571m
Top Messinian	061°	3067m	-590m	2222m	063°	3644m	-1443m	2400	054°	2844m	-927m

Table 4.1. Fault attributes for Faults 1, 2 and 3.

Length variations (Table 4.1) permit description of lateral fault tip geometries. Both Faults 1 and 3 have the same pattern of length variation in that length increases from the seabed to mid-Unit C and decreases by a significant amount to top Messinian level. They can therefore

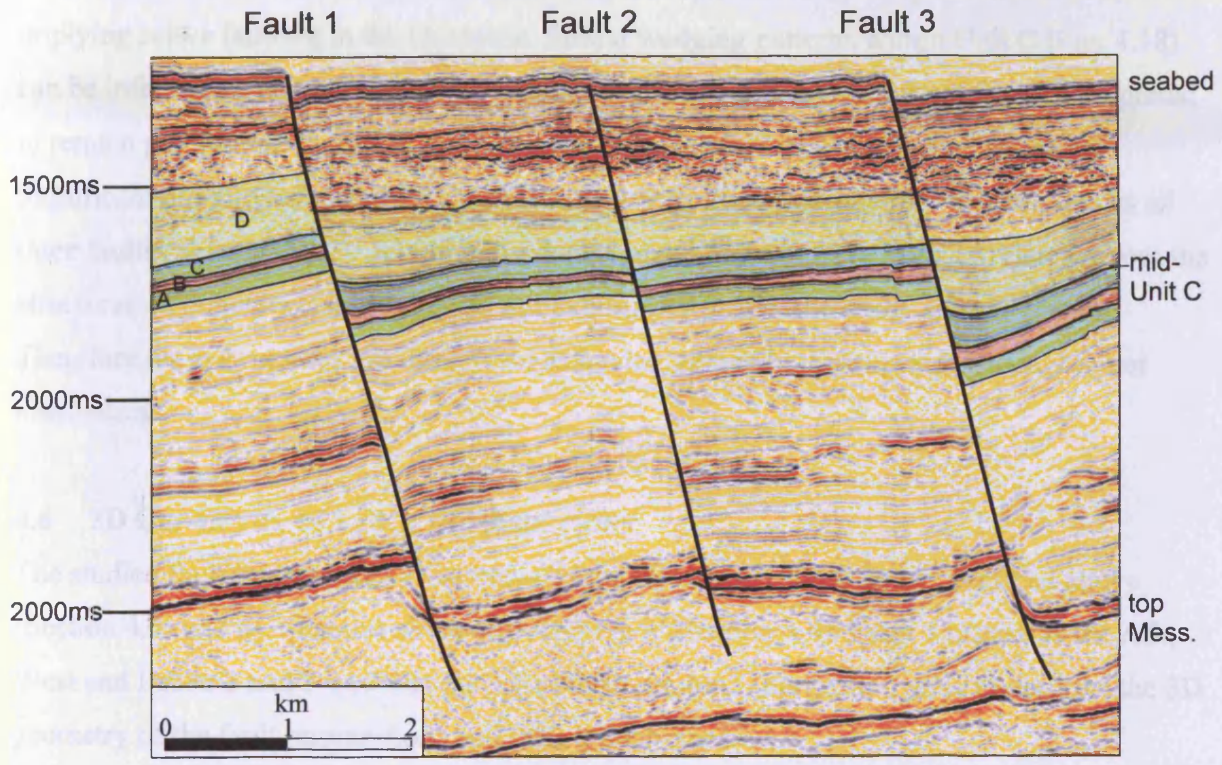

Figure 4.18. Seismic profile line showing the cross-sectional geometry of Faults 1- 3. They all dip toward the east and displace reflections with normal kinematics. They have fault scarps at the seabed surface and their basal tips detach in Unit B. Throw values are significantly greater on Faults 1 and 3 than on Fault 2. Coloured wedges represent packages A-D that demonstrate periods of syn-sedimentary deposition (see text for details).

be described as having an elliptical NE tip. Fault 2 has a constant length at the seabed and mid-Unit C horizons but decreases considerably by almost 1500m to top Messinian level and therefore has a rectangular-elliptical shape to its NE tip.

The faults dip to the east with average dip values of 50° ± 2° for Faults 1 and 3 and a steeper measurement of 57° for Fault 2. The upper tips are represented by scarps at the seabed, implying active faulting in the Holocene. Stratal wedging patterns within Unit C (Fig. 4.18) can be inferred to represent growth faulting (see Section 4.7.2.3). Fault planes are interpreted to remain predominantly planar and to detach at their lower tips within the Messinian. Significant dip-slip extensional motion is recorded from correlation of reflections across all three faults (Section 4.7.2). Where individual channel features have been correlated across the structures on coherence slices they do not exhibit any resolvable strike-slip movement. Therefore these structures are interpreted as having generally dip-slip extensional normal kinematics.

4.6 3D GEOMETRY OF FAULT INTERSECTIONS

The studied fault intersections exist between the three extensional faults described above (Section 4.5) and the sinistral strike-slip Afiq Fault (Section 4.4). Fault 1 intersects the Afiq West and Faults 2 and 3 intersect the Afiq North section. This section aims to describe the 3D geometry of the fault intersections and their branch lines.

The plan view geometry of intersections varies little with depth in the vertical section, but what variation there is can be described from the change in angle between the normal faults and the Afiq Fault. In particular, the angle variation relates to the relationship between the en-echelon faults in the shallow depth section and Faults 1 – 3. At the seabed surface Faults 1 – 3 are broadly parallel to, and extend from, the tips of the northern en-echelon fault set (Fig. 4.17a, Fig. 4.19).

Fault 3 joins with an en-echelon fault (E3 on Fig. 4.19) at the tip of the Afiq North at the seabed horizon (Fig. 4.17a, Fig. 4.19a). The slightly sigmoidal nature of E3 introduces a curvature to the SW extent of Fault 3 where they meet. In contrast, the Fault 3 intersection with the Afiq North is angular at mid-Unit C level and at the Top Messinian (Figs. 4.17b, c) where it is a sharp corner bounding a common footwall and hangingwall (Fig. 4.19b, c). Consequently, the angle of intersection increases from c. 40° at the seabed to c. 50° at the

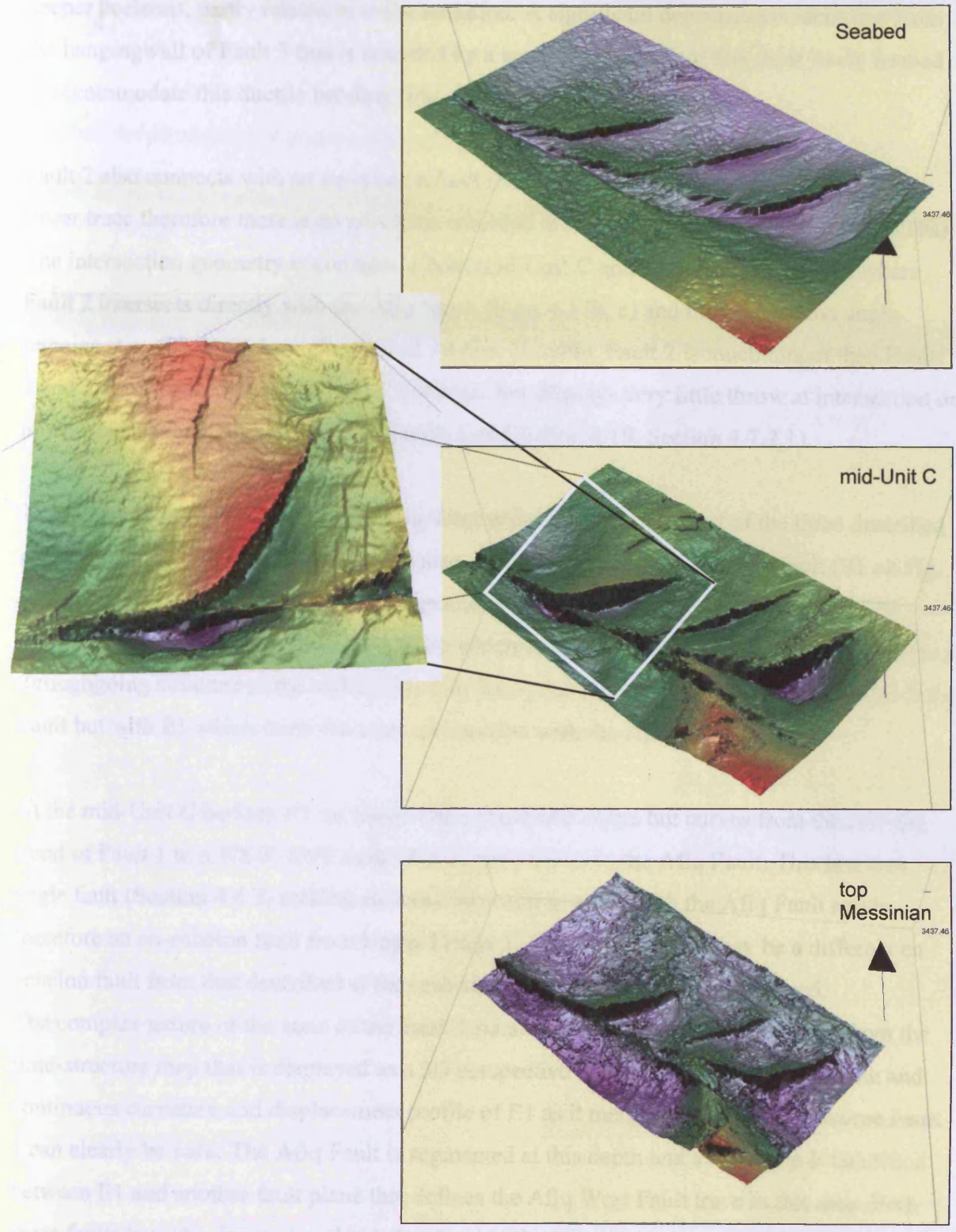

Figure 4.19. Time-structure maps of the seabed, mid-Unit C and top Messinian horizons in perspective view to illustrate the 3D nature of the intersections of Faults 1 - 3 with the Afiq Fault. The seabed horizon shows that Faults 1 - 3 are contiguous with en-echelon faults (E1 - E3) and E1 and E3 have significant seabed fault scarps. The intersections are curved at the seabed due to these relationships between Faults 1 - 3 and E1 - E3. The E1 - Fault 1 relationship at mid-Unit C is shown in detail in the inset. There is a significant depression adjacent to the intersection. Faults 1 - 3 have angular intersections with the Afiq Fault at top Messinian level. Faults 1 and 3 display a large throw value at the intersection location and link to the Afiq Fault.

deeper horizons, partly related to strike variation. A significant depression is identified from the hangingwall of Fault 3 that is bounded by a small antithetic fault that most likely formed to accommodate this ductile bending (Fig. 4.19).

Fault 2 also connects with an en-echelon fault (E2 on Fig. 4.19) at the seabed which has a linear trace therefore there is no curvature recorded at the intersection (fig. 4.17a, Fig. 4.19a). The intersection geometry is constant at both mid-Unit C and Top Messinian levels where Fault 2 intersects directly with the Afiq North (Figs. 4.17b, c) and the intersection angle remains at c. 40° throughout the vertical section. Notably, Fault 2 is much longer than Faults 1 and 3 at the seabed and mid-Unit C horizons, but displays very little throw at intersection on any horizons which also contrasts to Faults 1 and 3 (Fig. 4.19, Section 4.7.2.1).

The intersection of Fault 1 with the Afiq West is the most complicated of the three described intersections. At the seabed surface it is also contiguous with an en-echelon fault (E1 on Fig. 4.19a). E1 has a pronounced sigmoidal geometry and a scarp at the seabed. The NE-SW trending Fault 1 joins with E1 at its NW tip which is trending WNW-ESE. The Afiq Fault is a throughgoing structure at the seabed (Section 3.4.3) therefore intersection is not with the Afiq Fault but with E1 which itself forms an intersection with the Afiq West.

At the mid-Unit C horizon E1 no longer has a sigmoidal shape but curves from the NW-SE trend of Fault 1 to a WSW-ENE strike that is sub-parallel to the Afiq Fault. This is a low-angle fault (Section 4.4.2) making an acute intersection angle with the Afiq Fault and is therefore an en-echelon fault from Upper Fringe 1. This means that it may be a different en echelon fault from that described at the seabed, but this detail cannot be resolved.
The complex nature of the zone of the Fault 1 intersection can be further described from the time-structure map that is displayed as a 3D perspective image (Fig. 4.19). The smooth and continuous curvature and displacement profile of E1 as it merges seamlessly to become Fault 1 can clearly be seen. The Afiq Fault is segmented at this depth and a right step is identified between E1 and another fault plane that defines the Afiq West Fault trace in this area. Both these faults bound a depression that is localised to the intersection area. The southern limit of this depression is also fault-bounded and the geometry has similarities to a pull-apart structure (Dooley and McClay, 1997). Pull-apart structures are common in strike-slip fault systems (Sylvester, 1988) but it is unclear if this structure is related to tectonics of the Afiq Fault

development, or the intersection development, particularly as it is not identified from other horizons.

At the Top Messinian horizon the intersection geometry is a simple angular intersection between Fault 1 and the Afiq Fault (Fig. 4.17c and 4.19). The intersection becomes more angular with depth as a consequence of the relation of E1 to Fault 1 in the shallower sections and Fault 1 to the Afiq Fault at depth.

Also noteworthy from the 3D image (Fig. 4.19) is the relationship between the Afiq Fault and Faults 1 – 3. Their planform relationship is strikingly reminiscent of horsetail structures (e.g. Granier, 1985; Alessio and Martel, 2004) (see Section 4.8.2).

4.6.1 Branch line topology

Mapping of constituent faults of the intersections has made it possible to visualise the geometry of their branch lines (Fig. 4.20). The branch lines of Faults 2 and 3 with the Afiq Fault have simpler topologies than that of Fault 1 with the Afiq Fault. As the Afiq North Fault plane does not reach the surface these branch lines exist from an approximate depth of 1500ms TWT to the Messinian interval. Due to the vertical nature of the Afiq strike-slip planes, all branch lines display the same dip variations down-section as those described from the normal fault planes. Therefore, the branch lines of Faults 2 and 3 display near-constant dips of 57° and 50° respectively, but vary where localised changes are recognised e.g. shallowing described from within a slump unit.

The relative complexity of the Fault 1 branch line is related to its relationship with E1. In the upper c.350ms TWT there is a branch line between Fault 1 and E1, and between E1 and the Afiq West (Fig. 4.20). Below this a branch line exists directly between Fault 1 and the Afiq West. The branch line that is recorded on the Afiq Fault Plane (Fig. 4.20) therefore has a shallow dip and curved angle reflecting the en-echelon helicoidal geometry in the upper section, and steepens downward where it exists directly between Fault 1 and the Afiq Fault. The branch line between E1 and Fault 1 is also curved slightly with concave-up geometry. The evolution of the branch lines will be discussed in the context of the evolution of the constituent intersecting faults in Section 4.8.3.

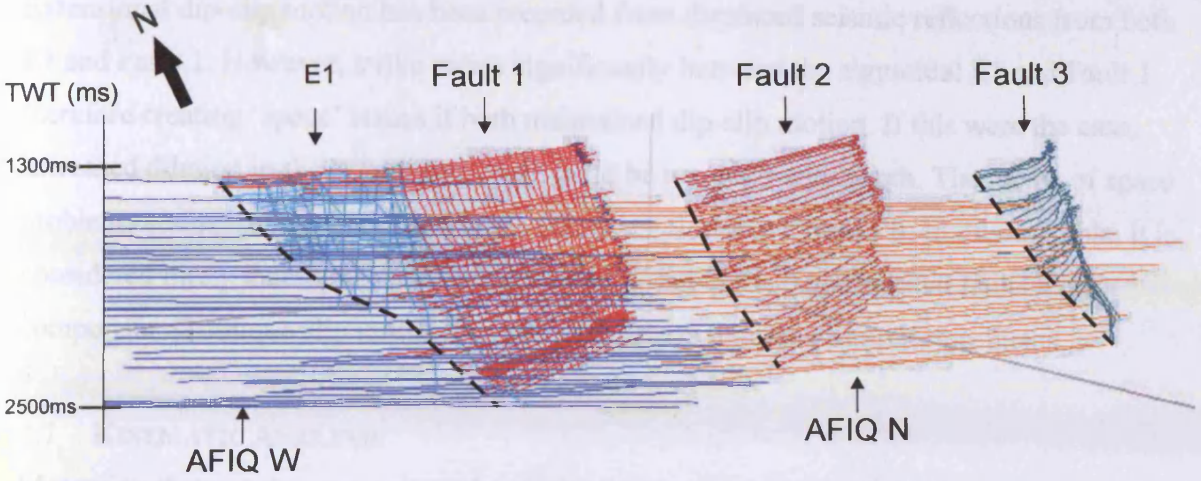

Figure 4.20. Mapped fault planes viewed in three-dimensions illustrating branch line topologies of intersections between Faults 1 - 3 and the Afiq Fault. Faults 3 and 2 have simple branch lines that have the same dip and dip direction as the Fault planes 1 - 3. The Fault 1 intersection is more complex. The intersection forms between E1 and the Afiq Fault in the shallow section and between Fault 1 and the Afiq Fault in the deeper section. Consequently, a branch line also forms between E1 and Fault 1. Branch lines are dashed lines.

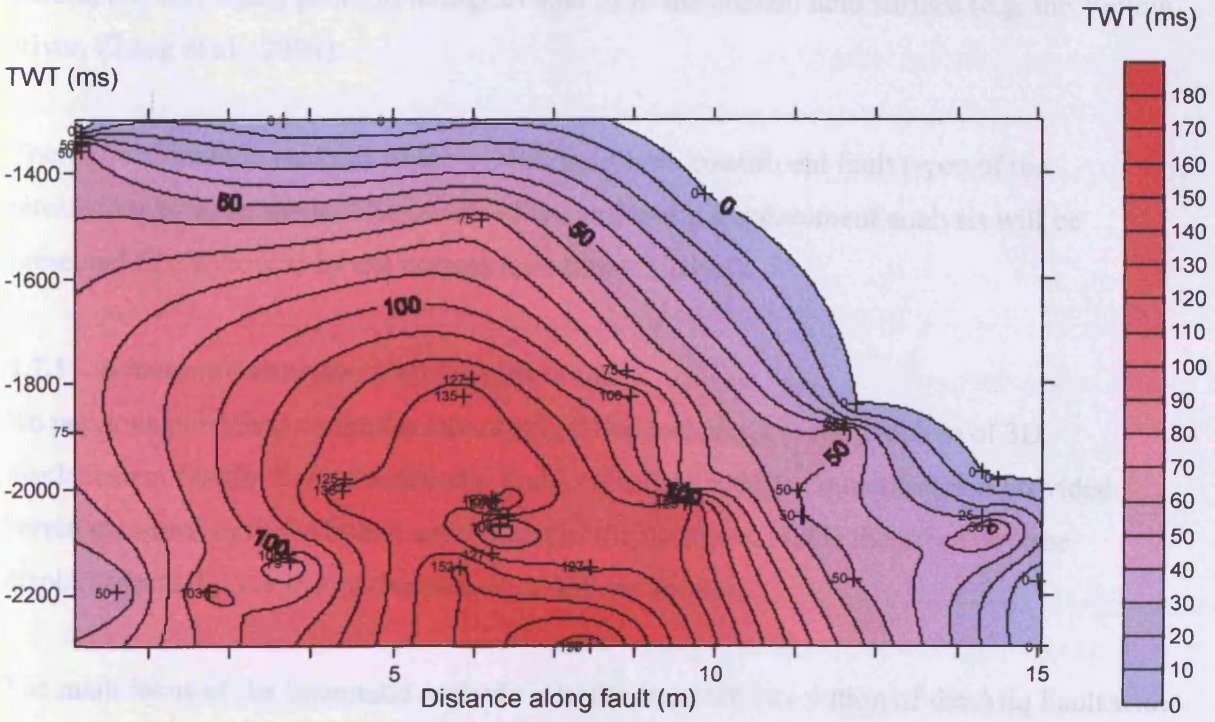

Figure 4.21. Strike-slip displacement distribution on the El-Arish fault plane represented on a vertical fault plane projection. Displacment contours at 10ms intervals. Data points are plotted as cross-line location of the northern piercement point against depth, and the plot is viewed looking NE onto the El-Arish Fault plane.

Extensional dip-slip motion has been recorded from displaced seismic reflections from both E1 and Fault 1. However, strike varies significantly between the sigmoidal E1 and Fault 1 therefore creating 'space' issues if both maintained dip-slip motion. If this were the case, increased dilation in the branch line area would be recorded with depth. The theme of space problems and accommodation structures will be explored in Chapter 6. In this example, it is considered likely that the en-echelon faults and possibly the larger normal faults have a component of oblique slip motion and this will help overcome any space problems.

4.7 KINEMATIC ANALYSIS

Measuring throw values as a proxy for displacement and mapping their distribution on a normal fault plane has been found to be a useful tool for interpreting the evolution of the fault within this work (Chapters 2 and 3). The methodology and assumptions to this technique are given in Chapter 1. An abundance of piercement marker points identified on horizontal coherence slices or mapped horizons have also permitted this technique to be developed for quantification of strike-slip displacement. This technique has been applied to strike-slip faults before, but only using geomorphological data from the present land surface (e.g. the Yellow River, Zhang et al., 2004).

Therefore kinematic analysis of the evolution of both constituent fault types of the intersections can be made. The results of the strike-slip displacement analysis will be presented first followed by the normal fault throw analysis.

4.7.1 Kinematic analysis of strike-slip faults

No previous published examples have applied this technique to the problem of 3D displacement distribution of strike-slip faults. The displacement quantification provided herein measures only the lateral component of displacement and is therefore not true displacement (if there is any component of oblique motion).

The main focus of the kinematic analysis is to document the evolution of the Afiq Fault with particular emphasis on its intersections with Faults 1 – 3. As was previously found, the El-Arish Fault provides an ideal analogue for the Afiq Fault as it is better imaged and at an earlier stage of evolution. A high level of confidence is given to El-Arish cross-fault marker correlation due to small displacement values in this system. Therefore, interpretation of the

more complicated Afiq Fault cross-fault correlation benefits from comparison with the El-Arish displacement distribution results, which will be provided first.

4.7.1.1 El-Arish Fault Displacement

Palaeo-channel markers that cross-cut the El-Arish Fault have been offset with sinistral motion (Fig. 4.12). Lateral offset values are contoured for displacement (Fig. 4.21). The contours indicate a rectangular to elliptical fault tip geometry which is constrained to the west by the edge of the dataset and at its base by the Messinian evaporite Unit B.

The displacement distribution decreases from a maximum value of approximately 150m in the centre of the plot within the lower stratigraphic levels of Unit C (Fig. 4.21). Displacement decreases toward the upper tip and eastern lateral tip. Due to a paucity of available offset markers, the western lateral tip is poorly constrained over the majority of Unit C. However, at the deeper stratigraphic levels, displacement values also decrease toward this tip. With particular focus on the eastern area of the distribution plot, the fault shape can be described as a 'three-quarter' ellipse. Displacement is not truly radial in that it does not decrease downward of the maximum value location but fits a radial description in that displacement variation decreases toward the other tips. There is a striking comparison between this 3D displacement distribution plots and those from normal faults. The displacement gradient from coherence slice 2020ms TWT is calculated at 0.02 (see Section 4.8.2).

Zero values from the upper tip indicate that dip-slip displacement is the dominant motion in the upper fringes and there is negligible or no resolvable strike-slip displacement from within the upper fringe zone.

4.7.1.2 Afiq Fault Displacement

Sinistral offset of palaeo-channel markers by the Afiq Fault is also documented. Due to regional structural dip and the component of dip-slip displacement on the Afiq Fault, it is preferable to conduct this analysis on mapped stratigraphic horizons rather than coherence volume slices. One such horizon is displayed as an amplitude map and used to illustrate displacement variation in the Afiq Fault system.

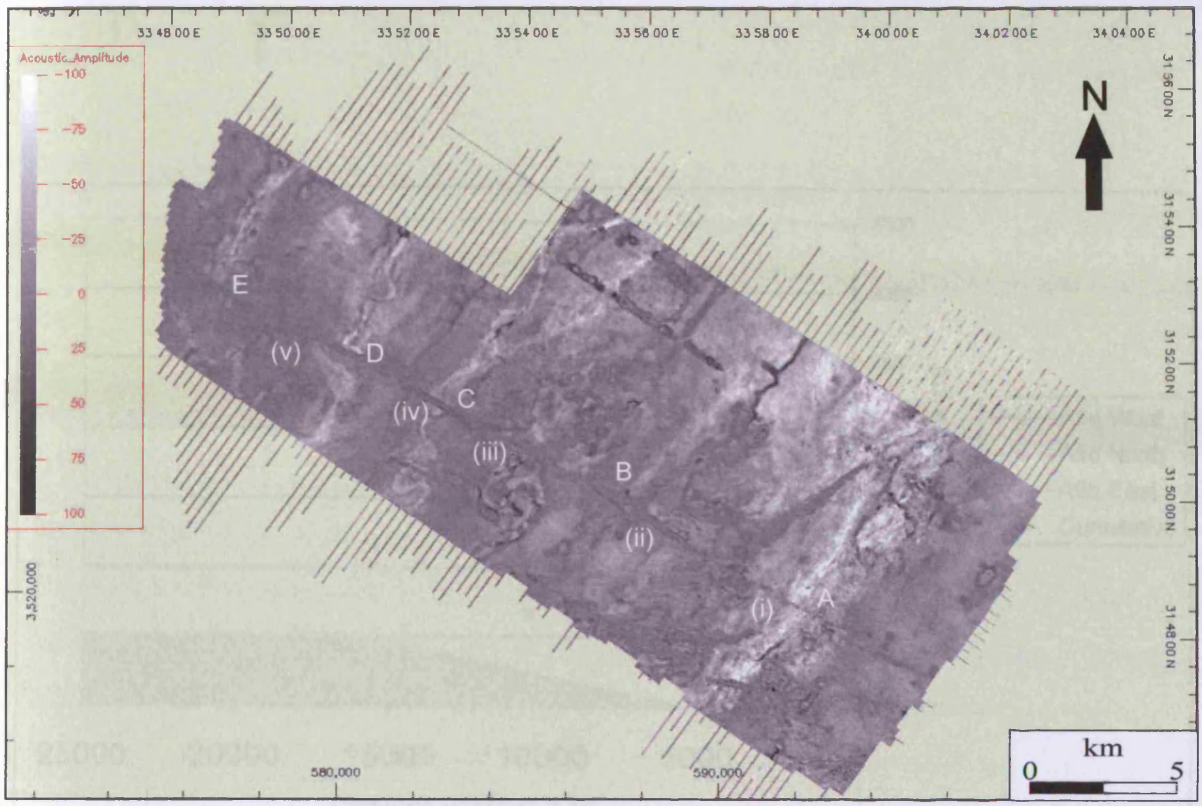

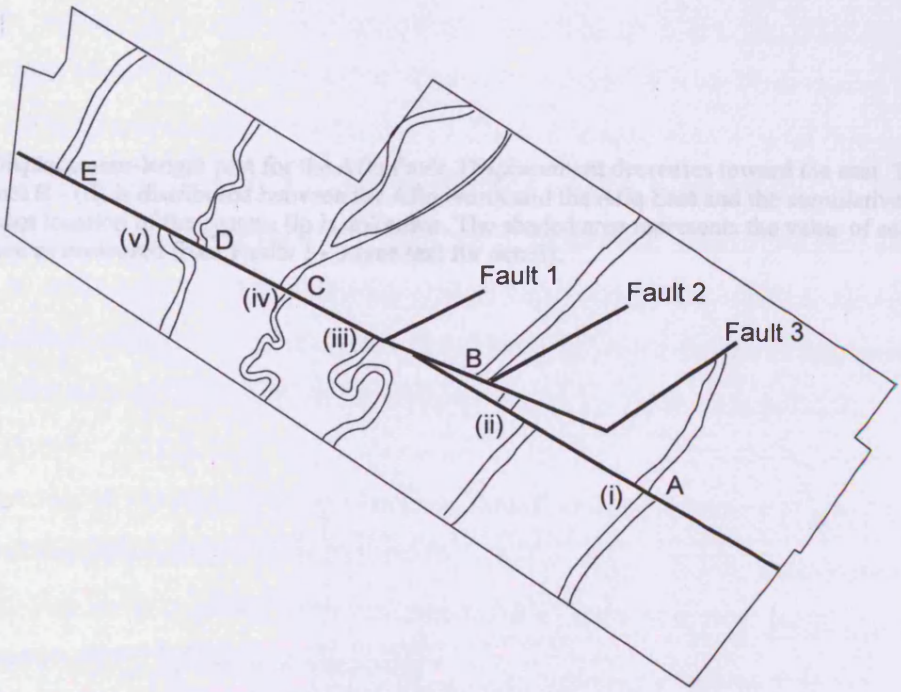

Figure. 4.22. Amplitude extraction of horizon map and line diagram showing channels offset by the Afiq Fault and correlation of the channels. Feature A correlated with Feature (i), offset = 460m; Feature B correlated with Feature (ii), offset = 1600m; Feature C correlated with Feature (iii), offset = 2700m; Feature D correlated with Feature (iv), offset = 2650m; Feature E correlated with Feature (v), offset = 2900m. Feature (v) shows a 90° change in trend from NE-SW to NW-SE approaching the Afiq Fault which supports the interpretation of correlation with E rather than D. Displacement on Feature B is distributed between the Afiq North and Afiq East.

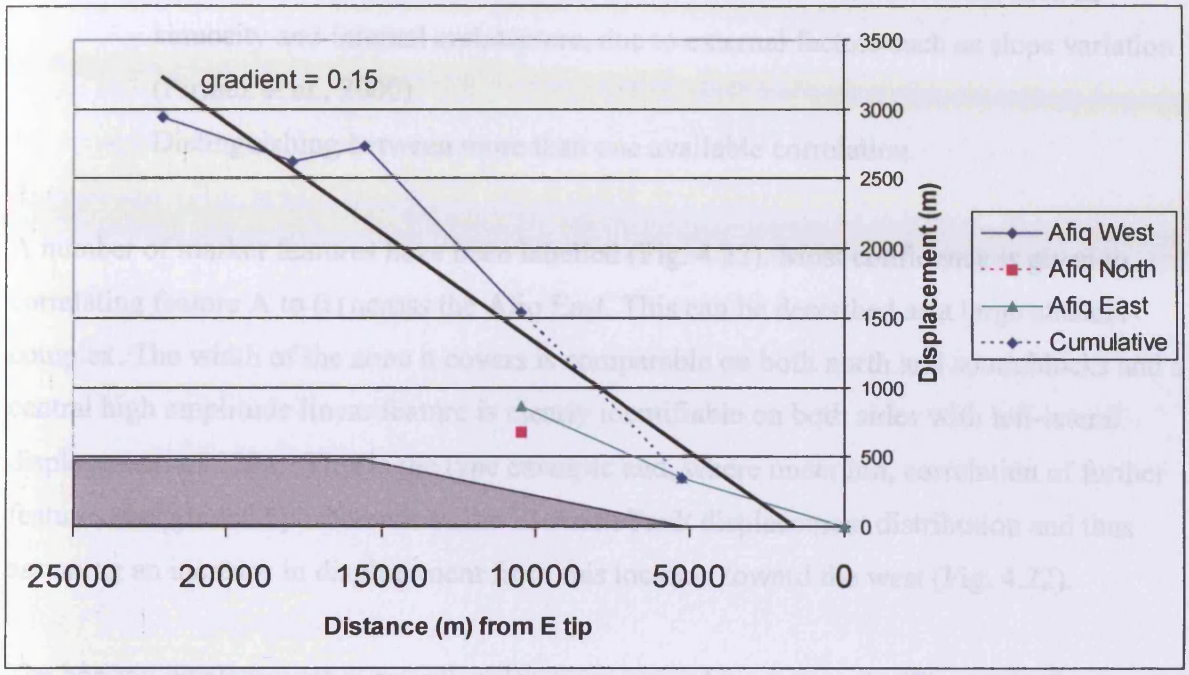

Figure 4.23. Displacement-length plot for the Afiq Fault. Displacement decreases toward the east. The total offset of channel B - (ii) is distributed between the Afiq North and the Afiq East and the cumulative point is shown. The exact location of the eastern tip is unknown. The shaded area represents the value of seismically resolvable heave as measured from Faults 1 - 3 (see text for detail).

Uncertainties in correlation of the channels are:

- Determination of true structural offset, rather than deflection along the strike-slip fault zone.
- Potential variations in channel characteristics across the fault zone, such as sinuosity and internal architecture, due to external factors such as slope variation (Pirmez et al., 2000).
- Distinguishing between more than one available correlation.

A number of marker features have been labelled (Fig. 4.22). Most confidence is given to correlating feature A to (i) across the Afiq East. This can be described as a large channel complex. The width of the zone it covers is comparable on both north and south blocks and a central high amplitude linear feature is clearly identifiable on both sides with left-lateral displacement of 350m. This is the type example and, where uncertain, correlation of further features was guided by reference to the El-Arish Fault displacement distribution and thus assuming an increase in displacement from this location toward the west (Fig. 4.22).

The horizon displacement distribution decreases toward an eastern tip (Fig. 4.23). Feature B is a 420m wide linear, high amplitude feature that is offset by both the Afiq East and Afiq North (Fig. 4.22). This observation indicates that displacement on the Afiq West is distributed between the Afiq North and East. Projection of the Afiq displacement trend through the B (ii) correlation cumulative displacement aligns with the Afiq East A (i) correlation displacement value, thus supporting a distribution of Afiq West displacement toward the east. However, a component of strike-slip displacement may also remain on the Afiq North in the tip region and this is not quantified in the cumulative plot. The Afiq North displacement is decreasing in its tip region through accommodation of strain by Faults 1 – 3 (Section 4.7.2.2).

The exact location of the eastern tip is uncertain therefore the displacement gradient is averaged over the data points (Fig. 4.23) and has a value of c.0.15. The decrease in value toward the eastern tip is expected to be representative of the whole fault plane as was found from the El-Arish 3D displacement variation.

The gradient value recorded for the Afiq Fault is an order of magnitude greater than that recorded from the El-Arish Fault. However, both these values lie within the reported range of gradients from strike-slip field studies e.g. 0.02 – 0.13 (Pachell et al., 2002); 0.084 – 0.2

(d'Alessio and Martel, 2004); 0.019 – 0.05 (Peacock and Sanderson, 1995). And these gradients lie within the ranges of other published slip data of 0.002 to 0.25 as compiled by Shipton and Cowie (2001) from predominantly normal faults.

It is beyond the scope of this chapter to further constrain displacement measurements from the Afiq Fault system. However, the observations of eastward decrease in displacement value can be integrated with observations from the fault zone architecture to interpret eastward propagation of the Afiq Fault system (Section 4.8.2).

4.7.2 Kinematic analysis of Faults 1 - 3

Kinematic analysis of Faults 1 – 3 includes study of the throw distribution, the heave relationship to strike-slip strain and investigation into the timing of growth of these faults. The results of this analysis permit interpretation of the evolution of the faults and consequently the intersections that they form with the Afiq Fault.

4.7.2.1 Throw Analysis

The throw distributions are firstly described from vertical fault projections (Fig. 4.24), which clearly show the differences in evolutionary style of the fault planes. Secondly, the throw distribution from the three mapped horizons is described from T-x plots (Figs. 4.25) and aids interpretation of the relationships between E1-3 and Faults 1-3.

Faults 1 and 3 clearly have a similar throw distribution with maximum throw recorded from a location that is close to or at the intersection with the Afiq Fault zone (Fig. 4.24). The throw contours decrease from the intersection location to their lateral NE tips with a largely 'fingerlike' pattern, maintaining the largest throw values from the same TWT depth across the plot. Fault 2 has a markedly different throw distribution with a central maximum throw (Tmax.) and a more radial (but diagonally skewed) contour pattern. Table 4.2 displays maximum throw values gained from the throw study and tip gradient values.

	Tmax.	Lateral tip West	Lateral Tip East	Upper Tip	Lower Tip (Top Messinian)	Lower Tip (Base Messinian)
Fault 1	171ms	-	0.06	0.23	0.06	0.14
Fault 2	73ms	0.028	0.026	0.06	0.04	-
Fault 3	189ms	-	0.06	0.26	0.06	0.16

Table 4.2 Maximum throw and tip gradients for Faults 1 to 3.

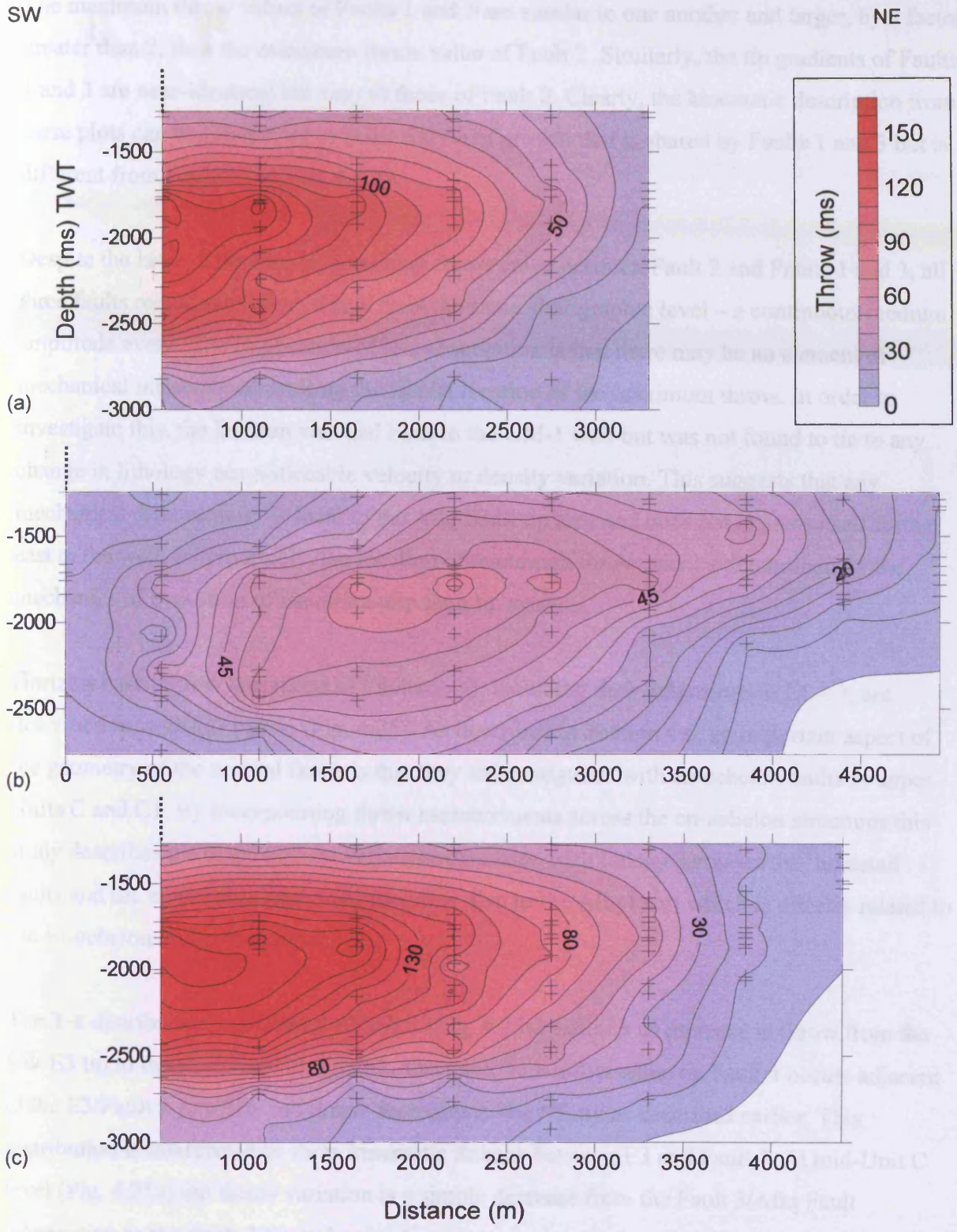

Figure 4.24. Throw distribution plots on vertical fault projections of (a) Fault 1, (b) Fault 2 and (c) Fault 3. Faults 1 and 3 have a similar distribution with maximum throw adjacent to intersection, decreasing toward their NE lateral tips. Fault 2 has a central maximum throw location and decreases radialy. Throw locations depicted by a cross. All three plots displayed at the same colour scale and contoured for throw on a 10ms interval. Dashed lines are measurement location closest to intersection location. The seabed horizon is the upper data limit.

The maximum throw values of Faults 1 and 3 are similar to one another and larger, by a factor greater than 2, than the maximum throw value of Fault 2. Similarly, the tip gradients of Faults 1 and 3 are near-identical but vary to those of Fault 2. Clearly, the kinematic description from these plots can be interpreted to show a style of growth that is shared by Faults 1 and 3 but is different from Fault 2 (Section 4.8.2).

Despite the large difference in maximum throw value between Fault 2 and Faults 1 and 3, all three faults record maximum throw from the same stratigraphic level – a continuous medium amplitude event. The implication of this observation is that there may be an element of mechanical influence controlling the spatial location of the maximum throw. In order to investigate this, the horizon was tied back to the GM-1 well but was not found to tie to any change in lithology nor noticeable velocity or density variation. This suggests that any mechanical discontinuity is local to the Afiq Fault tip area and does not express itself further east at the well. Alternatively, the location of maximum throw may be determined by the mechanics of evolution of the strike-slip fault tip system.

Horizon-based throw variations of Faults 1 – 3, including their extensions to E1 – 3, are described from the T-x plots (Fig. 4.25). As described in Section 4.6, an important aspect of the geometry of the normal faults is that they are contiguous with en-echelon faults in upper Units C and C1. By incorporating throw measurements across the en-echelon structures this study describes the displacement variation associated with linkage between the 'horsetail' faults and the en-echelon faults and therefore also to the Afiq Fault which is directly related to the en-echelon faults (Section 4.4).

The T-x distribution at seabed for Fault 3 (Fig. 4.25a) exhibits an increase in throw from the SW E3 tip to the junction with Fault 3. The maximum throw value on Fault 3 occurs adjacent to the E3/Fault 3 junction and throw decreases to the NE tip as described earlier. This distribution is interpreted to show kinematic linkage between E3 and Fault 3. At mid-Unit C level (Fig. 4.25a) the throw variation is a simple decrease from the Fault 3/Afiq Fault intersection to the Fault 3 tip and a similar pattern is also displayed at Top Messinian level (Fig. 4.25a). Both these plots show a first measurement that is slightly lower than the Tmax. value at the intersection location. The Tmax. value is the second measurement out from the intersection and this may be related to throw sharing at intersection or measurement error in

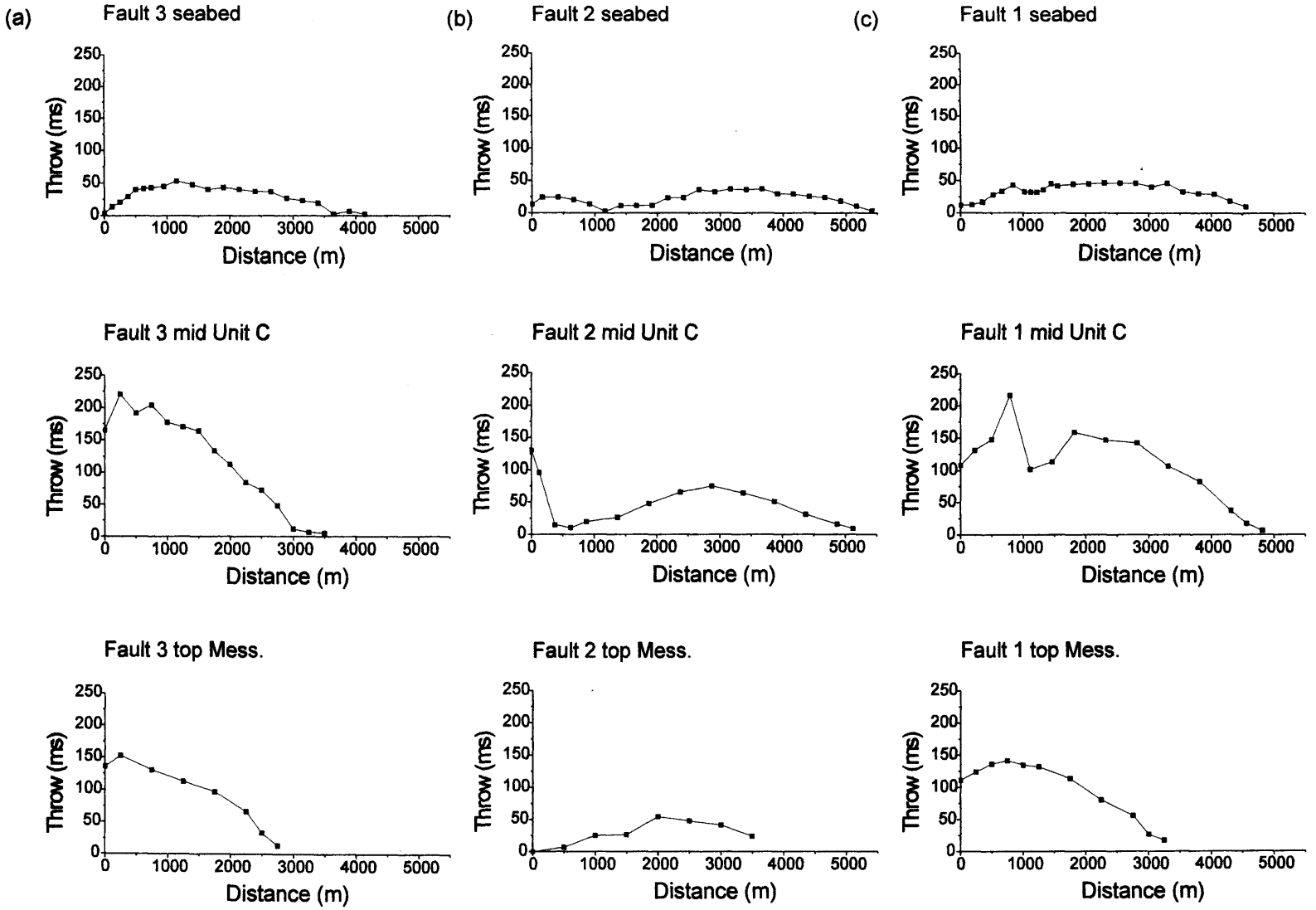

Figure 4.25. T-x plots for (a) Fault 3, (b) Fault 2 and (c) Fault 1.

this complex zone. Alternatively the location of maximum strain may exist at some small distance from the intersection.

The T-x distribution of Fault 2 at the seabed (Fig. 4.25b) exhibits a throw minima at the junction between Fault 2 and E2, thereby dividing the plot into throw from two separate fault segments. Both the E2 and the Fault 2 segments display a central throw maxima with throw values decreasing toward intersections and tips. The Fault 2 central throw maxima is also displayed by its throw distribution at mid-Unit C (Fig. 4.25b) and Top Messinian (Fig. 4.25b) horizons (c.f. Fig. 4.24). E2 and Fault 2 are not interpreted to be kinematically linked.

The T-x distribution for Fault 1 at the seabed exhibits a small throw decrease at the junction between E1 and Fault 1 (Fig. 4.25c). Despite this, the overall throw distribution from the E1/Afiq Fault intersection to the Fault 1 tip is broadly symmetrical with a near-central maximum throw value and E1 and Fault 1 are interpreted to be kinematically hard linked.

The throw minimum at the junction between E1 and Fault 1 is more pronounced at mid Unit C level (Fig. 4.25c). However, a measurement error is highlighted on the T-x plot where more than one fault has been sampled. E1 is sub-parallel to the main Afiq West Fault plane at this horizon (Section 4.6) therefore it is difficult to distinguish between these structures on seismic section due to resolution limitations. The throw maximum of Fault 1 is located approximately 400m from the intersection location.

The throw distribution for Fault 1 at Top Messinian level (Fig. 4.25c) again shows a gentle increase in throw from intersection to the Tmax. location followed by a decrease to its tip. Therefore, on all three horizon levels the Fault 1 throw maximum is located a small distance from the intersection location rather than directly adjacent to the intersection location.

4.7.2.2 Heave relation to strain

Heave measurements have been taken from the maximum throw horizon (near-mid Unit C level) at the approximate location of maximum throw on each fault, thus aiming to yield maximum heave measurements (Table 4.3).

Apparent heave values are greater in the orientation parallel to the strike-slip fault than in the direction normal to the strike of Faults 1 - 3. This perhaps suggests an element of oblique slip

motion on these faults. The cumulative maximum heave value of 475m gives a minimum estimate to the strike-slip displacement of the Afiq Fault, because these structures are interpreted to be integral to distribution of strain in the strike-slip tip region (Section 4.8.2).

	Fault 1	**Fault 2**	**Fault 3**	**TOTAL**
Heave parallel to Afiq Fault	200m	75m	200m	**475m**
Heave normal to Faults 1-3	168m	56m	152m	**376m**

Table 4.3. Maximum heave measurements taken oblique to Faults 1 – 3 and normal to Faults 1 – 3.

The only strike-slip measurement gained from the Afiq North has a value of 680m and is comparable to the maximum value of heave, given that many other normal faults with very small throw values also deform Unit C in the Afiq Fault tip region and will therefore also influence extension estimates.

4.7.2.3 Growth history of the Faults 1 - 3

Stratal thickness variations have been recognised across Faults 1 – 3 (Fig. 4.18) in the mid to upper section of Unit C. Package A is bounded at the base by a trough reflection and at the top by a peak and consists of a diagnostic wide, low amplitude peak at the base and a thin trough above this. This package does not display any quantifiable thickness variations across Faults 1 – 3. Package B is represented by a single trough in the footwall of Fault 1 but can be identified as a wedge encompassing an extra layer in the hangingwall of Fault 1 and is therefore interpreted to have been deposited while Fault 1 was active. This extra layer pinches out toward the east and the area of the footwall directly adjacent to Fault 2. No thickening is recorded of package B across Fault 2. However, package B thickens toward the area adjacent to the Fault 3 plane in its footwall, incorporating an extra layer. This same layer also exists in the hangingwall of Fault 3 and thickness variation is not immediately apparent. It is possible to discern, however, a widening of the peak that represents the upper boundary of package B/lower boundary of package C, and therefore a thickness increase. Packages C and D thicken significantly across Fault 1 and also across Fault 3 but do not vary across Fault 2. These thickness variations can be interpreted to represent growth periods on the faults whereby stratal wedging in the hangingwall represents time stages where accommodation space was created by fault growth.

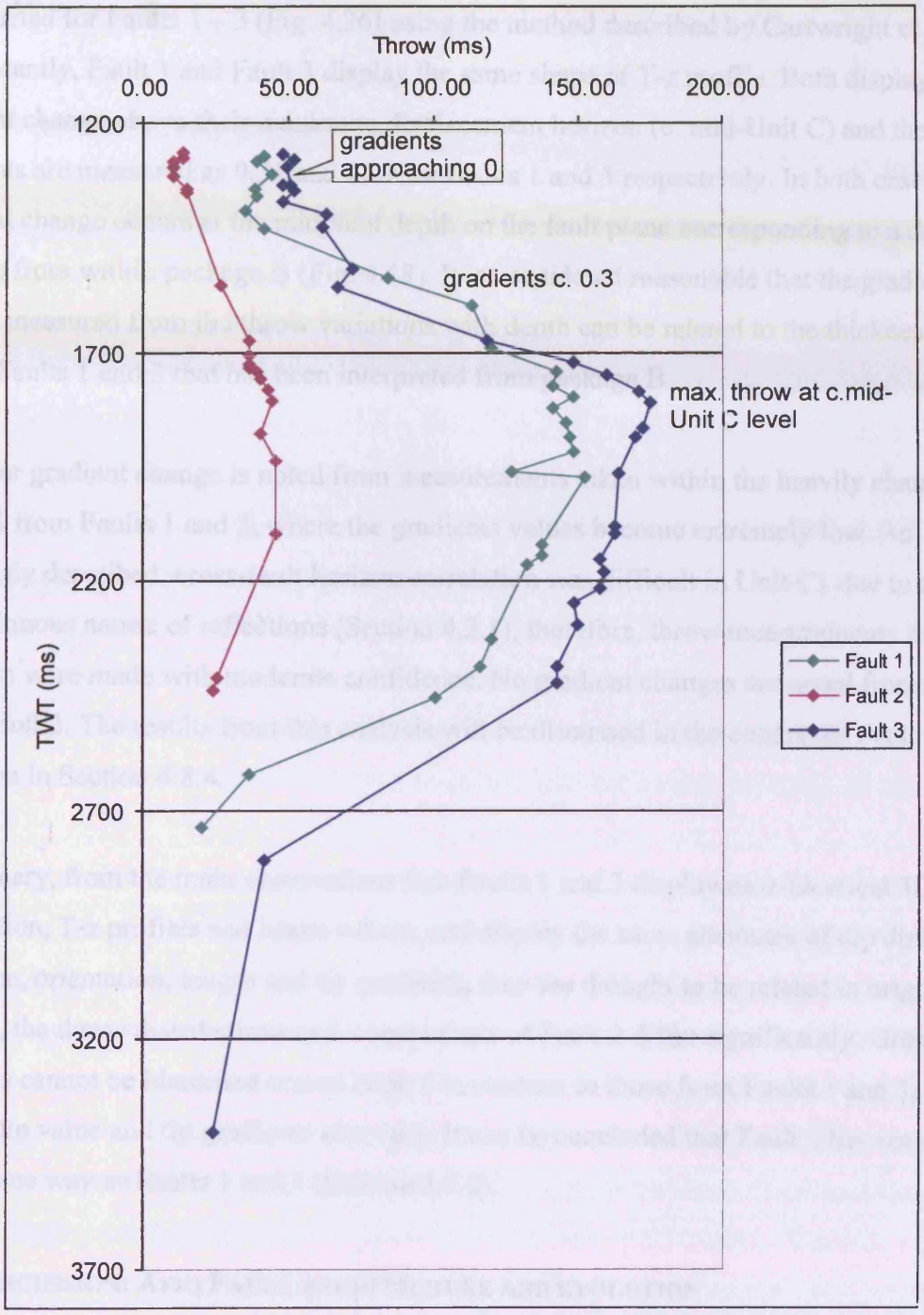

Figure 4.26. T-z plots for Faults 1 - 3.

To further investigate potential growth, high resolution throw variation with depth plots were constructed for Faults 1 – 3 (Fig. 4.26) using the method described by Cartwright et al., 1998. Significantly, Fault 1 and Fault 3 display the same shape of T-z profile. Both display a gradient change above their maximum displacement horizon (c. mid-Unit C) and these gradients are measured as 0.31 and 0.29 for Faults 1 and 3 respectively. In both cases, the gradient change occurs at the midpoint depth on the fault plane corresponding to a displaced horizon from within package B (Fig. 4.18). It is considered reasonable that the gradient change measured from the throw variations with depth can be related to the thickness increase across Faults 1 and 3 that has been interpreted from package B.

A further gradient change is noted from measurements taken within the heavily channelised Unit C1 from Faults 1 and 3, where the gradients values become extremely low. As previously described, cross-fault horizon correlation was difficult in Unit C1 due to the discontinuous nature of reflections (Section 4.2.1), therefore, throw measurements from the upper tip were made with moderate confidence. No gradient changes are noted from the upper tip of Fault 2. The results from this analysis will be discussed in the context of Fault 1 – 3 evolution in Section 4.8.4.

In summary, from the main observations that Faults 1 and 3 display near-identical 3D throw distribution, T-z profiles and heave values, and display the same attributes of dip direction and value, orientation, length and tip gradients, they are thought to be related in origin. In contrast, the throw distributions and heave values of Fault 2 differ significantly. Growth packages cannot be identified across Fault 2 in contrast to those from Faults 1 and 3, and fault length, dip value and tip gradients also vary. It can be concluded that Fault 2 has not evolved in the same way as Faults 1 and 3 (Section 4.8.4).

4.8 DISCUSSION: AFIQ FAULT ARCHITECTURE AND EVOLUTION

Through the detailed 3D description of Afiq Fault architecture and kinematic analysis provided above, the structural evolution of the Afiq Fault, and in particular its intersections with the horsetail faults, can be proposed. Observations of upper tip minor faults help discussion of a model for vertical propagation of strike-slip faults (Section 4.8.1). Lateral fault propagation (Section 4.8.2) focuses on evolution of the horsetail faults at the eastern tip of the Afiq Fault. Some consideration is given to the evolution of the Afiq Fault branch lines

(Section 4.8.3) which are complicated by relation of the horsetail faults to the en-echelon faults that also form integral minor structures to the evolution of the Afiq Fault.

4.8.1 Vertical propagation

The upper tips of the strike-slip faults described in this chapter are characterised by fringes of right-stepping en-echelon faults. Where detailed images were gained, a set of en-echelon faults, forming at a low angle to the underlying strike-slip principal plane, encompassed sets of shorter, en-echelon faults that formed a high angle with the strike-slip plane. Both high-angled and low-angled en-echelon fault sets consisted of a north-dipping fault that was paired with a south-dipping fault.

Analogous en-echelon tensile fractures recorded from the upper part of strike-slip faults are found from sandbox modelling experiments (Naylor et al., 1986; Tchalenko, 1970) and recognised from field studies e.g. Dasht-e-Bayaz Faults (Tchalenko and Ambraseys, 1970); the Cottage Grove Fault (e.g. Nelson and Krauss, 1981); faults at Gozo, Maltese Islands (e.g. Kim et al. 2000); the Kunlun Fault, northern Tibet (Fu et al. 2004); and the Pernicana fault system (Acocella et al., 2005). They have not previously been recorded from 3D seismic data.

Willemse et al. (1997) propose that extension faults that form parallel to local maximum compressive stress (~45deg to fault) represent the initial fracturing of rock prior to a through-going master fault. Scholtz (1989) explains that a mode III propagating tip forms from coalescence of mode I crack arrays. However, the en-echelon faults described here have shear motion.

Analogous faults with comparable three-dimensional geometries have been modelled in sandbox analogue experiments by Naylor (1986) and Ueta et al. (2000). These have helicoidal geometries and are termed Riedel shears. The Riedel Shears are interpreted to be the first representation of evolution of a strike-slip fault zone. Further predictable shear structures develop as strike-slip displacement accrues along the fault zone and anastomose before evolving to a through-going fault zone (e.g. Fig. 4.17). Therefore, Riedel Shears are generally found associated with the propagating tip.

The analogy with previous studies suggests that the upper fringe structures defined from this dataset represent the minor structures formed during upward propagation ahead of the

through-going fault zone and that the Afiq (and El-Arish) faults formed in a comparable way to the strike-slip structures from different tectonic settings. However, the main difference between reported Riedel shears from field studies (Tchalenko and Ambraseys, 1970), modelled Riedel shears (e.g. Naylor, 1987), and those reported from this study, is that two plan view sets of faults are recorded from the Afiq (and El-Arish) Faults rather than one set. This is a detail that is not recorded elsewhere but is recognised here as being integral to the development of the strike-slip systems. One possible interpretation is that the two sets, (e.g. those defining the upper tip of the El-Arish system), could have originated as a single set of Riedel Shears that 'split' and were offset by strike-slip motion. However, this is an unlikely interpretation as no resolvable strike-slip offset of marker features has been documented from within the upper fringe zone. In addition, the through-going fault zone exists at depth beneath these features and the El-Arish structure is in the early stages of development, therefore significant offset has not taken place. Furthermore, Kim et al. (2000) described the passive rotation of markers during further shear strain to create a sigmoidal plan view trace rather than dividing the en-echelon fault sets (see below). Therefore, it is interpreted that each upper fringe tier consists of a northern and a southern set of en-echelon faults in this system. From computerised X-ray tomography analysis of their sandbox experiments, Ueta et al. (2000) suggest that the Riedel shears propagate through the sand to join those on the other side and it may be possible that the two sets link at a later stage in evolution in this way.

A model of upward propagation with relation to the upper fringe en-echelon sets is proposed. The upward component of propagation was facilitated by development of an upper fringe consisting of two sets of en-echelon faults with fault strikes at a high angle to the main strike-slip fault trace below. This stage of fault development can be described as upward bifurcation or splaying (Fig. 4.13). Continued strike-slip motion causes rotation of the upper fringe 1 to a lower angle that is sub-parallel to the fault. Propagation through splaying of a second tier of high-angled faults then occurs (upper fringe 2). Eventually, the lower fringe, fringe 1, will be incorporated into the through-going fault zone.

From the variation in fault strike with increasing depth from high angles to the main strike-slip fault to sub-parallel at depth, the en-echelon faults deform with sinistral shear sense. Seismic profiles display a component of dip-slip motion on these planes and they are therefore interpreted to slip with oblique motion. It is envisaged that they are dominantly dip-slip in the shallow and dominantly strike-slip at depth as they are rooted to the strike-slip

fault. This is a form of kinematic partitioning whereby slip sense varies with vertical position on the fault.

4.8.2 Lateral propagation

One of the major conclusions of this study is that the Afiq fault propagated laterally toward the east. The main evidence for this is derived primarily from the novel approach of 3D strike-slip displacement mapping. It is also supported by observations of the elliptical tip shape where the eastern tip becomes limited in extent. Upper tip en-echelon faults are more sigmoidal on the Afiq West and become more planar toward the eastern tip of the Afiq North Fault and on the Afiq East Fault and this sigmoidal trace indicates passive rotation by a deformation that remained relatively homogenous (Tchalenko and Ambraseys. 1970). Further evidence that the Afiq West Fault is the most fully developed of the three sections is provided by the observation of a continuous, throughgoing fault trace at the seabed surface, but only upper fringe en-echelon faults in the Afiq East and North Faults.

There is a wealth of literature describing horsetail structures (also termed splay faults, pinnate joints, splay cracks, tail faults, tip cracks and wing cracks) from the termini of strike-slip faults. They are generally believed to form in the dilational quadrants to relieve stress concentrations caused by high displacement gradients at fault tips (e.g. Kim et al. 2000; Granier, 1985; Flodin and Aydin, 2004; Engelder, 1989; Martel et al., 1988; Cruikshank and Aydin, 1995; Kim et al., 2001 and Willemse and Pollard, 1998). Near mode II tips, the predominant sliding mode causes fracturing to initiate obliquely to the fault plane forming horsetail splay fractures or faults. Faults 1 – 3 occur in the dilational quadrant of the Afiq Fault tip, forming angles of c.40-50° (typical range 20-50°, Granier, 1985) and this fact, together with the observations that they are clearly kinematically associated with the Afiq Fault (see below) has permitted their interpretation as horsetail faults.

From analysis of the throw distribution plots of Faults 1 and 3, and in particular the observation that the maximum throw value is recorded from a location adjacent to the intersection and decreases in a finger-like pattern toward the NE tip, Faults 1 and 3 are interpreted to splay from the Afiq Fault. They can therefore be classed as branching intersections and interpreted to have nucleated at or near the intersection location and grown laterally to the NE (and upward and downward).

The kinematics of splaying or branching is poorly documented. The interpretation of evolution of Faults 1 and 3 described here, therefore, is perhaps the first time that such a kinematic connection has been established, at least at this scale. Maximum throw values from Faults 1 and 3 are not recorded directly at the intersection location, but rather some distance from it. This may suggest that initiation of the faults did not occur exactly at the Afiq fault plane but rather at some distance from it because the concentration of stress in this area was greater. Alternatively, the maximum throw location may have migrated in relation to linkage with the en-echelon faults E1 and E3. In either case, the evidence for the development of Fault 1 and Fault 3 by a splay process from the Afiq Fault is compelling.

In contrast, the different fault attributes, throw profiles and lower throw values recorded from Fault 2 support an alternative model of fault growth. Significantly, it has a radial distribution of throw with a centralised Tmax., and does not kinematically link with E2 toward the intersection location. A throw minimum is therefore recorded from both its NE tip and its intersection at its SW tip with E2 or the Afiq Fault. From these observations, it is argued that Fault 2 did not evolve as a splay from the Afiq Fault but rather as a radially propagating fault within Unit C. The Fault 2/Afiq Fault intersection therefore formed through accidental intersection. Despite this, it appears to belong to the system as it is situated exactly midway between Faults 1 and 3 with the same strike. The smaller values of throw recorded from this fault may indicate that it formed as a later structure (see Section 4.8.4). This has implications for formation of secondary structures in any strike-slip system, and suggests that later structures may infill between existing horsetail faults thus forming 'out of sequence' faulting.

The extensional component of the bulk strain is manifested by the development of fault heaves and the total heave measurement of 475m from Faults 1 – 3 provides a minimum estimate of 'apparent stretch' (Waldron, 2005). This figure compares reasonably well with the estimated displacement from channel offsets of 680m across Afiq North. However, Figures 4.22 and 4.23) show that the strike-slip displacement decreases from 2700m to 480m over a distance of c.10km, and this decrease in strike-slip displacement is clearly not matched by the cumulative heave across three major horsetail faults. Some minor faults are visible, but are insufficient to fill the strain imbalance. Hence it is concluded that there must be considerable extension within the region of the horsetail, or contraction in the opposing quadrant in order to accommodate the lateral gradient in the strike-slip displacement.

4.8.3 Branch line evolution

Analysis of the three-dimensional geometry of the Afiq Fault system allows recognition that branch lines exist between the en-echelon faults and the Afiq Fault plane, the secondary normal faults and the Afiq Fault plane, and between the en-echelon faults and the normal faults. The above sections have established the propagation styles of the upper fringes and the extensional horsetails therefore it is possible to briefly investigate the formation of these branch lines and to see how they relate to the evolution of the splay structures.

The en-echelon faults have been interpreted to evolve through upward splaying from the Afiq Fault plane. They are envisaged to initiate at a point or with a short, horizontal branch line at the top of, or slightly above, the Afiq Fault plane and most likely at an oblique angle to it (Fig. 4.27a). The en-echelon splay progressively steepens in intersection angle as it propagates upward (Fig 4.27b). The branch line will only form between the Afiq plane and the en-echelon faults when a through-going strike-slip plane propagates upward (Fig. 4.27c-d). The branch line topology is a function of the helicoidal geometry of the en-echelon plane and it will theoretically be curved and steepen upward from its original horizontal topology as recorded from E1.

Rather than the upward-splaying nature of the en-echelon faults whose branch line initiates at the top of the Afiq Fault plane, Faults 1 and 3 are interpreted to splay laterally from the intersection location and their branch lines are consequently dipping and sub-vertical. Nucleation of these faults is interpreted to be from near the mid-Unit C horizon. Consequently development of the branch line is both upward and downward as the normal faults propagate radially (Fig. 4.27e). In the circumstance of Fault 1 the branch line develops initially between E1 and the normal fault. With the downward element of fault propagation the branch line is established between the Fault 1 and the Afiq Fault. Consequently, at depth a branch line exists between Fault 1 and the Afiq Fault that continues upward between E1 and the Afiq Fault (Fig. 4.27). A further branch line develops upward from the junction of the Fault 1/Afiq and E1/Afiq branch lines between E1 and Fault 1 (Fig. 4.27). Fault 3 also establishes a branch line with E3 as it propagates upward from its nucleation position in the same way. The Fault 2 branch line is not considered in this section because the mode of propagation of Fault 2 is accidental but investigation into branch line evolution of accidental intersections will be developed in Chapter 6.

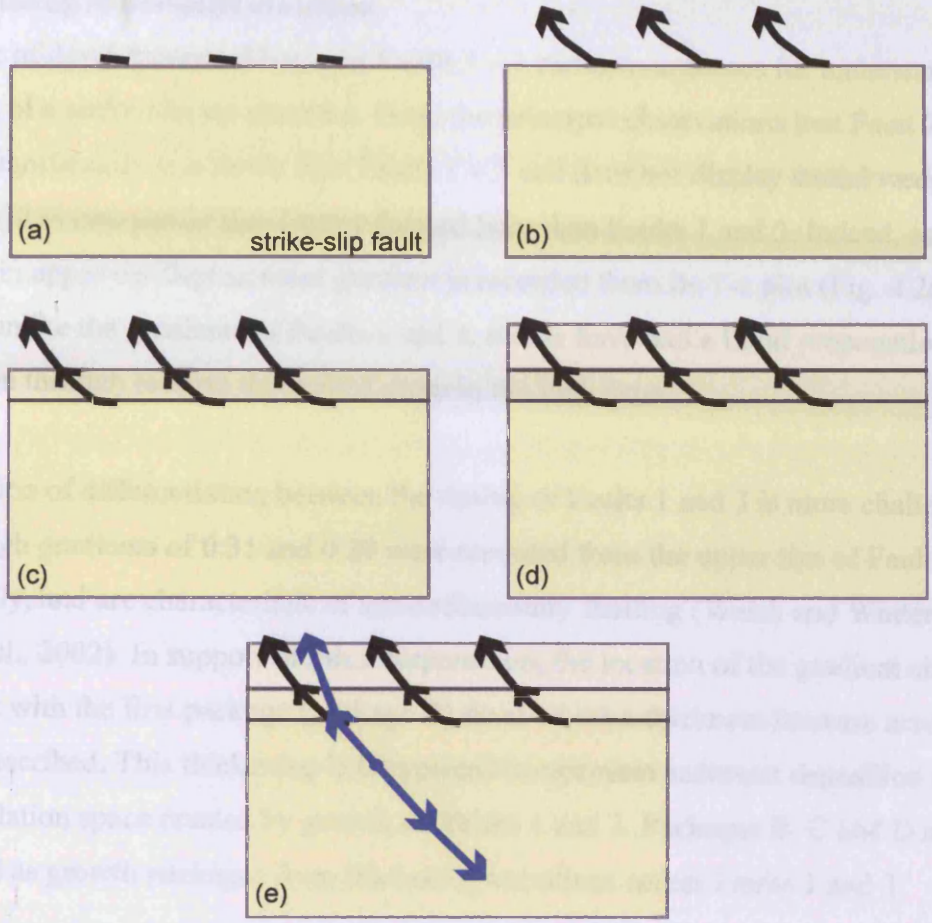

Figure 4.27. Cartoon of branch line evolution. (a) En-echelon faults (black lines) initiate above the upper tip of the strike-slip fault. (b) The en-echelon faults evolve. (c) - (d) The branch line evolves as the strike-slip fault propagates upward. (e) Example of Fault 1 (blue) which initiates (circle) at the Afiq Fault and propagates downward and upward where it links with the en-echelon fault and forms a further branch line with it.

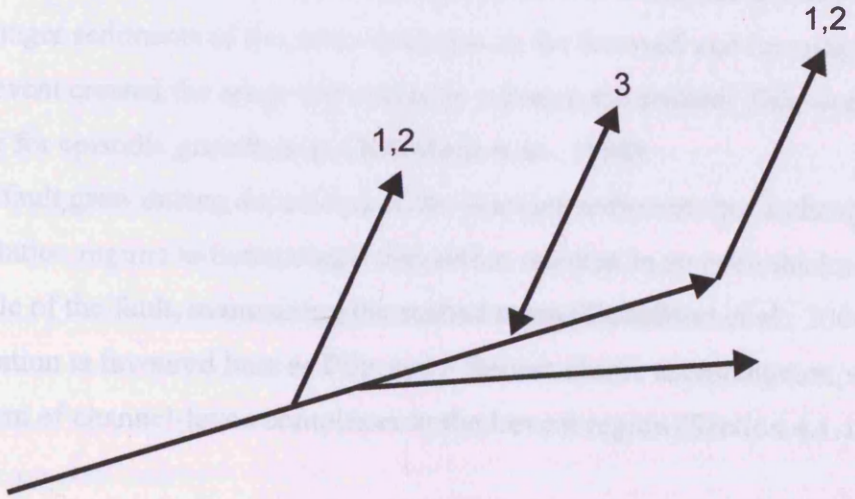

Figure 4.28. Cartoon of Afiq Fault horsetail evolution. Faults 1 and 3 evolve contemporaneously (1, 2) at the lateral tip of the Afiq Fault through branching from the main fault plane. Fault 2 evolves at a later stage(3) through radial propagation.

4.8.4 Timing of horsetail evolution

The order of development of horsetail Faults 1 – 3 has consequences for understanding the evolution of a strike-slip tip structure. From the principal observations that Fault 2 has accrued significantly less throw than Faults 1 – 3 and does not display stratal wedging related to growth, it is interpreted that Fault 2 formed later than Faults 1 and 3. Indeed, as no variation in upper tip displacement gradient is recorded from its T-z plot (Fig. 4.26, Section 4.7.2.3), unlike the gradients of Faults 1 and 3, it may have had a blind propagation upper tip and broken through to form the seabed scarp in the Holocene.

The question of differentiating between the timing of Faults 1 and 3 is more challenging. Similar high gradients of 0.31 and 0.29 were recorded from the upper tips of Faults 1 and 3 respectively, and are characteristic of syn-sedimentary faulting (Walsh and Watterson, 1989, Meyer et al., 2002). In support of this interpretation, the location of the gradient change is coincident with the first package (package B) from which a thickness increase across these faults is described. This thickening is interpreted to represent sediment deposition into accommodation space created by growth on Faults 1 and 3. Packages B, C and D are all interpreted as growth packages from thickening variations across Faults 1 and 3.

There are two possible interpretations for the extremely low gradient that is recorded from the upper tip of Faults 1 and 3:-

(1). The faults did not move after the growth periods B-D and the growth faults were buried with younger sediments of the same thickness in the footwall and hangingwall. A later, rapid growth event created the scarp that currently exists at the seabed. This would provide evidence for episodic growth (e.g. Cartwright et al., 1998).

(2). The fault grew during deposition of the younger sediments but a change in the sedimentation regime to hemipelagic deposition resulted in an even thickness of deposits on either side of the fault, maintaining the seabed scarp (Castelltort et al., 2004). The first interpretation is favoured here as Pliocene – Recent clastic sedimentation was predominantly in the form of channel-levee complexes in the Levant region (Section 4.1.1).

There is some evidence from seismic analysis of package B that growth of Fault 1 was earlier than that of Fault 3, though it is not conclusive. In addition, the seabed scarp of E1 is larger than that of E2 and it has a more sigmoidal plan view shape. This only supports the interpretation that E1 is older than E3. In contrast, Fault 3 records a larger maximum throw

value (which may infer a longer growth history) and Granier (1985) argues that horsetail evolution is initiated at the strike-slip tip and steps back toward the centre of the fault. From the above discussion, it is argued that the close relation of fault attributes, patterns of throw distribution and shapes of T-z plots supports an evolutionary history of Faults 1 and 3 that is related, and that they are therefore largely contemporaneous. There is not sufficient evidence to distinguish further between timing of evolution of Faults 1 and 3.

The evolution of the Afiq Fault can be summarised as follows (Fig. 4.28):

- Afiq Fault eastward and upward propagation with en-echelon fault fringes evolving at upper tips.
- Segmentation of the Afiq Fault to become Afiq East and Afiq North.
- Afiq North termination with near-contemporaneous Fault 1 and Fault 3 branching from the main fault plane.
- Fault 2 formation through radial propagation as a later strain-accommodating structure.

4.9 CONCLUSIONS

This case study has focused on two main themes: (1) the 3D fault architecture of a strike-slip fault and (2) the evolution of a strike-slip tip system. The major findings relating to these two themes are summarised below.

4.9.1 Strike-slip Architecture

- Two upper fringes of en-echelon faults are found at the upper tip of strike-slip faults. They form as two sets of en-echelon faults that dip toward one another and converge downwards to join the main fault zone, and the lower fringe bounds en-echelon faults of the upper fringe. This differs from model results that predict a single set of en-echelon faults that vary in dip direction across the fault zone.
- Extensional fault planes extend outward from the en-echelon fringes and their origin is therefore closely linked with the en-echelon faults (which in turn are linked to the strike-slip faults).
- Branch lines form near the seabed between extensional faults and en-echelon faults, and between extensional faults and the strike-slip fault at depth. Therefore intersections become more angular with depth and branch lines steepen with depth.

- Interpretation of strike-slip faults from a high resolution 3D seismic dataset has greatly improved understanding of three-dimensional strike-slip fault architecture.

4.9.2 Strike-slip fault evolution

- Upward propagation of strike-slip faults is facilitated by formation of upper fringes of sets of en-echelon faults. They propagate upward from the mode II strike-slip tip and are passively rotated to an orientation that is sub-parallel to the main fault zone, whereby another fringe set may then begin to propagate. They are eventually incorporated into the main fault zone.
- An elliptical fault plane shape is recorded from the strike-slip faults which indicates that faults evolve through lateral, in addition to upward, propagation.
- Lateral propagation gradients are recorded from strike-slip displacement analyses.
- 3D strike-slip displacement analysis using 3D seismic data has been documented for the first time.
- Termination of Afiq North propagation results in evolution of horsetail faults which dominantly form branching intersections and grow contemporaneously. Growth of these faults is initiated at c.mid-Unit C time.
- A later extensional fault forms mid-way between the splay faults to accommodate residual strain. It propagates blindly and radially. Horsetail faults can therefore form with out-of-sequence faulting.
- Predominantly dip-slip motion is recorded from Faults 1 – 3. They are linked to en-echelon faults E1 – 3, which also display a component of dip-slip motion, and form part of the strike-slip system. It is therefore interpreted that the en-echelon faults have predominantly oblique-slip shear sense and Faults 1 – 3 may also display a component of oblique slip motion.

CHAPTER 5: GRABENS FAULT ARRAY, CANYONLANDS NATIONAL PARK

5.1 INTRODUCTION

The study of the three-dimensional nature of intersecting fault geometries and kinematic interactions has previously benefited from analysis of 3D seismic datasets. However, this approach is limited by the resolution of the seismic data whereby it is not possible to image the intersection zone and its related deformation in detail. This study focuses on intersecting relationships that occur on a smaller scale.

This chapter will describe field analysis of the geometry and displacement variations of fault intersections. The field study offered the opportunity to describe intersection geometries on a comparable scale to seismic examples, but with additional detail gained at the sub-seismic scale.

The aim of this chapter is to present an evolutionary model for a set of intersecting faults from an exceptionally well-exposed array in the Canyonlands National Park, Utah. Field mapping updated current geological maps and important detail was captured in a new geological map that accurately describes displacement trends and fault tip locations. Displacement measurements of intersecting faults exposed in the study area form the basis to the kinematic interpretation. These are combined with analysis of sub-seismic scale structures in order to propose an evolutionary model for intersection that is thought to be applicable to other settings as well as to the Canyonlands array.

The chapter initially introduces the location of the study area and puts the investigated structures into regional stratigraphic (Section 5.2) and structural (Section 5.3) context, within which the origin and propagation styles of the intersecting fault trends are reviewed. The main descriptive section firstly describes the results of the geological mapping and introduces the mapped structures (Section 5.4). This is followed by detailed descriptions of fault intersection

geometries and displacement variations (Section 5.5). The results are then discussed in the context of intersecting fault kinematics and an evolutionary model is proposed (Sections 5.6).

5.1.1 Location of the study area

The study area is located south of the southern boundary of the Canyonlands National Park and on the eastern bank of Cataract Canyon on the Colorado River, SE Utah (Fig. 5.1). The study area is situated in the centre of the Colorado Plateau which is bordered by the Rocky Mountains to the east and the Basin and Range province to the west. A regional dip of c.4deg has resulted from its location on the NW flank of the Monument Upwarp, a compressional structure that was enhanced through the Laramide Orogeny (Baars and Stevenson, 1981).

Pronounced fluvial incision of the Colorado River, during the Late Pliocene – Recent, through a succession of Late Carboniferous – Late Permian sedimentary rocks has exposed evaporite rocks of the Late Carboniferous Paradox Formation. The resultant salt flowage created salt anticlines above basement trends and localised gravitational tectonics resulted in extension to form the Grabens structures of Canyonlands National Park (Baker, 1933; Huntoon, 1982).

5.1.2 Dataset and Methodology

Aerial photographs and a digital elevation model (DEM) of the Canyonlands region were available for the study. Eleven DEMs were generated using ERDAS OrthoMAX from 60% stereo-overlapped aerial photographs positives with a horizontal pixel size of 5m. They were prepared by A. Davies at Imperial College, London. Geological maps created by Huntoon (1982) and Lewis and Campbell (1965) include the study area.

Digital aerial photographs at various scales were used as base maps for geological mapping. Prior to fieldwork, lineaments were identified from these aerial photographs, and the DEM, and the interpretation of these lineaments as faults, and location of intersections and fault tips were verified in the field. Detailed mapping of the stratigraphic units established their spatial distribution and average thicknesses which aided acquisition of displacement measurements and delineation of fault tips.

Displacement measurements were made in the field from offset marker units, which were easily identified due to the excellent exposure of near-vertical normal fault scarps in the study area. Measurements of the angular change in elevation from footwall markers to hangingwall

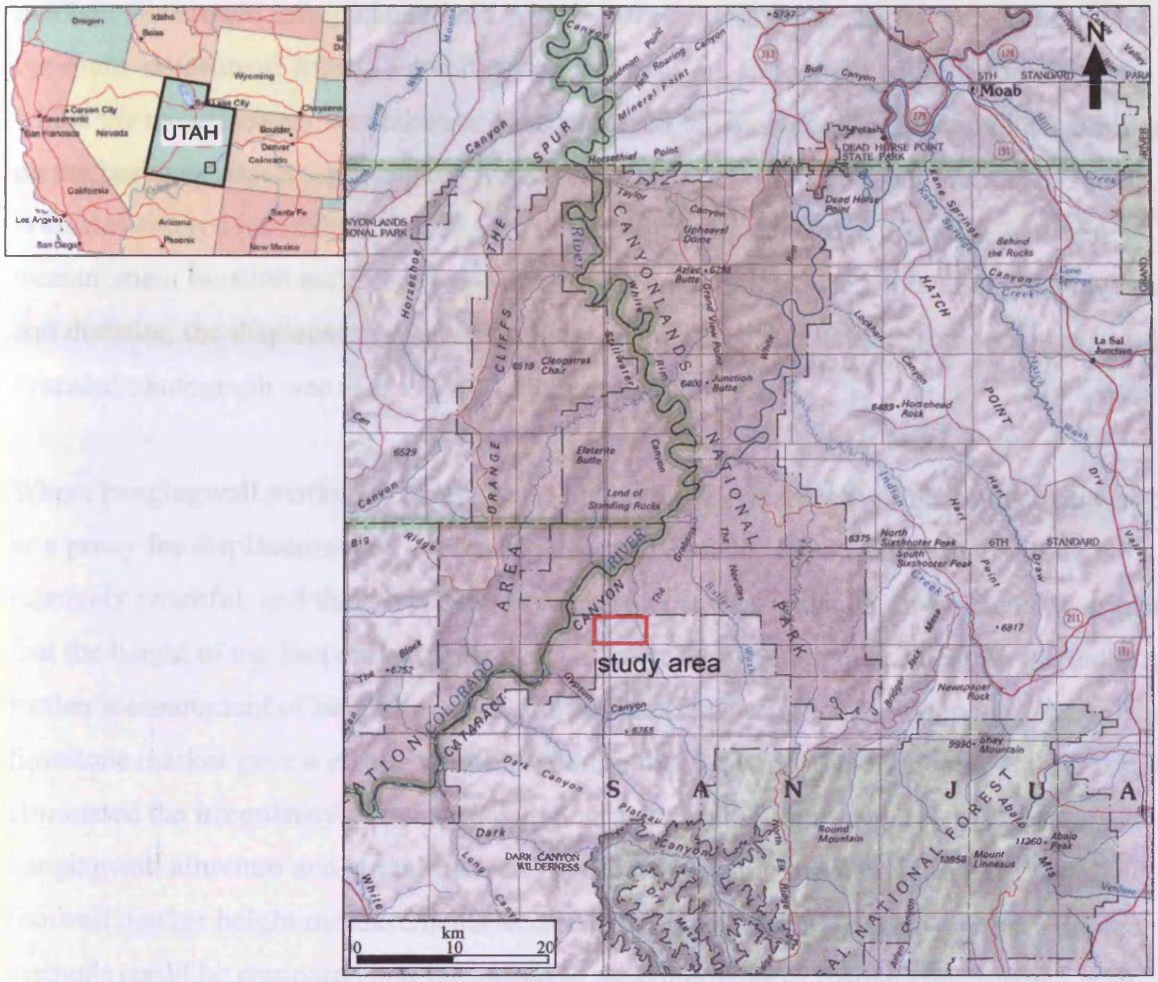

Figure 5.1. Study area location in SE Utah. The study area is situated south of the southern boundary of Canyonlands National Park on the eastern bank of Cataract Canyon on the Colorado River. Note the location of the Abajo Mountains in the SE of the map.

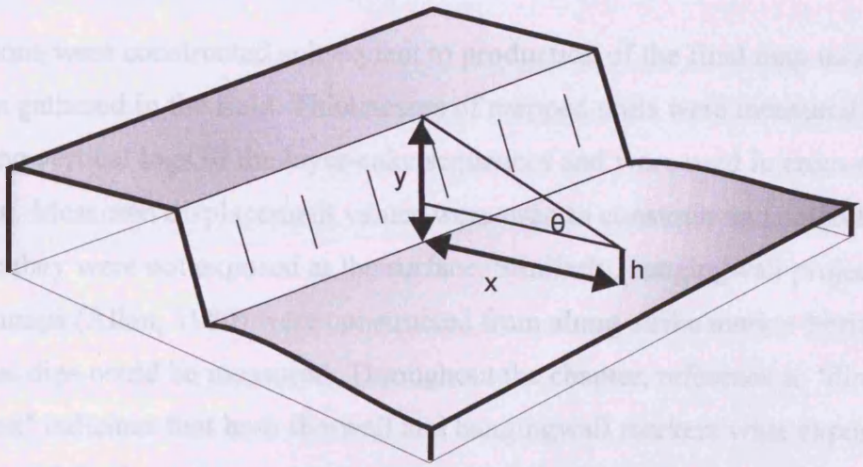

Figure 5.2. Schematic diagram of the trigonometric method used to measure the vertical component of displacement (throw) from the fault planes. The angle from the surveyors eye level to the top of the fault scarp or marker unit is measured using the Abney Level. The height from eye level to the measured unit is then calculated from $y = \tan\theta.x$ where y = height from eye level to the measured unit, θ = angle from the Abney Level and x =horizontal distance between the surveyor and the fault scarp measurement location. The height of the surveyor to eye level (h) was then added to y to obtain the throw value. This methodology was modified where the hangingwall intersection with the fault scarp lay below the surveyors feet.

markers were made using a hand-held Abney Level. Surveyed locations were chosen for optimum exposure of footwall and hangingwall markers and where both the location from which the measurement was taken and the surveyed location could be accurately determined on the basemap. Basemap locations were cross-checked with GPS locations and the co-ordinates entered into GIS software, ArcView, to calculate accurate distances between measurement location and surveyed point. From the field measurements of angular elevation and distance, the displacement value could be calculated using simple trigonometry (Fig. 5.2). A scaled photograph was also taken at each sample location.

Where hangingwall marker horizons could not be found, the height of the fault scarp was used as a proxy for displacement (c.f. Cartwright and Mansfield, 1998). Since the faulting is relatively youthful, and there has been little erosion, it was considered reasonable to assume that the height of the footwall scarp closely estimates the total displacement on the fault. A further measurement of height to limestone marker (see Section 5.2) was made. The height to limestone marker gave a closer approximation to the throw profile on the fault of interest, as it eliminated the irregularity of the surface topography. In addition, average thicknesses of hangingwall alluvium and stratal units to the top of the same marker could be added to footwall marker height measurements to calculate displacement. In this way, both indirect methods could be compared and integrated to measurements of displacement where both footwall and hangingwall markers were exposed in order to produce the most reliable displacement profile.

Cross-sections were constructed subsequent to production of the final map using stratal orientations gathered in the field. Thicknesses of mapped units were measured directly in the field or using vertical logs of the layer-cake sequences and were used in cross-section construction. Measured displacement values were used to constrain and project hangingwall units where they were not exposed at the surface. Similarly, hangingwall projections in Allan fault plane maps (Allan, 1980) were constructed from along-strike marker horizon exposures where stratal dips could be measured. Throughout the chapter, reference to 'direct measurement' indicates that both footwall and hangingwall markers were exposed and measurement of displacement could be gained using the Abney Level. 'Indirect' measurement refers to the above methods of along-strike projection and addition of thicknesses of buried to exposed strata.

5.1.2.1 Limitations

Hangingwall graben floors are infilled with a thin (<5m) cover of recent alluvial and aeolian sediments which limits the accuracy of displacement measurements. This cover is not uniform, and local outcrops form where the thin sediment cover has been removed by wind to expose hangingwall marker horizons allowing measurements to be made along the graben floors. Graben-central sink holes, (elongate depressions controlled by deeper structure), often expose bedrock beneath the alluvial cover permitting accurate measurement of its thickness and vertical depth below ground to a marker horizon. Therefore, the limitation of sediment infill is minimal in this study area and error from this source can be quantified at ±1m. Fault tips are accurately located as, in each instance, a hangingwall marker is identified adjacent to or in very close proximity to a footwall marker.

Other errors incurred in displacement measurements include those made from the Abney Level and calculation of distance between measurement location and sample point. These errors are estimated to be no more than 0.5° and 0.5m respectively, which results in an average error value of ±1m for an example measurement of 30m displacement taken from a distance of 100m.

5.2 STRATIGRAPHIC CONTEXT

The faults of the study area deform an approximately 500m thick succession of Carboniferous to Permian sedimentary rocks. The stratigraphy is summarised in Figure 5.3 and terminology used is based on Loope (1984, 1985). The lowermost unit is the Pennsylvanian Paradox evaporites of the Hermosa Formation, upon which the faults are gliding under gravitational forces (McGill and Stromquist, 1975). The study area is situated close to the western border of the Paradox Basin as shown by thinning of the salt unit whose presence defines the extent of the evaporite basin (Fig. 5.4a).

The overlying upper Hermosa Fm. comprises interbedded limestones, sandstones and shales (Loope, 1984). The Permian Rico Formation is recorded as an approximately 140m thick unit of interbedded limestone, sandstone and shale with an important regional limestone bed marking the top of the unit (Condon, 1997). The upper part of the Rico Formation is exposed in the study area and contains two regionally correlatable limestone markers. The Top Rico limestone is termed Upper Limestone in this text and the other, Lower Limestone marker, is situated approximately 12m below. The Cedar Mesa Sandstone Member of the Cutler

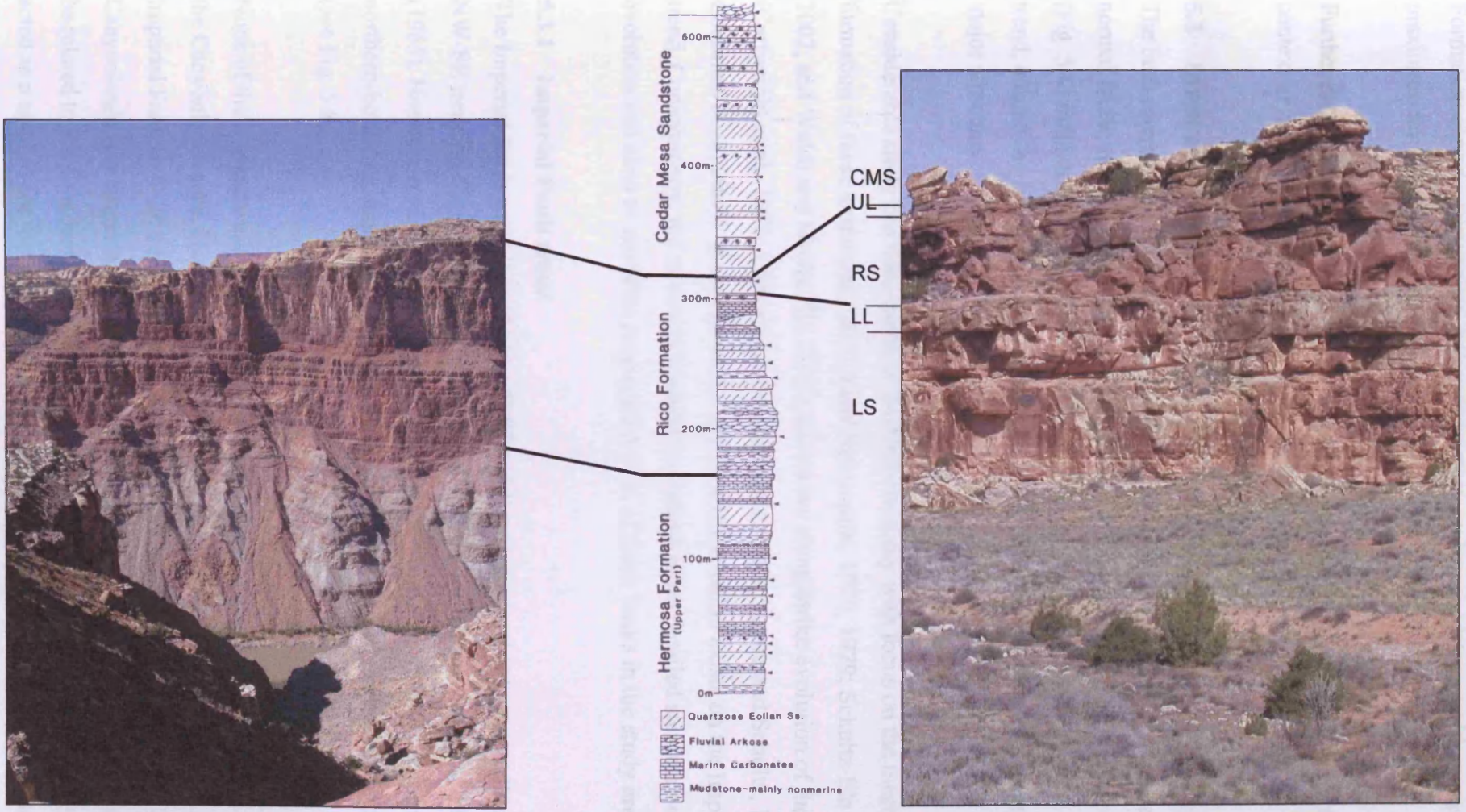

Figure 5.3. Summary of the stratigraphy exposed in the Canyonlands National Park. (a) photograph of the sedimentary layers exposed by the Colorado River showing the typical 450-500m of stratigraphy exposed in the deepest canyons in the area. (b) Generalised stratigraphic section of rocks displaced by the Canyonlands Grabens array (modified from Loope, 1984). Two regional correlative markers, UL and LL (see text) are indicated on this section. (c) Photograph of a fault scarp displaying the stratigraphy exposed and mapped in the study area. UL and LL markers are correlated to the stratigraphic column.

Formation caps the succession. It is a distinctive aeolian sandstone and is recorded as having a maximum thickness of approximately 200m (Loope, 1984, 1985).

Further details of the units that were mapped in the study area are given in Section 5.4.1 in the context of description of the geological mapping results.

5.3 STRUCTURAL CONTEXT

The fault intersections described in this chapter occur in the south of an arcuate array of normal faults, termed the Grabens of Canyonlands National Park. The plan view fault pattern (Fig. 5.4) indicates that the NE-SW trending grabens faults are cross-cut by an E-W fault trend, termed the Imperial Fault, and that all the fault intersections are thus formed with this major structure.

Considerable study has been made of the Grabens array with focus on the mechanics of formation of these structures (McGill and Stromquist, 1975, 1979; Schultz-Ela and Walsh, 2002; and Walsh and Shultz-Ela, 2003) and on the along-strike evolution of the faults (Cartwright et al., 1995; Cartwright and Mansfield, 1998; Moore and Schultz, 1999; and Commins et al., 2005). In comparison, very little information exists on the Imperial Fault trend. Consequently, the structural context provides a more detailed summary of the Grabens evolution and aims to establish propagation style of these faults in the study area.

5.3.1 Imperial Fault trend

The Imperial Fault was mapped as an E-W trending structure that has an oblique strike to the NW-SE trending Canyonlands Grabens in the south of the array by Lewis and Campbell (1965), Huntoon et al. (1982) and Woodward-Clyde Consultants (1983). It forms the northern-bounding fault to an approximately 400m wide graben termed the Imperial Graben (see Fig. 5.8).

None of the literature encountered in this study directly describes this E-W fault trend from the Canyonlands area. However, Huntoon (1987, his Fig. 4) linked an area that includes the Imperial Fault to E-W trending faults to the west of Cataract Canyon and further east of the Canyonlands (the Imperial Fault zone, Fig. 5.4). He implied that this extensional system can be related to the E-W trending Shay Fault Zone (Fig. 5.4) and argues that this system has acted as a conduit for the discharge of groundwater from lower Palaeozoic carbonates under

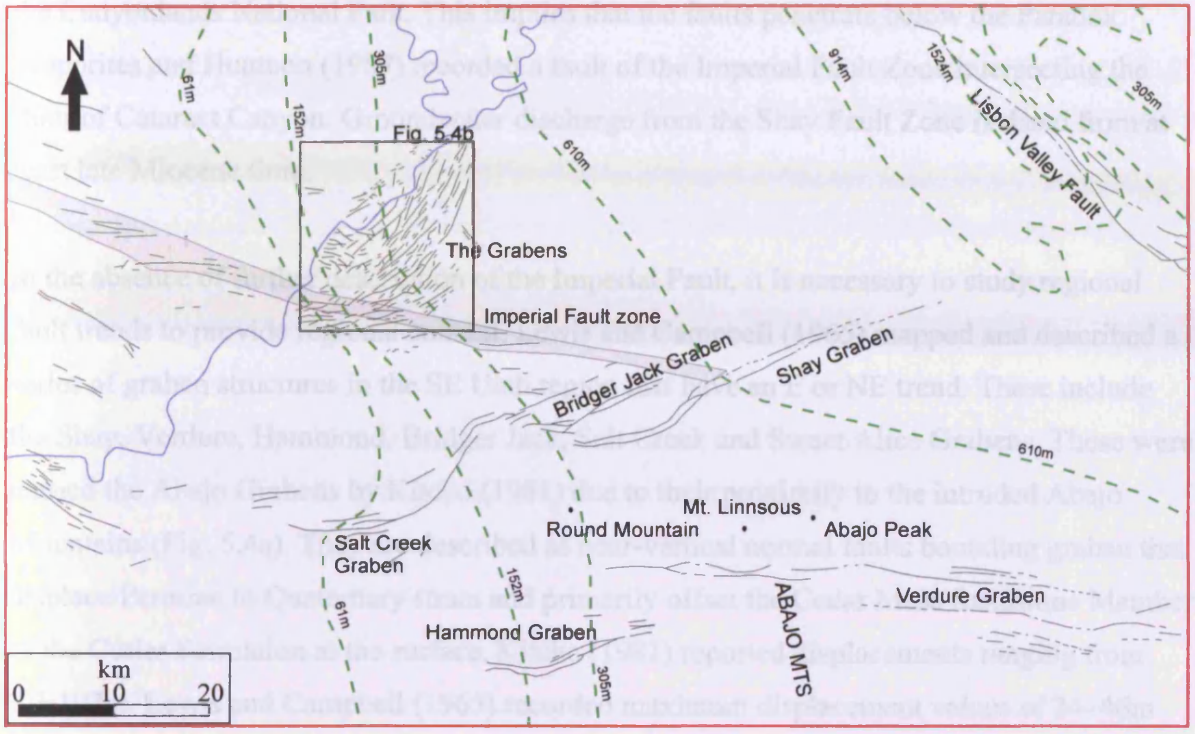

(a)

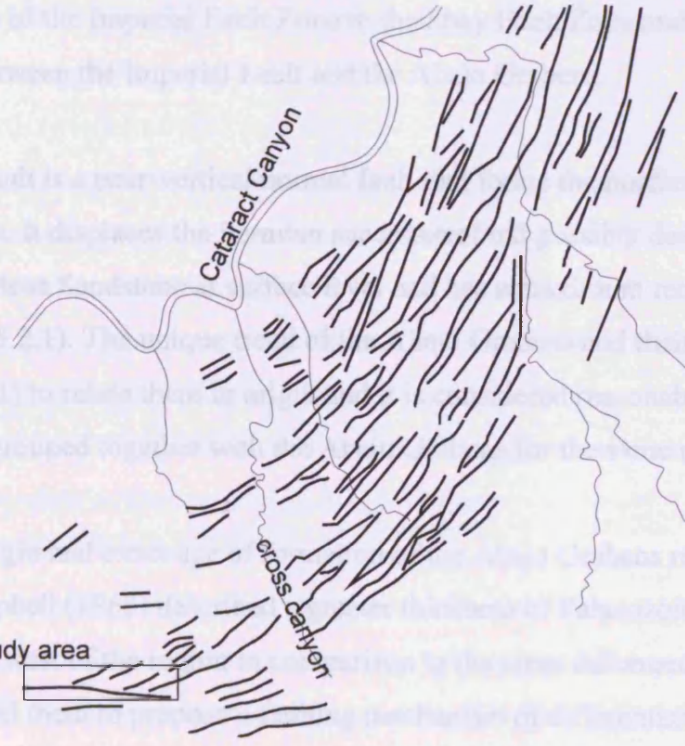

(b)

Figure 5.4. Regional structure. (a) Regional structure map showing the distribution of the Abajo Grabens (including the Salt Creek, Bridger Jack, Hammond, Verdure and Shay Grabens). The Imperial Fault trends E-W across the Grabens fault array and forms part of the Imperial Fault zone (shaded), after Huntoon, 1982. The contours represent thickness variation of the Paradox evaporites which thin toward the west, and the Lisbon Valley Fault is an example of a salt valley structure.

the Canyonlands National Park. This implies that the faults penetrate below the Paradox evaporites and Huntoon (1987) recorded a fault of the Imperial Fault Zone intersecting the floor of Cataract Canyon. Groundwater discharge from the Shay Fault Zone is dated from at least late Miocene time.

In the absence of further description of the Imperial Fault, it is necessary to study regional fault trends to provide regional context. Lewis and Campbell (1965) mapped and described a series of graben structures in the SE Utah region that have an E or NE trend. These include the Shay, Verdure, Hammond, Bridger Jack, Salt Creek and Sweet Alice Grabens. These were termed the Abajo Grabens by Kitcho (1981) due to their proximity to the intruded Abajo Mountains (Fig. 5.4a). They are described as near-vertical normal faults bounding graben that displace Permian to Quaternary strata and primarily offset the Cedar Mesa Sandstone Member of the Cutler Formation at the surface. Kitcho (1981) reported displacements ranging from 0.3-107m. Lewis and Campbell (1965) recorded maximum displacement values of 24–46m from faults of the Abajo Grabens. It was recorded above that Huntoon (1987, his Fig. 4) implied relation of the Imperial Fault Zone to the Shay Fault Zone and obvious comparisons can be made between the Imperial Fault and the Abajo Grabens.

The Imperial Fault is a near-vertical normal fault that forms the northern boundary to the E-W Imperial Graben. It displaces the Permian succession (and possibly deeper, Huntoon, 1987) and the Cedar Mesa Sandstone at surface level and has a maximum recorded displacement of 28m (section 5.5.2.1). The unique trend of the Abajo Grabens and their similar characteristics led Kitcho (1981) to relate them in origin and it is considered reasonable that the Imperial Graben can be grouped together with the Abajo Grabens for the same reasons.

The mode of origin and exact age of formation of the Abajo Grabens remains uncertain. Lewis and Campbell (1965) described a greater thickness of Palaeozoic and Mesozoic rocks in the north and west of the region in comparison to the areas deformed by the Abajo Grabens. This led them to propose a faulting mechanism of differential compaction in which greater compaction of the thick sediments overlying Pre-Cambrian crystalline rocks to the north and west creates tension causing large-scale graben failure.

Kitcho (1981) noted that most surface faults in the Paradox Basin are thought to be Laramide (late Cretaceous – early Eocene) or older. From the observations that the Abajo Grabens bend

and follow strike of beds round structural noses on the Monument Upwarp, Lewis and Campbell (1965) interpreted that formation of the Monument Upwarp post-dated initiation of faulting. The only direct evidence of the age of the faulting comes from Witkind (1964) who reported that dykes of diorite porphyry have been intruded along the faults of the Verdure Graben and suggested that the Grabens controlled placement of the Abajo laccoliths. From this, Lewis and Campbell (1965) surmised that faulting is at least as old as intrusion of the Abajo Mountains laccolith which Witkind (1975) later placed as c.42-48Ma (late Eocene).

In summary, from the available evidence, the onset and main activity of the Imperial Fault is considered to significantly pre-date the Recent formation of the Grabens Fault array.

5.3.2 The Canyonlands Grabens

The Canyonlands Grabens Fault array has been extensively studied due mainly to the excellent exposure and preservation of the recently faulted system. Work has focused on the origin and propagation mechanics of the grabens faults. This section aims to describe the characteristics of the fault array and to summarise the published literature in order to establish the propagation style of the grabens faults within the study area.

There is general agreement that the Canyonlands Grabens Fault array initiated through down slope gravitational collapse of the overburden when the Colorado River incision reached the depth of the Paradox evaporites (Baker, 1933; Lewis and Campbell, 1965; McGill and Stromquist, 1975, 1979; Huntoon, 1982; Walsh and Schultz-Ela, 2002). This created a lateral free surface allowing evaporite flow to the north-west due to the gentle regional north-west dip created by the Laramide Monument Upwarp. The brittle overburden fractured under tension caused by flow of the underlying evaporites toward the river.

The timing of graben development is poorly constrained. Based on Colorado River incision rates McGill and Stromquist (1974) estimated that graben initiation occurred at 0.5Ma. The oldest graben-fill sediments have been dated at 65Ka (Biggar, 1987) and 60Ka (Commins et al., 2005) which suggest some graben development prior to deposition of this alluvium. Evidence of recent and active faulting is recorded by sink-holes in graben-fill (Biggar and Adams, 1987), uprooting of trees such that they fall into graben faults (Trudgill and Cartwright, 1994) and live vegetation roots (dated as younger than 100 years old, Mansfield,

1996) existing in voids. There have been reports of visible changes and ground tremors within the last century (Baker, 1933; McGill and Stromquist, 1979; Lewis and Campbell, 1965).

5.3.2.1 Plan View Geometry

The Canyonlands Grabens are a spectacular array of normal faults that have significant scarps at the present-day surface allowing them to be clearly delineated on aerial photographs and digital elevation models. They are located to the east of the Colorado River, due south of its confluence with the Green River. The array reaches over 20km in length and up to 10km wide. There are over 100 individual faults that predominantly bound graben and have lengths of c.100-7000m (Cartwright and Mansfield, 1998). There is a general regularity in graben size and spacing with average graben-graben separations of 1km (measured centre to centre) and width ranges of 100-600m.

The Grabens array is an area of linked extensional fault segments that can be described as having an arcuate plan view geometry that is concave toward the river. It trends NNE-SSW in the north to ENE-WSW in the south with the change in orientation coincident with a NW-SE basement structure, the Chesler Lineament (Potter and McGill, 1978). McGill and Stromquist (1975) recorded larger and more complex graben near the Colorado River with decreasing complexity to the east. The study intersections form in the south of the array where graben geometries are not so well defined (Section 5.4.2).

The curvature of the fault array has been attributed to the presence of natural lateral boundaries to the system (McGill and Stromquist, 1975, 1979; Schultz-Ela and Walsh, 2002). The northern boundary is coincident with a change in regional dip adjacent to the canyon and the southern boundary is the pinch-out of the Paradox evaporites (Woodward Clyde Consultants, 1983; Fig. 5.4). Schultz-Ela and Walsh (2002) explained that these natural edge effects would act as restraining boundaries and inhibit gravity-driven extension at the array margins. McGill and Stromquist (1979) argued that this resulted in an increase in shear stress toward the boundaries and produced curvature of the intermediate and least principal stress orientations and therefore curvature of the array.

5.3.2.2 Cross-sectional Geometry

The importance of accurate cross-sectional description for the interpretation of mechanics of Graben array evolution was stressed by McGill and Stromquist (1975, 1979) and McGill et al.

(2000). Description of the cross-sectional geometry has resulted in different interpretations of vertical propagation mechanics (see Section 5.3.2.3). The cross-sectional geometry of the grabens is exposed in Cataract Canyon and its major tributaries. The faults are near-vertical within the top 100m of sediments then decrease in dip to ~75-85° (McGill and Stromquist, 1975, 1979; Trudgill and Cartwright, 1994; Moore and Schultz, 1999). The vertical nature of the faults in the near-surface relates to a close relationship between orientation of the Graben and that of a pervasive set of vertical joints that were present prior to faulting (McGill and Stromquist, 1975). Few examples exist of exposure of graben faults at or near their lower tip. Field evidence presented by McGill and Stromquist (1975, 1979) and McGill et al. (2000) suggests that graben-bounding faults meet at or above top salt although Cartwright et al. (2000) proposed that some faults may tip out in the salt.

Fault zones are recorded as open fissures up to 3m wide at the surface that remain open and are filled with colluvium down to 200-250m depth below surface (Cartwright et al., 1995; Mansfield, 1996; Ely, 1987). At greater depth they become thick, brecciated fault zones. Maximum displacement values are recorded from the surface and do not vary with depth (Cartwright et al., 1995, 1996; Cartwright and Mansfield, 1998) (suggesting rapid displacement decrease at lower tips consistent with detachment in salt). This indicates that displacement measurements at the surface are a valid representation of maximum slip over the whole fault plane. Maximum displacements recorded in the array vary from a few metres to 150m with a broad symmetry of displacement values recorded from individual graben-bounding fault pairs.

5.3.2.3 Vertical Propagation Mechanics

There are two significant interpretations of vertical fault propagation mechanics that have been proposed for the Grabens array. These are upward versus downward propagation and they are reviewed in this section. This is an important discussion as it impacts on interpretation of lateral fault propagation mechanics (see section 5.3.2.4) and consequently, how intersections are formed.

From their field descriptions of graben-bounding faults meeting at or above top salt level and the documentation of near-symmetrical distribution of graben-bounding fault slip McGill and Stromquist (1975, 1979) proposed that tensile graben fault initiation began at the top salt level and propagated upward to the surface. Their experimental models that replicate the grabens

geometry have a vertical σ_2 stress direction at surface creating a series of arcuate shear fractures. Therefore, they inferred that tensile fault initiation occurs at some depth, most probably at top salt, where the weight of the overburden is sufficient to cause σ_1 to be vertical, as required for normal faulting. In addition, they supported this interpretation by describing surface fault trace orientations that are oblique to predominant joint trends arguing that a surface fault initiation would trend exactly parallel to, and exploit these joints.

In contrast, Cartwright et al (1995, 1996, 2000), Cartwright and Mansfield (1998) and Mansfield (1996) argued the case for surface fault initiation and downward propagation. They based this interpretation on their field observations of maximum displacement values at surface and the existence of wide, open fissures at surface that remain open to half the thickness of the overburden and pass downward into brecciated fault zones. In addition, Cartwright and Mansfield (1998) showed that displacement patterns on graben-bounding fault pairs are not always symmetrical and therefore that fault pair evolution was not necessarily coupled as was suggested by McGill and Stromquist (1975, 1979). Mansfield (1996) and Cartwright et al. (2000) did not correlate structures across tributary canyons of Cataract Canyon. They argued that an upward-propagating structure would be unaffected by valley cuts and that the lack of continuity of faults across the canyons supports a downward propagation mechanism. This same argument is invoked from the observation that grabens faults do not cross-cut the Imperial Fault trend (Section 5.6).

Schult-Ela and Walsh (2003) were able to simulate graben geometry with 2D finite element models. The model results showed that that graben faults initiate at the surface and propagate downwards. They found that development of graben-bounding fault pairs is almost simultaneous with an antithetic fault forming almost immediately following failure of the first fault. The faults meet at depth as found from field observations and they therefore stated that initiation of the graben faults at the base of the overburden is not required to create the graben geometries as described from the field examples (McGill and Stromquist, 1975, 1979). A simple stress analysis is also used to show that the release of horizontal stress through Colorado River incision causes the top surface alone to reach tensile limit (through horizontal stress reduction within the overburden) whilst deeper levels in the overburden have not reached failure, thereby predicting surface fault initiation and reproducing the vertical upper portion of faults. In fact, McGill and Stromquist (1979) also predicted tensile failure near the surface from their discussion of the orientations of principal stress trajectories in the array.

From observations based on overall increase in size and complexity of the Graben towards the Colorado River, Stromquist (1976) and McGill and Stromquist (1979) proposed a sequential development of the graben away from the river. This interpretation is supported by Biggar (1987) from her analysis of the pattern of disturbed and abandoned drainages. Schult-Ela and Walsh (2002) and Walsh and Schultz-Ela (2003) presented numerical models that showed a sequential development away from the river as proposed by McGill and Stromquist (1974), Huntoon (1982) and Moore and Schultz (1999). They found that salt moving toward the canyon caused flexure of the brittle layer creating a horst structure closest to the canyon and a graben slightly further away. Continued salt expulsion and associated subsidence of the brittle overburden caused sequential development of additional grabens.

However, Mansfield (1996) argued that evidence exists of recent fault activity from scattered localities and that a simple eastward younging model does not hold. Commins (2003) also found evidence for out-of-sequence faulting. The kinematic models presented in this chapter also do not support simple eastward sequential faulting (see Section 5.5.1.8). From this it seems likely that the original development of the Grabens array may have been sequential but that subsequent movement was more randomly spaced.

In conclusion, the above discussion finds that downward propagation of grabens faults from the surface is the most viable vertical propagation mechanism. The following section will now investigate the interaction of the structures at the surface along-strike.

5.3.2.4 Lateral Propagation Mechanics

As surface fault initiation has been established (section 5.3.2.3) the lateral propagation styles recorded at the surface represent growth of the system in three-dimensions. The following section will introduce the detailed analyses of geometry and displacement distribution along-strike that has led to development of fault growth models by segment linkage in the Canyonlands (Cartwright et al., 1995).

The Canyonlands Grabens Array is described as segmented (Trudgill and Cartwright, 1994; Cartwright et al., 1995; Cartwright and Mansfield, 1998) and criteria for definition of segments and segment boundaries are given in Cartwright et al., (1996) as follows:

1. The presence of an abrupt change in strike or offset of adjacent segments.
2. Recognition of a change in fault throw between adjacent segments.

3. Recognition of a change in bedding attitude in the footwall exposed at the fault plane between adjacent segments.
4. The development of a relay structure at the segment boundary.

Relay ramp structures (Peacock and Sanderson, 1991) are described from areas where segments of the array overlap. Commonly both segments have the same sense of throw but Trudgill and Cartwright (1994) recorded a number of different geometries from the Canyonlands. The dips of strata in the ramps mapped in the Canyonlands range from a few degrees to over 50° (Cartwright et al., 1996).

The relay ramp is commonly breached by a fault trending obliquely to the two main fault strikes thereby joining the overlapping segments either via the footwall segment (footwall breached) leaving the hangingwall segment as an inactive splay, or by the hangingwall segment (hangingwall breached) leaving the footwall segment as an inactive splay (Trudgill and Cartwright, 1994). Relay ramp structures show internal deformation in the Canyonlands that can take the form of subsidiary faults that strike parallel to the main faults and divide the relay ramps longitudinally, minor extensional faults that form parallel to the rotation axis to accommodate stretching over the hinge and by lateral extension across joint surfaces along the ramps (Trudgill and Cartwright, 1994). The value of the displacement that can be measured from the breached fault (the breaching index, Cartwright et al., 1996) represents the value of added displacement since coherent linkage.

Cartwright and Mansfield (1998) described three main geometries of fault tip that they have identified in the area (Fig. 5.5). Type A tips are the most commonly reported from the Grabens array. As no process zone or monoclines associated with fault tip propagation (signifying Type B and Type C tips respectively) were identified in the study area, the investigated faults are recognised as having Type A tips and have propagated under mode III loading conditions.

In conclusion, fault growth by segment linkage is documented from the Canyonlands Grabens through documentation of abrupt strike changes and relay ramp geometries. Evidence of lateral displacement taper is indicative of lateral propagation direction.

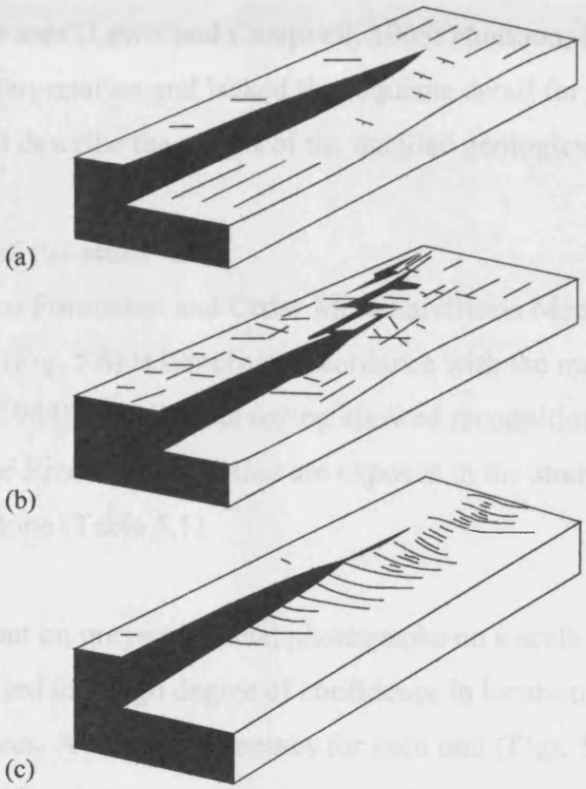

Figure 5.5. Types of lateral fault tips after Cartwright and Mansfield, 1998. (a) Type A: Characterised by a simple tapering of displacement on the main fault with no substantial complementary fracturing or folding adjacent to the fault. There is no recognisable 'process zone'. Bedding dip in the footwall and hangingwall flattens to regional approaching the tip. Fault propagated under mode III loading. (b) Type B: Characterised by a tensile 'process zone' constituting a zone of horizontal dilation of pre-existing joints and signifying tensional failure under mode I loading conditions. Close to the lateral tip, the fault plane generally passes laterally into a vertical ground 'fissure'. The decrease in displacement toward the transition from shear to tensile failure indicates mode III propagation therefore there is a mode III tip and a mode I tip along-strike from the transition. Type C: Characterised by a transition from a purely 'brittle' expression of the normal fault with vertical displacement of bedding, to a more 'ductile' expression of vertical displacement in the form of a monocline.

5.4 MAPPING RESULTS

Fulfilment of the objectives of the field study, i.e. to describe the geometry and particularly displacement variations on faults toward intersection, was greatly aided by production of the geological map at 1:8400 scale (Fig. 5.6). The map of the study area delineates the plan view geometry of the faults and the distribution of Permian stratigraphic units. Previous 1:62500 geological maps of the area (Lewis and Campbell, 1965; Huntoon, 1982) were mainly based on photogeological interpretation and lacked the requisite detail for fault analysis. The following sections will describe the results of the detailed geological mapping.

5.4.1 Stratigraphy of the study area

The distribution of Rico Formation and Cedar Mesa Sandstone Member (Cutler Formation) units presented herein (Fig. 5.6) is largely in accordance with the maps of Huntoon (1982) and Lewis and Campbell (1965). Detailed surveying allowed recognition and mapping of five distinct units within the Rico Formation that are exposed in the study area and are capped by the Cedar Mesa Sandstone (Table 5.1).

Mapping was carried out on greyscale aerial photographs on a scale of 1:6500. The detail of the aerial photographs led to a high degree of confidence in location of stratigraphic boundaries and structures. Average thicknesses for each unit (Figs. 5.6 and 5.7) vary little within the study area. All units are conformable, and sharp contacts, normally recognised by distinct colour changes, separate the units. The following section will briefly describe the distribution of the rock types.

Due to the weathering style of all units, particularly relating to rounding toward pervasive jointing, it is difficult to obtain reliable bedding orientations from anywhere except unit contacts where exposed.

In summary, the two regionally extensive limestone markers, UL and LL, are extremely well exposed in the study area, and are consequently most useful for displacement measurements.

Name	Rock Type	Colour	Distribution
Cedar Mesa Sandstone (CMS)	Coarse-grained aeolian sandstone	Pale yellow to white	Constitutes all topographic highs in study area, upper boundary is eroded.
Upper Limestone (UL)	Limestone	Dark grey	Top Rico Fm. Important regionally extensive marker, one single limestone bed that is exposed over the majority of the area.
Red Sandstone (RS)	Medium-grained, fissile sandstone	Purple-red (distinctive); lower beds are white	Exposed in all footwalls and in the hangingwall of the Imperial Fault. Purple-red scree slopes extend beyond the limits of RS exposure.
Lower Limestone (LS)	Limestone	Pale grey	Important regionally extensive marker, exposed on nearly all footwall scarps and in hangingwalls in the western study area.
Lower Sandstone (LS)	Coarse-grained sandstone	Buff	Constitutes the majority of large scarp exposures.
Lower Red Sandstone (LRS)	Coarse-grained sandstone exhibiting soft-sediment deformation	Brick Red	Only exposed in the EF5 and IFWa footwall cliff, no lower contact exposed in study area.

Table 5.1. Summary of the units mapped in the study area.

5.4.2 Structure of the study area

Geological mapping identified a series of NE-SW trending faults of the Grabens array that intersected with the Imperial Fault in its footwall. Fault scarps were easily identified in the study area and match well with those previously identified from the DEM/aerial photographs (Fig. 5.8). In contrast to the well-defined graben pairs to the north and northeast of Cross Canyon (Fig. 5.4b), fault trace patterns in the study area are more complex. Simple graben

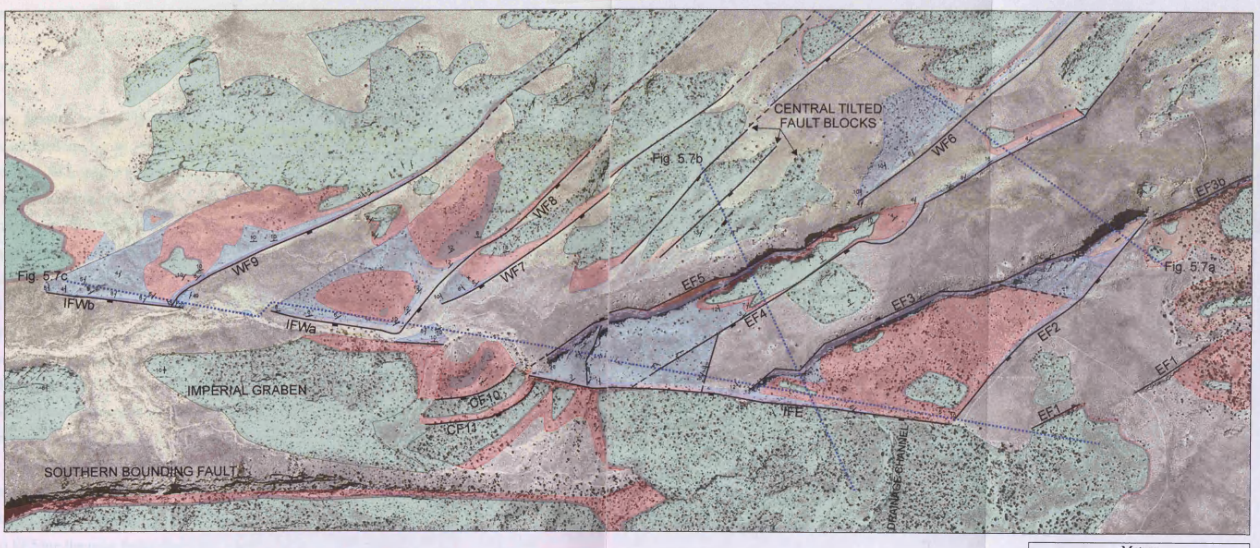

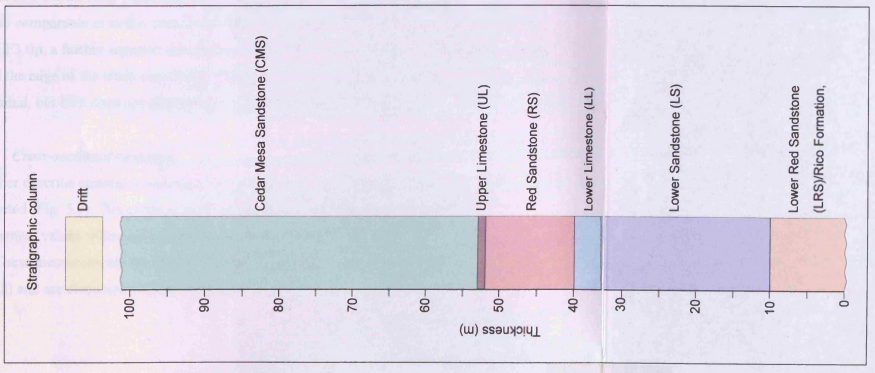

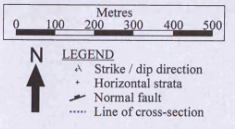

Figure 5.6. The geological map and stratigraphic column showing average thicknesses of mapped units. See text for geological description of units and their distribution. Areas of the basemap that are characterised by bright pale grey-to-white colours dotted with vegetation contrast to largely uniform grey-coloured areas that appear to be devoid of vegetation on the aerial photograph. These correspond to rock exposure and scrub-vegetated Quaternary deposits/alluvium respectively. Note lines of cross-sections (Fig. 5.7).

forms are not easily identified and half-grabens dominate instead. The dense faulting facilitates topographic height decrease toward the Colorado River. All faults have extensional kinematics.

The study area has been divided into east and west sections. The faults mapped in the study area are labelled in Figures 5.6 and 5.8 and their attributes summarised in Table 5.2. The E-W fault trend of the Imperial Fault has previously been mapped as a single trace (Huntoon, 1982) or as a segmented trace (Lewis and Campbell, 1965). Mapping in this study has revealed a segmented geometry with a break in fault trace continuity and a 75m northward shift of fault trace in the central area between the location of intersection with EF5 and with WF8. The Imperial Fault is thus separated into two areas, Imperial Fault East (IFE) and Imperial Fault West (IFW). Graben faults that intersect with the IFE are termed east faults (EF2-5), and those that intersect with the IFW are termed west faults (W8-9). The IFW is identified on the DEM and aerial photographs as a continuous lineation from the study area to the Colorado River. However, it only has surface expression in the study area as the two segments, IFWa and IFWb, where it intersects with WF8 and WF9 respectively, therefore if present elsewhere, it is concealed by the flat-lying topography.

Importantly, all the NE-SW trending faults of the Grabens array terminate at the Imperial Fault and do not continue to intersect with the Imperial Graben southern boundary fault. EF3 and EF5 are the only faults that form intersections in the study area to throw to the NW. They are comparable in strike, maximum throw and length with the exception that to the NE of the EF3 tip, a further segment on a continuous trend to EF3 is mapped. This fault continues beyond the edge of the study area and is termed EF3b. Thus EF3 as mapped is a segment of a larger trend, but EF5 does not display any continuation past its NE tip.

5.4.2.1 Cross-sectional structure

To further describe structural variation in the study area, cross sections A, B and C were constructed (Fig. 5.7). The cross-sections provide a means of indirectly interpreting displacement values where no surface hangingwall exposure exists as described in Section 5.1.2. These measurements are displayed on the cross-sections and on the displacement map (Fig. 5.8) and are discussed further in Section 5.5.

Name	Strike	Length segment (m)	Max. recorded displacement (m)	Slip direction	Graben-pair
Imperial Fault East (IFE)	095°	1180	24	S	Imperial Graben southern boundary fault
Imperial Fault West a (IFWa)	100°	360	28	S	Imperial Graben southern boundary fault
Imperial Fault West b (IFWb)	097°	250	20	S	Imperial Graben southern boundary fault
East Fault 1 (EF1)	056°	145	7	NW	EF2
East Fault 2 (EF2)	042°	730	22	SE	EF1
East Fault 3 (EF3)	064°	1130	59	NW	EF4
East Fault 4 (EF4)	059°	1300	29	SE	EF3
East Fault 5 (EF5)	066°	1100	63	NW	Central tilted fault blocks and WF7
West Fault 6 (WF6)	050°	1180	26	SE	Half graben
West Fault 7 (WF7)	055°	1250	Not sampled	SE	Half graben/EF5
West Fault 8 (WF8)	045°	1220	28	SE	Half graben
West Fault 9 (WF9)	065°	1500	27	SE	Half graben
Circular Fault 10 (CF10)	060°	320	8m	SW	Half graben
Circular Fault 11 (CF11)	060°	250	8m	SW	Half graben
Central Tilted Fault Blocks	044°	100 - 1000	Not sampled	SW	Half graben

Table 5.2. Attributes of faults mapped in the study area.

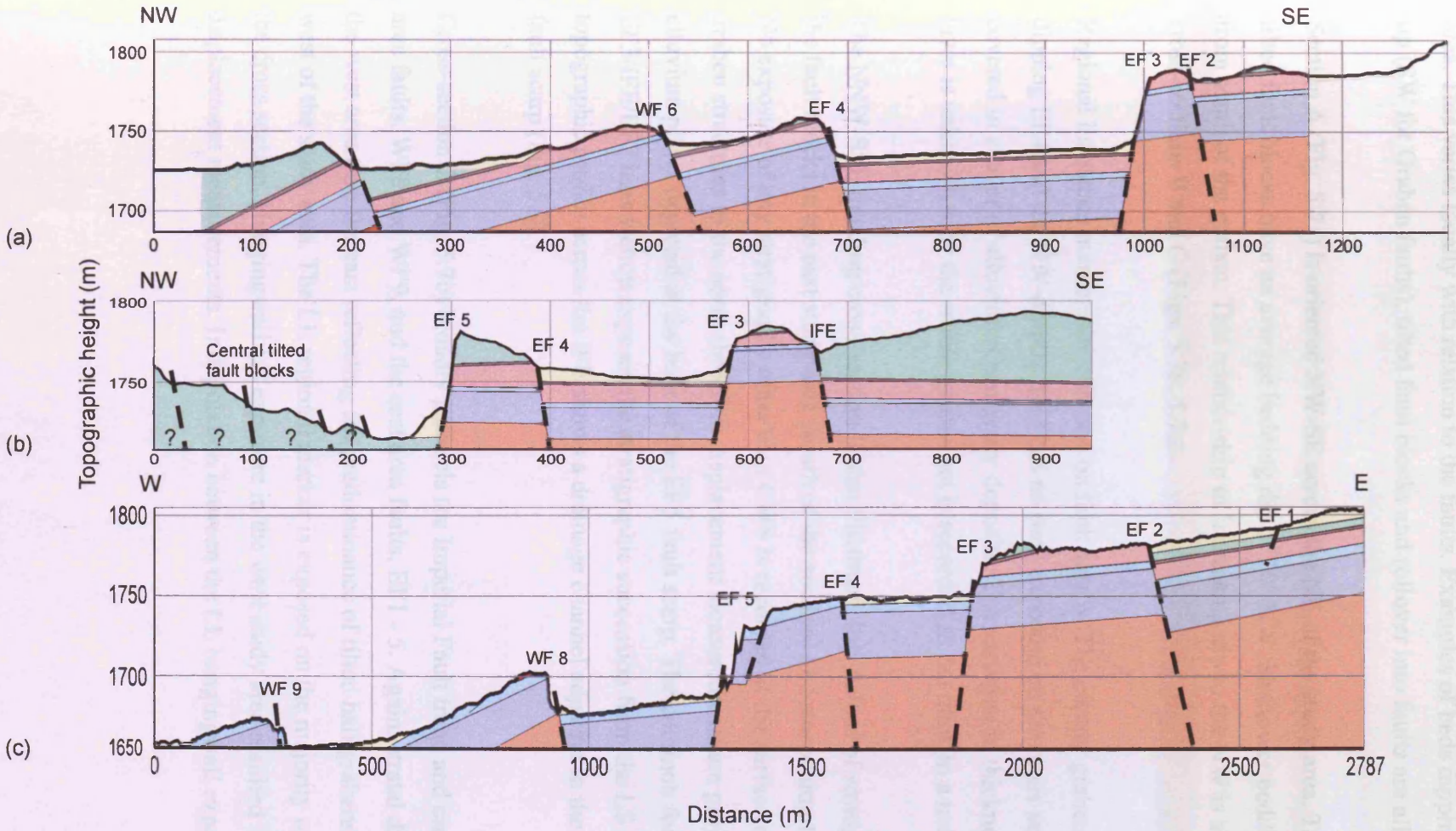

Figure 5.7. Cross-sectional structure of the study area. (a) Cross-section A. Average dips steepen toward the north-west where half-graben structures dominate. Graben-centre stratigraphy is projected on to the line of section from nearby hangingwall exposure. (b) Cross-section B. Average dips in the eastern study area are shallow. Graben-centre stratigraphy is projected on to the line of section from nearby hangingwall exposure. No units other than the CMS were mapped from the central tilted fault blocks on the northwest of the section line therefore the cross-sectional distribution of units is uncertain. (c) Cross-section C. The line of section is taken in the footwall of and near-parallel to the Imperial Fault. Dip values are greatest in the western study area. Two half-graben structures show that throw values on these faults are high in proximity to the Imperial Fault. In contrast, the eastern area has largely reduced throw in proximity to the Imperial Fault. Units are coloured as for the geological map (Fig. 5.6).

The average regional dip is 2-4°, and bedding dips of 3-10° NW are recorded in the study area. This varies locally with relation to the faults. Examples of beds dipping toward the fault tip (SW for Graben faults), tilted fault blocks and rollover into faults are all recorded.

Section A (Fig. 5.7a) is oriented NW-SE across the NE of the study area. To the NW, three tilted fault blocks have an average bedding dip of 10° NW. Shallower bedding dip is recorded from south of the graben. This relationship of increasing dip to the NW is also identified from cross-sections B and C (Figs. 5.7b, 5.7c).

Regional limestone markers are exposed on fault scarps. The central graben between the SE-dipping EF4 and the NW-dipping EF3 has no rock exposure on the cross-section and is covered in a layer of alluvium/Quaternary deposits. The variation in thickness of the alluvium layer is unknown over the whole graben but is recorded as 2m thick in a nearby sinkhole.

The NNW-SSE trending cross-section B also illustrates low values of stratigraphic dip from the fault blocks in the east study area (south of the section) and steepening toward the north. No exposure of any stratigraphy other than CMS is recorded at the surface of the four half graben structures to the north therefore displacement measurements are projected. A thick alluvium pile is depicted at the base of the EF5 fault scarp. The common footwall to the EF3/IFE/EF2 intersection exposes the stratigraphic succession from the LS to the CMS. The topographic profile across the IFE shows a drainage channel adjacent to the south-dipping fault scarp (Fig. 5.9).

Cross-section C (Fig. 5.7c) broadly parallels the Imperial Fault trend and cross-cuts the west area faults, WF8 and WF9, and the east area faults, EF1 - 5. Again, stratal dips are greater in the west area than the east reflecting the predominance of tilted half grabens in the north and west of the study area. The LL regional marker is exposed on the majority of fault scarps on the cross section. Hangingwall LL exposure in the west study area resulted in high quality displacement measurements. Interpolation between the LL hangingwall exposures shows a

Figure 5.8. Map of displacement values and distribution. Where displacement could not be gained, height to lower or upper limestone values are shown.

regional dip of 3° that is significantly increased in the tilted footwall blocks to approximately 10°.

In summary, the study area comprises a series of graben structures with shallow stratal dips in the east, and tilted half graben structures with steeper dips in the west area. A limited stratigraphy is exposed largely on footwall scarps and in some hangingwall graben-fills. It is therefore not possible to describe displacement measurements in three dimensions and concentration is on a horizon-based displacement interpretation. Description of individual intersection geometries and displacement distributions will be given below.

5.5 Description of Fault Intersections

This section aims to describe constituent faults of the intersections with particular reference to their displacement profiles and any associated deformation. The purpose of this detailed descriptive section is to summarise the intersection types documented in the study area in terms of their identifiable geometrical and displacement relationships. Four intersections with the Imperial Fault will be described from the east study area and a further two where grabens faults intersect with one another. This will be followed by description of two intersections with the Imperial Fault in the west study area. Some consideration will be given to evolution of the east and west study areas within this descriptive section (Sections 5.5.1.8 and 5.5.2.3).

5.5.1 The Eastern Study Area

The eastern study area has a distinctive plan view geometry that is made up of two triangular areas with a common southern boundary of the Imperial Fault East. The easternmost triangle constitutes Faults EF2, EF3 and IFE while Faults IF4, IF5 and IFE make up the western plan view triangle (Figs. 5.6, 6.8). Fault scarps show that the triangles represent the common footwalls of their constituent faults and form triangular horst blocks.

As the Imperial Fault East is common to four of the eastern area high-angled intersections its displacement profile will be described first. Where intersection angles are given below the measurement is defined as the angle of the corner of the common footwall bounded by the intersecting faults.

5.5.1.1 *Imperial Fault East*

In cross-section the fault is a trench with a near-vertical scarp forming the majority of the northern boundary, and a gentler slope being the more common morphology of the southern boundary (Fig. 5.9) The trench is a drainage channel and the course of an obvious N-S oriented channel (Fig. 5.8) to the south of the Imperial Fault is diverted westward on entering the Imperial Fault East trench. The diversion of this drainage suggests that fault formation occurred earlier than that of the drainage system.

The Imperial Fault East juxtaposes the younger CMS Formation in the south against older LS and LL sediments at the same topographic height in the north (Fig. 5.9). Therefore fault movement is defined as normal with downthrown displacement to the south (Fig. 5.6). The displacement profile (Fig 5.10) is near-symmetrical in shape with a central maximum displacement. Values on the western limb define a lateral displacement gradient of 0.02 which increases to 0.06 towards the EF5 intersection. Due to sparsity of measurements no gradient variations are recorded from the eastern limb which has a gradient of 0.03.

5.5.1.2 *Imperial Fault East/EF2 Intersection*

The EF2 forms an intersection with the IFE at its SW extent and with EF3 to the NW (Section 5.5.1.6). The IFE/EF2 intersection has an 'L'-shaped geometry (after classification, Chapter 2) with an intersection angle of 122°. There is no evidence in the field that either fault continues past the intersection location.

The EF2 displacement profile (Figs. 5.11, 5.12) displays a distinctive displacement decrease in the north-central section with displacement rising to 16ms at intersection with EF3 in the north. Toward the south there is a displacement increase then a decrease toward the Imperial Fault intersection to 8m. From the displacement profile Fault EF2 could be interpreted as two fault segments. An alternative explanation can be offered by the E-W trending fault that cuts across the common EF2/EF3 footwall and downthrows toward the north (Fig. 5.6). This fault may have brought its hangingwall stratigraphy into closer contact with the EF2 hangingwall stratigraphy (Fig. 5.12) thus reducing displacement in this central area. The intersection tip gradient of EF2 toward IFE, defined from the local Dmax. at approximately 200m from intersection to the intersection location with IFE, is 0.104, which is significantly steeper than that recorded from the IFE eastern limb.

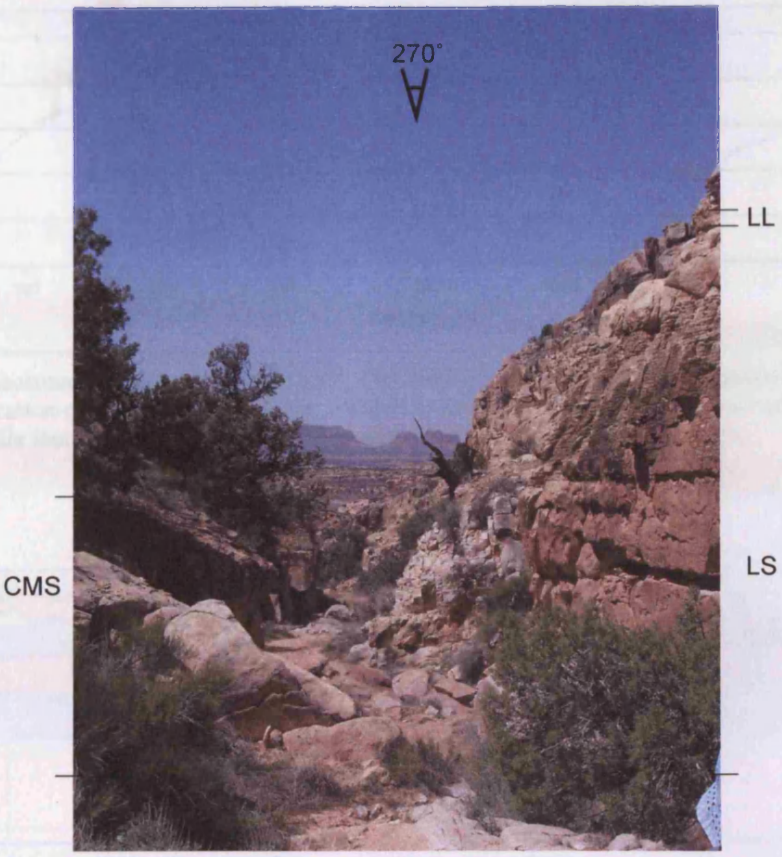

Figure 5.9. Photograph of the Imperial Fault East scarp (right hand side). The Imperial Fault juxtaposes LS sediments against CMS sediments. The course of a drainage channel runs along the Imperial Fault trench.

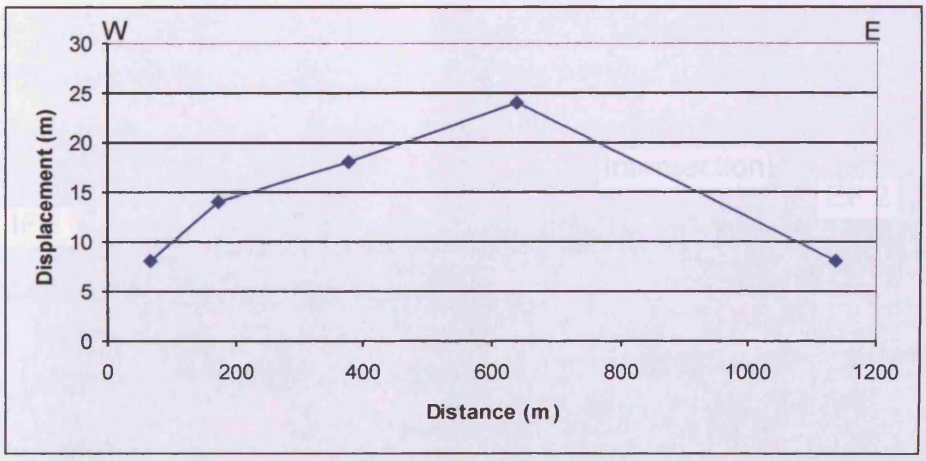

Figure 5.10. Displacement-length plot for the Imperial Fault East. Maximum displacement is recorded from a near-central location and decreases toward the western and eastern extents of the IFE segment. Importantly, neither extent of the fault segment reaches a zero value tip.

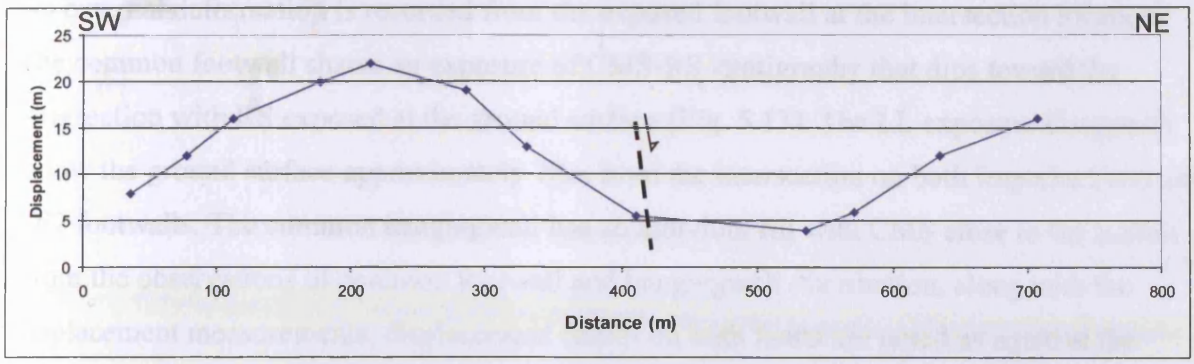

Figure 5.11. Displacement - length plot for the EF2. The displacement profile has a distinctive near-central minimum. The location of a cross-fault is shown. Neither extent of the EF2 reaches a zero value tip. The displacement profile increases toward the NE extent and decreases toward the SW extent.

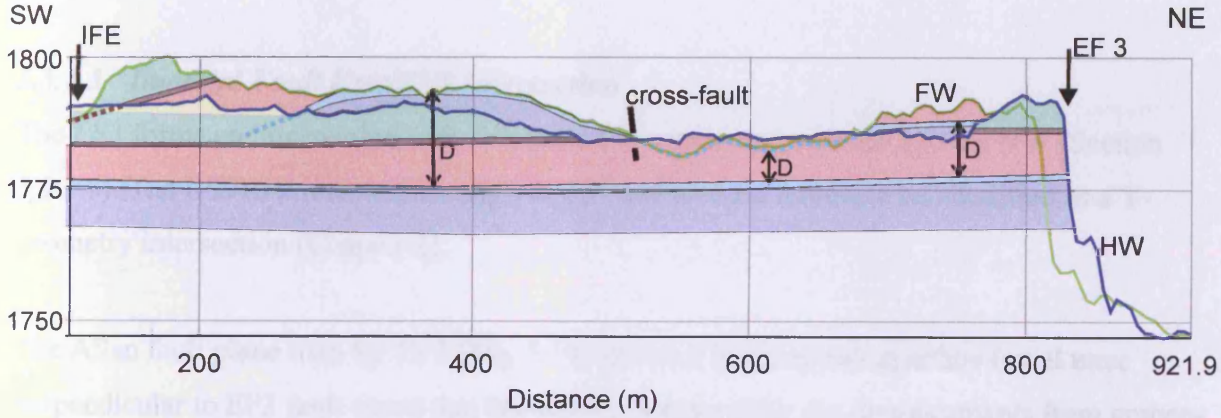

Figure 5.12 Allan fault plane map of EF 2. Hangingwall (HW) outline in navy, footwall (FW) outline in green. Double-headed arrows indicate displacment (D) measurements. Footwall units are dashed (short dashes) where they plunge below the hangingwall surface. Colours of units as for the geological map (Fig. 5.6). See Fig. 5.8 for location of section line.

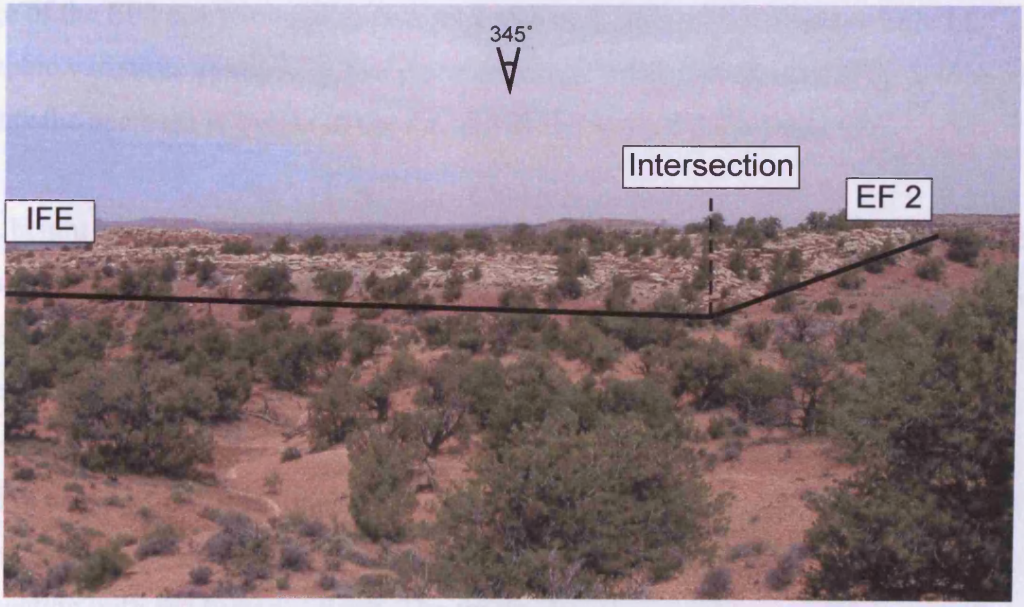

Figure 5.13. Photograph of the intersection between the IFE and the EF 2. The exposed stratigraphy of the footwall (CMS, UL and RS) is common to both faults, and the hangingwall succession is also shared.

No external deformation is recorded from the exposed footwall at the intersection location. The common footwall shares an exposure of CMS-RS stratigraphy that dips toward the intersection with RS exposed at the ground surface (Fig. 5.13). The LL exposure disappears below the ground surface approximately 70m from the intersection on both Imperial Fault and EF2 footwalls. The common hangingwall has an alluvium fill with CMS close to the surface. From the observations of common footwall and hangingwall distribution, along with the displacement measurements, displacement values on both faults are noted as equal at the intersection. This value is calculated as 8m however, cross-section C (Fig. 5.9c) suggests that it may have a greater value up to 13m. Importantly, neither fault reaches a zero value of displacement that would define a tip.

5.5.1.3 Imperial Fault East/EF3 Intersection

The EF3 forms an intersection with IFE at its SW extent and with EF2 to the NW (Section 5.5.1.6). The IFE/EF2 intersection angle is 50° and it could therefore be classified as a Y geometry intersection (Chapter 2).

The Allan fault plane map for EF3 (Fig. 5.14) shows a hangingwall syncline (axial trace perpendicular to EF3 fault trace) that has been constrained by dip measurements from graben-central exposures. Maximum displacement (Figs 5.14, 5.15) is recorded from a near-central position, decreasing toward the SW extent of the EF3 where the displacement gradient increases toward intersection. This displacement profile is illustrated further on a photo-montage of the EF3 scarp toward its NW extent (Fig. 5.16a) which displays little LL topographic variation, contrasting to a photo-montage in the SW tip area (Fig. 5.16b) which highlights the decrease in height of the LL and its dip toward the intersection.

The LL height profile (Fig. 5.15) can be seen to broadly follow the displacement curve but to underestimate it in the central section where the hangingwall LL is interpreted to be at its deepest. The footwall LL and UL tip gradient does not follow the same trend as the displacement profile as it does not account for the rising hangingwall trend.

At the SW extent of EF3, the footwall exposure of LL is brought into contact with HW LL (exposed adjacent to the IFE footwall scarp). Thus, EF3 reaches a zero displacement tip close to intersection with the Imperial Fault. The tip displacement profile has a high gradient value

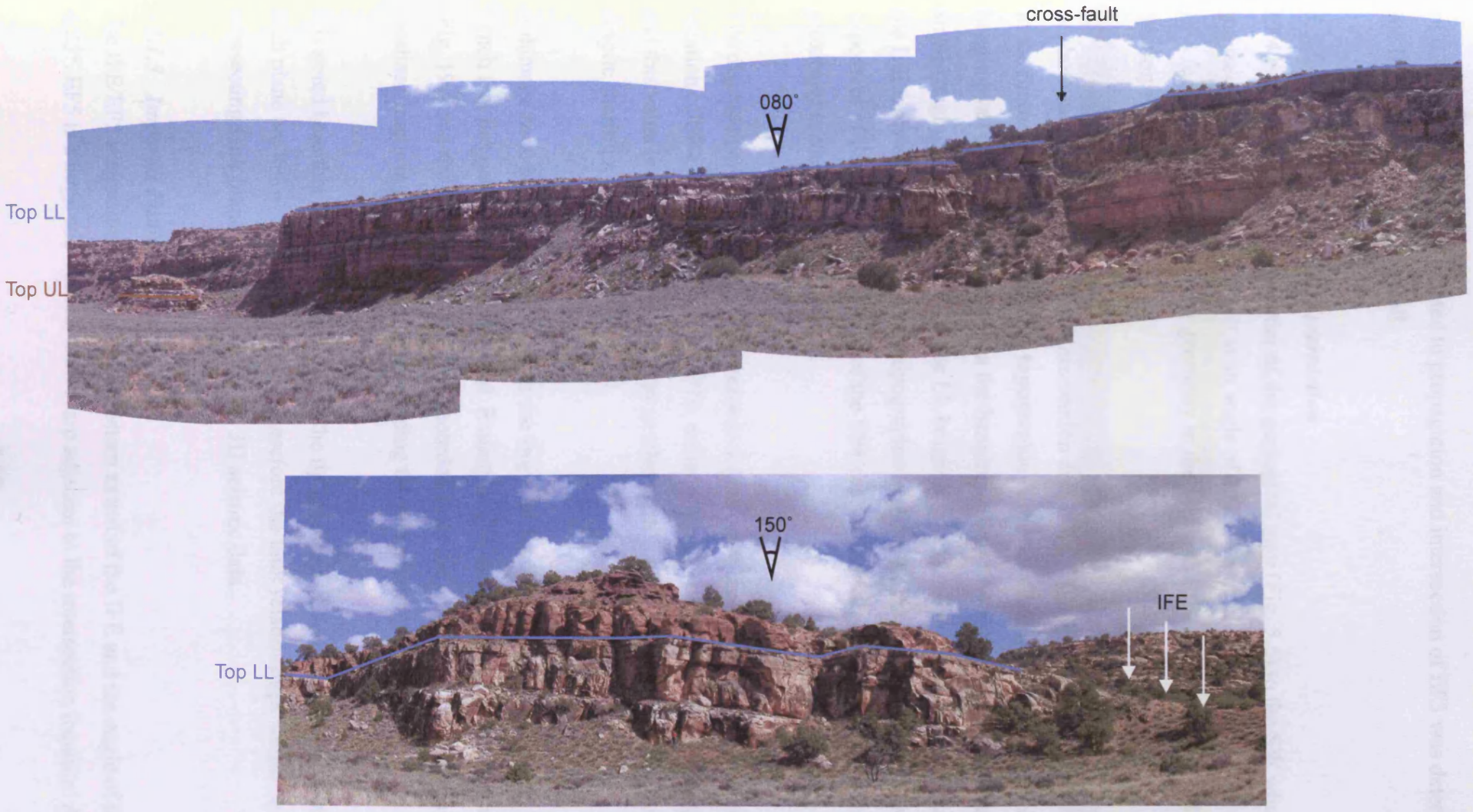

Figure 5.16. Photomontages of the EF3 fault scarp. (a) The LL unit shows little change in topographic profile over most of the length of the fault. (b) Toward the fault tip, the LL unit dips to the SW to meet with hangingwall LL thus defining the EF3 tip adjacent to the IFE fault trace.

of 0.306. No deformation related to propagation and intersection of EF3 was determined from the IFE footwall or hangingwall.

5.5.1.4 Imperial Fault/EF4 Intersection

EF4 extends from the north border of the geological map (Fig. 5.6) to the SW where it intersects with the Imperial Fault at an angle of 152°. A variation in strike is identified where EF4 forms an arcuate plan view geometry in the vicinity of the EF5 NE tip (Fig. 5.6, see Section 5.5.1.7).

A photo-montage of the IFE/EF4 intersection area (Fig. 5.17) demonstrates that exposed LL in the footwall of the EF4 has little topographic expression and lies very close to the EF4 hangingwall alluvium surface. LL in the hangingwall of EF4 is exposed in the scarp of a small hangingwall splay fault and the LL height is less than 1m. Further LL exposure from the IFE footwall exists at the same topographic level as the footwall and hangingwall exposures of the EF4. Thus, the tip of the EF4 can be defined and is reached in close proximity to the IFE, in its footwall.

The displacement profile (Fig. 5.18) records a gentle displacement decrease to zero at the tip location of EF4. The tip gradient is 0.039, defined from the inflexion to the tip (Fig. 5.18), and this value is approximately 10 times gentler in gradient than that of the EF3 profile, despite sharing a common hangingwall.

A damage zone has been recorded from the Imperial Fault hangingwall in an area within the trench that lies parallel to the EF4 trend. Examples of increased footwall fracture and collapse (Fig. 19a) and the only veining network recorded from the area (Fig. 19b) point to intense localised fracturing in the volume surrounding the intersection.

It is noted here that the distances between the tip locations of both EF3 and EF4 and the IFE fault plane are below seismic resolution, therefore the fault relationships would be imaged as intersecting fault planes on this horizon on 3D seismic data.

5.5.1.5 Imperial Fault/EF5 Intersection

The IFE/EF5 intersection occurs at the western extent of the IFE and the angle of intersection is 25°. EF5 is a large sub-vertical fault scarp adjacent to the intersection location. A N-S

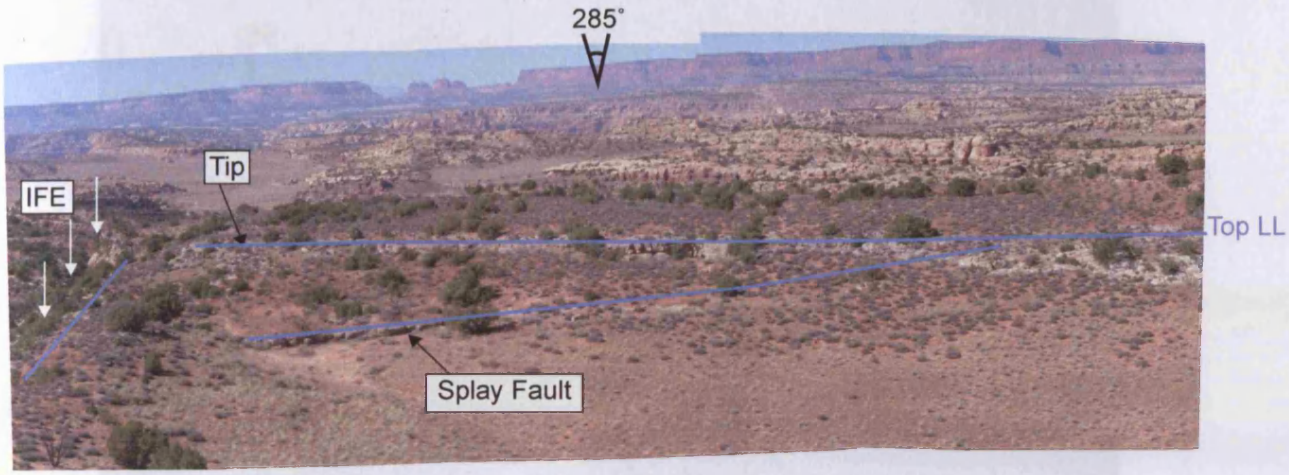

Figure 5.17. Photograph of the EF4 tip. Values of displacement are very low in proximity to the IFE. LL exposures in the footwall and hangingwall of the EF4 and in the footwall of the IFE are at the same topographic height indicating a fault tip.

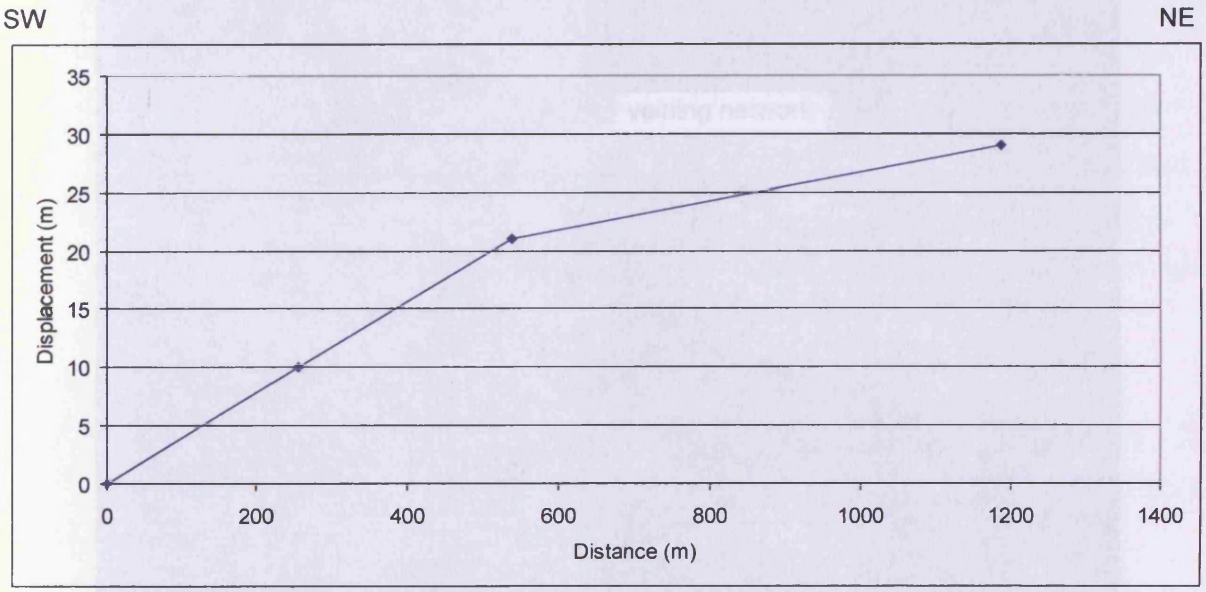

Figure 5.18. D-x profile of the SW tip region of the EF4. Displacement values decrease toward the SW and reach a zero value tip in the footwall of the IFE.

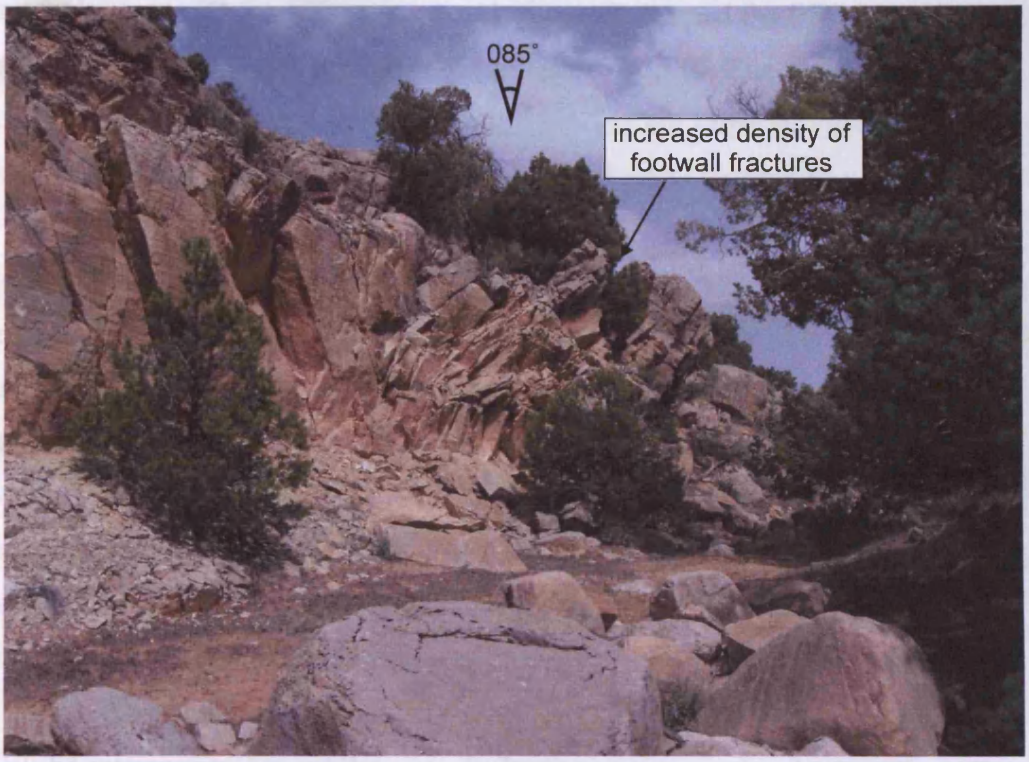

(a)

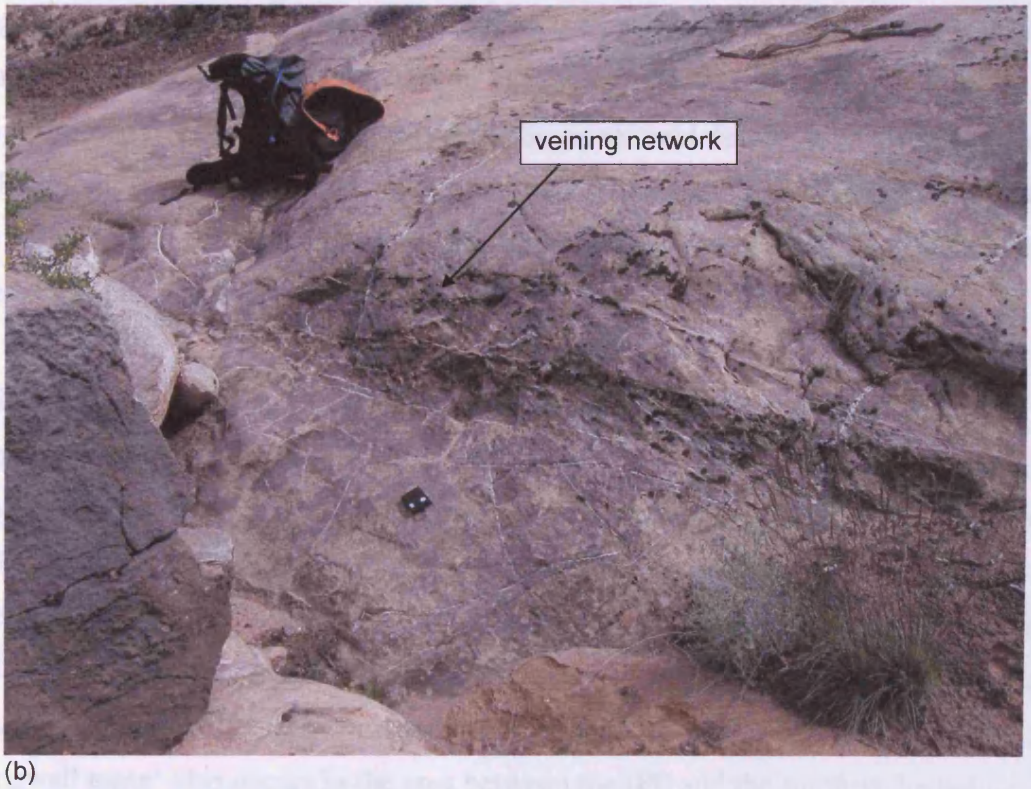

(b)

Figure 5.19 Photographs of damage recorded at the IFE, in a location along-strike from the EF4 fault tip. (a) sub-vertical joints and fractures are observed in the footwall scarp of the IFE at a greater density than other locations. (b) veining network and deformation bands are observed in the hangingwall of the IFE.

trending fault cross-cuts the IFE/EF5 common footwall, termed the EF5 cross-fault, and separates the main EF5 segment from a tip segment (Fig. 5.6). Two further faults have been mapped from the intersection area in the hangingwall of the Imperial Fault and are termed Circular faults 10 and 11 (Fig. 5.6) due to their curved plan view nature.

Excellent exposure of both footwall limestone markers provided good control on topographic profile variations. Little variation in the profile of the LL was recorded along the majority of the fault scarp with the exception of the intersection with the EF5 cross-fault which down-throws the LL by 15m to the SW (Fig. 5.20). Beds on the EF5 tip segment have an eastward dip toward the cross-fault (Fig. 5.6). A displacement value of c.45m was recorded close to the intersection location on EF5 (Fig. 5.20, Fig. 5.7c), signifying that the fault maintains a large value of displacement at intersection. The IFE has a recorded displacement value of approximately 8m from the intersection area (Fig. 5.8).

The IFE/EF5 intersection has greater complexity than those previously described. The plan view intersection geometry is simplified in a sketch figure (Fig. 5.21a). Importantly, a rectangular shaped promontory is identified from the common footwall of the intersection and bedding plane orientations show this area to be dipping steeply westward in contrast to the east dip recorded from the tip segment of EF5. Some internal deformation also exists with small E-W faults causing localised offset within the structure. The geometry of this structure can be defined as a footwall ramp where displacement decrease on the EF5 is facilitated by ductile bending of the beds in this area.

In addition, the Imperial Fault East hangingwall also dips westward (Fig. 5.21b) and is deformed by the circular faults (CF10, 11) that facilitate westward tilting, thus defining a hangingwall ramp. Interestingly, the plan view trace of these faults is sub-parallel to the strike of the EF5 fault and they emanate from the mapped intersection location. They have displacement values of c. 8-9m at their intersection with the Imperial Fault and decrease toward a SW tip. This observation suggests that they propagated outward from the Imperial Fault and it is possible that their presence is related to the intersection location. However, the 'hangingwall ramp' also occurs in the area between the IFE and the southern bounding fault of the Imperial Graben. The west study area has a lower topographic hangingwall datum (Fig. 5.21b) related to increasing values of displacement westward on this southern bounding fault of the Imperial Graben. Consequently, an alternative interpretation is that the hangingwall

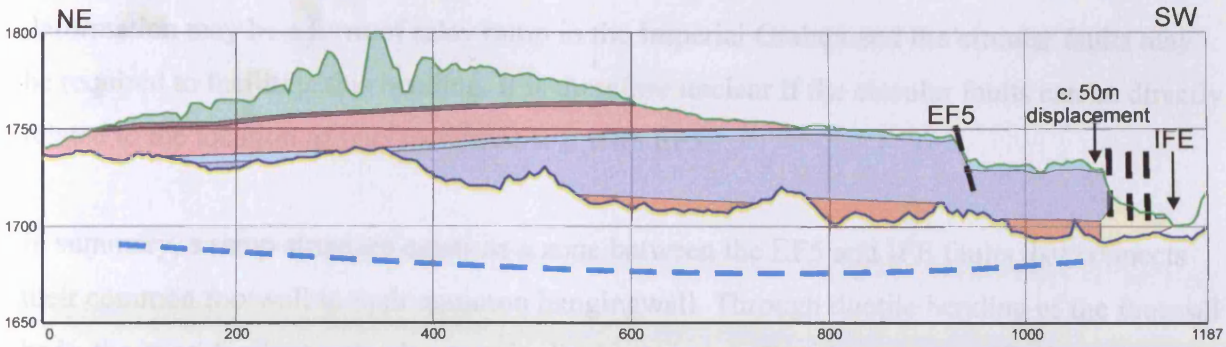

Figure 5.20. Allan fault plane map of EF5. Hangingwall outline in navy, footwall outline in green. The hangingwall profile shows that thick alluvium deposits are banked up against the EF5 scarp. Hangingwall LL is projected onto the line of section. The southwest extent of the fault scarp has a value of throw of c.50m. Throw decrease is via a ramp that is perpendicular to the line of section. A number of E-W faults cut the ramp. Colours of units as for the geological map (see Fig. 5.6). See Fig. 5.8 for line of section.

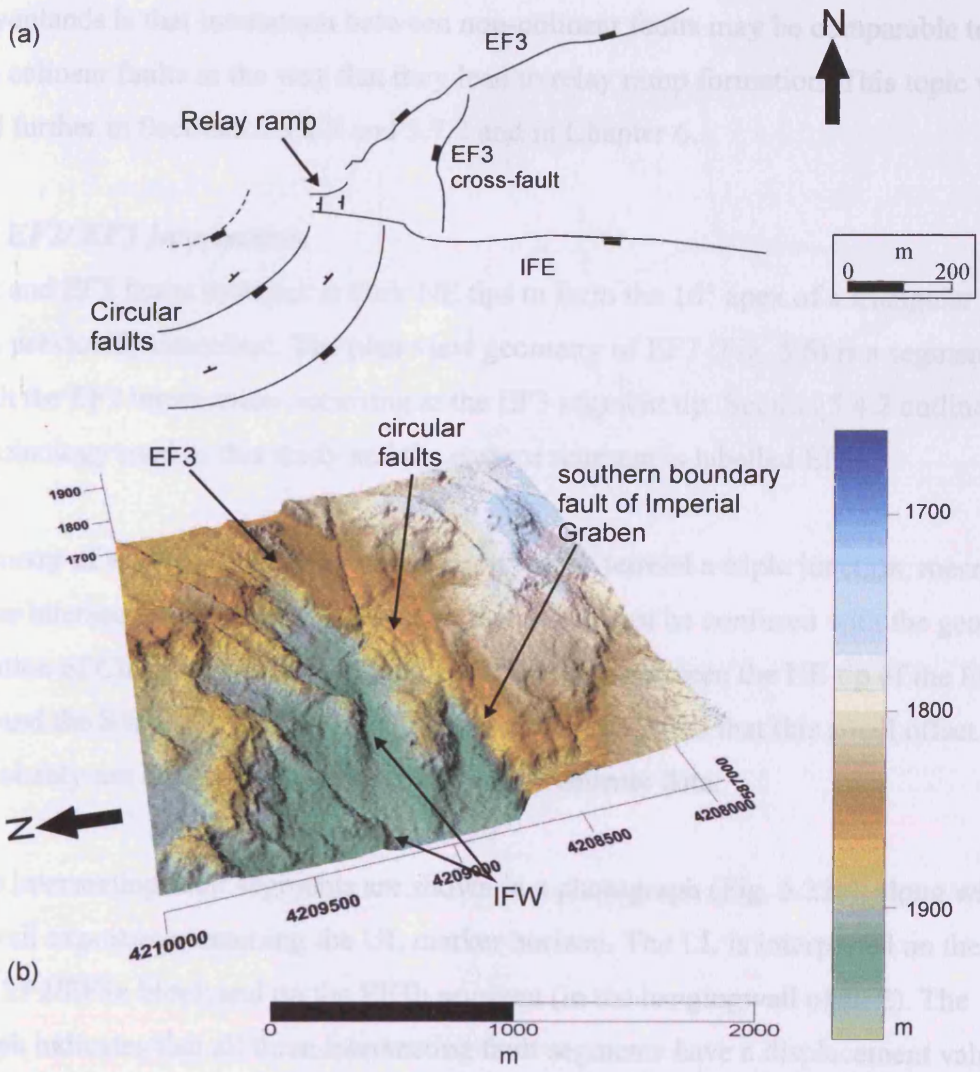

Figure 5.21. The EF3/IFE intersection. (a) Line drawing of the intersection area. A rectangular promontory (the relay ramp) is capped by LL that links the common footwall to the common hangingwall through bending of the bedding. Circular faults emanate from the intersection zone. (b) DEM of the study area. The circular faults form on the westward dipping area of the graben floor between the IFE and the southern bounding fault of the Imperial Graben. The topographic level of the western area is lower than that of the eastern area.

deformation may be a form of relay ramp in the Imperial Graben and the circular faults may be required to facilitate this bending. It is therefore unclear if the circular faults can be directly related to the location of intersection of IFE with EF5.

In summary, a ramp structure exists as a zone between the EF5 and IFE faults that connects their common footwall to their common hangingwall. Through ductile bending of the footwall beds, the ramp facilitates the decrease in displacement on EF5 from the significant value of 50m to zero. The southern boundary of this relay ramp is the IFE which has far lower values of displacement, as its hangingwall closely follows the same geometry.

The potential implication of this important observation from the high-angled intersections of the Canyonlands is that interaction between non-colinear faults may be comparable to that between colinear faults in the way that they lead to relay ramp formation. This topic will be explored further in Sections 5.5.2.3 and 5.7.2 and in Chapter 6.

5.5.1.6 EF2/ EF3 Intersection

The EF2 and EF3 faults intersect at their NE tips to form the 16° apex of a triangular horst block, as previously described. The plan view geometry of EF3 (Fig. 5.6) is a segmented fault trace with the EF2 intersection occurring at the EF3 segment tip. Section 5.4.2 outlined the fault terminology used in this study and the eastern segment is labelled EF3b.

The geometry of the EF2/EF3/EF3b intersection can be termed a triple junction, meaning that it involves intersection of three segments but this should not be confused with the geometrical classification of Chapter 2. There is a lateral shift of 25m between the NE tip of the EF3 segment and the SW tip of the EF3b segment. It should be noted that this small offset in trend would probably not be resolved on conventional 3D seismic data.

The three intersecting fault segments are shown in a photograph (Fig. 5.22a), along with a hangingwall exposure containing the UL marker horizon. The LL is interpreted on the common EF2/EF3a block and on the EF3b segment (in the hangingwall of EF2). The photograph indicates that all three intersecting fault segments have a displacement value at intersection. The value calculated from EF2 at the intersection is 16m and that for the EF3b segment is 29m. Interestingly, this adds up to 45m which is the value of displacement calculated from the EF3a segment at the intersection.

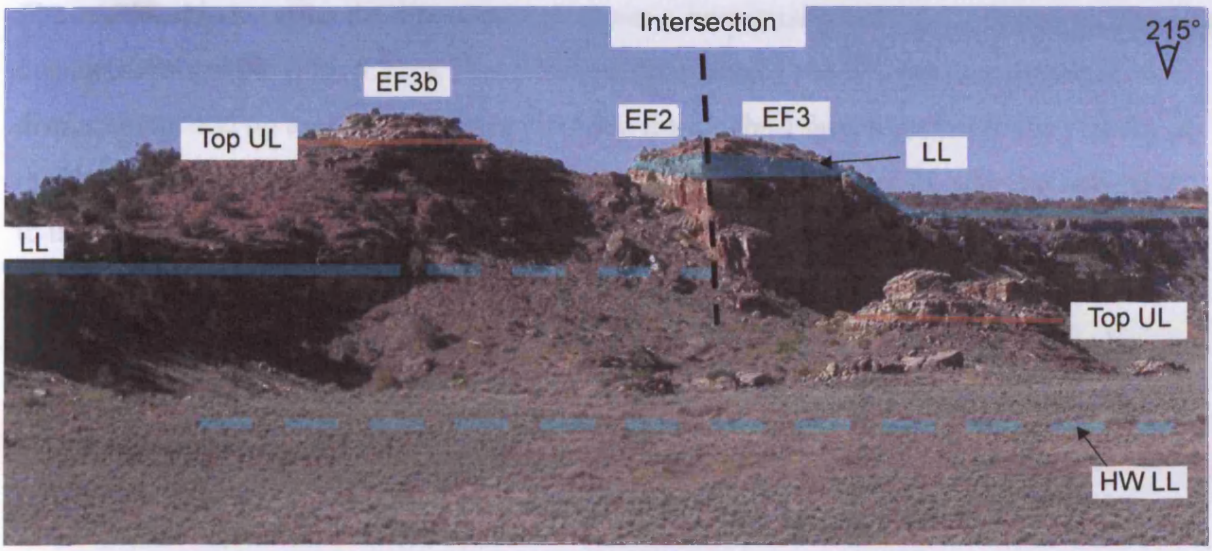

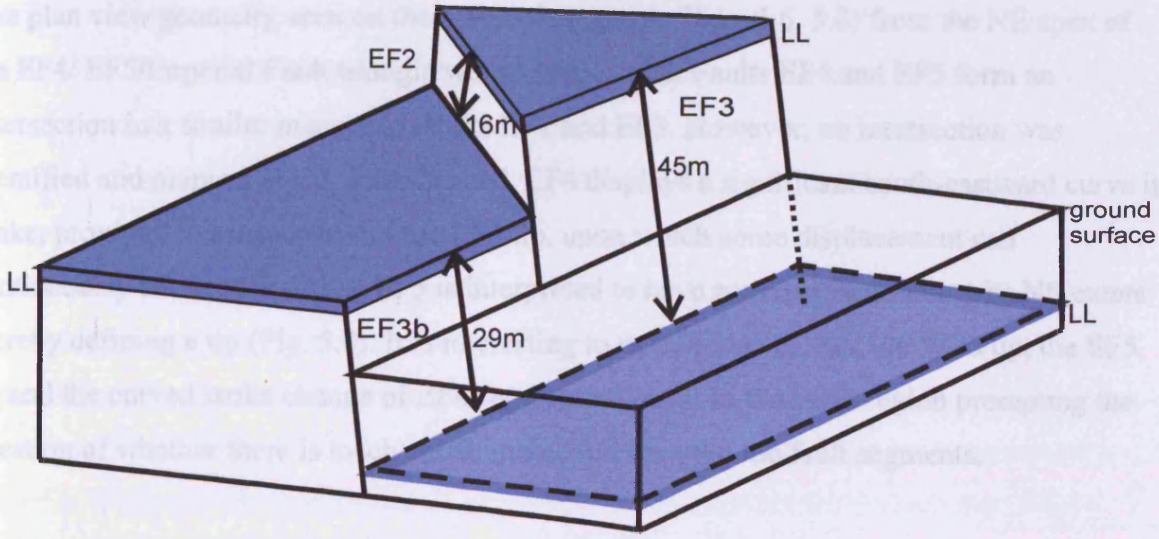

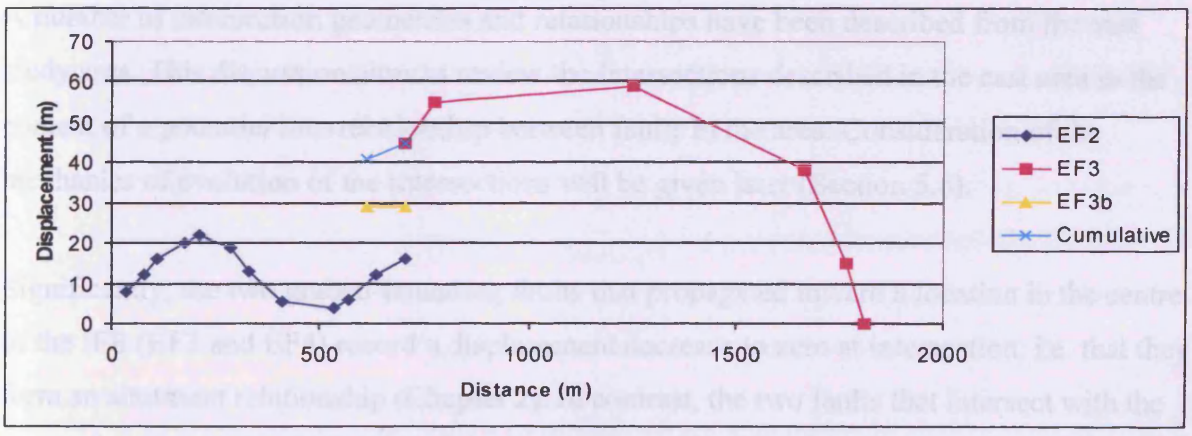

Figure 5.22. The EF2/EF3 intersection. (a) Photograph of the EF2/EF3 intersection. (b) Schematic block diagram of the EF2/EF3 intersection. (c) D-x plot of the EF2/EF3/EF3b faults. The cumulative value of displacement on faults EF2 and EF3b at intersection is equal to the value of displacement on EF3 at intersection.

The relationship between the three faults is shown schematically in Fig. 5.22b and on the joint displacement profile (Fig. 5.22c). This relationship, whereby the two smaller values of displacement add up to the larger value recorded from a third fault segment in the vicinity of the intersection, has been observed in the Gjallar Ridge PFS (Chapter 2), where it was taken to indicate an inter-relationship between all three faults at intersection. The near vertical nature of the Grabens faults results in a sub-vertical branch line which largely overcomes the issues described from shallower dipping fault planes e.g. slip vector re-orientation and dilation or overlap in the branch line area (see Chapter 6). For these reasons, branch lines in the polygonal fault system were interpreted as complex and likely to result in complex deformation but this complexity is not recorded in the Canyonlands study area.

5.5.1.7 EF4/EF5 Relationship

The plan view geometry seen on the aerial photograph (Figs. 5.6, 5.8) from the NE apex of the EF4/ EF5/Imperial Fault triangle would suggest that Faults EF4 and EF5 form an intersection in a similar manner to Faults EF2 and EF3. However, no intersection was identified and mapped in the field. Instead, EF4 displays a significant south-eastward curve in strike, proximal to the location of the EF5 tip, upon which some displacement can continuously be identified. The EF5 is interpreted to have zero displacement at its NE extent thereby defining a tip (Fig. 5.8). It is interesting to note, however, that the WF6 tip, the EF5 tip and the curved strike change of EF4 segment all occur in the same region prompting the question of whether there is mechanical interaction between the fault segments.

5.5.1.8 East Fault Intersections Discussion

A number of intersection geometries and relationships have been described from the east study area. This discussion aims to review the intersections described in the east area in the context of a potential interrelationship between faults in the area. Consideration of the mechanics of evolution of the intersections will be given later (Section 5.6).

Significantly, the two graben-bounding faults that propagated toward a location in the centre of the IFE (EF3 and EF4) record a displacement decrease to zero at intersection, i.e. that they form an abutment relationship (Chapter 2). In contrast, the two faults that intersect with the east and west extents of the IFE maintain a value of displacement at intersection, as does the IFE. This will be shown to be an important observation in Section 5.6. The potential implications of these observations raise the question: is there a mechanical reason for

abutment of the central intersections and linkages in the tip areas of the IFE? This will be further addressed in Section 5.6.2.

The observations of the plan view geometry of the eastern study area and the Grabens relationships with the IFE raise the question of whether growth of the entire area is interrelated. The schematic block diagram (Fig. 5.23) provides a synopsis of the geometry and displacement relationships formed in the eastern study area. D-x profiles from all constituent faults are plotted on the same profile (Fig. 5.24). There is a remarkable symmetry to the plot, discounting the EF4 profile, which may point toward a kinematic relationship between the east area faults.

The zero value at the left hand side of the plot relates to the zero displacement tip of EF4 in proximity to intersection with the IFE. From the D-L profile (Fig. 5.24) and previous description, EF5 has been interpreted to reach a tip at the surface location in proximity with EF4, whereas EF4 has been interpreted to continue along strike to the north-west. There is a significant displacement discrepancy between EF5 and IFE with approximately 50m displacement on EF5 and only 8m on the IFE. This intersection will be discussed in detail in Section 5.6.2. For this summary it is sufficient to note only that there is displacement on both faults at the site of intersection. The IFE/EF2 intersection records the same value of displacement from each fault and both show a decrease in displacement toward intersection. In contrast Fault EF2 and EF3 increase in displacement toward their intersection and have values of displacement at intersection, as does the EF3b segment with which they form a triple-segment intersecting relationship.

Based on the relationships described above, a kinematic model for the evolution of the east study area is proposed below and aims to provide a synthesis of the well constrained structural relationships. The Imperial Fault trend grew to something resembling its present form much earlier than the faults comprising the Grabens array. The propagation direction of the later grabens was toward the Imperial Fault. It is also striking that no graben faults cut across this trend thereby supporting an interpretation of lateral propagation toward intersection at the surface (Section 5.3.2.3).

Maximum displacement values, down-throw directions and strike of Faults EF3 and EF5 are strongly comparable. It is proposed that these faults propagated contemporaneously toward

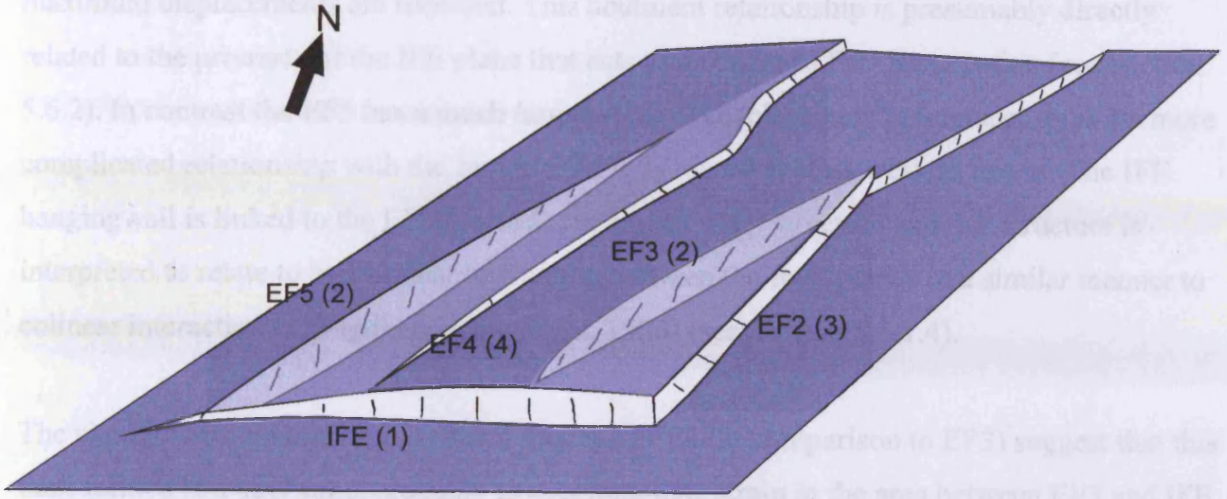

Figure 5.23. Schematic block diagram of the eastern study area. The IFE is interpreted as a pre-existing lineament (1). It forms linkages at its tips with EF5 and EF2. Propagation of the Grabens fault into the area adjacent to the IFE caused reactivation (2). EF3 and EF4 arrested propagation at the IFE. EF2 and EF4 may have been the latest to form (3, 4).

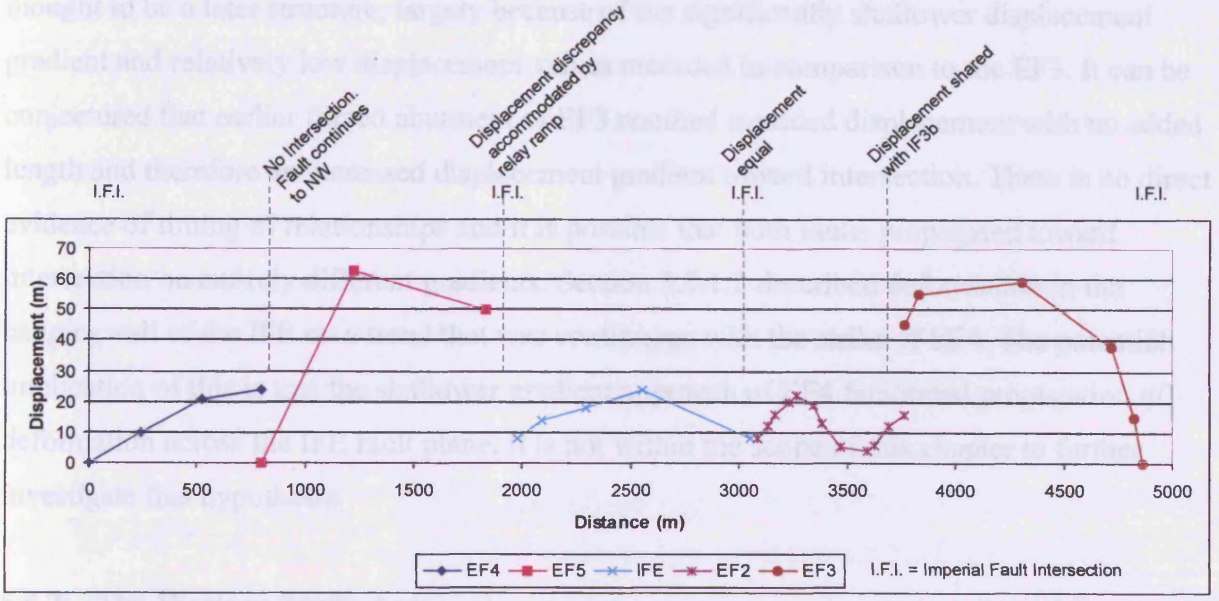

Figure 5.24. Combined D-x profile of the eastern study area faults. Faults are plotted from left to right: EF4, EF5, IFE, EF2 and EF3. The plot displays symmetry between the EF5 and the EF3.

the Imperial Fault. Interestingly, the displacement profile on EF3 decreases rapidly as it approaches the Imperial Fault in the centre of this fault plane, i.e. where present-day maximum displacements are recorded. This abutment relationship is presumably directly related to the presence of the IFE plane that acts as a barrier to EF3 propagation (see Section 5.6.2). In contrast the EF5 has a much larger value of displacement at intersection and a more complicated relationship with the Imperial Fault is recorded at its western extent. The IFE hangingwall is linked to the EF5 footwall via a relay ramp structure and this structure is interpreted to relate to mechanical interaction between the fault planes in a similar manner to colinear interaction (Trudgill and Cartwright, 1994) (see Section 5.5.1.4).

The significantly smaller displacement values of EF2 (in comparison to EF3) suggest that this fault formed at a later time, probably to accommodate strain in the area between EF3 and IFE caused by displacement inequalities. It is unclear if it formed as two segments or if the central displacement minimum relates to the E-W fault. EF2 forms a common footwall with the IFE and EF3 and is interpreted to be kinematically linked to both.

EF4 also shows an abutment relationship with the IFE where it has propagated toward a near-central location on the IFE where present-day displacement is high (c.f. EF3). It is also thought to be a later structure, largely because of the significantly shallower displacement gradient and relatively low displacement values recorded in comparison to the EF3. It can be conjectured that earlier forced abutment of EF3 resulted in added displacement with no added length and therefore an increased displacement gradient toward intersection. There is no direct evidence of timing of relationships and it is possible that both faults propagated toward intersection on entirely different gradients. Section 5.5.1.2 described deformation in the hangingwall of the IFE on a trend that was continuous with the strike of EF4. The potential implication of this is that the shallower gradient approach of EF4 facilitated propagation of deformation across the IFE fault plane. It is not within the scope of this chapter to further investigate this hypothesis.

5.5.2 The Western Study Area

The western study area includes all grabens faults to the west of the EF5 fault trace. They all displace strata to the SE with normal kinematics and all form half, rather than full graben structures. A series of tilted fault blocks are interpreted to reach zero displacement tips

without forming intersections (Fig. 5.8). Multi-directional fault intersections are formed between WF8 and the IFWa and the WF9 and IFWb.

5.5.2.1 Imperial Fault West/WF8 Intersection

The plan view geometry of the IFWa/WF8 intersection as mapped in the study area (Fig. 5.6) has an intersection angle of 119°. Stratal dips in the common footwall block are to the NW with strikes recorded trending mid-way between the strike of the constituent faults i.e. the dip direction is the bisector to the angles of fault strike and the fault block resultantly tilts away from the intersection location.

Displacement measurements are well constrained on the IFWa from exposure of both footwall LL and hangingwall LL at the ground surface (Figs. 5.6, 5.25). However, only one measurement was obtained from WF8 to the NE of the intersection location through indirect methods. Consequently there is less confidence in the interpretation of displacement increasing toward intersection on the WF8.

This IFWa reaches a zero displacement tip at its western extent at this surface location (Fig. 5.26). Displacement increases on a constant gradient of 0.09 toward intersection. The WF8 is also shown to increase in displacement toward intersection and this is the first example of an accidental intersection in this thesis where the maximum displacement from a high angled intersection is recorded on both faults at the intersection location. The implications for the kinematics of evolution of the intersection will be summarised in Section 5.6.2.

No deformation associated with the intersection is recorded from the IFWa/WF8 intersection and the branch line is near-vertical as are both fault planes. However, loose blocks, thought to be of the LS unit, are evident at the base of the fault scarps at the intersection location.

5.5.2.2 Imperial Fault West b/WF9 Intersection

The plan view geometry of the IFWb/WF9 intersection is almost identical to that of the IFWa/WF8 intersection. The WF9 forms an intersection angle of 119° with the IFWb segment. The intersection creates a similar tilted fault block geometry to that described from the IFWa/WF8 intersection; however, stratal dips are dominantly west rather than north-west.

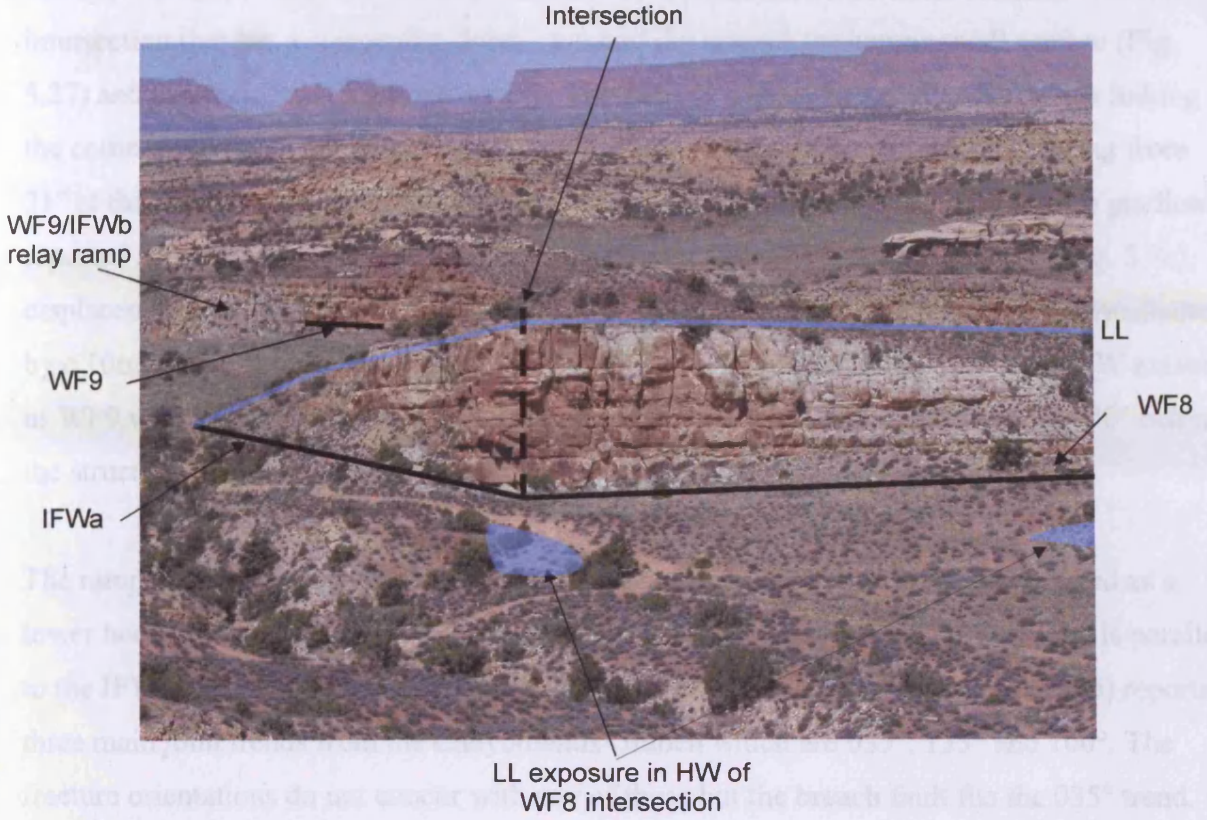

Figure 5.25. Photograph of the WF9/IFWa intersection. Displacement values are well-constrained from LL exposure in the hangingwall. Displacement values are equal at intersection. There is no associated deformation in the area of the branch line.

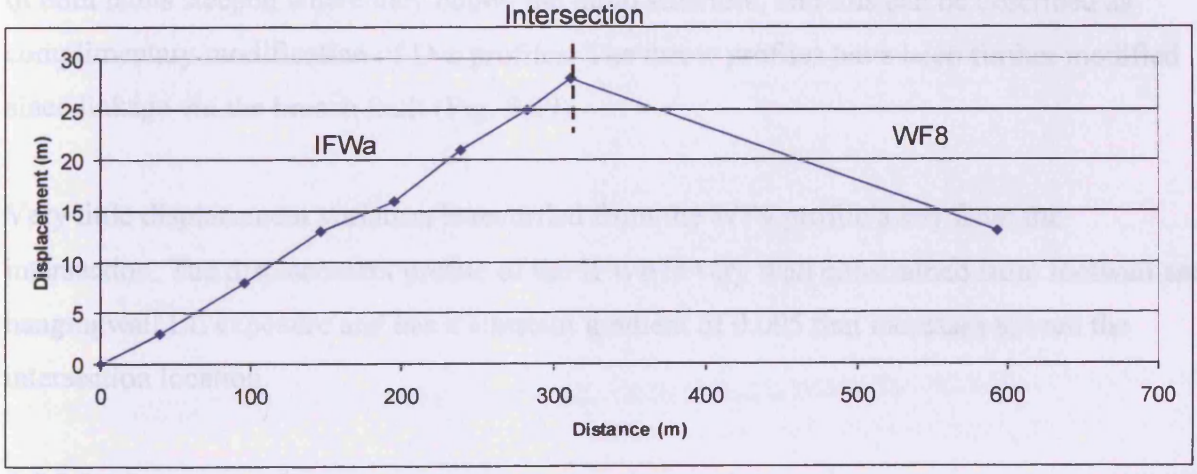

Figure 5.26. D-x plot of the IFWa and the WF 8. Both faults are plotted together. Distance is measured along the strike of the IFWa (left) from its western tip to the intersection location, then from the intersection location along the strike of the WF 8 (right) to its measured extent to the NE. Displacement is well-constrained on the IFWa. It displays a constant gradient of 0.09. The displacement profile of the WF 8 is less well constrained.

The main variation between the two intersections is that a structure exists at the IFWb/WF9 intersection that has a steepening-down eastward dip toward the hangingwall surface (Fig. 5.27) and can therefore be termed a ramp. The ramp is capped by LL (Fig.5.27) thus linking the common footwall LL with the common hangingwall LL. It has dip values ranging from 21° at the top to 49° at the base. It has a gradient of 0.41 which is larger than any tip gradient reported from elsewhere in the study area (Fig.5.29). The cross-sectional profile (Fig. 5.7c), displacement profile (Fig. 5.29) and photo (Fig.5.27) indicate that the structure is downfaulted by c.10m with respect to the common footwall block. This 'breaching fault' is the SW extent of WF9 which changes trend from the average 058° to a more N-S orientation of 030° behind the structure.

The ramp structure is heavily fractured with two main fracture orientations, displayed as a lower hemispheric stereoplot in Figure 5.28 equal to 090° and 180°. The 090° trend is parallel to the IFW but the 180° does not parallel WF9 nor the breach fault. Mansfield (1996) reports three main joint trends from the Canyonlands Graben which are 035°, 135° and 100°. The fracture orientations do not concur with any of these but the breach fault fits the 035° trend.

The combined displacement profile for the IFWb continuing to the WF9 is displayed as Fig. 5.29. The intersecting faults bound a common footwall block. The presence of the relay ramp modifies the displacement profiles of both the intersecting fault. The displacement gradients of both faults steepen where they bound the ramp structure, and this can be described as complimentary modification of D-x profiles. The throw profiles have been further modified since linkage via the breach fault (Fig. 5.29).

Very little displacement variation is recorded from the WF9 profile away from the intersection. The displacement profile of the IFWb is very well constrained from footwall and hangingwall LL exposure and has a constant gradient of 0.095 that increases toward the intersection location.

5.5.2.3 Summary of western area

The intersection relationships described from the west study area vary in geometry substantially from those of the east area. Both sets of intersections form between half-graben faults and a segment of the Imperial Fault West at the surface. In both cases the IFW segment

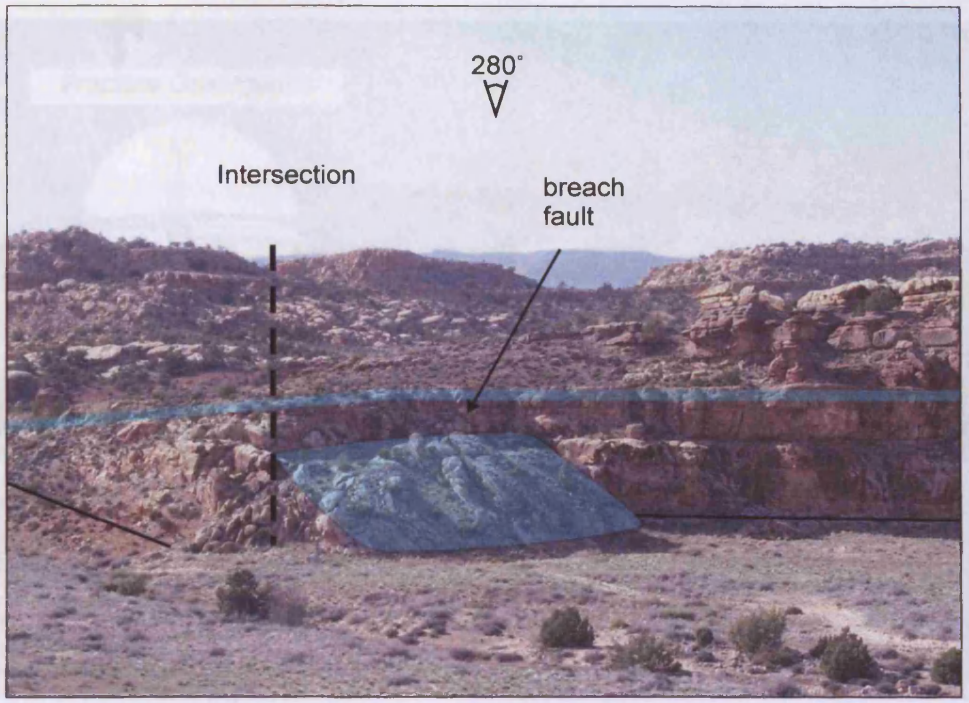

(a)

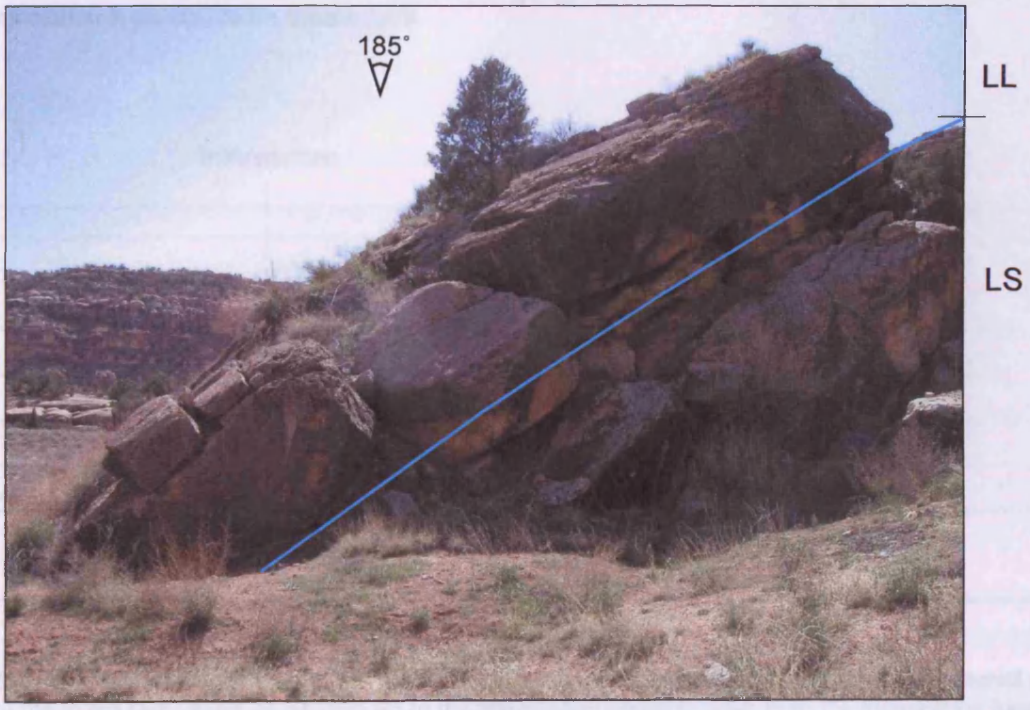

(b)

Figure 5.27. Photographs of the relay ramp that has formed at the intersection between IFWb and WF 9. (a) An area of rock is down-bent between the intersecting faults. A breach fault links the planes of the intersecting faults. The strike of the breach fault is not parallel to either the IFWb or WF 9. (b) View of the northern edge of the relay ramp. It is capped by the LL unit. It has a steep gradient and dip values increase downwards.

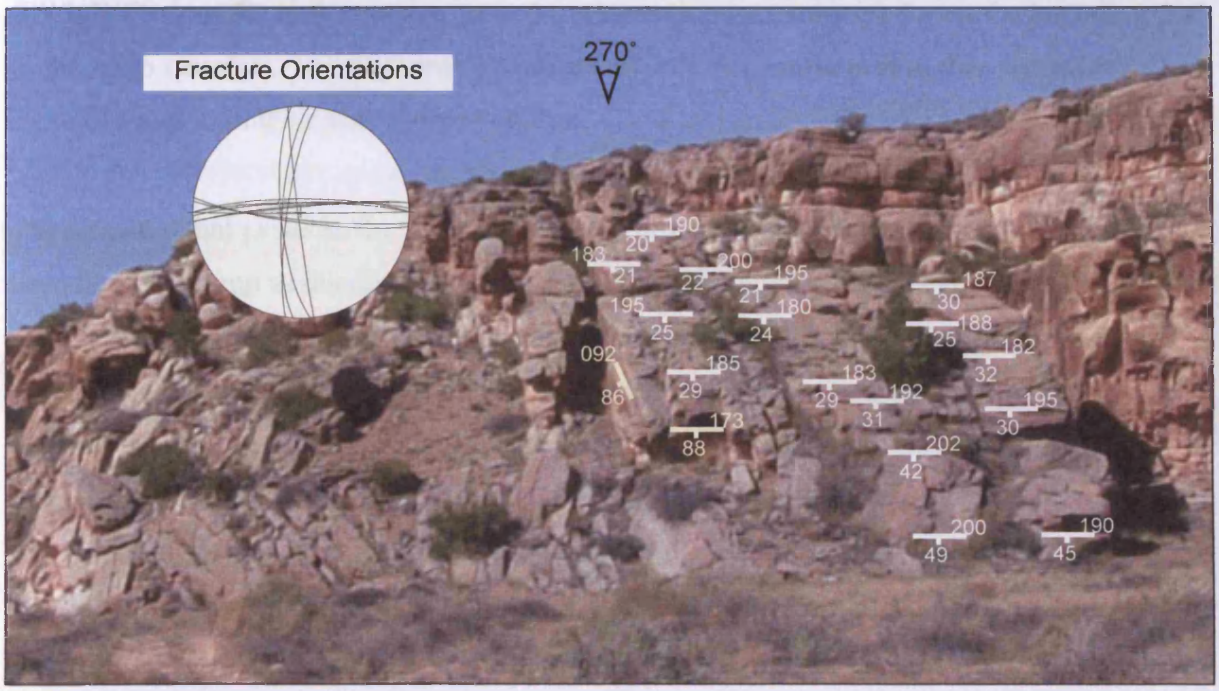

Figure 5.28. Orientation measurements of bedding plane dips (white) and fracture planes (yellow). There are two dominant fracture orientations - N-S and E-W (inset stereoplot). The E-W orientation is parallel to the IFWb. The N-S orientation is parallel to the breach fault.

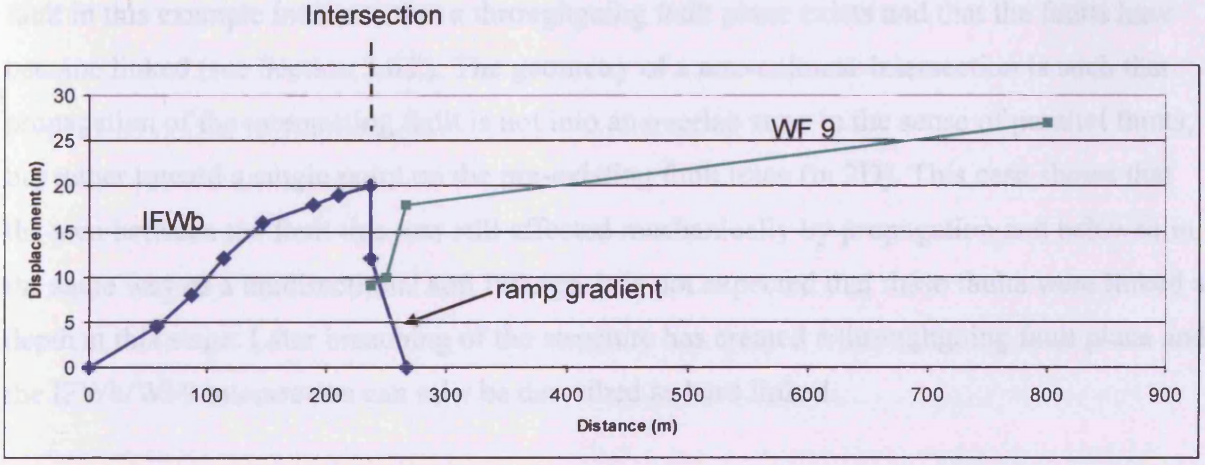

Figure 5.29. D-x profile of the IFWb and the WF 9. Both faults are plotted together. Distance is measured along the strike of the IFWb (left) from its western tip to the intersection location, then from the intersection location along the strike of the WF 9 (right) to its measured extent to the NE. Throw values on the IFWb increase toward the intersection location where it is downfaulted by the breach fault. The steep tip gradient of the ramp structure is labelled. The D-x profile of both faults is modified in the region of the intersection. Both D-x profiles have been modified by breaching.

increases in displacement from a zero tip to the intersection location. Only in intersection IFWb/WF9 does the IFW continue past the intersection location as it forms the bounding fault to the ramp structure. The west area intersections will be summarised in this section with some discussion of their kinematic evolution.

The structure that exists in the 'overlap' (see Section 5.6.2) between the IFWb and WF9 has been termed a ramp as ductile bending of beds is recorded from the area between the two fault trends. Steep displacement gradients are recorded from the D-L profiles of the two faults within this 'overlap' area. In this way it is analogous to a relay ramp in a colinear overlap of fault segments as reported from elsewhere in the Canyonlands study area and locations worldwide (e.g. Cartwright et al., 1996). The relay ramp described above, and that from the IFE/EF5 intersection are the only two examples of relay structures recorded from a multidirectional setting.

The relay ramp signifies that an evolutionary stage existed where the multidirectional faults were kinematically interdependent as displacement was transferred between the faults (i.e. soft linkage, Walsh and Watterson, 1991; Childs et al., 1995). It is potentially highly significant that the multidirectional faults should share displacement in this way. The breach fault in this example indicates that a throughgoing fault plane exists and that the faults have become linked (see Section 5.6.2). The geometry of a non-colinear intersection is such that propagation of the intersecting fault is not into an overlap zone in the sense of parallel faults, but rather toward a single point on the pre-existing fault trace (in 2D). This case shows that the area between the fault tips was still affected mechanically by propagation and behaved in the same way as a unidirectional soft linkage. It is not expected that these faults were linked at depth at this stage. Later breaching of the structure has created a throughgoing fault plane and the IFWb/WF9 intersection can now be described as hard linked.

A continuous fault plane from the IFWa to the WF8 is also identified with both faults having an equal value of throw at intersection location. This intersection is also hard linked and movement of both planes together has caused beds to dip away from the intersection location.

The WF8 is unique in this set of Grabens structures in that its maximum recorded displacement value exists at the intersection location rather than it decreasing in displacement toward intersection. This displacement distribution does not support simple determination of

kinematics from D-L distribution. However, the WF8 is interpreted as belonging to a set of half-grabens that are parallel, have stratal dip to the NW and cover the western study area. All other faults of this set decrease in displacement toward their SW extent which is commonly a tip. By analogy, interpretation of propagation direction on the WF8 to the SW is made with confidence. The increase in displacement toward intersection therefore may be anomalous as it is based on a single measurement. An alternative interpretation is offered as early linkage. Hard linkage may have occurred sufficiently early for the displacement profile to re-adjust as a single fault plane (Willemse, 1996). It is not possible to determine timing of linkage from the available data. It is possible that there was a soft linkage stage before hard linkage but that any potential ramp was not preserved.

The mode of propagation of the Imperial Fault is not known nor if the fault segments are linked at depth. It is interesting to note that both IFW segments have zero displacement tips at their western extent but maximum displacement values at intersection. One of the more interesting implications from these observations is that the propagation of the grabens faults toward the IFW segments may have actually caused reactivation of the IFW segments. This seems most likely if sigma 3 is oriented NW-SE and shear stresses are sufficiently high to overcome frictional stresses (Lisle and Srivastava, 2004). There are no sets of slip lineations that can help determine if this was the case.

5.6 DISCUSSION: EVOLUTION OF FAULT INTERSECTIONS

5.6.1 Fault Propagation

Fault displacement measurements are used in the study to interpret the propagation direction of faults and interrelationships between faults (e.g. Cartwright et al., 1996). However, it was only possible to describe variations from a limited stratigraphy and therefore not to understand evolution in three dimensions. It is therefore pertinent to consider the potential fault geometries in three dimensions. For example, would a fault relationship that does not actually intersect at the surface, form an intersecting relationship at depth?

The relationship with depth will be related to the shape of the propagating fault tip. For example, if the surface fault pattern samples a chord through the upper half of an elliptical fault, it can be assumed that fault lengths may be greater at depth and intersections may occur which are not recorded at the surface. In contrast, sampling a chord through the lower half of an ellipse predicts shorter fault lengths at depth.

Importantly, as described from Section 5.3.2.2, displacement values on faults in the Canyonlands array are not recorded to vary with depth (Cartwright and Mansfield, 1998) as would be expected from an elliptical fault. It was determined in section 5.5.2.3 that faulting initiated at the surface and therefore it is anticipated that fault length was established here. From these observations, the fault plane will have a rectangular tip geometry with fault lengths varying little with depth (although some tip line variation is expected). This suggests that branch lines that are identified from a surface location will be continuous with depth. In contrast, examples of described intersections where a tip on one fault is reached before formation of a branch line e.g. EF3/IFE, EF4/IFE and EF4/EF5 (where there was a particular question raised on intersection geometry with depth) are not predicted to form more evolved relationships at depth. Without further information, it is assumed that propagation and intersection kinematics identified at the surface hold over the entire depth section.

Fault tips have been identified that fit the type A tips described from Cartwright and Mansfield (1998). No process zones ahead of fault tips have been described (although they may be buried) and they are therefore thought to have formed under mode III loading conditions. However, the distinct lack of deformation and any kinematic indicators from fault planes is remarkable, and most likely implies some tensile component to failure. Indeed, Cartwright and Mansfield (1998) document mode III tips that pass laterally into mode I tips from their type B tips and these examples are thought to have initiated as mode I fractures. It is therefore possible that initial failure of the above investigated faults was under mode I loading conditions.

The displacement taper that has been recorded from the grabens faults toward intersection with the Imperial Fault, along with the identification of tips at the SW extent of grabens structures that do not intersect the Imperial Fault strongly argues for an evolution where propagation of the grabens was toward the intersection. Significantly, none of the grabens trend of faults cross-cut the Imperial Fault. This supports the interpretation of lateral propagation toward intersection and also fault initiation at the surface (as it is not thought that upward propagation would have been limited to the footwall of the Imperial Fault only, section 5.2.3.2). Beyond the eastern tip of the IFE, segments of the grabens trend, although not continuous, continue on the same strike past a projection of the eastern tip of the Imperial Fault. Therefore, in absence of the Imperial Fault, continued propagation to the SW is possible.

5.6.2 Kinematics of Intersection Relationships

The summary sections from the East (Section 5.5.1.8) and West (Section 5.5.2.3) study areas introduce the kinematics of the individual intersection relationships. This section intends to group together those intersections from either study area that display similar kinematics. The significance of these groups will be given further consideration in terms of a mechanical model in Section 5.6.3.

5.6.2.1 Abutment

The two grabens faults that decrease to a zero tip (Faults EF3 and EF4) before forming an intersection with the Imperial Fault both propagated toward its centre, which corresponds to the location of largest displacement values recorded from the Imperial Fault East. The implication of this is that the presence of the pre-existing Imperial Fault plane is the causative factor for abutment (see Section 5.6.3).

The EF3 intersection angle is acute and the displacement gradient is recorded to steepen toward intersection (c.f. T intersections, Chapter 2) to 0.3. In contrast, EF4 approaches intersection at the obtuse angle of 152° and shows no steepening of displacement gradient. Therefore, different intersection geometries, with different fault propagation styles, form the same type of intersection (Fig 5.30a).

5.6.2.2 Soft linkage

Two examples of intersections that record a soft linkage stage exist in the study area. Again, these occur with fault intersections of different plan view geometries. The simplest to identify in the field area was the WF9/IFWb intersection. This ramp structure that is preserved from the intersection records a stage of mechanical interaction before breaching to become a hard linked structure (Fig. 5.30b, Section 5.5.2.2). The WF9/IFWb intersection has an obtuse plan view geometry therefore an area of 'oblique overlap' can be defined (Fig. 5.31). In contrast, the EF5/IFE intersection is acute and the relay ramp that has been described from this intersection is not situated in a zone that could be termed an overlap (Fig. 5.31). The relationship between fault overlaps and intersection styles will be addressed in Chapter 6. This relay ramp is fractured but a single through-going fault could not be defined from the ramp area to create a hard linkage. The EF5 cross-fault does trend between the two intersecting structures and may act in this role. Alternatively, the acute angle of intersection may hinder the coherent action of both fault planes accruing slip together (but see below).

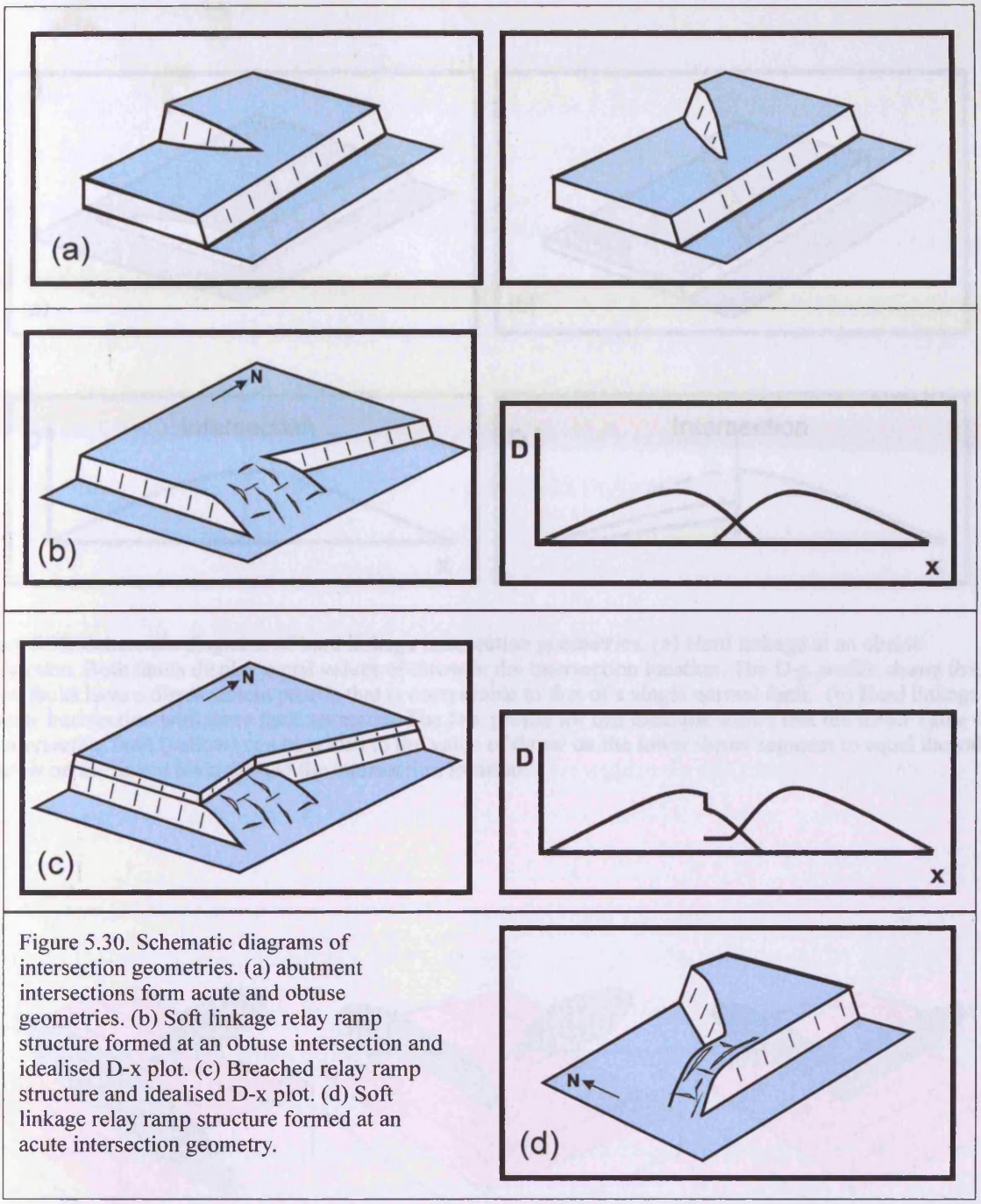

Figure 5.30. Schematic diagrams of intersection geometries. (a) abutment intersections form acute and obtuse geometries. (b) Soft linkage relay ramp structure formed at an obtuse intersection and idealised D-x plot. (c) Breached relay ramp structure and idealised D-x plot. (d) Soft linkage relay ramp structure formed at an acute intersection geometry.

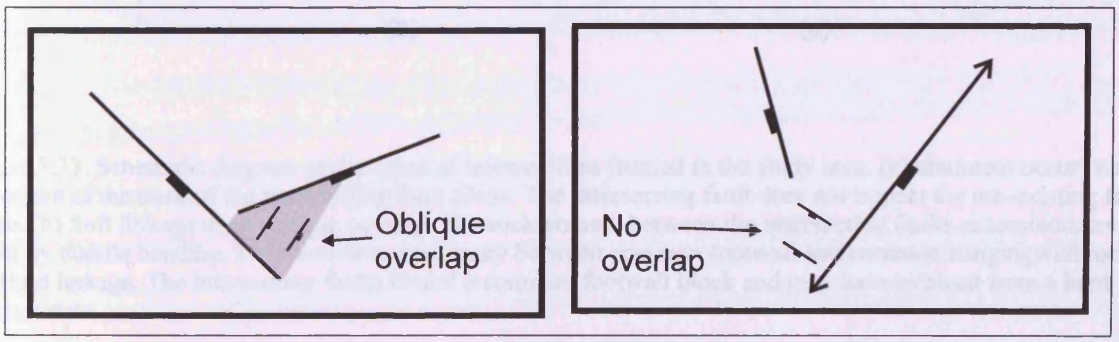

Figure 5.31. Simplified plan view diagram of (a) an obtuse intersection. A relay ramp structure forms in an area of oblique overlap between the faults. Faults dip concordantly. (b) an acute intersection. A relay ramp forms but faults are oppositely-dipping and do not overlap one another.

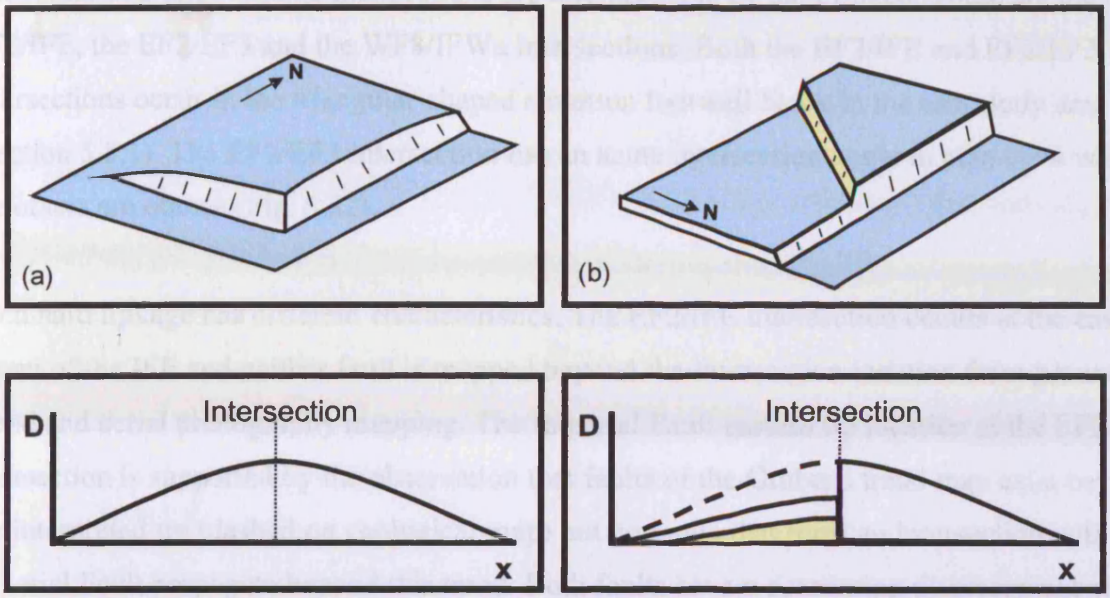

Figure 5.32. Schematic diagrams of hard linkage intersection geometries. (a) Hard linkage at an obtuse intersection. Both faults display equal values of throw at the intersection location. The D-x profile shows that the linked faults have a displacement profile that is comparable to that of a single normal fault. (b) Hard linkage at an acute intersection with three fault segments. The D-x profile for this example shows that the throw value on the intersecting fault (yellow) can be added to the value of throw on the lower throw segment to equal the value of throw on the linked main fault at the intersection location.

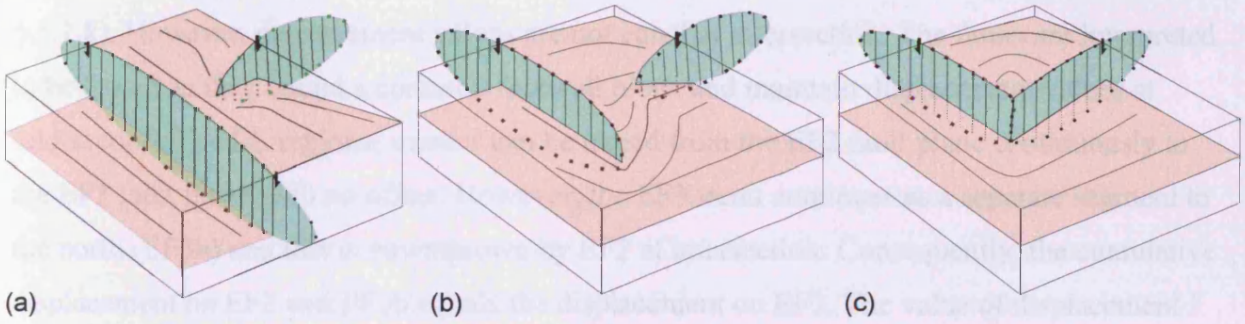

Figure 5.33. Schematic diagram of the types of intersections formed in the study area. (a) abutment occurs near the centre of the trace of the pre-existing fault plane. The intersecting fault does not impact the pre-existing fault plane. (b) Soft linkage at an oblique overlap. The rock volume between the intersecting faults accommodates strain by ductile bending. This facilitates continuity between common footwall and common hangingwall rocks. (c) Hard linkage. The intersecting faults bound a common footwall block and may have evolved from a hard linkage state.

5.6.2.3 *Hard Linkage*

The remaining three studied intersections are interpreted to be hard linked. These are the EF2/IFE, the EF2/EF3 and the WF8/IFWa intersections. Both the EF2/IFE and EF2/EF3 intersections occur in the triangular-shaped common footwall block in the east study area (Section 5.5.1). The EF2/EF3 intersection has an acute intersection angle in plan view while the others are obtuse (Fig. 5.32).

Each hard linkage has different characteristics. The EF2/IFE intersection occurs at the eastern extent of the IFE and neither fault is mapped beyond the intersection location from ground-based and aerial photography mapping. The Imperial Fault eastern tip location at the EF2 intersection is supported by the observation that faults of the Grabens trend may exist beyond the interpreted tip (dashed on geological map) but no faults that form an intersection with the Imperial Fault propagate beyond this trend. Both faults have a decreasing displacement profile toward intersection and equal values of displacement are recorded at intersection. This suggests that the faults are kinematically linked in a manner that is analogous to a hard linkage of colinear faults and that this occurred through propagation of EF2 toward the IFE tip. The value of displacement recorded at intersection equals the displacement that has accrued since linkage (see Section 5.6.3).

The EF2/EF3 intersection at the apex of the eastern triangular horst is also interpreted as a hard linkage indicating a kinematic relationship between the IFE, EF2 and EF3 (see Section 5.5.1.8). However, displacement values are not equal at intersection. The faults are interpreted to be linked as they bound a common footwall block and maintain displacement values at intersection. The LL regional marker can be traced from the EF2 fault plane continuously to the EF3 fault plane with no offset. However, the EF3 trend continues as a separate segment to the north (EF3b) and this is downthrown by EF2 at intersection. Consequently, the cumulative displacement on EF2 and EF3b equals the displacement on EF3. The value of displacement on EF2 at intersection is the value of post-linkage displacement on the linked EF2-EF3 and is equal to 16m.

This value is approximately double that of the value recorded at intersection of EF2 with the IFE (within error). This can lead to a number of interpretations related to the kinematics of the EF2: (a) linkage of EF2/IFE was later than that of EF2/EF3; (b) two segments of the EF2 exist or (c) the common footwall cross-fault was required to accommodate the displacement

discrepancy. Displacement sharing at a triple junction has been recorded by Tervoort (1998) and Nicol et al., (2003).

5.6.3 Mechanical Model

The above grouping of intersection relationships through consistency in their interaction with the Imperial Fault can be discussed in the context of mechanics of intersecting faults. In particular, the observations that no faults cross-cut the Imperial Fault but either form abutment or linkage relationships with it suggests that the mechanics of intersection can be related to the presence of the Imperial Fault embedded into an otherwise mechanically uniform region. The heterogeneity represented by the existing Imperial Fault trend was evidently sufficient to block the advance of the laterally propagating graben array.

The intersection observations can be summarised into two groups: those graben faults that intersect with a central portion of an Imperial Fault segment form abutment relationships; and those that intersect with an Imperial Fault segment tip form linkage relationships.

The tip areas were able to interact mechanically to form linkages and this is thought to relate to fault tip stress concentration allowing fault propagation in these areas. It is therefore argued that the propagation of the grabens faults to a proximal location to the IFE caused reactivation of the IFE. It is interesting that the IFE/EF2 intersection (and possibly the IFWa/WF8 intersection) show hard linkage at a 'corner', with no continuation of either plane past the intersection. It is not possible to rule out the possibility that the IFE trace continues past intersection but is not identified at the surface. However, other examples, namely the IFWb/WF9 intersection records soft linkage from such an 'oblique overlap'. Therefore, it seems most likely that this example records hard linkage at an 'L-geometry' intersection. It is thought that this would occur through interaction of any process zones at the segment tips where crack tip intensity is enhanced (although no associated deformation was recorded) and it is likely that this configuration is rare in nature.

The abutment relationships are comparable to those described from Subset 1 orthogonal intersection geometries from the Gjallar Ridge PFS (Chapter 2). If it is considered that the IFE has been reactivated by growth of the Grabens array then it is proposed here that propagation into the zone of greatest stress drop across the IFE plane, corresponding with greatest displacement on the IFE plane, led to the arrested propagation of faults EF3 and EF4.

Due to the lack of shear strength on the IFE plane, it cannot transmit crack tip stresses from the propagating faults and acts as a free surface. Alternatively, abutment may also occur during inter-slip periods. Because the Imperial Fault breaks the surface, there is almost no σ_3 acting on the fault plane. Since the fault plane is almost vertical there is a good chance that the fault zone is 'open' i.e. a fissure. This means that it is effectively a free surface. When an intersecting fault touches the 'zone' within 10s of metres of a free surface, the tip stress field must be altered considerably by the presence of this free surface, and this prevents ongoing propagation.

From the available evidence, the Imperial Fault can be viewed as a pre-existing lineament, related to tectonic events that significantly pre-dated the evolution of the Canyonlands Grabens (Section 5.3.1). It is unclear however, whether the fault remained active throughout the interval between initiation and the much more recent development of the grabens. The question of whether relatively earlier faults only cause mechanical interaction if they are kinematically active remains an interesting idea that would be suitable for further research. From the observation that grabens faults form hard linkages with IFW segments at the surface, it was suggested that as faults of the Grabens array propagate closer to the Imperial Fault, their zones of lateral tip stress concentration may lead to reactivation of the long inactive Imperial Fault. It is know that faulting locally perturbs the stress field (e.g. Mandl, 2000). The local reorientation of principal stresses, by decreasing $\sigma 2$ such that the intermediate and minimum principal stresses swap over, may be preferentially aligned for reactivation of the Imperial Fault segments (Lisle and Srivastava, 2004).

5.6.3.1 Evolutionary model

There is no evidence from the Canyonlands study that abutment can proceed to linkage from the evidence provided above. The two examples of abutment (EF3 and EF4) propagated toward a central surface location on the IFE plane that corresponded to the Dmax. location. If they were able to continue propagation to link with the IFE, they would have to effectively 'split' the Imperial Fault plane to succeed. This would separate the two triangular active horsts and leave a central inactive segment (combined hangingwall splays, Trudgill and Cartwright, 1994). There is little evidence that this can be achieved. However, it should not be discounted completely, since there is direct evidence for soft to hard linkage at the Imperial Fault segment tips

Breaching of the ductile relay structure that represents the soft linkage stage between interacting faults is reported from many unidirectional fault systems (Huggins, 1995, Peacock and Sanderson, 1991, Morley, 1990, Walsh and Watterson, 2001, Soliva et al., 2004). Here, there is evidence from the IFWb/WF9 intersection that the same process occurs for interacting faults that are non-colinear.

Three stages of mechanical interaction are recognised from the south of the Canyonlands National Park (Fig. 5.33):

1) Abutment – propagation on the intersecting fault is arrested where propagating toward the centre of the pre-existing fault plane which acts as a free surface.
2) Soft Linkage – propagation of the intersecting fault toward a tip zone of the pre-existing fault causes modification of stress fields which manifests as displacement gradient steepening and formation of a ductile relay ramp structure that forms a continuation between common footwall to common hangingwall.
3) Hard Linkage – either through breaching of a relay ramp or direct mechanical interaction at tips, a throughgoing fault plane is formed with a significant strike change at intersection. The intersected faults slip as a single structure.

No abutment relationships are recorded to evolve to a soft linkage stage but a transformation from soft-to-hard linkage is thought to be common. It is probable that an abutment intersection in close proximity to a tip of the pre-existing plane could evolve to a soft and then hard linkage. No examples of any type of intersection propagating across the pre-existing plane are documented and it is thought to be unlikely in this setting as intersections preferentially form mechanical relationships with the pre-existing fault.

5.7 CONCLUSIONS

This chapter has provided a detailed analysis of sub seismic-scale fault interactions from a well-exposed array in SE Utah. The main findings of this case study are summarised below:

- Updated geological mapping has increased detailed knowledge of the fault distribution and displacement variations.
- Displacement variations document lateral propagation towards the Imperial Fault to form intersections and mechanical interaction between the Grabens and the Imperial Fault trend.

- Relay ramp features have been identified from non-colinear intersections in locations close to the tips of the Imperial Fault segments. Relay ramp structures represent kinematic interaction between the intersecting faults.
- The geometry of the relay ramp and complimentary modifications of D-x profiles are analogous to those associated with soft linkage of colinear faults, indicating that the non-colinear faults form a soft linkage evolutionary stage.
- There are significant geometrical variations between colinear and non-colinear soft linkages. Firstly, a parallel overlap zone between the faults does not form. Instead, the intersecting fault propagates toward a single location on the pre-existing fault trace. Secondly, the intersecting faults bound a common footwall and common hangingwall therefore the ramp does not create a continuous layer from the footwall of one fault to the hangingwall of the other but rather from the footwall of both to the hangingwall of both.
- The intersecting faults in this study form one of three mechanical interaction stages: abutment, soft or hard linkage. Abutment is recorded from faults that propagate toward the centre of a pre-existing plane at the surface and soft or hard linkage from faults that propagate toward the tips. Abutment is related to the presence of the pre-existing fault which acts as a free surface in the area of greatest throw values. In contrast, the tip areas are able to link due to increased stress intensity at lateral tips.
- Evolution of a soft linkage stage to a hard linkage stage is recorded through breaching of a relay ramp to form a continuous plane and addition of slip on both intersecting faults after breaching.
- Propagation of the younger grabens faults into the area adjacent to the Imperial Fault caused reactivation of the older Imperial Fault lineament, thus permitting mechanical interaction between the intersecting faults.
- It is unlikely that the different stages of mechanical interaction would be distinguished from one another (particularly abutment from soft linkage) on conventional 3D seismic data. Correct interpretation of the intersection geometries has implications for understanding fluid flow and compartmentalisation of reservoirs.

CHAPTER 6: DISCUSSION

6.1 INTRODUCTION

In this study, fault systems from three 3D seismic datasets and a field study have been analysed to further understanding of the 3D geometries and evolutionary styles of fault plane intersections in non-colinear fault arrays.

Many of the issues addressed in this thesis have already been discussed in Chapters 2, 3, 4 and 5 and will not be discussed further in this chapter. In this chapter two key themes of (1) the evolutionary stages of intersection, and (2) branch line evolution are discussed in more detail based on observations made in the different case studies. The evolution of intersections described in this thesis can be grouped into those that form through accidental intersection and those that form through branching intersection. This chapter particularly focuses on the evolution of accidental intersections in Section 6.2 because a number of stages have been identified that are associated with this type of intersection. These stages are defined (Section 6.2.1. – 6.2.4) and the question of evolution between these stages is addressed (Section 6.2.5). The importance of branching intersections as a form of network evolution is discussed in Section 6.3. The style of evolution of the branch line in accidental intersections has implications for the specific evolutionary stages and this is addressed in Section 6.4. Finally, the implications of this thesis study for industrial applications are discussed and the chapter concludes with suggestions for further work.

6.2 ACCIDENTAL INTERSECTION EVOLUTION

Accidental intersections have been interpreted to be an important evolutionary style in a variety of natural fault systems (Chapters 2, 3, 4 and 5). Based on this sample of diverse structural settings, it can be inferred that it is common for non-colinear fault intersections to evolve through propagation of an intersecting fault toward a relatively older fault plane.

Accidental intersections are best defined as such from observations of throw decrease on the intersecting fault toward the intersection location. They can have a characteristic hooking geometry (e.g. Chapters 2 and 3), in which case accidental intersection is the most likely

interpretation. T class intersections generally form through accidental intersection (Chapter 2) but they are also recorded from Y class (Chapters 2 and 5) and TR class (Chapter 2) intersections. Importantly, accidental intersections are defined as forming between two separate structures that are entirely independent in (a) 3D geometry and (b) kinematic evolution, prior to intersection.

A number of stages of accidental intersection have been introduced throughout this thesis that describe the relationships between intersecting faults. These are termed abutment, soft linkage, hard linkage and cross-cutting. This section aims to define systematic criteria for identification of each stage of interaction. The terminology of soft and hard linkage was originally defined for fault systems that form in a stress regime with a dominant extensional orientation, thereby forming parallel, overlapping and underlapping colinear fault arrays, but elements of this terminology can be applied to non-colinear systems. This original terminology was defined on geometry alone (Walsh and Watterson, 1991) and only subsequently related to the kinematics of linkage.

Soft-linked faults have been defined as those between which a mechanical and geometric continuity is achieved by ductile strain of the rock volume between them, rather than by continuity of their fault surfaces (Walsh and Watterson, 1991). This zone of bending is the relay ramp (Peacock and Sanderson, 1994; Huggins et al., 1995; Trudgill and Cartwright, 1994). Displacement transfer at the relay ramp is accompanied by steep displacement gradients along normal fault segments that overlap in plan view (e.g. Peacock and Sanderson, 1994). Complimentary modifications of displacement patterns on overlapping faults are diagnostic of relay zones. Hard linkage is defined for faults in which fault surfaces are linked on the scale of the map or cross-section in use (Walsh and Watterson, 1991) and commonly evolves through breaching of the relay ramp to become a kinematically coherent structure (Peacock and Sanderson, 1994).

A fundamental question arising from simple consideration of the contrasting intersection geometry of non-colinear faults and colinear arrays is whether the phenomenology of linkage that has been derived in the past two decades from colinear systems can be used to explain the processes involved in linkage in non-colinear systems. For accidental intersection specifically, a number of subsidiary questions arise:-

- Should comparable stages of interaction to those derived from colinear arrays be expected in non-colinear arrays?
- Can the terms soft and hard linkage be applied for non-colinear faults?
- What is the significance of cumulative displacement profiles?
- Can an evolutionary sequence between stages be recognised uniquely?

The following discussion considers an idealised orthogonal intersection to address these questions, but this discussion would equally apply to any other geometrical form of accidental intersection.

6.2.1 Abutment

The abutment stage was described in Chapter 2 from the observation that the majority of intersecting faults terminate with their lateral tip abutting against the main fault, with seismically resolvable undeformed volume separating the tip from the main fault plane. From this, the presence of the pre-existing plane was inferred to act as a restriction to propagation of the intersecting tip (Nicol et al., 1996; Wilkins and Gross, 2002). Further, some of these intersecting faults displayed an anomalously high lateral tip gradient compared to the values recorded from 'free' or unrestricted lateral tips. Examples of abutment relationships from the Canyonlands were identified with both an increased tip gradient (EF3) and with no increased tip gradient (EF4) (Fig. 6.1, Section 6.2.5). Accepting that this is only a small sample, it can nonetheless be asked: should the criteria for abutment include a specification regarding an anomalously high lateral tip gradient on the intersecting fault in the vicinity of the abutment?

The increased lateral tip gradient signifies some form of mechanical interaction between the intersecting faults. Can we go further in this argument and ask whether the recognition of a mechanical relationship then necessarily indicates that a state a soft linkage exists between the intersecting faults? The increased lateral tip gradient most likely signifies skewing of accumulation of additional slip towards the restricted tip (Wilkins and Gross, 2002). The restriction caused by the presence of the main fault can be seen to affect the T-x profile of the intersecting fault, but a complimentary perturbation of slip accumulation is not observed on the main fault. The widely used definition of soft linkage in colinear systems included a criterion of a complimentary modification of displacement patterns of both fault segments (Huggins et al., 1995). It is therefore argued that if only the T-x profile of the intersecting fault is seen to be modified, then the interaction stage should be regarded as that of abutment.

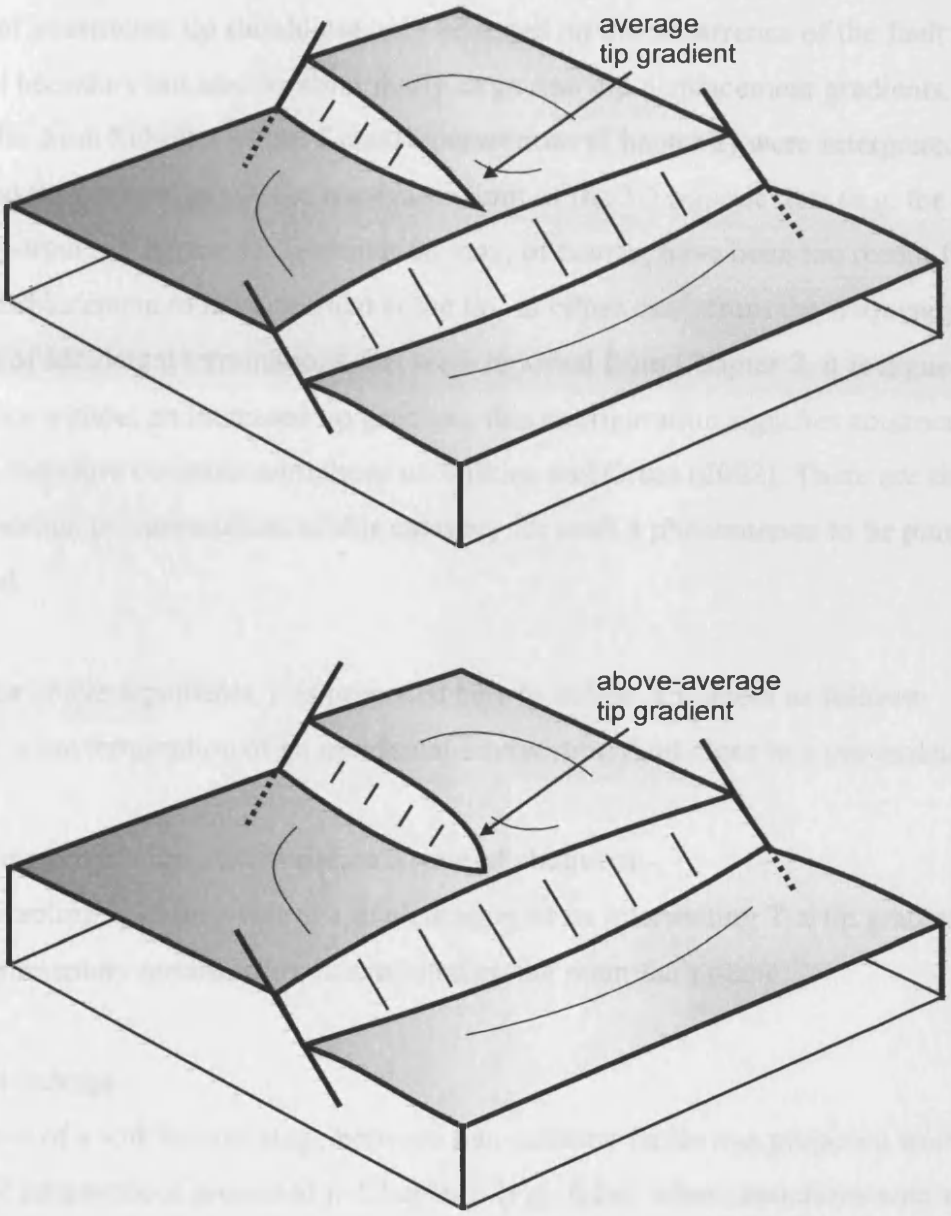

Figure 6.1 Schematic diagrams of abutment intersections. (a) The intersecting fault throw is decreasing to a zero value tip toward intersection on a constant tip gradient. (b) The intersecting fault throw is decreasing to a zero value tip toward intersection and the tip gradient is increased adjacent to the intersection location.

Following from the argument above, does a lack of increased tip gradient signify no mechanical relationship with the main fault, and that termination of the intersecting fault in this location is therefore purely coincidental? Wilkins and Gross (2002) concluded that a definition of a restricted tip should not only be based on the occurrence of the fault tip at a mechanical boundary but also by abnormally large near-tip displacement gradients. Many of the examples from Subset 1 of the T class intersections (Chapter 2) were interpreted to have an increased tip gradient below the resolvable limit of the 3D seismic data (e.g. the EF3 tip gradient reported in Chapter 5). Termination may, of course, have been too recent for enhanced displacement to have accrued at the tip. In either case, from the frequency of occurrence of accidental terminations that were reported from Chapter 2, it is argued that either with or without an increased tip gradient, this configuration signifies abutment and this conclusion therefore contrasts with those of Wilkins and Gross (2002). There are simply too high a proportion of intersections of this category for such a phenomenon to be purely coincidental.

Based on the above arguments, it is proposed here to define Abutment as follows:
"Abutment is the termination of an accidental intersecting fault close to a pre-existing fault plane".
The following criteria are used to define a state of abutment:-
1. The intersecting fault may record a modification of its intersecting T-x tip gradient.
2. No complimentary modification is exhibited by the main fault plane.

6.2.2 Soft linkage

The existence of a soft linkage stage between non-colinear faults was proposed from examples of intersections presented in Chapter 5 (Fig. 6.2a), where structures with all the usual geometrical characteristics of relay ramps were observed in oblique intersection configurations. Evidence of ductile deformation between non-colinear intersecting faults, and modification of T-x profiles of both intersecting faults, shows that distinct similarities exist with the description of colinear soft linkage in the fault analysis literature. This raises the interesting possibility that the progression from soft-hard linkage states now widely accepted for colinear systems, might also apply in the vastly contrasting geometrical situations investigated in this thesis. Could relay ramps be as commonly developed in non-colinear intersections and linkage as they are in segmented, colinear arrays?

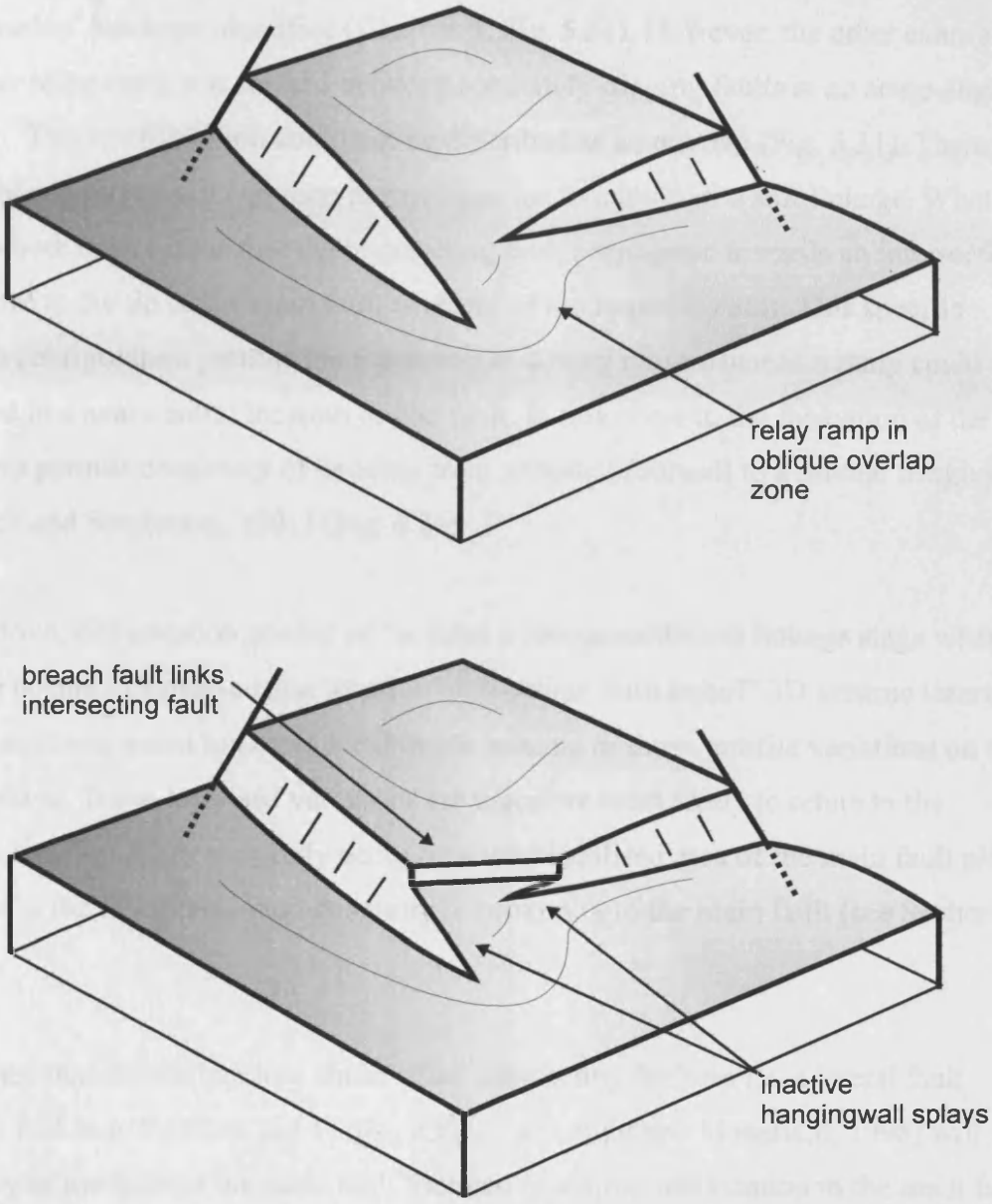

Figure 6.2. Schematic diagrams of non-colinear fault interaction at the 'oblique overlap' of the intersecting fault tips. (a) a relay ramp, signifying soft linkage, can form though intersection in this location. (b) breaching of the relay ramp forms a hard linkage.

The contrast in geometry does lead to certain basic differences in the soft-linked array configuration. For example, in non-colinear arrays, the development of true overlaps is precluded. One clear example of a relay ramp forming at what could be described as an 'oblique overlap' has been identified (Chapter 5, Fig. 5.31). However, the other example of a non-colinear relay ramp was formed between oppositely-dipping faults at an acute-angled intersection. This configuration could not be described as an overlap (Fig. 5.31). Therefore, the 'overlap' region is not a common prerequisite for formation of a soft linkage. What is common to both examples is that the intersecting fault propagated towards an intersection position close to the tip of the main fault segment of the Imperial Fault. This specific intersection configuration permits the formation of a relay ramp whereas a ramp could not have formed in a near-central location on the fault. In this context, the formation of the oblique ramp permits continuity of bedding from a mutual footwall to a mutual hangingwall (c.f. Peacock and Sanderson, 1991) (Fig. 6.2a).

From the above, one question arising is: 'Is there a recognisable soft linkage stage where an intersection occurs in a near-central location on the main fault trace?' 3D seismic intersection examples have been noted to record local throw minima or throw profile variations on the main fault plane. These localised variations are therefore most likely to relate to the intersection location. They may only occur on a very localised area of the main fault plane with respect to the full intersection geometry in proximity to the main fault (see Section 6.4.1).

It is envisaged that ductile bending ahead of an intersecting fault tip i.e. a lateral fault propagation fold (e.g. Peacock and Parfitt, 2002; Cartwright and Mansfield, 1998) will impact the geometry of the beds of the main fault footwall in a proximal location to the main fault plane, and this may result in the localised variations in T-x profile on the main fault (Fig. 6.3). From this, it can be asked: 'Is this variation actually an active slip response on the main fault plane, or is it a passive response of the slip profile to the geometry of its footwall bedding?' The very small inflections on the main fault profiles commonly show no variation away from the intersection location. Addition of the ductile component of displacement on the intersecting fault profile to the local minimum on the main fault may smooth out the variation. In this way, the main fault variation does appear to exhibit a mutually complementary displacement geometry at the intersection location. It is likely that at any stage, slip on the

main fault can continue independently of the intersecting fault, but continued slip on the intersecting fault will further modify the T-x profile on the main fault plane (Section 6.2.3).

To summarise, it is difficult to distinguish a soft linkage stage on 3D seismic data where the intersection occurs at a centralised location on the main fault trace and impacts the main fault slip profile only very locally. A putative soft-linked stage may be better considered as being equivalent to the abutment stage if the variation is locally related to propagation of the intersecting fault. Conversely, the recognition that a variation occurs may suggest that it has greater influence than can be confidently resolved by 3D seismic (See 6.2.5). The practical distinction (as opposed to a theoretical distinction) between abutment and soft linkage thus relates to recognition of the presence, or lack of, lateral tip folding and this variation may be related to independent factors such as rock mechanics and strain rate.

From the above, a state of soft linkage is defined by the following criteria:-
In the main fault tip region:
1. Formation of a relay ramp adjacent to the main fault tip.
2. Complimentary displacement anomalies on the intersecting and main fault planes.
In the main fault central region:
3. A localised variation on the main fault T-x profile such as a local minimum or profile gradient change at the intersection location, that records interaction with the intersecting fault.
4. Ductile displacement ahead of the propagating tip may be added to the T-x main fault profile to compliment the discrepancy.
5. The main fault can continue to slip independently of the intersecting fault.

6.2.3 Hard linkage

The hard linkage stage has been identified from intersections at segment boundaries in the Canyonlands array (Chapter 5) and rare examples were found in the Gjallar Ridge PFS (Chapter 2). It has been identified where intersecting faults have non-zero values of throw at the intersection position (branch line). It is thus easier to recognise the hard linkage stage than the soft linkage stage. However, it is not necessarily straightforward to differentiate accidental hard linkage from branching intersections (see Chapter 2). Hard linkage for non-colinear fault intersections is comparable in definition for those of colinear fault systems, as there is continuity in both the geometrical configuration and kinematic coherence can be demonstrated from throw values at the intersection position.

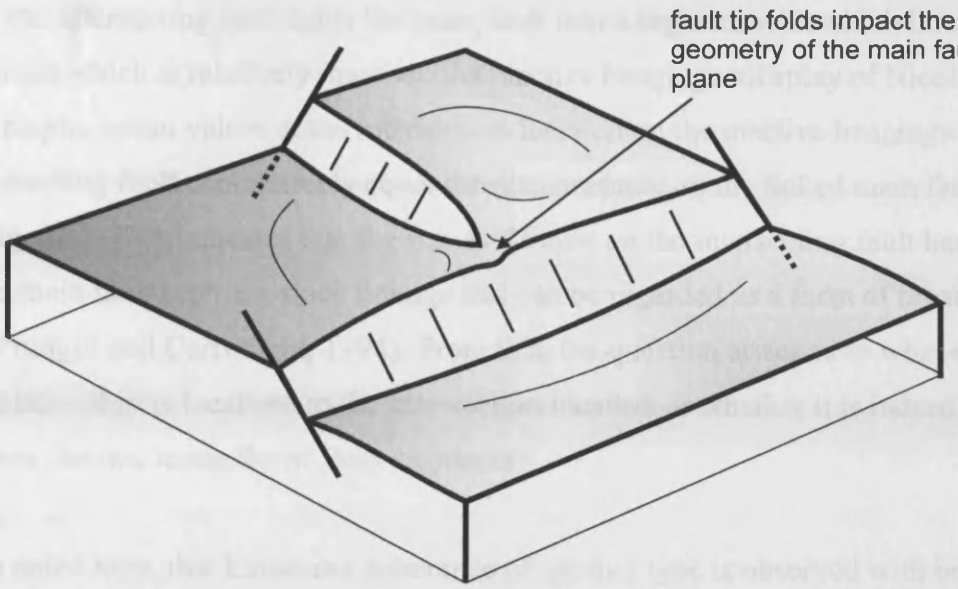

Figure 6.3. Schematic diagram showing the impact of ductile bending ahead of the propagating intersecting tip on the D-x profile of the main fault plane. The intersecting fault approaches the main fault in a near-central location on the main fault trace. Complimentary modification of the D-x profiles of the intersecting faults signifies non-colinear soft linkage.

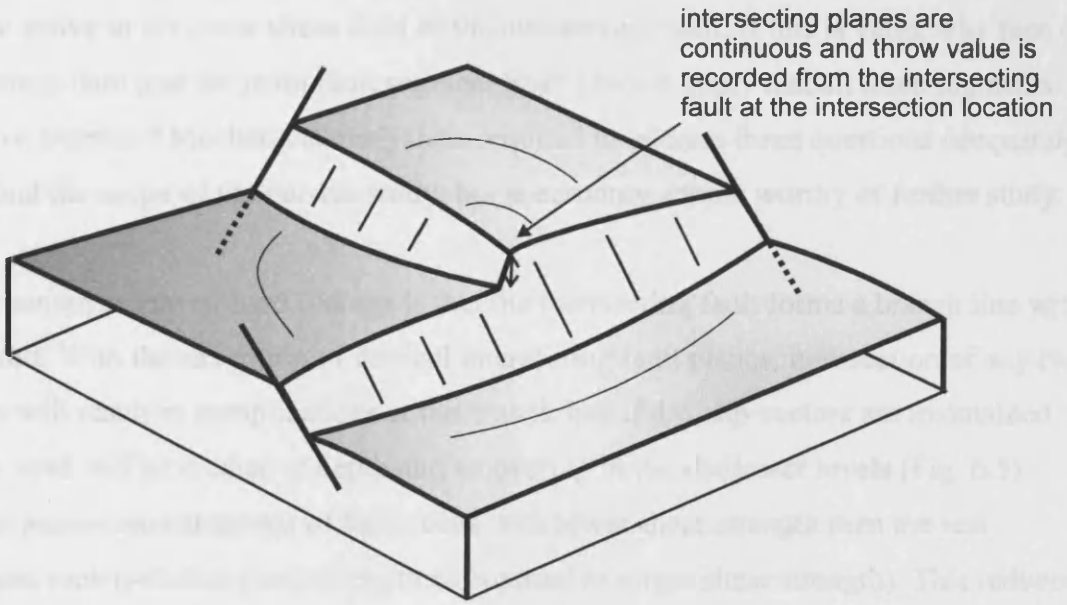

Figure 6.4. Schematic diagram of a hard linkage formed through accidental intersection. The intersecting fault approaches the main fault in a near-central location on the main fault trace. The value of throw that is measured from the intersecting fault at the intersection location (arrowed) is equal to the value of throw that has been added to the linked main fault segment since linkage. The cumulative value of throw that is measured from the intersecting fault and the inactive hangingwall splay is equal to the value of throw that is measured from the linked, active segment of the main fault, at the intersection location. This indicates kinematic coherence that is localised to the intersection location.

Hard linkages have been described from L class intersections (Chapter 5), from breaching of soft linkage at segment tips (Chapter 5, Fig. 6.2) and from T class intersections (Chapter 2). In the T class, the intersecting fault splits the main fault into a segment with which it links and a second segment which is relatively inactive (the inactive hangingwall splay of Nicol et al., 2003). The displacement values at the intersection location on the inactive hangingwall splay and the intersecting fault cumulatively equal the displacement on the linked main fault segment (Fig. 6.4). This indicates that the value of throw on the intersecting fault has been added to the main fault segment since linkage and can be regarded as a form of breaching index (c.f. Trudgill and Cartwright, 1994). From this, the question arises as to what extent the kinematic relationship is localised to the intersection location or whether it is indeed more extensive over the two lesser throw fault segments?

It should be noted here, that kinematic coherence of another type is observed with branching intersections, in that the cumulative profile over the extent of all three intersections creates a profile similar to a single fault (Willemse et al., 1996; Section 6.2).

The kinematic coherence that is exhibited at accidental intersections implies that the main fault can be active in the same stress field as the intersecting fault. If this is valid, why then do the intersecting fault and the main fault segment link? Does it imply that all three segments can be active together? Mechanical analysis is required to address these questions adequately, and is beyond the scope of the current study, but is certainly a topic worthy of further study.

One of the consequences of hard linkage is that the intersecting fault forms a branch line with the main fault. With the exception of vertical intersecting fault planes, intersection of any two fault planes will result in complications at the branch line if dip-slip vectors are maintained. In particular a void will be created at depth and an overlap in the shallower levels (Fig. 6.5). Active fault planes are composed of fault rocks with lower shear strength than the less damaged host rock (residual shear strength as opposed to virgin shear strength). This reduced strength allows faults to remain active, even when the external stress field and its principal directions have changed (due to localised perturbations). In general, these changes cause the direction of slip and resolved maximum shear stress to deviate from the initial slip direction (Mandl, 2000). Simultaneous operation of the differently striking faults must therefore require oblique slip vectors on the individual faults. This point is discussed in Section 6.3.

From the discussion of hard linkage above, it seems unlikely that all three segments can remain active (c.f. Nicol et al., 2003). If the 'inactive hangingwall splay' is truly inactive then reorientation of the slip vectors on the newly-linked intersecting fault plane will overlap with the inactive fault plane. This may be accommodated by intense localised deformation. Alternatively, the inactive plane may reorient slip vectors but cannot then be described as inactive. The PFS described in Chapter 2 was highly connected and highly interrelated. In such a setting, it is therefore unlikely that a state of inactivity will be maintained on a fault segment.

From the above, criteria used to define a state of hard linkage are as follows:-

1. There is continuity between the main fault plane and the intersecting fault plane.
2. Throw decreases on the intersecting fault toward the intersection (though may re-distribute with increased linkage).
3. A significant value of throw is recorded from the intersection location on the intersecting fault. It is equal to that of the main fault at an L class intersection, or can be added to that of the inactive hangingwall splay to equal that of the main active fault at a T or Y class intersection.

6.2.4 Cross-cutting

Cross-cutting through accidental intersection alone is briefly considered here, and develops as a result of penetrative propagation of one fault plane across another (e.g. Chapters 2 and 3). Despite their ubiquity on geological maps of faulted terrane at all scales, there are few specific studies of cross-cutting intersections in the literature and no kinematic description of how they form. Many geologists simply assume that one fault of the pair predates the other, with a rule of thumb being that the offset strike trace is the earlier fault.

The intersections analysed in this thesis are characterised by a throw decrease across the branch line (e.g. the Mississippi/Sabine X intersection in Chapter 3) and localised patches of slip that propagate through the pre-existing fault plane (Chapters 2 and 3). The ability for the intersecting fault to propagate across the intersection, rather than to form linkage with the pre-existing fault, suggests that slip vectors are not reoriented as was considered to be the case with the hard linkage stage. This topic is addressed further in Section 6.2.5.

The localised nature of sites of higher slip that have been interpreted as the location of propagation across the X type intersection raises the question of what localisation process promotes the specific breakthrough position across a pre-existing fault plane. Is it connected to spatial variations in the stress field, and the perturbation of regional (far-field) stress by the fault plane, or is it more related to a localised strength heterogeneity e.g. lithological or frictional variation on the fault plane? Alternatively, is it instead related to stress intensity geometry associated with the propagation of the intersecting fault (again modulated by heterogeneities in bulk moduli). It is even possible to speculate that the fault may regain sufficient traction after slip events to permit transmission of stresses in a localised manner (similar to that of slip patches). These various possibilities need to be tested in future by observation and modelling, and are simply speculated upon here, as logical derivatives from the limited observation set thus far obtained.

From the above, the following criteria are adopted for the definition of cross-cutting intersections:-

1. Intersecting faults form an X class geometry.
2. Throw values on the intersecting fault decrease toward intersection.
3. Throw gradient may be anomalously large toward the intersecting tip.
4. Throw values decrease across the intersection.

6.2.5 Accidental intersection evolutionary sequence

The importance of understanding evolution of colinear segment boundaries of isolated faults through soft to hard linkage in order to better understand evolution and kinematic coherence of fault arrays has been demonstrated by Peacock and Sanderson (1991, 1994), Trudgill and Cartwright (1994), Cartwright et al. (1996) and others. This section considers whether an evolutionary pathway(s) is developed in non-colinear arrays.

In the preceding discussion, it has been argued that an abutted intersecting fault has formed an intersection with the main fault, albeit of a restricted nature. In contrast, the soft-linked fault is specifically identified in those examples where lateral tip folds are developed ahead of the intersecting fault, and in the volume between the lateral tip of the intersecting fault and the main fault plane. It is suggested here that the abutment stage does not evolve in systematic progression to a soft linked stage. Restricted fault tips can accrue additional displacement in order to overcome a mechanical barrier (Nicol et al., 1996; Wilkins and Gross, 2002)

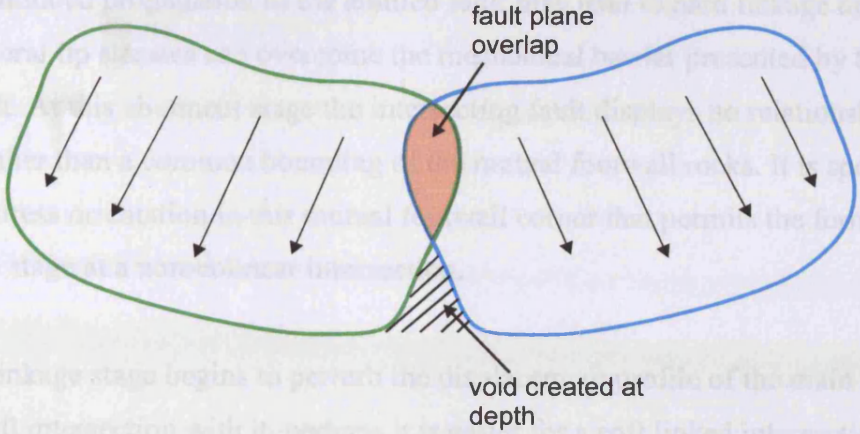

Figure 6.5. Schematic diagram of the intersecting fault planes in three-dimensions. If dip-slip vectors (arrowed) are maintained after intersection, faults will overlap in the shallower levels and create a void at depth.

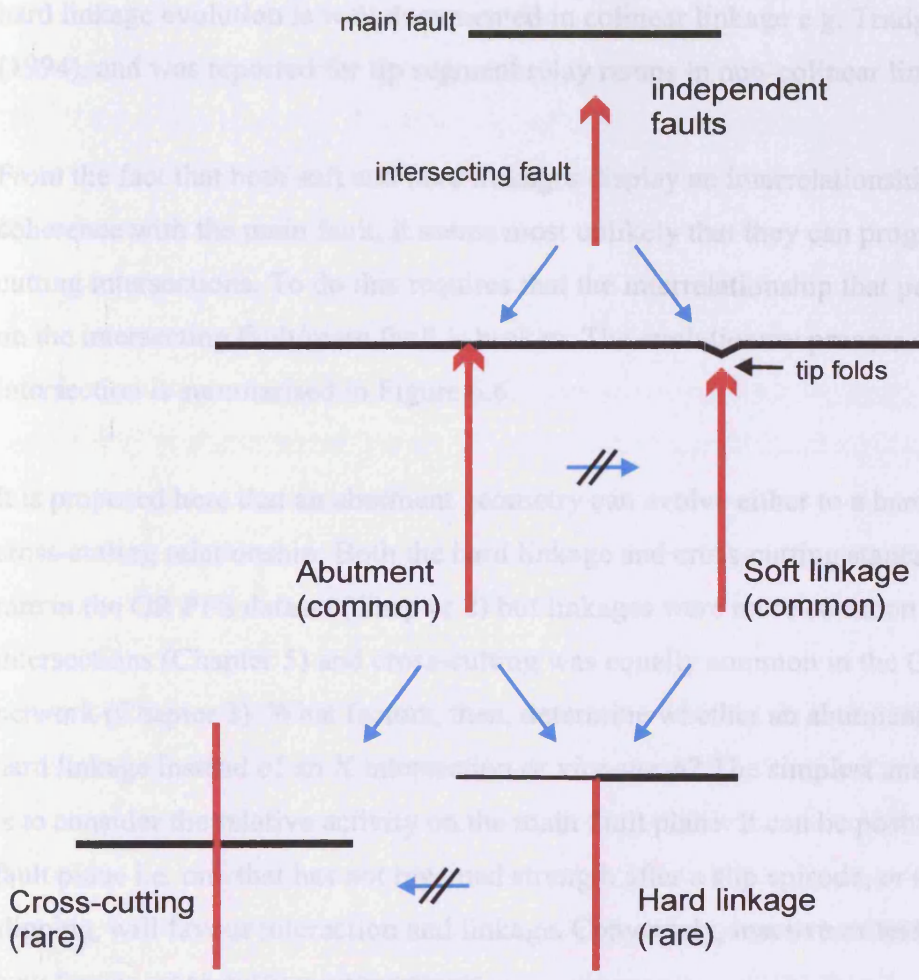

Figure 6.6. Summary of the evolution of non-colinear intersections. Independently propagating faults can interact through abutment of the intersecting fault against the main fault plane or through soft linkage. Both these stages are commonly reported from non-colinear fault intersections in this thesis. The soft linkage stage can evolve to hard linkage but not to cross-cutting. The abutment stage can evolve to hard linkage or to cross-cutting. Hard linkage cannot evolve to cross-cutting. Occurrences of non-colinear hard linkages and cross-cutting intersections have been rare in this thesis.

therefore continued propagation of the abutted fault may lead to hard linkage or to cross-cutting if lateral tip stresses can overcome the mechanical barrier presented by the pre-existing fault. At this abutment stage the intersecting fault displays no relationship with the main fault other than a common bounding of the mutual footwall rocks. It is speculated that it is the local stress orientation in this mutual footwall corner that permits the formation of a hard linkage stage at a non-colinear intersection.

As the soft linkage stage begins to perturb the displacement profile of the main fault before forming a full intersection with it, perhaps it is easier for a soft linked intersection to evolve to a hard linkage stage. If the two faults are interacting at some location on the main fault plane, ahead of the intersecting tip, then is seems likely that this interaction will continue. Soft to hard linkage evolution is well documented in colinear linkage e.g. Trudgill and Cartwright (1994), and was reported for tip segment relay ramps in non-colinear linkage (Chapter 5).

From the fact that both soft and hard linkages display an interrelationship and a kinematic coherence with the main fault, it seems most unlikely that they can progress to become cross-cutting intersections. To do this requires that the interrelationship that permits linked activity on the intersecting fault/main fault is broken. The evolutionary process of non-colinear intersection is summarised in Figure 6.6.

It is proposed here that an abutment geometry can evolve either to a hard linkage or to a cross-cutting relationship. Both the hard linkage and cross-cutting stages were found to be rare in the GR PFS dataset (Chapter 2) but linkages were more common in the Canyonlands intersections (Chapter 5) and cross-cutting was equally common in the Gulf of Mexico network (Chapter 3). What factors, then, determine whether an abutment evolves to form a hard linkage instead of an X intersection or vice-versa? The simplest answer to this question is to consider the relative activity on the main fault plane. It can be postulated that an active fault plane i.e. one that has not regained strength after a slip episode, or one that is constantly slipping, will favour interaction and linkage. Conversely, inactive or less active fault planes may favour cross-cutting intersections.

There is a complication to this postulate. If a fault originally abuts a pre-existing plane (as is thought to be the stage prior to cross-cutting e.g. the Mississippi/Sabine intersection, Chapter 3) then restriction of the intersecting fault has been related to the presence of the pre-existing

plane. At this stage, is the pre-existing plane active? Two possible interpretations can be given:

1. The pre-existing plane can cause abutment without being active – its presence alone is a heterogeneity in rock that restricts propagation.
2. Cycles of activity and inactivity may be the critical feature: i.e. reactivation causes abutment then cross-cutting.

The example of the IFE/EF4 intersection (Chapter 5) is interpreted as an abutment because the EF4 reaches a zero throw tip at the intersection location. However, this is the only intersection in the Canyonlands array where deformation was reported along-strike of the propagating tip in the hangingwall of the IFE. The EF4 tip gradient was not increased (c.f. the EF3 intersecting tip gradient). It can be interpreted from these observations that the EF4 was beginning to transmit crack tip stress across the IFE which therefore implies inactivity on the IFE, if the above is correct. However, the IFE had been reactivated through interaction with other grabens. The EF4 was interpreted to be a later fault and may have abutted against the IFE after it had re-gained strength.

A further example of cross-cutting associated with re-activation is given from the Mississippi/Sabine intersection (Chapter 3) whereby mutual offsetting of the fault planes as recorded by multiple branch points on coherence slices indicated that both faults were active during evolution of this intersection. There may have been periods of relative inactivity and the cross-cutting intersection may have evolved through inter-fingering of the constituent fault planes.

From observations of the frequency of occurrence of abutment or soft linkage relationships, as compared with recognition of hard linkage or cross cutting, it can be inferred that it is generally mechanically unfavourable for high-angled intersection to result in fault plane continuity via hard linkage or to propagate through another fault plane to form a clean cross-cut structure. One caveat should be noted here: the observations leading to these inferences are largely derived from the study of a PFS although partially supported by the relationships documented from the Canyonlands field study. As such, this is a highly restricted sample, and much more work is required before generalisations can be safely made, with much wider applicability.

6.3 EVOLUTION OF BRANCHING INTERSECTIONS

Branching intersections are defined by the propagation outward of the intersecting fault from the main fault. This is, in essence, a kinematic definition. The terminology of secondary faults, fault branches or splays is in common usage in structural geology literature, particularly amongst petroleum geologists (e.g. Fossen and Rornes, 1996; Needham et al., 1996), where splay trap types are widely mapped and exploited. A splay has been defined as a smaller fault that joins a larger fault to which it is related (Peacock et al., 2000). This description alone does not imply the kinematics of splay faulting and there has been little or no emphasis of the kinematics in the fault analysis literature.

Examples of branching intersections include release faults (e.g. Destro et al., 2003) and mode I fractures that initiate due to concentration of stress near mode II tips (Segall and Pollard, 1983) as are widely reported from strike-slip fault systems (e.g. Granier, 1983; Martel, 1988).

One potentially far-reaching result from this study, is that branching types of intersection are documented in several contrasting structural contexts: (1) as early-stage 'budding' from a pre-existing plane (Chapter 2), (2) as extensional faulting at a strike-slip tip (Chapter 4) and (3) as lateral tip bifurcation (Chapters 2 and 3). This discussion will focus on the latter type of branching intersection because the identification of lateral tip bifurcation style of intersection evolution impacts upon the general understanding of network development in many fault arrays.

Lateral branching geometries have previously been noted in salt-related arrays (Rowan et al., 1998; Dutton et al., 2004). Bifurcation of tip lines in the horizontal direction (e.g. Huggins et al., 1995) and the vertical direction (e.g. Childs et al., 1995; 1996b) have been described from analysis of 3D fault plane geometries. The irregularity of the tip line arises from any heterogeneities in the host rock material properties, such as the presence of a localised body or layer (e.g. Huggins et al., 1995) or due to non-uniformity of stress fields (Mandl, 2000). In these examples, the bifurcation of the tip line is a form of segmentation of the fault plane, where the bifurcation results in a sub-horizontal branch lines and segment propagation is parallel to that of the main fault plane (Fig. 6.7a). Thus, upper tip bifurcation results in a form of fringing segmentation of the upper and lower parts of fault surfaces. The segments are kinematically coherent and geometrically contiguous with the main fault plane through soft or

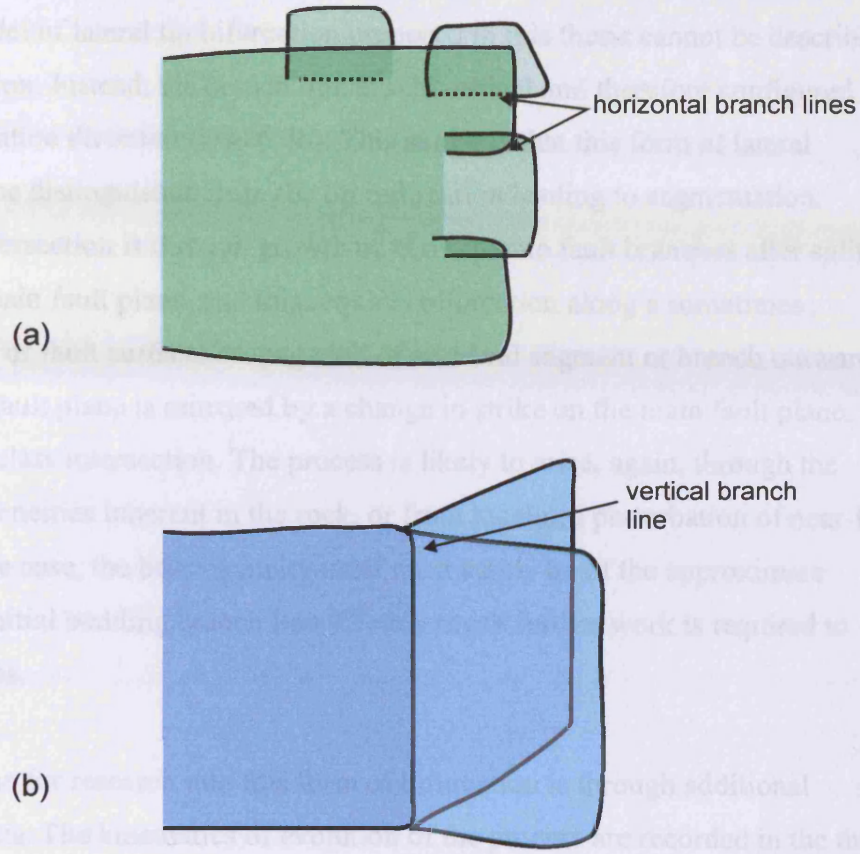

Figure 6.7. Schematic diagrams showing bifurcation of the main fault plane. (a) Segmentation of the main fault plane produces horizontal branch lines over short areas of the main fault plane. The tip segments are contiguous with the main fault plane. (b) Lateral tip bifurcation produces a vertical branch line that extends over the height of the main fault plane and fault segments propagate at a high angle to the propagation direction of the main fault plane.

hard linkage, and their presence at the propagating tip can therefore be likened to a process zone (Walsh et al., 2003).

In contrast, the model of lateral tip bifurcation proposed in this thesis cannot be described as a mode of segmentation. Instead, the branch line is sub-vertical and therefore configured at high angle to the propagation direction (Fig. 6.7b). This suggests that this form of lateral bifurcation should be distinguished from the tip bifurcation leading to segmentation. Evolution of the intersection is through growth of two separate fault branches after splitting or bifurcating of the main fault plane, and this requires bifurcation along a sometimes considerable length of fault surface. Propagation of a second segment or branch outward from the tip of the main fault plane is mirrored by a change in strike on the main fault plane, thus creating a Y or TR class intersection. The process is likely to arise, again, through the presence of heterogeneities inherent in the rock, or from localised perturbation of near-field stresses. If this is the case, the heterogeneity itself must surely be of the approximate dimensions as the initial budding branch line. Clearly much further work is required to elucidate this process.

One potential avenue for research into this form of bifurcation is through additional displacement analysis. The kinematics of evolution of the process are recorded in the throw distributions that decrease abruptly at the intersection location to the branch faults. The cumulative throw on the branches is equal to that on the main fault and typically, the cumulative profile will resemble that of a single normal fault, thus indicating kinematic coherence (Walsh and Watterson, 1991; Willemse et al., 1996). It is predicted that the T-z profiles of the branches will vary to the main fault as the 3D examples of TRA had similar heights of fault (where height equals the distance parallel to the dip-slip direction of the fault) to a vastly reduced throw (Fig. 6.7).

Despite the lack of current kinematic description of branching bifurcation, crack bifurcation of mode I fractures is prevalent in fracture mechanics and ceramics literature. In contrast, very little work has been done in the area of shear failure despite its vital importance in geological applications. Bifurcation is the response to mechanical heterogeneities e.g. a propagating tensile crack bifurcates at the boundary between layers of differing thickness and residual tensile stresses i.e. differential contraction upon cooling (Oeschner et al., 1996; Sanchez-Herencia et al., 1999).

Murphy et al. (2006) presented a model for bifurcating cracks and observed that branching occurs at a critical stress intensity factor, K_I, rather than at a critical crack velocity, therefore it is enhanced by stress concentrators e.g. pre-existing defects (Barquins and Petit, 1992). Branching was typically preceded by the formation of small out-of-plane crack-like defects ahead of the running crack. Ravi-Chandar and Knauss (1984) proposed the following method of growth. When K_I becomes sufficiently high, voids or other material flaws in the crack tip region start to grow themselves into micro-cracks ahead of the main crack front, which effectively becomes an ensemble crack front. The course of further crack propagation and its branching behaviour is then governed by the details of the interaction of these micro-cracks, which continuously communicate through stress waves. Bahat (1982) and Barquins and Petit (1992) consider the occurrence of branching faults in terms of mechanics and kinetics but there is no emphasis on the kinematics of evolution of branching intersections.

Therefore, the increased understanding of the kinematics of branching intersections in this thesis highlights the need for further work on this subject. The interpretation of lateral tip bifurcation as a mode of evolution of intersections in growing networks is an important new finding of this study.

6.4 BRANCH LINE EVOLUTION AND TOPOLOGY

The term branch line was originally defined from thrust faults to mean the intersection of two thrust surfaces (Butler, 1982). Hossack (1983) specifically refers to the branch line as forming through splaying of one thrust from another. Walsh et al. (1999) widens the application of the term to include normal faults and defines it as the intersection between a 'master' fault and a synthetic splay, or between two segments of a multi-strand fault. They specifically excluded unrelated faults and therefore the term was largely established to describe only branching intersections.

Previously published literature typically describes branch lines that are formed through bifurcation of a main fault (Huggins et al., 1995; Walsh et al., 2003) or segmentation related to attempts to form relay ramps (Walsh et al., 1999, 2003; Childs et al., 1995). Conjugate faults also display horizontal branch lines (Nicol et al., 1995). These examples can be grouped under branching intersections and therefore included in the definition provided above (Walsh et al., 1999).

This thesis defines a branch line as any line forming between two (or more) intersecting fault planes, independent of any kinematic relationships, and therefore includes branch lines that form through accidental intersection. This section will investigate the evolution of branch lines in accidental intersection with particular focus on the intersecting fault plane geometry. Geometrically, the branch line between two intersecting faults can be described as the line of intersection between two planes and its plunge and plunge direction can be simply resolved, using stereographic projections, from the 3D orientations of the planes. Therefore evolution of the branch line must necessarily depend upon evolution of the constituent faults. This is particularly true when visualising the branch line within the seismically resolvable scale, although sub-seismic scale variations in topology are likely. The process of establishing how a branch line evolves should help in the understanding of how fault tips develop at an intersection.

6.4.1 Fault tip shape

The shape of the propagating tip of the intersecting fault in an accidental intersection will impact fundamentally on the resulting evolution of the branch line. A schematic representation of fault tips (Fig 6.8) is used here to demonstrate the importance of the shape of the propagating fault as it approaches the pre-existing fault on the evolution of the branch line. A self-similar growth model is assumed in these schematics (c.f. Schlische et al., 1996; Cowie and Scholz, 1992a). The pre-existing fault plane topology is also of great importance in the evolution of the branch line. A slightly curved, dipping plane has been chosen for these schematic models. Intersections occur in the footwall based on the observation within this thesis that accidental footwall intersections predominate over hangingwall intersections.

In the schematic model of branch line evolution, the initial site of intersection between an elliptical tip of an intersecting fault (Fig. 6.8a) and the pre-existing main fault plane is in the upper part of both fault planes. This is the site of the shortest lateral distance between the fault planes and is a function of the dip of the pre-existing fault plane. The branch line evolves upward and downward in stages from this initial site of formation as the rest of the fault tip makes the intersection. The longest lateral distance between the fault planes is toward their basal tips. Again, this is a function of the dip of the pre-existing plane and of the elliptical shape of the intersecting fault tip. As a consequence of this geometry, more downward propagation is required in order to create a full branch line (see Section 6.4.2). An example of such an intersection is given as the TA case study (Appendix A1) whereby the intersection

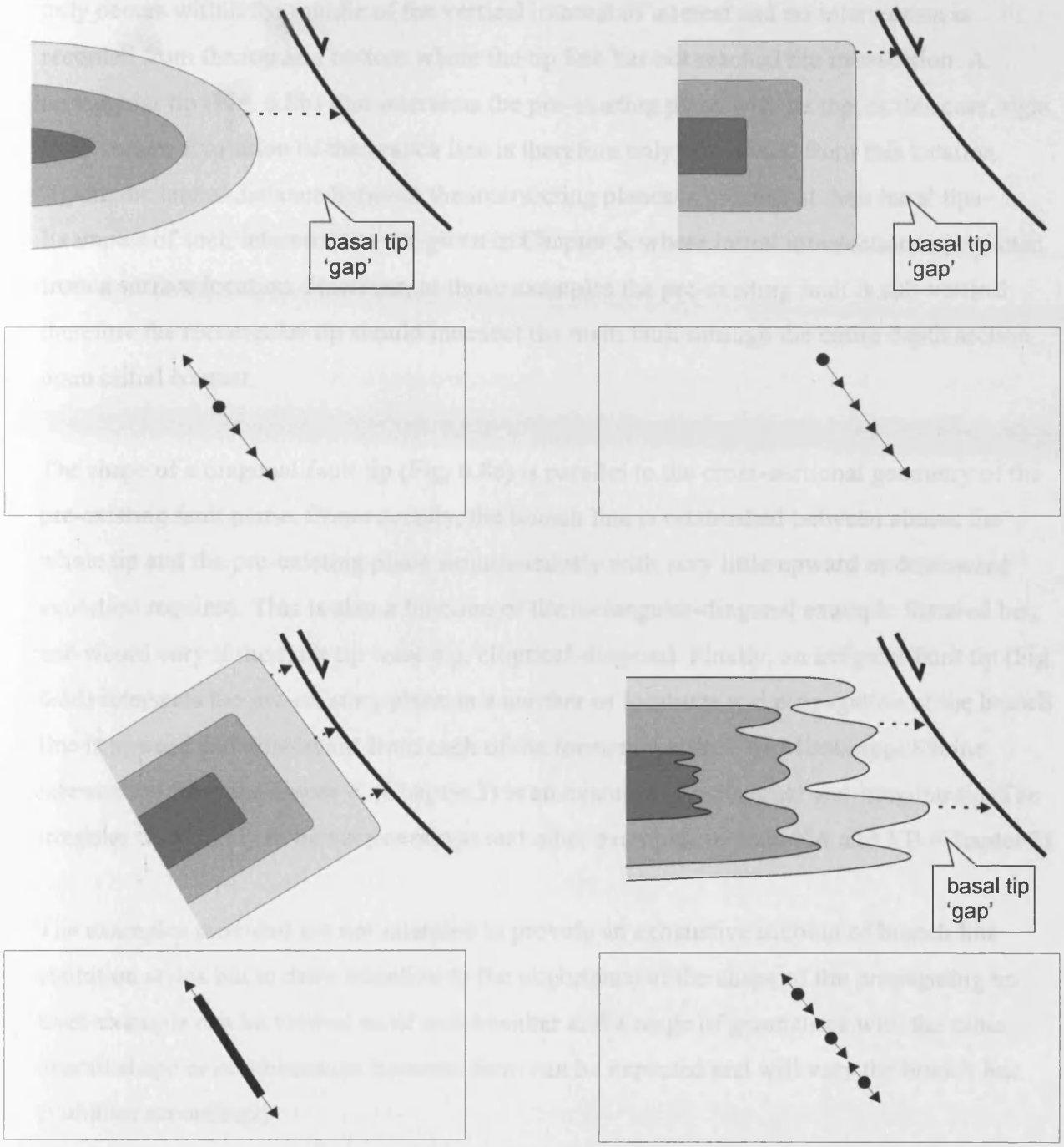

Figure 6.8. Schematic diagram of fault tips demonstrating the impact that the shape of the fault tip, that is propagating toward intersection with the dipping pre-existing fault, has on evolution of the branch line. In each diagram, the upper image is the view from the hangingwall of the intersecting fault as it propagates east toward an orthogonal intersection (and therefore the pre-existing fault is shown in cross-section only). Dotted arrows represent the shortest path to the pre-existing fault if propagation continues in the same way, and therefore the site of branch line nucleations. The lower box is the vertical projection of the pre-existing fault plane viewed from its hangingwall. Thick, black dots or lines represent the initial formation point of the branch line and arrows indicate propagation direction of the branch line after initial formation. a) Elliptical fault tip; b) rectangular fault tip; c) diagonal fault tip; d) irregular fault tip. Combinations are expected. See text for further details.

only occurs within the middle of the vertical interval of interest and no intersection is recorded from the top and bottom where the tip line has not reached the intersection. A rectangular tip (Fig. 6.8b) first intersects the pre-existing plane with its top, in this case, right hand corner. Evolution of the branch line is therefore only downward from this location. Again, the lateral distance between the intersecting planes is greatest at their basal tips. Examples of such intersections are given in Chapter 5, where initial intersection is predicted from a surface location. However, in those examples the pre-existing fault is sub-vertical therefore the rectangular tip should intersect the main fault through the entire depth section upon initial contact.

The shape of a diagonal fault tip (Fig. 6.8c) is parallel to the cross-sectional geometry of the pre-existing fault plane. Consequently, the branch line is established between almost the whole tip and the pre-existing plane simultaneously with very little upward or downward evolution required. This is also a function of the rectangular-diagonal example featured her, and would vary if the fault tip were e.g. elliptical-diagonal. Finally, an irregular fault tip (Fig. 6.8d) intersects the pre-existing plane in a number of locations and propagation of the branch line is upward and downward from each of the formation sites. The Mississippi/Sabine intersection from the Upper X (Chapter 3) is an example of a diagonal and irregular tip. The irregular tip is likely to be very common and other examples include XA and XB (Chapter 2).

The examples provided are not intended to provide an exhaustive account of branch line evolution styles but to draw attention to the importance of the shape of the propagating tip. Each example can be viewed as an end-member and a range of geometries with the same overall shape or combinations between them can be expected and will vary the branch line evolution accordingly.

Due to the seismic resolution, it has not been possible to map variations in branch line topology and to visualise these if they do occur. However, fault plane mapping and description of variations in fault plane with depth lead to the consideration that branch line topology must also be affected by localised fault variations. Examples of these are documented as down-dip fault plane changes in dip with lithological variations (Peacock and Zhang, 1994), along-strike folding of the fault plane (Grasemann et al., 1995), and along-strike variations in orientation. It must be assumed that these variations occur on both faults in

an intersection therefore it can be proposed that branch lines are actually more complex than the plunge and plunge direction resolutions suggest.

6.4.2 Fault tip modification

It is also clear from the examples in Figures 6.8a, b and d that full establishment of a branch line between the planes requires that the laterally propagating intersecting fault propagates further at its basal extent, i.e. into a 'gap' created if the pre-existing plane dips away from the propagating tip. This observation poses the question of how the fault propagates into this region? Once the initial contact has been made, in e.g. elliptical, rectangular and irregular laterally propagating tips, how does the rest of the fault continue to create a full branch line?

In contrast to purely lateral propagation, the diagonal growth toward the pre-existing fault plane effectively removes 'gap' issues. In comparison, if it is first considered that dip-slip vectors are maintained, a laterally propagating fault can only fill the gap if:
(a) Continued lateral propagation of the upper part of the fault cross-cuts the main fault to allow the lower area to reach the plane.
(b) The lateral propagation is arrested in the top part of the fault upon formation of an intersection but continues in the lower part of the fault thus modifying the fault tip shape.
(c) The propagating tip shape is modified at some distance from intersection to become sub-parallel to the cross-sectional geometry of the main fault.

Examples of cross-cutting intersections have been found to be relatively rare in the different case studies presented in this thesis. The few examples require transmission of enhanced fault tip stresses across the pre-existing fault that acts to restrict growth, therefore option (a) is likely to be less common. Options (b) and (c) require that the fault growth changes from the self-similar model and that the propagating tip is modified. Option (b) occurs in the evolutionary stage of abutment where an intersection is formed as the intersecting upper tip and the intersecting fault is modified to complete the branch line. Option (c) can occur as a pre-cursor to abutment, or as soft linkage as the tip modification at a distance from the pre-existing fault offers the possibility of ductile deformation ahead of the propagating intersecting fault tip. An interesting issue is raised through the discussion of the temporal evolution of a branch line – can an intersection be in two stages of spatial development at the same time? For example, cross-cutting at an upper tip and temporary abutment at the lower tip

(option (a)) or abutment at the upper tip and soft linkage at the lower tip (option (b)). Indeed cross-cutting and abutment were identified from examples XA and XB (Chapter 2).

Where dip-slip vectors are maintained, modification of the tip line for options (b, c) may require that propagation rate is slowed in the upper tip and more rapid at the lower tip to reach intersection at the same time. An alternative method to overcome the space problems would be adjustment of slip vectors on the intersecting fault plane. This allows propagation into the 'gap' through modification of the tip line shape. It was discussed in Section 6.2.3 that soft and hard linkages likely require oblique slip vectors. Perhaps it is the style of formation of the branch line that encourages linkage e.g. slip vector reorientation to link or dip-slip maintained for abutment or X.

A further interesting research topic is the effect of component dilatant and contractional regions around the pre-existing fault, and the relationship that these might have on the propagating intersecting tip (Fig. 6.9). In both cases of hangingwall or footwall intersection, the intersecting fault has to propagate further into the dilatant sector of the pre-existing fault (assuming relatively comparable sizes of faults) (Fig. 6.9).

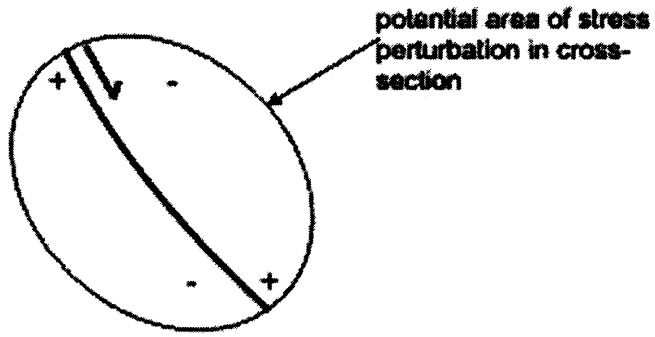

Figure 6.9. Cross-sectional area of potential stress field perturbation caused by a pre-existing fault. + = contractional sectors; - = dilatant sectors.

Kase and Kuge (1998) document that a secondary fault will trigger more easily in extensional jogs than in compressional jogs of a strike-slip fault: is it therefore easier to propagate in the extensional domain? The shape of the stress perturbation around a pre-existing fault has been considered in plan view with the distance of hooking geometries from intersection (Chapters 2 and 3) and a comparable study would be of great benefit in the vertical section.

6.5 IMPLICATIONS AND FUTURE RESEARCH

This research has used hydrocarbon industry datasets to study fault interaction in non-colinear fault arrays. Complex fault geometries are integral to sedimentary basins and the correct mapping of these structures can have a significant impact on exploration and production strategies. This section explores the implications of the major findings of this work for application to the hydrocarbon industry, and puts forward suggestions for further work.

6.5.1 Implications for hydrocarbon exploration

Normal fault zones play a key role in the development of sedimentary basins. Access to 2D and then 3D seismic data from industry has greatly enhanced research in this field, and consequently, understanding of the importance of fault interaction for controlling basin evolution. In particular, assessing the 3D evolution of fault networks is crucial as they influence fluid migration pathways, trapping geometries and reservoir architecture.

It was noted in Chapter 1 that non-colinear fault intersections are prevalent from basinal settings with salt tectonics (e.g. the Gulf of Mexico), those that are influenced by basement structure (e.g. the Gulf of Suez), those whose caprocks may be deformed by intraformational faulting (e.g. the North Sea) and many other examples. Active exploration for non-colinear intersecting faults as a typical trap geometry is common in e.g. the North Sea and the Gulf of Suez. Therefore it is of particular importance to understand the evolution of such geometries, particularly in areas of poor quality seismic data where interpretation will be driven by geological models.

The evolutionary style of intersection, and the stage of its development, will impact the mapped 3D geometry of the structure. For example, an accidental intersection that has formed an early stage linkage will exhibit a low value of throw at the intersection location. The structural crest will therefore occur at the location(s) of maximum throw which will be at some other site on the intersecting faults. Conversely, an accidental intersection displaying a well-developed hard linkage, or a branching intersection, may have a structural crest at the intersection location. The relationship between style of evolution, stage of development and 3D geometry clearly also impacts the column height that can be sustained by the structure and the lithological juxtaposition of units across the faults at the intersection location.

Similarly, the location of spill points will vary when using conventional software to assess trap integrity where fault segments of an intersection are modelled as a single, linked fault (where a central maximum throw location is assumed) versus two separate, unlinked fault segments (which assumes two sites of maximum throw separated by a throw minimum).

Finally, correct interpretation of the type of fault interaction will impact understanding of reservoir compartmentalisation. Using the results from study of the GR PFS as an example, it was found that abutment and soft linkage intersections are far more common than hard linkage intersections. From the map pattern alone, geologists commonly assume that faults in a mapped intersection are linked where they have a continuous trace. Despite the interconnectedness of the GR PFS, this network formed few cross-cutting or hard linked intersections which would potentially compartmentalise the reservoir and prevent extensive leakage through the system. In contrast, an abundance of soft linked intersections will enhance flow through a non-colinear fault network.

In summary, it is recommended that detailed displacement analysis be carried out in order to test the rigour of structural models and to provide robust interpretations of structural evolution. These displacement distributions can be compared to the models provided herein to assess the evolutionary style of the intersections and therefore the impact on variables of the hydrocarbon system as described above.

6.5.2 Future Research

Throughout this thesis, where applicable, suggestions for areas of future research have been highlighted. This work is one of the first to characterise fault interaction behaviour in non-colinear intersections and the results strongly encourage further work in this direction.

Fault strike changes (hooking geometries) have been described where intersecting faults become orthogonal to the main fault in response to its near-field stress perturbation. It would be interesting to pursue the topic of 3D characterisation of the area of stress perturbation around a fault. An extensive database of fault attributes of both the intersecting and main faults e.g. length, hook length, maximum throw, lithology, angle of approach of the intersecting fault, etc., should be gathered in order to attempt to relate hook geometry to a causative attribute.

In cross-section, the mechanical stratigraphy is known to vary the area of the rock volume affected by ductile strain caused by fault movement. Hook geometry variations within the vertical section should be compared to the areas affected by drag folding to help quantify the role of mechanical stratigraphy and to capture the 3D shape of the stress perturbation caused by an active fault. In addition, Section 6.4 suggested that the shape of the dilational and compressional zones around a pre-existing fault may affect the shape of the intersecting fault tip.

A related subject that requires further study is the role of reactivation in forming different types of intersection. It has been suggested that, where hook geometries form in limited vertical sections, they may indicate periods of activity on the main fault plane. Alternatively, their limited distribution could relate to lithological variations. This relationship should be studied from growth faults where intervals of fault activity can be well-constrained. Fault growth can therefore be related to types of intersection evolution e.g. T class versus X class formation.

In this study, models have been put forward to explain different types of fault interactions in non-colinear fault networks. Expansion of the database collated herein to include thrust faults, strike-slip faults and further examples of extensional faults at all scales would produce a statistically robust dataset and enable comparison of intersection types from different basinal settings and different stages of evolution. Further research into the determination of any predictable relationship between geometry and evolution could be conducted from this database.

Ongoing work has identified kinematically coherent 3D systems of non-colinear faults in basement-reactivated rift settings, through application of the techniques used herein to more developed systems. The areal extent of kinematic coherence should be investigated. Examples of branching intersection in this work demonstrated kinematic coherence along the entire length of all segments. Examples of accidental intersections were shown to be coherent in the area limited to the intersection i.e. cumulative throw on the intersecting fault and subordinate main fault segment equals the value of throw on the larger main fault segment at the intersection location. How far from intersection can the relationship between the intersecting fault and the minor main fault segment be extended? If the cumulative throw profile of the intersecting and lesser throw main fault segments mirrors the profile of the larger throw main

fault segment at some distance from intersection then the area of kinematic coherence is enlarged. It may also be possible to relate this area of kinematic coherence to an area of oblique slip movement.

CHAPTER 7: CONCLUSIONS

Fault intersections are an integral feature of all fault systems. This study has been one of the first to explore the geometries and kinematics of types of fault interactions from non-colinear arrays. The above summaries and discussions within the chapters demonstrate the range of new insights that have been added to the evolving literature of fault analysis through displacement studies on an as-yet under-considered but ubiquitous style of network. This section summarises the key findings and addresses the aims outlined in Chapter 1.

7.1 FAULT KINEMATICS

- Intersecting faults from non-colinear arrays demonstrate kinematic and mechanical interaction between their constituent faults. Growth histories and interrelationships are recorded from displacement distributions of the faults. Analysis of these displacement distributions can determine the evolutionary style of the intersection and the type of interrelationship that occurs. 3D studies are recommended for interpretation of intersection evolution.
- The evolution of intersections described in this thesis can be grouped into those that form through accidental intersection and those that form through branching intersection.

Accidental intersection

- Accidental intersections are defined as those that evolve through propagation of an intersecting fault toward the intersection location on a relatively older, main fault plane. Practically, this is identified where throw values on the intersecting fault decrease systematically toward intersection. Prior to intersection, both faults are separate structures that are entirely independent in (a) 3D geometry and (b) kinematic evolution.
- Fault intersections studied in this thesis formed predominantly through accidental intersection.

- There are four types of intersection relationship formed through evolution by accidental intersection: abutment, soft linkage, hard linkage and cross-cutting.
- *Abutment* is the termination of an intersecting fault close to a pre-existing fault plane. The gradient of the T-x profile may increase toward intersection. No complimentary modification is exhibited by the main fault plane.
- *Soft linkage* is identified where the main fault T-x profile is modified by the presence of the intersecting fault. Where the faults interact in their tip region, an oblique relay ramp structure can form, permitting continuity of bedding from a mutual footwall to a mutual hangingwall. Where the intersection occurs in a near-central location, soft linkage occurs where there is ductile displacement ahead of the propagating tip of the intersecting fault. The ductile component of displacement can be added to the main fault profile to compliment the discrepancy. The main fault can continue to slip independently of the intersecting fault.
- *Hard Linkage* occurs where the intersecting fault is contiguous with the main fault plane. Throw decreases on the intersecting fault toward the intersection (though throw profiles may re-distribute with increased development of linkage). A significant value of throw is recorded from the intersection location on the intersecting fault. This value is equal to the throw value of the main fault at intersection in an L class geometry, or can be added to that of the inactive hangingwall splay to equal that of the main active fault, in a T or Y class intersection. All three segments cannot remain active together post-linkage. Simultaneous operation of the differently-striking faults must require oblique slip vectors on the individual faults.
- *Cross-cutting* accidental intersections develop as a result of penetrative propagation of one fault plane across another. Throw values on the intersecting fault decrease toward and across the intersection. The throw gradient may be anomalously large toward the intersecting tip. The ability for the intersecting fault to propagate across the intersection, rather than to form a linkage with the pre-existing fault, suggests that slip vectors are not reoriented. Cross-cutting faults may form during periods of inactivity on the main fault plane.
- It may be easier to form linkages in the fault tip region of the main fault rather than in a near-central location. An active fault will act as a free surface and this will favour abutment intersections, but higher stresses in the tip regions may favour linkage.

Accidental intersection evolutionary sequence

- Abutment can evolve to hard linkage where both faults are active and the near-field stress orientation is preferentially aligned for high-angled linkage.
- Abutment can evolve to cross-cutting where lateral tip stresses of the intersecting fault can overcome the mechanical barrier presented by the pre-existing fault.
- Abutment cannot evolve to soft linkage as the abutted fault tip is adjacent to the main fault plane and the soft linkage stage requires ductile deformation of the rock volume between the intersecting fault tip and the main fault plane.
- Soft linkage can evolve to hard linkage. In the tip region of the main fault this can occur through breaching of a relay ramp. In a near-central region of the main fault trace, continued slip events on the intersecting fault may be conducive to evolution from soft to hard linkage.
- Neither soft nor hard linkage can evolve to a cross-cutting stage of interaction. Both these linkage states display a kinematic interrelationship with the main fault that would have to be broken, to allow progression to become cross-cutting.
- It is generally mechanically unfavourable for a high-angled intersection to result in fault plane continuity via hard linkage, or fault plane cross-cutting via continued propagation of the intersecting fault through another fault plane.
- An intersection can display more than one type of fault interaction relationship at a given time within the vertical section.

Branching intersection

- Branching intersections are defined by the propagation outward of the intersecting fault from the main fault and this is demonstrated by the throw distribution decreasing outward from the intersection location on the main fault plane.
- Branching types of intersection are documented in several contrasting structural contexts: (1) as early-stage 'budding' from a pre-existing plane, (2) as extensional faulting at a strike-slip tip and (3) as lateral tip bifurcation.
- *Lateral tip bifurcation* as a mode of evolution of intersections in growing networks is an important new finding of this study.
- *Lateral tip bifurcation* is the evolution of an intersection through growth of two separate fault branches after splitting or bifurcation of the main fault plane. Throw on the main fault is distributed between the subordinate faults.

Kinematic Coherence

- Soft-linked and hard-linked intersections that have evolved through accidental intersections are kinematically coherent in the area adjacent to intersection. That is, that addition of the value of throw on the intersecting fault at intersection can be added to the value of the subordinate main fault segment to equal the value of the larger main fault segment.
- Faults that have evolved through lateral bifurcation are kinematically coherent over the entire length of the intersecting structures. That is, that throw values on the two subordinate segments can be added together to produce a throw profile with the main fault that approximates that of an ideal isolated fault.
- Kinematically coherent cross-cutting faults do not modify the throw distribution on the fault planes of their constituent faults. Instead, the faults are able to grow simultaneously, and display only a single branch point indicating that slip vectors have modified to accommodate contemporaneous faulting.

Branch line evolution

- This thesis defines a branch line as any line forming between two (or more) intersecting fault planes, independent of any kinematic relationships, and therefore includes branch lines that form through both branching and accidental intersection.
- The shape of the propagating tip of the intersecting fault in an accidental intersection will impact fundamentally on the resulting evolution of the branch line.
- Full establishment of a branch line between the fault planes in an accidental intersection requires that the laterally propagating intersecting fault propagates further at its basal extent, i.e. into a 'gap' created if the pre-existing plane dips away from the propagating tip. This 'gap' issue is resolved if the intersecting fault tip shape is diagonal.
- Branch lines forming in branching intersections are sub-vertical. Therefore the mode of formation of a branch line in a lateral tip bifurcation differs from formation of the sub-horizontal branch lines that form through segmentation of the fault tip.

Strike-slip fault kinematics

- An elliptical fault plane shape is recorded from the strike-slip faults in the Levant Basin which indicates that the faults evolved through lateral, in addition to upward, propagation.

- Lateral propagation gradients are recorded from strike-slip displacement analyses.
- This work has been the first to document 3D strike-slip displacement analysis from interpretation of 3D seismic data.

7.2 GEOMETRY

- A classification for non-colinear fault intersections has been defined based on angles of intersection from plan view geometries.

  T class: The intersecting fault forms angles of 60-120° with the main fault. The main fault has a continuous strike across the intersection location.

  Y class: The intersecting fault forms angles of 10-60° with the main fault. The main fault has a continuous strike across the intersection location.

  TR class: Angles between all three segments are $\leq 145°$ with the ideal case being a perfect triple junction of all angles = 120°.

  X class: Four segments meet at a single intersection with any angle formed between the intersecting faults.

  L class: Two fault segments meet at any angle to form an intersection at their tips.
- The class of intersection can vary throughout the depth section.
- It is not possible to determine the style of intersection evolution and type of interrelationship from geometry alone, but there are some general trends.
- Accidental intersections most commonly occur in the footwall of the main fault.
- T class geometries commonly evolve as accidental intersections and display abutment relationships.
- Y class geometries, with acute intersection angles, and intersecting faults that have the same dip direction as the main fault, are commonly branching intersections.
- Hooking geometries displayed by intersecting faults are indicative of accidental intersection. Hook length values are comparable between examples from different basinal settings, suggesting that the shape and magnitude of the stress perturbation around a fault may be predictable.
- Intersections that form through lateral bifurcation have a characteristic ideal plan view geometry that consists of a long segment that diverges to form two shorter segments at its tip, and typically the main fault strike bisects the intersection angle between the two subordinate faults, thus creating a Y or TR class intersection.
- Displacement on cross-cutting faults with predominantly dip-slip motion will create two branch points which can be resolved on a slice through the coherence volume

(where the branch points are separated by a distance that is greater than the lateral resolution).

- End-members of fault tip shapes are elliptical, rectangular, diagonal and irregular. Their 3D form affects evolution of branch lines. A range of geometries with the same overall shape or combinations between them can be expected and will vary the branch line evolution accordingly.
- There are significant geometrical variations between colinear and non-colinear intersections. Interacting faults in a colinear array form parallel overlaps or underlaps. Where non-colinear fault interaction occurs near the fault tip regions, an oblique overlap may form. More commonly, a non-colinear intersection occurs at a point location in plan view.

APPENDIX A.

The results presented herein are appended to Chapter 2 and include additional case studies that were omitted from Chapter 2 for reasons of brevity.

A.1 3D ANALYSIS OF A T CLASS INTERSECTION

A.1.1 TA Geometry

The TA intersection has a near-orthogonal geometry at middle Miocene level (Fig. A.1a). Seismic cross-sections taken through both faults segments TAa and TAb (Fig. A.1b, c) indicate a fault trace, dipping ~50°, that has an upper tip at a depth of approximately 2050ms (300ms below seabed). The TAa – TAb is a Type 1 or Type 2 fault. A local throw minimum (Fig. A.1b) is identified from a depth of ~1100ms (-650ms below seabed) where the horizon is folded rather than offset and it is suggested that this fault has evolved through dip linkage. The seismic section through the TAc segment (Fig. A.1d) shows a fault that displaces to the NE and has both upper and lower tips in the Miocene to Pliocene section and can therefore be described as a Type 3 fault (section 3.2.2.2).

The middle Miocene plan view T class geometry does not persist throughout the depth section (Fig. A.1e). It varies between an L geometry where there are two distinct branch points (e.g. 2296ms) to a T intersection with a single branch point (e.g. 2260ms) to isolated faults (e.g. 2348ms). In 3D, two branch lines exist in the top ~500ms where the main fault appears to 'split' and form two intersections with the intersecting fault, TAc (Fig. A.2a). In addition, due to the westward dip of the main fault the TAa-TAc branch line does not persist through the entire depth section that is cut by the TAc intersecting fault. There is a resultant 'gap' at depth (Fig. A.2) which has implications for understanding the stability of the branch line.

The time-structure map of the middle Miocene horizon (Fig. A.2b) shows that the common footwall of the TAa and TAc segments is contoured such that this is a coherent block with an

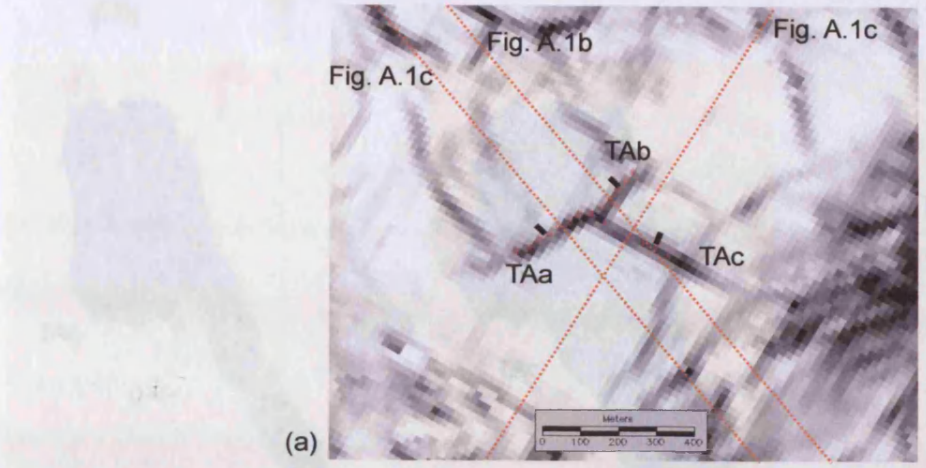

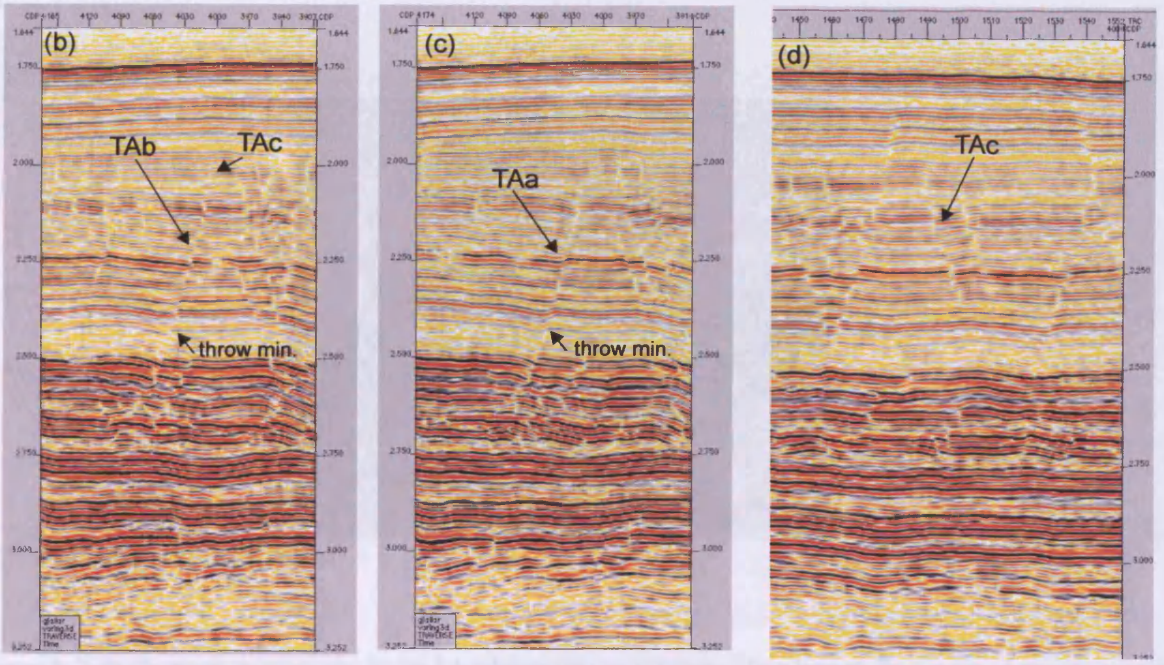

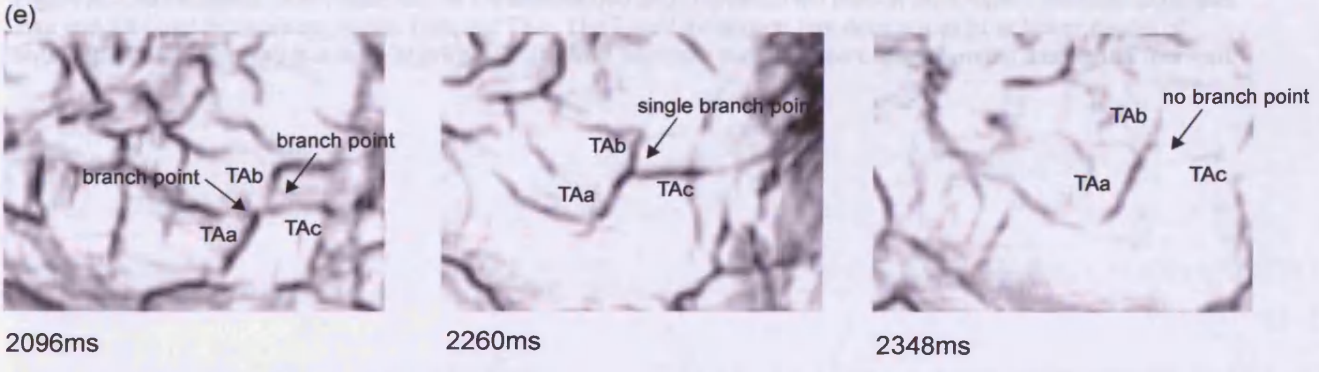

Figure A.1. 3D geometry of the TA intersection. (a) Coherence extraction of the mid-Miocene horizon showing plan view geometry at that level. Note location of seismic profile lines. (b) Seismic profile line through TAb. The steep segment at the upper tip of the TAa fault is an oblique section of the TAc fault (c) Seismic profile line through TAa. (d) Seismic profile line through TAc. (e) Coherence slices showing the variation in plan view geometry of the TA intersection.

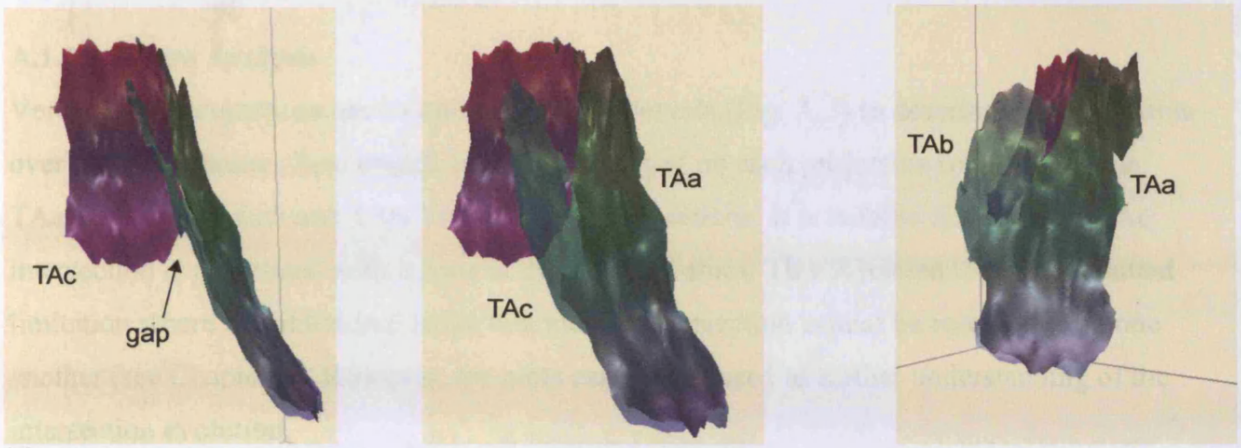

(a)

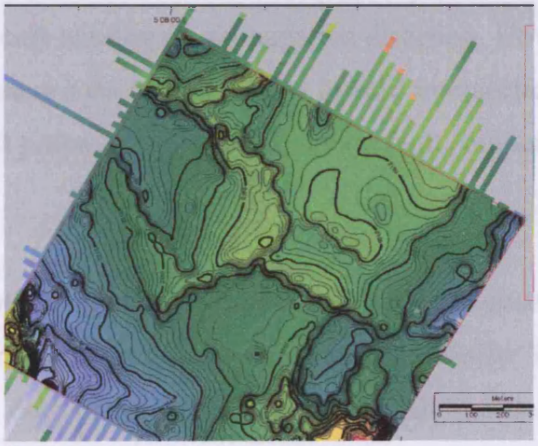

(b)

Figure A.2. (a) Mapped fault planes of the TA intersection in 3D space. Two branch lines exist - between segments TAa and TAc and between segments TAb and TAc. The TAa/TAc branch line does not exist at lower depths of segment TAc where a gap has been highlighted. (b) Mid Miocene time-structure map showing a common footwall.

overall south-westward dip. In contrast, the TAc hangingwall contours are parallel to that fault segment and appear unrelated to the TAb footwall block.

A.1.1.2 Throw analysis

Vertical fault projections are contoured at 1ms intervals (Fig. A.3) to describe throw variation over the fault planes. Two branch lines are displayed on each projection representing the TAa-TAc intersection and TAb-TAc intersection locations. It is notable that the TAa-TAc intersection is associated with a zone of high throw values. This is related to a measurement limitation where the individual faults that meet at intersection cannot be resolved from one another (see Chapter 1). However, the plots can still be used to further understanding of the intersection evolution.

Throw values are fairly consistent on the intersecting fault plane and the high values at intersection make it difficult to interpret propagation direction. However, the middle Miocene T-x data (Fig. A.3c) displays a decrease in throw toward intersection, therefore suggesting that this intersecting fault propagated toward the main fault, supporting a footwall linkage interpretation.

The main fault throw distribution is complicated but some observations can be made. The TAb segment has a central throw maxima that decreases radially. The minimum that separates it from the TAa segment does not coincide with the branch line so an interpretation of slip minima at intersection (Maerten, 1999) can be discounted. Combined with the geometrical observation that this segment is offset from the main fault TAa segment in the shallow section, the TAb segment is thought to have largely evolved separately from TAa.

However, the 3D fault plane images (Fig. A.2) show that the TAa and TAb segments are coherent below a depth of 500ms below seabed (TWT). The throw distribution shows a horizontal minimum and this suggests that dip linkage has occurred. It is therefore envisaged that any kinematic linkage between fault planes TAa and TAb is driven by linkage at depth.

From the geometrical and throw distribution observations, the branch lines are proposed to evolve through accidental intersection. The TAb segment has propagated toward the TAc segment forming an abutting relationship. The TAa-TAc branch line has evolved through footwall capture as the TAc segment has linked with segment TAa. This section does not aim

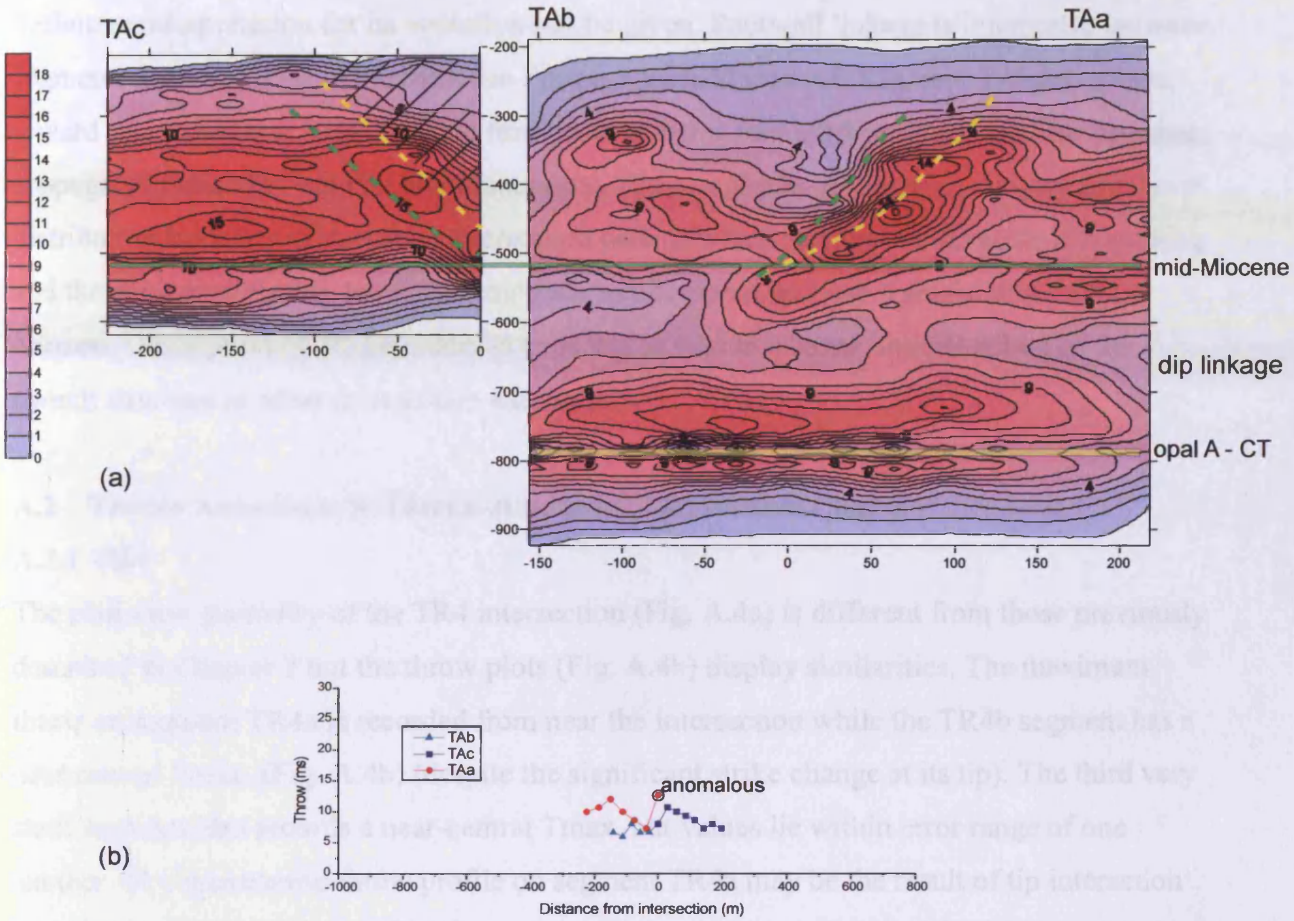

Figure A.3. Vertical fault plane projections showing throw variation over fault segmetns TAc and TAb to TAa. There are two branch lines (yellow = TAc to TAa; green = TAc to TAb). Anomalously high throws are concentrated at the branch line between segment TAc and TAa. There is a dip linkage between the lower part of the TAa-TAb fault and the upper part. (b) T-x profile of the TA interscting faults. The TAc segment decreases in throw toward intersection, showing it to be an accidental intersection, and an anomalous measurement is displayed from the intersection location.

to answer all questions posed by this complex intersection, particularly in light of seismic resolution issues. In summary, it is clear from both the variation in plan view geometry down-section and the vertical projection throw plots that this intersection is complex and that no definitive interpretation for its evolution can be given. Footwall linkage is interpreted between segments TAa and TAc in the Miocene-Pliocene vertical interval. Segment TAb has grown toward its intersection with TAc and formed an abutting relationship. Thus, all three segments propagated separately but contemporaneously. The complexity of the 3D geometry and throw distribution highlight important interpretation pitfalls which include the 3D seismic resolution and the danger of placing too much emphasis in interpretation from a single stratigraphic horizon. Description of 3D geometry is expected to lead to a better understanding of the overall structure in other intersection examples.

A.2 THROW ANALYSES OF TRIPLE-JUNCTION (TR) INTERSECTIONS

A.2.1 TR4

The plan view geometry of the TR4 intersection (Fig. A.4a) is different from those previously described in Chapter 2 but the throw plots (Fig. A.4b) display similarities. The maximum throw on segment TR4a is recorded from near the intersection while the TR4b segment has a near-central Tmax. (Fig. A.4b) (despite the significant strike change at its tip). The third very short segment also records a near-central Tmax. but values lie within error range of one another. The aysmmetric throw profile on segment TR4a may be the result of tip interaction with TR4b. If both TR4a and TR4b segments propagated separately and intersected at their tips then TR4c can be thought of as a strain accommodation structure. An alternative interpretation is that TR4a and TR4c were originally linked and intersection with TR4b provides a further example of footwall capture.

A.2.2 TR5

The plan view geometry of the TR5 intersection (Fig. 2.13) has a near-perfect triple-junction geometry with angles of intersection of 129° (a to b), 124° (a to c) and 105° (c to b). The throw profile (Fig. A.5) differs from those previously described. The largest throw values are recorded from segment TR5a that has a rather flat profile. The throw profile of segment TR5b can clearly be described as increasing toward intersection on a throw gradient of 0.03. However, a local minimum is recorded from the intersection location which may be anomalous or may be related to the intersection location. Discounting this local minimum, there is little variation in throw value from the TR5a to b segments and they may be

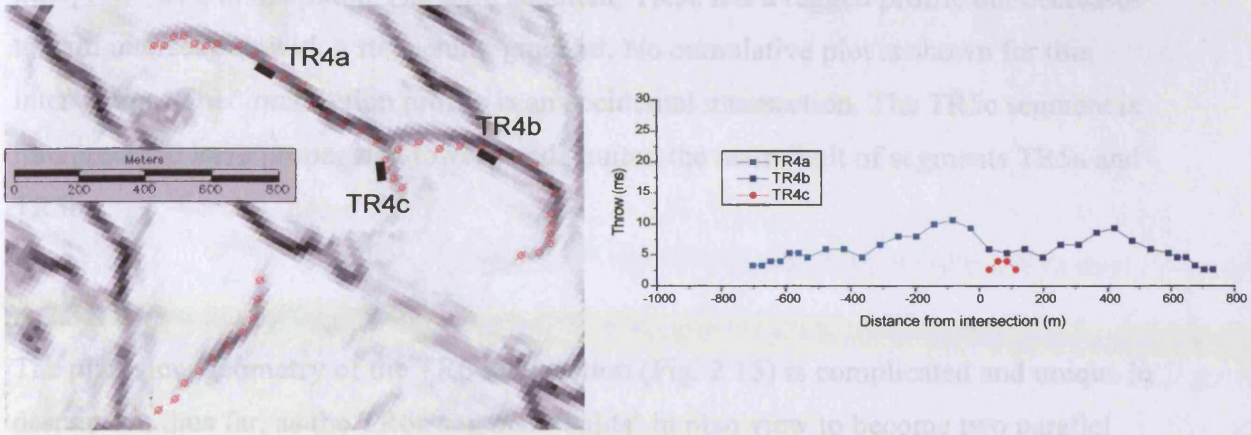

Figure A.4. (a) Coherence extraction of the middle Miocene horizon showing the plan view geometry and measurement locations of the TR4 intersection. (b) T-x plot of the TR4 intersection.

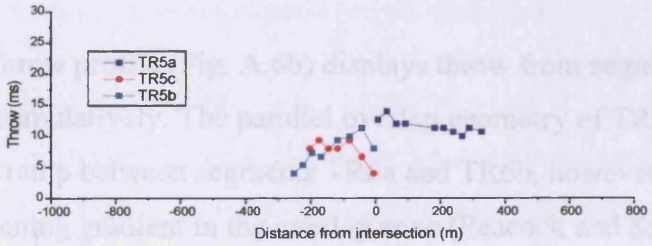

Figure A.5. T-x plot fo the TR5 intersection.

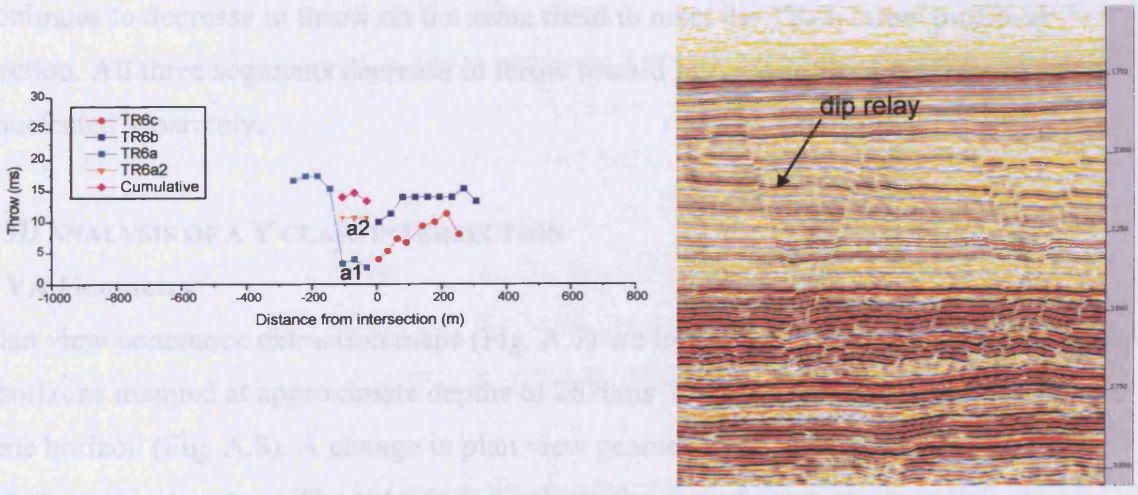

Figure A.6. (a) T-x profile of TR6 intersection. Throw decreases where parallel segments overlap (a1 and a2) but the cumulative throw is continuous to segment TR6a. (b) Seismic profile line through the relay ramp.

interpreted as a linked fault. The third segment, TR5c has a ragged profile but decreases toward intersection with a steepening gradient. No cumulative plot is shown for this intersection. This intersection profile is an accidental intersection. The TR5c segment is interpreted to have propagated toward and abutted the main fault of segments TR5a and TR5b.

A.2.3 TR6

The plan view geometry of the TR6 intersection (Fig. 2.13) is complicated and unique in description thus far, as the TR6a segment 'splits' in plan view to become two parallel segments (TR6a1 + TR6a2) approaching the intersection. The seismic profile taken through the parallel segments (Fig. A.6a) shows that they are synthetic and overlap in the dip section between ~2000ms and 2300ms TWT.

The throw profile (Fig. A.6b) displays throw from segments TR6a1 and TR6a2 separately and also cumulatively. The parallel overlap geometry of TR6a1 and TR6a2 can be described as a relay ramp between segments TR6a and TR6b, however the throw profile does not show a steepening gradient in the overlap zone (Peacock and Sanderson, 1991). Rather, a significant decrease in throw on both segments TR6a and TR6b is recorded. The cumulative TR6a1 and TR6a2 profile has a throw value that is near-equal to the value of throw on the TR6a profile and continues to decrease in throw on the same trend to meet the TR6b throw profile at intersection. All three segments decrease in throw toward intersection and are interpreted to have nucleated separately.

A.3 3D ANALYSIS OF A Y CLASS INTERSECTION

A.3.1 YA Geometry

The plan view coherence extraction maps (Fig. A.7) are images of the same intersection taken from horizons mapped at approximate depths of 2630ms TWT, 2470ms TWT and the middle Miocene horizon (Fig. A.8). A change in plan view geometry can clearly be seen down through the vertical section. The YAa fault displaces the section from an upper tip in the Pleistocene, ~1850ms, to a lower tip within the Oligocene section at ~2750ms (Fig. A.8). The maximum throw is recorded from near the middle Miocene horizon. The main and intersecting faults have parallel dips of c.50°. The intersecting fault is a Type 2 fault that displaces strata from the Miocene through the Oligocene section.

On the mid-Miocene horizon (Fig. A.7a), where this intersection was first selected as a Y geometry, the intersecting fault YAc makes an acute angle of intersection of 053° with the main fault. However, it incurs a significant strike change to do this from 069° where it near-parallels the main fault, to 016°. The strike change on the intersecting fault, YAc, in mid-Miocene is also seen at the 2470ms level (Fig. A.7b). However it is a less angular change from 082° to 035° with an acute intersection angle of 063°. The length of the YAb fault segment is greater than at mid Miocene level and parallels in strike, and equals in length, the intersecting fault segment.

At the 2630ms level (A.7c), the most significant observation is that the northern fault segment, previously interpreted as the intersecting fault, YAc, does not actually intersect with the main fault. Instead it parallels the main fault on a strike of 086° and the chord through this fault plane has two free tips as seen at this level.

A.3.2 Throw analysis

The distribution of throw varies significantly between the three horizons as did the plan view geometry. Throw values on the middle Miocene horizon (Fig. A.7a) show an abrupt decrease across the intersection from a value of 19ms on the YAa segment to 4ms on the YAb segment. An overall decrease in throw is recorded from west to east on the main fault YAa segment toward intersection on an approximate gradient of 0.03. A similar throw gradient decreasing away from intersection is seen on the intersecting fault which has a value near intersection of 11ms. This example also shows the cumulative throw for the YAb and YAc segments. The small average throw values of c.5ms recorded from segment YAb can be described as showing a near central Tmax. However, all values exist within error bar range of one another (Fig. A.7a) which leaves this profile open to interpretation and impacts the cumulative throw profile. The cumulative throw shows a localised maximum but can be described as bridging the throw profiles between the main fault YAa segment and the intersecting fault YAc segment. Similarly, throw decrease at intersection is recorded from the 2470ms horizon (Fig. A.7b). However, values of throw are almost equal from the YAb and intersecting, YAc, segments and this is reflected in the symmetry of the plan view mapped geometry (Fig. A.7b). The intersecting fault again shows an increasing trend toward intersection on a gradient of 0.02. However, a throw minimum near intersection is recorded which can be interpreted in different ways. The cumulative throw profile has a value of throw

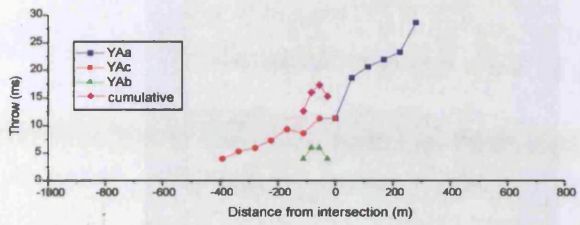

(a)

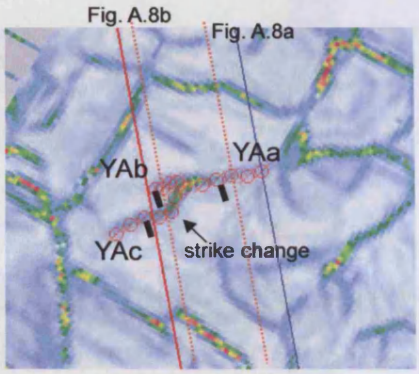

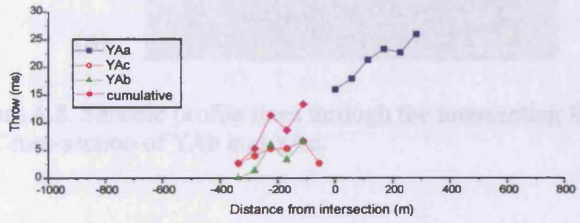

(b)

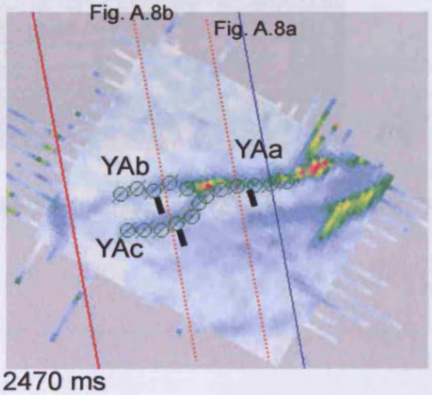

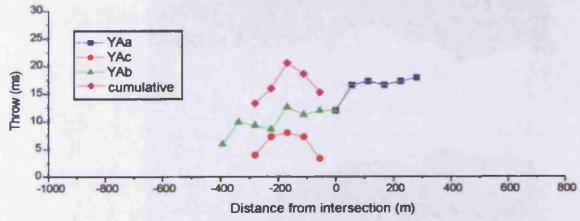

(c)

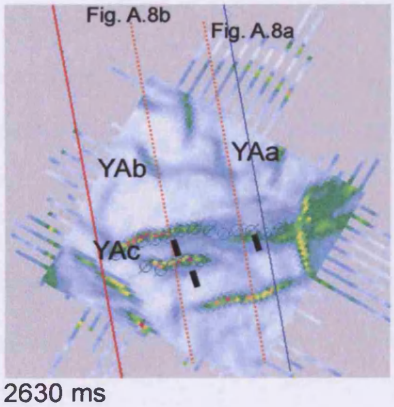

Figure A.7. T-x profiles and associated plan view geometries of the YA intersection from three horizons: (a) Middle Miocene; (b) 2470ms and (c) 2630ms.

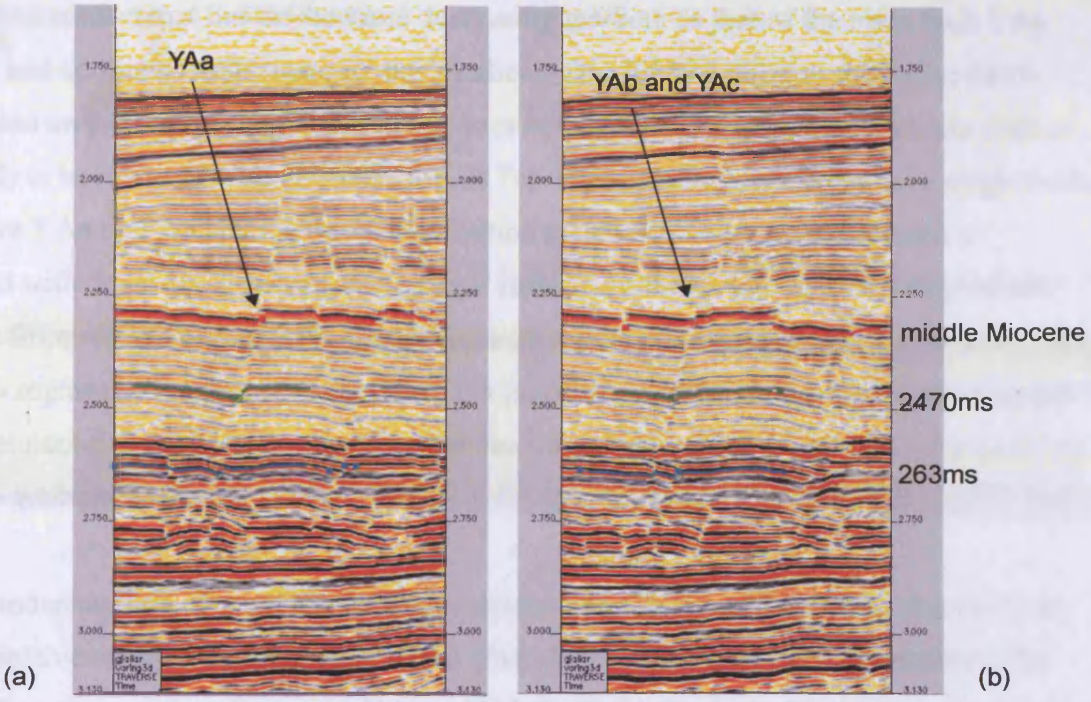

Figure A.8. Seismic profile lines through the intersecting faults of the YA intersection. (a) cross-section of YAa. (b) Cross-section of YAb and YAc.

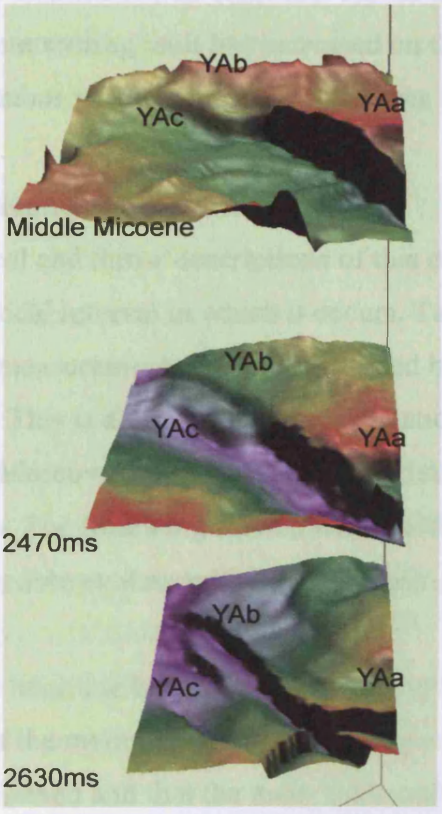

Figure A.9. 3D perspective image of mapped horizons (see Fig A.8) showing fault interrelationships.

nearest intersection that lies on the same decreasing gradient as that of the main fault YAa segment and continues to decrease on this gradient. The 2630ms horizon shows the throw distribution on the intersecting fault (which does not actually intersect with the main fault at this level) to have a near-central Tmax (Fig. A.7c). The main fault is mapped as a single fault trace from YAa to YAb and the throw distribution contrasts to both those previously described with the YAb segment having larger recorded values. An overall throw gradient decrease from west to east of 0.01 is recorded with a throw decrease of 5ms between the YAa and YAb segments. In contrast to the other T-x plots, the cumulative profile does not appear to be continuous to the YAa profile, although the throw value nearest intersection does lie on the same gradient decrease.

Further understanding of the 3D horizon geometries and throw variations can be given from the perspective view of the mapped horizons (Fig. A.9). At 2630ms the faults appear to be distinct from one another. Segments YAa to YAb display a single fault trace that decreases in throw toward the east. The 2470ms horizon shows that throw value has increased on the main YAa fault plane and apparently decreased on the YAb and YAc segments. The YAc segment now shows an extension to its trace that curves to meet with the main fault plane. Throw value on the intersecting fault has increased on the middle Miocene horizon and the profile appears continuous to the main fault YAa plane as described from the T-x plots above.

A.3.3 Interpretation of YA intersection

The geometrical and throw descriptions of this case study clearly show that variations occur within the vertical interval in which it occurs. Taken separately the plan view geometry and related throw measurements from each studied horizon allow for a different growth interpretation. This is a limitation to interpretations based on one horizon in complex intersections. Moreover, it allows for a more detailed interpretation of the (near) 3D evolution of this horizon. The following section will describe an interpretation for each horizon then discuss the possible evolution histories for case study YA.

On the middle Miocene horizon the intersecting fault throw distribution is closer in value and trend to that of the main YAa segment. It may be interpreted that these segments are kinematically linked and that the main YAb segment has intersected in the footwall of YAa-YAc throughgoing fault. However, the interpretation must still account for a significant strike change and a decrease in throw across the fault at intersection. It should also be noted that the

plan view geometry and throw distribution shown here is analogous to a hangingwall breached relay in a unidirectional system. An interpretation of lateral bifurcation could also be considered here, where the 'intersecting' fault segment has become the dominant splay.

Interpretation of the 2470ms horizon focuses on the observation of a significant throw decrease on the YAa segment at the intersection to approximately equal values on YAc and YAb segments. This can be interpreted as throw sharing between YAb and YAc i.e. lateral bifurcation. This does not entirely account for the minimum at intersection recorded from the YAc segment that suggests it is not linked to the system. However, the throw profiles certainly suggest that throw is distributed between the YAb and YAc segments from the main fault YAa segment.

The 2630ms horizon shows two separate faults from its plan view geometry. This is also reflected in the intersecting fault, YAc, throw distribution which has a near central Tmax. profile that is concurrent with radial propagation. The throw distribution that is decreasing to the east from the main fault YAa to YAb segments, suggests lateral propagation in this direction. The only noticeable variation from this interpretation is that a decrease in throw values from main YAa-YAb is recorded near the location of the YAc tip that may suggest some kinematic interaction between the two faults.

The three interpretations related to the three different horizons are clearly not the same and not immediately recognisable as related. They afford the proposition of three interpretations for this system. These are (a) footwall linkage; (b) hangingwall linkage; (c) lateral bifurcation.

(a) Footwall linkage. Throw distribution on the mid-Miocene horizon suggested that the intersecting fault, YAc to YAa are linked and that the YAb segment could be a separate segment propagating in the footwall. From the 2470ms horizon the relative 'importance' of this segment is increased as reflected by its increase in length and throw and the corresponding decrease in throw on the intersecting fault. At the 2630ms horizon the YAb to YAa segments show evidence of linkage from the T-x profile and plan view map image. The YAc segment is entirely separate. The footwall linkage interpretation suggests that the YAa to YAc linked fault was intersected in the footwall by the YAb segment that then linked with the YAa segment to leave the YAc segment as a hangingwall splay. This interpretation is not thought to be the most likely case due to the extreme strike change identified in plan view

(Fig. A.7a, b). It is unlikely that the fault would be interpreted as a single segment when such a strike change exists and another straight segment exists (YAb). It may also be interpreted to suggest downward propagation of the system which has not been supported from the data presented in this polygonal fault system.

(b) Hangingwall linkage. The 2630ms horizon indicates that both faults are parallel and separate at this level. However, the middle Miocene and the 2470ms horizon plan view images show that the intersecting fault changes strike to intersect the hangingwall of the straight main fault. The YAc segment has been described as sharing the throw of the YAa segment with the YAb segment on the middle horizon. It has a larger throw value on the middle Miocene and a more continuous T-x profile with the main fault YAa segment. This could be described as a hard linkage that has formed between the intersecting fault and the YAa segment leaving the YAb as an inactive footwall splay. This may also be interpreted as hangingwall breach in a unidirectional system as these faults are parallel at depth. It may also require a dominantly upward propagation of this system which has been recorded from polygonal faults.

(c) the third interpretation suggest that the structure evolved through lateral bifurcation and this is based largely on the observation from the middle horizon of throw sharing on the intersecting fault and the YAb segment that equals the main fault YAa throw profile. Radial propagation of this system shows that more throw is added to the YAc segment in the shallow section, whereas the YAb segment is the dominant fault at depth. If this is the case, then the intersecting fault is no longer part of the system at depth and all throw is transferred to the YAb segment.

An interpretation of either hangingwall capture or lateral bifurcation are proposed as the most likely evolution style for this intersection. The section of the intersecting fault that coincides with the change in strike between the intersecting fault and the main fault appears to be the linkage structure between the main and intersecting faults and this strongly resembles a hangingwall breach fault in a soft-linked unidirectional system. The cumulative throw profiles suggest that all three segments are kinematically related in this system. The above analysis again highlights the potential over-simplication of analysing T-x plots from one horizon only.

A.4 THROW ANALYSIS OF X CLASS INTERSECTION, X3

The plan view geometry of intersection X3 (Fig. A.10a) shows that the intersection is near-orthogonal and that fault plane strikes and dips are maintained in opposite segments across intersection. An elliptical feature overlaps the X3c segment and is interpreted as a pock mark. The 3D geometry of the middle Miocene horizon (Fig. A.10b) describes variations in throw that can be linked to the T-x profiles from the middle Miocene (Fig. A.10c). Throw values decrease across intersection from segment X3a to X3b. However, no variation in the throw profile is notably related to the intersection location. In contrast, both segments X3c + X3d record a significant decrease in throw toward intersection. This is reflected on the 3D horizon by ductile bending of the rock volume close to intersection on segment X3d. Segment X3c does not appear to reach intersection in this 3D perspective image, however it is complicated by the pock mark and a further fault that trends parallel to segment X3a to X3b. At the deeper horizon level, segment X3d still decreases in throw toward intersection though it has some expression and X3c cannot be traced to the intersection. Interestingly, the X3b fault is not apparent, however, the seismic expression of this fault is folded at this horizon but shows brittle offset one loop above. Lithological effects cannot be quantified from this analysis and it is not possible to estimate the effects that lithological heterogeneities can have.

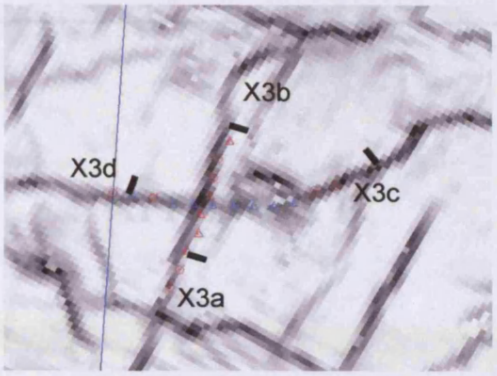

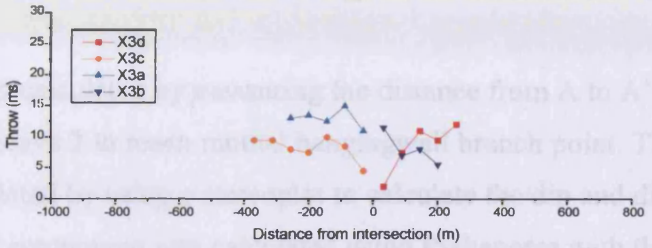

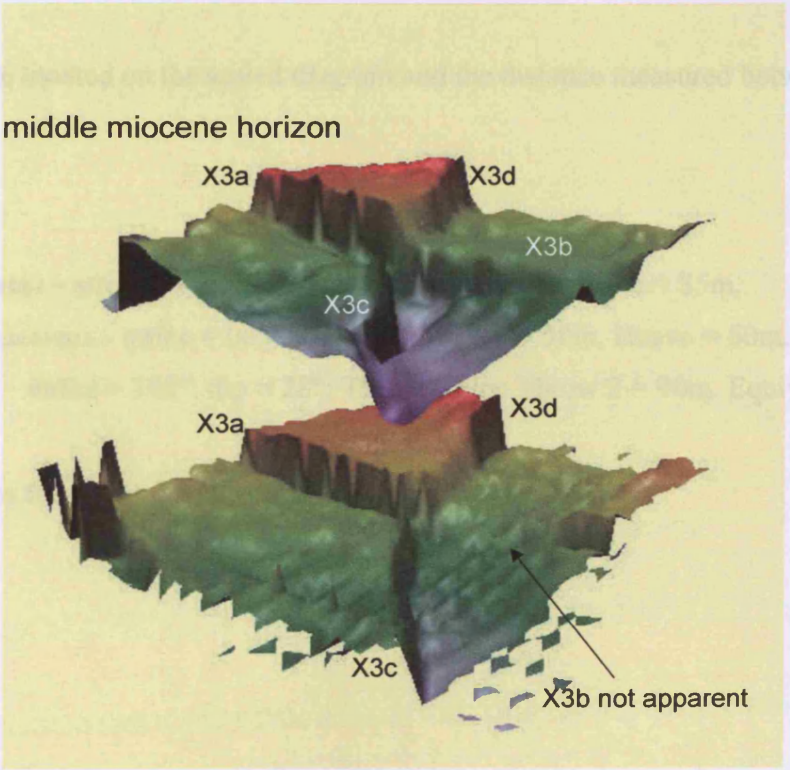

Figure A.10. 3D geometry and throw variation of the X3 intersection. (a) Coherence extraction of the middle Miocene horizon, showing the X3 plan view geometry. (b) T-x plot of the X3 fault segments. (c) 3D time-structure maps showing the continuity of fault segments over the intersction.

APPENDIX B.

This section is appended to Chapter 3. It describes the methodology used to construct a scaled diagram of lateral offset on a horizontal slice through the deformed rock volume.

The scaled diagram was calculated by measuring the distance from A to A'' that was moved by values of heave 1 and heave 2 to reach mutual hangingwall branch point. The mutual footwall branch point was calculated by using a stereoplot to calculate the dip and dip azimuth of the branch line. The lateral component was calculated using Pythagoras with the known dip of the branch line and the throw on both fault planes.

The two points were located on the scaled diagram and the distance measured between them (Fig. B.1).

Input values:

Fault 1 (Texas) – strike = 023°; dip = 35°; throw = 60m. Heave = 85m.

Fault 2 (Louisiana) – strike = 085°; dip = 30°; throw = 30m. Heave = 50m.

Branch line – strike = 158°; dip = 28°; Throw 1 plus Throw 2 = 90m. Equivalent heave = 169m.

Approximate time slice 1700ms

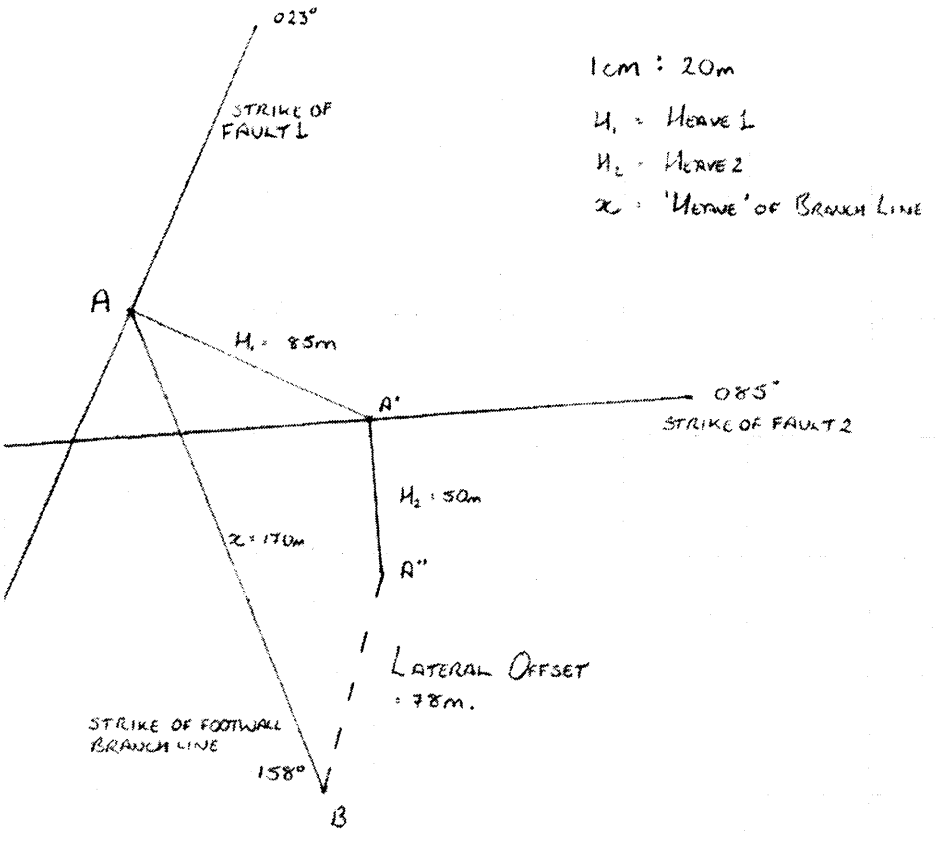

Figure B.1. Scaled diagram of the lateral offset between the footwall branch point and the hangingwall branch point of the Lower X intersection (Chapter 3) on a coherence slice at 1700ms TWT.

REFERENCES

A

Abreu, V., Sullivan, M., Pirmez, C. & Mohrig, D. 2003. Lateral accretion packages (LAPs): an important reservoir element in deep water sinuous channels. *Marine and Petroleum Geology* 20(6-8), 631-648.

Ackermann, R. V. & Schlische, R. W. 1997. Anticlustering of small normal faults around larger faults. *Geology* 25(12), 1127-1130.

Acocella, V. & Neri, M. 2005. Structural features of an active strike-slip fault on the sliding flank of Mt. Etna (Italy). *Journal of Structural Geology* 27(2), 343-355.

Allan, U. S. 1980. A model for the migration and entrapment of hydrocarbons. *American Association of Petroleum Geologists Research Conference on Seals for Hydrocarbons.*

Atkinson, B. K. 1987. *Fracture mechanics of rocks.* Academic Press, London.

B

Baars, D. L. & Stevenson, G. M. 1981. Tectonic evolution of the Paradox Basin, Utah and Colorado. In: *Geology of the Paradox Basin* (edited by Wiegand, D. L.). Rocky Mountain Association of Geologists, Denver, 23-32.

Badawy, A. & Horvath, F. 1999. The Sinai subplate and tectonic evolution of the northern Red Sea region. *Journal of Geodynamics* 27(4-5), 433-450.

Badley, M. E. 1985. *Practical seismic interpretation.* International Human Resources Development Corporation, Boston.

Bahat, D. 1982. Extensional Aspects of Earthquake Induced Ruptures Determined by an Analysis of Fracture Bifurcation. *Tectonophysics* 83(3-4), 163-183.

Bahorich, M. & Farmer, S. 1995. 3-D seismic discontinuity for faults and stratigraphic features: The coherence cube. *The Leading Edge* 14, 1053-1058.

Bai, T., Maerten, L., Gross, M. R. & Aydin, A. 2002. Orthogonal cross joints: do they imply a regional stress rotation? *Journal of Structural Geology* 24(1), 77-88.

Baker, A. A. 1933. Geology and oil possibilities of the Moab district, Grand and San Juan Counties, Utah. *US Geological Survey Bulletin* 841, 95.

Barnett, J. A. M., Mortimer, J., Rippon, J. H., Walsh, J. J. & Watterson, J. 1987. Displacement Geometry in the Volume Containing a Single Normal Fault. *Aapg Bulletin-American Association of Petroleum Geologists* 71, 925-937.

Barquins, M. & Petit, J. P. 1992. Kinetic Instabilities During the Propagation of a Branch Crack - Effects of Loading Conditions and Internal-Pressure. *Journal of Structural Geology* 14(8-9), 893-903.

Ben-Avraham, Z., Ginzburg, A., Makris, J. & Eppelbaum, L. 2002. Crustal structure of the Levant Basin, eastern Mediterranean. *Tectonophysics* 346(1-2), 23-43.

Berndt, C., Bunz, S. & Mienert, J. 2003. Polygonal fault systems on the mid-Norwegian margin: a long-term source for fluid flow. In: *Subsurface sediment mobilization* (edited by Van Rensbergen, P., Hillis, R. R., Maltman, A. J. & Morley, C. K.). Geological Society Special Publication 216, 283-290.

Bertoni, C. & Cartwright, J. 2005. 3D seismic analysis of circular evaporite dissolution structures, Eastern Mediterranean. *Journal of the Geological Society* 162, 909-926.

Bertoni, C. & Cartwright, J. A. 2006a. Controls on the basinwide architecture of late Miocene (Messinian) evaporites on the Levant margin (Eastern Mediterranean). *Sedimentary Geology: The Messinian Salinity Crisis Revisited* 188-189, 93-114.

Bertoni, C. & Cartwright, J. A. 2006b. Clastic depositional systems at the base of the Messinian (late Miocene) evaporitic series of the Eastern Mediterranean: Evidence from 3D seismic data. *Special publications, Geological Society of London.*

Biggar, N. E. & Adams, J. A. 1987. Dates derived from quaternary strata in the vicinity of Canyonlands National Park. In: *Geology of Cataract Canyon and vicinity 1987; field symposium.* (edited by Campbell, J. A.) 10. Four Corners Geological Society, Durango, Colorado, 127-136.

Bjornseth, H. M., Grant, S. M., Hansen, E. K., Hossack, J. R., Roberts, D. G. & Thompson, M. 1997. Structural evolution of the Voring Basin, Norway, during the Late Cretaceous and Palaeogene. *Journal of the Geological Society* 154, 559-563.

Bourne, S. J. & Willemse, E. J. M. 2001. Elastic stress control on the pattern of tensile fracturing around a small fault network at Nash Point, UK. *Journal of Structural Geology* 23(11), 1753-1770.

Brekke, H., Dahlgren, S., Nyland, B. and Magnus, C. 1999. The prospectivity of the Voring and More basins in the Norwegian Sea continental margin. *In: Fleet. A.J. and Boldy, S.A.R. (eds) Petroleum Geology of Northwest Europe: Proceedings of the 5th Conference*, 261-274.

Bruhn, R. L., Yonkee, W. A. & Parry, W. T. 1990. Structural and fluid-chemical properties of seismogenic normal faults. *Tectonophysics* 175, 139-157.

Burgmann, R., Pollard, D. D. & Martel, S. J. 1994. Slip distributions on faults: effects of stress gradients, inelastic deformation, heterogeneous host-rock stiffness, and fault interaction. *Journal of Structural Geology* 16, 1675-1690.

Butler, R. W. H. 1982. The terminology of structures in thrust belts. *Journal of Structural Geology* 4(3), 239-245.

C

Cartwright, J., Bouroullec, R., James, D. & Johnson, H. 1998. Polycyclic motion history of some Gulf Coast growth faults from high-resolution displacement analysis. *Geology* 26, 819-822.

Cartwright, J., James, D. & Bolton, A. 2003. The genesis of polygonal fault systems; a review. In: *Subsurface sediment mobilization* (edited by van-Rensbergen, P., Hillis, R. R., Maltman, A. J. & Morley, C. K.) 216. Geological Society Special Publication, 223-243.

Cartwright, J., Trudgill, B. & Mansfield, C. 2000. Fault growth by segment linkage: an explanation for scatter in maximum displacement and trace length data from the Canyonlands grabens of SE Utah: Reply. *Journal of Structural Geology* 22(1), 141-143.

Cartwright, J. A. 1994. Episodic basin-wide fluid expulsion from geopressured shale sequences in the North Sea basin. *Geology* 22(5), 447-450.

Cartwright, J. A. 1996. Polygonal fault systems: A new type of fault structure revealed by 3D seismic data from the North Sea Basin. In: *Applications of 3D seismic data to exploration and production* (edited by Weimer, P. & Davis, T. L.). AAPG Studies in Geology No. 42 and SEG Geophysical Developments Series, No. 5, 225-230.

Cartwright, J. A. & Dewhurst, D. N. 1998. Layer-bound compaction faults in fine-grained sediments. *Geological Society of America Bulletin* 110, 1242-1257.

Cartwright, J. A. & Lonergan, L. 1996. Volumetric contraction during the compaction of mudrocks: a mechanism for the development of regional-scale polygonal fault systems

doi:10.1046/j.1365-2117.1996.01536.x. *Basin Research* 8(2), 183-193.
Cartwright, J. A. & Mansfield, C. S. 1998. Lateral displacement variation and lateral tip geometry of normal faults in the Canyonlands National Park, Utah. *Journal of Structural Geology* 20, 3-19.
Cartwright, J. A., Mansfield, C. S. & Trudgill, B. 1996. The growth of normal faults by segment linkage. In: *Modern developments in structural interpretation, validation and modelling* (edited by Buchanan, P. C. & Nieuwland, D. A.) 99. Special Publication of the Geological Society of London, pp. 163-177.
Cartwright, J. A., Trudgill, B. D. & Mansfield, C. S. 1995. Fault growth by segment linkage: an explanation for scatter in maximum displacement and trace length data from the Canyonlands Grabens of SE Utah. *Journal of Structural Geology* 17, 1319-1326.
Castelltort, S., Pochat, S. & Van Den Driessche, J. 2004. Using T-Z plots as a graphical method to infer lithological variations from growth strata. *Journal of Structural Geology* 26(8), 1425-1432.
Childs, C., Watterson, J. and Walsh, J.J. 1995. Fault overlap zones within developing normal fault systems. *Journal of the Geological Society, London* 152, 535-549.
Childs, C., Watterson, J. and Walsh, J.J. 1996. A model for the structure and development of fault zones. *Journal of the Geological Society, London* 153, 337-340.
Chopra, S. 2002. Coherence Cube and beyond. *First Break* 20, 27-33.
Commins, D., Gupta, S. & Cartwright, J. 2005. Deformed streams reveal growth and linkage of a normal fault array in the Canyonlands graben, Utah. *Geology* 33(8), 645-648.
Condon, S. M. 1997. Geology of the Pennsylvanian and Permian Cutler Group and Permian Kaibab Limestone in the Paradox Basin, Southeastern Utah and Southwestern Colorado. *U. S. Geological Survey Bulletin* 2000-P.
Corfield, S. M., Wheeler, W., Karpuz, R., Wilson, M. & Helland, R. 2004. Exploration 3D seismic over the Gjallar Ridge, mid-Norway; visualization of structures on the Norwegian volcanic margin from Moho to seafloor. In: *3D seismic technology; application to the exploration of sedimentary basins.* (edited by Davies, R. J., Cartwright, J., Stewart, S., Lappin, M. & Underhill, J. R.) 29. Memoirs of the Geological Society of London, 177-185.
Cotterell, B. & Rice, J. R. 1980. Slightly curved or kinked cracks. *International Journal of Fracture* V16(2), 155-169.
Cowie, P. A. & Scholz, C. H. 1992. Displacement-length scaling relationship for faults: data synthesis and discussion. *Journal of Structural Geology* 14, 1149-1156.
Cowie, P. A. & Scholz, C. H. 1992. Physical explanation for the displacement-length relationship of faults using a post-yield fracture mechanics model. *Journal of Structural Geology* 14, 1133-1148.
Cruikshank, K. M. & Aydin, A. 1995. Unweaving the joints in Entrada Sandstone, Arches National Park, Utah, U.S.A. *Journal of Structural Geology* 17(3), 409-421.

D

d'Alessio, M. A. & Martel, S. J. 2004. Fault terminations and barriers to fault growth. *Journal of Structural Geology* 26(10), 1885-1896.

Davies, R. J. & Cartwright, J. 2002. A fossilized Opal A to Opal C/T transformation on the northeast Atlantic margin: support for a significantly elevated Palaeogeothermal gradient during the Neogene? *Basin Research* 14(4), 467-486.
Dawers, N. H. & Anders, M. H. 1995. Displacement-Length Scaling and Fault Linkage. *Journal of Structural Geology* 17(5), 607-&.

Destro, N., Szatmari, P., Alkmim, F. F. & Magnavita, L. P. 2003. Release faults, associated structures, and their control on petroleum trends in the Reconcavo rift, northeast Brazil. *Aapg Bulletin* 87, 1123-1144.

Destro, N., Szatmari, P., Alkmim, F. F. & Magnavita, L. P. 2003. Release faults, associated structures, and their control on petroleum trends in the Reconcavo rift, northeast Brazil. *Aapg Bulletin* 87, 1123-1144.

Dewhurst, D. N., Cartwright, J. A. & Lonergan, L. 1999. The development of polygonal fault systems by syneresis of colloidal sediments. *Marine and Petroleum Geology* 16, 793-810.

Dickinson, G. 1954. Subsurface interpretation of intersecting faults and their effects upon stratigraphic horizons. *AAPG Bulletin* 38(5), 854-877.

Donath, F. A. 1962. Analysis of Basin-Range structure, south-central Oregon. *Geological Society of America Bulletin* 73, 1-16.

Dooley, T. & McClay, K. 1997. Analog modeling of pull-apart basins. *AAPG Bulletin* 81, 1804-1826.

Dutton, D. M., Lister, D., Trudgill, B. & Pedro, K. 2004. Three-dimensional geometry and displacement configuration of a fault array from a raft system, Lower Congo Basin, Offshore Angola: implications for the Neogene turbidite play. In: *3D Seismic Technology* (edited by Davies, R. J., Cartwright, J., Stewart, S. A., Lappin, M. & Underhill, J. R.) 29. Geological Society Memoir, 133-142.

Dyer, R. 1988. Using joint interactions to estimate paleostress ratios. *Journal of Structural Geology* 10(7), 685-699.

E

Ely, R. W. 1987. Colluvium-filled fault fissures in the Needles fault zone, Cataract Canyon, Utah. In: *Geology of Cataract Canyon and vicinity 1987; field symposium.* (edited by Campbell, J. A.) 10. Four Corners Geological Society, Durango, Colorado, 69-73.

Engelder, T. 1989. Analysis of pinnate joints in the Mount Desert Island granite: Implications for postintrusion kinematics in the coastal volcanic belt, Maine. *Geology* 17(6), 564-567.

Engelder, T. 1993. *Stress regimes in the lithosphere.* Princeton University Press, Princeton, New Jersey.

F

Faerseth, R. B., Knudsen, B. E., Liljedahl, T., Midboe, P. S. & Soderstrom, B. 1997. Oblique rifting and sequential faulting in the Jurassic development of the northern North Sea. *Journal of Structural Geology* 19(10), 1285-1302.

Flodin, E. A. & Aydin, A. 2004. Evolution of a strike-slip fault network, Valley of Fire State Park, southern Nevada. *Geological Society of America Bulletin* 116(1-2), 42-59.

Fossen, H., Johansen, T. E. S., Hesthammer, J. & Rotevatn, A. 2005. Fault interaction in porous sandstone and implications or reservoir management; examples from southern Utah. *Aapg Bulletin* 89(12), 1593-1606.

Fossen, H. & Rornes, A. 1996. Properties of fault populations in the Gullfaks Field, northern North Sea. *Journal of Structural Geology* 18(2-3), 179-190.

Frey Martinez, J., Cartwright, J. & Hall, B. 2005. 3D seismic interpretation of slump complexes: examples from the continental margin of Israel. *Basin Research* 17(1), 83-108.

Fu, B., Awata, Y., Du, J. & He, W. 2004. Surface deformations associated with the 2001 Mw-7.8 Kunlun earthquake, northern Tibet: geomorphic growth features along a major strike-slip fault. *Engineering Geology* 75(3-4), 325-339.

Fu, B., Awata, Y., Du, J. & He, W. 2005. Late Quaternary systematic stream offsets caused by repeated large seismic events along the Kunlun fault, northern Tibet. *Geomorphology* 71(3-4), 278-292.

G

Garfunkel, Z. & Almagor, G. 1985. Geology and structure of the continental margin off northern Israel and the adjacent part of the Levantine Basin. *Marine Geology* 62(1-2), 105-131.

Garfunkel, Z., Arad, A. & Almagor, G. 1979. The Palmahim Disturbance and its Regional Setting. *Geological Survey of Israel Bulletin* 72.

Gartrell, A., Lisk, M. and Underschultz, J. 2002. Controls on the trap integrity of the Skua oil field, timor sea. *In: Keep, M., Moss, S.J. (Eds), The Sedimentary Basins of Western Australia 3. Proceedings of Petroleum Exploration Society of Australia, Perth*, 389-407.

Gaullier, V., Mart, Y., Bellaiche, G., Mascle, J., Vendeville, B. C., Zitter, T. & Party, S. L. P. I. S. 2000. Salt tectonics in and around the Nile deep-sea fan: insights from the PRISMED II cruise. In: *Salt, shale and igneous diapirs in and around Europe* (edited by Vendeville, B. C., Mart, Y. & Vigneresse, J. L.) Special Publications 174. Geological Society of London, London, 111-129.

Goulty, N. R. 2001. Mechanics of layer-bound polygonal faulting in fine-grained sediments. *Journal of the Geological Society, London* 159, 239-246.

Granier, T. 1985. Origin, Damping, and Pattern of Development of Faults in Granite. *Tectonics* 4, 721-737.

Grasemann, B., Martel, S. & Passchier, C. 2005. Reverse and normal drag along a fault. *Journal of Structural Geology* 27(6), 999-1010.

Guerin, G. & Goldberg, D. 1996. Acoustic and elastic properties of calcareous sediments across a siliceous diagenetic front on the eastern US continental slope. *Geophysical Research Letters* 23(19), 2697-2700.

Gupta, A. & Scholz, C. H. 2000. A model of normal fault interaction based on observations and theory. *Journal of Structural Geology* 22, 865-879.

H

Hansen, D. M., Shimeld, J. W., Williamson, M. A. & Lykke-Andersen, H. 2004. Development of a major polygonal fault system in Upper Cretaceous chalk and Cenozoic mudrocks of the Sable Subbasin, Canadian Atlantic margin. *Marine and Petroleum Geology* 21(9), 1205-1219.

Hansen, J. P. V., Cartwright, J. A., Huuse, M. & Clausen, O. R. 2005. 3D seismic expression of fluid migration and mud remobilization on the Gjallar Ridge, offshore mid-Norway *Basin Research* 17(1), 123-139.

Harding, T. P. 1985. Seismic characteristics and identification of negative flower structures, positive flower structures, and positive structural inversion. *AAPG Bulletin* 69, 582-600.

Hesthammer, J. & Fossen, H. 2001. Structural core analysis from the Gullfaks area, northern North Sea. *Marine and Petroleum Geology* 18(3), 411-439.

Hjelstuen, B. O., Eldholm, O. & J, S. 1997. Voring Plateau diapir fields and their structural and depositional settings. *Marine Geology* 144, 33-57.

Hossack, J. R. 1983. A cross-section through the Scandinavian Caledonides constructed with the aid of branch-line maps. *Journal of Structural Geology* 5(2), 103-111.

Hsü, K. J., Cita, M. B. & Ryan, W. B. F. 1973. The origin of the Messinian evaporites. *Initial Reports of the Deep Sea Drilling Project* 13, 1249.

Huggins, P., Watterson, J., Walsh, J. J. & Childs, C. 1995. Relay zone geometry and displacement transfer between normal faults recorded in coal-mine plans. *Journal of Structural Geology* 17, 1741-1755.

Huntoon, P. W. 1982. The meander anticline, Canyonlands, Utah. An unloading structure resulting from horizontal gliding on salt. *Geological Society of America Bulletin* 93, 941-950.

Huntoon, P. W. 1987. The case for regional discharge of ground water from the lower Palaeozoic carbonates through the Shay fault zone, Canyonlands, Utah. In: *Geology of Cataract Canyon and vicinity 1987; field symposium.* (edited by Campbell, J. A.) 10. Four Corners Geological Society, Durango, Colorado, 185-191.

Huntoon, P. W., Billingsley, G. H. J. & Breed, W. J. 1982. *Geological map of Canyonalds National Park and vicinity, Utah.* The Canyonlands Natural History Association.

J

James, D. M. D. 2000. Discussion on geometry and origin of a polygonal fault system. *Journal of the Geological Society, London* 157, 1261-1264.

K

Kase, Y. & Kuge, K. 1998. Numerical simulation of spontaneous rupture processes on two non-coplanar faults: the effect of geometry on fault interaction. *Geophysical Journal International* 135(3), 911-922.

Kempler, D., Mart, Y., Herut, B. & McCoy, F. W. 1996. Diapiric features in the southeastern Mediterranean Sea: possible indication of extension in a zone of incipient continental collision. *Marine Geology* 134(3-4), 237-248.

Kim, Y.-S., Andrews, J. R. & Sanderson, D. J. 2000. Damage zones around strike-slip fault systems and strike-slip fault evolution, Crackington Haven, southwest England. *Geoscience Journal* 4, 53-72.

Kim, Y.-S., Andrews, J. R. & Sanderson, D. J. 2001. Extension fractures, secondary faults and segment linkage in strike-slip fault systems at Rame Head, Southern Cornwall. *Proceedings of the Ussher Society* 10(2), 123-133.

Kitcho, C. A. 1981. Characteristics of surface faults in the Paradox Basin. In: *Geology of the Paradox Basin* (edited by Wiegand, D. L.). Rocky Mountain Association of Geologists, Denver, 1-22.

Krantz, R. W. 1988. Multiple fault sets and three-dimensional strain: Theory and application. *Journal of Structural Geology* 10, 225-237.

L

Lachenbruch, A. H. 1962. Mechanics of thermal contraction cracks and ice-wedge polygons in permafrost. In: *Geological Society of America Special Papers* 70, 1-69.

Lawn, B. R. & Wilshaw, T. R., 1975. 1975. *Fracture of brittle solids.* Cambridge University Press, New York.

Lewis, R. Q. & Campbell, R. H. 1965. Geology and Uranium Deposits of Elk Ridge and Vicinity San Juan County, Utah.

Lindsey, J. P. 1989. The Fresnel zone and its interpretive significance. *Geophysics: The Leading Edge of Exploration* 8, 33-39.

Lisle, R. J. & Srivastava, D. C. 2004. Test of the frictional reactivation theory for faults and validity of fault-slip analysis. *Geology* 32(7), 569-572.

Lonergan, L., Cartwright, J. & Jolly, R. 1998. The geometry of polygonal fault systems in Tertiary mudrocks of the North Sea. *Journal of Structural Geology* 20, 529-548.

Loope, D. B. 1984. Eolian origin of upper Paleozoic sandstones, southeastern Utah. *Journal of Sedimentary Petrology* 54, 563-580.

Loope, D. B. 1985. Episodic deposition and preservation of eolian sands: A late Paleozoic example from southeastern Utah. *Geology* 13, 73-76.

M

Maerten, L. 2000. Variation in slip on intersecting normal faults: Implications for paleostress inversion. *Journal of Geophysical Research-Solid Earth* 105, 25553-25565.

Maerten, L., Gillespie, P. & Pollard, D. D. 2002. Effects of local stress perturbation on secondary fault development. *Journal of Structural Geology* 24(1), 145-153.

Maerten, L., Willemse, E. J. M., Pollard, D. D. & Rawnsley, K. 1999. Slip distributions on intersecting normal faults. *Journal of Structural Geology* 21, 259-271.

Mandl, G. 2000. *Faulting in brittle rocks: an introduction to the mechanics of tectonic faults.* Springer.

Mansfield, C. S. 1996. Fault growth by segment linkage. *Unpublished PhD thesis.*

Marchal, D., Guiraud, M. & Rives, T. 2003. Geometric and morphologic evolution of normal fault planes and traces from 2D to 4D data. *Journal of Structural Geology* 25(1), 135-158.

Martel, S. J. 1990. Formation of compound strike-slip fault zones, Mount Abbot quadrangle, California. *Journal of Structural Geology* 12(7), 869-882.

Martel, S. J., Pollard, D. D. & Segall, P. 1988. Development of simple strike-slip fault zones, Mount Abbot Quadrangle, Sierra Nevada, California. *Geological Society of America Bulletin* 100(9), 1451-1465.

Mascle, J., Benkhelil, J., Bellaiche, G., Zitter, T., Woodside, J., Loncke, L. & , P. I. S. P. 2000. Marine geologic evidence for a Levantine-Sinai plate, a new piece of the Mediterranean puzzle. *Geology* 28(9), 779-782.

McGill, G. E., Schultz, R. A. & Moore, J. M. 2000. Fault growth by segment linkage: an explanation for scatter in maximum displacement and trace length data from the Canyonlands grabens of SE Utah: Discussion. *Journal of Structural Geology* 22(1), 135-140.

McGill, G. E. & Stromquist, A. W. 1974. A model for graben formation by subsurface flow, Canyonalds National Park, Utah. *Dept. of Geology Contribution No. 15, University of Massachusetts, Amherst, Massachusetts.*

McGill, G. E. & Stromquist, A. W. 1975. Origin ofGraben in the Needles District, Canyonlands National Park, Utah. In: *Canyonlands, Frou Corners Geological Society Eight Field Conference Guidebook*, Durango, Colorado, 235-244.

McGill, G. E. & Stromquist, A. W. 1979. The grabens of Canyonlands National Park, Utah: geometry, mechanics and kinematics. *Journal of Geophysical Research* 84(B9), 4547-4563.

Meyer, V., Nicol, A., Childs, C., Walsh, J. J. & Watterson, J. 2002. Progressive localisation of strain during the evolution of a normal fault population. *Journal of Structural Geology* 24(8), 1215-1231.

Moore, J. M. & Schultz, R. A. 1999. Processes of faulting in jointed rocks of Canyonlands National Park, Utah. *Geological Society of America Bulletin* 111(6), 808-822.

Muraoka, H. & Kamata, H. 1983. Displacement distribution along minor fault traces. *Journal of Structural Geology* 5, 483-495.

Murphy, N., Ali, M. & Ivankovic, A. 2006. Dynamic crack bifurcation in PMMA. *Engineering Fracture Mechanics:Fracture of Polymers, Composites and Adhesives* 73(16), 2569-2587.

N

Naylor, M. A., Mandl, G. & Supesteijn, C. H. K. 1986. Fault geometries in basement-induced wrench faulting under different initial stress states. *Journal of Structural Geology* 8(7), 737-752.

Needham, T., Yielding, G. & Fox, R. 1996. Fault population description and prediction using examples from the offshore U.K. *Journal of Structural Geology* 18(2-3), 155-167.

Nelson, W. J. & Krausse. 1981. *The Cottage Grove fault system in southern Illinois.* Illinois State Geological Survey, Circular 522.

Newhouse, W. H. 1942. Ore deposits as related to structural features. In: *Ore deposits as related to structural features* (edited by Newhouse, W. H.).

Nicol, A., Walsh, J. J., Watterson, J. & Bretan, P. G. 1995. Three-dimensional geometry and growth of conjugate normal faults. *Journal of Structural Geology* 17(6), 847-862.

Nicol, A., Walsh, J. J., Watterson, J., Nell, P. A. R. & Bretan, P. 2003. The geometry, growth and linkage of faults within a polygonal fault system from South Australia. In: *Suburface sediment mobilization* (edited by Van Rensbergen, P., Hillis, R. R., Maltman, A. J. & Morley, C. K.) 216. Geological society special publication, 245-262.

Nicol, A., Watterson, J., Walsh, J. J. & Childs, C. 1996. The shapes, major axis orientations and displacement patterns of fault surfaces. *Journal of Structural Geology* 18(2-3), 235-248.

O

Oechsner, M., Hillman, C. & Lange, F. F. 1996. Crack bifurcation in laminar ceramic composites. *Journal of the American Ceramic Society* 79(7), 1834-1838.

P

Pachell, M. A. & Evans, J. P. 2002. Growth, linkage, and termination processes of a 10-km-long strike-slip fault in jointed granite: the Gemini fault zone, Sierra Nevada, California. *Journal of Structural Geology* 24, 1903-1924.

Park, C. F. & MacDiarmid, R. A. 1970. *Ore Deposits*. W. H. Freeman and Company.

Park, R. G. 1989. *Foundations of structural geology*. Third edition. Chapman and Hall.

Patton, T. L., Moustafa, A. R., Nelson, R. A. & Abdine, A. S. 1994. Tectonic evolution and structural setting of the Suez Rift. In: *Interior rift basins* 59, 9-55.

Peacock, D. C. P. 1991. Displacements and segment linkage in strike-slip fault zones. *Journal of Structural Geology* 13, 1025-1035.

Peacock, D. C. P., Knipe, R. J. & Sanderson, D. J. 2000. Glossary of normal faults. *Journal of Structural Geology* 22(3), 291-305.

Peacock, D. C. P. & Parfitt, E. A. 2002. Active relay ramps and normal fault propagation on Kilauea Volcano, Hawaii. *Journal of Structural Geology* 24(4), 729-742.

Peacock, D. C. P. & Sanderson, D. J. 1994. Geometry and Development of Relay Ramps in Normal-Fault Systems. *Aapg Bulletin-American Association of Petroleum Geologists* 78, 147-165.

Peacock, D. C. P. & Sanderson, D. J. 1995. Strike-slip relay ramps. *Journal of Structural Geology* 17(10), 1351-1360.

Peacock, D. C. P. & Zhang, X. 1994. Field Examples and Numerical Modeling of Oversteps and Bends Along Normal Faults in Cross-Section. *Tectonophysics* 234(1-2), 147-167.

Pirmez, C., Beaubouef, R. T., Friedmann, S. J. & Mohrig, D. 2000. Equilibrium profile and baselevel in submarine channels: examples from late pleistocene systems and implications for the architecture of deepwater reservoirs. In: *Deep-Water Reservoirs of the World* (edited by Weimer, P., Slatt, R. M., Coleman, J., Rossen, N. C., Nelson, H.,

Bouma, A. H. & Styzen, M. J.). GCSSEPM Foundation 20th Annual Research Conference, 782-805.

Potter, D. B. & McGill, G. E. 1978. Field analysis of a pronounced topographic lineament, Canyonlands National Park, Utah. In: *Proceedings of the Third International Conference on Basement Tectonics* (edited by O'Leary, D. W. & Earle, J. L.) 3. Basement Tectonics Committee, Inc., Durango, Colorado.

R

Ravi-Chandar, K. & Knauss, W. G. 1984. An experimental investigation into dynamic fracture: III. On steady-state crack propagation and crack branching. *International Journal of Fracture* V26(2), 141-154.

Reches, Z. 1983. Faulting of rocks in three-dimensional strain fields II. Theoretical analysis. *Tectonophysics* 95, 133-156.

Rippon, J. H. 1985. Contoured patterns of the throw and hade of normal faults in the Coal Measures (Westphalian) of north-east Derbyshire. *Proceedings of the Yorkshire Geological Society* 45, 147-161.

Rowan, M. G., Hart, B. S., Nelson, S., Flemings, P. B. & Trudgill, B. D. 1998. Three-dimensional geometry and evolution of a salt-related growth-fault array: Eugene Island 330 field, offshore Louisiana, Gulf of Mexico. *Marine and Petroleum Geology* 15(4), 309-328.

Rowan, M. G., Jackson, M. P. A. & Trudgill, B. D. 1999. Salt-related fault families and fault welds in the northern Gulf of Mexico. *Aapg Bulletin-American Association of Petroleum Geologists* 83(9), 1454-1484.

S

Sanchez-Herencia, A. J., Pascual, C., He, J. & Lange, F. F. 1999. ZrO2/ZrO2 layered composites for crack bifurcation. *Journal of the American Ceramic Society* 82(6), 1512-1518.

Schlische, R. W., Young, S. S., Ackermann, R. V. & Gupta, A. 1996. Geometry and scaling relations of a population of very small rift-related normal faults. *Geology* 24(8), 683-686.

Scholz, C. H. 1989. Mechanics of Faulting. *Annual Review of Earth and Planetary Sciences* 17, 309-334.

Schultz-Ela, D. D. & Walsh, P. 2002. Modeling of grabens extending above evaporites in Canyonlands National Park, Utah. *Journal of Structural Geology* 24, 247-275.

Segall, P. & Pollard, D. D. 1983. Nucleation and growth of strike slip faults in granite. *Journal of Geophysical Research* 88, 555-568.

Shipton, Z. K. & Cowie, P. A. 2001. Damage zone and slip-surface evolution over [mu]m to km scales in high-porosity Navajo sandstone, Utah. *Journal of Structural Geology* 23, 1825-1844.

Stewart, S. A. & Clark, J. A. 1999. Impact of salt on the structure of the central North Sea hydrocarbon fairways. In: *Petroleum geology of Northwest Europe; proceedings of the 5th conference.* (edited by Fleet, A. J. & Boldy, S. A. R.). The Geological Society of London. London, United Kingdom.

Suppe, J. 1985. *Principles of structural geology.*

Sylvester, A. G. 1988. Strike-slip faults. *Geological Society of America Bulletin* 100, 1666-1703.

T

Talbot, C. J., Ronnlund, P., Schmeling, H., Koyi, H. & Jackson, M. P. A. 1991. Diapiric spoke patterns. *Tectonophysics* 188(1-2), 187-201.

Talwani, P. 1999. Fault geometry and earthquakes in continental interiors. *Tectonophysics* 305, 371-379.

Tchalenko, J. S. 1970. Similarities between shear zones of different magnitude. *Geological Society of America Bulletin* 81, 1625-1640.

Tchalenko, J. S. & Ambraseys, N. N. 1970. Structural analysis of the Dasht-e-Bayaz (Iran) earthquake fractures. *Geological Society of America Bulletin* 81, 41-60.

Tervoort, E. 1998. Structural analyses of the polygonal fault systems in the central north sea.

Trudgill, B. & Cartwright, J. 1994. Relay-Ramp Forms and Normal-Fault Linkages, Canyonlands National-Park, Utah. *Geological Society of America Bulletin* 106(9), 1143-1157.

Tuckwell, G. W., Lonergan, L. and Jolly, R.J.H. 2003. The control of stress history and flaw distribution on the evolution of polygonal fracture networks. *Journal of Structural Geology.*

U

Ueta, K., Tani, K. & Kato, T. 2000. Computerized X-ray tomography analysis of three-dimensional fault geometries in basement-induced wrench faulting. *Engineering Geology* 56(1-2), 197-210.

W

Waldron, J. W. F. 2005. Extensional fault arrays in strike-slip and transtension. *Journal of Structural Geology* 27(1), 23-34.

Walsh, J. J., Bailey, W. R., Childs, C., Nicol, A. & Bonson, C. G. 2003. Formation of segmented normal faults: a 3-D perspective. *Journal of Structural Geology* 25, 1251-1262.

Walsh, J. J. & Watterson, J. 1987. Distributions of cumulative displacement and seismic slip on a single normal fault surface. *Journal of Structural Geology* 9, 1039-1046.

Walsh, J. J. & Watterson, J. 1988. Analysis of the relationship between displacements and dimensions of faults. *Journal of Structural Geology* 10, 239-247.

Walsh, J. J. & Watterson, J. 1989. Displacement gradients on fault surfaces. *Journal of Structural Geology* 11(3), 307-316.

Walsh, J. J. & Watterson, J. 1991. Geometric and kinematic coherence and scale effects in normal fault systems. In: *The geometry of normal faults* (edited by Roberts, A. M., Yielding, G. & Freeman, B.) 56. Geological Society of London special publication, 193-203.

Walsh, J. J., Watterson, J., Bailey, W. R. & Childs, C. 1999. Fault relays, bends and branch-lines. *Journal of Structural Geology* 21, 1019-1026.

Walsh, P. & Schultz-Ela, D. D. 2003. Mechanics of graben evolution in Canyonlands National Park, Utah. *Geological Society of America Bulletin* 115, 259-270.

Watterson, J. 1986. Fault dimensions, displacements and growth. *Pure and applied geophysics* 124, 365-373.

Watterson, J., Walsh, J., Nicol, A., Nell, P.A.R. and Bretan, P.G. 2000. Geometry and origin of a polygonal fault system. *Journal of the Geological Society, London* 157, 151-162.

Wilkins, S. J. & Gross, M. R. 2002. Normal fault growth in layered rocks at Split Mountain, Utah: influence of mechanical stratigraphy on dip linkage, fault restriction and fault scaling. *Journal of Structural Geology* 24(9), 1413-1429.

Willemse, E. J. M., Peacock, D. C. P. & Aydin, A. 1997. Nucleation and growth of strike-slip faults in limestones from Somerset, U.K. *Journal of Structural Geology* 19(12), 1461-1477.

Willemse, E. J. M. & Pollard, D. D. 1998. On the orientation and patterns of wing cracks and solution surfaces at the tips of a sliding flaw or fault. *Journal of Geophysical Research, B, Solid Earth and Planets* 103(2), 2427-2438.

Willemse, E. J. M., Pollard, D. D. & Aydin, A. 1996. Three-dimensional analyses of slip distributions on normal fault arrays with consequences for fault scaling. *Journal of Structural Geology* 18, 295-309.

Witkind, I. J. 1964. Age of the grabens in southeast Utah. *Geological Society of America Bulletin* 75, 99-106.

Woodward-Clyde-Consultants. 1983. *Overview of the Regional Geology of the Paradox Basin Study Rgion: ONWI-92*. Office of Nuclear Waste Isolation, Battelle Memorial Institute, Columbus, Ohio.

www.npd.no

Y

Yilmaz, O. 1987. *Seismic data processing*. Society of Exploration Geophysicists, Tulsa, OK.

Younes, A. I. & McClay, K. 2002. Development of accommodation zones in the Gulf of Suez-Red Sea rift, Egypt. *Aapg Bulletin* 86(6), 1003-1026.

Z

Zeng, H., Henry, S. C. & Riola, J. P. 1998. Stratal slicing, Part II: Real 3-D seismic data. *Geophysics* 63(2), 502-513.

Zhang, K., Liu, K. & Yang, J. 2004. Asymmetrical valleys created by the geomorphic response of rivers to strike-slip fault. *Quaternary Research* 62(3), 310-315.